POLISH SOCIETY OF THEORETICAL AND APPLIED MECHANICS

JOURNAL OF THEORETICAL AND APPLIED MECHANICS

No. 4 • Vol 53

Quarterly

WARSAW, OCTOBER 2015

JOURNAL OF THEORETICAL AND APPLIED MECHANICS
(until 1997 Mechanika Teoretyczna i Stosowana, ISSN 0079-3701)

Beginning with Vol 45, No. 1, 2007, *Journal of Theoretical and Applied Mechanics* (JTAM) has been selected for coverage in Thomson Reuters products and custom information services. Now it is indexed and abstracted in the following:

- **Science Citation Index Expanded** (also known as SciSearch®)
- **Journal Citation Reports/Science Edition**

* * * * *

Editorial Office
Building of Civil Engineering Warsaw University of Technology
Al. Armii Ludowej 16, room 650
00-637 Warszawa, Poland
phone (+48 22) 825 7180, e-mail: biuro@ptmts.org.pl

www.ptmts.org.pl/jtam.html

* * * * *

Publication supported by Ministry of Science and Higher Education of Poland

JOURNAL OF THEORETICAL
AND APPLIED MECHANICS
53, 4, pp. 767-774, Warsaw 2015
DOI: 10.15632/jtam-pl.53.4.767

NEURAL NETWORK CONTROL DESIGN CONSIDERATIONS FOR THE ACTIVE DAMPING OF A SMART BEAM

Piotr Cupiał
AGH University of Science and Technology, Kraków, Poland; e-mail: pcupial@agh.edu.pl
Łukasz Łacny
Cracow University of Technology, Mechanical Faculty, Kraków, Poland; e-mail: llacny@pk.edu.pl

In this study, possible options for the active damping of a smart beam with piezoelectric patches using neural network control algorithm, are presented. The algorithms used for the control are Neural Direct Inverse and Feedback Linearisation (NARMA-L2). Additionally, several possible modifications used for the purpose of improving the control, such as different values of control gain or sampling time of the training data, as well as step-wise control are tested.

Keywords: neural network control, smart structures, vibration damping

1. Introduction

In the recent years, the interest in the so-called "smart structures" and their application in real-life systems has greatly increased. The advantages of such structures – to monitor even subtle changes in their environment and actively respond and react to them – cannot be overlooked. Numerous possible uses of this technology have already been developed and discussed, e.g., structural health monitoring, active vibration and noise damping, energy harvesting (Choi, 2002; Crawley and Luis, 1987; Cupiał, 2008; Preumont, 1997; Tylikowski, 1993).

Neural networks, on the other hand, have been successfully used mostly for the purpose of identification and pattern recognition (Flasiński, 2011; Rutkowski, 2009), but also to some extent in the control of both linear and non-linear systems (Hagan and Demuth, 1999; Narendra *et al.*, 1990; Nøorgaard *et al.*, 2003; Omidvar and Elliot, 1997; Passino, 2005). The possibility of combining smart materials with neural network control could provide us with systems responding to external excitation and adjusting to it accordingly.

This paper focuses on the possibility of using such a combination in order to improve the damping performance of an oscillating system, i.e., a clamped beam with piezoelectric patches. The option of using neural networks for the damping of similar "smart structures" has already been attempted by several authors. In these studies, the neural network was either used to emulate an existing control method (Smyser and Chandrashekhara, 1997) and to adjust the parameters of such a method, e.g., find the optimal values for K_P, K_I and K_D of an PID controller (Qiu *et al.*, 2012) or the network was of a recurrent type (Valoor *et al.*, 2001).

Each of these methods is correct from the analytical point of view and some have been proved (both numerically and by means of an experiment) to reduce the vibration of an oscillating object efficiently. However, it would be preferable if the neural control method were not derived from an existing control algorithm and would be derived from the dynamics of the systems alone. Additionally, it is necessary that the artificial neural network used for the control is both simple to implement and use.

In this paper, the damping is performed by methods that utilize neural networks of the feedforward type, while the training is based only on the samples from the existing model (without assuming any pre-existing control). In addition to that, several adjustments to control are considered for the purpose of increasing the performance even further.

2. Model of the smart beam

In this paper, an effort is made to present possible means of damping the vibration of a smart beam using artificial neural networks. The "smart beam" in question is a clamped-free beam with two piezoelectric patches attached next to the clamping end, as shown in the simplified model (Fig. 1). The patches operate as a collocated pair – one acting as a sensor while the other one as an actuator (Preumont, 1997). It is assumed in the model presented in this work that the external excitation is applied in the form of an impulse at the free end of the beam, perpendicular to the beam. This assumption allows for the model to be simplified by considering only the transverse vibration of the beam, while it also ensures that the higher vibration modes are excited as well.

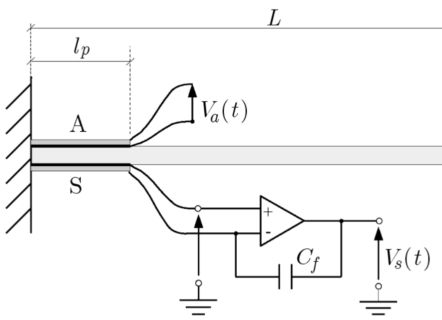

Fig. 1. Simplified model of a smart beam with piezoelectric patches (A – actuator, S – sensor) and a charge amplifier (C_f)

The dimensions and material properties of the beam considered in the analysis are given as follows

$L = 1.5 \cdot 10^{-1}\,\mathrm{m}$	–	length of beam
$h = 1.5 \cdot 10^{-3}\,\mathrm{m}$	–	height of beam
$b = 10^{-2}\,\mathrm{m}$	–	thickness of beam
$\rho = 7.9 \cdot 10^{3}\,\mathrm{kg/m^3}$	–	beam material density
$E = 2.1 \cdot 10^{11}\,\mathrm{N/m^2}$	–	Young's modulus

Using these parameters and one of the available methods (Rayleigh-Ritz, Galerkin, etc., see Nixioł, 1996) the natural frequencies of the beam can be obtained.

For the additional simplification of the model, the effect of the piezoelectric patches can be defined using the following equations (Preumont, 1997)

$$M(t) = cV_a(t) \qquad V_s(t) = s\left[\frac{\partial w(x,t)}{\partial x}\Big|_{x=x_b} - \frac{\partial w(x,t)}{\partial x}\Big|_{x=x_a}\right] \tag{2.1}$$

Equation $(2.1)_1$ relates the moments at both ends of the piezo-actuator with coordinates x_a, x_b to the applied voltage. The variable x in this equation defines the position on the beam, while the parameter w is the deflection of the beam at a given point and time. Equation $(2.1)_2$, on the other hand, gives the relation between the angle of rotation of both ends of the piezo-sensor and the voltage generated in the sensor. Each of these equations contains additional parameters c

and s which are dependent on the material properties and the dimensions of the patches. These parameters can be calculated using the following formulas (Preumont, 1997)

$$c = \frac{E_p|d_{31}|b_p(h+h_p)}{2} \qquad s = \frac{E_p|d_{31}|b_p(h+h_p)}{2}\frac{1}{C_f} \tag{2.2}$$

in which h is the height of the beam, E_p and d_{31} are Young's modulus and the piezoelectric constant of the patches, while b_p and h_p is the thickness and height of the patches, respectively. C_f appearing in Eq. $(2.2)_2$ is the capacitance of the charge amplifier. For the purpose of this analysis, these parameters are chosen as follows

$$\begin{array}{lll} E_p = 50 \cdot 10^9\,\mathrm{N/m^2} & d_{31} = -150 \cdot 10^{-12}\,\mathrm{C/V} & b_p = 10^{-2}\,\mathrm{m} \\ h_p = 1.5 \cdot 10^{-3}\,\mathrm{m} & l_p = 2 \cdot 10^{-2}\,\mathrm{m} & C_f = 10^{-7}\,\mathrm{C} \end{array}$$

Additional information about piezoelectric materials and their application both as sensors and actuators can be found in the literature (Crawley and Luis, 1987; Cupiał, 2008; Preumont, 1997).

3. Artificial neural network control

3.1. Control considerations

Before an attempt at any actual control by neural networks can be made, several important aspects of this control need to be considered. This step is essential, due to the complex nature of neural networks the behaviour of which may be influenced by many different factors. Below, the listing of the most relevant factors is presented along with a short explanation for each one of these decisions as well as for the choices made during the control design:

- **type of control** – although the model considered in this paper could be regarded as MIMO, the control becomes much simpler if it is considered as SISO, which is especially true when trying to train the appropriate network for control. The input in this case is the voltage applied to the actuator. As for the output – either the voltage measured by the patch sensor or the displacement of the beam free end seem appropriate. In fact both of these have been tested for this paper and the results are similar;
- **neural controller type** – even though there are several types of neural controllers available in the literature (Hagan and Demuth, 1999; Korbicz *et al.*, 1994; Nøorgaard *et al.*, 2003), not all of them can be efficient when applied to the model in question. Although the control using one of the direct method controllers (Direct Inverse and Feedback Linearisation) proved possible, albeit with slight modifications, an attempt to damp the beam by means of Predictive Control was found to be inefficient;
- **neural network design** – specifically: number of layers, number of regressors, size of layers (especially the hidden ones) and the type of activation functions. All of these parameters influence the way the network behaves, and how well it can perform;
- **training data** – the data collected from the model (either experimental or generated numerically) needs to be adequate for the training of the network. First of all, the training samples should contain, if possible, the whole range within which the control will be performed. This, in turn, requires the input (excitation) to be chosen correctly, either as a random- or as a chirp function. Additionally, a decision needs to be made regarding the sampling time and the amount of samples – in both of these cases, an optimal value must be found or the network may not operate as intended;

- **training method and performance** – in the case of dynamical neural networks the preferable method of training is the so-called Lavenberg-Margquardt method (although not always, e.g, with Model Reference Control). As for the training performance (in this case calculated as a mean square error between the target- and the actual output value), it can be shown that problems may occur both when it is too low (inefficient control) or too high (super-efficient control, but with the control effort reaching unrealisable values). Similar to the training data generation, an optimum needs to be found.

The two neural control methods used for damping of the smart beam are: the Direct Inverse- and Feedback Linearisation (NARMA-L2) Control. In the former method, an assumption is made that the neural network can be trained to emulate the behaviour of the inverse of the system. By supplying the already trained controller with a desired reference value, the network can calculate the control force needed to reach that reference. The equation describing the inverse function is given as follows

$$\widehat{u}(k) = \widehat{f}^{-1}(y_r(k+1), y(k), \dots, y(k-n), u(k-1), \dots, u(k-m)) \tag{3.1}$$

with $\widehat{u}(k)$ representing the control force, $y_r(k+1)$ – the reference value, $u(k), \dots, u(k-m)$ – control regressors and $y(k), \dots, y(k-n)$ – output regressors.

The second control method (NARMA-L2) defines the control value using the linearised equation

$$\widehat{u}(k) = \frac{y_r(k) - f(k)}{g(k)} \tag{3.2}$$

where $y_r(t)$ is the reference signal, while $f(k)$ and $g(k)$ are non-linear functions of the control and output regressors

$$\begin{aligned} f(k) &= f(y(k), \dots, y(k-n+1), u(k-1), \dots, u(k-m)) \\ g(k) &= g(y(k), \dots, y(k-n+1), u(k-1), \dots, u(k-m)) \end{aligned} \tag{3.3}$$

Both non-linear functions are trained using separate neural networks using the data generated (or obtained) from the model.

A more detailed description of these NN control methods can be found in the papers by Nøorgaard *et al.* (2003), Hagan and Demuth (1999), Medsker and Jain (1999).

3.2. Neural network control

The data used for the training of the neural controllers are generated using the available smart beam model, described in Section 2. The voltage applied to the piezo-actuator during the data generation is limited to the range [−250 V, 250 V]. It is necessary to impose these limits to ensure that a feasible value of voltage is applied during the simulation and eventual control. In the simulation studies an additional saturation block has therefore been added.

Although the two control methods used in this paper differ in terms of the network structure, the results of control are similar with only minor differences noticeable. Therefore, only the results of one of these methods are shown in the following tests. Apart from the active damping, additional passive modal damping of value $\zeta = 0.001$ for each mode is present in the model. Unless stated otherwise, the default values used for the tests discussed below are as follows: control gain $g = 0.01$, sampling time $\Delta t = 0.002$ s.

3.2.1. NN control – relation to training data

Figure 2 shows how the sampling time of the data used for the training of the neural controller influences its behaviour. It needs to be noted that in each case the network architecture as well as the number of training iterations and the desired training performance is the same. It is imperative that the sampling time Δt is small enough to include the dynamics of the controlled system with enough precision. However, as can be seen in Fig. 2, the higher the sampling frequency, the faster the network tries to regulate the system, which leads to a much higher control voltage. If not for the saturation block, this would have caused the voltage applied to the piezo-actuator exceed the values imposed during the design. On the other hand (Fig. 2c), if the sampling time Δt is too small, the active damping is less effective. Therefore, it can be seen that the control performance of the neural network controller is related to the training data chosen, and it should be considered beforehand.

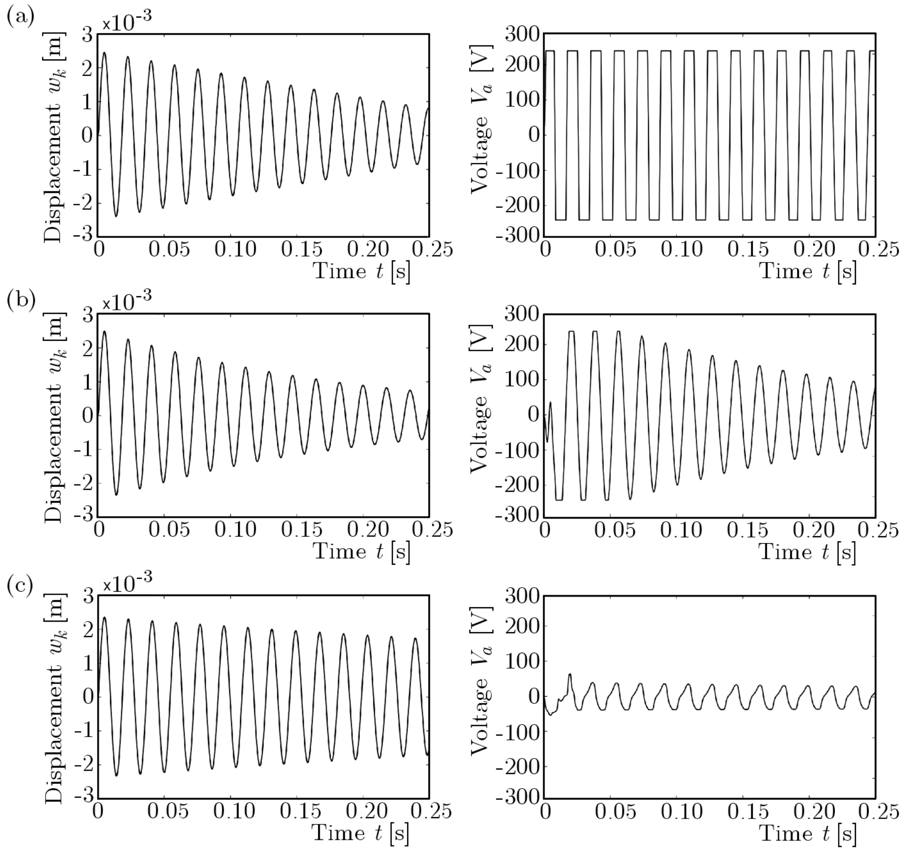

Fig. 2. Displacement of the free end of the beam w_k and control voltage V_a for different training data sampling times: (a) $\Delta t = 0.001\,\mathrm{s}$, (b) $\Delta t = 0.002\,\mathrm{s}$, (c) $\Delta t = 0.005\,\mathrm{s}$

3.2.2. NN control – relation to gain value

The results of using three different values of the control gain are shown in Fig. 3. The efficiency of damping can be improved by increasing the gain, but obviously at a cost of the increased voltage.

3.2.3. NN Control with the step-wise change of target value

As neural network controllers show a tendency to choose the best possible (mostly highest) control value to reach the desired point, it may be possible to improve their behaviour by setting

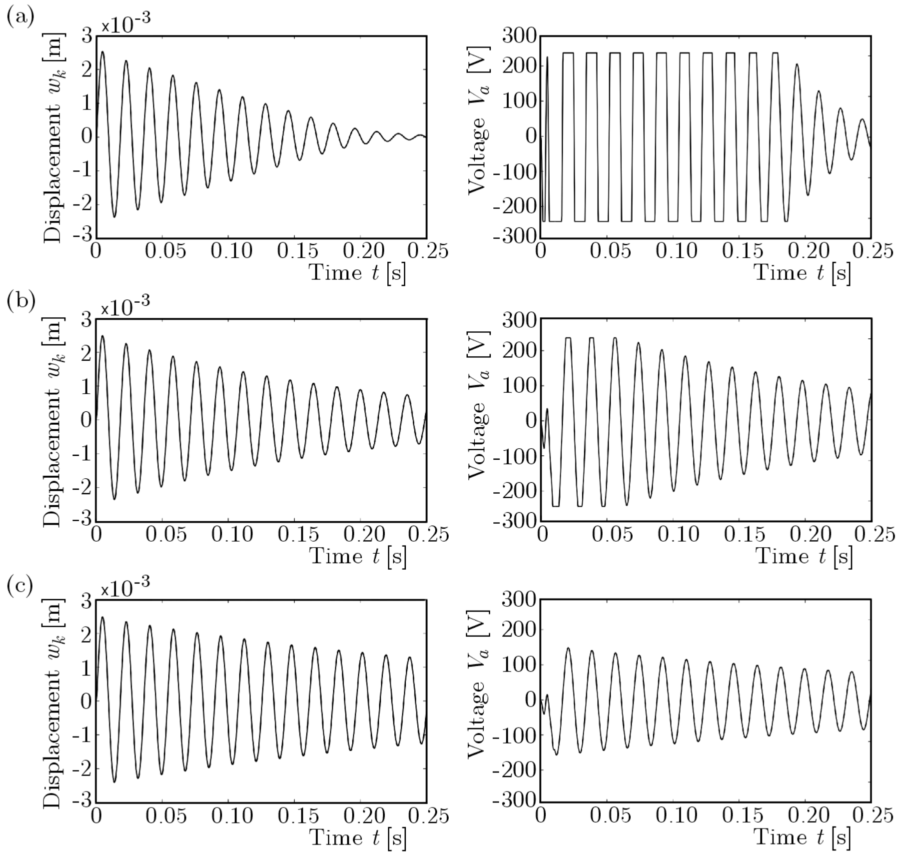

Fig. 3. Displacement of the free end of the beam w_k and control voltage V_a for different values of gain: (a) $g = 0.1$, (b) $g = 0.01$, (c) $g = 0.005$

interim goals for the controller, leading to the final goal. In this case, an additional step-wise change block is added, which in each step replaces the setpoint value t of the displacement of the free end of the beam by a value that lies between the actual value y and the setpoint. This new target value can, in general, be found using the following equation

$$\widehat{t} = y(1-d) + td \tag{3.4}$$

where $d \in [0,1]$ is the descent ratio. In our case this is simplified since $t = 0$. If $d = 1$, the control is changed to default (as if no modification were introduced). On the other hand, when $d = 0$, no control can be performed as the actual output y is the same as the modified target output $\widehat{t}$. By adjusting the value of ratio d, the controller can be forced to reach the target more slowly and, in turn, to decrease the required control voltage. In Fig. 4, it can be seen that for $d = 0.1$ the control values are visibly lower with no noticeable difference in the control performance.

3.2.4. NN Control with stepwise control (higher modes)

The control of several modes (in this case the 1st and 2nd one) can be seen in Fig. 5, respectively, with the standard- and stepwise control. The results are similar to those discussed before. It should be noted that the control in this case is performed using the controller trained only for the first mode and then modified to operate for both modes. In this approach, the controller sampling time remains unchanged. On the other hand, the system sampling time is made shorter by dividing the controller sampling time by a natural number r. This means that instead of using the output regressor $y(k-n)$, the regressor $y(k-r\cdot n)$ is used. The same rule applies to the input regressors. However, one should be careful when using this modification.

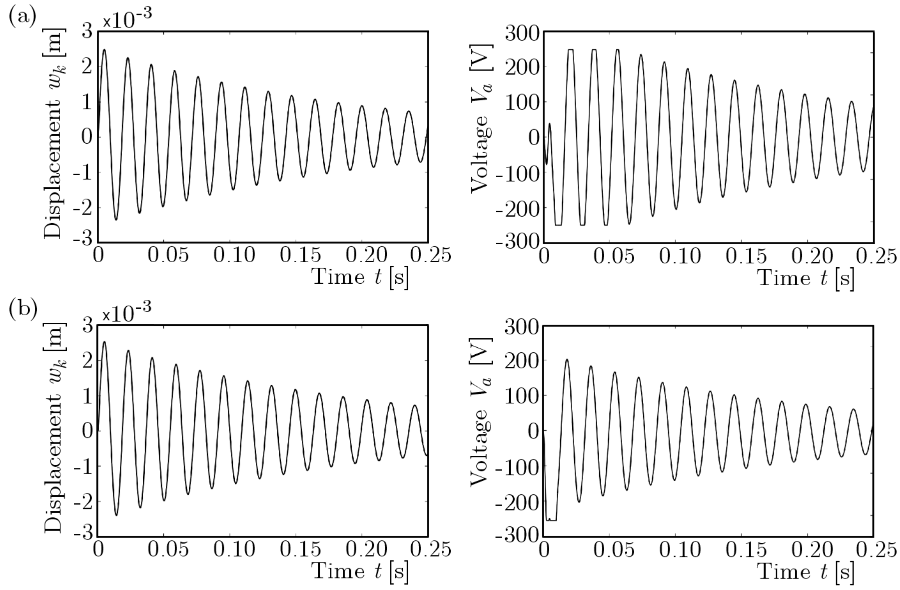

Fig. 4. Displacement of the free end of the beam w_k and control voltage V_a with step-wise change (fundamental mode); (a) $d = 1$, (b) $d = 0.1$

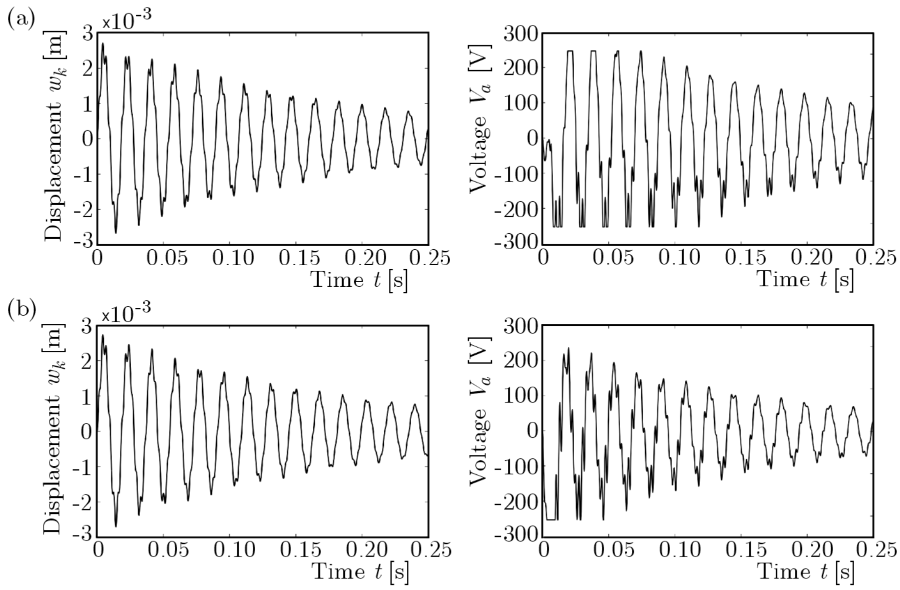

Fig. 5. Displacement of the free end of the beam w_k and control voltage V_a with step-wise change (two lowest modes); (a) $d = 1$, (b) $d = 0.1$

When applying this procedure, one should exercise caution, since when the value of r is too high, the neural control system may become unstable and some additional measures to prevent this from happening would need to be taken.

4. Summary

The purpose of this paper is to present possible options for the active vibration damping of a clamped-free beam with piezoelectric patches using neural network control. Two control methods have been chosen and used for this purpose. Due to the complex nature of neural network control, several factors have to be considered. Several changes to the most important of these factors are presented in this study. It can be shown that by properly setting and adjusting these parameters the control can become faster and more effective.

Although the paper has been limited to the simulation studies, the results obtained and the techniques used are belived to be of help in the design of a neural controller of a physical smart beam.

References

1. Choi S., 2002, *Vibration Control – Encyclopedia of Smart Materials*, John Wiley & Sons, New York
2. Crawley E., De Luis J., 1987, Use of piezoelectric actuators as elements of intelligent structures, *AIAA Journal*, **25**, 1373-1385
3. Cupiał P., 2008, *Coupled Electromechanical Vibration Problems for Piezoelectric Distributed-Parameter Systems*, Politechnika Krakowska, Kraków
4. Flasiński M., 2011, *Introduction to Neural Networks* (in Polish), Wydawnictwo Naukowe PWN
5. Hagan M.T., Demuth H.B., 1999, Neural networks for control, *Proceedings of the 1999 American Control Conference*, San Diego, 1642-1656
6. Korbicz J., Obuchowicz A., Uciński D., 1994, *Artificial Neural Networks* (in Polish), Akademicka Oficyna Wydawnicza PLJ
7. Medsker L., Jain L.C., 1999, *Recurrent Neural Networks: Design and Applications*, CRC Press, 325-354
8. Narendra K.S., Parthasarathy K., 1990, Identification and control of dynamical systems using neural networks, *IEEE Transactions on Neural Networks*, **1**, 4-26
9. Nizioł J., 1989, *Principles of Machine Vibration* (in Polish), Wydawnictwo PK, Kraków
10. Nørgaard M., Ravn O., Poulsen N,K., Hansen L.K., 2003, *Neural Networks for Modelling and Control of Dynamic Systems*, Springer
11. Omidvar O., Elliot D.L., edit., 1997, *Neural Systems for Control*, Academic Press
12. Passino K.M., 2005, *Biomimicry for Optimization, Control and Automation*, Springer
13. Preumont A., 1997, *Vibration Control of Active Structures*, Kluwer Academic Publisher
14. Qiu Z., Zhang X., Ye C., 2012, Vibration suppresion of a flexible piezoelectric beam using BP neural network controller, *Acta Mechanica Solida Sinica*, **25**, 417-428
15. Rutkowski L., 2009, *Methods and Algorithms of Artificial Inteligence* (in Polish), Wydawnictwo Naukowe PWN
16. Smyser C.P., Chandrashekhara K., 1997, Robust vibration control of composite beams using piezoelectric devices and neural networks, *Smart Materials and Structures*, **6**
17. Tylikowski A., 1993, Stabilization of beam parametric vibrations, *Journal of Theoretical and Applied Mechanics*, **31**, 657-670
18. Valoor M.T., Chandrashekhara K., Agarwal S., 2001, Self-adaptive vibration control of smart composite beams using recurrent neural architecture, *International Journal of Solids and Structures*, **38**, 7857-7874

Manuscript received December 5, 2013; accepted for print March 22, 2015

JOURNAL OF THEORETICAL
AND APPLIED MECHANICS
53, 4, pp. 775-788, Warsaw 2015
DOI: 10.15632/jtam-pl.53.4.775

DYNAMIC BEHAVIOUR OF THREE-LAYERED ANNULAR PLATES WITH VISCOELASTIC CORE UNDER LATERAL LOADS

Dorota Pawlus
University of Bielsko-Biala, Faculty of Mechanical Engineering and Computer Science, Bielsko-Biała, Poland
e-mail: dpawlus@ad.ath.bielsko.pl

This paper presents the dynamic behaviour of three-layered, annular plates with a linear viscoelastic core. The annular plate is loaded in plane of facings with variable in time forces acting on the inner or outer plate edges. The analysed plate structure is symmetric and composed of three-layers: thin facings and a thicker, soft core. The core material is considered as linear with viscoelastic properties. Analytical and numerical solution will be presented including the wavy forms of dynamic loss of plate stability. In the analytical and numerical solution, two approximation methods: orthogonalization and finite difference have been applied to obtain the system of differential equations for the analysed problem of dynamic deflections of the examined plate with the viscoelastic core. Additionally, the suitable plate model using the finite element method has been built. The numerical calculations carried out in ABAQUS system show the results which are compatible with those obtained for the analytical and numerical solution. Presented in figures time histories of plate deflections and velocity of deflections as well as buckling forms of the plate model show the dynamic response of the examined plate on time-dependent loads and core material properties.

Keywords: sandwich plate, viscoelastic core, dynamic stability

1. Introduction

The examinations of three-layered plates have been undertaken in numerous works. Rarely, they concern annular plates under lateral loads variable in time and plate structures where damping properties of the layer material is taken into account. A wide range of possible applications of annular layered plates in aerospace industry, mechanical and nuclear engineering presented in works by Dumir and Shingal (1985), Paydar (1990), Chen *et al.* (2006), Wang and Chen (2004) causes the evaluation of dynamic behaviour of such complex composite plates still important.

The following, exemplary papers by Wang and Chen (2002, 2004), Chen *et al.* (2006) belong to the group of works, where the plate dynamic problems like vibrations or dynamic instability have been analysed. The examinations concern the plates composed of three layers: the thin outer constraining layer, the thin middle viscoelastic damping layer and the bottom outer host layer of the plate. The evaluation of the influence of the viscoelastic core thickness on the improvement of damping plate properties was presented in work by Wang and Chen (2002). In many works, the problem of the loss of plate stability wss often limited to only the axisymmetric case. Whereas, full evaluation also requires analysis of circumferentially waved plate buckling forms. In the work by Krizhevsky and Stavsky (1996), the asymmetric instability problem of a three-layered plate with a relatively thin core was shown. The results of critical loads were presented.

The evaluation of dynamic behaviour of a three-layered annular plate with a viscoelastic core loaded in facings plane is presented in this work. The type of the three-layered structure is characteristic, transversally symmetrical and composed of thin facings and a suitable thicker, soft core. The asymmetric buckling modes of examined, dynamic loaded plates are also observed.

Including in the description of physical relations the rheological properties of the plate core made of polyurethane foam correctly approximates the critical real plate behaviour. It could be supposed that the noticed in the work by Romanów (1995) sensitivity of foam materials on the long duration of load could be important particularly in supercritical plate work under a load constant in time or slowly increasing.

Such observations together with dynamic stability analyses of three-layered annular plates with viscoelastic cores are the main goal of this work. The presented way of problem solution and detailed results refer to analyses presented in works by Pawlus (2010, 2011a,b,c).

2. Problem formulation

The three-layered annular plate with the soft foam core and with the symmetric cross-section structure is the subject of consideration. The scheme of the plate is presented in Fig. 1. The facings are elastic. The core material is treated as elastic or viscoelastic. The plate is loaded on the inner or/and outer perimeter of facings with uniformly distributed stress linearly increasing in time, according to Equation (2.1) or constant in time (see, Eq. (6.1))

$$p = st \tag{2.1}$$

where p is compressive stress, s – rate of growth of the plate loading, t – time.

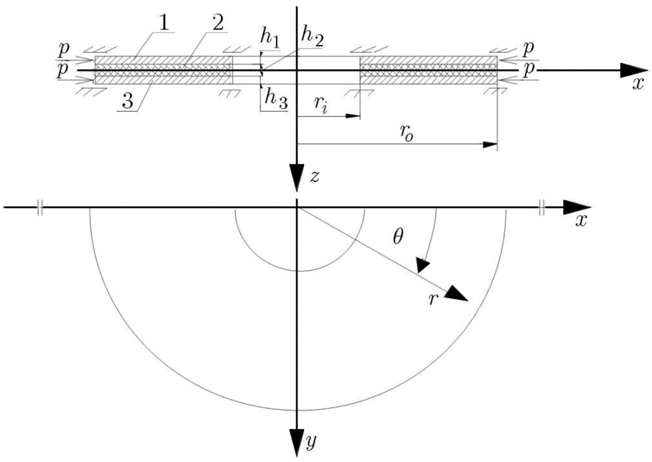

Fig. 1. A scheme of the three-layered annular plate composed of facings – layers 1, 3 and core – layer 2

The plate with bilaterally slidably clamped edges is undertaken in the presented considerations. The form of plate predeflection corresponds with the plate buckling form. The circumferentially waved forms of the loss of plate dynamic stability are analysed, too. The classical theory of sandwich plates with the broken line hypothesis, presented by Volmir (1967), and the decomposition of basic stresses to normal and shearing components, carried by facings and the core, respectively, have been accepted in the mathematical formulation of the problem. In numerical solution, the approximate finite difference method and finite element method have been used.

As the criterion of the loss of plate stability, the criterion presented by Volmir (1972) has been adopted. According to this criterion, the loss of plate stability occurs at the moment of time when the speed of the plate point of the maximum deflection reaches the first maximum value. The essence of the accepted criterion of the loss of plate stability connected with the evaluation of values of dynamic critical loads in the region of significant increase in plate deflections corresponds to the Budiansky-Roth criterion. This criterion is used in the buckling analysis of laminated shells, presented for example by Tanov and Tabiei (1998).

3. Basic equations

Solution to the considered problem is based on the relations typical for the edge-initial problem: dynamic equilibrium equations, geometrical and physical relations and initial and boundary conditions. Dynamic equilibrium equations have been formulated for each layer of the plate. Core deformation is described by the angles β and α in the radial and circumferential directions, respectively

$$
\begin{aligned}
\beta &= \frac{u_1 - u_3}{h_2} - \frac{1}{2}\frac{h_1 + h_3}{h_2} w_{d,r} + w_{o,r} \\
\alpha &= \frac{v_1 - v_3}{h_2} - \frac{1}{2r}\frac{h_1 + h_3}{h_2} w_{d,\theta} + \frac{1}{r} w_{o,\theta}
\end{aligned}
\tag{3.1}
$$

where w_d is additional plate deflection, w_o – preliminary plate deflection, $u_{1(3)}$, $v_{1(3)}$ – displacements of the points of the middle plane of facings (layers 1, 3) in the radial and circumferential directions, respectively.

Linear physical relations of Hooke's law for facings and linear viscoelastic relations of the standard model (see Fig. 2) for the plate core are applied. The physical relations of the viscoelastic core material subjected to shearing stresses are presented by the equations

$$
\tau_{rz_2} = \widetilde{G}_2 \gamma_{rz_2} \qquad \tau_{\theta z_2} = \widetilde{G}_2 \gamma_{\theta z_2}
\tag{3.2}
$$

where γ_{rz_2}, $\gamma_{\theta z_2}$ are shearing strains of the plate core in the radial and circumferential direction, respectively, expressed by

$$
\gamma_{rz_2} = u_{2,z}^{(z)} + w_{d,r} \qquad \gamma_{\theta z_2} = v_{2,z}^{(z)} + \frac{1}{r} w_{d,\theta}
\tag{3.3}
$$

where: $u_2^{(z)} = u_2 - z\beta + zw_{o,r}$, $v_2^{(z)} = v_2 - z\alpha + zw_{o,\theta}/r$ are the radial and circumferential displacements of the points in the distance z between the point and the middle surface of the plate core; u_2, v_2 – displacements of the points of the middle plane of the core layer in the radial and circumferential direction, respectively; $\widetilde{G}_2$ – modulus expressed by the formula corresponding to the form of the constitutive equation of the standard model

$$
\widetilde{G}_2 = \frac{C + D\frac{\partial}{\partial t}}{E + F\frac{\partial}{\partial t}}
\tag{3.4}
$$

where C, D, E, F are the quantities formulated by the elastic G_2, G_2' and viscosity η' constants of the core material, presented by Skrzypek (1986)

$$
C = \frac{G_2 G_2'}{G_2 + G_2'} \qquad D = \frac{\eta' G_2}{G_2 + G_2'} \qquad E = 1 \qquad F = \frac{\eta'}{G_2 + G_2'}
\tag{3.5}
$$

and $\partial/\partial t$ – differential operator.

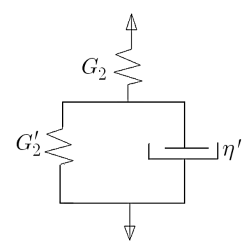

Fig. 2. The standard model of a viscoelastic layer material

Using the equations of the nonlinear Kármán's plate, the sectional forces and moments in the facings are established. Then, the resultant transverse radial and circumferential forces and the resultant membrane forces expressed by the introduced stress function are formulated.

The initial conditions, loading and boundary conditions as well as relations connected with the slidably clamped both inner and outer plate edges are established as follows

$$\begin{aligned}
&w\big|_{t=0} = w_o \qquad w_{,t}\big|_{t=0} = 0 \qquad w_d\big|_{t=0} = 0 \qquad w_{d,t}\big|_{t=0} = 0\\
&\sigma_r\big|_{r=r_i(r_o)} = -p(t)d_{1(2)} \qquad \sigma_{r,t}\big|_{r=r_i(r_o)} = -(p(t))_{,t}d_{1(2)} \qquad \tau_{r\theta}\big|_{r=r_i(r_o)} = 0\\
&w\big|_{r=r_i(r_o)} = 0 \qquad w_{,r}\big|_{r=r_i(r_o)} = 0 \qquad \delta = \gamma\big|_{r=r_i(r_o)} = 0 \qquad \delta_{,r}\big|_{r=r_i(r_o)} = 0
\end{aligned} \tag{3.6}$$

where w is the total deflection, w_d – additional deflection, w_o – preliminary deflection, σ_r – radial stress, $\tau_{r\theta}$ – shear stress, d_1, d_2 – quantities equal to 0 or 1, determining the loading of the inner or/and outer plate perimeter, δ, γ – differences of radial and circumferential displacements of the points in middle surfaces of facings, respectively.

Finally, after some calculations the basic differential equation expressed the deflections of the analysed sandwich plate with the viscoelastic core are determined

$$\begin{aligned}
&N_1 w_{d,rrrr} + \frac{2N_1}{r}w_{d,rrr} - \frac{N_1}{r^2}w_{d,rr} + \frac{N_1}{r^3}w_{d,r} + \frac{N_1}{r^4}w_{d,\theta\theta\theta\theta} + \frac{2(N_1+N_2)}{r^4}w_{d,\theta\theta}\\
&\quad + \frac{2N_2}{r^2}w_{d,rr\theta\theta} - \frac{2N_2}{r^3}w_{d,r\theta\theta} - \widetilde{G}_2\frac{H'}{h_2 r}\Big(\gamma_{,\theta} + \delta + r\delta_{,r} + H'\frac{1}{r}w_{d,\theta\theta} + H'w_{d,r} + H'rw_{d,rr}\Big)\\
&\quad = \frac{2h'}{r}\Big(\frac{2}{r^2}\Phi_{,\theta}w_{,r\theta} - \frac{2}{r}\Phi_{,r\theta}w_{,r\theta} + \frac{2}{r^2}w_{,\theta}\Phi_{,r\theta} - \frac{2}{r^3}w_{,\theta}\Phi_{,\theta} + w_{,r}\Phi_{,rr} + \Phi_{,r}w_{,rr}\\
&\quad + \frac{1}{r}\Phi_{,\theta\theta}w_{,rr} + \frac{1}{r}\Phi_{,rr}w_{,\theta\theta}\Big) - Mw_{d,tt}
\end{aligned} \tag{3.7}$$

where N_1, N_2 are expressed by the material and geometrical parameters of plate layers; $H' = h' + h_2$; $h'(h_1 = h_3 = h')$ – facing thickness, h_2 – core thickness.

4. Problem solution

In the solution, the following dimensionless quantities and the expressions have been assumed

$$\begin{aligned}
&\zeta = \frac{w}{h} \qquad \zeta_1 = \frac{w_d}{h} \qquad \zeta_o = \frac{w_o}{h} \qquad F = \frac{\Phi}{Eh^2}\\
&\rho = \frac{r}{r_o} \qquad \overline{\delta} = \frac{\delta}{h} \qquad \overline{\gamma} = \frac{\gamma}{h} \qquad t^* = tK_7 \qquad K_7 = \frac{s}{p_{cr}}\\
&\zeta_1(\rho,\theta,t) = X_1(\rho,t)\cos(m\theta) \qquad \zeta_o(\rho,\theta) = X_a(\rho) + X_b(\rho)\cos(m\theta)\\
&\zeta = \zeta_1 + \zeta_o \qquad F(\rho,\theta,t) = F_a(\rho,t) + F_b(\rho,t)\cos(m\theta) + F_c(\rho,t)\cos(2m\theta)\\
&\overline{\delta}(\rho,\theta,t) = \overline{\delta}(\rho,t)\cos(m\theta) \qquad \overline{\gamma}(\rho,\theta,t) = \overline{\gamma}(\rho,t)\sin(m\theta)
\end{aligned} \tag{4.1}$$

where m is the number of circumferential waves corresponding to the form of plate buckling, $h = h_1 + h_2 + h_3$ is the total thickness of plate, p_{cr} – critical static stress.

Using the orthogonal method to elimination of the angular variable θ, Eq. (3.7) has been replaced by the approximate one obtained from the following condition

$$\int\limits_0^{2\pi} \psi\cos(m\theta)\,d\theta = 0 \tag{4.2}$$

where ψ is the difference of the left and right side of transformed Equation (3.7).

Using the physical relations, relations of sectional forces and moments in the facings with stresses and equations of resultant membrane forces expressed by the introduced stress function after elimination of the quantities described by sums of the radial $(u_1 + u_3)$ and circumferential $(v_1 + v_3)$ facing displacements, the following equation has been obtained

$$
\begin{aligned}
&\Phi_{,rrrr} + \frac{2}{r}\Phi_{,rrr} - \frac{1}{r^2}\Phi_{,rr} + \frac{1}{r^3}\Phi_{,r} + \frac{1}{r^4}\Phi_{,\theta\theta\theta\theta} + \frac{4}{r^4}\Phi_{,\theta\theta} - \frac{2}{r^3}\Phi_{,r\theta\theta} + \frac{2}{r^2}\Phi_{,rr\theta\theta} \\
&\quad = E\Big[\frac{1}{r}w_{o,rr}\Big(w_{o,r} + \frac{1}{r}w_{o,\theta\theta}\Big) - \frac{1}{r^2}\Big(\frac{1}{r}w_{o,\theta} - w_{o,r\theta}\Big)^2 - \frac{1}{r}w_{,rr}\Big(w_{,r} + \frac{1}{r}w_{,\theta\theta}\Big) \\
&\quad + \frac{1}{r^2}\Big(\frac{1}{r}w_{,\theta} - w_{,r\theta}\Big)^2\Big]
\end{aligned}
\tag{4.3}
$$

The quantities δ and γ, unknown in Equation (3.7), have been obtained determining the differences of the radial and circumferential displacements u_1, u_3 and v_1, v_3 of the points of the middle surface of the plate facings. The equilibrium equations for forces acting on the non-deformed outer plate layers in the u and v direction are used.

After insertion of Equations (4.1) describing the functions w, w_o, Φ and after comparison of the expressions by the same trigonometric functions, Equation (4.3) has been presented in form of three equations.

In the solution, the finite difference method has been used for the approximation of the derivatives with respect to ρ by central differences in the discrete points. The form of the system of differential equations expressing the deflections of three-layered annular plate with the viscoelastic core is as follows

$$
\begin{aligned}
&\mathbf{PU} + \mathbf{Q} + \mathbf{P}_L\dot{\mathbf{U}} + \mathbf{Q}_L - W_1\ddot{\mathbf{U}} = W_2\dddot{\mathbf{U}} \\
&\mathbf{M}_Y\mathbf{Y} = \mathbf{Q}_Y \qquad \mathbf{M}_Y\dot{\mathbf{Y}} = \dot{\mathbf{Q}}_Y \\
&\mathbf{M}_V\mathbf{V} = \mathbf{Q}_V \qquad \mathbf{M}_V\dot{\mathbf{V}} = \dot{\mathbf{Q}}_V \\
&\mathbf{M}_Z\mathbf{Z} = \mathbf{Q}_Z \qquad \mathbf{M}_Z\dot{\mathbf{Z}} = \dot{\mathbf{Q}}_Z \\
&\mathbf{M}_{DL}\dot{\mathbf{D}} = \mathbf{M}_D\mathbf{D} + \mathbf{M}_U\mathbf{U} + \mathbf{M}_{UL}\dot{\mathbf{U}} + \mathbf{M}_G\mathbf{G} + \mathbf{M}_{GL}\dot{\mathbf{G}} \\
&\mathbf{M}_{GGL}\dot{\mathbf{G}} = \mathbf{M}_{GG}\mathbf{G} + \mathbf{M}_{GU}\mathbf{U} + \mathbf{M}_{GUL}\dot{\mathbf{U}} + \mathbf{M}_{GD}\mathbf{D} + \mathbf{M}_{GDL}\dot{\mathbf{D}}
\end{aligned}
\tag{4.4}
$$

where

$$
W_1 = K_7\frac{h'}{h}r_o h_2 M E_L \qquad W_2 = K_7^3\frac{h'}{h}r_o h_2 M F_L
$$

and M is the expression: $M = 2h'\mu + h_2\mu_2$; μ, μ_2 – facing and core mass density, respectively; r_o – outer radius; E_L, F_L – quantities determined by elastic and viscosity constants of the core standard material; $\mathbf{U}, \mathbf{Y}, \mathbf{V}, \mathbf{Z}, \dot{\mathbf{U}}, \ddot{\mathbf{U}}, \dddot{\mathbf{U}}, \dot{\mathbf{Y}}, \dot{\mathbf{V}}, \dot{\mathbf{Z}}$ – vectors of plate additional deflections and components F_a, F_b, F_c of the stress function $F_{a'\rho} = y$, $F_b = v$, $F_c = z$ and their derivatives with respect to time t, respectively; $\mathbf{P}$, $\mathbf{P}_L$ – matrices with elements composed of geometric and material plate parameters, the quantity b (b – length of the interval in the finite difference method), dimensionless radius ρ and the number m of buckling waves and its derivative with respect to time t, respectively; $\mathbf{Q}$, $\mathbf{Q}_L$ – vectors of expressions composed of the initial and additional deflections, geometric and material parameters, components of the stress function, radius ρ, quantity b, coefficients δ, γ and the number m and their derivatives with respect to time t, respectively; $\mathbf{M}_Y$ – matrix of elements composed of the radius ρ and quantity b, respectively; $\mathbf{M}_V, \mathbf{M}_Z$ – matrices of elements composed of the radius ρ, quantity b and number m; $\mathbf{Q}_Y, \mathbf{Q}_V, \mathbf{Q}_Z, \dot{\mathbf{Q}}_Y, \dot{\mathbf{Q}}_V, \dot{\mathbf{Q}}_Z$ – vectors of expressions composed of the initial and additional deflections, radius ρ, quantity b and the number m and their derivatives with respect to time t, respectively; $\mathbf{M}_D, \mathbf{M}_G, \mathbf{M}_{GG}, \mathbf{M}_{GD}, \mathbf{M}_{DL}, \mathbf{M}_{GL}, \mathbf{M}_{GGL}, \dot{\mathbf{M}}_{GDL}$ – matrices of elements composed of geometric and material parameters, quantity b and the number m and their derivatives with respect to time t, respectively; $\mathbf{M}_U, \mathbf{M}_{UL}$ – matrices of elements composed of material parameters and quantity b and their derivatives with respect to time t, respectively; $\mathbf{M}_{GU}, \mathbf{M}_{GUL}$ – matrices of elements composed of geometric parameters, material parameters and the number m and their derivatives with respect to time t, respectively; $\mathbf{D}, \mathbf{G}, \dot{\mathbf{D}}, \dot{\mathbf{G}}$ – vectors of expressions composed of coefficients δ and γ and their derivatives with respect to time t, respectively.

The system of Equations (4.4) has been solved using Runge-Kutta's integration method for the initial state of plate.

Eliminating from the system of Equations (4.4) Equations $(4.4)_{3,5,7}$ and the expressions connected with the differential operator $\partial/\partial t$ applied in physical relations of the viscoelastic material of the plate core, a system of equations for plate with elastic core has been obtained (Pawlus, 2010, 2011b,c). The critical static stress p_{cr} has been calculated solving the eigenproblem for the problem of the disk state neglecting the inertial components and nonlinear expressions (Pawlus, 2010, 2011b,c).

5. Finite element plate models

In the analysis carried out with use the finite element method, two models have been built:

- basic model in form of the complete model of the annular plate, circularly symmetrical (Fig. 3a),
- simplified model built of axisymmetrical elements (Fig. 3b).

The facings are built of shell elements but the core mesh is built of solid elements. The grids of facings elements are tied with the grid of core elements using the surface contact interaction. The calculations were carried out at the Academic Computer Center CYFRONET-CRACOW (KBN/SGI_ORIGIN_2000/PŁódzka/030/1999) using the ABAQUS system.

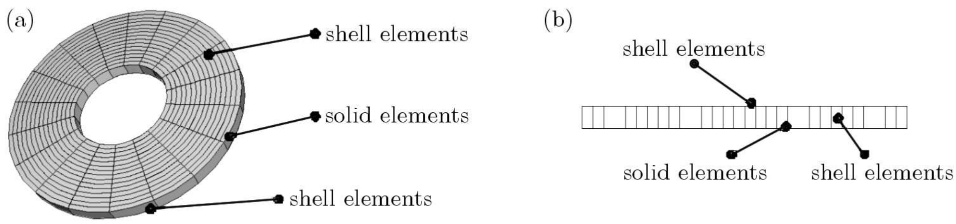

Fig. 3. (a) Basic model, (b) simplified model

The viscoelastic properties of the core material have been described by a single term of the Prony series for the shear relaxation modulus (Hibbitt *et al.*, 2000)

$$G_R(t) = G_o\Big(1 - q_1^p\Big(1 - \mathrm{e}^{-t/\tau_1^G}\Big)\Big) \tag{5.1}$$

where q_1^p, τ_1^G are material constants, G_o – instantaneous shear G_2.

The values of material constants q_1^p, τ_1^G for the standard model of the plate core have been calculated from the following equations

$$q_1^p = \frac{G_2}{G_2 + G_2'} \qquad\qquad \tau_1^G = \frac{\eta'}{G_2 + G_2'} \tag{5.2}$$

6. Exemplary calculations

Exemplary numerical calculations were carried out for the plate with the following geometrical dimensions: inner radius $r_i = 0.2\,\mathrm{m}$, outer radius $r_o = 0.5\,\mathrm{m}$, facing thickness $h' = 0.001\,\mathrm{m}$, core thickness $h_2 = 0.005\,\mathrm{m}$, $0.01\,\mathrm{m}$ or $0.02\,\mathrm{m}$. The parameters of steel facing are: Young's modulus $E = 2.1 \cdot 10^5\,\mathrm{MPa}$, Poisson's ratio $\nu = 0.3$, mass density $\mu = 7.85 \cdot 10^3\,\mathrm{kg/m^3}$. Polyurethane foam is the core material. Two kinds of foam presented in works by Romanów (1995) and Majewski and Mackowski (1975) have been accepted:

- with the values of constants G_2, G_2', η', μ_2 presented in work by Romanów (1995) equal to: $G_2 = 15.82\,\mathrm{MPa}$, $G_2' = 69.59\,\mathrm{MPa}$, $\eta' = 7.93 \cdot 10^4\,\mathrm{MPa{\cdot}s}$, $\mu_2 = 93.6\,\mathrm{kg/m^3}$,
- with the data presented in work by Majewski and Mackowski (1975) the Kirchhoff's modulus equal to: $G_2 = 5\,\mathrm{MPa}$, the creep function $\varphi = 0.845(2 - \mathrm{e}^{-0.36t} - \mathrm{e}^{-0.036t})$ and mass density equal to: $\mu_2 = 64\,\mathrm{kg/m^3}$.

The creep function presented in the work by Majewski and Mackowski (1975) allows for calculation of the values of elastic and viscous constants of the five-parameters rheological model composed of two Kelvin-Voigt models and the spring element connected in series. Because the solution presented in this paper is for the core material described by the three-parameters standard model (see, Fig. 2), hence the presented characteristic of function $\varphi(t)$ has been approximated by the function of the standard model. The numerical analysis has been carried out for the following values of standard constants of the plate core: $G_2 = 5\,\mathrm{MPa}$, $G_2' = 3.13\,\mathrm{MPa}$, $\eta' = 212.92 \cdot 10^4\,\mathrm{MPa{\cdot}s}$, (Pawlus, 2010). According to the standard specification PN-84/B-03230 the value of Poisson's ratio is equal $\nu = 0.3$. The values of Young's modulus calculated treating the foam material as an isotropic are equal, respectively, to $E_2 = 41.13\,\mathrm{MPa}$, $E_2 = 13\,\mathrm{MPa}$. The values of material constants q_1^p, τ_1^G, expressed by Equations (5.2), in Prony series (see, Eq. (5.1)) are as follows:

- $q_1^p = 0.615$, $\tau_1^G = 26.19 \cdot 10^4\,\mathrm{s}$ for the foam with $G_2 = 5\,\mathrm{MPa}$,
- $q_1^p = 0.185$, $\tau_1^G = 928.46\,\mathrm{s}$ for the foam with $G_2 = 15.82\,\mathrm{MPa}$.

Rapidly increasing loading acting on the edge is expressed by Equation (2.1). The rate of plate loading growth s is equal for each numerically analysed plate. The value of the rate s is the result of the following equation: $s = K_7 p_{cr}$ (see Eq. (4.1)). The value of parameter K_7 is accepted as $K_7 = 20\,\mathrm{s}^{-1}$. Solving the eigenproblem, the value of critical stress p_{cr} is $p_{cr} = 217.32\,\mathrm{MPa}$ calculated for the plate compressed on the inner perimeter with the facing thickness $h' = 0.001\,\mathrm{m}$, core thickness $h_2 = 0.01\,\mathrm{m}$ and value of core Kirchhoff's modulus $G_2 = 15.82\,\mathrm{MPa}$ and $p_{cr} = 46.58\,\mathrm{MPa}$ for the plate model with $N = 26$ number of discrete points radially compressed on the outer perimeter with the number of buckling waves $m = 7$, the facing thickness $h' = 0.001\,\mathrm{m}$, core thickness $h_2 = 0.005\,\mathrm{m}$ and value $G_2 = 15.82\,\mathrm{MPa}$ (see Table 1).

The calculations by the finite difference method have been preceded by selection of the number N of discrete points from numbers N, equal to $N = 11, 14, 17, 21, 26$. The values of critical dynamic loads p_{crdyn} of plates with the viscoelastic core and values of critical static loads p_{cr} have been evaluated. The numerical calculations show that the number $N = 14$ allows us to achieve the accuracy up to 5% of technical error. The calculations have been carried out for this number. Table 1 presents exemplary results of the analysis.

The treating of the polyurethane foam as isotropic is one of the accepted assumptions in the description of the plate core material. In FEM numerical analysis, the value of the material Young's modulus has been calculated using the following equation: $G_2 = E_2/[2(1+\nu)]$. Table 2 presents exemplary results of the critical time t_{cr} and the critical additional deflection w_{dcr} for the basic elastic plate model compressed on the inner edge with the core parameters: thickness $h_2 = 0.005\,\mathrm{m}$, Young's modulus E_2 presented in Table 2, Poisson's ratio $\nu = 0.3$, Kirchhoff's modulus $G_2 = 15.82\,\mathrm{MPa}$. The axisymmetric form $m = 0$ of plate buckling has been examined.

In the wide range of the assumed values of Young's modulus E_2, the results for the critical time t_{cr}, and after calculations, also the values of the critical dynamic loads p_{crdyn} do not change.

Table 1. Critical loads p_{cr}, p_{crdyn} of the plates with the viscoelastic core loaded on the outer edge $G_2 = 15.82$ MPa $G_2' = 69.59$ MPa, $\eta' = 7.93 \cdot 10^4$ MPa·s, $h_2 = 0.005$ m, $h' = 0.001$ m, $\mu_2 = 93.6$ kg/m^3, $K_7 = 20\,\mathrm{s}^{-1}$

m	N									
	11		14		17		21		26	
	p_{cr} [MPa]	p_{crdyn} [MPa]	p_{cr} [MPa]	p_{crdyn} [MPa]	p_{cr} [MPa]	p_{crdyn} [MPa]	p_{cr} [MPa]	p_{crdyn} [MPa]	p_{cr} [MPa]	p_{crdyn} [MPa]
0	73.97	81.47	74.46	81.38	76.23	81.47	76.27	81.47	76.30	81.47
1	70.28	79.42	70.73	79.42	72.51	79.51	72.56	79.51	72.59	79.51
2	61.14	69.54	61.67	69.64	63.44	69.73	63.53	69.82	63.59	69.92
3	53.01	67.96	53.39	68.05	55.10	68.15	55.21	68.33	55.30	68.33
4	48.33	66.28	48.64	66.38	50.02	66.47	50.13	66.47	50.21	66.66
5	46.11	53.43	46.36	52.59	47.45	52.50	47.55	52.21	47.62	52.03
6	45.39	51.01	45.58	49.05	46.45	50.54	46.53	50.26	46.60	50.17
7	45.60	47.84	45.75	47.47	46.45	47.65	46.52	47.93	46.58	47.84
8	46.44	45.69	46.56	45.32	47.14	45.04	47.20	44.86	47.25	44.67

Table 2. Values of the critical time t_{cr} and maximum deflection w_{dcr} depending on core Young's modulus E_2

E_2 [MPa]	1.0	5.0	13.0	50.0	100.0
t_{cr} [s]	0.019	0.02	0.02	0.02	0.02
$w_{dcr} \cdot 10^3$ [m]	4.14	4.48	4.15	3.85	3.73

The values of the plate maximum critical deflection w_{dcr} change according to prediction. The analysis shows that the accepted core material could be treated as an isotropic in the presented evaluation focused on the critical plate loads.

The calculation results of the plates with the standard core material subjected to momentary loads (duration in the range of 0.1 s) do not differ significantly from the results for the plates with the elastic core. The time histories of deflections of the plates with the viscoelastic and elastic core for the number $m = 0$ are presented in Fig. 4. The results are presented using two kinds of

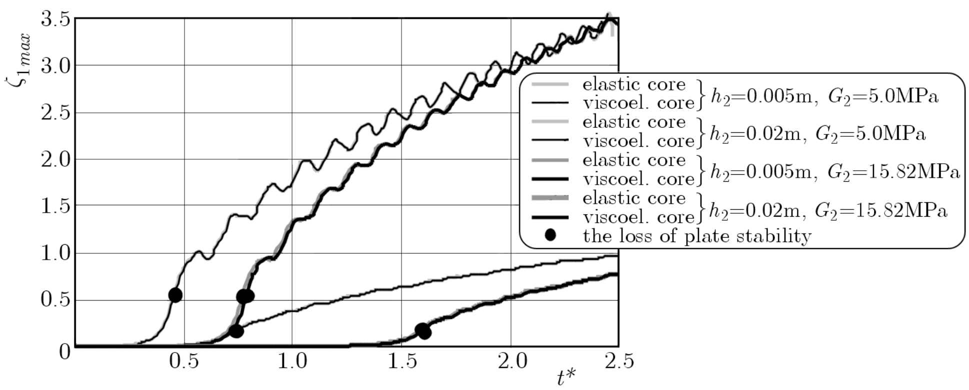

Fig. 4. A comparison of deflection time histories of plates loaded on the inner edge with the viscoelastic and elastic core

lines grey and black for the pairs: elastic and viscoelastic plate core with the same parameters h_2, G_2. The compatibility of deflection time histories is observed for the plates loaded on the inner perimeter with the viscoelastic and elastic core and compressed on the outer edge, too (see Fig. 5). The values of the critical time t_{cr} and critical dynamic loads p_{crdyn} are practically the same. The critical deflections are comparable for the plates with core thickness: $h_2 = 0.005\,\mathrm{m}$ and $h_2 = 0.02\,\mathrm{m}$. Of course, the values of the critical time and load increase for the plate with the stiffer core (higher value of modulus G_2 and thickness h_2). Then, supercritical vibrations disappear.

Figure 5 shows characteristic time histories of plate deflections for a selected number of buckling $m = 0$, $m = 3$, $m = 5$, $m = 8$ in two respective groups. Some differences are observed in supercritical responses of the plates. The minimal value of plate critical parameters is for the waved plate with the number $m = 5$ of buckling modes.

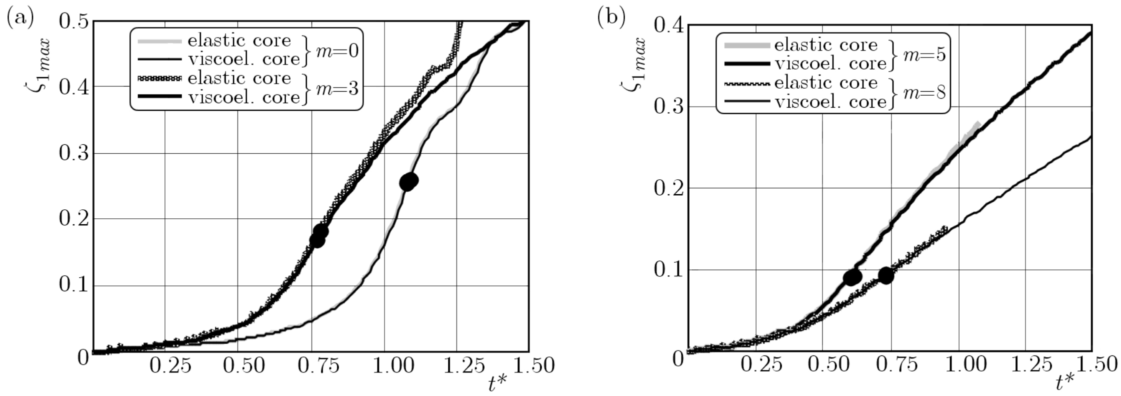

Fig. 5. A comparison of deflection time histories of plates ($G_2 = 5\,\mathrm{MPa}$, $h_2 = 0.01\,\mathrm{m}$) loaded on the outer edge with the viscoelastic and elastic core for the buckling wave number: (a) $m < 4$, (b) $m > 4$

The image of behaviour of the plates with the standard core is enriched by comparison with the results obtained for the plates with the core expressed by a simpler two-element model. The accepted in observations Maxwell model built of elastic and viscous elements connected in series takes attracts attention on the influence of the core material viscosity constant on the plate time histories of deflection. The numerical calculations have been carried out for quantities (3.5) assuming $G_2' = 0$. The comparison of deflection time histories of the plates compressed on the outer perimeter with the standard core ($G_2 = 15.82\,\mathrm{MPa}$) and the core expressed by the Maxwell model with parameters: $G_2 = 15.82\,\mathrm{MPa}$ and viscosity constant $\eta' = 7.93 \cdot 10^4\,\mathrm{MPa{\cdot}s}$ is shown in Fig. 6. The results are presented for selected buckling forms, which entirely show

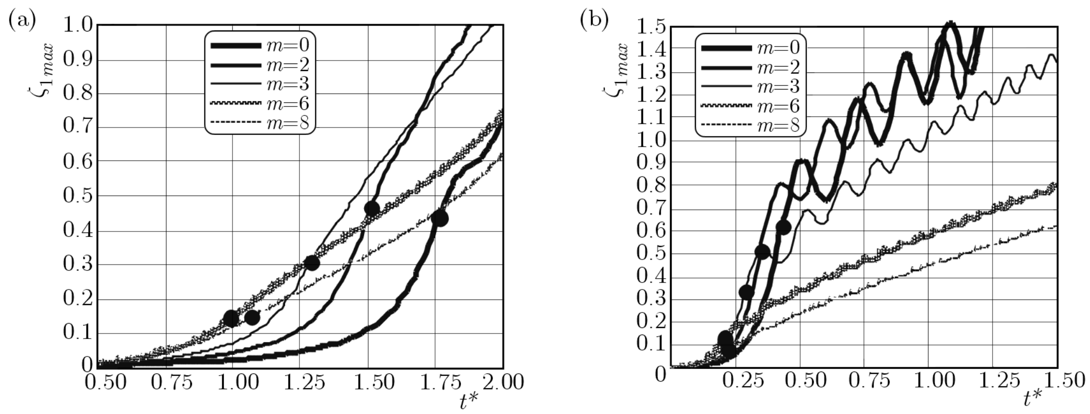

Fig. 6. The time histories of deflections of plates ($G_2 = 15.82\,\mathrm{MPa}$, $h_2 = 0.005\,\mathrm{m}$) compressed on outer edge with: (a) standard core, (b) Maxwell core

the character of curves. The standard model of solid body clearly extends the time to the loss of plate stability. In the case of the Maxwell model, the character of time histories of deflections of the plates with various numbers of circumferential waves m is comparable – increasing in the plate loading time. One can observe that the deflection time histories for the plate with the standard core model differ for plates with higher and lower numbers of the buckling mode. Figure 5 shows this character of curves too.

Figure 7 shows the comparison of curves $\zeta_{1max} = f(t^*)$ of the plates with the elastic and viscoelastic core compressed on the outer edge with the number of circumferential waves corresponding to the minimal values of the critical dynamic load for different values of material parameters and core thickness. The same lines (gray and black) are used to present the results for the plates with the elastic and viscoelstic core. The diagram presents the results for the plates with the Maxwell core, too. For this simple model, the change of material parameters ($G_2 = 15.82$ MPa, $\eta' = 7.93 \cdot 10^4$ MPa·s and $G_2 = 5$ MPa, $\eta' = 212.92 \cdot 10^4$ MPa·s) does not influence the deflection time histories and the critical time. Whereas, the plate core thickness has a great importance. The results show the relevant sensibility of the plate structure with three elements and the standard core on the material and geometrical parameters. It confirms an obvious and better approximation of the structure behaviour of the expected responses of the actual object. The results obtained for the plate compressed on the outer edge confirm earlier observations that the critical time prolongs for the plates with the stiffer core. For these plates, the minimal critical dynamic load is for the mode m = 5-7. It depends on the core parameters G_2, h_2. The value of the critical additional deflection is about 0.1 of the total plate thickness (see Eq. (4.1)). It is slightly higher for the plate with the modulus $G_2 = 15.82$ MPa.

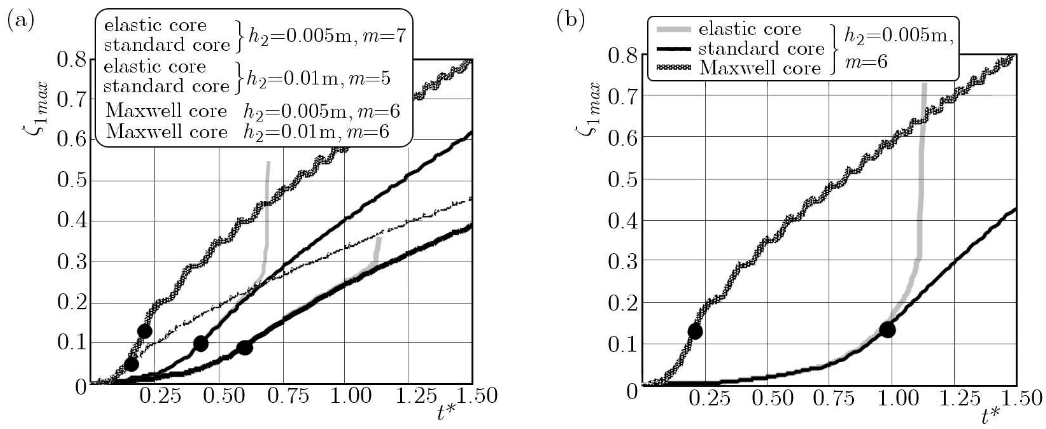

Fig. 7. Time histories of deflections of plates compressed on the outer edge for the elastic standard and Maxwell core with: (a) $G_2 = 5$ MPa, (b) $G_2 = 15.82$ MPa

The viscoelastic properties of the foam material relevantly depend on the viscosity constant η'. The deflection results for the plates with the viscoelastic core of significantly lower viscosity constant η' differ. Figure 8 shows the deflection time histories of the plates loaded on the inner edge with various values of the viscosity constant η' of the viscoelastic core material.

Large differences could be observed for the core material with very small values of the constant η' within the range $7.93 \cdot 10^{-2}(10^{-3})$ MPa·s. The time to the loss of plate stability shortens. The increase in values of the constant η' does not change the critical or supercritical deflections of the plates with the viscoelastic core. They are compatible with the results obtained for the plates with the elastic core.

The numerical FEM calculations of the simplified plate model confirm these observations. The critical dynamic loads distribution depending on values of the constant η' is presented for two kinds of the core viscoelastic materials in Fig. 9. The plates are loaded on the inner edge. A large theoretical decrease in values of the number η' up to a value about 10^{-8} times lower influences the contraction of the time to the loss of dynamic stability and decreases critical dynamic loads. These observations have an important practical meaning. In a wide range of accepted values of

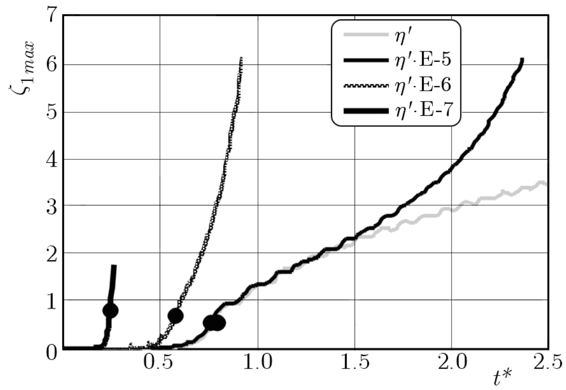

Fig. 8. The influence of viscosity constant η' on the deflection time histories of plate ($G_2 = 15.82\,\mathrm{MPa}$, $h_2 = 0.005\,\mathrm{m}$) loaded on the inner edge

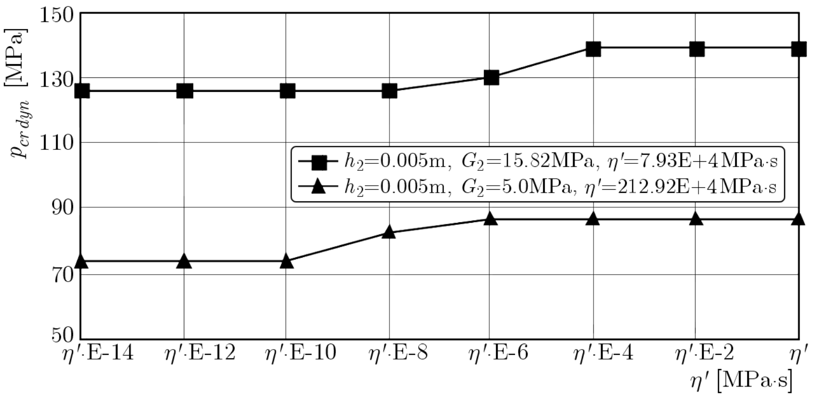

Fig. 9. Influence of the viscosity constant η' on the critical dynamic loads p_{crdyn} of the FEM plate model loaded on the inner edge

the viscosity constant, the dynamic response of the plate subjected to quickly increasing loads does not change. Here, it should be noticed that for true materials, precise determination of viscous material parameters is a great problem. Smaller sensitiblity to fluctuation of values of the viscoelastic material parameters seems to be the advantageous dynamical behaviour of such plates.

Exemplary time histories of deflections and velocity of deflections as well as critical deformations of the FEM simplified plate model with the elastic and viscoelastic core with $\eta' = 212.92 \cdot 10^{-6}$ (10^{-10} times decrease) are presented in Fig. 10. In general, there are no differences in the character of curves. A slightly less critical time and also dynamic load with higher deflection are noticed for the plate with a strongly reduced value of the viscosity constant η'. For a higher parameter η', the response of the plate with the viscoelastic core is consistent with that with the elastic one.

The influence of rheological properties of the core material on the increase of plate deflections is observed for the plates subjected to the load constant in time. The supercritical response has been analysed for both plates with the viscoelastic and elastic core compressed on the inner or outer edge in the case of the load constant in time. The assumed load function is expressed as follows

$$p(t) = \begin{cases} st & \text{for} \quad t \leqslant nt_{cr} \\ np_{crdyn} & \text{for} \quad t > nt_{cr} \end{cases} \tag{6.1}$$

where t_{cr} is the critical time of the loss of plate dynamic stability, n – assumed number.

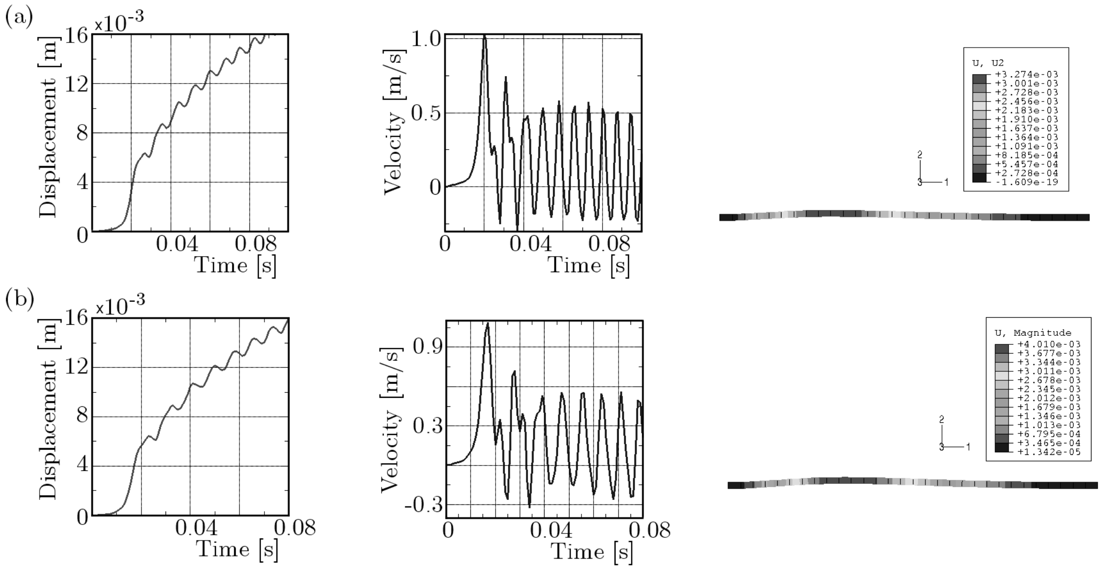

Fig. 10. Time histories of deflections, velocity of deflections and buckling forms of the plates ($G_2 = 5\,\mathrm{MPa}$, $h_2 = 0.005\,\mathrm{m}$) with: (a) elastic core, (b) viscoelastic core loaded on the inner edge

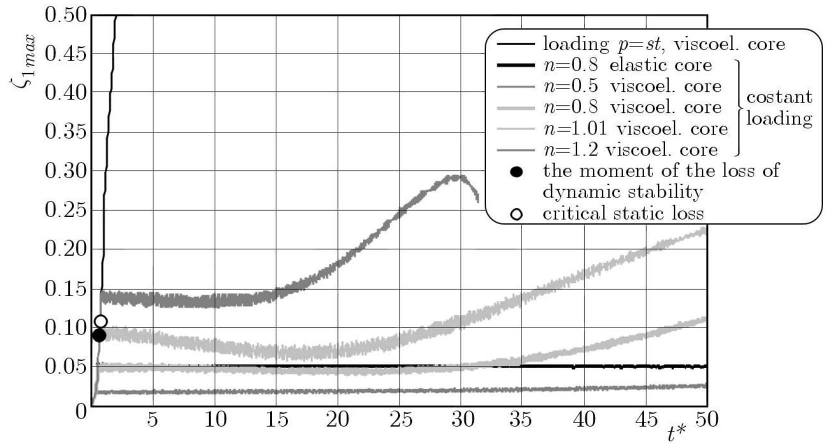

Fig. 11. Time histories of deflections of plates $G_2 = 5\,\mathrm{MPa}$, $h_2 = 0.01\,\mathrm{m}$, $m = 5$ with the elastic and viscoelastic core subjected to the load constant in time acting on the outer edge

Figure 11 shows the time histories of deflections of the plates with the elastic and viscoelastic core compressed on the outer edge with the waved form of predeflection and buckling. The number m is equal 5. The value of the number n is equal 0.5, 0.8 (undercritical load) and $n = 1.01, 1.2$. Additionally, Fig. 11 presents the curve $\zeta_{1max} = f(t^*)$ obtained for a linear ($p = st$) increase in the load acting on the plate with the viscoelastic core. The marked points show the moment of the loss of plate dynamic stability and static stability after suitable miscalculations in the value of the critical static load. The course of deflection time histories of the plates with the elastic and viscoelastic core under increasing linear load are consistent. The differences could be observed in the range for the loading constant in time. In a short time ($t = 2.5\,\mathrm{s}$) of the loading, an increase in the deflection of the plate with the viscoelastic core can be significant. An increase in the deflection rises in the critical ($n = 0.8$, 1.01) and supercritical ($n = 1.2$) range of plate operation. The sensitivity of the plate structure with the viscoelastic core material subjected to the load constant in time is clear. It is interesting that the course of these curves is observed for the plates examined in the short loading time. Doubtlessly, a quick increase in the dynamic loads, which involves the basic part of plate operation, influences such behaviour. One can find that the course of curves for the plates subjected to the load constant in time corresponds to the characteristic rheological curve with zones of the stationary and final creep.

The influence of dynamics of the increasing loading on the course of constant deflections of the plate with the viscoelastic core compressed on the outer perimeter is shown in Fig. 12. The rate of loading growth expressed by the parameter K_7 is not out of meaning in the response of the examined plate under the supercritical load (the number n is equal 1.01) constant in time. The dynamic behaviour with an increase in deflections of the plate initially linearly loaded with different values of the parameter K_7 in a longer time of the loading with a constant value is observed. The thickness h_2 of the plate with the viscoelastic core has here the influence, too. The results confirm dynamic sensitivity of the sandwich plate with the viscoelastic core. They also show importance of the general solution with the accepted description of the physical relations for the core rheological material in the analysed problem.

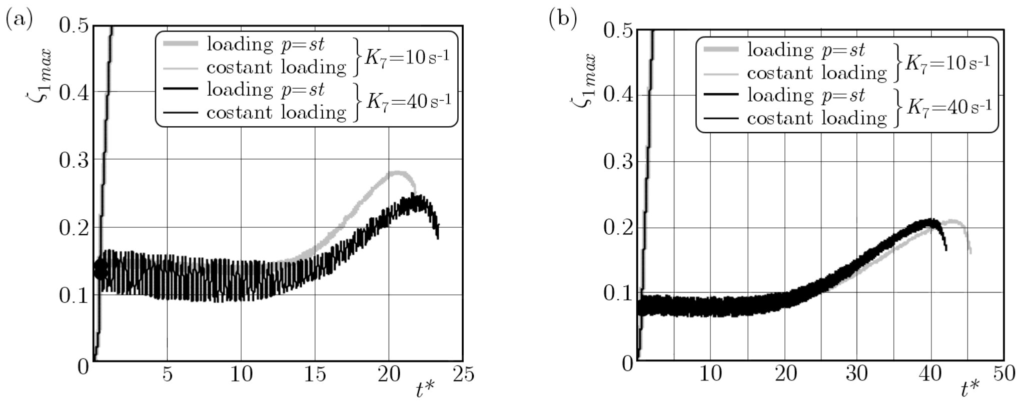

Fig. 12. Time histories of deflections of plates with the viscoelastic core subjected to the load constant in time acting on the outer edge depending on the rate of loading growth K_7 for different core thicknesses h_2: (a) $h_2 = 0.005\,\mathrm{m}$, $G_2 = 5\,\mathrm{MPa}$, $n = 1.01$, $m = 7$, (b) $h_2 = 0.01\,\mathrm{m}$, $G_2 = 5\,\mathrm{MPa}$, $n = 1.01$, $m = 6$

7. Conclusion

Summarizing the presented results and observations, it could be stated that, in general, the calculations of plates with an viscoelastic core could be replaced by calculations of similar plates but with an elastic core. Then, the solution of the problem could be significantly easier. However, the presented results show plate responses to its rheological properties. It has been observed that the plate behaviour differ for plates subjected to short critical time loadings and for plates loaded longer. The reactions on viscoelastic material parameters of the plate structure under longer duration of loading are quite clear. The indicate that the use of viscoelastic expressions in the plate physical relations is relevant. Then, the practical calculations become more difficult and should be carried out solving a more complicated problem formulation. Additional plate parameters connected with the effects of external factors like higher temperature make the problem more complex, which requires the achievement of the generalized solution.

The computational results also showed the influence of dynamics of the preliminary loading on the growth of rheological deflections of plates loaded constant in time. Both loading time histories expressed by the assumed function, in this paper by Eq. (6.1), as well as the speed of loading growth have an important meaning in this problem. A detailed analysis could expand the knowledge about dynamic behaviour of such a plate structure.

The carried out numerical experiments allow one to formulate the following statements:

- the use of proper constitutive relations for the plate material with rheological properties is essential in the solution to the dynamic deflection problem,

- determination of the material model of the viscoelastic layer and the values of its constants is a problem in itself. This multiparameter problem requires some compromise between the attempt to find an exact problem description and the assumption of a rationally sophisticated one,
- action of loads in longer duration on the plate structure identifies its rheological properties.

References

1. Chen Y.R., Chen L.W., Wang C.C., 2006, Axisymmetric dynamic instability of rotating polar orthotropic sandwich annular plates with a constrained damping layer, *Composite Structures*, **73**, 2, 290-302
2. Dumir P.C., Shingal L., 1985, Axisymmetric postbuckling of orthotropic thick annular plates, *Acta Mechanica*, **56**, 229-242
3. Hibbitt, Karlsson & Sorensen, Inc., 2000, ABAQUS/Standard User's Manual, version 6.1
4. Krizhevsky G., Stavsky Y., 1996, Refined theory for vibrations and buckling of laminated isotropic annular plates, *International Journal of Mechanical Sciences*, **38**, 5, 539-555
5. Majewski S., Maćkowski R., 1975, Creep of foamed plastics used as the core of a sandwich plate (in Polish), *Inżynieria i Budownictwo*, **3**, 127-131
6. Pawlus D., 2010, Dynamic stability of three-layered annular plates with a viscoelastic core (in Polish), *Scientific Bulletin of the Technical University of Łódź*, **1075**
7. Pawlus D., 2011a, Critical loads calculations of annular three-layered plates with soft elastic or viscoelastic core, *Archives of Civil and Mechanical Engineering*, **XI**, 4, 993-1009
8. Pawlus D., 2011b, Dynamic stability of three-layered annular plates with wavy forms of buckling, *Acta Mechanica*, **216**, 123-138
9. Pawlus D., 2011c, Solution to the problem of axisymmetric and asymmetric dynamic instability of three-layered annular plates, *Thin-Walled Structures*, **49**, 660-668
10. Paydar N., 1990, Axisymmetric buckling of an annular sandwich plate of varying thickness, *Composite Structures*, **15**, 149-159
11. Romanów F., 1995, Strength of Sandwich Constructions (in Polish), WSI in Zielona Góra, Poland
12. Skrzypek J., 1986, Plasticity and Creep (in Polish), Warszawa, PWN
13. Standard, PN-84/B-03230, *Lightweight curtain walls and roofs of sandwich and rib panels. Static calculation and design* (in Polish), Standardization Publishers "Alfa", Warszawa, 1985
14. Tanov R., Tabiei A., 1998, Static and dynamic buckling of laminated composite shells, *Proceedings of the 5-th International LS-DYNA Users Conference*, South Field, MI.
15. Volmir C., 1967, *Stability of Deformed Systems* (in Russian), Moskwa, Science
16. Volmir C., 1972, *Nonlinear Dynamics of Plates and Shells* (in Russian), Moskwa, Science
17. Wang H.J., Chen L.W., 2002, Vibration and damping analysis of a three-layered composite annular plate with a viscoelastic mid-layer, *Composite Structures*, **58**, 563-570
18. Wang H.J., Chen L.W., 2004, Axisymmetric dynamic stability of rotating sandwich circular plates, *Journal of Vibration and Acoustics*, **126**, 407-415

Manuscript received February 21, 2014; accepted for print March 26, 2015

JOURNAL OF THEORETICAL AND APPLIED MECHANICS
53, 4, pp. 789-798, Warsaw 2015
DOI: 10.15632/jtam-pl.53.4.789

DIFFERENCES IN ENERGY FLOW IN THREE DIRECTIONS IN HUMAN-TOOL BIOMECHANICAL SYSTEMS BASED ON SPATIAL HUMAN PHYSICAL MODELS SPECIFIED IN THE ISO 10068:2012 STANDARD

Marian Witalis Dobry, Tomasz Hermann
Poznan University of Technology, Institute of Applied Mechanics, Poznań, Poland
e-mail: marian.dobry@put.poznan.pl; tomasz.hermann@put.poznan.pl

The article presents the differences in energy flow for two human physical models from ISO 10068:2012. The models are compared on the basis of a numerical simulation of energy flow implemented with MATLAB/simulink software. For purposes of comparison, the dynamics of the two Human-Tool systems is mathematically modelled and then used to derive their energy models. The model dynamic structures are fully specified in order to determine and compare three kinds of powers. The study revealed differences between the model characteristics when analysed along different directions of vibrations and as a whole.

Keywords: biomechanical system, energy flow, hand-arm vibrations

1. Introduction

Every physical model of a system requires a corresponding mathematical model. Developing a valid mathematical model is essential for purposes of analysing the system behaviour in different conditions (Cannon, 1973; Żółtowski, 2002). The construction of an appropriate model is not an easy task and should always be preceded by numerous verification studies. In an effort to create more complex models, it is sometimes more practical to take advantage of a model that has already been verified and use it as a component of a larger system. This approach may prove problematic when there is a number of competing models that can be used to describe a given system and each one is supposed to correctly represent the way the system functions. This is the kind of problem we are faced with when trying to choose a model representing responses of the human body to mechanical vibrations (Dobry and Hermann, 2014, 2015).

Research focused on developing discrete models of the human body dates back to the 1970s. Major contributions in this area were made in the studies by Griffin (1990), Meltzer (1981), Reynolds and Soedel (1972) and many others. Nowadays the impact of vibrations on the human body can be analysed by selecting one of many existing biomechanical models of the hand or the hand-arm system (Dobry and Hermann, 2014; Książek, 1996; Rakheja *et al.*, 2002; ISO 10068:1998 and ISO 10068:2012). It is worth pointing out that in order to create a physical model, and hence a mathematical model of a system, one needs to have a wide knowledge of its structure and properties as well as relationships and processes that occur within it. It should also be remembered that a model is, by definition, a certain idealised or simplified representation of reality (Cannon, 1973; Żółtowski, 2002). This is exactly the kind of situation we are facing when trying to choose a model to analyse theoretically the impact of vibration on the human body. The available models differ from one another with respect to the number of components included in their dynamic structure, the kinds of joints and the number of degrees of freedom. This affects the extent to which the reality is simplified and the way the components are connected. Figure 1 shows selected structures of human biomechanical models used in the dynamic analysis of the impact of local vibrations. What is more, the character and the degree of simplification is related to the knowledge, awareness and needs of the researcher. Finally, it should be added that in this case all models must presuppose the same characteristic of motion of the model and the real system.

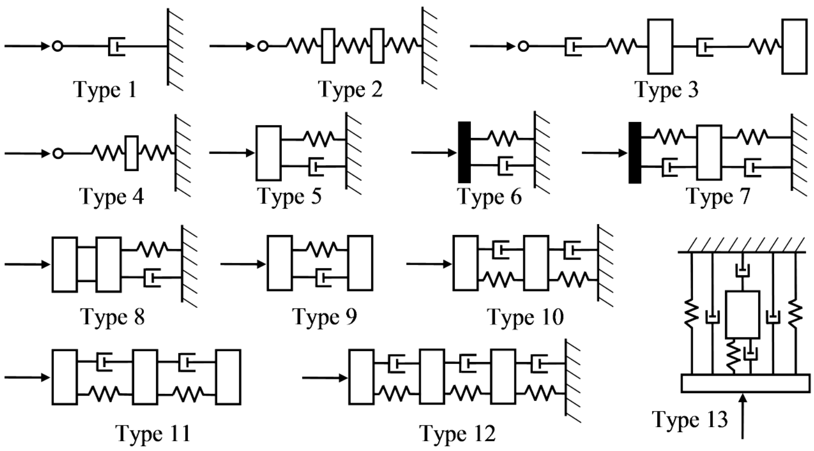

Fig. 1. Structures of human biomechanical models used to analyze the impact of local vibrations (Książek, 1996)

Hence, while constructing a model, it is, above all, necessary to ensure the same response of the model and the real system to the excitation. However, the model should not be determined only on the basis of the relationship between input and output values or else the system to be analysed will resemble a black box. As a result, any conclusions drawn from such a model will most likely be imprecise, especially with respect to the impact of vibrations on the human body. It can be demonstrated that a system modelled with this approach disregards some unknown properties. Hence, while the response of the model is important, what also needs to be taken into account is adequate internal structure of the model. Only this kind of similarity between the model and the original system can ensure the most accurate information (Żółtowski, 2002).

Consequently, one can ask what distinguishes the models used to analyse the human response to mechanical vibrations? This question is particularly justified when one considers that the relevant standards, ISO 10068:1998 and ISO 10068:2012, contain a number of different human physical models. The fact is that work on the development of new models (ISO 10068:2012) has been conducted for a few years and presented in numerous publications, e.g. (Dong *et al.*, 2007, 2010, 2013). Models described in the withdrawn standard ISO 10068:1998 have also been verified and approved and have been in use all over the world for many years. The facts mentioned above may help to appreciate the complex nature of modelling and model verification and the difficulty faced by those who need to choose one of the available models.

The present article describes an energy method used for comparative assessment of human physical models, specifically the Human-Tool model. The application of this procedure facilitates a comparison of the biomechanical Human-Tool systems (Dobry, 1998, 2001, 2012; Dobry and Herman, 2014). It is a synchronous method, in which values resulting from the dynamic analysis are used in real time as the input in the energy analysis. By applying an energy model of the system, it is possible to switch from the conventional dynamic analysis to the energy analysis conducted in the domain of energy flow. In the present study, the criterion for assessing the model validity is the equality of energy phenomena occurring in the dynamic structure during operation (Dobry, 1998, 2001, 2012; Dobry and Herman, 2014). The aim of the study is to analyse two models of the Human-Tool system, which are constructed using the physical models specified in ISO 10068:2012 – models 1 and 2.

2. Energy models of Human-Tool systems

Physical models of the Human-Tool systems are constructed using human dynamic models from ISO 10068:2012. The models specified in the standard are discrete models, where specific points of reduction are connected by means of spring and damping systems. Basic parameters of the models are specified in ISO 10068:2012 – see Table 1 and 2.

The Human-Tool systems in question are constructed by combining human models with tool models. The purpose of the modelling process is to create a simple model of a person operating a power tool, e.g. an angle grinder. For this purpose, the energy analysis needs to account for the tool mass m_N, its vibration frequency f and the character of the driving force $F(t)$.

Table 1. Values of dynamic parameters for the model with two points of reduction – model 1 (ISO 10068:2012)

Parameter	Unit	k-th direction of vibration		
		x	y	z
m_{1k}	kg	0.5479	0.5374	1.2458
m_{2k}	kg	0.0391	0.0100	0.0742
k_{1k}	N/m	400	400	1000
k_{2k}	N/m	0	17648	50000
c_{1k}	N·s/m	22.5	38.3	108.1
c_{2k}	N·s/m	202.6	75.5	142.4

Table 2. Values of dynamic parameters for the model with three points of reduction – model 2 (ISO 10068:2012)

Parameter	Unit	k-th direction of vibration		
		x	y	z
m_{1k}	kg	0.4129	0.7600	1.1252
m_{2k}	kg	0.0736	0.0521	0.0769
m_{3k}	kg	0.0163	0.0060	0.0200
m_{4k}	kg	0.0100	0.0028	0.0100
k_{1k}	N/m	400	500	1000
k_{2k}	N/m	200	100	12000
k_{3k}	N/m	4000	4907	43635
k_{4k}	N/m	8000	17943	174542
c_{1k}	N·s/m	20.0	28.1	111.5
c_{2k}	N·s/m	100	39.7	39.3
c_{3k}	N·s/m	144.6	50.7	86.8
c_{4k}	N·s/m	79.9	14.3	121.0

In the study, the tool model is limited to one mass $m_N = 5\,\mathrm{kg}$. To enable comparisons between the models, it is assumed that a sinusoidally varying driving force $F(t)$ with an amplitude of 200 N acts on the biomechanical systems in every direction. This kind of force is usually generated in angle grinders due to mechanical wear. The last parameter, namely the vibration frequency, is set at $f = 30\,\mathrm{Hz}$ and is taken into account in the driving force. Figure 2 shows the final models of the Human-Tool systems.

The following step involves development of mathematical models of the dynamic structures using Lagrange equations of the second kind given by (Cannon, 1973; Żółtowski, 2002)

$$\frac{d}{dt}\Big(\frac{\partial E}{\partial \dot{q}_j}\Big) - \frac{\partial E}{\partial q_j} = Q_j + Q_{jP} + Q_{jR} \qquad j = 1, 2, \ldots, s \tag{2.1}$$

where E is the kinetic energy of the system, q_j – generalized coordinates, $\dot{q}_j$ – generalized velocities, Q_j – external active forces, Q_{jP} – potential forces, Q_{jR} – forces of dissipation, s – number of degrees of freedom.

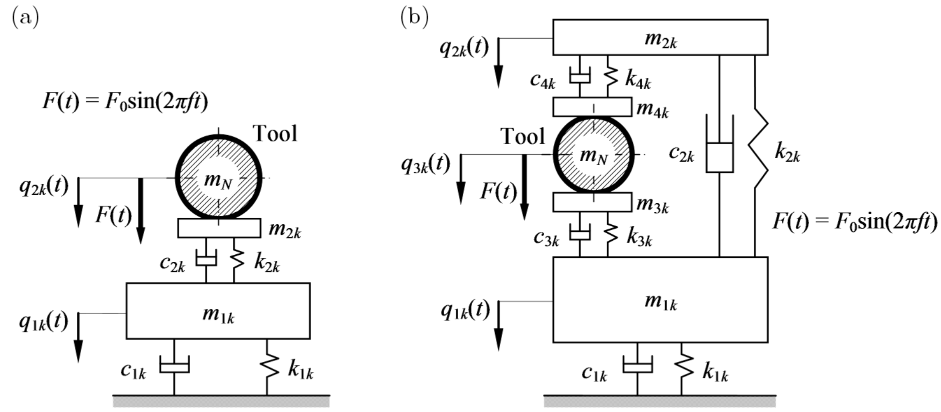

Fig. 2. A synthesis of the ISO 10068:2012-based human physical models with the tool model: (a) model 1 and tool; (b) model 2 and tool (ISO 10068:2012)

The mathematical models of the Human-Tool systems are constructed using generalized coordinates. Since three directions of vibration are taken into account, it is necessary to formulate three differential equations of motion. Hence, a complete analysis of the impact of vibration on the human body (along the x, y and z axes), requires:

a) for the model with two points of reduction (Fig. 2a) – 6 generalized coordinates and 6 differential equations of motion, since the model has 2 two points of reduction and 6 degrees of freedom,
b) for the model with three points of reduction (Fig. 2b) – 9 generalized coordinates and 9 differential equations of motion, since the model has 3 two points of reduction and 9 degrees of freedom.

Since the models of interest have the same structure in each direction of vibrations, in accordance with the ISO standard, it is sufficient to present 2 general differential equations of motion for the model with two points of reduction and 3 general differential equations of motion for the model with three points of reduction. The equations for the x, y and z directions can be obtained by substituting the values of dynamic parameters for each direction, see Table 1 and 2, and introducing generalized coordinates for this direction.

The first step in the formulation of general differential equations involves introduction of generalized coordinates. For the model shown in Fig. 2, the following generalized coordinates are used (Fig. 2a)

$j = 1 \quad \Rightarrow \quad q_{1k} = u_{1k}(t) \quad$ – displacement of mass m_{1k} in the k-th direction

$j = 2 \quad \Rightarrow \quad q_{2k} = u_{2k}(t) \quad$ – displacement of mass m_{2k} and m_N in the k-th direction, where m_N is the mass of the hand-held power tool for each direction

For the combination of the ISO 10068:2012-based model – model 2 and the tool model (Fig. 2b), the following generalized coordinates are used

$j = 1 \quad \Rightarrow \quad q_{1k} = u_{1k}(t) \quad -$ displacement of mass m_{1k} in k-th direction

$j = 2 \quad \Rightarrow \quad q_{2k} = u_{2k}(t) \quad -$ displacement of mass m_{2k} in k-th direction

$j = 3 \quad \Rightarrow \quad q_{3k} = u_{3k}(t) \quad -$ displacement of mass m_{3k}, m_{4k} and m_N in k-th direction

After applying the generalized coordinates defined above, the general mathematical model of the Human-Tool system (Fig. 2a), can be written down as

$$\begin{aligned} j=1 \qquad & m_{1k}\ddot{u}_{1k} + (c_{1k}+c_{2k})\dot{u}_{1k} + (k_{1k}+k_{2k})u_k - c_{2k}\dot{u}_{2k} - k_{2k}u_{2k} = 0 \\ j=2 \qquad & (m_{2k}+m_N)\ddot{u}_{2k} + c_{2k}\dot{u}_{2k} + k_{2k}u_{2k} - c_{2k}\dot{u}_{1k} - k_{2k}u_{1k} = F_0\sin(2\pi f t) \end{aligned} \tag{2.2}$$

The general mathematical model of the combined model consisting of the ISO 10068:2012-based model and the tool model (Fig. 2b) is given by three equations

$$\begin{aligned} j=1 \qquad & m_{1k}\ddot{u}_{1k} + (c_{1k}+c_{2k}+c_{3k})\dot{u}_{1k} + (k_{1k}+k_{2k}+k_{3k})u_{1k} - c_{3k}\dot{u}_{3k} - k_{3k}u_{3k} \\ & -c_{2k}\dot{u}_{2k} - k_{2k}u_{2k} = 0 \\ j=2 \qquad & m_{2k}\ddot{u}_{2k} + (c_{2k}+c_{4k})\dot{u}_{2k} + (k_{2k}+k_{4k})u_{2k} - c_{2k}\dot{u}_{1k} - k_{2k}u_{1k} - c_{4k}\dot{u}_{3k} \\ & -k_{4k}u_{3k} = 0 \\ j=3 \qquad & (m_{3k}+m_{4k}+m_N)\ddot{u}_{3k} + (c_{3k}+c_{4k})\dot{u}_{3k} + (k_{3k}+k_{4k})u_{3k} - c_{4k}\dot{u}_{2k} \\ & -k_{4k}u_{2k} - c_{3k}\dot{u}_{1k} - k_{3k}u_{1k} = F_0\sin(2\pi f t) \end{aligned} \tag{2.3}$$

General differential equations of motion (2.2) and (2.3) are used to construct energy models of the Human-Tool systems of interest by applying the First Principle of Energy Flow in a Mechanical System (Dobry, 1998, 2001, 2012). This approach enables switching from the conventional dynamic analysis conducted in terms of displacement amplitudes, velocities and accelerations to the energy analysis in terms of energy flow. The general energy model of the Human-Tool system with two points of reduction, Fig. 2a, has the following form

$$\begin{aligned} j=1 \qquad & \int_0^t |m_{1k}\ddot{u}_{1k}\dot{u}_{1k}|\,dt + \int_0^t |(c_{1k}+c_{2k})\dot{u}_{1k}^2|\,dt + \int_0^t |(k_{1k}+k_{2k})u_k\dot{u}_{1k}|\,dt \\ & -\int_0^t |c_{2k}\dot{u}_{2k}\dot{u}_{1k}|\,dt - \int_0^t |k_{2k}u_{2k}\dot{u}_{1k}|\,dt = 0 \\ j=2 \qquad & \int_0^t |(m_{2k}+m_N)\ddot{u}_{2k}\dot{u}_{2k}|\,dt + \int_0^t |c_{2k}\dot{u}_{2k}^2|\,dt + \int_0^t |k_{2k}u_{2k}\dot{u}_{2k}|\,dt \\ & -\int_0^t |c_{2k}\dot{u}_{1k}\dot{u}_{2k}|\,dt - \int_0^t |k_{2k}u_{1k}\dot{u}_{2k}|\,dt = \int_0^t |F_0\sin(2\pi f t)\dot{u}_{2k}|\,dt \end{aligned} \tag{2.4}$$

The general energy model of the second Human-Tool system, Fig. 2b, is given by

$$\begin{aligned} j=1 \qquad & \int_0^t |m_{1k}\ddot{u}_{1k}\dot{u}_{1k}|\,dt + \int_0^t |(c_{1k}+c_{2k}+c_{3k})\dot{u}_{1k}^2|\,dt + \int_0^t |(k_{1k}+k_{2k}+k_{3k})u_{1k}\dot{u}_{1k}|\,dt \\ & -\int_0^t |c_{3k}\dot{u}_{3k}\dot{u}_{1k}|\,dt - \int_0^t |k_{3k}u_{3k}\dot{u}_{1k}|\,dt - \int_0^t |c_{2k}\dot{u}_{2k}\dot{u}_{1k}|\,dt - \int_0^t |k_{2k}u_{2k}\dot{u}_{1k}|\,dt = 0 \\ j=2 \qquad & \int_0^t |m_{2k}\ddot{u}_{2k}\dot{u}_{2k}|\,dt + \int_0^t |(c_{2k}+c_{4k})\dot{u}_{2k}^2|\,dt + \int_0^t |(k_{2k}+k_{4k})u_{2k}\dot{u}_{2k}|\,dt \\ & -\int_0^t |c_{2k}\dot{u}_{1k}\dot{u}_{2k}|\,dt - \int_0^t |k_{2k}u_{1k}\dot{u}_{2k}|\,dt - \int_0^t |c_{4k}\dot{u}_{3k}\dot{u}_{2k}|\,dt - \int_0^t |k_{4k}u_{3k}\dot{u}_{2k}|\,dt = 0 \\ j=3 \qquad & \int_0^t |(m_{3k}+m_{4k}+m_N)\ddot{u}_{3k}\dot{u}_{3k}|\,dt + \int_0^t |(c_{3k}+c_{4k})\dot{u}_{3k}^2|\,dt + \int_0^t |(k_{3k}+k_{4k})u_{3k}\dot{u}_{3k}|\,dt \\ & -\int_0^t |c_{4k}\dot{u}_{2k}\dot{u}_{3k}|\,dt - \int_0^t |k_{4k}u_{2k}\dot{u}_{3k}|\,dt - \int_0^t |c_{3k}\dot{u}_{1k}\dot{u}_{3k}|\,dt - \int_0^t |k_{3k}u_{1k}\dot{u}_{3k}|\,dt \\ & = \int_0^t |F_0\sin(2\pi f t)\dot{u}_{3k}|\,dt \end{aligned} \tag{2.5}$$

The energy models of two Human-Tool systems (2.4) and (2.5) are solved using a simulation programme implemented in the MATLAB/simulink software. The simulation time t was 300 seconds. Additionally, integration time steps used in the simulation were set to range from a maximum of 0.0001 to a minimum of 0.00001 second, with a tolerance of 0.001. Simulation-based inputs of the energy of inertia, dissipation and elasticity were used to compare the models. The models were regarded as comparable when the inputs of respective types of energy were equal.

3. Energy comparison of the human-tool systems

On the basis of the First Principle of Energy Flow in a Mechanical System (Dobry, 1998, 2001, 2012) it is possible to determine the precise amounts of the three kinds of energy for each Human-Tool system. Energy inputs of inertia, dissipation and elasticity can be obtained by integrating the absolute values of dynamic forces. In this particular case, these are simply sums in which the absolute values of specific types of power are integrated within simulation time equal to 300 seconds.

For the Human-Tool system based on the model with three points of reduction from ISO 10068:2012 – Fig. 2b, the energy inputs are calculated using the following formulas:
a) energy of inertia for the k-th direction, expressed in [J]

$$E_{3k-\mathrm{INE}} = \int\limits_0^t |m_{1k}\ddot{u}_{1k}\dot{u}_{1k}|\,dt + \int\limits_0^t |m_{2k}\ddot{u}_{2k}\dot{u}_{2k}|\,dt + \int\limits_0^t |(m_{3k}+m_{4k}+m_N)\ddot{u}_{3k}\dot{u}_{3k}|\,dt \tag{3.1}$$

b) energy of dissipation for the k-th direction, expressed in [J]

$$E_{3k-\mathrm{DIS}} = \int\limits_0^t |(c_{1k}+c_{2k}+c_{3k})\dot{u}_{1k}^2|\,dt + \int\limits_0^t |(c_{2k}+c_{4k})\dot{u}_{2k}^2|\,dt + \int\limits_0^t |(c_{3k}+c_{4k})\dot{u}_{3k}^2|\,dt \tag{3.2}$$

c) energy of elasticity for the k-th direction, expressed in [J]

$$\begin{aligned}E_{3k-\mathrm{ELA}} &= \int\limits_0^t |(k_{1k}+k_{2k}+k_{3k})u_{1k}\dot{u}_{1k}|\,dt + \int\limits_0^t |(k_{2k}+k_{4k})u_{2k}\dot{u}_{2k}|\,dt \\ &+ \int\limits_0^t |(k_{3k}+k_{4k})u_{3k}\dot{u}_{3k}|\,dt\end{aligned} \tag{3.3}$$

For the second Human-Tool system – Fig. 2a, the following formulas are derived to calculate:
a) energy of inertia for the k-th direction, expressed in [J]

$$E_{2k-\mathrm{INE}} = \int\limits_0^t |m_{1k}\ddot{u}_{1k}\dot{u}_{1k}|\,dt + \int\limits_0^t |(m_{2k}+m_N)\ddot{u}_{2k}\dot{u}_{2k}|\,dt \tag{3.4}$$

b) energy of dissipation for the k-th direction, expressed in [J]

$$E_{2k-\mathrm{DIS}} = \int\limits_0^t |(c_{1k}+c_{2k})\dot{u}_{1k}^2|\,dt + \int\limits_0^t |c_{2k}\dot{u}_{2k}^2|\,dt \tag{3.5}$$

c) energy of elasticity for the k-th direction, expressed in [J]

$$E_{2k-\mathrm{ELA}} = \int\limits_0^t |(k_{1k}+k_{2k})u_{1k}\dot{u}_{1k}|\,dt + \int\limits_0^t |k_{2k}u_{2k}\dot{u}_{2k}|\,dt \tag{3.6}$$

Table 3 presents the amounts of three types of energy, the combined energy input in each direction and the total energy input for the two Human-Tool systems of interest.

Table 3. Energy flow in the models of the Human-Tool systems

Model		Model 1 2 points of reduction			Model 2 3 points of reduction		
Direction		x	y	z	x	y	z
Energy input of	inertia $E_{\mathrm{INE}}(t)$ [J]	3749	4211	4406	3782	4078	4309
	dissipation $E_{\mathrm{DIS}}(t)$ [J]	2047	1266	2669	3591	1195	3967
	elasticity $E_{\mathrm{ELA}}(t)$ [J]	5	813	2226	486	1107	8950
Energy input – in one direction [J]		5801	6290	9301	7859	6380	17226
Total energy input [J]		21392			31465		

Using the values obtained by applying the energy method, it is possible to compare the two models from ISO 10068:2012. Figure 3 shows the percentages of the three kinds of energy in the two models in three directions. The percentages are calculated as ratios of energy kinds for the model with 3 points of reduction to their corresponding values for the model with 2 points of reduction. The relation can be written as

$$D_K = \frac{E_{3k-\mathrm{X}}}{E_{2k-\mathrm{X}}} \cdot 100\% \tag{3.7}$$

where: $E_{3k-\mathrm{X}}$ – energy input of inertia, dissipation and elasticity in the whole system, calculated as a sum of energy inputs from all points of reduction and obtained by adopting model 2 with three points of reduction – expressed in [J], $E_{2k-\mathrm{X}}$ – energy input of inertia, dissipation and elasticity in the whole system, calculated as a sum of energy inputs from all points of reduction and obtained by adopting model 1 with two points of reduction – expressed in [J].

A value exceeding 100% means that the energy input in model b is higher than in model a – see Fig. 2.

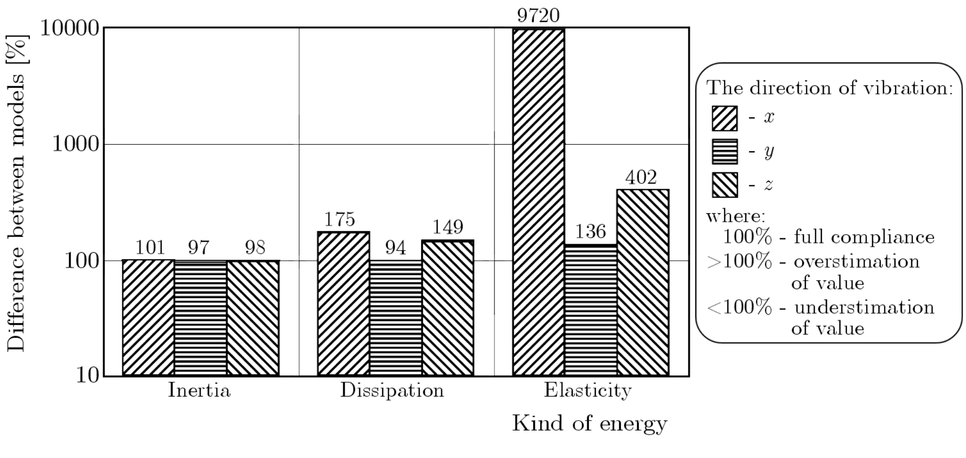

Fig. 3. Energy difference between the models depending on the direction of vibrations

The results shown in Fig. 3 indicate a lack of similarity between the models. The degree of similarity depends on two factors. The first one is the kind of energy. In this respect, the differences between the models range from:

- energy of inertia – between 1 and 3%,
- energy of dissipation – between 6 and 75%,
- energy of elasticity – between 36 and 9620%.

It should be noted that the 96-fold underestimation of the energy of elasticity evidently results from the model structure. With respect to the model with two points of reduction (Fig. 2a), the structure along the x direction of vibrations differs from the structure along the other directions. The authors of the model choose not to account for elasticity along this direction – denoted as k_{2x} (Table 1). The value of the dynamic parameter for this element equals 0, which contributes to model simplification and results in a considerably lower flow of energy through the model.

This fact does not affect the order of energy kinds in terms of the degree of similarity between the models, which is the same in all directions, with the highest level of equivalence for the energy of inertia, followed by the energy of dissipation and the lowest for the energy of elasticity.

The second factor which affects the degree of similarity is the direction of vibrations. The highest level of equivalence between the models is observed in the y direction – Fig. 3. In this case, differences in energy inputs between the levels are 3% for inertia, 6% for dissipation and 36% for elasticity.

For other directions, the order is not so consistent. In terms of the kind of energy, there is clearly more similarity between the models along the z direction than in the x direction.

The next aspect of the analysis is related to the combined energy input along one direction. If one looks only at the directional flow of the combined energy input consisting of the three kinds of energy, the resulting order is reverse. Figure 4 shows the percentage difference in combined energy inputs along the three directions between the two models.

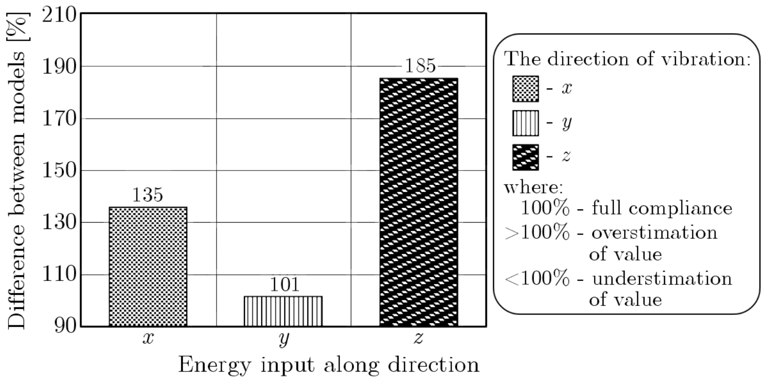

Fig. 4. The influence of the direction of vibrations on the increase in combined energy input along one direction

The two models of interest can also be analysed in terms of total energy input, which is calculated by summing up the directional flows for each model. From this point of view, the flow of energy in the model with three points of reduction is higher by 47% compared with the model with two points of reduction, see Table 3. This means that the human model chosen in the analysis plays a crucial role in determining the level of protection that is intended for the human operator of hand-held power tools: the technical standards that must be met by hand-held tools are significantly higher when the assessment of the impact of vibrations is based on the model with three points of reduction (Fig. 2b) compared to those based on the model with two points of reduction (Fig. 2a).

If we assume the acceptable tolerance between the models of no more than 5%, we considerably limit the extent to which the two models can be used interchangeably. With such a margin of error, the only aspect of the two models that can be regarded as comparable is the energy of inertia, see Fig. 3. Consequently, the models are not energy equivalent and can yield incomparable results in the theoretical analysis of the impact of vibrations on the human body.

4. Conclusions

Based on the above energy comparison of the Human-Tool models, we must conclude that the two models display considerable differences in terms of the similarity criterion, which is the equivalence between the predicted values of the three kinds of energy. The simulation results reveal the highest degree of similarity with respect to the energy of inertia (Fig. 3) with a difference of no more than 3%. There is no similarity in terms of the energy of dissipation or elasticity.

The differences are also manifested in the energy levels predicted by the models along the x, y and z directions (Fig. 4). In this case, the highest degree of equivalence can be observed along the y direction, with a difference of only 1%. It should be remembered, however, that the models are characterised by different internal structures. It can therefore be concluded that it is the internal structure of the models that directly affects the level of equivalence between the three kinds of energy. It is also worth pointing out that for both models the highest energy input can be observed along the z direction, which is shown in Table 3. This suggests that it is the most crucial direction from the point of view of the impact of vibrations of the human body.

When analysed in terms of total energy input along the three directions, the models differ from each other by as much as 47%. This means that the ISO 10068:2012 model with three points of reduction, see Fig. 2b, used in the theoretical study of the impact of vibrations on the human body will result in raising the technical requirements used in the assessment of power tools, which has to do with the increased flow of energy predicted by this model. It can be expected that the use of this model in the energy assessment of power tools will increase the requirements concerning their vibroisolation.

Acknowledgments

The study was co-financed by the Ministry of Science and Higher Education and was part of the research project (02/21/DSMK/3458) entitled: *Energy, diagnostic and acoustic problems in vibroacoustics.*

References

1. Cannon R.H. Jr., 1973, *Dynamics of Physical Systems* (in Polish), Wydawnictwa Naukowo-Techniczne
2. Dobry M.W., 1998, *Optimization of the Energy Flow in the Human-Tool Base System* (in Polish), Rozprawa habilitacyjna, Seria "Rozprawy" nr 330, ISSN 0551-6528, Wydawnictwo Politechniki Poznańskiej, Poznań
3. Dobry M. W., 2001, Energy diagnostics and assessment of dynamics of mechanical and biomechatronics systems, *Machine Dynamics Problems*, **25**, 35-54
4. Dobry M.W., 2012, *Fundamentals of Energy Diagnostics of Mechanical and Biomechanical Systems* (in Polish), Wydawnictwo Naukowe Instytutu Technologii Eksploatacji – PIB, Radom
5. Dobry M.W., Hermann T., 2014, Comparison of human physical models specified in ISO 10068:2012 based on the distribution of power, *Vibrations in Physical Systems*, **26**, 49-56
6. Dobry M.W., Hermann T., 2015, A comparison of human physical models based on the distribution of power in a dynamic structure in the case of hand-arm vibrations, *Journal of Theoretical and Applied Mechanics*, **53**, 1, 3-13
7. Dong R.G., Dong J.H., Wu J.Z., Rakheja S., 2007, Modelling of biodynamic responses distributed at the fingers and the palm of the human hand-arm system, *Journal of Biomechanics*, **40**, 2335-2340
8. Dong R.G., Rakheja S., McDowell T.W., Welcome D.E., Wu J.Z., 2010, Estimation of the biodynamic responses distributed at fingers and palm based on the total response of the hand-arm system, *International Journal of Industrial Ergonomics*, **40**, 425-436

9. Dong R.G., Welcome D.E., McDowell T.W., Wu J.Z., 2013, Modelling of the biodynamic responses distributed at the fingers and palm of the hand in three orthogonal directions, *Journal of Sound and Vibration*, **332**, 1125-1140

10. Griffin M.J., 1990, *Handbook of Human Vibration*, Academic Press, London

11. ISO 10068:1998, Mechanical vibration and shock – free, mechanical impedance of the human hand-arm system at the driving point

12. ISO 10068:2012, Mechanical vibration and shock – mechanical impedance of the human hand-arm system at the driving point

13. Książek A.M., 1996, Analysis of the existing biodynamic hand-arm models to isolation of a human – operator from vibrations emitted by the hand-held tools (in Polish), *Czasopismo Techniczne*, Wydawnictwo Politechniki Krakowskiej, 87-114

14. Meltzer G., 1981, A vibration model for the human hand-arm-system, *Studies in Environmental Science*, **13**, 210-221

15. Rakheja S., Wu J.Z., Dong R.G., Schopper A.W., 2002, A comparison of biodynamic models of the Human hand-arm system for applications to hand-held power tools, *Journal of Sound and Vibration*, **249**, 55-82

16. Reynolds D.D., Soedel W., 1972, Dynamic response of the hand-arm system to a sinusoidal input, *Journal of Sound and Vibration*, **21**, 339-353

17. Żółtowski B., 2002, *Study of the Dynamics of Machines* (in Polish), Markar – B.Ż., Bydgoszcz

Manuscript received January 23, 2015; accepted for print March 27, 2015

JOURNAL OF THEORETICAL
AND APPLIED MECHANICS
53, 4, pp. 799-809, Warsaw 2015
DOI: 10.15632/jtam-pl.53.4.799

EVALUATION OF SPECIFIC PROCESS PARAMETERS AND ULTRASONICALLY ACTIVATED INJECTION AFFECTING THE QUALITY OF FILLING IN THIN WALLED PLASTIC PARTS

Andrei Adam, Daniel Stan, Aurel Tulcan

Politehnica University Timisoara, Department of Materials and Manufacturing Engineering, Romania

e-mail: andreiadam83@yahoo.com

The paper presents a set of experiments focused on the study of rheological behavior of a polymer flowing through a narrow section at the forming by injection of thin-walled plastic parts. The paper addresses the use of ultrasonically activated injection for fabrication of polymeric parts with thin wall features. In the experiment, a part with six different geometric features has been created. The design-of-experiments approach is applied to correlate the quality of the parts with the processing parameters. Four processing parameters are investigated using a screening factorial experimentation plan to determine their possible effect on the filling quality of the moulded parts. The experiments have been conducted on a hot runner mould with two nests in which the final (nest) nozzle has been modified to host, as the central element, the ultrasonic horn of a sonic system. It has been found that the ultrasonic activation applied on the active part of the mould does not play an important role as a stand-alone factor but could amplify or strengthen the effect of classical setting parameters (and influence factors) of the process: the melt temperature and injection pressure. Because it is easier to stimulate and to control rheological properties of the melt by setting the intensity of ultrasonic energy and, more important, the effect is forthwith, the paper recommends the runner systems with ultrasonic activation as an alternative for the hot runner with heating elements.

Keywords: ultrasonic activation, design-of-experiments, rheological behavior of the polymer, thin-walled plastic parts

1. Introduction

Injection moulding is the most common forming method for the manufacturing of plastic parts. With high productivity, it is based on accurate replication of the nest. In the industrial design and manufacturing, it is always a challenge to make a proper compromise between the most desirable shape of parts, tooling cost, their weight and as well as strength and rigidity (Adam *et al.*, 2013). The primary concern is to respect the quality requirements for the moulded parts. Especially for thin-walled parts, difficulties in the process are due to poor rheological capabilities of the melt flowing through thin section (negative of the thin-walled).

Based on the previous research results, for the ultrasonic activation of the extrusion (Stan, 1999; Stan *et al.*, 2000), we supposed that the so called "thermo-pellicular effect" of the sonic activation of the polymer melt under pressure could also be obtained in injection conditions to improve the flow and replication capability of the melt in the above mentioned conditions.

The main approach to identify influential processing parameters in thin-wall injection moulding was by changing one parameter at a time while keeping the others constant, and then observing the effects of that parameter (Wimberger-Friedl, 2000). This approach was inherited from conventional injection moulding. It was useful in drawing basic conclusions about how each parameter affects the filling quality of the moulded part. This approach, however, has two main limitations (Eriksson *et al.*, 2008): the first limitation is that it is relatively time consuming when many parameters are being investigated, the second drawback is that it does not take into consideration the effect of the interaction between two or more parameters, which is relevant consideration in a complex process such as ultrasonically activated injection used on thin-walled plastic parts.

In this paper, the design-of-experiments (DOE) approach is introduced into the research domain as a useful alternative to conventional methods. A number of research groups have used a variety of DOE experimentation plans to investigate the relation between processing parameters and part filling quality (Attia *et al.*, 2009). The responses chosen for the experiments included filling quality of micro-sized channels (Mönkkönen *et al.*, 2002), part dimensions (Zhao *et al.* 2003; Aufiero, 2005; Baltes and Tierean, 2009; Pirskanen *et al.* 2005; Malloy, 1994) and flow length (Jung *et al.*, 2007).

Results presented in the literature show that different DOE designs yield different outputs. For example, there is disagreement about the importance of holding pressure and injection speed. Furthermore, certain experiments have highlighted interactions between processing parameters which have not been seen in other works. These differences in experimental results may be due to different geometrical shapes as well as polymers and experimental set-ups used in each experiment (Baltes and Tierean, 2009). It would, therefore, seem reasonable to claim that, at present, significant processing parameters in thin wall injection are identified on case-by-case basis and cannot be generalized for all situations.

This paper addresses the effects of ultrasonically activated injection and specific processing parameters on the filling quality for thin walled plastic parts through the design-of-experiments (DOE) approach.

2. Experimental part

2.1. Mould design

Mould flow simulations have been carried out using the finite element method (FEM) which is one of the best methods to perform various computer and engineering simulations. This method incorporates programs that have become essential parts of modern computer aided design (Bariani *et al.*, 2007).

Generally, using computer aided simulation in plastics technology, consists in assumption of various scenarios with a certain number of injection points with different locations in relation to the 3D configuration of the part to be injected with various injection point lengths and diameters, and determining the correct size of the gate. For parts with thin walls this kind of the engineering approach is very important because the location of the injection point should be achieved as effectively as possible, so as to provide balanced mold filling (Chang, 2007).

For the experiment, a geometric part has been created that has flow channels with thickness (gap, i) of 0.2 mm, 0.3 mm, 0.4 mm, 0.5 mm and 0.6 mm (Fig. 1).

The experiments were done with the following injection parameters:

1. $T_{inj} = 230°\mathrm{C}$, $P_{inj} = 200\,\mathrm{MPa}$ (2000 bar),
2. $T_{inj} = 280°\mathrm{C}$, $P_{inj} = 200\,\mathrm{MPa}$ (2000 bar).

In the first case, the results show that in the flow channels with smaler gaps the injected material (ABS) does not completely fill the whole volume (Fig. 2). The significance of the colours are: orange shows no problems with the flow rate and red/grey that there will be problems with flow and maybe no complete filling of the cavity.

In the second case, at a higher injection temperature, the results show that the flow channels are completly filled, but for smaller gaps ($i = 0,\,2$ and $0,\,3$), there are still some issues (Fig. 3).

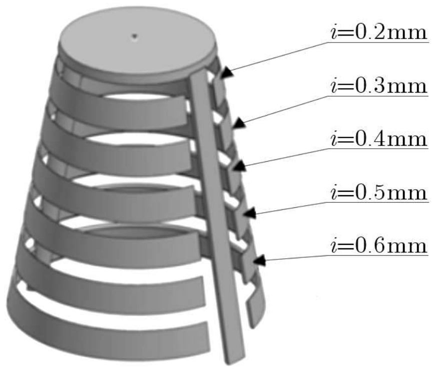

Fig. 1. Proposed geometrical model of the injected part

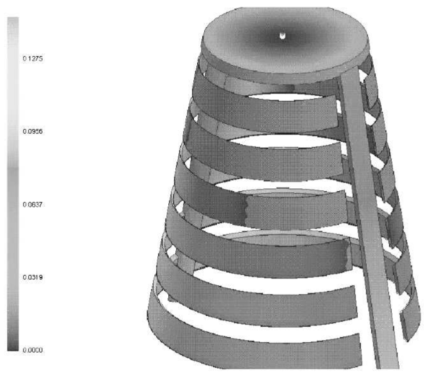

Fig. 2. Flow simulations, first case

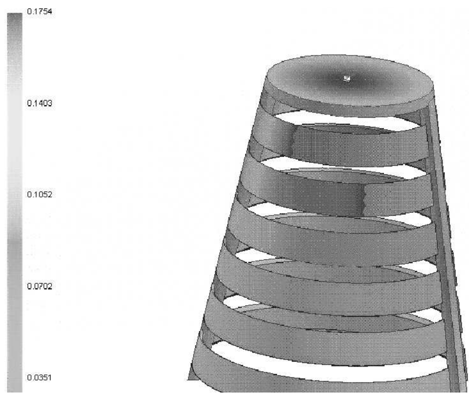

Fig. 3. Flow simulations, second case

2.2. Factorial experiment

For the experiment, we have chosen a patented invention (Fig. 4). The patent (Patent No. 118576 B/2003) relates to an inventive concept for the design of hot-runner injection molds in which to improve the nests filling and quality of the parts, an ultrasonic converter (ultrasonic transducer (1) + concentrator wave adapter (2)) is placed in the hot block (plate) (3) centered on each final nozzle (4), so that in the proximity of the injection point (gate) (5) a powerful thermo-pellicular effect is created in the molten plastic flowing in contact with the wave adapter and to the top of this (Iclanzan *et al.*, 2008). In order to estimate the effects of ultrasonic activation, the second nest was placed in the mould with a classic (without ultrasonic activation) final injection nozzle.

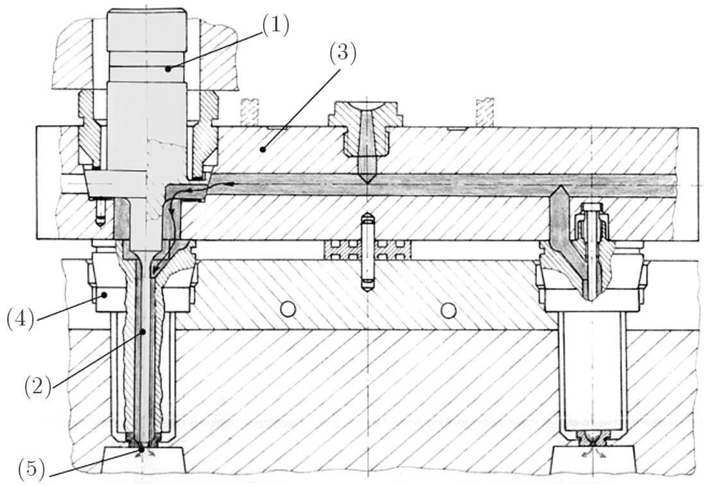

Fig. 4. Ultrasonically activated mould

The material used for the tests was acrylonitrile-butadiene-styrene (ABS) because of its higher injection load resistance and a significant melt flow rate (MFI=35 g/10 min).

The tests were carried out on an injection mould (Fig. 5) that was mounted on the Krauss Maffei KM 200-700 C2 injection machine.

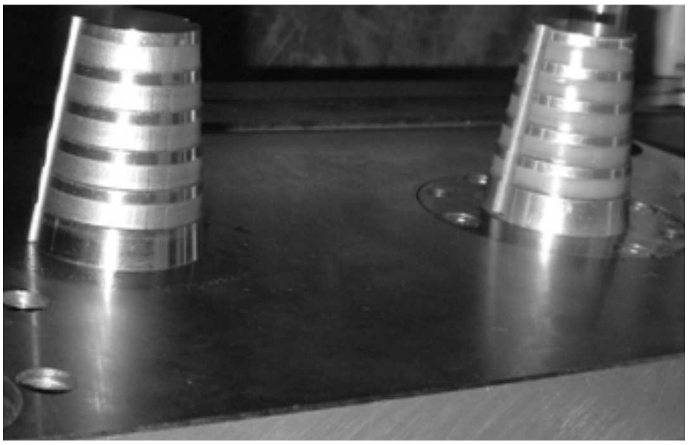

Fig. 5. Cores of the injection mould

The injected parts that were obtained during the experiments (Fig. 6) were measured along the length traveled by the plastic flow through the narrow cavities of the "ribs", as the amount of rheological capability of the melt.

The experimental plan was designed for four influence factors (independent variables), three of them being the classical setting parameters for the control of rheological properties of the melt: pressure, temperature and gap (opening of the free flowing section) plus the fourth factor, ultrasonic activation of the injection (nest) nozzle. The response (dependent) variable considered to be relevant for the assessment of rheological capabilities of the melt was the length of the flow until solidification. The levels of the independent variables are presented in Table 1.

Experimental results obtained with and without ultrasonic activation are presented in Table 2.

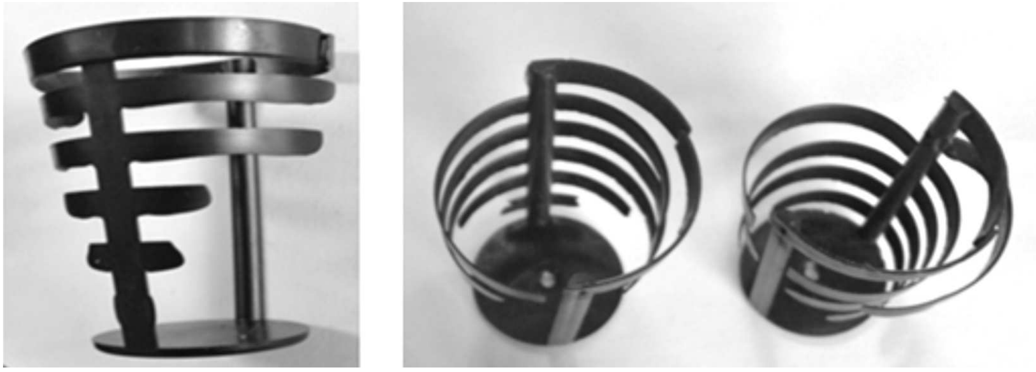

Fig. 6. Parts obtained for different p-T combinations

Table 1. Levels of the independent variables

Pressure [bar]		Temperature [°C]		Gap [mm]		Ultrasonic activation at maximum amplitude (US)	
−1	+1	−1	+1	−1	+1	−1	+1
1500	2000	230	280	0.2	0.5	without US	US of the injection nozzle: Frequency: 35 kHz Power: 10% ($P_{nom} = 1$ kW)

Table 2. Experimental design results

Exp. ctr.	Independent variables of the experimental design (coded)				Dependent variable
	Pressure P [bar]	Temperature T [°C]	Gap i [mm]	Ultrasoinc activation US [−1 =NO; +1 =YES]	Lenght of the rib L [mm]
1	+1	−1	+1	+1	30
2	+1	+1	+1	+1	43
3	+1	−1	−1	−1	2
4	−1	+1	+1	−1	32
5	−1	−1	−1	−1	0
6	−1	−1	+1	+1	24
7	−1	+1	−1	−1	5
8	+1	−1	+1	−1	26
9	−1	+1	+1	+1	36
10	−1	+1	−1	+1	14
11	−1	−1	+1	−1	21
12	+1	−1	−1	+1	7
13	−1	−1	−1	+1	6
14	+1	+1	−1	−1	10
15	+1	+1	+1	−1	41
16	+1	+1	−1	+1	18

3. Experimental results

For the processing of the results, the Statgraphics^{TM} program has been used. The primary influence factors that are taken into consideration are pressure, temperature and gap. Table 3 shows each of the estimated effects and interactions. Also shown is the standard error of each effect, which measures their sampling error, and that the largest variance inflation factor (V.I.F.)

equals 1.0. For a perfectly orthogonal design, all factors would be equal to 1. Standard errors are based on the total error with 5 d.f.

Table 3. Estimated effects for the travelled length

Effect	Estimate	Stnd. error	V.I.F.
Average	19.6875	0.232177	
A: Injection pressure	4.875	0.464354	1.0
B: Injection temperature	10.375	0.464354	1.0
C: Gap	23.875	0.464354	1.0
D: Ultrasonic activation	5.125	0.464354	1.0
AB	1.375	0.464354	1.0
AC	1.875	0.464354	1.0
AD	−0.375	0.464354	1.0
BC	2.375	0.464354	1.0
BD	0.625	0.464354	1.0
CD	−1.875	0.464354	1.0

In order to test the statistical significance of the effects, the analysis of variance, called ANOVA has been used. The results obtained are shown in Table 3. The four independent variables are encoded by A, B, C and D, and the interaction by AB, AC, AD, BC, BD and CD which are products of the independent factors.

Table 4. ANOVA chart for the travelled length

Source	Sum of squares	D.f.	Mean square	F-ratio	P-value
A: Injection pressure	95.0625	1	95.0625	110.22	0.0001
B: Injection temperature	430.563	1	430.563	499.20	0.0000
C: Gap	2280.06	1	2280.06	2643.55	0.0000
D: Ultrasoinc activation	105.063	1	105.063	121.81	0.0001
AB	7.5625	1	7.5625	8.77	0.0315
AC	14.0625	1	14.0625	16.30	0.0099
AD	0.5625	1	0.5625	0.65	0.4560
BC	22.5625	1	22.5625	26.16	0.0037
BD	1.5625	1	1.5625	1.81	0.2361
CD	14.0625	1	14.0625	16.30	0.0099
Total error	4.3125	5	0.8625		
Total (corr.)	2975.44	15			

R-squared = 99.8551%, R-squared (adjusted for d.f.) = 99.5652%
standard error of est. = 0.928709, mean absolute error = 0.445313
Durbin-Watson statistic = 1.7971 ($P = 0.4020$)
lag 1 residual autocorrelation = −0.0226449

The program determines, for each effect individually, the Fisher criteria which compare it with the F-distribution table (critical values), and finally establishes the importance of that factor which has a significant influence. In this case, the main factors and other three interactions have P-values less than 0.05, indicating that they are significantly different from zero at the 95.0% confidence level. The R-squared statistic indicates that the model as fitted explains 99.85% of the variability in the Travelled length. The adjusted R-squared statistic, which is more suitable for comparing models with different numbers of independent variables, is 99.56%, which shows that the mathematical modeling of the phenomenon is very good.

The influence of the travelled lenght can be seen in the Pareto chart (Fig. 7), where the vertical line represented for $P = 0.05$ separates the significant factors from the others. The fact that the release is random can also be seen in Fig. 8, where it can be observed that there is no systematic arrangement between the experimentally obtained results and the residual dispersion from the values estimated by the mathematical model.

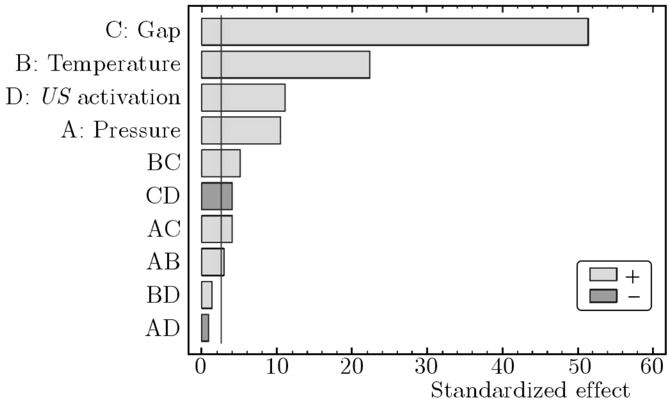

Fig. 7. Pareto chart for the traveled length

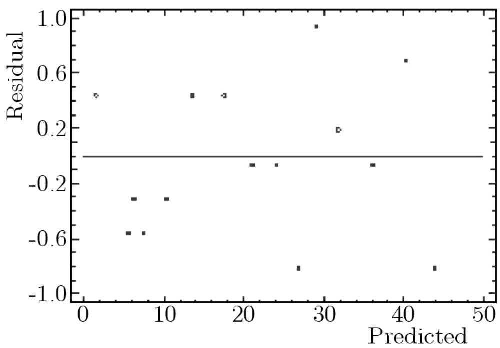

Fig. 8. Diagram of the residual

Based on the regression coefficients associated with the significant factors P, T, G, and ultrasonic activation (US), Table 5, the length travelled by the plastic material a mathematical model could be predicted Mathematical model

$$\begin{aligned}\text{Traveled length} &= 19.6875 + 2.4375P + 5.1875T + 11.9375G + 2.5625(US) \\ &\quad + 0.6875PT + 0.9375PG - 0.1875P(US) + 1.1875TG + 0.3125T(US) \\ &\quad - 0.9375G(US)\end{aligned} \tag{3.1}$$

In Fig. 9, the main effects of the response function, i.e. the length traveled are shown. It is noted that the four determinant factors and their interactions lead to an increase in the value of the travelled lenght by increasing their minimum to maximum.

In the next figures, variation of the estimated response surface (a) and its contours (b) corresponding to the length travelled by the plastic material depending on combinations of the four factors is shown.

4. Conclusions

The results of this paper show that for all the analyzed cases, with or without ultrasonic injection, the gap i is the main influence factor. This situation is expected because, as in the scientific literature, the lower limit usually considered for the gap (thinnest wall of the part) is

Table 5. Estimated regression coefficients for the length travelled by the plastic material

Coefficient	Estimate
Constant	19.6875
A: Presure	2.4375
B: Temperature	5.1875
C: Gap	11.9375
D: *US* activation	2.5625
AB	0.6875
AC	0.9375
AD	−0.1875
BC	1.1875
BD	0.3125
CD	−0.9375

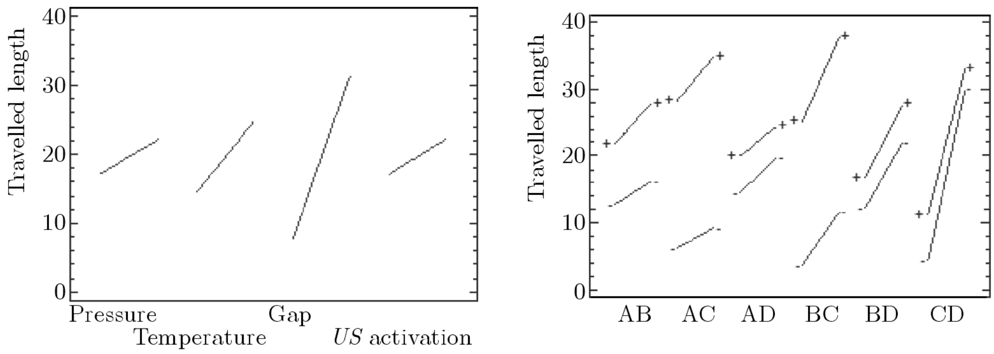

Fig. 9. Main effects on the travelled length

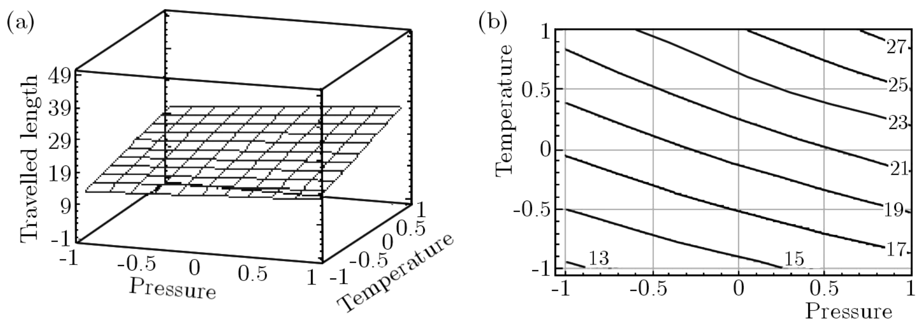

Fig. 10. The influence of pressure and temperature

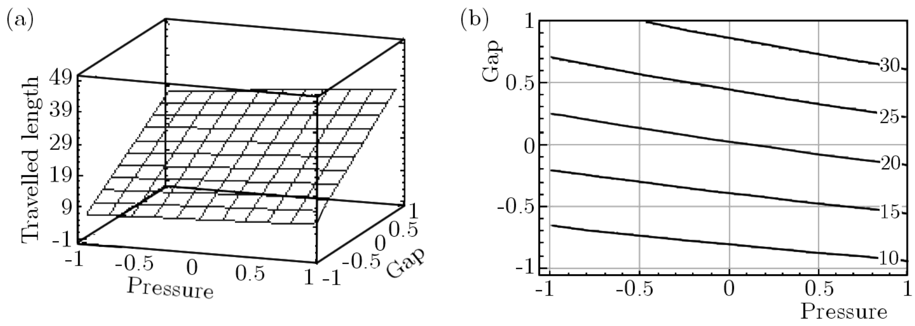

Fig. 11. The influence of pressure and gap

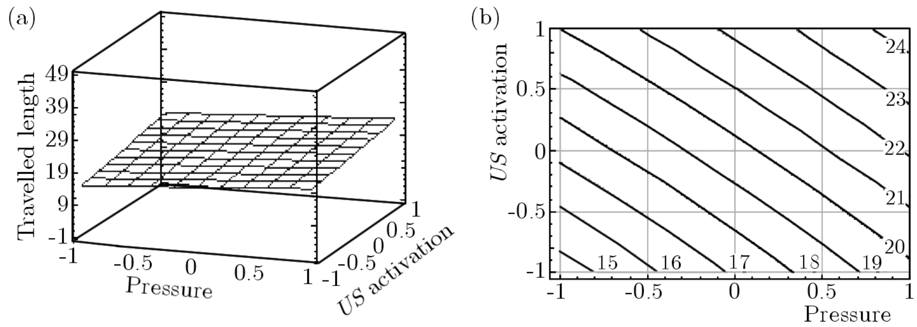

Fig. 12. The influence of pressure and US activation

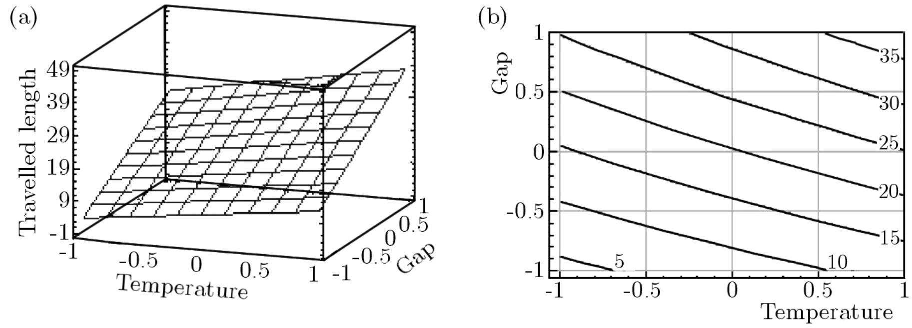

Fig. 13. The influence of temperature and gap

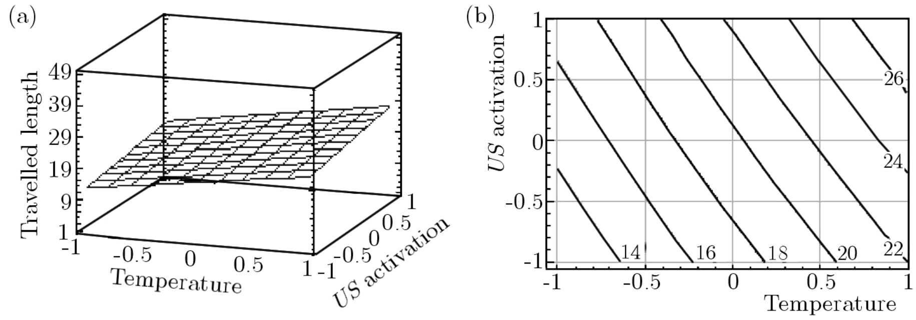

Fig. 14. The influence of temperature and US activation

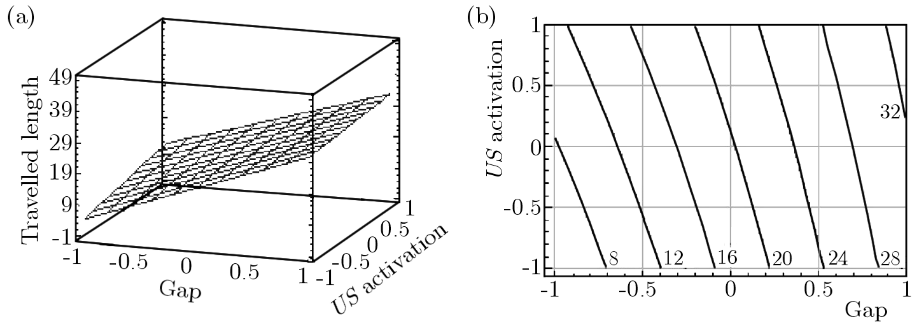

Fig. 15. The influence of gap an US activation

$i_{min} = 0.5$ mm. Any increase of the flowing gap, even by 0.1 mm, can decide on the capacity of the melt to fill that area and may dramatically affect the quality of the injected product.

Also the temperature T, shown in the Pareto chart (Fig. 7), is the second most important factor influencing the value of the objective function L.

Note that the ordering of the gap and the temperature in the first two positions is not affected by including the ultrasonic activation in the study. This situation shows no major interactions of the combined the i-US or T-US, excluding the possibility of spectacular effects from the ultrasonic activation.

However, the sets of factorial experiments 2^4 in which the nozzle is ultrasonically activated designate the US asthe third influencing factor after the contribution that it has to increase the flow path.

Moreover, comparing the Pareto chart, one can conclude that the ultrasonic activation is more important for the quality of the filling than the injection pressure (exceeding the influence of the pressure in the Pareto charts) that conventionally has an outstanding influence on the length travelled by the melt.

This situation is a solid argument for the implementation of the industrial ultrasonic activation in injection moldings.

Acknowledgment

This paper has been supported by the Sectoral Operational Programme Human Resources Development POSDRU/159/1.5/S/137516 financed from the European Social Fund and by the Romanian Government.

References

1. Adam A., Cosma C., Dume A.I., Jadaneantu S., Pop A., 2013, Integration of CAD CAM techniques in the development of an injection mould for automotive parts, *Proceedings of AMS 2013 International Conference*, Timisoara, Romania, 25-27

2. Attia U.M., Marson S., Alcock J.R., 2009 Micro-injection moulding of polymer microfluidic devices, *Microfluid Nanofluid*, **7**, 1-28

3. Aufiero R., 2005, The effect of process conditions on part quality in microinjection molding, *ANTEC: Proceedings of Annual Technical Conference*, Boston, MA, 36-40

4. Baltes L., Tierean M., 2009, Influence of the part shape on the polymer flow inside mould and overall strength, *Annals of DAAM for 2009, Proceedings of the 20th International DAAM Symposium*, **20**, 1, 1107-1108, ISSN: 1726-9679

5. Bariani P.F., Salvador M., Lucchetta G., 2007, Development of a test method for the rheological characterization of polymers under the injection molding process conditions, *Journal of Materials Processing Technology*, **191**, 1/3, 119-122

6. Chang D.H., 2007, *Rheology and Processing of Polymeric Materials*, Vol. 2, Polymer Processing, Oxford University Press Inc., New York, www.oup.com, ISBN: 978-0-19-518783-0

7. Eriksson L., Johansson N., Kettaneh-Wold N., Wikstrom C., Wold S., 2008, *Design of Experiments: Principles and Applications*, 3rd ed., Umetrics, Umeå

8. Iclanzan T., Serban I., Rotar D., Tut V., 2010, Ultrasonic activation, a possible alternative application in the microinjection molding, *International Journal of Material Forming*, **3**, suppl. 1, 547-550

9. Iclanzan T., Stan D., Abadie M., 2008, A possible new ultrasonic thermo-pellicular effect and applications, *International Journal of Material Forming*, 743-746, doi: 10.1007/s12289-008-0282-y

10. Jung W.-C., Heo Y.-M., Shin K.-H., Yoon G.-S., Chang S.-H,, 2007, An experimatal study on micro injection paramaters, *ANTEC: Proceedings of Annual Technical Conference*, Cincinnati, OH, 638-642

11. Malloy R., 1994, *Plastic Part Design for Injection Molding*, Carl Hanser Verlag, Munchen-New York

12. Mönkkönen K., Hietala J., Pääkkönen P., Pääkkönen E.J., Kaikuranta T., Pakkanen T.T., Jääskeläinen T., 2002, Replication of sub-micron features using amorphous thermoplastics, *Polymer Engineering and Science*, **42**, 1600-1608

13. Patent No. RO118576 B, 2003, *Ultrasonic activated mould* (in Romanian)

14. Pirskanen J., Immonen J., Kalima V., Pietarinen J., Siitonen S., Kuittinen M., Mönkkönen K., Pakkanen T., Suvanto M., Pääkkönen E.J., 2005, Replication of submicrometre features using microsystems technology, *Plastics Rubber and Composites*, **34**, 222-226

15. Stan D., 1999, Activation ultrasonique des thermo-plastiques lors de la mise en oeuvre par injection et extrusion, PhD Thesis, Univ. Montpellier, France

16. Sîrbu A.N., 2009, Theoretical and experimental research on the ultrasonic activation effect on the molten polymers rheology, PhD Thesis, Politehnica University of Timisoara

17. Sîrbu N.A., Iclănzan T., Oancă O., 2008, Conception, design and realization of the ultrasonic assembly for flow activation devices of the polymeric media, *Symposium of the Institute of Solid Mechanics, SISOM, Symposium of Acoustics*, Bucharest

18. Stan D., 1999, The ultrasonic activation of the thermo-plastics in forming processes by injection and extrusion (in French), PhD Thesis, 1999, USTL Montpellier 2, France, www.sudoc.fr/06769939, accessed: 20 febr. 2015

19. Stan D., Iclanzan T., Abadie M., 2000, The surface effect in the case of the ultrasonic activation of the visco-ellastically pressurized media (in French), *Synthetic Polymer Journal*, **VII**, 84-93

20. Wimberger-Friedl R., 2000, Injection molding of sub-μm grating optical elements, *Journal of Injection Molding Technology*, **4**, 78-83

21. Zhao J., Mayes R., Chen G., Xie H., Chan P., 2003, Effects of process parameters on the micro molding process, *Polymer Engineering and Science*, **43**, 1542-1554

Manuscript received July 27, 2014; accepted for print March 30, 2015

JOURNAL OF THEORETICAL
AND APPLIED MECHANICS
53, 4, pp. 811-822, Warsaw 2015
DOI: 10.15632/jtam-pl.53.4.811

PERFORMANCE COMPARISON OF ACTIVE AND SEMI-ACTIVE SMC AND LQR REGULATORS IN A QUARTER-CAR MODEL

Urszula Ferdek, Jan Łuczko
Cracow University of Technology, Faculty of Mechanical Engineering, Kraków, Poland
e-mail: uferdek@mech.pk.edu.pl; jluczko@mech.pk.edu.pl

In this paper, an analysis is performed on a quarter-car model of car suspension with semi--active and active damper utilizing the sliding mode (SMC) and linear-quadratic control (LQR). The effect of control parameters and time delays in the transmission of control signal on the factors related to the safety and comfort of driving is investigated. The results obtained from numerical simulations are shown in form of frequency characteristics for several selected performance factors.

Keywords: active damping, semi-active damping, vibration reduction, car suspension

1. Introduction

For the purpose of checking the chosen concepts of active or semi-active control of car suspension, either quarter-car (Huang and Chen, 2006; Rajeswari and Lakshmi, 2008; Lin *et al.*, 2009; Snamina *et al.*, 2011) or, less often, half-car (Sam *et al.*, 2008; Sapiński and Rosół, 2008) vehicle models are used. These are usually linear models with two- or four-degrees of freedom depending on the chosen type. They consist of both spring-supported masses (1/4 or 1/2 car body) and non--spring supported ones (wheels with the reduced mass of the suspension system). The performance factor of the acting vibroisolation system should provide a compromise between the passengers' comfort level and their safety during driving (Łuczko and Ferdek, 2012). Several indexes of the driving comfort are introduced, either related to the displacements and velocities (Yoshimura *et al.*, 2001; Chen and Huang, 2005; Sam and Osman, 2005) or to accelerations (Fischer and Isermann, 2004; Rao and Narayanan, 2009) of the so-called spring-supported mass, i.e. car body. Most often, the values used for this purpose are either mean or peak ones. The measure of the safety level is on the other hand derived form the net reaction or its dynamic component (Ahmadian and Vahdati, 2006), e.g. Eusam's index. With a decrease in the net reaction, the adhesion of the wheels and the steering decreases as well. The same happens to the performance of force transmission of driving and braking.

In the numerical simulations performed to analyze the behavior of a driving vehicle, the knowledge of the function describing the kinematic excitation acting on the vehicle is essential. Several different approaches to describing the irregularities in the road are presented in the literature. The road profile can be defined using a random function (Snamina *et al.*, 2011) or a harmonic one of constant (Chen and Huang, 2005) or modulated frequency. If a vehicle is crossing some obstacles (e.g. bumps) either an impulse function of unit step type (Ahmadian and Vahdati, 2006) or other of more complex form (Lin *et al.*, 2009; Łuczko, 2011) are used.

In the active systems, several different types of control can be used. These are usually based on algorithms for the linear-quadratic regulation LQR (Rao and Narayanan, 2009; Orman and Snamina, 2009), PID regulation (Yildirim, 2004; Maciejewski, 2012) or sliding mode control (SMC) (Huang and Chen, 2006; Sam *et al.*, 2008; Tomera, 2010). Theoretically, in the case of active damping, there are no limitations imposed on the function defining the control force.

In the semi-active systems (Wu and Griffin, 1997; Fischer and Isermann, 2004; Liu *et al.*, 2005) the basic restriction imposed on the control is based on the condition of preventing the introduction of energy to the system. This condition is fulfilled if the product of the control force and the velocity of spring-supported mass to the non-spring supported one (power) is less than zero. It is most often considered for the purpose of controlling damping properties of magneto-rheological dampers (Sapiński and Rosół, 2008; Makowski *et al.*, 2011).

In this study, the emphasis is placed on analyzing the efficiency of two active control algorithms, utilizing LQR and SMC regulation, respectively. Additionally, an analysis of performance of semi-active systems, based on these regulators, is made. In the numerical simulations, the influence of time delay present between the control signal and the actuator is included.

2. Quarter-car suspension model

In this study, a quarter-car model is used as shown in Fig. 1. The motion of both masses: the non--spring-supported m_w and the spring-supported one m_b are defined by the variables y_w and y_b. The displacement $w(t)$ is the given kinematic excitation, while $u(t)$ is the active or semi-active system influence on the mass elements m_w and m_b. The parameters k_w and c_w define the spring and damping properties of the wheel, while the parameters k_b and c_b define the properties of the suspension system. Due to the negligible effect of damping of rubber on the results, this parameter is omitted in the analysis ($c_w = 0$).

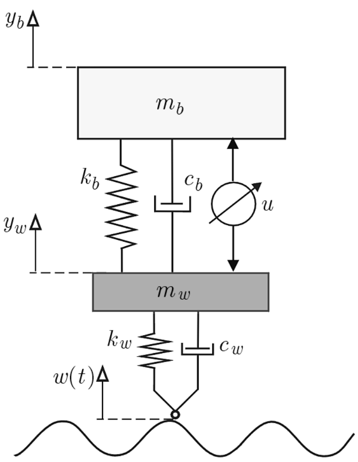

Fig. 1. Quarter-car model

Motion of the system around the static equilibrium position can be describen using the following matrix differential equation

$$\mathbf{M}\ddot{\mathbf{y}} + \mathbf{C}\dot{\mathbf{y}} + \mathbf{K}\mathbf{y} = \widetilde{\mathbf{B}}u + \widetilde{\mathbf{F}}w(t) \tag{2.1}$$

where $\mathbf{y} = [y_w, y_b]^{\mathrm{T}}$. The matrices: mass $\mathbf{M}$, damping $\mathbf{C}$ and stiffness $\mathbf{K}$ are given as

$$\mathbf{M} = \begin{bmatrix} m_w & 0 \\ 0 & m_b \end{bmatrix} \qquad \mathbf{C} = \begin{bmatrix} c_b & -c_b \\ -c_b & c_b \end{bmatrix} \qquad \mathbf{K} = \begin{bmatrix} k_w + k_b & -k_b \\ -k_b & k_b \end{bmatrix} \tag{2.2}$$

while the $\widetilde{\mathbf{B}}$ and $\widetilde{\mathbf{F}}$ vectors are of form

$$\widetilde{\mathbf{B}} = \begin{bmatrix} -1 \\ 1 \end{bmatrix} \qquad \widetilde{\mathbf{F}} = \begin{bmatrix} k_w \\ 0 \end{bmatrix} \tag{2.3}$$

A modified state space vector is introduced, which includes generalized velocities

$$\mathbf{x} = \begin{bmatrix} \mathbf{x}_1 \\ \mathbf{x}_2 \end{bmatrix} = \begin{bmatrix} \mathbf{y} \\ \dot{\mathbf{y}} \end{bmatrix} \tag{2.4}$$

thus allowing one to write Eq. (2.1) in form of the first-order differential equation

$$\dot{\mathbf{x}} = \mathbf{A}\mathbf{x} + \mathbf{B}u + \mathbf{F}w \tag{2.5}$$

There is a relation between the matrix $\mathbf{A}$ and matrices present in Eq. (2.1)

$$\mathbf{A} = \begin{bmatrix} \mathbf{0}^{(2\times2)} & \mathbf{I}^{(2\times2)} \\ -\mathbf{M}^{-1}\mathbf{K} & -\mathbf{M}^{-1}\mathbf{C} \end{bmatrix} \tag{2.6}$$

in which the matrices $\mathbf{0}^{(2\times2)}$ and $\mathbf{I}^{(2\times2)}$ are respectively the empty and singular matrix of size 2×2. The same relation is for the matrices

$$\mathbf{B} = \begin{bmatrix} \mathbf{0}^{(2\times1)} \\ \mathbf{M}^{-1}\widetilde{\mathbf{B}} \end{bmatrix} \qquad \mathbf{F} = \begin{bmatrix} \mathbf{0}^{(2\times1)} \\ \mathbf{M}^{-1}\widetilde{\mathbf{F}} \end{bmatrix} \tag{2.7}$$

where $\mathbf{0}^{(2\times1)}$ is an empty vector of length 2.

3. Linear-quadratic regulator (LQR)

Linear-quadratic regulation is often used for vibration reduction (Rao and Narayanan, 2009; Orman and Snamina, 2009). The control signal generated by the controller depends on the actual state of the system

$$u = -\mathbf{L}\mathbf{x} \tag{3.1}$$

The control if found using the minimal performance factor condition

$$J = \int\limits_0^\infty (\mathbf{x}^{\mathrm{T}}\mathbf{Q}\mathbf{x} + Ru^2)\, dt \tag{3.2}$$

in which $\mathbf{Q}$ is a positive half-defined weight matrix related to the state vector, while R in the case of a single-input control is a positive weight coefficient When minimizing the car body vibration, it can be assumed that $\mathbf{Q} = \operatorname{diag}(0, q_x, 0, q_v)$. Such a form of the weight matrix should ensure the minimum of the second and fourth of the state vector variables, i.e. the displacement and velocity of the spring-supported mass. After the matrix $\mathbf{W}$, which is the solution to the Ricatti equation

$$\mathbf{A}^{\mathrm{T}}\mathbf{W} + \mathbf{W}\mathbf{A} - \mathbf{W}\mathbf{B}R^{-1}\mathbf{B}^{\mathrm{T}}\mathbf{W} + \mathbf{Q} = \mathbf{0} \tag{3.3}$$

is obtained, the matrix $\mathbf{L}$ (transposed vector) can be found from the formula

$$\mathbf{L} = R^{-1}\mathbf{B}^{\mathrm{T}}\mathbf{W} \tag{3.4}$$

4. Sliding mode control (SMC)

An alternative option for the active control of the car suspension is to use the algorithm of sliding mode control SMC (Yoshimura *et al.*, 2001; Sam and Osman, 2005; Huang and Chen, 2006). During the process of regulation, two phases can be distinguished: the approach phase which lasts till the point that describes the dynamics of the system reaches the so-called "sliding plane", and the sliding phase. In the analyzed example, the sliding plane can be described using the formula

$$S = \kappa_x e + \kappa_v \dot{e} \tag{4.1}$$

in which e is the regulation error. When minimizing the displacements of the spring-supported mass, this error can be assumed to be equal to the displacement of this mass, meaning $e = x_2 = y_b$. Therefore, after the introduction of the transposed vector

$$\mathbf{D} = [0, \kappa_x, 0, \kappa_v] \tag{4.2}$$

the sliding plane equation can be written in the form

$$S = \mathbf{D}\mathbf{x} \tag{4.3}$$

The approach to the sliding plane is ensured by the so-called compensation (equivalent) component of the control, which can be found from the relation

$$\dot{S} = \mathbf{D}\dot{\mathbf{x}} = \mathbf{D}(\mathbf{A}\mathbf{x} + \mathbf{B}u + \mathbf{F}w) = 0 \tag{4.4}$$

The product $\mathbf{DF}$ of the transposed vector $\mathbf{D}$ and the vector $\mathbf{F}$ defined this way is equal to zero, which means that the equivalent component in this example does not depend on the excitation. If the model is well-known and no disturbance is present, the equivalent control defined by the formula

$$u^{eq}(t) = -(\mathbf{DB})^{-1}\mathbf{DAx} \tag{4.5}$$

compensating all the other forces acting on the spring-supported mass. In theory, the vibration of the system can be completely damped. Most often, the parameters of the model are not known, while the structure of the system is more complex, with the model being usually nonlinear. In a physical system, both the disturbances of the control signal and the time delay between the regulator and actuator are present. Due to these reasons, additional discontinuous control is added in form of a switching component: usw(t) (switching control)

$$u^{sw}(t) = -K^{sw}(\mathbf{DB})^{-1}\,\mathrm{sgn}\,(S) = -K^{sw}(\mathbf{DB})^{-1}\,\mathrm{sgn}\,(\mathbf{Dx}) \tag{4.6}$$

The final form of the control signal is given by the formula

$$u(t) = -(\mathbf{DB})^{-1}[\mathbf{DAx} + K^{sw}\,\mathrm{sgn}\,(\mathbf{Dx}) \tag{4.7}$$

in which K^{sw} is found based on the numerical simulation.

5. Semi-active systems

In semi-active systems, the realization of actual LQR or SMC control is not possible because of their active behavior. Therefore, these algorithms are usually modified to ensure that the momentary power is always negative (which means that no energy is introduced to the system).

Additionally, see Orman and Snamina (2009), some sort of limitation is usually imposed on the control (clipped LQR). For such semi-active control systems, the control is found using the equation

$$u^{clipped} = \varphi(u, u_{max}, v) \tag{5.1}$$

in which φ is of form

$$\varphi(u, u_{max}, v) = \begin{cases} 0 & vu \geqslant 0 \\ u & vu < 0 \quad \text{and} \quad |u| < u_{max} \\ u_{max} & vu < 0 \quad \text{and} \quad u \geqslant u_{max} \\ -u_{max} & vu < 0 \quad \text{and} \quad u \leqslant -u_{max} \end{cases} \tag{5.2}$$

where u is the control found from the condition of minimizing functional (3.2) or from Eq. (4.7), u_{max} is the maximal permissible value of control, while $v = v_b - v_w$ is the velocity of spring-supported mass with relation to the non-spring-supported one. The effectiveness of semi-active damping can be estimated through numerical simulations.

6. Results of numerical simulations

The proposed algorithms of active and semi-active damping are based on the assumption that the model of the system is a precise description of the actual physical system. In practice, some sort of uncertainty of the model needs to be taken into account, mostly due to the simplified and usually linear description of the object and inaccurately determined parameters. Additionally, the disturbances and the time delay between the control signal and the actuator influence the performance of regulation. The analysis below is limited to finding the sensitivity of the designed regulator to the time delay only on the assumption that the acting force U is related to the control signal u by the equation of a first-order filter

$$\dot{U} = -\sigma(U - u) \tag{6.1}$$

where σ is the inverse of the time constant. In the numerical calculations, the following values of parameters of the quarter-car model have been chosen: $m_w = 28\,\text{kg}$, $m_b = 510\,\text{kg}$, $k_w = 180000\,\text{N/m}$, $k_b = 20000\,\text{N/m}$, $c_b = 1000\,\text{Ns/m}$.

Below, the effect of parameters present in the control algorithms LQR and SMC on the indexes, describing the driving comfort and safety is presented. In order to measure the discomfort experienced by the passengers, both the displacement and velocity characteristics of the spring-supported mass are used. The driving safety is measured using the Eusam index W_E, which calculates the wheel-surface adhesion. Eusam's index is defined as a ratio of the maximum force to the static force acting on the wheel.

The values of indexes related to the driving comfort and safety reach maximum in different regions of excitation frequency. In the case of the vibration of frequency within the first vibration mode region, the car body displacements are dominant, which means that the driving comfort is worse. When the frequency of vibration is within the region close to the second natural mode, the displacements of car suspension are larger, and the wheel adhesion to the road is decreased. In order to evaluate the global performance of the regulator, it is advised to use either the frequency characteristics of the system or analyze the response of the system to the excitation of modulated frequency, e.g. the function "chirp". Below, the function of "chirp" type is used with a variable amplitude of the excitation. The proposed modification is introduced due to the fact that the frequency of excitation related to the velocity of the vehicle is increased, with an increase in the amplitude or, more precisely, with a decrease in the irregularities of the road. The noticeable effect of such a correction to the excitation are more realistic values of the Eusam index. Without this modification, when the amplitude of excitation is too high, the Eusam index is negative within the high frequency range (which denotes the loss of adhesion), and practically independent of the used vibroisolation system.

Further, it is assumed that with an increase in the excitation frequency, the amplitude decreases according to the formula

$$a = \frac{\alpha_1}{(\alpha_2 + \omega)^2} \tag{6.2}$$

The value of coefficients α_1 and α_2 are found from the condition that the amplitude value close to the first resonance frequency ($\omega = 8.396\,\mathrm{rad/s}$) is equal $\alpha_0 = 0.005\,\mathrm{m}$, and around the second resonance frequency ($\omega = 84.39\,\mathrm{rad/s}$) the amplitude is $0.0004\,\mathrm{m}$ ($\alpha_1 = 914.2631\,\mathrm{ms^2/rad^2}$ and $\alpha_2 = 21.3806\,\mathrm{rad/s}$). Additionally, it is assumed that the frequency increases proportionally to the square of time

$$\omega = \omega_1 + \varepsilon t^2 = \omega_1 + (\omega_2 - \omega_1)\Big(\frac{t}{T_{sim}}\Big)^2 \tag{6.3}$$

while in the region limited by the frequencies ω_1 and ω_2 ($\omega_1 = 1\,\mathrm{rad/s}$, $\omega_2 = 100\,\mathrm{rad/s}$) both resonance frequencies are present. The parameter T_{sim} is the large enough duration of simulation. Figure 2 shows the kinematic excitation in the function of time

$$w(t) = a\sin\Big(\omega_1 t + \varepsilon\frac{t^3}{3}\Big) \tag{6.4}$$

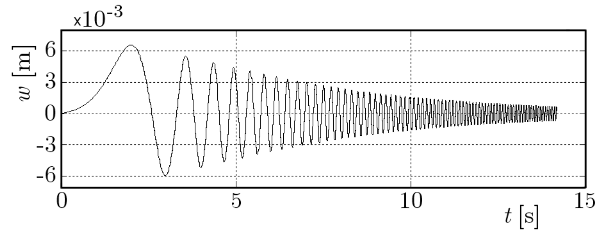

Fig. 2. Kinematic excitation $w(t)$

The effectiveness of both considered regulators depends on three parameters (q_x, q_v and R for LQR, κ_x, κ_v and K^{sw} for SMC). As the units of the parameters in both these cases are different, it is better to use dimensionless control parameters defined as follows: $\alpha_x = q_x K_x^2$, $\alpha_v = q_v K_v^2$, $\rho = R K_u^2$ for LQR and $\beta_x = \kappa_x K_x$, $\beta_v = \kappa_v K_v$, $\gamma = K^{sw}/\omega_0$ for SMC, with: $K_x = a_0$, $K_v = \omega_0 a_0$, $K_u = k_b a_0$, $\omega_0 = \sqrt{k_b/m_b}$.

In the case of a linear-quadratic regulator, one of the parameters: α_x, α_v or ρ can be chosen arbitrarily due to the form of functional (3.2). In the numerical simulation presented here, the value $\alpha_v = 1$ is chosen. The ratio between the parameters α_x and ρ highly influences the results. With an increase in this ratio, the amplitudes of displacements, velocities and accelerations are decreased, especially within the range of the first resonance. Additionally, the Eusam index is decreased, which means that the wheel adhesion to the road is worse.

For the values $\alpha_x = 100$ and $\rho = 0.1$ in the wide frequency range, both the amplitude of vibration (Fig. 3a) and the Eusam index (Fig. 3b) are satisfactory. For example, within the range of the first resonance, a reduction in the displacement amplitude by eight times is visible ($x_{2\,max} < 0.6\,\mathrm{mm}$ for $\omega \approx 8.4\,\mathrm{rad/s}$ and $a = 5\,\mathrm{mm}$), while in the range of the second resonance, the index $W_E > 0.8$.

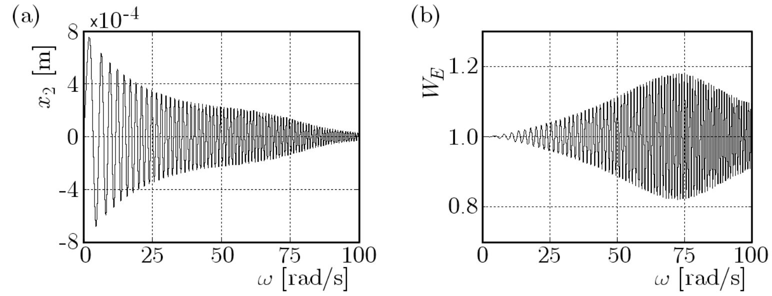

Fig. 3. LQR controller ($\alpha_x = 100$, $\alpha_v = 1$, $\rho = 0.1$, $\sigma = 100\,\mathrm{s}^{-1}$): (a) displacement x_2, (b) Eusam index W_E

In order to better illustrate the effect of control parameters on the selected frequency characteristics, in the following figures (Figs. 4, 5, 6) the maximum (or minimal in the case of the Eusam index) values of the response of the system to the excitation defined by Eqs. (6.2)-(6.4) are shown.

Figure 4 shows the velocities (Fig. 4a) and the Eusam index (Fig. 4b) as functions of the excitation frequency acquired for the system with LQR for six different values of parameter α_x and $\alpha_v = 1$, $\rho = 0.1$, $\sigma = 100\,\mathrm{s}^{-1}$. With an increase in the parameter α_x, a decrease in the displacement, velocities and accelerations in the low-frequency range is noticeable, but the Eusam index (as well as the momentary power) is increased near the second resonance.

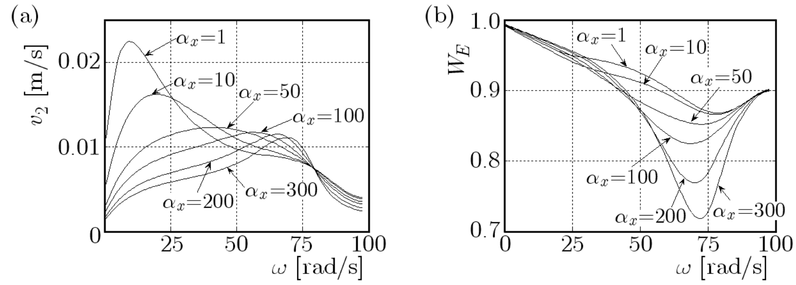

Fig. 4. LQR controller – effect of parameter α_x ($\alpha_v = 1$, $\rho = 0.1$ and $\sigma = 100\,\mathrm{s}^{-1}$): (a) velocity v_2, (b) Eusam index W_E

Figure 5 shows the effect of the parameter ρ on the frequency characteristics of the system. When the value ρ decreases, both the velocities and displacements decrease as well (Fig. 5a), while the acceleration of the spring-supported mass are relatively low within the low-frequency range (Fig. 5b). As the lower values of the parameter ρ require less restrictions imposed on the control signal, with a decreasing of its value, the control forces, Eusam index (Fig. 5c) and the momentary power (Fig. 5d) begin to rise (rapidly at $\rho < 0.05$).

The effect of time delay between the control signal u – force U, (Fig. 6; velocities and power), is notice within the high-frequency range. In a relatively wide range, with an increase in the parameter σ (larger time delay), both the vibration of the spring-supported mass (Fig. 6a) and the value of dynamic reaction increase, which causes the minimum value of Eusam index to decrease. Within this range, high values of the power (Fig. 6b), denoting changes in energy introduced to the system, can be observed. Although the parameters of control are chosen to be optimal, the active system is not very effective in this range of frequencies.

Figure 7 shows the displacements and Eusam index for the SMC regulator obtained in the similar way as for LQR (Fig. 3). The numerical simulations are performed for $\beta_x = \beta_v = 1$, $\gamma = 0.1$ and $\sigma = 100\,\mathrm{s}^{-1}$. The function $\mathrm{sgn}\,(S)$, present in Eq. (4.6), is approximated by a continuous function $2/\pi \arctan(\eta S)$ with the parameter $\eta = 100$. In the case of SMC regulator, much better vibration reduction can be accomplished (Fig. 7a) than for LQR (Fig. 3a) especially

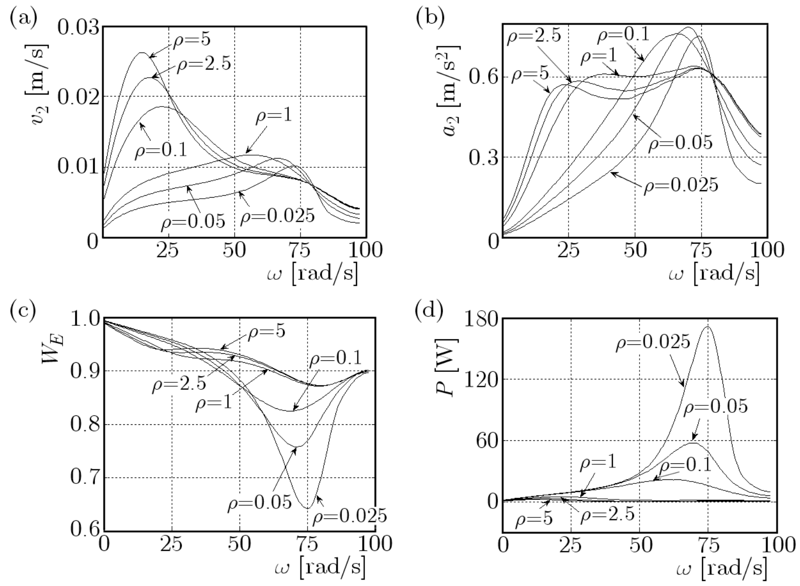

Fig. 5. LQR controller – effect of parameter ρ ($\alpha_x = 100$, $\alpha_v = 1$, $\sigma = 100\,\mathrm{s}^{-1}$): (a) velocity v_2, (b) acceleration a_2, (c) Eusam index W_E, (d) momentary power P

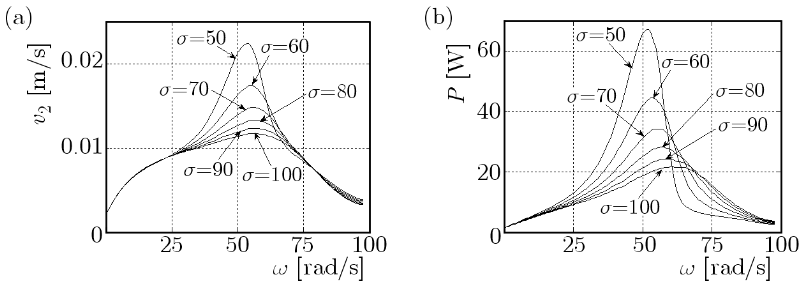

Fig. 6. LQR regulator – effect of parameter σ ($\alpha_x = 100$, $\alpha_v = 1$, $\rho = 0.1$): (a) velocity v_2, (b) momentary power

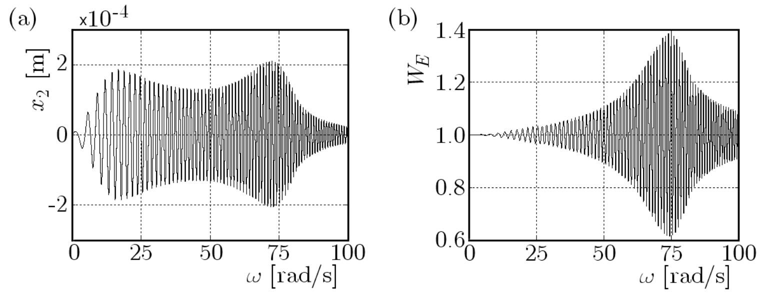

Fig. 7. SMC regulation ($\beta_x = \beta_v = 1$, $\gamma = 0.1$, $\sigma = 100\,\mathrm{s}^{-1}$): (a) displacement x_2, (b) Eusam index W_E

in the low-frequency range. Similarly, as with LQR, within the high-frequency range both the Eusam index (Fig. 7b) and the momentary power (not shown here) are unsatisfactory.

Figure 8 shows the characteristics of the SMC regulator obtained for six different values of the parameter β_x. The effect of the parameter β_x on the frequency characteristics is, apart from the slightly different plot, similar to the parameter α_x for LQR (Fig. 4). With an increase in β_x, the amplitude of vibration decreases in the lower frequency range. However, if this value is too high, the so-called effect of "chattering" might occur, which causes the characteristic of the system to greatly deteriorate in the high-frequency range.

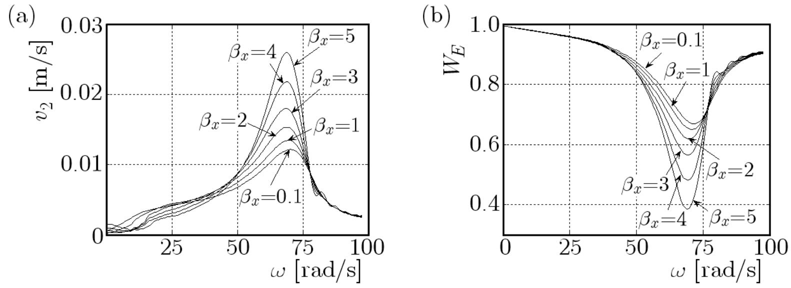

Fig. 8. SMC regulation – effect of parameter β_x ($\beta_v = 1$, $\gamma = 0.1$, $\sigma = 100\,\mathrm{s}^{-1}$): (a) velocity v_2, (b) Eusam index W_E

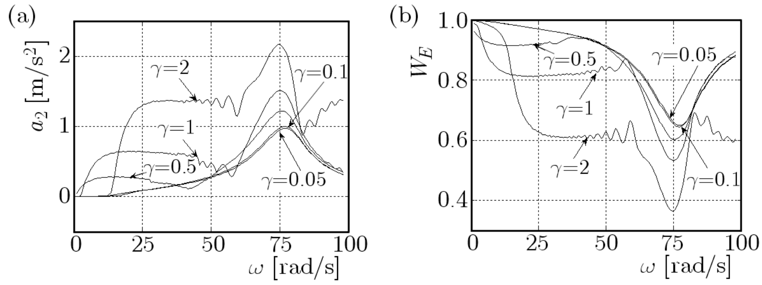

Fig. 9. SMC regulation – effect of parameter γ ($\beta_x = \beta_v = 1$, $\sigma = 100\,\mathrm{s}^{-1}$): (a) acceleration a_2, (b) Eusam index W_E

The "chattering" effect – the appearance of high frequency oscillation, is caused mostly by the switching component of control $u^{sw}(t)$, visible in the time plots. This effect is also the cause of irregular frequency characteristics plots. Figure 9a (maximum accelerations) and Fig. 9b (Eusam index) obtained for $\beta_x = \beta_v = 1$, $\sigma = 100\,\mathrm{s}^{-1}$ and five different values of γ partially illustrate the effect of "chattering". From the analysis of numerous results of numerical simulations, a conclusion can made that with an increase in the parameter γ (and also β_x) the vibration amplitudes decrease in the range of the first resonance, but for the excitation of high frequency, the maximal value of the control force is increased, while the minimal value of the Eusam index is decreased (Fig. 9b). Additionally, after exceeding certain values (for $\gamma > 0.1$), a rapid rise in accelerations in noticeable (Fig. 9a) and the possibly of occuring of the "chattering" effect is high.

The frequency characteristics of the system depend also on the value of the parameter σ. This influence is visible in Fig. 10, obtained for six values of σ and $\beta_x = \beta_v = 1$, $\gamma = 0.1$. With an increase in σ, the regulator is more effective in the low-frequency range (see Fig. 10a for velocities, Fig. 10b for accelerations), however its efficiency is greatly decreased in the second resonance range, and the power requirement is much higher, especially for high values of the parameter β_x (for $\beta_x > 1$).

Figure 11 shows the frequency characteristics of semi-active LQR (denoted as LQR-S) for $\alpha_x = \alpha_v = 1$ and $\rho = 0.1$, and also SMC (SMC-S) for $\beta_x = \beta_v = 1$ and $\gamma = 0.1$. Additionally, a characteristic of the system without regulator is presented (LIN).

For the parameters chosen as such, the efficiency of the semi-active damper is satisfactory both in terms of driving comfort (Fig. 11a) and safety (Fig. 11b). Within the range of the first resonance, both semi-active systems are thrice as effective as the passive system. In the high-frequency range on the other hand, the performance of semi-active and passive systems is compatible. Semi-active regulators, when compared to the active ones, are less vulnerable to changes in the parameter σ. In the calculations, these values have been assumed as $\sigma = 100\,\mathrm{s}^{-1}$ and $u_{max} = 10K_u$.

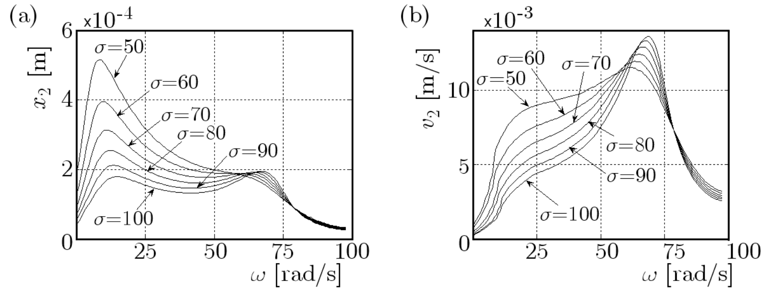

Fig. 10. SMC regulation – effect of parameter σ ($\beta_x = \beta_v = 1$, $\gamma = 0.1$): (a) velocity v_2, (b) momentary power

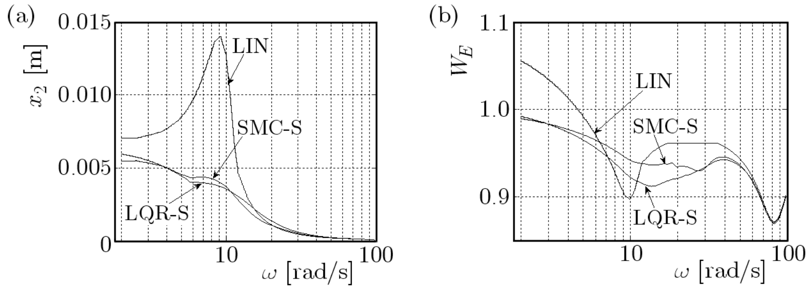

Fig. 11. Comparison of semi-active LQR-S, SMC-S and passive LIN system ($\sigma = 100\,\mathrm{s}^{-1}$): (a) displacement x_2, (b) Eusam index W_E

It needs to be pointed out that the value of the parameter α_x for LQR-S is different from the one used for LQR. For the previously used parameters α_x, α_v and ρ, the system with LQR-S controller does not behave well in the low-frequency regime (below to 60 rad/s). The SMC-S regulator works well when the parameters β_x and γ are low, but the effect of the parameter β_x is less significant than in the case of active control – that is why the same value as for the SMC is used in the calculations.

Both semi-active systems reduce the amplitude of displacement to the same degree. Although both areless effective in the minimization of vibration when compared to the active systems, but when compared in terms of driving safety both are better due to much higher minimum values of the Eusam index.

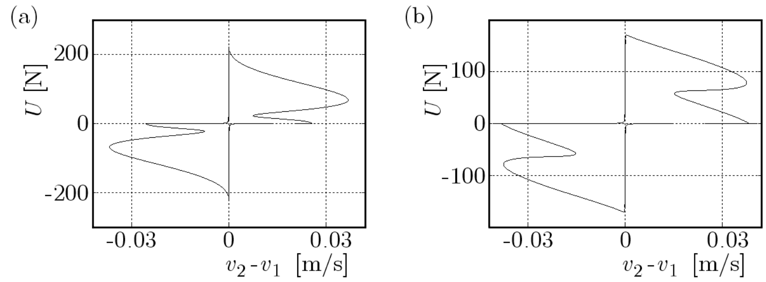

Fig. 12. Control force characteristic ($\omega = 8.396$ rad/s and $a = 5$ mm, $\sigma = 100\,\mathrm{s}^{-1}$): (a) LQR-S, (b) SMC-S

The similar operation of LQR-S and SMC-S, is most probably the effect of similar force characteristics generated by both regulators. Figures 12 and 13 show the relation between the control force and the relative velocity for LQR-S ($\alpha_x = \alpha_v = 1$, $\rho = 0.1$) and SMC-S ($\beta_x = \beta_v = 1$, $\gamma = 0.1$) systems.

It is assumed that the system is exposed to harmonic excitation defined by the parameters: $\omega = 8.396$ rad/s and $a = 0.005$ m (first resonance) and $\omega = 84.39$ rad/s and $a = 0.0004$ m

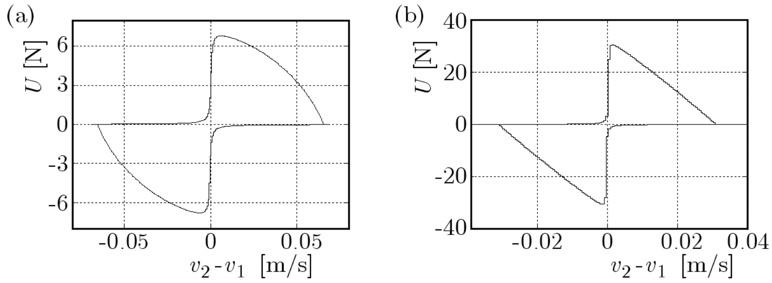

Fig. 13. Control force characteristic ($\omega = 84.39\,\mathrm{rad/s}$, $a = 0.4\,\mathrm{mm}$, $\sigma = 100\,\mathrm{s}^{-1}$): (a) LQR-S, (b) SMC-S

(second resonance). The plot of the characteristics in the first and third quadrant of the system is due to the condition imposed on the momentary power. A less-than-ideal plot of the curve in those quadrants is the result of replacing the discontinuous function (5.2) by a continuous one. For the angular frequency $\omega = 8.396\,\mathrm{rad/s}$, both characteristics are similar qualitatively and quantitaviley. For the second resonance, the differences are more significant with the visibly higher control force values of SMC-S.

7. Conclusions

From the analysis of the results and observations obtained from numerical simulations performed under different conditions, several conclusions can be drawn:

- The application of both active systems, especially the SMC algorithm, greatly reduces the amplitude, velocity and acceleration within the frequency range close to the first resonance, which in turn slightly increases the comfort of passengers during driving.
- Active systems are however unsatisfactory, within the range of the second resonance frequency, as they decrease the Eusam index describing how well the wheel-road adhesion is, and also increase the momentary power, and so the energy that needs to be introduced to the system.
- The analyzed systems, especially the active controllers, are sensible to time delay between the regulator and the actuator. This fact should be taken into consideration when choosing the parameters of the regulator.
- The semi-active systems are visibly less effective within the region of the first resonance frequency, however due to their lower cost and higher resistance to control signal time delays, they can become an alternative to the active systems.

References

1. Ahmadian M., Vahdati N., 2006, Transient dynamics of semiactive suspensions with hybrid control, *Journal of Intelligent Material Systems and Structures*, **17**, 2, 145-153
2. Chen P.-C., Huang A.-C., 2005, Adaptive sliding control of non-autonomous active suspension systems with time-varying loadings, *Journal of Sound and Vibration*, **282**, 1119-1135
3. Fischer D., Isermann R., 2004, Mechatronic semi-active and active vehicle suspensions, *Control Engineering Practice*, **12**, 1353-1367
4. Huang S.-J., Chen H.-Y., 2006, Adaptive sliding controller with self-tuning fuzzy compensation for vehicle suspension control, *Mechatronics*, **16**, 607-622
5. Lin J., Lian R.-J., Huang C.-N., Sie W.-T., 2009, Enhanced fuzzy sliding mode controller for active suspension systems, *Mechatronics*, **19**, 1178-1190

6. Liu Y., Waters T.P., Brennan M.J., 2005, A comparison of semi-active damping control strategies for vibration isolation of harmonic disturbances, *Journal of Sound and Vibration*, **280**, 21-39

7. Łuczko J., 2011, Comparison of dynamical responses of semi-active dampers described by the Bouc-Wen and Spencer models (in Polish), *Czasopismo Techniczne*, **2**, 1-M 127-136

8. Łuczko J., Ferdek U., 2012, Comparison of different control strategy in semi-active vehicle suspension system (in Polish), *Czasopismo Techniczne*, **11**, 6-M, 81-92

9. Maciejewski I., 2012, Control system design of active seat suspensions, *Journal of Sound and Vibration*, **331**, 1291-1309

10. Makowski M., Knap L., Grzesikiewicz W., 2011, Modelowanie i identyfikacja parametrów sterowanych tłumików magnetoreologicznych, *Modelowanie Inżynierskie*, **41**, 261-269

11. Orman M., Snamina J., 2009, Comparison of effectiveness of semi-active and active cable vibration dampers (in Polish), *Czasopismo Techniczne*, **12**, 3-M, 71-83

12. Rajeswari K., Lakshmi P., 2008, GA tuned distance based fuzzy sliding mode controller for vehicle suspension systems, *International Journal of Engineering and Technology*, **5**, 1, 36-47

13. Rao LVV Gopala, Narayanan S., 2009, Sky-hook control of nonlinear quarter car model traversing rough road matching performance of LQR control, *Journal of Sound and Vibration*, **323**, 515-529

14. Sam Y.M., Osman J.H.S., 2005, Modeling and control of the active suspension system using proportional integral sliding mode approach, *Asian Journal of Control*, **7**, 2, 91-98

15. Sam Y.M., Suaib N.M., Osman J.H.S., 2008, Hydraulically Actuated Active Suspension System with Proportional Integral Sliding Mode Control, *WSEAS Transactions on Systems and Control*, **9**, 3, 859-868

16. Sapiński B., Rosół M., 2008, Autonomous control system for a 3 DOF pitch-plane suspension model with MR shock absorbers, *Computers and Structures*, **86**, 379-385

17. Snamina J., Kowal J., Wzorek T., 2011, Analysis of the energy dissipation in vehicle suspensions for selected control algorithm (in Polish), *Czasopismo Techniczne*, **2**, 1-M, 233-240

18. Tomera M., 2010, Nonlinear controller design of a ship autopilot, *International Journal of Applied Mathematics and Computer Science*, **20**, 2, 271-280

19. Wu X., Griffin M.J., 1997, A semi-active control policy to reduce the occurrence and severity of end-stop impacts in a suspension seat with an electrorheological fluid damper, *Journal of Sound and Vibration*, **203**, 5, 781-793

20. Yildirim S., 2004, Vibration control of suspension systems using a proposed neural network, *Journal of Sound and Vibration*, **277**, 1059-1069

21. Yoshimura T., Kume A., Kurimoto M., Hino J., 2001, Construction of an active suspension system of a quarter car model using the concept of sliding mode control, *Journal of Sound and Vibration*, **239**, 2, 187-199

Manuscript received December 5, 2013; accepted for print April 1, 2015

JOURNAL OF THEORETICAL
AND APPLIED MECHANICS
53, 4, pp. 823-836, Warsaw 2015
DOI: 10.15632/jtam-pl.53.4.823

EFFECT OF DAMAGES ON CRACK DEVELOPMENT IN COATING ON ELASTIC FOUNDATION

Vagif M. Mirsalimov
Institute of Mathematics and Mechanics of NAS of Azerbaijan, Baku, Azerbaijan Republic
e-mail: vagif.mirsalimov@imm.az

Shahin G. Hasanov
Azerbaijan Technical University, Baku, Azerbaijan Republic; e-mail: iske@mail.ru

A fracture mechanics problem for a coating linked to the basis made of another elastic material is considered. It is assumed that in the vicinity of technological defect (crack) in the process of loading in the coating, there will arise prefracture zones (damages) that are modeled as the areas of weakened interparticle bonds of the material. In the prefracture zones (interlayers of the overstressed material), the coating material is deformed beyond the limit of elasticity. It is considered that during loading in the cross section of the coating in the vicinity of the crack, there is an arbitrary number of rectilinear prefracture zones. The condition determining the limiting value of the external load at which the crack growth happens is obtained.

Keywords: coating, elastic foundation, crack with plastic end zones, prefracture zones

1. Introduction

Analysis of the present state of coatings revealed that the coating materials have crack-visible discontinuities. In the cross sections of the coating, there arise transition zones where physico-mechanical features of the material differ from the features of the basic coating. The indicated damages in the coating cross section may have both natural origin (lamination, inclusions, pores) or be caused by technological processes. In spite of importance of the enumerated factors on coating strength, up today, these issues have not found due consideration in calculation methods. Development of calculation models of investigation of damage of a coating on an elastic foundation is a very urgent problem. A problem on interactions of damages on crack growth (Mirsalimov and Rustamov, 2012a,b) is an important problem of strength theory. Wide literature, e.g. Kulchytsky-Zhyhailo and Rogowski (2007), Haj-Ali (2009), Tukashev and Adilhanova (2010), Ameri *et al.* (2011), Hasanov (2010, 2013), Hasanov and Mirsalimov (2014) and others has been devoted to investigation of the stress strain state and fracture of the coating on an elastic foundation.

2. Formulation of problem

Consider with respect to Cartesian coordinates x, y a double-layer body consisting of a coating of thickness h with the elastic characteristics G_1 (shear modulus) and μ_1 (Poisson ratio) linked with an elastic half-plane with characteristics G_2 and μ_2 (Fig. 1).

Consider a fracture mechanics problem for a double layer body when the normal load P is applied to the external surface of the coating. The remaining part of the coating is not loaded. It is accepted that the coating material has a crack with end plastic zones (Leonov-Panasyuk-Dugdale

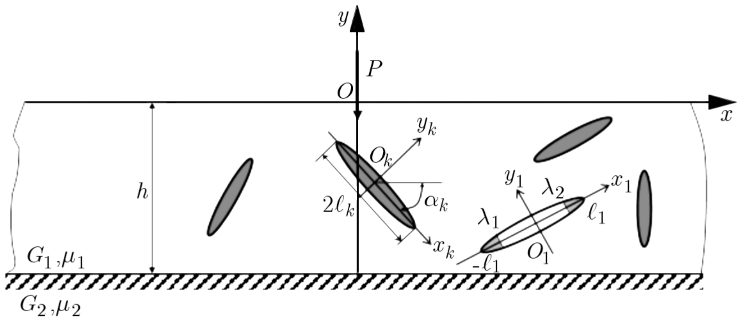

Fig. 1. A scheme of the problem of interaction of prefracture zones and cracks with end zones in the coating

crack model), see Leonov and Panasyuk (1959), Dugdale (1960). It is assumed that in the coating material in the vicinity of the crack, after repeated loading, there appear damages (prefracture zones) that are modeled as areas of interparticle bonds of the material. At the loading with external loading in the interlayer of the overstressed material a plastic flow is formed. Let, for definiteness, the power loadings change so that plastic deformation is realized in the area of weakened interparicle bonds of the material. Interaction of the faces of prefracture zones is modeled by the lines of plastic flow between them (degenerated plastic deformation zones). Under constant stress the sizes of plastic flow zones (prefracture zones) depend on the form of the material. General tendency to formation of areas with a broken structure of the material at early stages of fracture in the form of narrow layers occupying slight volume of the body compared with its elastic zone (Panasyuk, 1991; Mirsalimov, 1987; Rusinko and Rusinko, 2011) is known well from practice. The sizes of prefracture zones at the end plastic deformation zones at the crack tips are unknown beforehand and should be defined. Interaction of the prefracture zones in the vicinity of technological defect (crack) may reduce to the loss of crack stability, appearance of new cracks. It is assumed that the prefracture zones are oriented in the direction of action of maximal tensile stresses appearing in the coating.

Since the indicated zones are small compared with the remaining elastic part of the coating, one can mentally remove them changing it by cuttings whose surfaces interact between themselves by some law corresponding to the action of the removed material. In the coating cross section the crack with end zones is of length $2l_1$ along the axis x_1. Let in the coating in the vicinity of the crack there will be $(N-1)$ prefracture zones of length $2l_k$ $(k = 1, 2, \dots, N)$ (Fig. 1). In the centers of prefracture zones and the crack with end zones, we locate the origin of a local system of coordinates $x_k O_k y_k$ whose axes x_k coincide with the prefracture zones and the crack, and make the angles a_k with the axis x (Fig. 1).

Under the action of the external power load P on the coating surface in bonds connecting the prefracture zone faces and the cracks in end zones, there will arise normal $q_{y_k} = \sigma_S$ and tangential $q_{x_k y_k} = \tau_S$ stresses $(k = 1, 2, \dots, N)$, where σ_S is the yield point of the coating material for tension; τ_S is the yield point of the material for shear.

The boundary conditions of the problem are written in the form (the upper index 1 corresponds to the coating, the upper index 2 to the half-plane):

— for $y = 0$

$$\sigma_y^{(1)} = -P\delta(x) \qquad \tau_{xy}^{(1)} = 0 \tag{2.1}$$

— for $y = -h$

$$u^{(1)} + \mathrm{i}v^{(1)} = u^{(2)} + \mathrm{i}v^{(2)} \qquad \sigma_y^{(1)} + \mathrm{i}\tau_{xy}^{(1)} = \sigma_y^{(2)} + \mathrm{i}\tau_{xy}^{(2)} \tag{2.2}$$

— for $y_1 = 0$

$$\lambda_{11} < x < \lambda_{21} \qquad \sigma_y^{(1)} = 0 \qquad \tau_{xy}^{(1)} = 0 \tag{2.3}$$

— for $y_1 = 0$, $-\ell_1 \leqslant x_1 \leqslant \lambda_{11}$ and $\lambda_{21} \leqslant x_1 \leqslant \ell_1$

$$\sigma_{y_1}^{(1)} = \sigma_s \qquad \tau_{x_1 y_1}^{(1)} = \tau_s \tag{2.4}$$

and

$$\sigma_{y_k}^{(1)} = \sigma_s \qquad \tau_{x_k y_k}^{(1)} = \tau_s \qquad \text{on} \qquad L_k \qquad (k = 1, 2, \dots, N) \tag{2.5}$$

where L_k are the faces of the k-th prefracture zone; $\delta(x)$ is Dirac's impulse function, $\sigma_x, \sigma_y, \tau_{xy}$ are stress tensor components; u, v are displacement vector components: as $y \to -\infty$ the displacements and stresses disappear.

3. The method of the boundary-value problem solution

For the solution of the problem under consideration we use the superposition principle. Then we can represent the state of a double-layer body in the form of the sum of two stress-strain states:

1) adhesive connection of materials without a crack and prefracture zones under the action of the external normal load P on the external surface of the coating;
2) stress-strain state of a coating with a crack and prefracture zones on the faces of which the stresses equal in value and opposite in sign, defined by the first stress-strain state for $y_1 = 0$ and on L_k are additionally applied.

The boundary conditions for the first stress state are of the form (2.1)-(2.2).

For the solution of boundary value problem (2.1), (2.2), we use Papkovich-Neiber's four functions $F_n^m(x, y)$ $(n, m = 1, 2)$. Two of them are for the coating (upper index 1) and two for the half-plane (upper index 2).

The stresses and strains are expressed by the Parkovich-Neiber function by the known formulae (Uflyand, 1967)

$$\begin{aligned}
\frac{\sigma_y^{(m)}}{2G_m} &= 2(1-\mu_m)\frac{\partial F_2^m}{\partial y} - \frac{\partial^2 F_1^m}{\partial y^2} - y\frac{\partial^2 F_2^m}{\partial y^2} \\
\frac{\tau_{xy}^{(m)}}{2G_m} &= \frac{\partial}{\partial x}\Big[(1-2\mu_m)F_2^m - \frac{\partial F_1^m}{\partial y} - y\frac{\partial F_2^m}{\partial y}\Big] \\
u^{(m)} &= -\frac{\partial F_1^m}{\partial x} - y\frac{\partial F_2^m}{\partial x} \qquad v^{(m)} = (3-4\mu_m)F_2^m - \frac{\partial F_1^m}{\partial y} - y\frac{\partial F_2^m}{\partial y}
\end{aligned} \tag{3.1}$$

Taking into account the symmetry of the problem in x, we use the Fourier cos-transformation. Accept that

$$\begin{aligned}
F_1^1 &= \int_0^\infty (A\sinh\alpha y + B\cosh\alpha y)\cos\alpha x \, d\alpha \\
F_2^1 &= \int_0^\infty (C\sinh\alpha y + D\cosh\alpha y)\alpha\cos\alpha x \, d\alpha \\
F_1^2 &= \int_0^\infty E e^{\alpha y}\cos\alpha x \, d\alpha \qquad F_2^2 = \int_0^\infty F e^{\alpha y}\alpha\cos\alpha x \, d\alpha
\end{aligned} \tag{3.2}$$

Satisfying by functions (3.1), (3.2) boundary conditions (2.1), (2.2), we get a system of six linear algebraic equations with respect to six unknown functions $A(\alpha)$, $B(\alpha)$, $C(\alpha)$, $D(\alpha)$, $E(\alpha)$, $F(\alpha)$

$$\begin{aligned}
&2(1-\mu_1)(C\cosh\alpha h + D\sinh\alpha h) - A\sinh\alpha h - B\cosh\alpha h\\
&\qquad - \alpha h(C\sinh\alpha h + D\cosh\alpha h) = -\frac{P}{2\pi G_1\alpha^2}\\
&(1-2\mu_1)(C\sinh\alpha h + D\cosh\alpha h) - A\cosh\alpha h - B\sinh\alpha h\\
&\qquad - \alpha h(C\cosh\alpha h + D\sinh\alpha h) = 0\\
&B = E \qquad (3-4\mu_1)D - A = (3-4\mu_2)F - E\\
&G_1[2(1-\mu_1)C - B] = G_2[2(1-\mu_2)F - E]\\
&G_1[(1-2\mu_1)D - A] = G_2[(1-2\mu_2)F - E]
\end{aligned} \tag{3.3}$$

Solving algebraic system of equations (3.3) by the method of successive exclusion of unknowns, we find the coefficients $A(\alpha)$, $B(\alpha)$, $C(\alpha)$, $D(\alpha)$, $E(\alpha)$, $F(\alpha)$

$$\begin{aligned}
&D = \frac{\varDelta_1}{\varDelta} \qquad F = \frac{\varDelta_2}{\varDelta} \qquad E = B\\
&A = \frac{1}{a_{11}}(B_1 - a_{12}B - a_{13}C - a_{14}D - a_{15}F)\\
&B = \frac{1}{c_{11}}\Big(B_2 - \frac{a_{21}}{a_{11}}B_1 - c_{12}C - c_{13}D - c_{14}F\Big)\\
&C = \frac{1}{A_{11}^*}\Big(b_2^* - \frac{c_{21}}{c_{11}}b_1^* - A_{12}^*D - A_{13}^*F\Big)
\end{aligned}$$

Here

$$\begin{aligned}
&a_{11} = -\sinh\alpha h \qquad a_{12} = -\cosh\alpha h \qquad a_{13} = 2(1-\mu_1)\cosh\alpha h - \alpha h\sinh\alpha h\\
&a_{14} = 2(1-\mu_1)\sinh\alpha h - \alpha h\cosh\alpha h \qquad a_{15} = 0 \qquad a_{21} = -\cosh\alpha h\\
&a_{22} = -\sinh\alpha h \qquad a_{23} = (1-2\mu_1)\sinh\alpha h - \alpha h\cosh\alpha h\\
&a_{24} = (1-2\mu_1)\cosh\alpha h - \alpha h\sinh\alpha h \qquad a_{25} = 0 \qquad a_{31} = -1 \qquad a_{32} = 1\\
&a_{33} = 0 \qquad a_{34} = 3-4\mu_1 \qquad a_{35} = -(3-4\mu_1) \qquad a_{41} = -G_1 \qquad a_{42} = 1\\
&a_{43} = 0 \qquad a_{44} = G_1(1-2\mu_1) \qquad a_{45} = -G_2(1-2\mu_2) \qquad a_{51} = 0\\
&a_{52} = 1-2G_1(1-\mu_1) \qquad a_{53} = 2G_1(1-\mu_1) \qquad a_{54} = 0\\
&a_{55} = -2G_2(1-2\mu_2) \qquad B_1 = -\frac{P}{2\pi G_1\alpha^2} \qquad B_2 = 0\\
&B_3 = 0 \qquad B_4 = 0 \qquad B_5 = 0\\
&c_{11} = a_{22} - a_{12}\frac{a_{21}}{a_{11}} \qquad c_{12} = a_{23} - a_{13}\frac{a_{21}}{a_{11}} \qquad c_{13} = a_{24} - a_{14}\frac{a_{21}}{a_{11}}\\
&c_{14} = a_{25} - a_{15}\frac{a_{21}}{a_{11}} \qquad c_{21} = a_{32} - a_{12}\frac{a_{31}}{a_{11}} \qquad c_{22} = a_{33} - a_{13}\frac{a_{31}}{a_{11}}\\
&c_{23} = a_{34} - a_{14}\frac{a_{31}}{a_{11}} \qquad c_{24} = a_{35} - a_{15}\frac{a_{31}}{a_{11}} \qquad c_{31} = a_{42} - a_{12}\frac{a_{41}}{a_{11}}\\
&c_{32} = a_{43} - a_{13}\frac{a_{41}}{a_{11}} \qquad c_{33} = a_{44} - a_{14}\frac{a_{41}}{a_{11}} \qquad c_{34} = a_{45} - a_{15}\frac{a_{41}}{a_{11}}\\
&c_{41} = a_{52} - a_{12}\frac{a_{51}}{a_{11}} \qquad c_{42} = a_{53} - a_{13}\frac{a_{51}}{a_{11}} \qquad c_{43} = a_{54} - a_{14}\frac{a_{51}}{a_{11}}\\
&c_{44} = a_{55} - a_{15}\frac{a_{51}}{a_{11}} \qquad A_{11}^* = c_{22} - c_{12}\frac{c_{21}}{c_{11}} \qquad A_{12}^* = c_{23} - c_{13}\frac{c_{21}}{c_{11}}
\end{aligned}$$

$$A_{13}^* = c_{24} - c_{14}\frac{c_{21}}{c_{11}} \qquad A_{21}^* = c_{32} - c_{12}\frac{c_{31}}{c_{11}} \qquad A_{22}^* = c_{33} - c_{13}\frac{c_{31}}{c_{11}}$$
$$A_{23}^* = c_{34} - c_{14}\frac{c_{31}}{c_{11}} \qquad A_{31}^* = c_{42} - c_{12}\frac{c_{41}}{c_{11}} \qquad A_{32}^* = c_{43} - c_{13}\frac{c_{41}}{c_{11}}$$
$$A_{33}^* = c_{44} - c_{14}\frac{c_{41}}{c_{11}}$$
$$b_1^* = -\frac{a_{21}}{a_{11}}B_1 \qquad b_2^* = -\frac{a_{31}}{a_{11}}B_1 \qquad b_3^* = -\frac{a_{41}}{a_{11}}B_1 \qquad b_4^* = -\frac{a_{51}}{a_{11}}B_1$$
$$\Delta = \Big(A_{22}^* - A_{12}^*\frac{A_{21}^*}{A_{11}^*}\Big)\Big(A_{33}^* - A_{13}^*\frac{A_{31}^*}{A_{11}^*}\Big) - \Big(A_{23}^* - A_{13}^*\frac{A_{21}^*}{A_{11}^*}\Big)\Big(A_{32}^* - A_{12}^*\frac{A_{31}^*}{A_{11}^*}\Big)$$
$$\Delta_1 = M_1\Big(A_{33}^* - A_{13}^*\frac{A_{31}^*}{A_{11}^*}\Big) - M_2\Big(A_{23}^* - A_{13}^*\frac{A_{21}^*}{A_{11}^*}\Big)$$
$$\Delta_2 = M_2\Big(A_{22}^* - A_{12}^*\frac{A_{21}^*}{A_{11}^*}\Big) - M_1\Big(A_{32}^* - A_{12}^*\frac{A_{31}^*}{A_{11}^*}\Big)$$
$$M_1 = b_3^* - \frac{c_{31}}{c_{11}}b_1^* - \Big(b_2^* - \frac{c_{21}}{c_{11}}b_1^*\Big)\frac{A_{21}^*}{A_{11}^*} \qquad M_2 = b_4^* - \frac{c_{41}}{c_{11}}b_1^* - \Big(b_2^* - \frac{c_{21}}{c_{11}}b_1^*\Big)\frac{A_{31}^*}{A_{11}^*}$$

By means of formulae (3.1), (3.2), we find the stress components $|x_1| \leqslant \ell_1$, $y_1 = 0$ and L_k ($|x_k| \leqslant \ell_k$, $y_k = 0$, $k = 1, 2, \ldots, N$).

The boundary conditions of the problem for the second stress-strain state take the form:
— for $y = 0$

$$\sigma_y^{(1)} = 0 \qquad \tau_{xy}^{(1)} = 0 \tag{3.4}$$

— for $y = -h$

$$\sigma_y^{(1)} = 0 \qquad \tau_{xy}^{(1)} = 0 \tag{3.5}$$

— for $y_1 = 0$

$$\sigma_{y_1} - \mathrm{i}\tau_{x_1y_1} = \begin{cases} -(\sigma_{y_1}^1 - \mathrm{i}\tau_{x_1y_1}^1) & \text{on the crack faces} \\ \sigma_s - \mathrm{i}\tau_s - (\sigma_{y_1}^1 - \mathrm{i}\tau_{x_1y_1}^1) & \text{on the end zone faces of the crack} \end{cases} \tag{3.6}$$

— for $y_k = 0$, $|x_k| \leqslant \ell_k$

$$\sigma_{y_k} - \mathrm{i}\tau_{x_ky_k} = \sigma_s - \mathrm{i}\tau_s - (\sigma_{y_k}^1 - \mathrm{i}\tau_{x_ky_k}^1) \qquad (k = 1, 2, \ldots, N) \tag{3.7}$$

By means of the Kolosov-Muskhelishvili formulae (Muskhelishvili, 1977), we represent boundary conditions (3.5)-(3.7) in the form of the boundary value problem for finding the two analytic functions $\Phi(z)$ and $\Psi(z)$

$$\begin{aligned} y &= 0 && \Phi(z) + \overline{\Phi(z)} + z\overline{\Phi'(z)} + \overline{\Psi(z)} = 0 \\ y &= -h && \Phi(z) + \overline{\Phi(z)} + z\overline{\Phi'(z)} + \overline{\Psi(z)} = 0 \\ y_k &= 0 && \Phi(x_k) + \overline{\Phi(x_k)} + x_k\overline{\Phi'(x_k)} + \overline{\Psi(x_k)} = F_k \end{aligned} \tag{3.8}$$

where

$$F_1 = \begin{cases} -(\sigma_{y_1}^1 - \mathrm{i}\tau_{x_1y_1}^1) & \text{on the crack faces} \\ \sigma_S - \mathrm{i}\tau_S - (\sigma_{y_1}^1 - \mathrm{i}\tau_{x_1y_1}^1) & \text{on the end zone faces of the crack} \end{cases}$$
$$F_k = \sigma_S - \mathrm{i}\tau_S - (\sigma_{y_k}^1 - \mathrm{i}\tau_{x_ky_k}^1) \qquad (k = 1, 2, \ldots, N)$$

We look for the complex potentials $\Phi(z)$ and $\Psi(z)$ (Panasyuk *et al.*, 1977) in the form

$$\begin{aligned}\Phi(z) &= \frac{1}{2\pi}\sum_{k=0}^{N+1}\int\limits_{-\ell_k}^{\ell_k}\frac{g_k(t)}{t-z_k}\,dt\\ \Psi(z) &= \frac{1}{2\pi}\sum_{k=0}^{N+1}\mathrm{e}^{-2\mathrm{i}\alpha_k}\int\limits_{-\ell_k}^{\ell_k}\Big[\frac{\overline{g_k(t)}}{t-z_k}-\frac{\overline{T_k}\mathrm{e}^{\mathrm{i}\alpha_k}}{(t-z_k)^2}g_k(t)\Big]\,dt\end{aligned} \tag{3.9}$$

where

$$T_k = t\mathrm{e}^{\mathrm{i}\alpha_k}+z_k^0 \qquad\qquad z_k=\mathrm{e}^{-\mathrm{i}\alpha_k}(z-z_k^0)$$

Using transformation formulae (Muskhelishvili, 1977) in transfoming into the new system of coordinates

$$\begin{aligned}\Phi_k(z_k) &= \Phi\Big(z_k\mathrm{e}^{\mathrm{i}\alpha_k}+z_k^0\Big)\\ \Psi_k(z_k) &= \mathrm{e}^{2\mathrm{i}\alpha_k}\Big[\Psi\Big(z_k\mathrm{e}^{\mathrm{i}\alpha_k}+z_k^0\Big)+\overline{z}_k^0\Phi'\Big(z_k\mathrm{e}^{\mathrm{i}\alpha_k}+z_k^0\Big)\Big]\end{aligned} \tag{3.10}$$

we write complex potentials $\Phi_n(z_n)$ and $\Psi_n(z_n)$ for the considered problem in the system of coordinates $x_nO_ny_n$

$$\begin{aligned}\Phi_n(z_n) &= \frac{1}{2\pi}\sum_{k=0}^{N+1}\int\limits_{-\ell_k}^{\ell_k}\frac{g_k(t)}{t-z_k}\,dt\\ \Psi_n(z_n) &= \frac{1}{2\pi}\sum_{k=0}^{N+1}\mathrm{e}^{2\mathrm{i}\alpha_{nk}}\int\limits_{-\ell_k}^{\ell_k}\Big[\frac{\overline{g_k(t)}}{t-z_k}-\frac{(\overline{T_k}-z_n)\mathrm{e}^{\mathrm{i}\alpha_k}}{(t-z_k)^2}g_k^0(t)\Big]\,dt\end{aligned} \tag{3.11}$$

where

$$z_k=\mathrm{e}^{-\mathrm{i}\alpha_k}\Big(z_n\mathrm{e}^{\mathrm{i}\alpha_n}+z_n^0-z_k^0\Big) \qquad\qquad \alpha_{nk}=\alpha_n-\alpha_k$$

Having defined by the Kolosov-Muskhelishvili formula (Muskhelishvili, 1977) the stresses on the axis x_n and substituting into boundary condition (3.8), after some transformations, we get a system of $N+2$ integral equations:
— for $|x|<\infty$

$$\begin{aligned}&\int\limits_{-\infty}^{\infty}\Big[\frac{g_0^0(t)}{t-x}+g_{N+1}^0(t)K_{0,N+1}(t-x)+\overline{g_{N+1}^0(t)}L_{0,N+1}(t-x)\Big]\,dt\\ &\qquad=-\sum_{k=1}^{N}\int\limits_{-\ell_k}^{\ell_k}[g_k^0(t)K_{0,k}(t,x)+\overline{g_k^0(t)}L_{0,k}(t,x)]\,dt\\ &\int\limits_{-\infty}^{\infty}\Big[\frac{g_{N+1}^0(t)}{t-x}+g_0^0(t)K_{N+1,0}(t-x)+\overline{g_0^0(t)}L_{N+1,0}(t-x)\Big]\,dt\\ &\qquad=-\sum_{k=1}^{N}\int\limits_{-\ell_k}^{\ell_k}[g_k^0(t)K_{N+1,k}(t,x)+\overline{g_k^0(t)}L_{N+1,k}(t,x)]\,dt\end{aligned} \tag{3.12}$$

— for $|x| < \ell_n$ $(n = 1, 2 \ldots, N)$

$$\begin{aligned}
&\int\limits_{-\ell_k}^{\ell_k} \frac{g_n^0(t)}{t-x} + \sum_{k\neq n}\Bigg[\int\limits_{-\ell_k}^{\ell_k} g_k^0(t)K_{nk}(t,x) + \overline{g_k^0(t)}L_{nk}(t,x)\Bigg]\,dt\\
&\quad + \int\limits_{-\infty}^{\infty}[g_0^0(t)K_{n,0}(t,x) + \overline{g_0^0(t)}L_{n,0}(t,x)]\,dt\\
&\quad + \int\limits_{-\infty}^{\infty}[g_{N+1}^0(t)K_{n,N+1}(t,x) + \overline{g_{N+1}^0(t)}L_{n,N+1}(t,x)]\,dt = \pi F_n(x)
\end{aligned} \tag{3.13}$$

Here

$$\begin{aligned}
&K_{0,N+1}(x) = K_{N+1,0}(x) = \frac{x}{x^2+h^2} \qquad\qquad L_{0,N+1}(x) = \overline{L_{N+1,0}(x)} = \frac{\mathrm{i}h}{(x+\mathrm{i}h)^2}\\
&K_{0,k}(t,x) = \frac{\mathrm{e}^{\mathrm{i}\alpha_k}}{2}\Big(\frac{1}{T_k - x - \mathrm{i}h/2} + \frac{1}{\overline{T}_k - x + \mathrm{i}h/2}\Big)\\
&L_{0,k}(t,x) = \frac{\mathrm{e}^{-\mathrm{i}\alpha_k}}{2}\frac{\overline{T}_k - T_k + \mathrm{i}h}{(\overline{T}_k - x + \mathrm{i}h/2)^2}\\
&K_{n,0}(t,x) = \frac{1}{2}\Big(\frac{1}{t + \mathrm{i}h/2 - X_n} + \frac{\mathrm{e}^{-2\mathrm{i}\alpha_n}}{t - \mathrm{i}h/2 - \overline{X}_n}\Big)\\
&L_{n,0}(t,x) = \frac{1}{2}\Big(\frac{1}{t - \mathrm{i}h/2 - \overline{X}_n} - \frac{t + \mathrm{i}h/2 - X_n}{(t - \mathrm{i}h/2 - \overline{X}_n)^2}\mathrm{e}^{-2\mathrm{i}\alpha_n}\Big)\\
&K_{N+1,k}(t,x) = \frac{\mathrm{e}^{\mathrm{i}\alpha_k}}{2}\Big(\frac{1}{T_k - x + \mathrm{i}h/2} + \frac{1}{\overline{T}_k - x - \mathrm{i}h/2}\Big)\\
&L_{N+1,k}(t,x) = \frac{\mathrm{e}^{-\mathrm{i}\alpha_k}}{2}\frac{\overline{T}_k - T_k - \mathrm{i}h}{\Big(\overline{T}_k - x - \mathrm{i}h/2\Big)^2}\\
&K_{n,N+1}(t,x) = \frac{1}{2}\Big(\frac{1}{t - \mathrm{i}h/2 - X_n} + \frac{\mathrm{e}^{-2\mathrm{i}\alpha_n}}{t + \mathrm{i}h/2 - \overline{X}_n}\Big)\\
&L_{n,N+1}(t,x) = \frac{1}{2}\Big(\frac{1}{t + \mathrm{i}h/2 - \overline{X}_n} - \frac{t - \mathrm{i}h/2 - X_n}{\Big(t + \mathrm{i}h/2 - \overline{X}_n\Big)^2}\mathrm{e}^{-2\mathrm{i}\alpha_n}\Big)\\
&K_{nk}(t,x) = \frac{\mathrm{e}^{\mathrm{i}\alpha_k}}{2}\Big(\frac{1}{T_k - X_n} + \frac{\mathrm{e}^{-2\mathrm{i}\alpha_n}}{(\overline{T}_k - \overline{X}_n)^2}\Big)\\
&L_{nk}(t,x) = \frac{\mathrm{e}^{-\mathrm{i}\alpha_k}}{2}\Big(\frac{1}{\overline{T}_k - \overline{X}_n} - \frac{T_k - X_n}{(\overline{T}_k - \overline{X}_n)^2}\mathrm{e}^{-2\mathrm{i}\alpha_n}\Big)\\
&X_n = x\mathrm{e}^{\mathrm{i}\alpha_n} + z_n^0
\end{aligned} \tag{3.14}$$

For convenience, in (3.12) and (3.13) and further, we omit the index in x_n. From the system of $N+2$ singular integral equations (3.12) and (3.13) we exclude two unknown functions $g_0^0(t)$ and $g_{N+1}^0(t)$.

We can write the solutions to equations (3.12) in the following way

$$\begin{aligned}
g_0^0(t) = &\int\limits_{-\infty}^{\infty}[D_0(t)W_1(x-t) + \overline{D_0(t)}W_2(x-t) + D_{N+1}(t)W_3(x-t)\\
&+\overline{D_{N+1}(t)}W_4(x-t)]\,dt
\end{aligned} \tag{3.15}$$

$$g^0_{N+1}(t) = \int\limits_{-\infty}^{\infty} [D_0(t)\overline{W_3}(x-t) + \overline{D_0(t)}\,\overline{W_4}(x-t) + D_{N+1}(t)\overline{W_1}(x-t)$$
$$+ \overline{D_{N+1}(t)}\,\overline{W_2}(x-t)]\, dt$$

Here

$$\begin{aligned}
&D_0(x) = -\frac{1}{\pi}\sum_{k=1}^{N}\int\limits_{-\ell_k}^{\ell_k}[g^0_k(t)K_{0,k}(t,x) + \overline{g^0_k(t)}L_{0,k}(t,x)]\, dt \\
&D_{N+1}(x) = -\frac{1}{\pi}\sum_{k=1}^{N}\int\limits_{-\ell_k}^{\ell_k}[g^0_k(t)K_{N+1,k}(t,x) + \overline{g^0_k(t)}L_{N+1,k}(t,x)]\, dt \\
&W_1(x) = \frac{1}{2}[M_1(x) + N_1(x)] \qquad W_2(x) = \frac{1}{2}[M_2(x) + N_2(x)] \\
&W_3(x) = \frac{1}{2}[M_2(x) - N_2(x)] \qquad W_4(x) = \frac{1}{2}[M_1(x) - N_1(x)] \\
&M_1(x) = -\frac{\mathrm{i}}{4\pi}\int\limits_{-\infty}^{\infty}\frac{\operatorname{sgn} s[\mathrm{e}^{h|s|} + h(|s|+s)]}{\sinh|s|h + |s|h}\mathrm{e}^{\mathrm{i}sx}\, ds \\
&M_2(x) = \frac{\mathrm{i}}{4\pi}\int\limits_{-\infty}^{\infty}\frac{\operatorname{sgn} s}{\sinh|s|h + |s|h}\mathrm{e}^{\mathrm{i}sx}\, ds \\
&N_1(x) = -\frac{\mathrm{i}}{4\pi}\int\limits_{-\infty}^{\infty}\frac{\operatorname{sgn} s\{[\mathrm{e}^{h|s|} - h(|s|+s)]\mathrm{e}^{\mathrm{i}sx} - (1+\mathrm{i}sx) + hs\}}{\sinh|s|h - |s|h}\, ds \\
&N_2(x) = -\frac{\mathrm{i}}{4\pi}\int\limits_{-\infty}^{\infty}\frac{\operatorname{sgn} s(\mathrm{e}^{\mathrm{i}sx} - 1 - \mathrm{i}sx)}{\sinh|s|h - |s|h}\, ds
\end{aligned} \tag{3.16}$$

Now substituting into (3.15) the expressions for $D_0(x)$ and $D_{N+1}(x)$ from (3.16), we find

$$\begin{aligned}
&g^0_0(x) = -\sum_{k=1}^{N}\int\limits_{-\ell_k}^{\ell_k}[g^0_k(u)M_{0,k}(u,x) + \overline{g^0_k(u)}N_{0,k}(u,x)]\, du \\
&g^0_{N+1}(x) = -\sum_{k=1}^{N}\int\limits_{-\ell_k}^{\ell_k}[g^0_k(u)M_{N+1,k}(u,x) + \overline{g^0_k(u)}N_{N+1,k}(u,x)]\, du
\end{aligned} \tag{3.17}$$

Here

$$\begin{aligned}
&M_{0,k}(u,x) = \frac{1}{\pi}\int\limits_{-\infty}^{\infty}[W_1(x-t)K_{0,k}(u,t) + W_2(x-t)\overline{L_{0,k}(u,t)} \\
&\quad + W_3(x-t)K_{N+1,k}(u,t) + W_4(x-t)\overline{L_{N+1,k}(u,t)}]\, dt \\
&N_{0,k}(u,x) = \frac{1}{\pi}\int\limits_{-\infty}^{\infty}[W_1(x-t)L_{0,k}(u,t) + W_2(x-t)\overline{K_{0,k}(u,t)} \\
&\quad + W_3(x-t)L_{N+1,k}(u,t) + W_4(x-t)\overline{K_{N+1,k}(u,t)}]\, dt \\
&M_{N+1,k}(u,x) = \frac{1}{\pi}\int\limits_{-\infty}^{\infty}[\overline{W_3(x-t)}K_{0,k}(u,t) + \overline{W_4(x-t)}\,\overline{L_{0,k}(u,t)} \\
&\quad + \overline{W_1(x-t)}K_{N+1,k}(u,t) + \overline{W_2(x-t)}\,\overline{L_{N+1,k}(u,t)}]\, dt
\end{aligned} \tag{3.18}$$

$$N_{N+1,k}(u,x)=\frac{1}{\pi}\int\limits_{-\infty}^{\infty}[\overline{W_3(x-t)}L_{0,k}(u,t)+\overline{W_4(x-t)}\,\overline{K_{0,k}(u,t)}$$
$$+\overline{W_1(x-t)}L_{N+1,k}(u,t)+\overline{W_2(x-t)}\,\overline{K_{N+1,k}(u,t)}]\;dt$$

Now substituting these formulas into (3.13), after some transformations, we get a system of N singular integral equations of the considered problem for $|x|\leqslant \ell_n$ $(n=1,2,\ldots,N)$

$$\int\limits_{-\ell_k}^{\ell_k}\frac{g_k^0(t)}{t-x}\;dt+\sum_{k=1}^{N}\int\limits_{-\ell_k}^{\ell_k}[g_k^0(t)R_{nk}(t,x)+\overline{g_k^0(t)}S_{nk}(t,x)]\;dt=\pi F_n(x_n) \tag{3.19}$$

where

$$R_{nk}(t,x)=(1-\delta_{nk})K_{nk}(t,x)+r_{nk}(t,x)\qquad S_{nk}(t,x)=(1-\delta_{nk})L_{nk}(t,x)+s_{nk}(t,x) \tag{3.20}$$

and

$$\begin{aligned}r_{nk}(t,x)&=\int\limits_{-\infty}^{\infty}[K_{n,0}(\tau,x)M_{0,k}(t,\tau)+L_{n,0}(\tau,x)\overline{N_{0,k}(t,\tau)}\\&\quad+K_{n,N+1}(\tau,x)M_{N+1,k}(t,\tau)+L_{n,N+1}(\tau,x)\overline{N_{N+1,k}(t,\tau)}]\;d\tau\\s_{nk}(t,x)&=\int\limits_{-\infty}^{\infty}[K_{n,0}(\tau,x)N_{0,k}(t,\tau)+L_{n,0}(\tau,x)\overline{M_{0,k}(t,\tau)}\\&\quad+K_{n,N+1}(\tau,x)N_{N+1,k}(t,\tau)+L_{n,N+1}(\tau,x)\overline{M_{N+1,k}(t,\tau)}]\;d\tau\end{aligned} \tag{3.21}$$

After substituting into (3.21) integrals (3.18), the kernels $r_{nk}(t,x)$ and $s_{nk}(t,x)$ will be represented by three-fold iterated integrals. After integration, these expressions may be represented by single integrals.

Omitting very bulky calculations, for the kernels $r_{nk}(t,x)$ and $s_{nk}(t,x)$ we finally find

$$\begin{aligned}r_{nk}(t,x)&=\int\limits_{0}^{\infty}\Big[\Big(\frac{1}{\sinh hs+hs}+\frac{1}{\sinh hs-hs}\Big)H_{nk}(X_n,T_k,s,\alpha_n,\alpha_k)\\&\quad+\Big(\frac{1}{\sinh hs+hs}-\frac{1}{\sinh hs-hs}\Big)G_{nk}(X_n,T_k,s,\alpha_n,\alpha_k)\Big]\;ds\\s_{nk}(t,x)&=\int\limits_{0}^{\infty}\Big[\Big(\frac{1}{\sinh hs+hs}-\frac{1}{\sinh hs-hs}\Big)H_{nk}(X_n,\overline{T}_k,s,\alpha_n,-\alpha_k)\\&\quad+\Big(\frac{1}{\sinh hs+hs}+\frac{1}{\sinh hs-hs}\Big)G_{nk}(X_n,\overline{T}_k,s,\alpha_n,-\alpha_k)\Big]\;ds\end{aligned} \tag{3.22}$$

where

$$\begin{aligned}H_{nk}(X_n,\overline{T}_k,s,\alpha_n,-\alpha_k)&=\frac{\mathrm{e}^{\mathrm{i}\alpha_k}}{4}\{\sin(X_n-\overline{T}_k)s\\&\quad-\sin(T_k-\overline{X}_n)s\langle hs+\mathrm{e}^{-2\mathrm{i}\alpha_n}[1-hs+s^2(T_k-\overline{T}_k)(\overline{X}_n-X_n)+h^2s^2]\rangle\\&\quad+\langle s(T_k-\overline{T}_k)-\mathrm{e}^{-2\mathrm{i}\alpha_n}[(T_k-\overline{T}_k)+hs^2(\overline{X}_n-X_n-T_k+\overline{T}_k)]\rangle\cos(T_k-\overline{X}_n)s\\&\quad+\mathrm{e}^{-hs}[\sin(T_k-X_n)s+\mathrm{e}^{-2\mathrm{i}\alpha_n}\sin(\overline{T}_k-\overline{X}_n)s]\}\\G_{nk}(X_n,T_k,s,\alpha_n,\alpha_k)&=\frac{\mathrm{e}^{\mathrm{i}\alpha_k}}{4}\{-[1+\mathrm{e}^{-2\mathrm{i}\alpha_n}(-1+hs)]\sin(\overline{T}_k-\overline{X}_n)s-hs\sin(T_k-X_n)s\\&\quad-s(T_k-\overline{T}_k)\cos(T_k-X_n)s-\mathrm{e}^{-2\mathrm{i}\alpha_n}(\overline{X}_n-X_n)s\cos(\overline{T}_k-\overline{X}_n)s+\mathrm{e}^{-hs}[\sin(T_k-\overline{X}_n)s\\&\quad-\mathrm{e}^{-2\mathrm{i}\alpha_n}\sin(T_k-\overline{X}_n)s+\mathrm{e}^{-2\mathrm{i}\alpha_n}\sin(\overline{X}_n-X_n-T_k+\overline{T}_k)s\cos(T_k-\overline{X}_n)s]\}\end{aligned} \tag{3.23}$$

Note that the functions $r_{nk}(t,x)$ and $s_{nk}(t,x)$ are regular. They define the effect of faces of the band on the stress state near the crack tips. To the system of singular equations (3.19) for internal cracks, we should add the additional conditions

$$\int_{-\ell_k}^{\ell_k} g_k^0(t)\,dt = 0 \qquad (k = 1,2,\ldots,N) \tag{3.24}$$

Using the procedure for converting (Panasyuk *et al.*, 1977; Mirsalimov, 1987) at conditions (3.24), the system of complex singular integral equations (3.19) is reduced to a system of $N \times M$ algebraic equations for determining the $N \times M$ unknowns $g_k^0(t_m)$ ($k = 1,2,\ldots,N$; $m = 1,2,\ldots,M$)

$$\begin{aligned} &\frac{1}{M}\sum_{m=1}^{M}\sum_{k=1}^{N}\ell_k[g_k^0(t_m)R_{nk}(\ell_k t_m,\ell_n x_r) + \overline{g_k^0(t_m)}S_{nk}(\ell_k t_m,\ell_n x_r)] = F_n^0(x_r^0)\\ &\sum_{m=1}^{M} g_n^0(t_m) = 0 \qquad (n = 1,2,\ldots,N)\end{aligned} \tag{3.25}$$

If in (3.25) we pass to complex conjugate values, we get one more $N \times M$ algebraic equations.

For completeness of algebraic equations, we need $2 \times N$ complex equations determining the sizes of prefracture zones.

The solution of the system of integral equations is sought in the class of everywhere bounded functions (stresses). Consequently, it is necessary to add to system (3.25) the conditions of stress boundedness at the ends of the crack and prefracture zones $x_k = \pm l_k$ ($k = 1,2,\ldots,N$). These conditions are of the form

$$\begin{aligned} &\sum_{m=1}^{M}(-1)^m g_n^0(t_m)\cot\frac{2m-1}{4M}\pi = 0 \qquad (n = 1,2,\ldots,N)\\ &\sum_{m=1}^{M}(-1)^{M+m} g_n^0(t_m)\tan\frac{2m-1}{4M}\pi = 0\end{aligned} \tag{3.26}$$

The obtained resolving systems of equations can be determines under the given external load the stress-strain state of the coating linked with elastic foundation in the availability of a crack and arbitrary number of prefracture zones in the coating. The united resolving system of equations becomes nonlinear because of the unknown values l_k ($k = 1,2,\ldots,N$). For its solution, we use the method of successive approximations the essence of which is the following. We solve system (3.25) at some definite values l_k^* ($k = 1,2,\ldots,N$) of the sizes of prefracture zones and the crack end zones with respect to the remaining unknowns. The remaining unknowns enter into the system linearly. The values of l_k^* and the found quantities $g_k(t_m)$ are substituted into (3.26), i.e. into the unused equations of the system. The taken values of the parameters l_k^* and the appropriate values $g_k(t_m)$ will not, generally speaking, satisfy equations (3.26). Therefore, by selecting the values of the parameters l_k^*, we will repeat the calculations until equations (3.26) of system (3.25) and (3.26) are satisfied with the given accuracy. At each approximation, the algebraic system is solved by the Gauss method with choosing the principal element.

Using the solution of the problem, calculate the opening on the faces of the crack and prefracture zones

$$-\frac{1+\kappa}{2G_1}\frac{\pi\ell_k}{M}\sum_{m=1}^{M_1} g_k(t_m) = v_k(x_{0k},0) - \mathrm{i}u_k(x_{ok},0) \qquad (k = 1,2,\ldots,N)$$

Here, M_{1k} is the number of nodal points contained in the interval $(-l_k, x_{0k})$.

For the displacement vector modulus on the faces of the crack and prefracture zone for $x = x_{0k}$, we have

$$V_{0k} = \sqrt{u_k^2 + v_k^2} = \frac{1+\kappa}{2G_1}\frac{\pi\ell_k}{M}\sqrt{A_k^2 + B_k^2} \tag{3.27}$$

where

$$A_k = \sum_{m=1}^{M_{1k}} v_k(t_m) \qquad B_k = \sum_{m=1}^{M_1k} u_k(t_m) \qquad (k = 1, 2, \dots, N)$$

To determine the external load at which the crack propagation occurs, we use the criterium of critical opening of crack faces at the foundation of the plastic deformations zone. Then the condition determining the limiting value of the external load will be the equality

$$V_{01}(\lambda_{11}) = \delta_c \qquad V_{01}(\lambda_{21}) = \delta_c \tag{3.28}$$

where δ_c is a characteristic of the fracture toughness of the coating material defined experimentally.

The obtained solution of the problems allows one to predict the appearance of new cracks in the coating material. Tp achieve that, the problem statement should be complemented with the condition (criterion) of the crack appearance (discontinuity of interparticle bonds of the material). In place of such a condition, we accept the criterium of critical opening of prefracture zone faces

$$|(v_k^+ - v_k^-) - \mathrm{i}(u_k^+ - u_k^-)| = \delta_{cr} \qquad (k = 2, \dots, N) \tag{3.29}$$

where δ_{cr} is the characteristics of resistance of the material to cracking.

Using the obtained solution, we can write the limit condition in the form

$$V_{0k}(x_k^*) = \delta_{cr} \qquad (k = 2, \dots, N) \tag{3.30}$$

where x_k^* is the coordinate of the point of the prefracture zone at which discontinuity of the material interparticle bonds occurs.

These additional conditions enables finding the coating parameters at which new cracks appear in the coating cross section. Dependences of the length of the crack-tip zone $d_1 = (l_1 - \lambda_{11})/l_1$ on the value of the load $p_* = P/h\sigma_s$ for different values of the crack length $l_* = (\lambda_{21} - \lambda_{11})/l_1$ for $\alpha_1 = 45°$ and $z_0 = (0.05h - \mathrm{i}0.25h)$ are depicted in Fig. 2. The dependences of the prefracture zone length l_2/h on the dimensionless value of the external load $P/h\sigma_s$ under different orientation angles of the prefracture zone location in the case $l_* = 0.75$ are depicted in Fig. 3. The dependences of the opening of prefracture zone faces δ/δ_0 along the prefracture zone x_2/l_2 at different orientation angles of the prefracture zone location in the case $l_* = 0.75$ are depicted in Fig. 4. Here $\delta_0 = \pi E_1\delta_c/8\sigma_s$. Figure 5 represents the dependence of the critical load $p_c = P/h\sigma_s$ on the dimensionless length of the crack $\lambda = l_*/h$ for $\alpha_1 = 45°$.

4. Conclusions

Experimental data from operational practice of the pair "coating-elastic foundation" convincingly show that at the design stage it is necessary to take into attention the cases when the coating may have damages and cracks. The existing methods of strength analysis of the pair "coating-elastic foundation" ignore this case. Such a situation makes it impossible to design a pair "coating-foundation" with minimal specific consumption of materials at guaranteed reliability and durability.

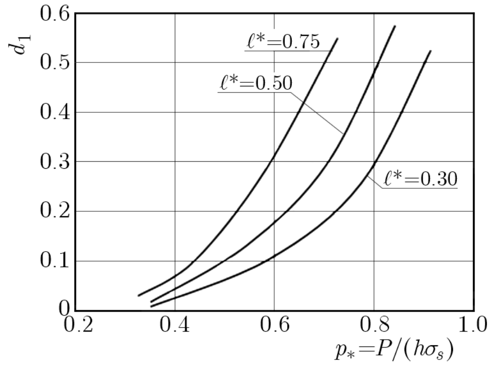

Fig. 2. Dependence of the length of the left end zone $d_1 = (\ell_1 - \lambda_{11})/R_1$ on the dimensionless external load $p_* = P/h\sigma_s$ for different values of the crack length $\ell_* = (\lambda_{21} - \lambda_{11})/\ell_1$ for $\alpha_1 = 45°$ and $z_0 = 0.05h - \mathrm{i}0.25h$

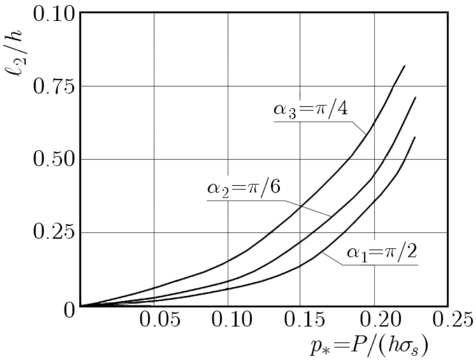

Fig. 3. Dependence of the prefracture zone length ℓ_2/h on the dimensionless length of the external load $P/h\sigma_s$ at different orientation angles of the prefracture zone location for the case $\ell_* = 0.75$

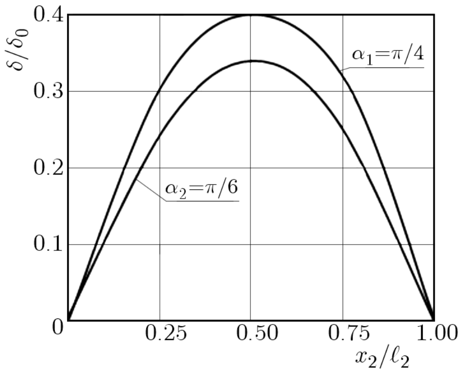

Fig. 4. Dependence of the prefracture zone faces opening δ/δ_0 along the prefracture zone at different orientation angles of the prefracture zone location for the case x_2/ℓ_2. Here $\delta_0 = \pi E_1 \delta_c / 8\sigma_s$

In this connection, it is necessary to realize the limit analysis of the pair "coating-foundation" in order to establish ultimate loads at which cracking and crack growth in the coating occurs. The size of the limiting minimal prefracture zone at which a crack appears should be considered as a design characteristic of the coating material.

Based on the suggested designed model that takes into account the availability of damages (zones of weakened interparticle bonds of the material) and cracks with end zones in the coating, we developed a method of calculation of coating parameters at which cracking and crack growth occurs. Knowing the basic values of critical parameters of cracking and the effect of materials properties on them, cracking and crack growth phenomenon may be controlled by means of design-technological decisions at the design stage.

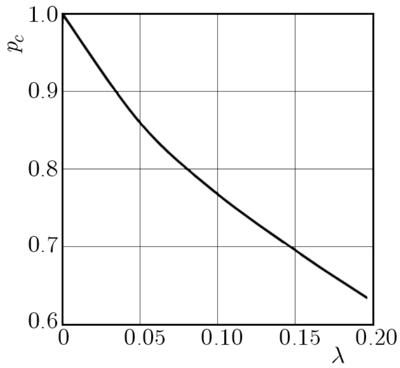

Fig. 5. Dependence of the critical load $p_c = P/h\sigma_s$ on the dimensionless length of the crack $\lambda = \ell_1/h$ for $\alpha_1 = 45°$

Numerical realization of the obtained equations enables solution of the following practically important design problems:

1) to estimate the guaranteed resource of the pair "coating-elastic foundation" with regard to expected defects and loading conditions;
2) to establish the admissible deficiency level and maximum values of workload ensuring sufficient reliability reserve;
3) to choose materials with necessary complex of static and cyclic fracture toughness characteristics.

References

1. Ameri M., Mansourian A., Heidary Khavas M., Aliha M.R.M., Ayatollahi M.R., 2011, Cracked asphalt pavement under traffic loading – a 3D finite element analysis, *Engineering Fracture Mechanics*, **78**, 8, 1817-1826
2. Dugdale D.S., 1960, Yielding of steel sheets containing slits, *Journal of the Mechanics and Physics of Solids*, **8**, 100-108
3. Haj-Ali R., 2009, Cohesive micromechanics: a new approach for progressive damage modeling in laminated composites, *International Journal of Damage Mechanics*, **18**, 8, 691-720
4. Hasanov Sh.H., 2010, Calculated method of research of fatigue fracture of the road covering, *Structural Mechanics of Engineering Constructions and Buildings*, **2**, 14-20
5. Hasanov Sh.H., 2013, Solution of fracture mechanics for the transverse crack in the cross section of road cover, *Journal of Mechanics of Machines, Mechanisms and Materials*, **2**, 23, 35-40
6. Hasanov Sh.H., Mirsalimov V.M., 2014, Modeling of stress-strain state of road covering with cracks, *Acta Polytechnica Hungarica*, **11**, 215-234
7. Leonov M.Ya., Panasyuk V.V., 1959, Propagation of fine cracks in solid body (in Russian), *Prikladnaya Mekhanika*, **5**, 391-401
8. Kulchytsky-Zhyhailo R., Rogowski G., 2007, Stresses of hard coating under sliding contact, *Journal of Theoretical and Applied Mechanics*, **45**, 4, 753-771
9. Mirsalimov V.M., Rustamov B.E., 2012, Effect of damages on crack-visible of the cavity opening displacement in burning solid fuel, *International Journal of Damage Mechanics*, **21**, 373-384
10. Mirsalimov V.M., Rustamov B.E., 2012, Interaction of prefracture zones and crack-visible cavity in a burning solid with mixed boundary conditions, *Acta Mechanica*, **223**, 627-643
11. Mirsalimov V.M., 1987, *Non-One Dimensional Elastoplastic Problems* (in Russian), Nauka, Moscow

12. Muskhelishvili N.I., 1977, *Some Basic Problem of Mathematical Theory of Elasticity*, Kluwer, Amsterdam
13. Panasyuk V.V., 1991, *Mechanics of Quasibrittle Fracture of Materials* (in Russian), Naukova Dumka, Kiev
14. Panasyuk V.V, Savruk M.P., Datsyshyn A.P., 1977, A general method of solution of two-dimensional problems in the theory of cracks, *Engineering Fracture Mechanics*, **9**, 481-497
15. Rusinko A., Rusinko K., 2011, *Plasticity and Creep of Metals*, Springer, Berlin
16. Tukashev J.B., Adilhanova L.A., 2010, Investigation of stress-strain state of road covering, *Geology, Geography and Global Energy*, **37**, 2, 163-165
17. Uflyand Ya.S., 1967, *Integral Transforms in the Theory of Elasticity* (in Russian), Nauka, Leningrad

Manuscript received October 20, 2014; accepted for print April 6, 2015

JOURNAL OF THEORETICAL
AND APPLIED MECHANICS
53, 4, pp. 837-846, Warsaw 2015
DOI: 10.15632/jtam-pl.53.4.837

EXPERIMENTAL AND NUMERICAL INVESTIGATION OF FRICTION COEFFICIENT EFFECTS ON DEFECTS IN HORIZONTAL TUBE BENDING PROCESS

Jalal Taheri Kahnamouei
Memorial University of NewFoundland, Canada; e-mail: jtk441@mun.ca

A.M. Fattahi
Department of Mechanical Engineering, Tabriz Branch, Islamic Azad university, Tabriz, Iran

The aim of this paper is to investigate defects in a thin-walled tube bending process (without using mandrel and booster) and effects of friction between the dies and tube on wrinkles. In the tube bending process, there are several effective parameters such as wall thickness, outer diameter-to-wall thickness ratio, centerline bending radius-to-outer diameter ratio and friction coefficient. Any mismatch in the selection of the process parameters would cause defects inducing undesirable variations in wall thickness and cross-section distortion. In this work, firstly, tubes with several wall thickness values are bent, and the final depths of wrinkling and wall thickness change are reviewed. Then, to study the process numerically, numerical simulations are carried out. Then, a series of experimental tests are carried out to verify the simulation results. A comparison between numerical and experimental results shows a reasonable agreement. Finally, in order to obtain a suitable friction condition, the effects of friction coefficients on defects are studied. For this purpose, a series of simulations has been carried out. It shows that at a certain friction coefficient, a minimum wrinkling depth can be observed and variations in the friction coefficient between the dies and tube has no effective influence on wall thinning and thickening.

Keywords: tube bending, wrinkle, simulation, friction, wall thickness change

1. Introduction

Recently, curved thin-walled tubular elements have been attracting more applications in automobile, aerospace, and oil industries. Tube bending is used as a hydroforming process and application that needs high strength/weight ratio products (Manabe and Amino, 2002; Koc and Altan, 2001). There are some parameters to be controlled in order to reduce the defect. For example, geometry parameters and friction conditions are modified to restrain instability of the process. In the tube forming process, wrinkling can be avoided, but the wall thickness change is almost inevitable. From among the considerable number of studies dealing with the wrinkling and thinning of wall thickness in tube bending, only few studies have focused on methods to reduce the defect. Tang (2000) employed plastic-deformation theory to investigate the plastic deformation in pipe and tube bending and also explained the seven phenomena in tube bending, also mentioning their practical formulas. An experimental sample was also tested to illustrate that the results of the formulae are very similar to the experimental results. Yang *et al.* (2006) investigated the effect of friction on the cross-section quality of thin-walled tube NC bending. His results showed that the effects of frictions between all dies and tube on wall thinning are smaller than their effects on section distortion. Therefore, in order to improve the section quality, frictions between mandrel, wiper and tube should be decreased, but the frictions between the pressure die, bending die and tube should increase. Gaoa and Strano (2004) made a research on the effect of friction on the quality of tube pre-bending and hydroforming. In that paper, process variables such as the friction coefficient, tube material and pre-bent tube radius were analyzed. It was found that a lower friction coefficient can reduce thinning in the pre-bending process, and that a large pre-bending radius is beneficial to both pre-bending and subsequent hydroforming.

Zeng and Li (2002) introduced a tube push-bending process combining axial forces and internal pressure. Moreover, they also made research on effects of the internal pressure, friction condition and push distance on the tube deformation push-bending process. Yang and Lin (2004) studied the wrinkling in the tube bending process, where the effects of bending angle, geometrical dimensions, material properties and the original radius and strength coefficient of tubes on the minimum bending radius were analyzed. The role of the filling material on defects in the of thin--walled tube bending process was reported as a numerical and experimental study by Sedighi and Taheri Kahnamouei (2014). That paper investigated approaches to avoid common defects such as the wrinkling, cross section distortion and wall thickness variation in the bending process of a thin-walled tube. So, a series of experimental tests was carried out by filling the tube with melted lead and different types of rubbers. They showed that wrinkle initiation and cross section distortion can be avoided with a lost core made of low temperature melting metal like lead or tin. Jiang *et al.* (2011) used a three-dimensional finite element method to investigate deformation behavior of medium-strength TA18 high-pressure tubes during NC bending with different bending radii. The article showed that if a mandrel is used, the thickening ratio increases from the initial bending section to the bending section.

In the present study, firstly, the wrinkle phenomenon and the wall thickness change in a thin-walled tube are studied using theoretical, experimental and FE methods. In order to verify the finite element analysis results, some experiments have been done and comparisons drawn between the experimental and numerical results in Section 2. In Section 3, FEM analysis of effects of friction between the dies and tube on these defects is studied. Finally, in Section 4 the results are presented and discussed. The results show that at a certain friction coefficient a minimum wrinkling depth can be observed and variations in the friction coefficient between the dies and tube have no effective influence on the wall thinning and thickening.

2. Methodology

2.1. Analytical approach

Changes in wall thickness is related to many factors, such as material, size and shape, bending and wall factors, bending method, tooling and bending operation. When a tube is bent, then tensile or compressive stresses cause wall thinning or thickening. The wrinkling in the inner wall of the bending radius is one of the common defects in the tube bending process. It has a direct relation with the outer diameter-to-wall thickness ratio and the centerline bending radius-to-outer diameter ratio (Fig. 1).

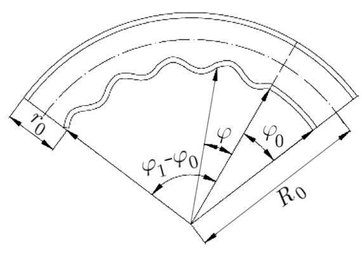

Fig. 1. Example of a wrinkled bending section of a tube and its parameters (Yang and Lin, 2004)

Based on the known energy principle, the critical moment of wrinkling onset is when the internal energy of the wrinkled shell (U) is equal to the work done by the external forces (T), and the wrinkling happens if the external forces are larger than the internal energy of the wrinkled shell (Yang and Lin, 2004). According to the wrinkling wave function proposed by Wang and Cao (2001) and Yang and Lin (2004), the depth of wrinkling in the normal direction w can be characterized with the following function

$$w = w_0\sqrt{\frac{R\cos\theta}{R_0}}\Big(1-\cos\frac{2\pi m\varphi}{\phi_1-\phi_0}\Big) \qquad w_0 = \frac{\sqrt{r_0R_0}(\phi_1-\phi_0)}{\pi m} \tag{2.1}$$

where r_0 is the tube diameter, R_0 is the bending radius, m is the wave number along the circumferential direction of the tube, φ is the curve coordinate in the tube bending direction which changes from ϕ_1 to ϕ_2.

When a tube is bent, two typical stress zones can be defined. One is the tension zone at the extrados of the bend; the other is the compressive zone at the intrados of the bend. These cause tube thickening at the intrados and thinning at the extrados, respectively, as shown in Fig. 2.

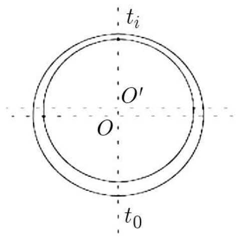

Fig. 2. Cross section of tube after bending

Based on plastic deformation theory, equations (2.2) give the rate of wall thinning and wall thickening for the extrados and intrados of the bend which has been proposed by Tang (2000)

$$t_{0\,max} = \Big(1-\frac{r_0}{4R_0}\Big)t \qquad t_{i\,max} = \Big(1+\frac{2R_0r_0+3r_0^2}{8R_0^2}\Big)t \tag{2.2}$$

where t is tube wall thickness.

2.2. Material properties and geometry

A uniaxial tension test is used to obtain mechanical properties of steel (USt37) and is listed in Table 1. The hardening behavior can be described by equation $\sigma = K(\varepsilon)^n$. The Coulomb friction model is used in the simulation process.

Table 1. Mechanical properties of the tube

Poisson's ratio	0.3
Maximum elongation [%]	44.2
Elasticity modulus [GPa]	210
Yield stress [MPa]	270
K	345
n	0.05

The tooling parameters are shown in Table 2. Circular tubes of diameter $r_0 = 50$ mm, wall thickness of $t_0 = 1.5$, 1.25, 0.9 mm, bending radius 150 mm and bending angle 45° were used in the experiments.

Table 2. Tooling geometry dimensions

Tooling parameter	Length [mm]	Dimension [mm]
Bend die	300(D)	52
Rotary die	150	52

2.3. Experimental setup

The experiment is performed to provide a general concept of the tube bending process and to verify the FE modeling. For this purpose, a hydraulic horizontal tube bending machine has been used. The horizontal bending is widely used for bending tubes, particularly for tight bending radii and thin wall tubes. The dies setup on the horizontal bending machine is shown in Fig. 3. The work piece is held between the bend die and rotary dies. The bend die strokes linearly and, synchronically, rotary dies are actuated to rotate on the tube, and the work piece bends to any requested angle.

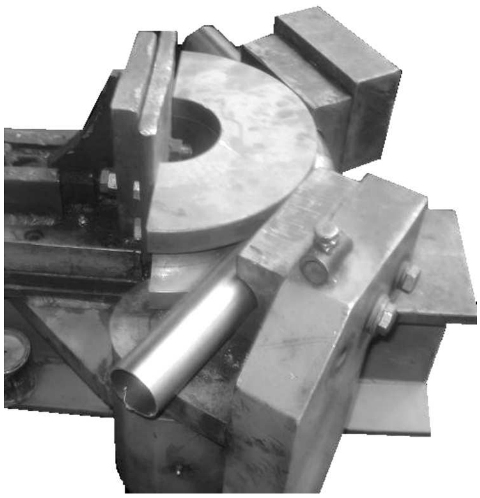

Fig. 3. Sketch of the tube horizontal bending

2.4. The FE model

A 3D finite element model is built using ANSYS software. The tube is modeled by shell 143 which is well suited to model nonlinear, flat or wrapped, thin to moderately thick shell structures. Three dimensional rigid elements for the dies models have been used. Shell 143 is 4-node 3D space shell element and has six degrees of freedom at each node: translations in the nodal x, y, and z-directions and rotations about the nodal x, y, and z-axis. The geometry, node locations, and the coordinate system for this element are shown in Fig. 4 (ANSYS Help, 2007).

The Coulomb friction coefficient between the tube and dies are assumed to be equal to 0.15 (Trana, 2002) and all dies and tube geometric parameters are the same as used in the experimental setup. In the tube bending process, there are three contact surfaces between the tube/bend die, tube/rotary dies. The “surface-to-surface contact” method has been employed to describe the mechanical constraints for different contact pairs using CONTACT174 and TARGET169. Figure 5 shows a representative finite element model with the initial tube blank and the tool set.

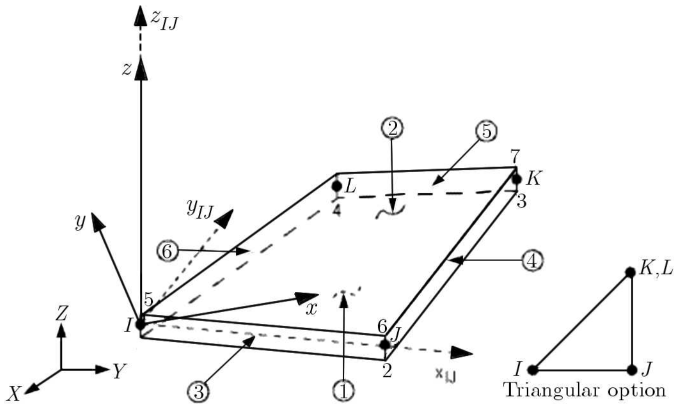

Fig. 4. Shell (143) geometry (ANSYS Help, 2007)

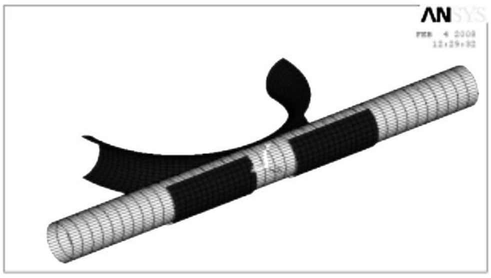

Fig. 5. FE model for the horizontal bending process

3. Experimental verification of the numerical model

In order to verify the finite element analysis results, some experiments have been done. In Fig. 6, a comparison between the experimental and numerical results are presented. No wrinkling can be seen in the tube with 1.5 mm thickness but in the tube with 1.25 mm and 0.9 mm thickness wrinkling is observed.

Also the wrinkling depth in the experimental and FE modeling results is compared in Fig. 7. It can be seen that the amount of wrinkling in the tube is in direct correlation with the tube wall thickness. An increasing in the wall thickness decreases the possibility of wrinkling. From Fig. 6 and Fig. 7 it can be concluded that the FE results are reasonable and can be used for further investigation of the friction coefficients effect on wrinkling.

FEM simulations and experimental results for the extrados wall thickness at the bend zone have been compared and they are shown in Fig. 8. It can be seen that the wall thickness at the outside of the bend is always decreased. Also by an increase in d/t ratio, the thinning value decreases. The maximum thinning reduction in 1.5 mm tube is equal to 6.5% and the minimum thinning reduction in 0.9 mm tube is equal to 3%. It can also be observed from Fig. 8 that the wall thickness has a great influence on the thinning when the bending radius and tube diameters are fixed.

Also experimental and FEM results for the intrados wall thickness at the bend zone have been compared and shown in Fig. 9. It can be seen that the thickness at the inside of the bend is increased, and the maximum thickness thickening reduction is equal to 10%.

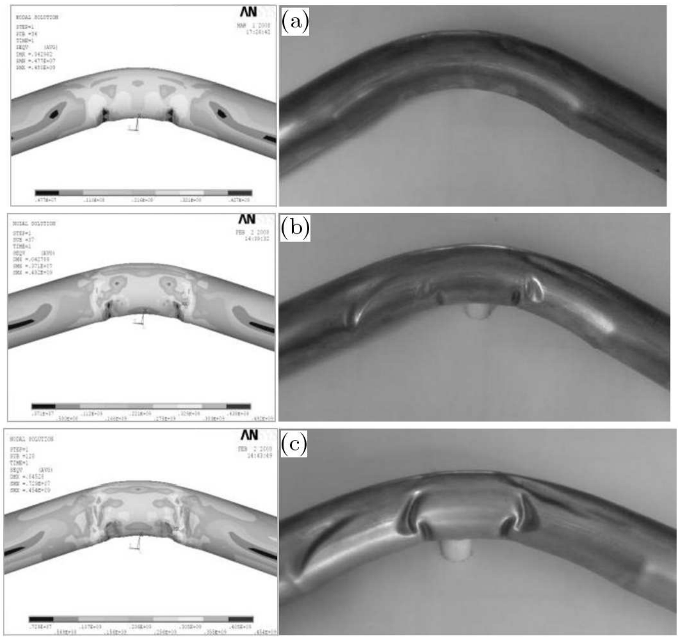

Fig. 6. Verification of the FE results by experiments. Wall thickness: (a) 1.5 mm, (b) 1.25 mm, (c) 0.9 mm

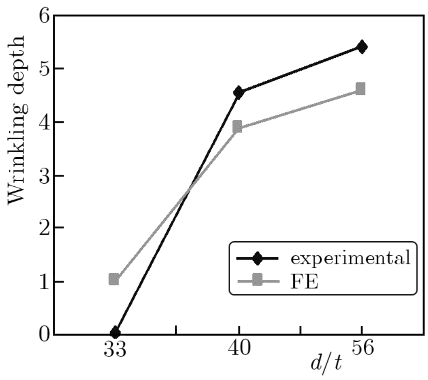

Fig. 7. Comparison of FE and experimental results

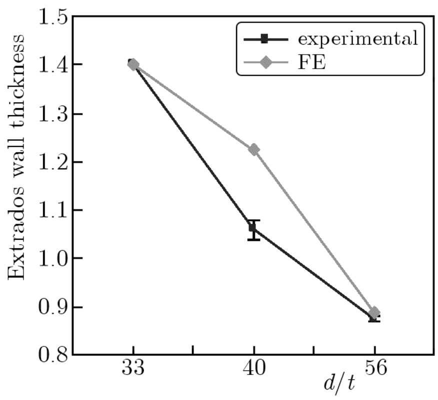

Fig. 8. Comparison of the thickness distribution in FE and experimental results at the extrados radius (without considering hardening and friction parameters)

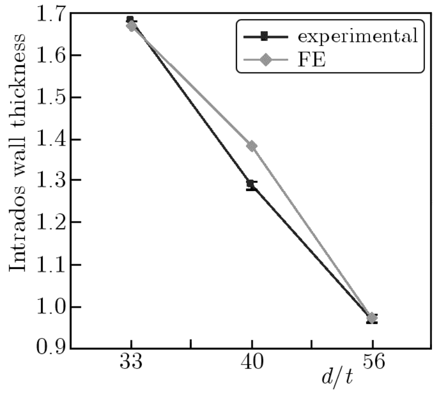

Fig. 9. Comparison of the thickness distributions in FE and experimental results at the intrados radius (without considering hardening and friction parameters)

4. Results and discussion

The friction conditions between the bend die, rotary die and tube have a large effect on the wrinkling in thin-walled tube horizontal bending, especially for small R/D and large D/t. In order to study the effects of friction on defects after verification of the FE model, a set of runs have been implemented. There are two different cases of friction in the horizontal bending process. One refers to friction between the bend die and tube; another refers to friction between the tube and rotary dies. For this purpose, two series of friction conditions are employed. These runs include values of the friction coefficient between the bend die and tube as 0.05, 0.1, 0.2, 0.3, 0.4, 0.5 and friction between the rotary dies and tube as 0.05, 0.1, 0.2, and 0.3. In the following, the obtained results will be discussed for four different subsections separately.

4.1. The effect of friction between rotary dies and tube on wrinkling

The FE modeling of the bending process for different amounts of friction between the rotary dies and tube have been carried out. Variations in the friction coefficient and wrinkling depths are shown in Fig. 10. It shows that the depth of wrinkling for all three thicknesses are decreased when the friction coefficient is decreased from 0.3 to 0.2 and the depth of the wrinkling is increased when the friction coefficient is reduced from 0.2 to 0.05. This shows that the least wrinkling depth will happen at a certain friction coefficient.

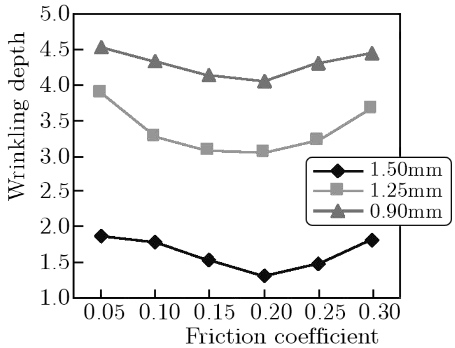

Fig. 10. Variations in wrinkling depth vs. friction coefficient between the tube and rotary dies

4.2. The effect of friction between rotary dies and tube on the wall thickness change

The effects of the friction coefficient between the rotary die and tube on the wall thickness are shown in Figs. 11 and 12. It can be found that it has no influence on the thinning and thickening of the tube wall.

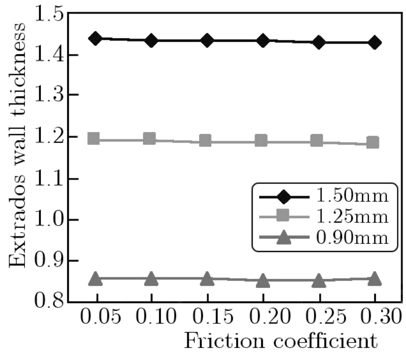

Fig. 11. Variations in wall thinning vs. friction coefficient between the tube and rotary dies (without considering hardening and friction parameters)

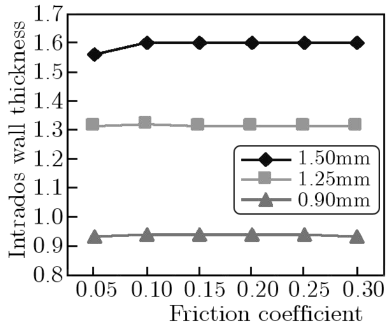

Fig. 12. Variations in wall thickening vs. friction coefficient between the tube and rotary dies (without considering hardening and friction parameters)

4.3. The effect of friction between bend die and tube on the wrinkling

Variations in the friction coefficient and wrinkling depths for different thicknesses (1.5, 1.25, 0.9 mm) are presented in Fig. 13. It shows that for all three thicknesses, the depth of wrinkling is decreased when the friction coefficient is reduced from 0.5 to 0.2. But when the friction coefficient is reduced from 0.2 to 0.05, the depth of wrinkling increases. It is found that the minimum wrinkling depth takes place at friction coefficient of 0.2.

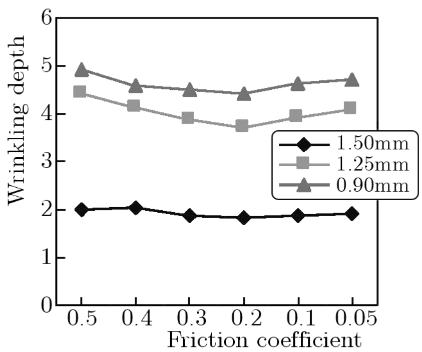

Fig. 13. Variations in wrinkling depth vs. friction coefficient between the tube and bend die

4.4. The effect of friction between bend die and tube on the wall thickness change

The effects of the friction between the bend die and tube on the wall thickness are shown in Figs. 14 and 15. Same as in the previous Subsection, it can be found that friction between the bend die and tube has no influence on the thinning and thickening of the tube wall.

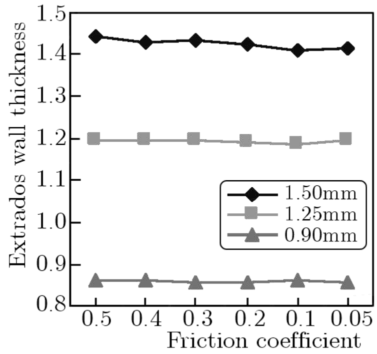

Fig. 14. Variations in wall thinning vs. friction coefficient between the tube and bend die (without considering hardening and friction parameters)

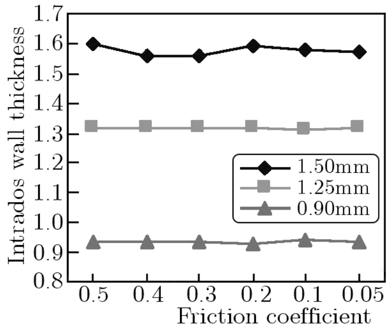

Fig. 15. Variations in wall thickening vs. friction coefficient between the tube and bend die (without considering hardening and friction parameters)

According to the results given in these figures, it can be concluded that friction between the tube, bend die and rotary dies have a significant and important effect on the wrinkling, and have no influence on the thinning and thickening of tube wall thickness in the tube horizontal bending process.

5. Conclusion

A 3D FE model has been created to study the effect of friction on defects in the bending process. The FE results have been verified by experimental tests and they are in good agreement. According to the results of the analysis, it can be concluded that:

- The minimum wrinkling depth occurs at a certain value of the friction coefficient.
- Friction conditions may affect the balance of internal energy between the wrinkled shell and the work done by the external forces. So, there should be a certain friction coefficient value for which a stable state exists between the two mentioned energies.
- Extremely low or high friction conditions are detrimental for the tube bending process. A perfect tubular part can be obtained at a suitable friction condition.
- Variations in the friction coefficient between the dies and tube have no influence on the thinning and thickening of the tube wall.

Finally, it should be noticed that there are other effective parameters in the tube bending such as bending speed, bending radius. Future works should address these factors in detail.

References

1. ANSYS Inc., "ANSYS Help", Release 11.0, Documentation, Copyright 2007
2. Gaoa L., Strano M., 2004, FEM analysis of tube pre-bending and hydroforming, *Journal of Materials Processing Technology*, **151**, 294-297
3. Jiang Z., Zhan M., Yang H., Xu X., Li G., 2011, Deformation behavior of medium-strength TA18 high-pressure tubes during NC bending with different bending radii, *Chinese Journal of Aeronautics*, **24**, 657-664
4. Koc M., Altan T., 2001, an overall review of the tube hydroforming (THF) technology, *Journal of Materials Processing Technology*, **108**, 384-393
5. Manabe K., Amino M., 2002, Effects of process parameters and material properties on deformation process in tube hydroforming, *Journal of Materials Processing Technology*, **123**, 285-291
6. Sedighi M., Taheri Kahnamouei J., 2014, Role of filling material on defects of thin-walled tube bending process, *Journal of Theoretical and Applied Mechanics*, **52**, 1, 227-233
7. Tang N.C., 2000, Plastic-deformation analysis in tube bending, *International Journal of Pressure Vessels and Piping*, **77**, 751-759
8. Trana K., 2002, Finite element simulation of the tube hydroforming process-bending, performing and hydroforming, *Journal of Materials Processing Technology*, **127**, 401-408
9. Wang X., Cao J., 2001, Wrinkling limit in tube bending, *Trans. ASME*, **123**, 430-435
10. Yang H., Lin Y., 2004, Wrinkling analysis for forming limit of tube bending processes, *Journal of Materials Processing Technology*, **152**, 363-369
11. Yanh H., Gu R.-J., Zhan M., Li H., 2006, Effect of frictions on cross se ction quality of thin-walled tube NC bending, *Transactions of Nonferrous Metals Society of China*, **16**, 878-886
12. Zeng Y., Li Z., 2002, Experimental research on the tube push-bending process, *Journal of Materials Processing Technology*, **122**, 237-240

Manuscript received December 2, 2013; accepted for print April 17, 2015

JOURNAL OF THEORETICAL AND APPLIED MECHANICS
53, 4, pp. 847-858, Warsaw 2015
DOI: 10.15632/jtam-pl.53.4.847

ANALYZING SQUARE PLATE IN DIAGONAL COMPRESSION USING BELTRAMI-MICHELL METHODOLOGY

Djelloul Rezini
LCGE Laboratory, USTO – Mohamed Boudiaf University of Oran, Algeria
e-mail: redjellou@yahoo.fr

Abdelkrim Khaldi
LRTTFC Laboratory, USTO – Mohamed Boudiaf University of Oran, Algeria

Kouider Bouzid
Metallurgy Department, USTO – Mohamed Boudiaf University of Oran, Algeria

Yahia Rahmani
LRTTFC Laboratory, USTO – Mohamed Boudiaf University of Oran, Algeria

This paper is concerned with the "Study of photoelasticity and a photoelastic theoretical investigation of the stress distribution in Square Blocks subjected to concentrated diagonal loads", a thesis topic by M.M. Frocht who developed the well-known semi empirical Shear Stress Difference method. Indeed, the use of the Beltrami-Michell methodology remains quick, when complemented by photoelasticity to acquire Dirichlet's conditions. The synergy of both methods is enhanced with the use of the finite difference method. In addition, a finite element analysis has provided results that will be a supplementary reference for validation. The results obtained have been of lower cost than those obtained by Frocht.

Keywords: photoelasticity, hybrid method, Beltrami-Michell, square-plate, diagonal compression

1. Introduction

The objective of this paper is to present an alternative solution to the stress distribution in square blocks to that presented in Frocht's thesis entitled "Study of photoelasticity and a photoelastic theoretical investigation of the stress distribution in Square Blocks subjected to concentrated diagonal loads" (Frocht, 1931). Furthermore, some features of the stress distribution are examined by both techniques. We will show, moreover, maps of the whole field of each of the stress components individually, which the method by Frocht cannot provide. In addition, the finite element analysis has provided results that will be a supplementary reference for the validation.

Stress analysis is a classical subject in the field of elasticity theory. Exact solutions to practical problems are not easily determined because of the exact incorporation of the associated physical conditions. The usually used displacement approach degrades the order of the approximation, especially when the state of stress is of principal interest. Therefore, in the alternative direct formulation in terms of stress, the tensor stress field is used as the principal unknown variable (Boresi *et al.*, 2011). This technique is associated with the elliptic equation of Beltrami-Michell forming a well-posed Dirichlet's problem which can be partitioned into two parts; the first approach provides a harmonic field function subject to certain boundary conditions, while the second one investigates the behavior of this function in the neighbourhood of the boundary. Actually, a correct treatment of boundary conditions is one of the major obstacles to the reliable solution to practical problems.

Although, photoelasticity provides an incomplete solution within the field, nevertheless it always gives a complete one on the boundaries (Frocht, 1941). Isoclinic information will not be needed here, since the isochromatics on the boundaries is the sufficient information (Rezini, 1984) and will be thoroughly used for the proposed stress analysis. However, enhanced with the use of Finite Difference Method (FDM), the aim of this paper is to propose a photoelastic-numerical hybrid method for stress analysis within any irregularly shaped domain in plane stress conditions. Thus, the Square Block will be an appropriate application for the validation of the present model.

2. Elastic plane stress boundary value problem

The plane stress problem considered is referred to as an elastic planar layer subjected to symmetric in-plane loading in the case of the diagonal compressed Square Block. Given the plane stress assumptions, this problem is firstly governed by the necessary equilibrium conditions. As a result of the forces applied at the boundary, the stress tensor $\boldsymbol{\sigma}$, a symmetric rank two tensor field, satisfies the following equilibrium condition either in the absence or for constant body forces for each i

$$\sum_{j=1}^{2} \frac{\partial \sigma_{ij}}{\partial x_j} = 0 \tag{2.1}$$

Moreover, the plane stress problem is defined as the elastic planar layer Ω on the stress assumption that ($\sigma_{33} = \sigma_{13} = \sigma_{23} = 0$); $(x_1, x_2, x_3) \in \Omega$. Furthermore, the stress field in the middle layer is reasonably described by the three field components $\sigma_{11}(x_1, x_2)$, $\sigma_{22}(x_1, x_2)$, and $\sigma_{12}(x_1, x_2)$ which form the symmetrical stress tensor, of which the trace is expressed as follows

$$\mathrm{trace}(\boldsymbol{\sigma}) = \Sigma_\sigma(x_1, x_2) = \sigma_{11} + \sigma_{22} \tag{2.2}$$

In terms of stress, the invariant $\Sigma_\sigma(x_1, x_2)$ has the fundamental properties of a harmonic function that satisfies the Laplace-potential equation. In fact, if the Laplace operator is applied to the trace of the stress tensor given in (2.2), the well-known Laplace potential equation for the stress sum is obtained

$$\sum_{j=1}^{2} \frac{\partial^2 \Sigma_\sigma(x_1, x_2)}{\partial x_j^2} = 0 \tag{2.3}$$

Equation (2.3) as stated is the compatibility condition in terms of stress for planar version. When equilibrium equations (2.1) are derived in a suitable form and subtracted from each other, the following equality in terms of the second order derivatives will result

$$\frac{\partial^2 \sigma_{11}}{\partial x_1^2} = \frac{\partial^2 \sigma_{22}}{\partial x_2^2} \tag{2.4}$$

In a similar way, by adding both equations, the determining Poisson equation for the shear stress is obtained, and is given as follows

$$\Delta \sigma_{12} = -\frac{\partial^2 (\sigma_{11} + \sigma_{22})}{\partial x_1 \partial x_2} \tag{2.5}$$

where Δ is referred to as the two-dimensional Laplace operator. Laplace's potential equation (2.3) may be rewritten in the extended form shown below

$$\Delta \sigma_{11} = -\frac{\partial^2 \sigma_{22}}{\partial x_1^2} - \frac{\partial^2 \sigma_{22}}{\partial x_2^2} \tag{2.6}$$

The incommoding member in equation (2.6) will be replaced by its equivalent one given in equation (2.4), so that an equation of the Poisson type for the normal stress component is obtained

$$\Delta\sigma_{11} = -\frac{\partial^2(\sigma_{11}+\sigma_{22})}{\partial x_1^2} \tag{2.7}$$

In a cyclic permutation, the equation for the normal stress in the other direction is established likewise

$$\Delta\sigma_{22} = -\frac{\partial^2(\sigma_{11}+\sigma_{22})}{\partial x_2^2} \tag{2.8}$$

Equations (2.5), (2.7) and (2.8) are the well-known Beltrami-Michell equations; with the requirement that the potential equation solution of the sum of stresses given in (2.3) at the stress field must be available. Other formulations shown in the literature may lead to the same equations (Hetnarski and Ignaczak, 2011). Furthermore, it is essential, however, to notice the fact that the Beltrami-Michell equations are independent of elastic constants for the two-dimensional case (Muskhelishvili, 1975).

3. Photoelasticity treatment of the problem

The photoelastic experiment (Ramesh, 2008; Frocht, 1941, 1948) provides only two experimental parameters for each point: the isochromatic fringe order N which is proportional to $(\sigma_1 - \sigma_2)$ and θ, the isoclinic parameter. However, three characteristics are needed to fully define the stress state. Photoelasticity provides therefore an incomplete solution as is symbolically sketched below

$$(\sigma_{11},\sigma_{22},\sigma_{12}) \Longleftrightarrow \begin{cases} N & \text{isochromatic order} \\ \theta & \text{isoclinic parameter} \end{cases}$$

Both the two-dimensional basic equation of photoelasticity and the procedure are well documented in the literature (Sharafutdinov, 2012). Photoelasticity and the SSD-method form a single semi empirical hybrid method which calculates stress components within a grid starting from initial values at the boundary points. The SSD-method is based on the step-by-step integration of one of the differential equations of equilibrium. In a Cartesian (x,y) plane, for any particular y-ordinate, equation (2.1) can be integrated in the x-direction

$$\sigma_x(x_1) = \sigma_x(x_0) - \int_{x_0}^{x_1} \frac{\partial\tau_{xy}}{\partial y}\,dx \tag{3.1}$$

where the partial derivative $\partial\tau_{xy}/\partial y$ is a function of the x-coordinate. In practice, τ_{xy} is determined by photoelasticity from the isochromatic fringe order N and the isoclinic parameter θ viewed in the (x,y)-plane (Fig. 1) using the following photoelasticity law

$$\tau_{xy} = \frac{Nf}{2t}\sin 2\theta \tag{3.2}$$

where f and t are the material constant and thickness of the model, respectively. When the loaded Square Block model is viewed in the polariscope, a fringe pattern called isochromatic is apparent.

The Square Block photoelastic data are shown in Fig. 1 where the stress patterns are on the right-hand side, and the corresponding isoclinics are on the left-hand side. The stress separation

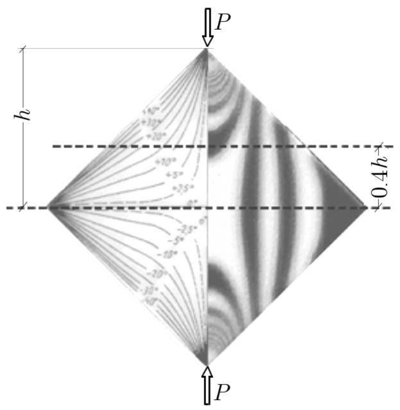

Fig. 1. Isoclinics and isochromatic fringes data of the diagonally compressed Square Block

will be carried out along the straight line, indicated by X. Along the horizontal line $y =$ const, for the SSD-method, the central-difference between 2 auxiliary lines parallel to y at a distance of Δy, the partial differential quotient of the shear stress is approximated as follows

$$\frac{\partial \tau_{xy}}{\partial y} \cong \frac{\Delta \tau_{xy}}{\Delta y} \tag{3.3}$$

Substituting expression (3.3) into equation (3.1) and using elementary summation along the grid nodes in the photoelasticity law, equation (3.2) leads to the following separated stresses both in the x and y-directions

$$\sigma_y\big|_i = \sigma_y\big|_0 + \sum_{k=1}^{i}\Big(\frac{\Delta\tau}{\Delta x}\Delta y\Big)_k \qquad \sigma_x\big|_i = \sigma_x\big|_0 + \sum_{k=1}^{i}\Big(\frac{\Delta\tau}{\Delta y}\Delta x\Big)_k \tag{3.4}$$

It is shown that even if the error introduced by the measurement of the isochromatic parameter may not be important, the error due to the isoclinic (stress direction) measurement can be very significant (Kuske, 1959, 1971). Since the SSD-method involves step-by-step integration, the error introduced will be cumulative.

Concerning the boundary values, the state of stress is most evident on the free boundaries. At each point of the free boundary either σ_1 or σ_2 vanishes; the stress fringe pattern gives immediately the numerical value of the remaining principal stress. In addition, the sign of the boundary stress can be determined by considering the external loading or by "nail" pressure on the boundary (Kuske and Robertson, 1974). The required boundary potentials arise automatically from photoelastic study of the specimen in which the principal stress sum can be obtained readily because they are identical to the principal stress difference on the free boundary (Mangal and Ramesh, 1999; Petrucci, 1997; Pinit and Umezaki, 2007), from which the equality of their absolute values at the boundary is deduced

$$\sigma_B = \Big|(\sigma_1 + \sigma_2)_{\partial\Omega}\Big| = \Big|(\sigma_1 - \sigma_2)_{\partial\Omega}\Big| \tag{3.5}$$

Besides, the harmonic state of the stress invariant satisfies Laplace equation (2.3); and it is usually used to determine the interior potential of the stress sum with the necessary knowledge of boundary conditions (Fernàndez *et al.*, 2010). The accuracy of the boundary values of the stress sum is absolutely decisive for the results. This is true because the stress sum occurs each time as a source function of the set of the Beltrami-Michell equations. According to the law of photoelasticity, the stress sum is proportional to the fringe order on the free boundaries

$$(\sigma_x + \sigma_y)\big|_{\partial\Omega} = \kappa N(x,y)\big|_{\partial\Omega} \tag{3.6}$$

Knowing the inclination angle θ (or the slope) at a given point on the model edge and the tangential stress $\sigma_B = \kappa N(x,y)$ at the same point, the Cartesian stresses components are easily computed using separately the equilibrium conditions as follows

$$\sigma_x = \sigma_B \cos^2\theta \qquad \sigma_y = \sigma_B \sin^2\theta \qquad \tau_{xy} = -\sigma_B \sin\theta\cos\theta \tag{3.7}$$

Commonly, only one black-and-white photograph of the boundary-isochromatic fringe patterns of the model for the input data is needed. The simplest way of fringe data recording is to use a digitizing tablet and to "click" (pick up) on the centre of each fringe at a density that adequately represents the fringe centreline (such as Gauss distribution) on the breadth (Rezini, 1984). This simple acquisition technique has the significant advantage of allowing the user maximum control of the number and location data. Per boundary, the coordinates of the boundary points are recorded along with their isochromatic values and tabulated in an array (x_i, y_i, N_i), where $i = 1, \ldots, n$ labelling each recorded point in this array. It is also all of the entire work necessary for the data input procedure. It is to be pointed out that the matrices of each system of the finite difference algebraic equations will be automatically occupied, taking into account the recorded boundary values, as described above. In the next step, a processing subprogram (solver) is started in order to perform the numerical analysis. An output program shall be provided.

4. Finite difference implementation on the Square Block

Due to its definition, the FDM is the most important and certainly still dominant numerical method in the partial differential equations modelling. In order to approximate the solution of a partial differential equation by its nodal values at a set of grid points, the FDM often requires the mesh points to be uniformly placed, so that the derivatives of the unknown function at grid points can be accurately approximated. Difficulties principally occur in the FDM discretization of the homogeneous and mixed derivatives at irregular shaped boundaries. To overcome this restriction and in order to solve partial differential equations that are defined on domains with irregular geometry, numerous variants are proposed in several works (Collatz, 1960; McKenney *et al.*, 1996). Many procedured exist on this subject; e.g. McKenney *et al.* (1996) propose a fast Poisson solver for complex geometries. In this way, Zhang (1998) developed a multigrid solution to Poisson's equation. In the present implementation, a flexible 5-point stencil is systematically used for the discretization of the homogeneous and the mixed partial derivatives occurring in both Laplace equation (2.3) and in the right-hand side of Poisson equations (2.5), (2.7) and (2.8).

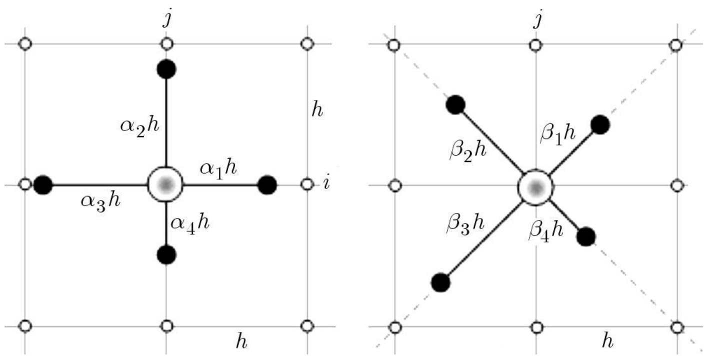

Fig. 2. Unequal armed difference star: (a) normal grid, (b) skewed grid

Consider the general case of a group of five points, of which spacing is non-uniform, arranged in an unequal-armed star. We represent each distance by $\alpha_i h$, where α_i represent the respective fractions of the standard spacing h from the discretization central point as shown in Fig. 2a. Based on Taylor's theorem, the derivative of a function at a point can be approximated by the linear combination of function values at nearby points including the function itself (Dahlquist and Bjorck, 1974; Smith, 1985). The definition of difference quotients and of the discrete Laplace operator also has to be modified. This leads to the Shortley-Weller approximation (Shortley and Weller, 1938)

$$\Delta\phi\big|_h = C_0^+\Phi_0 + C_1^+\Phi_1 + C_2^+\Phi_2 + C_3^+\Phi_3 + C_6^+4\Phi_4 = \begin{cases} 0 & \text{Laplace} \\ f\big|_{k=0} & \text{Poisson} \end{cases} \tag{4.1}$$

In this symbolic equation, (4.1), the coefficients of the finite difference equations are defined depending on the spacing to the boundaries. The Shortley-Weller coefficients for the discrete Laplace operator $\Delta|_h$ will be distinctly expressed as follows

$$\begin{aligned} C_1^+ &= \frac{1}{h^2\alpha_1(\alpha_1+\alpha_3)} & C_2^+ &= \frac{1}{h^2\alpha_2(\alpha_2+\alpha_4)} \\ C_3^+ &= \frac{1}{h^2\alpha_3(\alpha_3+\alpha_1)} & C_4^+ &= \frac{1}{h^2\alpha_4(\alpha_4+\alpha_2)} \\ C_0^+ &= -\sum_{k=1}^{4} C_k^+ \end{aligned} \tag{4.2}$$

The motivation of the following approach is to produce an accurate method for treating mixed derivatives. Near the boundary, the approximation of the second order mixed derivatives requires a 9-point stencil. This task is not easy to handle with respect to the aimed "automatization" of the method. A transformation by rotation 45° of the grid (stencil) to obtain a 5-point formula is also suggested. Notice that the 2-dimensional Taylor series approach, according to the approximation of mixed derivatives, leads to a similar form of Shortley-Weller's coefficients in a 45° skewed stencil as shown in Fig. 2b

$$\frac{\partial^2\phi}{\partial x\partial y}\Big|_h = C_0^\times\Phi_0 + C_1^\times\Phi_1 + C_2^\times\Phi_2 + C_3^\times\Phi_3 + C_4^\times\Phi_4 \tag{4.3}$$

The finite difference coefficients for mixed derivates (4.3) can be expressed in individual terms as follows

$$\begin{aligned} C_1^\times &= \frac{1}{2h^2\beta_1(\beta_1+\beta_3)} & C_2^\times &= \frac{-1}{2h^2\beta_2(\beta_2+\beta_4)} \\ C_3^\times &= \frac{1}{2h^2\beta_3(\beta_3+\beta_1)} & C_4^\times &= \frac{-1}{2h^2\beta_4(\beta_4+\beta_2)} \\ C_0^\times &= -\sum_{k=1}^{4} C_k^\times \end{aligned} \tag{4.4}$$

The above symbols $(+, \times)$ are used for normal and skewed network stencil, respectively. By definition, the irregular 5-point-difference star is present when at least one of its star boughs (arms) becomes smaller than the mesh size h. The irregular difference star is the most general case and for the regular ones, the following condition is required $\alpha_k = \beta_k = 1$, $k \in \{1, 2, 3, 4\}$.

Furthermore, in this study, the direct method which produces an exact solution in a finite number of operations is used (Duff *et al.*, 1986). When solving successively the Laplace and the Poisson systems of equations, the errors in the solutions arise only from the rounding off and truncation errors in the computational calculation (Smith, 1985; Collatz, 1960). This method is tested on several application examples and is found to produce very good results (Rezini, 1984).

5. Results of methods and discussion

Before the PCs had appeared, the SSD-method was done by manual calculations. One imagines the excess of labour to investigate the Square Block problem. However, because we already have the results of Frocht (1948, pp. 265-269), the feasibility of this method will be proved on this application example. Isochromatics (in orders) have been superimposed for convenience over the isoclinic parameters in the field around the straight line X, as depicted in Fig. 1. The stress-integration can be started from the initial values, and the stress-separation will be accomplished according to numerical integrations (3.4), as mentioned previously. The initial stress values are obtained from the boundary values at a point from conditions (3.7). For the stress-separation along the straight line, instead of using relation (3.4), Frocht proceeds as follows

$$\begin{aligned} \sigma_x\Big|_i &= \sigma_x\Big|_0 - \sum_0^i \varDelta\tau_{xy}\Big(\frac{\varDelta x}{\varDelta y}\Big) \\ \sigma_y &= \sigma_x \pm \sqrt{(\sigma_1-\sigma_2)^2 - 4\tau_{xy}^2} \end{aligned} \tag{5.1}$$

The plus or minus signs in front of the radical in $(5.1)_1$ correspond to the two possible positions of the centre of Mohr's circle. Accordingly, σ_1 lies furthermost on the right and σ_2, being the furthermost, on the left of the circle.

The initial value of $\sigma_x|_0$ for the step-by-step integration is evaluated from the boundary value of q_0 (fringe order negative) and θ_0, which are 0.80 fringe and 45°, respectively. The initial stresses in both the x direction and the y direction get the following respective values

$$\sigma_x\Big|_0 = q_0\cos^2 45° = -0.8\cdot 0.5 = -0.40\,\text{fringe} \tag{5.2}$$

and

$$\sigma_y\Big|_0 = q_0\sin^2 45° = -0.8\cdot 0.5 = -0.40\,\text{fringe} \tag{5.3}$$

The initial shear stress value becomes

$$\tau_{xy}\Big|_0 = -q_0\sin 45°\cos 45° = -\frac{q_0}{2} = +0.8\cdot 0.5 = +0.40\,\text{fringe} \tag{5.4}$$

In this case, it is important to point out the difference between both procedures: in Frocht's SSD-process, the stress component σ_y is determined by means of Mohr's circle statement $(5.1)_2$; while the isoclinic parameter θ is used for the integration. The cumulative error in the integration process has also an effect on the stress-separation. It is noted that the determination of θ isoclinic parameter in its physical range remains, generally, a difficult problem (Fernàndez, 2011). Several works have been published concerning this topic; see for example (Mangal and Ramesh, 1999; Siegmann *et al.*, 2011; Ajovalasit and Zuccarello, 2000). Besides, in the Beltrami-Michell Boundary Value Problem (B-M BVP), each stress component being subject to its values on the boundary form a BVP individually. In addition, it is noted that the Square Block edges direction (slope) is a principal stress direction itself in the case of a free boundary. Otherwise, this shows the long process in achieving the results by means of the SSD-method (see diagram; Fig. 3). Mainly, the fact it is noticed that the separation of stresses is established along a straight line only.

The need for full-field separation of stresses is more advantageous, and this is why B-M BVP is more appropriate. In order to make full comparisons, the same representation as that of Frocht (Fig. 3) is adapted.

In order to re-examine the stress distribution for further validation, a numerical analysis has been carried out using the finite element analysis for the same Square Block loading situation.

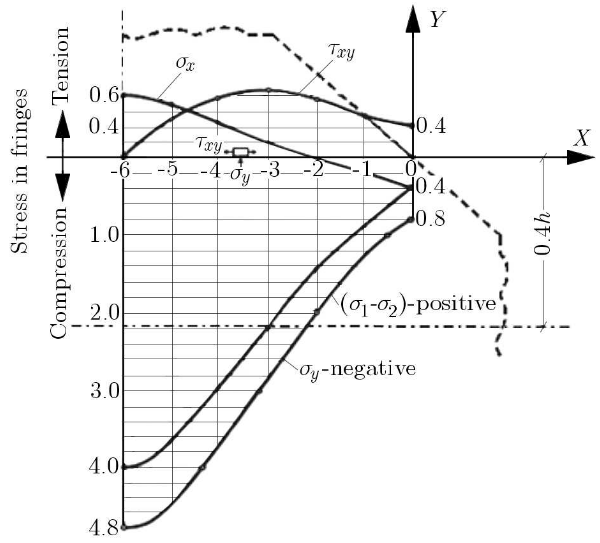

Fig. 3. Cartesian stress components distributions on section X (Frocht, 1948, pp. 265-269)

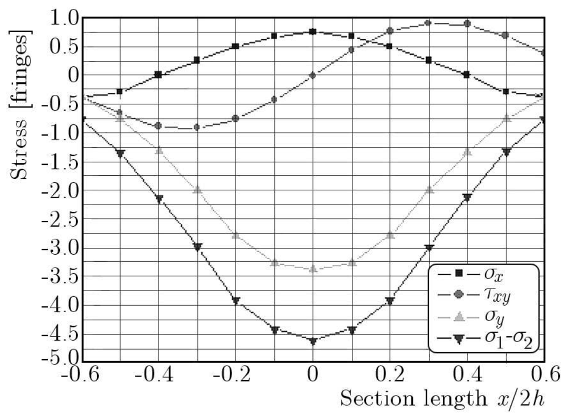

Fig. 4. Cartesian stress component distributions on section X (referring to this work)

The FEA has been performed using ANSYS software. PLANE82 elements have been used to model the Square Block subjected to diagonal compression. This type of element provides more accurate results for mixed (quadrilateral-triangular) automatic meshes and can tolerate irregular shapes without as much loss of accuracy. Such 8-node elements have compatible displacement shapes and are well suited to model curved boundaries (Madenci and Guven, 2005).

After preliminary tests, the meshing configuration shown in Fig. 5 has been opted for; a number of 3491 PLANE82-elements (10720 Nodes) have been used.

The static balance across section X is then stated when the sum of vertical forces vanishes. This condition of equilibrium in the loading direction provides the necessary (check) verification of each method used, permitting the comparison of the numerical results. All geometrical dimensions and the load necessary for the result verification are shown in Fig. 5. The units are also kept Anglo-American. Furthermore, the stress distributions along the straight line X will be compared with those of the SSD-method and of FEA. Accordingly, the equilibrium across the horizontal section may be re-examined. The normal stress σ_y acting within each cross section must balance the load P_y each time. The area under the σ_y-curve (Fig. 3) has been measured by means of a planimeter and found to be $11.2\,\mathrm{in}^2$. The length of the half section $0.6h$ has been found to be 4.065 in (Frocht, 1941, pp. 270). Hence

$$\sigma y = \frac{11.2}{4.065} = 2.75\,\mathrm{in} = 2.2\,\mathrm{fringes}$$

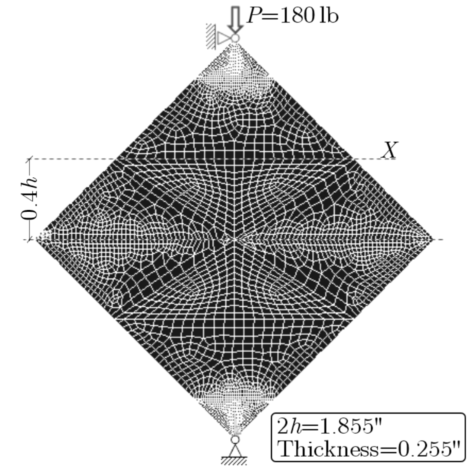

Fig. 5. Meshing configuration of the Square Block and associated boundary conditions

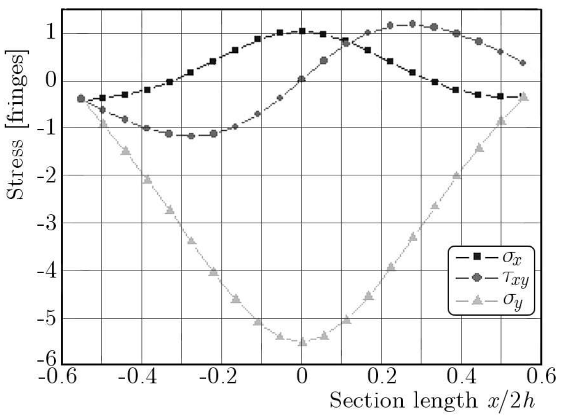

Fig. 6. Cartesian stress component distributions on section X using FEA

Multiplying this value by the model compressive fringe value of 284 psi, we have: $\sigma_y = 2.2 \cdot 284 = 625$ psi. The force P_y acting on the section of length $0.6h$ is then given by: $P_y = 625 \cdot 1.855 \cdot 0.255 \cdot 0.6 = 177.5$ lb. This result differs from the applied load of 180 lb approximately by -1.5%. Concerning our results, the integral of the σy-curve (Fig. 6) is calculated. By taking into account our scale, the following result is obtained: $\sigma_y = 2.18 \cdot 284 = 619$ psi. Hence, the calculated force resulting from our calculation method is: $P_y = 619 \cdot 1.855 \cdot 0.255 \cdot 0.6 = 175.7$ lb.

Therefore, the error induced is approximately -2.4%. This discrepancy is not a crucial one. The reasons leading to this error magnitude will be discussed later. In contrast, the FEA results are the most accurate (see Table 1) in this analysis.

Table 1. Comparison of present results with Frocht's and FEA

Result of	P_y [lb]	Error [%]
Frocht	177.50	-1.5
FEA	179.75	-0.1
this work	175.70	-2.4

Referring to the available experimental results, those achieved by the photoelastic-numerical hybrid method are in good agreement with a relative difference of about -1%. Furthermore, it is worth emphasizing that the occurring small deviations in the results obtained are due to the procedure of the graphical representation rather than to inaccuracy in the calculation.

Moreover, the component stress distribution is automatically interpolated at the grid points in the neighbourhood of the straight line X, which explains once more the deviation of the results. On the one hand, the designated lines along which the results will be compared cannot be identical in the absolute. Moreover, there is a significant difference in terms of the process used to expose stress distribution maps in the reference work (Fig. 4) likewise for FEA (Fig. 6). Separating the result data in individual components usually provides stresses at only discrete locations. For this purpose, the field results are presented in Figs. 7 and 8.

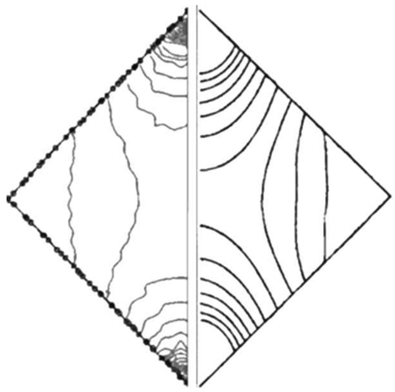

Fig. 7. Isopachic stress patterns; LHS calculated and RHS measured

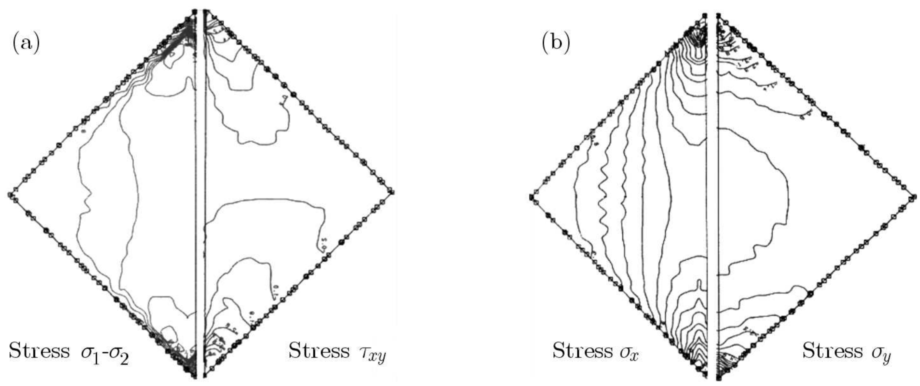

Fig. 8. Full-field distributions of each stress

6. Conclusion

In the present study, validation of the stress state results obtained by two comparative methods has been carried out using supplementary FEA numerical models. A very good qualitative agreement between the three methods has been found. As treated by Frocht, the true whole field isoclinic angle and phase difference are the key data to obtain the stress distribution in a birefringent model. The feasibility of this method has been proved by the Square Block experiment under in-plane compression, wherein only boundary isochromatic fringe data are needed. Furthermore, the developed SSD-method by Frocht still provides accurate results. The aim of this paper is to show the efficiency of an additional method for stress-separation without needing field information as in the case of the SSD-method; and to quickly obtain results with an acceptable accuracy. Based on the numerical solving of the B-M BVP of Dirichlet's type, this method reduces the photoelastic data to the minimum, in order to separate the prevailing stresses. Further, the method facilitates the automatic process for generating stress component maps (Ajovalasit and Zuccarello, 1998) and reconstructing the full-field stress tensor using little equipment. In regard to large utilization in the experimental-numerical photoelasticity, the next step will be to develop an automatic system that allows the computer to control both the image acquisition of boundary isochromatic fringes and the shape recognition simultaneously. In fact, the present paper has shown that the successful use of a hybrid method can thereby reduce the amount of measurements required, increase the accuracy of numerical results and, at the same time, allow quick determination of the complete stress distribution within the studied part.

References

1. Ajovalasit A., Zuccarello B., 2000, Limitation of Fourier transform photoelasticity: influence of isoclinics, *Experimental Mechanics*, **4**, 384-392
2. Ajovalasit A., Barone S., Petrucci G., 1998, A review of automated methods for the collection and analysis of photoelastic data, *Strain*, **33**, 75-91
3. Boresi A.P., Chong K.P., Lee J.D., 2011, *Elasticity in Engineering Mechanics*, 3rd Edit., John Wiley & Sons, Inc.
4. Collatz L., 1960, *The Numerical Treatment of Differential Equations*, Springer
5. Dahlquist G., Bjorck A., 1974, *Numerical Methods*, Prentice-Hall, Englewood Cliffs, NJ
6. Duff I., Erisman A., Reid J., 1986, *Direct Methods for Sparse Matrices*, Oxford University Press, England
7. Fernàndez M.S.-B., 2011, Towards uncertainty evaluation in photoelastic measurements, *Journal of Strain Analysis*, **45**, 275-285
8. Fernàndez M.S-B., Alegre Calderón J.M., Bravo Diez P.M., Cuesta Segura I.I., 2010, Stress-separation techniques in photoelasticity, *Strain*, **1**, 1-17
9. Frocht M., 1931, A Study of Photoelasticity and a Photoelastic Theoretical Investigation of the Stress Distribution in Square Blocks Subjected to Concentrated Diagonal Loads, Dissertation Topic, Advisor Stephen Prokofyevich Timoshenko. Ph.D. Dissertation, University of Michigan, USA
10. Frocht M., 1941, *Photoelasticity*, Volume I, John Wiley & Sons, New York
11. Frocht M., 1948, *Photoelasticity*, Volume II, John Wiley & Sons, New York
12. Hetnarski R.B., Ignaczak J., 2011, *The Mathematical Theory of Elasticity*, Taylor Francis
13. Kuske A., 1959, *Introduction of Photoelasticity* (in German), Stuttgart, Wissenschaftliche Verlagsgesellschaft
14. Kuske A., 1971, *Handbook of Photoelasticity* (in German), Stuttgart: Wiss. Verl. Ges.
15. Kuske A., Robertson G., 1974, *Photoelastic Stress Analysis*, London, New York, Sydney John Wiley & Sons
16. Madenci E., Guven I., 2005, *The Finite Element Method and Applications in Engineering Using ANSYS*, Springer
17. Mangal S.K., Ramesh K., 1999, Use of multiple loads to extract continuous isoclinic fringes by phase-shifting, *Strain*, **35**, 15-17
18. McKenney A., Greengard L., Mayo A., 1996, A fast Poisson solver for complex geometries, *Journal of Computation Physics*, **2**, 348-355
19. Muskhelishvili N.I., 1975, *Some Basic Problems of the Mathematical Theory of Elasticity*, 4th Edit., English translation, L. Noordhoff International Publishing, Leyden
20. Petrucci G., 1997, Full-field automatic evaluation of an isoclinic parameter in white light, *Experimental Mechanics*, **37**, 4, 420-426

21. Pinit P., Umezaki E., 2007, Digitally whole field analysis of isoclinic parameter in photoelasticity by four-step color phase-shifting technique, *Optics and Lasers in Engineering*, **45**, 7, 795-807

22. Ramesh K., 2008, *Photoelasticity, Springer Handbook of Experimental Solid Mechanics*, Springer Handbook of Experimental Solid Mechanics

23. Rezini D., 1984, Randisochromaten als ausreichende Information zur Spannungstrennung und Spannungsermittelung in der Spannungsoptik, Ph.D. Dissertation, TU-Clausthal, FR Germany

24. Sharafutdinov G. Z., 2012, Basic relations of photoelasticity (I. Allerton Press, Ed.), *Allerton Press, Inc.*, **67**, 1, 1-4

25. Shortley G. H., Weller R., 1938, The numerical solution of Laplace's equation, *Appl. Phys.*

26. Siegmann P., Colombo C., Daz-Garrido F., Patterson E., 2011, Determination of the isoclinic map for complex photoelastic fringe patterns, *Experimwntal and Applied Mechanics*, **6**, 79-85, Conf. Proc. of the SEM Series 17

27. Smith G., 1985, *Numerical Solution of Partial Differential Equations: Finite Difference Methods*, Oxford Ed., Clarendon Press

28. Zhang J., 1998, Fast and high accuracy multigrid solution of the three dimensional Poisson equation, *Journal of Computation Physics*, **2**, 449-461

Manuscript received October 7, 2013; accepted for print April 17, 2015

JOURNAL OF THEORETICAL
AND APPLIED MECHANICS
53, 4, pp. 859-872, Warsaw 2015
DOI: 10.15632/jtam-pl.53.4.859

A STUDY ON LOW VELOCITY IMPACT RESPONSE OF FGM RECTANGULAR PLATES WITH 3D ELASTICITY BASED GRADED FINITE ELEMENT MODELING

Kamran Asemi
Department of Mechanical Engineering, Tehran North Branch, Islamic Azad University, Tehran, Iran
Sattar Jedari Salami
Department of Mechanical Engineering, Damavand Branch, Islamic Azad University, Damavand, Iran
e-mail: sattar.salami@damavandiau.ac.ir

Low velocity impact behavior of rectangular plates made of functionally graded materials (FGMs) based on three-dimensional theory of elasticity is studied in this paper. The modified Hertz contact law, which is appropriate for graded materials, is employed. On the basis of the principle of minimum potential energy and the Rayleigh Ritz method, the graded finite element modeling is applied. Solution of the nonlinear resulted system of equations in the time domain is accomplished via an iterative numerical procedure based each time on Newmark's integration method. The effects of various involved parameters, such as the graded property profile, projectile velocity and projectile density on time histories of contact force, lateral deflection and normal stresses are investigated in detail. To present efficiency of the present work, several numerical examples are included. The main novelty of the present research, which has not been reported in literature, is considering the difference of lateral deflection through the thickness of the FGM plate due to analyzing three-dimensional elasticity of the plate.

Keywords: low velocity impact, functionally graded plate, three dimensional elasticity, graded finite element

1. Introduction

Functionally graded materials yield as a category of novel composite materials in which mechanical properties vary in one, two or even three specific direction(s). FGMs are mainly composed of metal and ceramic components. Unlike the traditional composites, which are piecewise homogeneous mixtures or layered structures, material properties of FGMs are affected by those of all constituent materials, so that mechanical properties of the FGMs can be monitored to vary continuously throughout the structure. Advantages of FGMs over laminated composites are the elimination of the delamination mode of failure, reduction thermal stresses, residual stresses and stress concentration factors.

Low velocity impact response of solid structures is a conventional topic in structural mechanics. There are various approaches to model the contact between the projectile and target. Spring mass models, energy balance technique and a direct approach are the commonly utilized methods. A complete survey of these approaches with their defects or advantages may be found in a book by Abrate (1998).

A wide range of studies has been carried out on dynamic analysis of FGM structures which mostly used the plate and shell theories (Asemi *et al.*, 2010; Qian *et al.*, 2004; Sun and Luo, 2011; Behjat *et al.*, 2009; Kiani *et al.*, 2012; Noda *et al.*, 2012; Derras *et al.*, 2013; Ghannad and Nejad, 2013; Yaghoobi and Torabi, 2013). For thin plates, the classical plate theory (CPT) is used to analyze FG plates. Due to neglecting the effect of shear deformation through the thickness of

FG plates, the application of this theory to moderately thick or thick plate structures can lead to considerable errors. Therefore, for eliminating the lack of CPT for moderately thick and thick FG plates, the first, third and higher shear deformation theories and also the 3D elasticity solutions, some modifications are done to include the effects of transverse shear deformation. Among these analyses, 3D elasticity analysis of plates not only provides accurate results but also allows further physical insights, which cannot otherwise be estimated by the other two dimensional or plate theory analyses.

A literature review on the subject of FGM structures under low velocity impact as a dynamic analysis discloses that researches on this topic are rare in the open literature. There are a class of works dealing with the simulation of low velocity impact response of FGMs using the commercial software. For instance, Gunes and Aydin (2010) modeled the three dimensional response of FGM media using the commercial finite element software. In that research an FGM circular plate was divided into a number of layers in the thickness direction, where each one was supposed as an isotropic homogeneous layer. Gunes *et al.* (2011) developed their previous work for the case of elasto-plastic impact response of circular FGM plates. Mori-Tanaka scheme was applied to obtain the equivalent properties of each single layer. For the case of a sandwich beam with FGM core, Etemadi *et al.* (2009) extended a three dimensional simulation on the low velocity impact response of the structure.

To achieve the low velocity impact response of FGM plates, Larson and Palazotto (2009) and Larson *et al.* (2009) developed a combined experimental, computational and analytical method. In those investigations, a property estimation sequence was introduced for specifying the local elastic properties of a two-phased, two constituent FGM plate subjected to impact loading. Numerical simulations and experimental tests were carried out on Ti-TiB FGM plates. The evaluated results were then used to accomplish a finite element model of the problem. It was indicated that the low-velocity impact response of the plate based on FEM results were in good agreement with those obtained experimentally. To date, a few works have been studied on dynamic behavior of plates made of functionally graded materials in two directions. Wirowski (2009) studied free vibrations of thin annular plates made of a functionally graded material that is made of a two-phase functionally graded composite. The plate has a periodically inhomogeneous microstructure slowly varying along a circular coordinate, but smoothly graded properties in the radial direction. Also, Wirowski (2011, 2012) analyzed the free vibration response of a thin rectangular plate band made of a nonlinear functionally graded material. The material properties varied periodically in one direction and non-linearly in the other one. The effect of the material distribution on the overall response of the composite was studied. As might be concluded, a very strong dependency of frequency of free vibrations of the plate band on the material distribution was observed for the bracket and very weak for the simple support on both sides.

There are only a few investigations related to the mathematical formulation of low velocity impact in FGMs. The main reason may be the contact force modeling between the projectile and target. Giannakopoulos and Suresh (1997) studied the indentation of solids into a graded half-space. Two types of grading profiles, i.e. the exponential distribution and polynomial type of dispersion were considered in their works. In addition, the two-dimensional contact was also studied by Giannakopoulos and Pallot (2000). Those investigations may be useful to deduce the contact-force expression for graded materials. For example, Mao *et al.* (2011) analyzed the response of a shallow spherical shell under the low velocity impact in a thermal field. Properties of the FGM media were distributed across the thickness based on an exponential function. The immovable case of clamped edges was considered and the resulted equations were solved via the Galerkin method. The developed contact force formulation for the exponential property distribution revealed that the force-indentation relation in exponential FGMs was similar to the Hertz contact force, where force is proportional to $\alpha^{3/2}$. The contact stiffness, however, was related to geometrical and material parameters of contacting structures, impacting a sphere and an FGM shallow spherical shell. For media with transversely isotropic characteristics, Conway (1956) and Turner (1980) concluded a force-indentation relation through the Hertz contact force expression. In those researches, also only the contact stiffness was influenced by a property variation of the structure and again, force was proportional to $\alpha^{3/2}$.

Such a character motivates the investigators to modify the Hertz contact force of finite thickness media in a way to account the graded profile through the thickness. For instance, Larson and Palazotto (2006) developed a Hertzian type of the contact force in which the contact stiffness was modified to account the grading profile. The impact response of a circular FGM plate was analyzed in their work. Shariyat and Jafari (2013) obtained the low velocity impact behavior of a circular plate with both radial and transverse graded profiles. In their work, symmetrical motion equations were obtained based on the first order shear deformation plate theory and the results were found via the Galerkin method. In another study, Shariyat and Farzan (2013) investigated the response of an FGM plate in rectangular shape under the eccentric impact. In that research, the first order shear deformation beam theory was used and the effect of in--plane loads was also taken into consideration. Khalili *et al.* (2013) studied the response of a thin FGM plate in rectangular shape that was subjected to low velocity impact. However in that research, in-plane inertia effects were neglected. With the introduction of Airy stress function, the in-plane motion equations were replaced by the compatibility equation. Besides, a linear contact force model was employed in which the contact force varied linearly with respect to indentation. The contact stiffness was obtained based on the mass-spring model and the results were compared with the ABAQUS software. In another study, Dai *et al.* (2012) studied the low velocity impact behaviour of shear deformable FGM circular plates. In that investigation, also the contact formulation of Giannakopoulos and Suresh (1997) was implemented. The solution in space and time domains was obtained based on the orthogonal collocation point method and Newmark's method, respectively.

According to the above literature review, to date, the equivalent single-layer theories have been applied to analyze the low velocity impact response of FGM plates. Due to difficulty in obtaining solutions for low velocity impact analysis of FGM plates based on 3D elasticity, solutions are available only through a number of problems by the use of plate theories. Therefore, powerful numerical methods are needed to solve the governing equations. The graded finite element method (GFEM) is a relatively new numerical technique in structural analysis. Kim and Paulino (2002), and Zhang and Paulino (2007), developed a GFEM approach for modeling nonhomogeneous structures. In their studies, it was shown that the conventional FE formulations cause a discontinuous stress field in the direction perpendicular to the material property gradation, while the graded elements gave a continuous and smooth variation. Also, Asemi *et al.* (2012) studied the dynamic response of thick short length FGM cylinders under an internal impact loading using the graded finite element method. Ashrafi *et al.* (2013) presented a comparative study between the graded finite element and boundary element formulations capable of modeling nonhomogeneous behavior of FGM structures. They showed that using the conventional finite element modeling such that the material property is constant within an element for dynamic problems leads to considerable discontinuities and inaccuracies. On the other, hand by using the graded finite element method in which the material property is graded continuously through the elements, the accuracy of results can be improved without increasing the mesh size.

To the best knowledge of the authors, there are no accessible documents in literature on involving effects of the material inhomogeneity of the FGM plates based on the graded elements and three dimensional elasticity theory on low velocity impact response of FGM plates. So, the present study aims at developing a numerical approach for low velocity impact of FGM rectangular plates based on the three-dimensional theory of elasticity. The governing equations are derived based on the principle of minimum potential energy and the Rayleigh Ritz method. In this regard, variations of the material properties are interpolated using general shape functions.

An iterative numerical procedure in the space domain is used which is suitable for an arbitrary case of boundary conditions. This style accompanied with Newmark's method is employed to solve the nonlinear resulted field equations. The modified contact force model of Larson and Palazotto (2006), which considered the property variations through the thickness, is utilized. The influences of various involved parameters such as projectile velocity, power law index, projectile mass on time histories of the contact force and lateral deflection of the target are studied in detail.

2. The governing equations

2.1. Description of variations of the material properties

A functionally graded rectangular plate whose length, width, and thickness are marked by a, b, and h, respectively, is considered as it is shown in Fig. 1. The top surface of the plate is made of pure metal and the bottom surface of pure ceramic. The material properties of the plate vary continuously through the thickness direction according to a power law distribution

$$P = P_c + (P_m - P_c)\Big(\frac{z}{h}\Big)^n \tag{2.1}$$

where P is material property such as elasticity modulus and mass density. n is the non-negative volume fraction index and the z coordinate is measured from the bottom surface of the plate. The subscripts c and m are referred to a ceramic and metal, respectively.

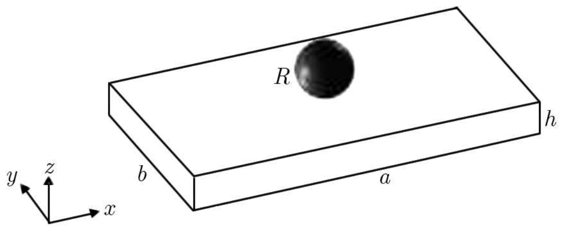

Fig. 1. Geometry of the plate and the impactor

2.2. The effective stiffness of the contact region

Integrating the local volume fraction of the constituent material of the top layer leads to the total volume fraction of the mentioned material

$$V_m = \frac{1}{h}\int\limits_0^h \Big(\frac{z}{h}\Big)^n\,dz = \frac{1}{1+n} \qquad\qquad V_c = 1 - V_m \tag{2.2}$$

Therefore, the apparent material properties of the FGM plate at the impact region can be expressed as

$$\begin{aligned} E_z &= \Big(\frac{V_c}{E_{z_c}} + \frac{V_m}{E_{z_m}}\Big)^{-1} \qquad && G_{xz} = G_{yz} = \Big(\frac{V_c}{G_c} + \frac{V_m}{G_m}\Big)^{-1} \\ E_x &= E_y = E_c V_c + E_m V_m && \rho = \rho_c V_c + \rho_m V_m \end{aligned} \tag{2.3}$$

where G is the shear modulus of the material.

Based on the investigation carried out by Olsson (1992), the impact load applied by a spherical projectile may be related to the indentation value of an isotropic half space through the following Hertz-type relation

$$F(\alpha) = K_h \alpha^{3/2} \tag{2.4}$$

where α is the indentation value, and the impact stiffness is

$$K_h = \frac{4}{3}Q_\alpha\sqrt{R} \tag{2.5}$$

where R is the indenter nose radius, and Q_α is defined as

$$\frac{1}{Q_\alpha} = \frac{1}{Q_{zi}} + \frac{1}{Q_{zp}} \qquad Q_{zk} = \frac{E_{zk}}{1-\nu_{zk}^2} \qquad k = i,p \tag{2.6}$$

where E_{zk} is the elastic modulus in the transverse direction and ν_{zk} is Poisson's ratio of the plate (p) or impactor (i). For the case in which the rigidity of the impactor is much more than that of the impacted half space, Eq. (2.6) may be reduced to

$$Q_\alpha = Q_{zp} \tag{2.7}$$

It is evident that the impact force and the indentation value are considerably smaller when the same indenter impacts a very thin plate instead of a half space. For this reason, Swanson (2005) modified Eq. (2.4) in the following form for a transversely isotropic plate with a finite thickness

$$F(\alpha) = \beta K_h\alpha^{3/2} \tag{2.8}$$

where β is an empirical correction factor that tends to unity for thickness to indentation ratios exceeding three. On the other hand, Turner (1980) proved that the apparent modulus of a plate that incorporates influences of the transverse variations of material properties at the impact region may be determined as follows

$$Q_\alpha = \frac{2}{\alpha_1\alpha_3} \tag{2.9}$$

where

$$\begin{aligned} \alpha_1 &= \sqrt{\frac{1}{1-\nu_{xy}^2}\Big(\frac{E_x}{E_z} - \nu_{xz}^2\Big)} \qquad \alpha_2 = \frac{1}{1-\nu_{xy}^2}\Big[\frac{E_x}{2G_{xz}} - \nu_{xz}(1+\nu_{xy})\Big] \\ \alpha_3 &= \sqrt{\frac{\alpha_1+\alpha_2}{2}}\Big(\frac{1-\nu_{xy}}{G_{xy}}\Big) \end{aligned} \tag{2.10}$$

2.3. Equations of motion of an FGM plate

In absence of the body forces, the equations of motion for an FGM rectangular plate can be written as follows

$$\sigma_{ij,j} = \rho(z)\ddot{u}_i \tag{2.11}$$

where $i,j = x,y,z$, and the comma denotes partial differentiation with respect to Cartesian coordinate variables. Hence, $u_x = u$, $u_y = v$, $u_z = w$ are displacement components along the x, y and z axes, respectively. Also, ρ is mass density which depends on the z coordinate, and σ_{ij} are the stress components.

2.4. Stress-strain relations

The constitutive relation based on the three- dimensional theory of elasticity is as follows

$$\boldsymbol{\sigma} = \mathbf{D}\boldsymbol{\varepsilon}$$

$$\mathbf{D} = \frac{E(z)(1-\nu)}{(1+\nu)(1-2\nu)}\begin{bmatrix} 1 & \frac{\nu}{1-\nu} & \frac{\nu}{1-\nu} & 0 & 0 & 0 \\ \frac{\nu}{1-\nu} & 1 & \frac{\nu}{1-\nu} & 0 & 0 & 0 \\ \frac{\nu}{1-\nu} & \frac{\nu}{1-\nu} & 1 & 0 & 0 & 0 \\ 0 & 0 & 0 & \frac{1-2\nu}{2(1-\nu)} & 0 & 0 \\ 0 & 0 & 0 & 0 & \frac{1-2\nu}{2(1-\nu)} & 0 \\ 0 & 0 & 0 & 0 & 0 & \frac{1-2\nu}{2(1-\nu)} \end{bmatrix} = E(z)\boldsymbol{\Lambda} \tag{2.12}$$

where $\mathbf{D}$ is the elastic coefficients matrix. It is assumed that the elasticity modulus E varies in the z direction while Poisson's ratio ν is constant. The constant part of the matrix $\mathbf{D}$ is defined as $\mathbf{\Lambda}$.

2.5. Strain-displacement relations

The strain displacement relations of the infinitesimal theory of elasticity in the rectangular Cartesian coordinates are

$$\varepsilon_{ij} = \frac{1}{2}(u_{i,j} + u_{j,i}) \tag{2.13}$$

Strain-displacement relations (2.13) may be written as

$$\boldsymbol{\varepsilon} = \mathbf{dq} \qquad \mathbf{d} = \begin{bmatrix} \frac{\partial}{\partial x} & 0 & 0 \\ 0 & \frac{\partial}{\partial y} & 0 \\ 0 & 0 & \frac{\partial}{\partial z} \\ \frac{1}{2}\frac{\partial}{\partial y} & \frac{1}{2}\frac{\partial}{\partial x} & 0 \\ 0 & \frac{1}{2}\frac{\partial}{\partial z} & \frac{1}{2}\frac{\partial}{\partial y} \\ \frac{1}{2}\frac{\partial}{\partial z} & 0 & \frac{1}{2}\frac{\partial}{\partial x} \end{bmatrix} \qquad \mathbf{q} = \begin{bmatrix} u \\ v \\ w \end{bmatrix} \tag{2.14}$$

2.6. Boundary and initial conditions

For a simply supported plate, the essential boundary conditions are defined as

$$\begin{aligned} &w(0,y,z) = w(a,y,z) = w(x,0,z) = w(x,b,z) = 0 \\ &v(0,y,z) = v(a,y,z) = u(x,0,z) = u(x,b,z) = 0 \end{aligned} \tag{2.15}$$

And initial conditions for the system of equations are as follows

$$\mathbf{q}_0 = \dot{\mathbf{q}}_0 = 0 \qquad \alpha_0 = 0 \qquad \dot{\alpha}_0 = V_0 \tag{2.16}$$

3. Graded finite element modeling

The three-dimensional 8-node linear brick element is considered. In contrast to the conventional solid (brick) elements, material properties are interpolated using the shape functions. Following the common FE approximation, the displacement components vector $\mathbf{q}$ of an arbitrary point of the element may be related to the nodal displacement vectors of the element $\boldsymbol{\delta}^{(e)}$ through the shape function matrix $\mathbf{N}$, as

$$\begin{gathered} \mathbf{q}(\xi,\eta,\zeta) = \mathbf{N}(\xi,\eta,\zeta)\boldsymbol{\delta}^{(e)} \qquad \boldsymbol{\delta}^{(e)} = \Big\{U_1 \quad V_1 \quad W_1 \quad \dots \quad U_8 \quad V_8 \quad W_8\Big\}^{\mathrm{T}} \\ \mathbf{N} = \begin{bmatrix} N_1 & 0 & 0 & N_2 & 0 & 0 & N_3 & 0 & 0 & N_4 & 0 & 0 & N_5 & 0 & 0 & N_6 & 0 & 0 & N_7 & 0 & 0 & N_8 & 0 & 0 \\ 0 & N_1 & 0 & 0 & N_2 & 0 & 0 & N_3 & 0 & 0 & N_4 & 0 & 0 & N_5 & 0 & 0 & N_6 & 0 & 0 & N_7 & 0 & 0 & N_8 & 0 \\ 0 & 0 & N_1 & 0 & 0 & N_2 & 0 & 0 & N_3 & 0 & 0 & N_4 & 0 & 0 & N_5 & 0 & 0 & N_6 & 0 & 0 & N_7 & 0 & 0 & N_8 \end{bmatrix} \end{gathered} \tag{3.1}$$

The components of the shape matrix may be expressed in terms of the natural coordinates (Zienkiewicz and Taylor, 2005)

$$N_i(\xi,\eta,\zeta) = \frac{1}{8}(1+\xi_i\xi)(1+\eta_i\eta)(1+\zeta_i\zeta) \tag{3.2}$$

where $-1 \leqslant \xi \leqslant 1$, $-1 \leqslant \eta \leqslant 1$ and $-1 \leqslant \zeta \leqslant 1$.

In addition to the displacement field, the heterogeneity of the material properties of the FGM may also be determined based on their nodal values. Therefore, a graded finite element method (GFEM) may be used to effectively trace smooth variations of the material properties at the element level. Using GFEM for the modeling of gradation of the material properties leads to more accurate results than dividing the solution domain into homogenous elements. In this regard, the shape functions similar to those of the displacement field may be used

$$E = \sum_{i=1}^{8} E_i N_i = \mathbf{N}\boldsymbol{\Xi} \qquad \rho = \sum_{i=1}^{8} \rho_i N_i = \mathbf{N}\boldsymbol{\mathcal{R}} \tag{3.3}$$

where E_i and ρ_i are the modulus of elasticity and mass density corresponding to node i. $\mathbf{N}$, $\boldsymbol{\Xi}$ and $\boldsymbol{\mathcal{R}}$ are vectors of shape functions, modulus of elasticity and mass densities of each element, and they are as

$$\mathbf{N} = [N_1, \ldots, N_8]_{1\times 8} \qquad \boldsymbol{\Xi} = [E_1, \ldots, E_8]^{\mathrm{T}}_{1\times 8} \qquad \boldsymbol{\mathcal{R}} = [\rho_1, \ldots, \rho_8]^{\mathrm{T}}_{1\times 8} \tag{3.4}$$

Therefore, Eq. (2.12) may be rewritten as

$$\mathbf{D} = \boldsymbol{\Lambda}\mathbf{N}\boldsymbol{\Xi} \tag{3.5}$$

Substituting (3.1) into (2.14) gives the strain matrix of the element (e) as

$$\boldsymbol{\varepsilon}^{(e)} = \mathbf{d}\mathbf{N}^{(e)}\boldsymbol{\delta}^{(e)} = \mathbf{B}\boldsymbol{\delta}^{(e)} \tag{3.6}$$

The governing equations of the FE model may be derived based on the principle of minimum potential energy and the Rayleigh Ritz method. The total potential energy of the plate may be expressed as

$$\begin{aligned}\Pi^{(e)} &= \frac{1}{2}\int\limits_{V^{(e)}} (\boldsymbol{\varepsilon}^{(e)})^{\mathrm{T}}\boldsymbol{\sigma}^{(e)}\, dV - \int\limits_{A^{(e)}} \mathbf{q}^{\mathrm{T}}\mathbf{p}\, dA + \int\limits_{V^{(e)}} \boldsymbol{\rho}\mathbf{q}^{\mathrm{T}}\ddot{\mathbf{q}}^{(e)}\, dV \\ &\quad + m_p w_p \ddot{w}_p - \frac{2}{5}K_h\Big[w_p - W\Big(\frac{a}{2}, \frac{b}{2}, h\Big)\Big]^{\frac{5}{2}}\end{aligned} \tag{3.7}$$

where $W(a/2, b/2, h)$ is nodal transverse displacement of the contact node, m_p and w_p are the mass and displacement value of the impactor.

By employing (3.5) and (3.6) in (3.7), the following equation could be derived

$$\begin{aligned}\Pi^{(e)} &= \frac{1}{2}\int\limits_{V^{(e)}} (\boldsymbol{\delta}^{(e)})^{\mathrm{T}}\mathrm{B}^{\mathrm{T}}\boldsymbol{\Lambda}\mathbf{N}\boldsymbol{\Xi}\mathbf{B}\boldsymbol{\delta}^{(e)}\, dV - \int\limits_{A^{(e)}} (\boldsymbol{\delta}^{(e)})^{\mathrm{T}}\mathbf{N}^{\mathrm{T}}\mathbf{p}\, dA \\ &\quad + \int\limits_{V^{(e)}} \mathbf{N}\boldsymbol{\mathcal{R}}(\boldsymbol{\delta}^{(e)})^{\mathrm{T}}\mathbf{N}^{\mathrm{T}}\mathbf{N}\ddot{\boldsymbol{\delta}}^{(e)}\, dV + m_p w_p \ddot{w}_p - \frac{2}{5}K_h\Big[w_p - W\Big(\frac{a}{2}, \frac{b}{2}, h\Big)\Big]^{\frac{5}{2}}\end{aligned} \tag{3.8}$$

where $V^{(e)}$ and $A^{(e)}$ are respectively the volume and area of the element, $\mathbf{p}$ is the traction vector and the two last terms of Eq. (3.8) represent the work of inertial loads.

Therefore, employing the principle of minimum total potential energy leads to the following result

$$\begin{aligned}\frac{\partial \Pi^{(e)}}{\partial(\boldsymbol{\delta}^{(e)})^{\mathrm{T}}} &= 0 \Rightarrow \Bigg(\int\limits_{V^{(e)}} \mathbf{N}\boldsymbol{\mathcal{R}}\mathbf{N}^{\mathrm{T}}\mathbf{N}\, dV\Bigg)\ddot{\boldsymbol{\delta}}^{(e)} + \Bigg(\int\limits_{V^{(e)}} \mathbf{B}^{\mathrm{T}}\boldsymbol{\Lambda}\mathbf{N}\boldsymbol{\Xi}\mathbf{B}\, dV\Bigg)\boldsymbol{\delta}^{(e)} \\ &\quad - \int\limits_{A^{(e)}} \mathbf{N}^{\mathrm{T}}\mathbf{p}\, dA + K_h\Big[w_p - W\Big(\frac{a}{2}, \frac{b}{2}, h\Big)\Big]^{\frac{3}{2}} = 0\end{aligned} \tag{3.9}$$

Equation (3.9) for each element of the FGM plate may be written in a compact form as

$$\mathbf{M}^{(e)}\ddot{\boldsymbol{\delta}}^{(e)} + \mathbf{K}^{(e)}\boldsymbol{\delta}^{(e)} = \mathbf{F}^{(e)} \tag{3.10}$$

where

$$\begin{aligned}
&\mathbf{K}^{(e)} = \int\limits_{V^{(e)}} \mathbf{B}^{\mathrm{T}}\boldsymbol{\Lambda}\mathbf{N}\boldsymbol{\Xi}\mathbf{B}\, dV \qquad \mathbf{M}^{(e)} = \int\limits_{V^{(e)}} \mathbf{N}\boldsymbol{\mathcal{R}}\mathbf{N}^{\mathrm{T}}\mathbf{N}\, dV \\
&\mathbf{F}^{(e)} = \int\limits_{A^{(e)}} \mathbf{N}^{\mathrm{T}}\mathbf{p}\, dA - K_h\Big[w_p - W\Big(\frac{a}{2}, \frac{b}{2}, h\Big)\Big]^{\frac{3}{2}}
\end{aligned} \tag{3.11}$$

It should be noted that the contact force should be set equal to zero after separation of the impactor from the plate.

Also by minimizing the total potential energy with respect to the displacement of the impactor, we have

$$\frac{\partial \Pi^{(e)}}{\partial w_p} = 0 \Rightarrow m_p\ddot{w}_p - K_h\Big[w_p - W\Big(\frac{a}{2}, \frac{b}{2}, h\Big)\Big]^{\frac{3}{2}} \tag{3.12}$$

On the other hand, the governing equation of the impactor is as follows

$$F(\alpha) = -m_p\ddot{w}_p = K_h\alpha^{\frac{3}{2}} \tag{3.13}$$

Based on the deformation kinematics

$$\alpha = w_p - W\Big(\frac{a}{2}, \frac{b}{2}, h\Big) \tag{3.14}$$

Equation (3.12) may be rewritten as

$$\ddot{W}\Big(\frac{a}{2}, \frac{b}{2}, h\Big) = -\frac{K_h}{m_p}\alpha^{\frac{3}{2}} - \ddot{\alpha} \tag{3.15}$$

Now, by assembling the element matrices, the global dynamic equilibrium equations for the FGM plate can be obtained as

$$\mathbf{M}\ddot{\boldsymbol{\delta}} + \mathbf{K}\boldsymbol{\delta} = \mathbf{F} \tag{3.16}$$

Various numerical methods can be employed to solve Eq. (3.16) in the space and time domains. The Newmark direct integration algorithm (Zienkiewicz 2005) is used to discretize the system of ordinary differential Eq. (3.16) in time domain. With the given initial conditions shown in Eq. (2.16), Eq. (3.15) and Eq. (3.16) have to be solved simultaneously. However, since the system of equations is nonlinear, the Newton-Raphson technique has to be used in each time step to reach a convergent solution. For each time step, the iteration lasts until the difference between the previous two iterative steps is smaller than 0.1%.

4. Results and discussion

4.1. Verification of the results

To validate the current work, the low velocity impact response of a homogenous plate is considered. So the geometry and material properties of the plate are considered as: $a = 0.2\,\mathrm{m}$,

$b = 0.1\,\mathrm{m}$, $E = 70\,\mathrm{GPa}$, $\rho = 2707\,\mathrm{kg/m^3}$, and for the rigid spherical impactor: $R = 15\,\mathrm{mm}$, $V_0 = 1\,\mathrm{m/s}$.

Due to inaccessibility to experimental results, the empirical constant β of Swanson's equation (Eq. (2.8)) is presumed unity in the present analysis (Turner, 1980). The calculated time histories of the contact force and mid-plane deflection ($x = a/2$, $y = b/2$, $z = h/2$) for the simply supported FGM rectangular plate is compared with the numerical results obtained by commercial FEM software ANSYS Workbench as shown in Fig. 2. In order to model the problem in ANSYS Workbench, $25 \times 25 \times 4$ brick elements through the x, y and z directions are utilized. The frictionless type of contact between surfaces of the projectile and plate is used. The results are in good agreement with those obtained from software simulation. The differences are probably due to using a real contact in ANSYS Workbench and modified Hertz contact law in the present research.

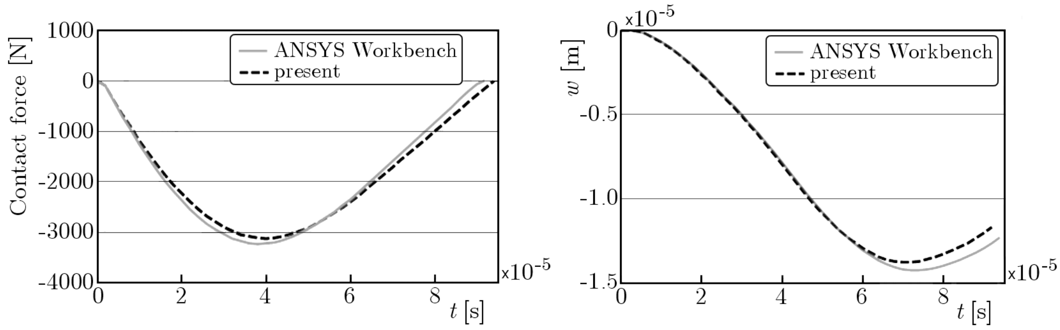

Fig. 2. Time history of the contact force and mid-plane deflection of the plate compared with ANSYS Workbench

4.2. Evaluation of effects of different parameters on the low velocity impact responses of the FGM plate

In this Section, an effective analysis is employed based on various parameters. The FGM rectangular plate and a rigid spherical impactor are specified as the following: $a = 200\,\mathrm{mm}$, $b = 100\,\mathrm{mm}$, $h = 20\,\mathrm{mm}$, $R_i = 15\,\mathrm{mm}$, $\rho_i = 7800$, 8900, 9850 and $11300\,\mathrm{kg/m}s$, $V_0 = 1$, 2, 3, $4\,\mathrm{m/s}$, $E_m = 70\,\mathrm{GPa}$, $\rho_m = 2707\,\mathrm{kg/m^3}$, $E_c = 380\,\mathrm{GPa}$, $\rho_c = 3800\,\mathrm{kg/m^3}$, $\nu = 0.3$.

The effects of the volume fraction index on the time histories of the contact force, projectile velocity, mid-plane ($x = a/2$, $y = b/2$, $z = h/2$) deflection of the plate, top displacement ($x = a/2$, $y = b/2$, $z = h$) of the plate, and normal stress components of the mid-plane are shown in Figs. 3-5, respectively, for $n = 1, 3, 5$. The results are obtained for $V_0 = 1\,\mathrm{m/s}$ and $m_p = 110\,\mathrm{gr}$, ($\rho_i = 7800\,\mathrm{kg/m^3}$). According to Fig. 3a, it may be observed that since the volume fraction index of the material properties increases, the volume fraction of the ceramic part and the stiffness of the FGM plate increases so that the peak contact force is increased and, as a result of this, the contact time duration is decreased. Figure 3b indicates that whatever the material property index of FGM plate is increased, the departure velocity of projectile is elevated. This result reveals that by increasing the stiffness of the FGM plate, the stored energy in the plate is reduced. Furthermore, as illustrated in Fig. 3b, the higher index case yields a more rapid velocity reduction compared with the lower one, because the FGM plate is strengthened by an increase in the index of material property.

On the other hand, according to Fig. 4a increasing the volume fraction index and, consequently, enhancing the stiffness of the plate leads to a decrease in the deflection of the plate. As a result of this occurrence, the curvature of the plate decreases and the in-plane normal stress component σ_{yy} is reduced, see Fig. 5a. The observed result for peel stress σ_{zz} is vague. That is probably affected by the material nonlinearity of the FGM plate, see Fig. 5b. Also Figs. 4a

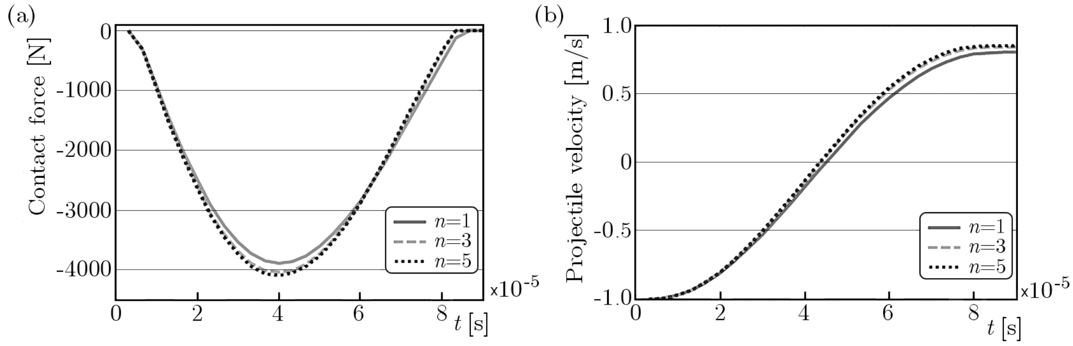

Fig. 3. A comparison among time histories of the contact force (a) and of the projectile velocities (b) for different volume fraction indices

and 4b illustrate that the top displacement of the FGM plate is greater than the mid-plane one, because the FGM plate is analyzed by three dimensional theory of elasticity, therefore, the lateral compressibility of the plate is considered. The mentioned result has not been reported due to using Equivalent Single Layer (ESL) theories in such works in the literature.

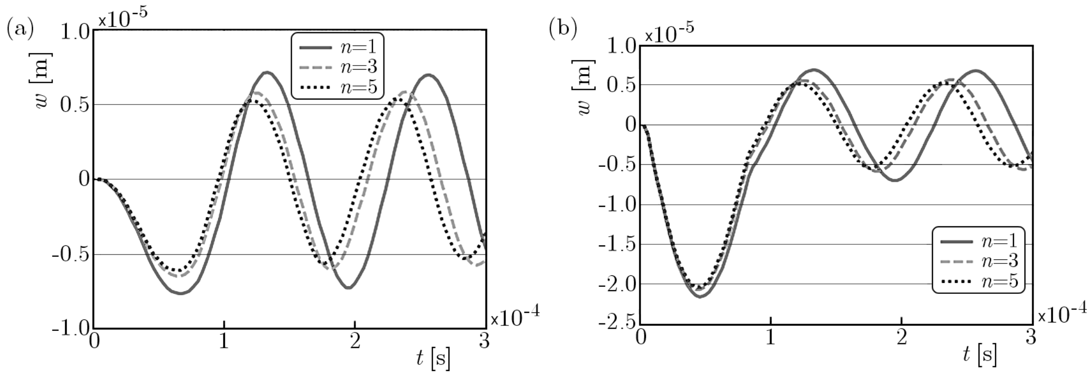

Fig. 4. A comparison among time histories of the mid-plane deflections (a) and of the top displacement (b) for different volume fraction indices

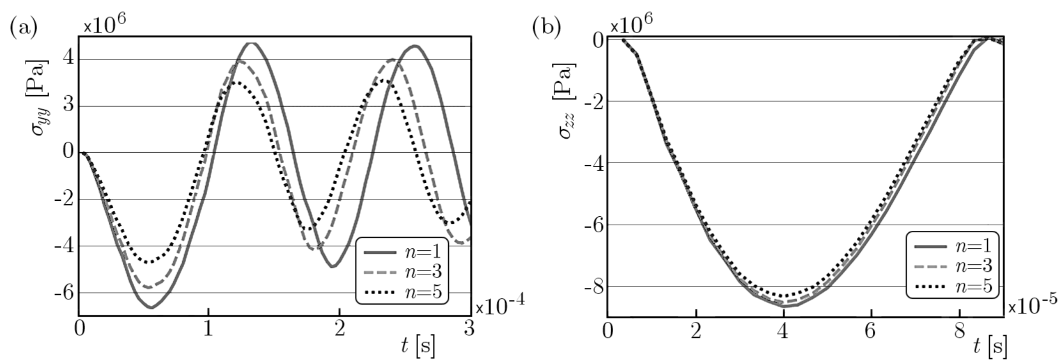

Fig. 5. A comparison among time histories of the in-plane stress σ_{yy} (a) and of the peel stress σ_{zz} (b) for different volume fraction indices

The effects of the initial velocity of the projectile on the contact force, mid-plane deflection of the plate and departure velocity of the projectile are depicted in Figs. 6a,b and 7, respectively ($n = 1$, $m_p = 110\,\mathrm{gr}$). It may be concluded that increasing the initial velocity of the projectile causes enhancement of the peak contact force. However, the high initial velocity of projectile decreases the contact time duration. Figure 7 reveals how the departure velocity may vary as the initial velocity of the projectile increases. According to this result, the ratio of the departure to the initial velocity of the projectile is decreased by increasing the initial velocity of the projectile. This is because that by increasing the initial velocity, the stored energy in the plate is increased. On the other hand, whatever the initial velocity of projectile is increased, the velocity during the contact time is reduced more rapidly.

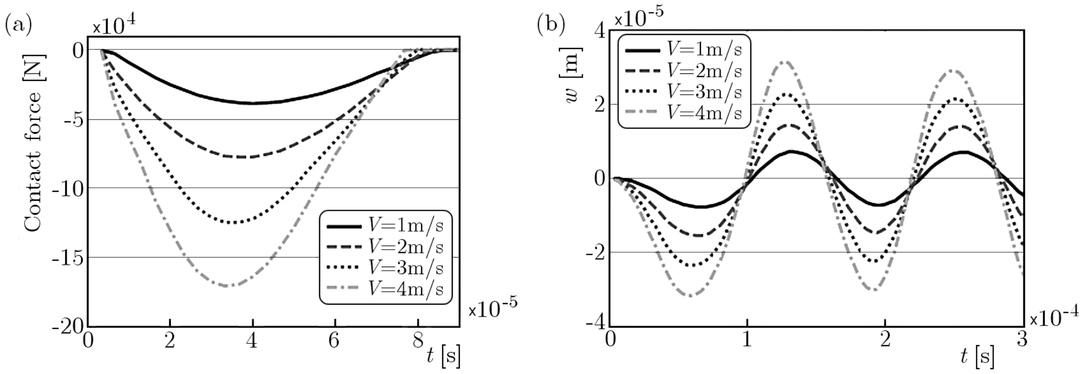

Fig. 6. Influence of the initial velocity of the projectile on the time history of the contact force (a) and of the lateral deflection of the plate (b); $n = 1$

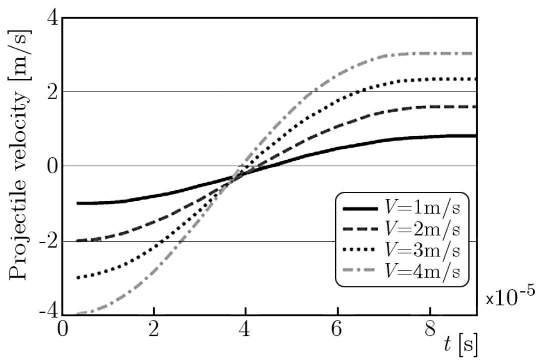

Fig. 7. Influence of the initial velocity of the projectile on the departure velocity of the projectile; $n = 1$

The effects of the projectile mass on the contact force and mid-plane lateral deflection of the plate for the simply supported FGM plate are presented in Figs. 8a and 8b, respectively for $n = 1$ and $V_0 = 1\,\mathrm{m/s}$. As it may be deduced from Fig. 8a, an increase in the projectile mass increases the peak contact force due to increasing the impact energy. Also, it elevates the contact time duration, and this result is in contrast with the effect of initial velocity of the projectile. It is because the increase in the mass of projectile highlights the inertia effect. As it may be observed in Fig. 8b, an increase in the projectile mass reduces the deflection wave propagation because this increase raises the contact duration time. Also, by increasing the projectile mass, the maximum deflection is enhanced.

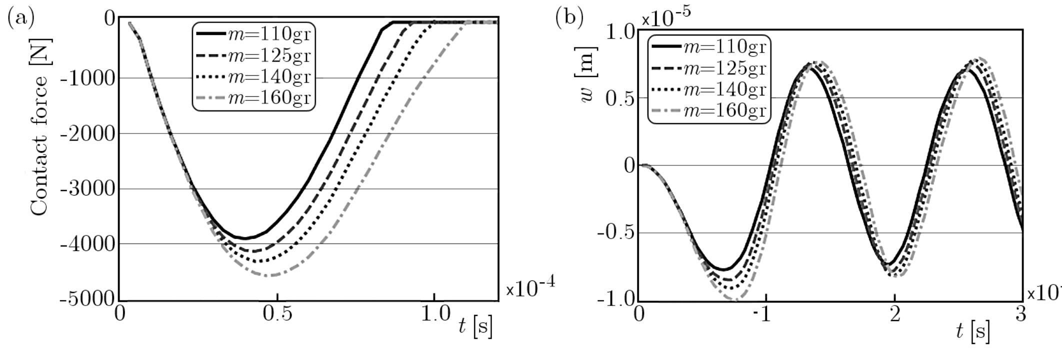

Fig. 8. Effect of the projectile mass on the time history of the contact force (a) and of the lateral deflection of plate (b); $n = 1$

5. Conclusion

In this research, a numerical approach for the low-velocity impact of FGM plates based on the three-dimensional theory of elasticity is extended. By applying the three-dimensional graded elements for analysis of the plates, discontinuities of the stress distribution that are present in the conventional FE results, are eliminated. The influence of the volume fraction index of the FGM plate, initial velocity of the projectile and projectile mass on the parameters such as time histories of the contact force, velocity of the projectile, lateral deflection and normal stresses are studied. The main novelty of the present research which has not been reported in literature is the consideration of the difference of lateral deflection through the thickness of the FGM plate due to analysis of three-dimensional elasticity of the plate.

References

1. Abrate S., 1998, *Impact on Composite Structures*, Cambridge University Press
2. Asemi K., Salehi M., Akhlaghi M., 2010, Dynamic analysis of functionaly graded thick truncated cone, *International Journal of Mechanics and Materials in Design*, **6**, 367-378
3. Asemi K., Akhlaghi M., Salehi M., 2012, Dynamic analysis of thick short FGM cylinders, *Meccanica*, **47**, 1441-1453
4. Ashrafi H., Asemi K., Shariyat M., Salehi M., 2013, Two-dimensional modeling of heterogeneous structures using graded finite element and boundary element methods, *Meccanica*, **48**,663-680
5. Behjat B., Salehi M., Sadighi M., Armin A., Abbasi M., 2009, Static, dynamic and free vibration analysis of functionally graded piezoelectric panels using finite element method, *Journal of Intelligent Materials Systems and Structures*, **20**, 1635-1646
6. Conway H.D., 1956, Analytical model for delamination growth during small mass impact on plates, *ZAMP*, **7**, 80-85
7. Dai H.L., Guo Z.Y., Yang L., 2012, Nonlinear dynamic response of functionally graded materials circular plates subject to low-velocity impact, *Journal of Composite Materials*, DOI: 10.1177/0021998312458132
8. Derras M., Kaci A., Draiche K., Tounsi A., 2013, Non-linear analysis of functionally graded plates in cylindrical bending based on a new refined shear deformation theory, *Journal of Theoretical and Applied Mechanics*, 51, 339-348
9. Etemadi E., Afaghi Khatibi A., Takaffoli M., 2009, 3D finite element simulation of sandwich panels with a functionally graded core subjected to low velocity impact, *Composite Structures*, **89**, 28-34

10. Ghannad M., Nejad M.Z., 2013, Elastic solution of pressurized clamped-clamped thick cylindrical shells made of functionally graded materials, *Journal of Theoretical and Applied Mechanics*, **51**, 1067-1079
11. Giannakopoulos A.E., Suresh S., 1997, Indentation of solids with gradients in elastic properties: part I. Point force, *International Journal of Solids and Structures*, **34**, 2357-2392
12. Giannakopoulos A.E., Pallot P., 2000, Two-dimensional contact analysis of elastic graded materials, *Journal of Mechanics and Physics of Solids*, **48**, 1597-1631
13. Gunes R., Aydin M., 2010, Elastic response of functionally graded circular plates under a drop--weight, *Composite Structures*, **92**, 2445-2456
14. Gunes R., Aydin M., Apalak M.K., Reddy J.N., 2011, The elasto-plastic impact analysis of functionally graded circular plates under low-velocities, *Composite Structures*, **93**, 860-869
15. Khalili S.M.R., Malekzadeh K., Veysi Gorgabad A., 2013, Low velocity transverse impact response of functionally graded plates with temperature dependent properties, *Composite Structures*, **96**, 64-74.
16. Kiani Y., Shakeri M., Eslami M.R., 2012, Thermoelastic free vibration and dynamic behaviour of an FGM doubly curved panel via the analytical hybrid Laplace-Fourier transformation, *Acta Mechanica*, **223**, 1199-1218
17. Kim J.H., Paulino G.H., 2002, Isoparametric graded finite elements for nonhomogeneous isotropic and orthotropic materials, *Journal of Applied Mechanics*, **69**, 502-514
18. Larson R.A., Palazotto A., 2006, Low velocity impact analysis of functionally graded circular plates, *Proceedings of IMECE2006 2006 ASME International Mechanical Engineering Congress and Exposition*, Chicago, Illinois, USA, paper No.: IMECE2006-14003
19. Larson R.A., Palazotto A.N., 2009, Property estimation in FGM plates subjected to low--velocity impact loading, *Journal of Mechanics of Materials and Structures*, **4**, 1429-1451
20. Larson R.A., Palazotto A.N., Gardenier H.E., 2009, Impact Response of titanium and titanium boride monolithic and functionally graded composite plates, *AIAA Journal*, **47**, 676-691
21. Mao Y.Q., Fu Y.M., Chen C.P., Li Y.L., 2011, Nonlinear dynamic response for functionally graded shallow spherical shell under low velocity impact in thermal environment, *Applied Mathematical Modelling*, **35**, 2887- 2900
22. Noda N., Ootao Y., Tanigawa Y., 2012, Transient thermoelastic analysis for a functionally graded circular disk with piecewise power law, *Journal of Theoretical and Applied Mechanics*, **50**, 831-839
23. Olsson R., 1992, Impact response of orthotropic composite plates predicted from a one-parameter differential equation, *AIAA Journal*, **30**, 1587-1596.
24. Qian L.F., Batra R.C., Chen L.M., 2004, Static and dynamic deformations of thick functionally graded elastic plates by using higher-order shear and normal deformable plate theory and meshless local Petrov-Galerkin method, *Composites, Part B: Engineering*, **35**, 685-697
25. Shariyat M., Jafari R., 2013, Nonlinear low-velocity impact response analysis of a radially preloaded two-directional-functionally graded circular plate: a refined contact stiffness approach, *Composites, Part B: Engineering*, **45**, 981-994
26. Shariyat M., Farzan F., 2013, Nonlinear eccentric low-velocity impact analysis of a highly prestressed FGM rectangular plate, using a refined contact law, *Archive of Applied Mechanics*, **83**, 623-641
27. Sun Dan., Luo S.N., 2011, The wave propagation and dynamic response of rectangular functionally graded material plates with completed clamped supports under impulse load, *European Journal of Mechanics – A/Solids*, **30**, 396-408
28. Swanson S.R., 2005, Contact deformation and stress in orthotropic plates, *Composites A*, **36**, 1421-1429

29. Turner J.R., 1980, Contact on a transversely isotropic half-space, or between two transversely isotropic bodies, *International Journal of Solids and Structures*, **16**, 409-419

30. Wirowski A., 2009, Free vibrations of thin annular plates made from functionally graded material, *Proceedings in Applied Mathematics and Mechanics*, **9**, 261-262

31. Wirowski A., 2011, Different methods of modelling vibrations of plates made of functionally graded materials, *Electronic Journal of Polish Agricultural Universities*, **14**, 3

32. Wirowski A., 2012, Self-vibration of thin plate band with non-linear functionally graded material, *Archives of Mechanics*, **64**, 603-615

33. Yaghoobi H., Torabi M., 2013, An analytical approach to large amplitude vibration and post--buckling of functionally graded beams rest on non-linear elastic foundation, *Journal of Theoretical and Applied Mechanics*, **51**, 39-52

34. Zhang Z., Paulino G.H., 2007, Wave propagation and dynamic analysis of smoothly graded heterogeneous continua using graded finite elements, *International Journal of Solids and Structures*, **44**, 3601-3626

35. Zienkiewicz O.C., Taylor R.L., 2005, *The Finite Element Method for Solid and Structural Mechanics*, Sixth Edition, Elsevier Butterworth-Heinemann, Oxford

Manuscript received July 31, 2014; accepted for print April 25, 2015

JOURNAL OF THEORETICAL
AND APPLIED MECHANICS
53, 4, pp. 873-884, Warsaw 2015
DOI: 10.15632/jtam-pl.53.4.873

GREEN'S FUNCTION IN FREQUENCY ANALYSIS OF CIRCULAR THIN PLATES OF VARIABLE THICKNESS

Krzysztof Kamil Żur
Bialystok University of Technology, Faculty of Management, Kleosin, Poland
e-mail: k.zur@pb.edu.pl

Free vibration analysis of homogeneous and isotropic circular thin plates with variable distribution of parameters by using Green's functions (solution to homogeneous ordinary differential equations with variable coefficients) is considered. The formula of Green's function (called the influence function) depends on the Poisson ratio and the coefficient of distribution of plate flexural rigidity, and the thickness is obtained in a closed-form. The limited independent solutions to differential Euler equations are expanded in the Neumann power series using the Volterra integral equations of the second kind. This approach allows one to obtain the analytical frequency equations as the power series rapidly convergens to exact eigenvalues for different values of the power index and different values of the Poisson ratio. The six lower natural dimensionless frequencies of axisymmetric vibration of circular plates of constant and variable thickness are calculated for different boundary conditions. The obtained results are compared with selected results presented in the literature.

Keywords: circular plates, Green's function, Neumann series

1. Introduction

The study of vibration of a thin circular plate is basic in structural mechanics because it has many applications in civil and mechanical engineering. Circular plates are the most critical structural elements in high speed rotating engineering systems such as circular saws, rotors, turbine flywheels, etc. In reality, a lot of complicating factors may come into play: non-uniform thickness, elastic constraints, anisotropic or composite materials, etc. The natural frequencies of the plates have been studied extensively for more than a century, if only because when the frequency of external load matches the natural frequency of the plate, destruction may occur.

The free vibration of circular plates of constant and variable thickness has received considerable attention in the literature. The vibration of circular plates has been discussed by many authors. The work of Leissa (1969) is an excellent source of information about methods used for free vibration analysis of plates. Free vibration analysis has been carried out by using a variety of weighting function methods (Leissa, 1969) such as the Ritz method, the Galerkin method or the finite element method. Conway (1957, 1958) analyzed the axisymmetric vibration of thin circular plates with a power function thickness variation for a particular Poisson ratio in terms of the Bessel functions. Jain *et al.* (1972) studied the axisymmetric vibration of thin circular plates with linearly varying thickness using by the Frobenius method. Yang (1993) studied the same problem using by perturbation method. Wang (1997) used the power series method for free vibration analysis of circular thin plates with power variable thickness. Wu and Liu (2001, 2002) proposed a generalized differential quadrature rule (GDQR) for free vibration analysis of circular thin plates of constant and variable thickness. Jaroszewicz and Zoryj (2006) studied free vibration of circular thin plates with variable distribution of parameters using the method of partial discretization (MPD). Taher *et al.* (2006) studied free vibration of circular and annular plates with variable thickness and different combinations of boundary conditions. Gupta *et* *al.* (2006) analyzed free vibration of nonhomogeneous circular plates with nonlinear thickness variation by using the differential quadrature method (DQM). Yalcin *et al.* (2009) studied free vibration of circular plates by using the differential transformation method (DTM). Zhou *et al.* (2011) applied the Hamiltonian approach to solution of the free vibration problem of circular and annular thin plates. Duan *et al.* (2014) proposed the DSC element method for free vibration analysis of circular thin plates with constant and stepped thickness.

In the works by Leissa (1969), Conway (1957, 1958) the solutions for free axisymmetric vibration of clamped circular plates with a power function thickness variation were presented. Those solutions were possible to obtain only for few combinations of the Poisson ratios and Bessel functions. That kind of solutions have limited practical applications. The aim of the paper is frequency analysis of circular plates with different values of the power index m of the plate parameters and different values of the Poisson ratios. The characteristic equations are obtained for two different values of the Poisson ratio and different boundary conditions such as free, clamped, simply supported, sliding and elastic supports. The limited independent solutions of differential Euler equations are expanded in the Neumann power series using the properties of integral equations. This approach allows one to obtain analytical frequency equations as the power series rapidly converges to the exact eigenvalues. The numerical results of investigation are in good agreement with selected results presented in the literature.

2. Statement of the problem

Consider an isotropic, homogeneous circular thin plate of variable thickness $h = h_R r^{m/3}$ and flexural rigidity $D = D_R r^m$ in the cylindrical coordinate system (r, θ, z) with the z-axis along the longitudinal direction. h_R and D_R are thickness and flexural rigidity of circular plates on the edge $(r = R)$, respectively. The geometry and coordinate system of the considered plate are shown in Fig. 1. For free axisymmetric vibration of circular plates, the deflection is independent of θ. The partial differential equation for free vibration of thin circular plates has the following form (Timoshenko and Woinowsky-Krieger, 1959)

$$D\frac{\partial}{\partial r}\Big(\frac{\partial^2 W}{\partial r^2} + \frac{1}{r}\frac{\partial W}{\partial r}\Big) + \frac{\partial D}{\partial r}\Big(\frac{\partial^2 W}{\partial r^2} + \frac{\nu}{r}\frac{\partial W}{\partial r}\Big) + \frac{1}{r}\int\limits_0^r \rho h \frac{\partial^2 W}{\partial t^2} r\, dr = 0 \qquad (2.1)$$

where ρ is mass density, r is the radial coordinate and $W(r,t)$ is the small axisymmetric deflection compared with the thickness h of the plate.

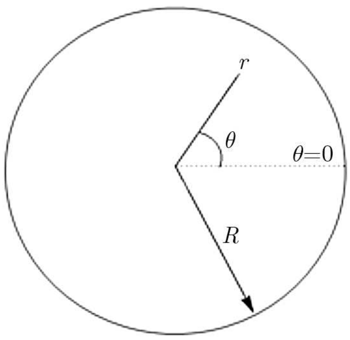

Fig. 1. Geometry and coordinate system of the circular plate

The axisymmetric deflection of a circular plate may be expressed as follows

$$W(r,t) = w(r)e^{i\omega t} \qquad (2.2)$$

where $w(r)$ is the radial mode function and ω is natural frequency. Substituting Eq. (2.2) into Eq. (2.1) and using the dimensionless coordinate $\xi = r/R$, the governing differential equation of the circular plate becomes

$$L(w) - \lambda^2 \xi^{-2m/3} w = 0 \tag{2.3}$$

where $L(w)$ is the operator defined by

$$L(w) \equiv \frac{d^4 w}{d\xi^4} + \frac{2(m+1)}{\xi}\frac{d^3 w}{d\xi^3} + \frac{m^2+m+\nu m-1}{\xi^2}\frac{d^2 w}{d\xi^2} + \frac{m^2\nu - m\nu - m + 1}{\xi^3}\frac{dw}{d\xi} \tag{2.4}$$

and the dimensionless frequency λ of vibration is given by

$$\lambda = \omega R^{m/3}\sqrt{\frac{\rho h_R}{D_R}} \tag{2.5}$$

The governing differential equation for the circular plate of constant thickness has the form

$$L(w) - \lambda^2 w = 0 \tag{2.6}$$

where

$$L(w) \equiv \frac{d^4 w}{d\xi^4} + \frac{2}{\xi}\frac{d^3 w}{d\xi^3} - \frac{1}{\xi^2}\frac{d^2 w}{d\xi^2} + \frac{1}{\xi^3}\frac{dw}{d\xi} \qquad \lambda = \omega R^2\sqrt{\frac{\rho h_R}{D_R}} \tag{2.7}$$

The boundary conditions at the outer edge ($\xi = 1$) of the circular plate may be one of the following: clamped, simply supported, free, sliding supports and elastic supports. These conditions may be written in terms of the radial mode function $w(\xi)$ in the following form:

— clamped

$$w(\xi)\Big|_{\xi=1} = 0 \qquad \frac{dw}{d\xi}\Big|_{\xi=1} = 0 \tag{2.8}$$

— simply supported

$$w(\xi)\Big|_{\xi=1} = 0 \qquad M(w)\Big|_{\xi=1} = \Big(\frac{d^2 w}{d\xi^2} + \frac{\nu}{\xi}\frac{dw}{d\xi}\Big)_{\xi=1} = 0 \tag{2.9}$$

— free

$$M(w)\Big|_{\xi=1} = 0 \qquad V(w)\Big|_{\xi=1} = \Big(\frac{d^3 w}{d\xi^3} + \frac{1}{\xi}\frac{d^2 w}{d\xi^2} - \frac{1}{\xi^2}\frac{dw}{d\xi}\Big)_{\xi=1} = 0 \tag{2.10}$$

— sliding (vertical) supports

$$\frac{dw}{d\xi}\Big|_{\xi=1} = 0 \qquad V(w)\Big|_{\xi=1} = 0 \tag{2.11}$$

— elastic supports

$$\begin{aligned} \varPhi(w)\Big|_{\xi=1} &= \Big[\Big(\frac{d^2 w}{d\xi^2} + \nu\frac{dw}{d\xi}\Big) + \phi\frac{dw}{d\xi}\Big]_{\xi=1} = 0 \\ \varPsi(w)\Big|_{\xi=1} &= \Big[\Big(\frac{d^3 w}{d\xi^3} + \frac{d^2 w}{d\xi^2} - \frac{dw}{d\xi}\Big) - \psi w\Big]_{\xi=1} = 0 \end{aligned} \tag{2.12}$$

$M(w)$ and $V(w)$ are the normalized radial bending moment and the normalized effective shear force, respectively. $\phi = K_\phi R/D_R$ and $\psi = K_\psi R^3/D_R$ are parameters of the elastic supports. K_ϕ and K_ψ are the rotational and translational spring constants (Fig. 2), respectively.

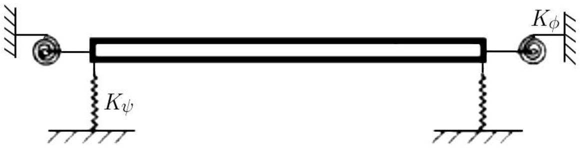

Fig. 2. Cross-section of a uniform circular plate with elastic supports

3. Finding Green's functions

The characteristic equation of a homogeneous differential Euler equation for thin circular plates with variable thickness, see Eq. (2.4)

$$L(w) = 0 \tag{3.1}$$

has the following form

$$s^4 + (2m-4)s^3 + (m^2 + m\nu - 5m + 4)s^2 + (-m^2 + m^2\nu - 2m\nu + 2m)s = 0 \tag{3.2}$$

The roots of Eq. (3.2) are

$$s_1 = 0 \qquad s_2 = 2 - m \qquad s_3 = 1 - \frac{m}{2} - \mathcal{H} \qquad s_4 = 1 - \frac{m}{2} + \mathcal{H} \tag{3.3}$$

where

$$\mathcal{H} = \frac{1}{2}\sqrt{m^2 - 4m\nu + 4} \tag{3.4}$$

The general solution to Eq. (3.1) is

$$w(\xi) = C_1 + C_2\xi^{2-m} + C_3\xi^{1-\frac{m}{2}-\mathcal{H}} + C_4\xi^{1-\frac{m}{2}+\mathcal{H}} \tag{3.5}$$

Green's function (solution to the homogeneous Euler equation $L(K_m(\xi,\alpha)) = 0$) for different values of the power index m may be received from a formula presented in the following form (Jaroszewicz and Zoryj, 2005)

$$K_m(\xi,\alpha) = \frac{A_m}{W(\alpha)_m p_0(\alpha)} \tag{3.6}$$

where $p_0(\alpha) = 1$ is a coefficient placed before the highest order of the derivative of Euler differential equation (3.1) and

$$
\begin{aligned}
A_m &= \begin{vmatrix}
1 & \alpha^{2-m} & \alpha^{1-\frac{m}{2}-\mathcal{H}} & \alpha^{1-\frac{m}{2}+\mathcal{H}} \\
0 & \dfrac{d\alpha^{2-m}}{d\alpha} & \dfrac{d\alpha^{1-\frac{m}{2}-\mathcal{H}}}{d\alpha} & \dfrac{d\alpha^{1-\frac{m}{2}+\mathcal{H}}}{d\alpha} \\
0 & \dfrac{d^2\alpha^{2-m}}{d\alpha^2} & \dfrac{d^2\alpha^{1-\frac{m}{2}-\mathcal{H}}}{d\alpha^2} & \dfrac{d^2\alpha^{1-\frac{m}{2}+\mathcal{H}}}{d\alpha^2} \\
1 & \xi^{2-m} & \xi^{1-\frac{m}{2}-\mathcal{H}} & \xi^{1-\frac{m}{2}+\mathcal{H}}
\end{vmatrix} \\
W(\alpha)_m &= \begin{vmatrix}
1 & \alpha^{2-m} & \alpha^{1-\frac{m}{2}-\mathcal{H}} & \alpha^{1-\frac{m}{2}+\mathcal{H}} \\
0 & \dfrac{d\alpha^{2-m}}{d\alpha} & \dfrac{d\alpha^{1-\frac{m}{2}-\mathcal{H}}}{d\alpha} & \dfrac{d\alpha^{1-\frac{m}{2}+\mathcal{H}}}{d\alpha} \\
0 & \dfrac{d^2\alpha^{2-m}}{d\alpha^2} & \dfrac{d^2\alpha^{1-\frac{m}{2}-\mathcal{H}}}{d\alpha^2} & \dfrac{d^2\alpha^{1-\frac{m}{2}+\mathcal{H}}}{d\alpha^2} \\
0 & \dfrac{d^3\alpha^{2-m}}{d\alpha^3} & \dfrac{d^3\alpha^{1-\frac{m}{2}-\mathcal{H}}}{d\alpha^3} & \dfrac{d^3\alpha^{1-\frac{m}{2}+\mathcal{H}}}{d\alpha^3}
\end{vmatrix}
\end{aligned} \tag{3.7}
$$

The functions 1, α^{2-m}, $\alpha^{1-\frac{m}{2}-\mathcal{H}}$, $\alpha^{1-\frac{m}{2}+\mathcal{H}}$ are linear independent solutions, then the Wronskian must satisfy the condition (Stakgold and Holst, 2011)

$$W(\alpha)_m = -\frac{\mathcal{H}}{8}(-2+m)[(-2+m)^2 - 4\mathcal{H}^2]^2\alpha^{-2(1+m)} \neq 0 \qquad \text{for} \quad m \neq 0 \ \wedge \ m \neq 2 \tag{3.8}$$

After calculations, Green's function (GF) has the following form

$$\begin{aligned} K_m(\xi,\alpha) = {} & \frac{2\xi^{-m-\mathcal{H}}\alpha^{1-\mathcal{H}}}{\mathcal{H}(m-2)(4-4m+m^2-4\mathcal{H}^2)} \\ & \cdot \Big[(2-m)\xi^{1+\frac{m}{2}+2\mathcal{H}}\alpha^{1+\frac{m}{2}} + 2\xi^{m+\mathcal{H}}\mathcal{H}\alpha^{2+\mathcal{H}} - 2\xi^{2+\mathcal{H}}\mathcal{H}\alpha^{m+\mathcal{H}} + (m-2)\xi^{1+\frac{m}{2}}\alpha^{1+\frac{m}{2}+2\mathcal{H}}\Big] \end{aligned} \tag{3.9}$$

and satisfies the conditions

$$\begin{aligned} & K_m(\alpha,\alpha) = \frac{\partial K_m(\xi,\alpha)}{\partial\xi}\Big|_{\xi=\alpha} = \frac{\partial^2 K_m(\xi,\alpha)}{\partial\xi^2}\Big|_{\xi=\alpha} = 0 \\ & \frac{\partial^3 K_m(\xi,\alpha)}{\partial\xi^3}\Big|_{\xi=\alpha} = 1 \end{aligned} \tag{3.10}$$

according to the properties of influence functions (Kukla, 2009; Stakgold and Holst, 2011).

The function $K_m(\xi,\alpha)$ is indeterminate for $m = 0$ and $m = 2$. After calculation of lthe imits of the function $K_m(\xi,\alpha)$ for $m \to 0$ and $m \to 2$, the determinate Green function have the following form

$$\lim_{m\to 0} K_m(\xi,\alpha) = \frac{\alpha}{4}\Big[\alpha^2 - \xi^2 + (\xi^2+\alpha^2)\ln\frac{\xi}{\alpha}\Big] \tag{3.11}$$

when Poisson ratio $\nu = 0.25$

$$\lim_{m\to 2} K_m(\xi,\alpha) = \frac{1}{9}\xi^{-\sqrt{\frac{3}{2}}}\alpha^3\Big[\sqrt{6}\alpha^{-\sqrt{\frac{3}{2}}}(\xi^{\sqrt{6}} - \alpha^{\sqrt{6}}) - 6\xi^{\sqrt{\frac{3}{2}}}(\ln\xi + \ln\alpha)\Big] \tag{3.12}$$

and $\nu = 0.33$

$$\lim_{m\to 2} K_m(\xi,\alpha) = \frac{3\alpha^3}{16}\Big[\sqrt{3}\xi^{-\frac{2}{\sqrt{3}}}\alpha^{-\frac{2}{\sqrt{3}}}\Big(\xi^{\frac{4}{\sqrt{3}}} - \alpha^{\frac{4}{\sqrt{3}}}\Big) - 4\ln\xi + 4\ln\alpha\Big] \tag{3.13}$$

Examples of the formulas of Green's function $K_m(\xi\alpha)$ for different values of the power index m $m \in \{-3,-2,-1,0,2,3,4\}$ are presented as in the following:
— for Poisson ratio $\nu = 0.25$

$$\begin{aligned} K_{-3}(\xi,\alpha) &= \frac{1}{45\alpha^2}\Big(4\xi^5 - 5\xi^{\frac{9}{2}}\sqrt{\alpha} + 5\sqrt{\xi}\alpha^{\frac{9}{2}} - 4\alpha^5\Big) \\ K_{-2}(\xi,\alpha) &= \frac{1}{30\alpha}\Big(5\xi^4 - 5\alpha^4 - 2\sqrt{10}\xi^{2+\sqrt{\frac{5}{2}}}\alpha^{2-\sqrt{\frac{5}{2}}} + 2\sqrt{10}\xi^{2-\sqrt{\frac{5}{2}}}\alpha^{2+\sqrt{\frac{5}{2}}}\Big) \\ K_{-1}(\xi,\alpha) &= \frac{2}{9}\Big(2\xi^3 - 2\alpha^3 - \sqrt{6}\xi^{\frac{3}{2}+\sqrt{\frac{3}{2}}}\alpha^{\frac{3}{2}-\sqrt{\frac{3}{2}}} + \sqrt{6}\xi^{\frac{3}{2}-\sqrt{\frac{3}{2}}}\alpha^{\frac{3}{2}+\sqrt{\frac{3}{2}}}\Big) \\ K_0(\xi,\alpha) &= \frac{\alpha}{4}\Big[\alpha^2 - \xi^2 + (\xi^2+\alpha^2)\ln\frac{\xi}{\alpha}\Big] \\ K_2(\xi,\alpha) &= \frac{1}{9}\xi^{-\sqrt{\frac{3}{2}}}\alpha^3\Big[\sqrt{6}\alpha^{-\sqrt{\frac{3}{2}}}(\xi^{\sqrt{6}} - \alpha^{\sqrt{6}}) - 6\xi^{\sqrt{\frac{3}{2}}}(\ln\xi + \ln\alpha)\Big] \\ K_3(\xi,\alpha) &= \frac{2}{45}\Big(-10\alpha^3 + \frac{10\alpha^4}{\xi} + \sqrt{10}\xi^{-\frac{1}{2}+\sqrt{\frac{5}{2}}}\alpha^{\frac{7}{2}-\sqrt{\frac{5}{2}}} - \sqrt{10}\xi^{-\frac{1}{2}-\sqrt{\frac{5}{2}}}\alpha^{\frac{7}{2}+\sqrt{\frac{5}{2}}}\Big) \\ K_4(\xi,\alpha) &= \frac{(\xi-\alpha)^3\alpha^2(\xi+\alpha)}{12\xi^3} \end{aligned} \tag{3.14}$$

— for Poisson ratio $\nu = 0.33$

$$
\begin{aligned}
K_{-3}(\xi,\alpha) &= \frac{1}{170}\Big(\frac{17r^5}{\alpha^2} - 17\alpha^3 - 5\sqrt{17}\xi^{\frac{1}{2}(5+\sqrt{17})}\alpha^{\frac{1}{2}-\sqrt{\frac{17}{2}}} + 5\sqrt{17}\xi^{\frac{5}{2}-\sqrt{\frac{17}{2}}}\alpha^{\frac{1}{2}(1+\sqrt{17})}\\
K_{-2}(\xi,\alpha) &= \frac{3}{32\alpha}\Big(2\xi^4 - 2\alpha^4 - \sqrt{6}\xi^{2+2\sqrt{\frac{2}{3}}}\alpha^{2-2\sqrt{\frac{2}{3}}} + \sqrt{6}\xi^{2-2\sqrt{\frac{2}{3}}}\alpha^{2+2\sqrt{\frac{2}{3}}}\Big)\\
K_{-1}(\xi,\alpha) &= \frac{1}{38}\Big(19\xi^3 - 19\alpha^3 - 3\sqrt{57}\xi^{\frac{1}{6}(9+\sqrt{57})}\alpha^{\frac{1}{6}(9-\sqrt{57})} + 3\sqrt{57}\xi^{\frac{1}{6}(9-\sqrt{57})}\alpha^{\frac{1}{6}(9+\sqrt{57})}\Big)\\
K_0(\xi,\alpha) &= \frac{\alpha}{4}\Big[\alpha^2 - \xi^2 + (\xi^2+\alpha^2)\ln\frac{\xi}{\alpha}\Big]\\
K_2(\xi,\alpha) &= \frac{3\alpha^3}{16}\Big[\sqrt{3}\xi^{-\frac{2}{\sqrt{3}}}\alpha^{-\frac{2}{\sqrt{3}}}\Big(\xi^{\frac{4}{\sqrt{3}}} - \alpha^{\frac{4}{\sqrt{3}}}\Big) - 4\ln\xi + 4\ln\alpha\Big]\\
K_3(\xi,\alpha) &= \frac{(\xi-\alpha)^3\alpha^2}{6\xi^2}\\
K_4(\xi,\alpha) &= \frac{3\alpha^3}{176}\Big(\frac{11\alpha^2}{\xi^2} + \sqrt{33}\xi^{-1+\sqrt{\frac{11}{3}}}\alpha^{1-\sqrt{\frac{11}{3}}} - \sqrt{33}\xi^{-1-\sqrt{\frac{11}{3}}}\alpha^{1+\sqrt{\frac{11}{3}}} - 11\Big)
\end{aligned}
\tag{3.15}
$$

4. Solution of the problem

The ordinary differential equations with constant or variable coefficients can be transformed to the Volterra or Fredholm integral equations by using e.g. Fubini's method (Pogorzelski, 1958). The solutions to these equations are solutions to the transformed ordinary differential equation. If Green's function (kernel of integral equation) is well known (or determined), the linear independent solutions can be expanded in the Neumann (called Liouville-Neumann) power series rapidly convergent to the eigenvalues (spectrum of integral kernel) based onthe method of successive approximations (Tricomi, 1957; Shestopalov and Smirnov, 2002).

The limited (for $\xi = 0$) independent solutions of Eq. (3.1) are $w_1(\xi) = 1$ and $w_2(\xi) = \xi^{2-m}$ (or $w_2(\xi) = \xi^{1-\frac{m}{2}+\mathcal{H}}$ for $m \geqslant 2$). These solutions are expanded in the Neumann power series in the following form

$$
\begin{aligned}
K_m(\xi,\lambda)_u &= K_0(\xi)_u + \sum_{i=1}^{\eta} K_i(\xi)_u\lambda^{2i} \qquad \lambda \in \mathcal{R}^+\\
K_m(\xi,\lambda)_v &= K_0(\xi)_v + \sum_{i=1}^{\eta} K_i(\xi)_v\lambda^{2i}
\end{aligned}
\tag{4.1}
$$

where $K_i(\xi)_u$ and $K_i(\xi)_v$ are integral iterated kernels given by

$$
\begin{aligned}
K_i(\xi)_u &= \int_0^{\xi} K_m(\xi,\alpha)\alpha^{-\frac{2}{3}m}K_{i-1}(\alpha)_u\,d\alpha \qquad K_0(\alpha)_u = \chi_u\\
K_i(\xi)_v &= \int_0^{\xi} K_m(\xi,\alpha)\alpha^{-\frac{2}{3}m}K_{i-1}(\alpha)_v\,d\alpha \qquad K_0(\alpha)_v = \chi_v
\end{aligned}
\tag{4.2}
$$

and η is the degree of approximations. χ_u and χ_v are limited independent solutions to Eq. (3.1) for $\xi = 0$. $\chi_u = 1$ for all values of the parameter m. Values of χ_v depend on the power index m and the Poisson ratio ν (for $m \geqslant 2$). They are shown in Table 1.

Table 1. Values of χ_v for some considered values of the power index m

m	-3	-2	-1	0	2	3	4
χ_v	α^5	α^4	α^3	α^2	$\alpha^{2\sqrt{3}/3}$	α	$\alpha^{-1+\sqrt{11/3}}$

The characteristic equations $\Delta_m = 0$ for different boundary conditions and different values of the parameter m are obtained from well known characteristic determinants given by:
— clamped

$$\Delta_m(\lambda) \equiv \left. \begin{vmatrix} K_m(\xi,\lambda)_u & K_m(\xi,\lambda)_v \\ \dfrac{\partial K_m(\xi,\lambda)_u}{\partial \xi} & \dfrac{\partial K_m(\xi,\lambda)_v}{\partial \xi} \end{vmatrix} \right|_{\xi=1} \tag{4.3}$$

— simply supported

$$\Delta_m(\lambda) \equiv \left. \begin{vmatrix} K_m(\xi,\lambda)_u & K_m(\xi,\lambda)_v \\ M[K_m(\xi,\lambda)_u] & M[K_m(\xi,\lambda)_v] \end{vmatrix} \right|_{\xi=1} \tag{4.4}$$

— free

$$\Delta_m(\lambda) \equiv \left. \begin{vmatrix} M[K_m(\xi,\lambda)_u] & M[K_m(\xi,\lambda)_v] \\ V[K_m(\xi,\lambda)_u] & V[K_m(\xi,\lambda)_v] \end{vmatrix} \right|_{\xi=1} \tag{4.5}$$

— sliding supports

$$\Delta_m(\lambda) \equiv \left. \begin{vmatrix} \dfrac{\partial K_m(\xi,\lambda)_u}{\partial \xi} & \dfrac{\partial K_m(\xi,\lambda)_v}{\partial \xi} \\ V[K_m(\xi,\lambda)_u] & V[K_m(\xi,\lambda)_v] \end{vmatrix} \right|_{\xi=1} \tag{4.6}$$

— elastic supports

$$\Delta_m(\lambda) \equiv \left. \begin{vmatrix} \Phi[K_m(\xi,\lambda)_u] & \Phi[K_m(\xi,\lambda)_v] \\ \Psi[K_m(\xi,\lambda)_u] & \Psi[K_m(\xi,\lambda)_v] \end{vmatrix} \right|_{\xi=1} \tag{4.7}$$

For all boundary conditions, the formula of Δ_m has the following form

$$\Delta_m = a_0 + \sum_{i=1}^{\eta} (-1)^i a_i \lambda^{2i} \tag{4.8}$$

where $a_0, a_1, \ldots, a_\eta$ are coefficients of characteristic equations depending on the boundary conditions and the parameter m.

5. Results and discussion

The numerical results for dimensionless frequencies of the uniform and non-uniform circular plates with different boundary conditions are presented in Tables 2-5. The Neumann power series (Eq. (4.1)) expanded only for $\eta = 15$ allows one to obtained six lower exact eigenvalues for all considered cases. The numerical dimensionless frequencies of the uniform circular plates are presented in Table 2 with comparison to the results by Duan *et al.* (2014), Leissa (1969), Wu and Liu (2002) and Yalcin *et al.* (2009). The numerical results for uniform circular plates with elastic supports are shown in Table 3 with comparison to the results by Wu and Liu (2002).

Table 2. The first six lower dimensionless frequencies $\lambda = \omega R^2 \sqrt{\rho h_R / D_R}$ of the uniform circular plates

λ		Boundary conditions					
		Clamped	Simply supported		Free		Sliding supports
			$\nu = 0.3$	$\nu = 0.25$	$\nu = 0.3$	$\nu = 0.25$	
λ_0	GF	10.216	4.935	4.860	9.003	8.889	14.682
	Duan *et al.* (2014)	10.215	4.935	–	9.003	–	–
	Wu and Liu (2002)	10.216	4.935	–	9.003	–	14.682
	Yalcin *et al.* (2009)	10.215	4.935	–	9.003	–	–
λ_1	GF	39.771	29.72	29.66	38.443	38.335	49.218
	Duan *et al.* (2014)	39.771	29.72	–	38.443	–	–
	Wu and Liu (2002)	39.771	29.72	–	38.443	–	49.218
	Yalcin *et al.* (2009)	39.771	29.72	–	38.443	–	–
λ_2	GF	89.104	74.156	74.101	87.750	87.645	103.499
	Duan *et al.* (2014)	89.104	74.155	–	87.753	–	–
	Wu and Liu (2002)	89.104	74.156	–	87.750	–	103.499
	Yalcin *et al.* (2009)	89.104	74.156	–	87.750	–	–
λ_3	GF	158.184	138.318	138.26	156.818	156.71	177.521
	Duan *et al.* (2014)	158.184	138.317	–	156.826	–	–
	Wu and Liu (2002)	158.184	138.318	–	156.816	–	177.521
	Yalcin *et al.* (2009)	158.184	138.318	–	156.818	–	–
λ_4	GF	247.006	222.215	222.25	245.634	245.53	271.282
	Duan *et al.* (2014)	247.006	222.213	–	245.651	–	–
	Wu and Liu (2002)	247.007	222.215	–	245.634	–	271.282
	Yalcin *et al.* (2009)	247.006	222.215	–	245.633	–	–
λ_5	GF	355.569	325.849	325.79	354.6	354.08	384.782
	Leissa (1969)	355.568	–	–	–	–	–
	Wu and Liu (2002)	355.569	325.849	–	–	–	–

GF – Green's function

Table 3. The first six lower dimensionless frequencies $\lambda = \omega R^2 \sqrt{\rho h_R / D_R}$ of the uniform circular plates with elastic supports, Poisson ratio $\nu = 0.3$

λ		Elastic parameters		
		$\phi = 0.1$, $\Psi = 100$	$\phi = 10$, $\Psi = 100$	$\phi = 100$, $\Psi = 100$
λ_0	GF	4.854	7.790	8.809
	Wu and Liu (2002)	4.854	7.790	8.809
λ_1	GF	22.097	22.128	22.142
	Wu and Liu (2002)	22.098	22.128	22.143
λ_2	GF	44.938	49.253	51.441
	Wu and Liu (2002)	44.938	49.254	51.442
λ_3	GF	90.469	98.741	104.413
	Wu and Liu (2002)	90.469	98.741	104.413
λ_4	GF	158.359	168.599	177.926
	Wu and Liu (2002)	158.359	168.599	177.926
λ_5	GF	246.673	258.213	271.391
	Wu and Liu (2002)	246.673	258.213	271.391

Table 4. The first six lower dimensionless frequencies $\lambda = \omega R^{m/3}\sqrt{\rho h_R/D_R}$ of the non-uniform circular plates

m	λ	Boundary conditions							
		Clamped		Simply supported		Free		Sliding supports	
		$\nu = 0.33$	$\nu = 0.25$	$\nu = 0.33$	$\nu = 0.25$	$\nu = 0.33$	$\nu = 0.25$	$\nu = 0.33$	$\nu = 0.25$
-3	λ_0	16.902	17.209	10.851	10.981	25.643	25.501	36.543	36.676
	λ_1	86.044	86.188	67.382	67.403	90.847	90.722	114.63	114.75
	λ_2	197.11	197.25	167.37	167.38	210.79	201.67	236.94	237.07
	λ_3	352.64	352.78	311.75	311.76	357.14	357.01	403.59	403.71
	λ_4	552.55	552.69	500.53	500.54	556.94	556.82	614.61	614.74
	λ_5	796.86	796.99	733.71	733.72	801.18	801.05	870.03	870.16
-2	λ_0	15.147	15.331	9.280	9.314	19.555	19.398	28.537	28.625
	λ_1	68.932	69.027	53.458	53.440	71.203	71.062	90.109	90.192
	λ_2	156.66	156.75	132.43	132.41	158.85	158.71	186.69	186.77
	λ_3	279.52	279.61	246.49	246.47	281.60	281.46	318.33	318.41
	λ_4	437.46	437.54	395.64	395.61	439.47	439.33	485.04	485.13
	λ_5	630.48	630.56	579.87	579.85	632.45	632.31	686.84	686.92
-1	λ_0	12.868	12.951	7.302	7.256	14.041	13.868	21.254	21.297
	λ_1	53.504	53.551	40.917	40.860	53.762	53.604	68.307	68.349
	λ_2	120.65	120.70	101.37	101.31	120.86	120.70	142.21	142.25
	λ_3	214.70	214.74	188.69	188.63	214.85	214.69	242.97	243.01
	λ_4	335.61	335.65	302.88	302.82	335.72	335.57	370.60	370.64
	λ_5	483.38	483.42	443.93	443.87	483.48	483.32	525.09	525.13
2	λ_0	8.894	9.111	3.297	3.334	5.302	5.412	8.876	9.193
	λ_1	25.837	26.306	19.076	19.410	22.951	23.296	28.472	29.011
	λ_2	51.575	52.278	42.759	43.337	48.776	49.363	56.510	57.279
	λ_3	86.082	87.017	75.135	75.949	83.323	84.144	93.262	94.260
	λ_4	129.36	130.52	116.25	117.30	126.62	127.67	138.76	139.99
	λ_5	181.41	182.81	166.13	167.41	178.68	179.97	193.03	194.49
3	λ_0	8.719	8.965	3.002	3.073	4.686	4.843	8.787	7.170
	[1]	8.720	–	–	–	–	–	–	–
	[7]	8.708	–	–	–	–	–	–	–
	[16]	8.719	8.965	–	–	–	–	–	–
	λ_1	21.145	21.609	15.761	16.110	18.152	18.520	21.638	22.170
	[1]	21.15	–	–	–	–	–	–	–
	[16]	21.145	21.609	–	–	–	–	–	–
	λ_2	38.453	39.122	32.031	32.595	35.607	36.187	40.402	41.133
	[1]	38.45	–	–	–	–	–	–	–
	[16]	38.453	39.122	–	–	–	–	–	–
	λ_3	60.680	61.551	53.108	53.879	57.892	58.677	63.964	64.894
	λ_4	87.834	88.910	79.076	80.052	85.077	86.066	92.411	93.577
	λ_5	119.91	121.19	109.95	111.03	117.18	118.31	125.78	126.78
4	λ_0	8.458	8.705	2.877	2.965	4.395	4.569	3.644	4.273
	λ_1	16.735	17.137	12.781	13.096	14.093	14.427	15.778	16.236
	λ_2	27.094	27.643	22.827	23.299	24.645	25.131	27.042	27.639
	λ_3	39.611	40.303	34.898	35.418	37.240	37.872	40.255	41.007
	λ_4	54.305	55.139	49.123	49.866	51.975	52.751	55.925	56.484
	λ_5	70.806	71.542	65.087	66.243	68.884	69.791	70.875	74.118

[1] – Conway (1957), [7] – Jaroszewicz and Zoryj (2006), [16] – Wang (1997)

Table 5. The first six lower dimensionless frequencies $\lambda = \omega R^{m/3}\sqrt{\rho h_R/D_R}$ of the non-uniform circular plates with elastic supports

m	λ	Elastic parameters					
		$\phi = 0.1$, $\Psi = 10$		$\phi = 100$, $\Psi = 10$		$\phi = 10$, $\Psi = 10$	
		$\nu = 0.33$	$\nu = 0.25$	$\nu = 0.33$	$\nu = 0.25$	$\nu = 0.33$	$\nu = 0.25$
-3	λ_0	3.595	3.670	2.965	3.011	0.317	0.322
	λ_1	27.042	26.920	36.525	36.650	33.285	33.379
	λ_2	91.487	91.369	113.22	113.34	104.64	104.72
	λ_3	202.25	202.13	233.81	233.93	218.85	218.90
	λ_4	357.53	357.41	398.25	398.37	376.43	376.46
	λ_5	557.30	557.18	606.59	606.71	577.83	577.84
-2	λ_0	3.818	3.873	3.344	3.377	0.354	0.357
	λ_1	21.143	21.012	28.709	28.790	26.104	26.164
	λ_2	71.857	71.723	89.165	89.246	82.728	82.772
	λ_3	159.29	159.16	184.49	184.58	173.21	173.23
	λ_4	281.972	281.83	314.55	314.63	297.95	297.95
	λ_5	439.81	439.67	479.34	479.42	457.28	457.27
-1	λ_0	3.860	3.886	3.749	3.769	0.394	0.396
	λ_1	15.947	15.818	21.624	21.662	19.520	19.546
	λ_2	54.447	54.297	67.746	67.787	63.101	63.114
	λ_3	121.29	121.14	140.76	140.80	132.60	132.60
	λ_4	215.20	215.04	240.43	240.47	228.33	228.31
	λ_5	336.06	335.88	366.76	366.77	350.51	350.48
2	λ_0	3.140	3.168	7.330	7.148	0.729	0.723
	λ_1	9.061	9.195	8.855	9.317	8.250	8.546
	λ_2	23.752	24.096	28.495	29.027	26.982	27.482
	λ_3	49.197	49.784	56.260	57.022	53.862	54.581
	λ_4	83.620	84.442	92.740	93.731	89.265	90.204
	λ_5	126.86	127.918	137.94	139.16	133.27	134.43
3	λ_0	3.100	3.156	21.623	22.157	1.050	1.023
	λ_1	8.804	8.954	40.302	41.028	6.374	6.733
	λ_2	18.947	19.309	63.727	64.651	20.771	21.271
	λ_3	36.010	36.589	92.023	93.149	38.923	39.615
	λ_4	58.170	58.955	125.22	126.24	61.783	62.668
	λ_5	85.295	86.304	153.08	155.33	89.454	90.552
4	λ_0	3.166	3.239	15.354	15.859	2.642	1.999
	λ_1	8.651	8.803	26.962	27.562	15.401	15.832
	λ_2	14.881	15.204	40.184	40.919	26.395	26.966
	λ_3	25.028	25.512	55.473	56.347	39.575	40.040
	λ_4	37.810	38.129	72.903	73.921	48.253	55.200
	λ_5	45.062	52.949	92.495	93.111	59.544	72.493

The dimensionless frequencies of the non-uniform circular plates with different boundary conditions are presented in Table 4 with comparison to the results by Conway (1957), Jaroszewicz and Zoryj (2006), Wang (1997). The numerical results for the non-uniform circular plates with elastic supports are shown in Table 5.

The dimensionless frequencies of the non-uniform circular plate (Table 4) decrease when values of the power index increase. However, the absolute values of frequencies ω increase if the power index increases, which is according to physical properties of this kind of plates with variable thickness (Wu and Liu, 2002). Additionally, the dimensionless frequencies depend on functions describing the distribution of plate parameters such as thickness or rigidity. The dimensionless frequencies and absolute values ω for the uniform and the non-uniform circular plates with elastic constraints (Table 3 and 5) depend on combination of values of the elastic parameters.

6. Conclusions

In this paper, Green's functions have been employed to solve the problem of natural vibration of uniform and non-uniform circular thin plates with different boundary conditions. The universal Green function for different power indices m and different Poisson ratios is defined. The limited solutions to the Euler equation expanded in the Neumann power series allow one to obtain characteristic equations of circular plates rapidly convergent to the exact eigenvalues. The characteristic equations have been obtained for different values of the parameter m, different values of Poisson's ratio and different boundary conditions. The considered values of Poisson's ratio have not large influence on the dimensionless eigenvalues, but the numerical results of the investigation can be used to validate the accuracy of other numerical methods as benchmark values. The obtained results are in good agreement with the results obtained by other methods presented in the literature. The calculations have been carried out with the help of Mathematica v10, which is a symbolic calculation software.

References

1. Conway H.D., 1957, An analogy between the flexural vibrations of a cone and a disc of linearly varying thickness, *Journal of Applied Mathematics and Mechanics*, **37**, 9, 406-407
2. Conway H.D., 1958, Some special solutions for the flexural vibrations of discs of varying thickness, *Ingenieur-Archiv*, **26**, 6, 408-410
3. Duan G., Wang X., Jin Ch., 2014, Free vibration analysis of circular thin plates with stepped thickness by the DSC element method, *Thin-Walled Structures*, **85**, 25-33
4. Gupta U.S., Lal R., Sharma S., 2006, Vibration analysis of non-homogeneous circular plate of nonlinear thickness variation by differential quadrature method, *Journal of Sound and Vibration*, **298**, 892-906
5. Jain R.K., Prasad C., Soni S.R., 1972, Axisymmetric vibrations of circular plates of linearly varying thickness, *ZAMP*, **23**, 941-947
6. Jaroszewicz J., Zoryj L., 2005, *Methods of Free Axisymmetric Vibration Analysis of Circular Plates Using by Influence Functions*, Bialystok University of Technology, Poland
7. Jaroszewicz J., Zoryj L., 2006, The method of partial discretization in free vibration problems of circular plates with variable distribution of parameters, *International Applied Mechanics*, **42**, 364-373
8. Kukla S., 2009, *Green's Functions and their Properties*, Czestochowa University of Technology, Poland
9. Leissa A.W., 1969, *Vibration of Plates*, Washington
10. Pogorzelski W., 1958, *Integral Equations and their Applications*, Vol. 1, PWN Warszawa
11. Shestopalov Y.V, Smirnov Y.G., 2002, *Integral Equations*, Karlstad
12. Stakgold I., Holst M., 2011, *Green's Functions and Boundary Value Problem*, Edition 3rd, Wiley

13. Taher H.R., Omidi M., Zadpoor A.A., Nikooyan A.A., 2006, Free vibration of circular and annular plates with variable thickness and different combinations of boundary conditions, *Journal of Sound and Vibration*, **296**, 1084-1092

14. Timoshenko S., Woinowsky-Krieger S., 1959, *Theory of Plates and Shells*, McGraw-Hill, New York

15. Tricomi F.G., 1957, *Integral Equations*, New York

16. Wang J., 1997, General power series solution of the vibration of classical circular plates with variable thickness, *Journal of Sound and Vibration*, **202**, 593-599

17. Wu T.Y., Liu G.R., 2001, Free vibration analysis of circular plates with variable thickness by the generalized differential quadrature rule, *International Journal of Solids and Structures*, **38**, 7967-7980

18. Wu T.Y., Liu G.R., 2002, Free vibration analysis of circular plates using generalized differential quadrature rule, *Computer Methods in Applied Mechanics and Engineering*, **191**, 5365-5380

19. Yalcin H.S., Arikoglu A., Ozkol I., 2009, Free vibration analysis of circular plates by differential transformation method, *Applied Mathematics and Computation*, **212**, 2, 377-386

20. Yang J.S., 1993, The vibration of circular plate with variable thickness, *Journal of Sound and Vibration*, **165**, 178-185

21. Zhou Z.H., Wong K.W., Xu X.S., Leung A.Y.T., 2011, Natural vibration of circular and annular plates by Hamiltonian approach, *Journal of Sound and Vibration*, **330**, 5, 1005-1017

Manuscript received October 2, 2014; accepted for print May 4, 2015

**JOURNAL OF THEORETICAL
AND APPLIED MECHANICS**
53, 4, pp. 885-894, Warsaw 2015
DOI: 10.15632/jtam-pl.53.4.885

THEORETICAL STUDY OF A TWIN-TUBE MAGNETORHEOLOGICAL DAMPER CONCEPT

Janusz Gołdasz
Technical Center Krakow, BWI Group, Kraków, Poland and
Cracow University of Technology, Department of Control and Information Technology, Kraków, Poland
e-mail: janusz.goldasz@bwigroup.com

In this study, the author presents a theoretical model of a semi-active magnetorheological (MR) twin-tube damper concept. The model relies on geometric variables and material properties and can be used in engineering and research studies on damper structures. Other non-linear characteristics, namely, the fluid chamber compressibility, fluid inertia, cylinder elasticity, friction, one-way check valves are included into the model as well. The author studies the performance of the damper model as design variables are varied, and the results are analysed and discussed.

Keywords: MR damper, twin-tube damper concept, lumped parameter model

1. Introduction

Magnetorheological (MR) fluids have always been attractive to engineers and researchers within the automotive industry. The material adapts to changing external conditions within milliseconds. Automotive (vehicle) dampers utilizing MR fluids are now found in a number of semi-active platforms in vehicles. In the industry, the monotube damper configuration (de Carbon, 1952) is the most common structure of a flow-mode MR damper. The cylinder tube houses the floating piston (gas cup) separating the fluid from the gas-filled chamber. The piston divides the MR fluid volume into the compression chamber (fluid volume between the floating piston and the main piston assembly) and the rebound chamber (fluid volume between the rod guide and the main piston). The piston assembly contains an annular gap to permit the fluid to flow between the chambers and secondary flow paths (bypasses) for tuning the MR damper low-speed performance. In a typical MR damper, the rod is attached to the vehicle body and the cylinder to the wheel hub. The relative motion of the wheel and the body drives the fluid flow between the chambers through the annulus in the piston. The design has been a natural choice for MR applications due to its simplicity, however, high operating pressures and packaging limit its scope. Moreover, manufacturing issues due to high surface finish requirements of the cylinder tube are a factor here, too. Also, gas high pressures in monotube dampers would translate into rod guide friction well above that of twintube hardware. Therefore, the research on other structures of MR dampers continues (Poynor, 2001). A standard twin-tube damper features concentric cylinder tubes. The inner cylinder houses a piston valve for controlling the flow between the adjacent fluid chambers and a base (foot) valve for regulating the flow between the fluid chamber below the piston in the inner cylinder and a reservoir (fluid volume contained between the outer tube and the inner one). The reservoir is partially filled with oil to accommodate volume changes due to rod displacement. The dampers work at a lower gas pressure, but only upright positions are possible in vehicles, and they incorporate more valves. However, research efforts on MR twin-tube structures have not fully succeeded. Two studies focused on a twin-tube structure of an MR damper in which the MR control valve was located in the piston inside the inner cylinder

(Poynor, 2001; Jensen *et al.*, 2001). In the design of Jensen *et al.* (2001), a standard base valve was used for controlling the MR fluid flow into the outer reservoir. The damper structure, however, might suffer from hydraulic imbalance (a common problem affecting twintube dampers), and the range of damping forces that can be achieved with this design could be limited. The imbalance phenomenon occurs when the damper is in compression and the pressure drop across the piston is larger than the pressure drop across the base valve. As a result, most of the fluid volume is pushed through the base valve causing lags in the chamber above the piston. Another study revealed a twin-tube damper in which the MR valve regulates the fluid flow from the upper chamber above the piston into the reservoir volume between the cylinders (Oakley, 2006). Two one-way check valves are used for directing the flow between the fluid chambers. Another feature of this concept is its ability to tune its non-energized condition with passive valves. Apparently, there is no published research on the twin-tube design of Oakley (2006) related to its performance. The proposed model fulfills this gap. Briefly, the generic goal of this study was to provide a lumped parameter model of a twin-tube MR damper for component as well as vehicle level analyses. The task is complicated – damper and flow channel geometry, magnetic field induced yield stress and resistance-to-flow build-up, fluid compliance, cavitation, friction, gas absorption, etc. have been among the contributors to the force output of MR dampers (Hong *et al.*, 2006). At the same time, vehicle dampers have been a subject of intensive modelling work. In the past, researchers developed various models of dampers to copy their non-linear characteristics. For example, Lang (1977) as well as Segel and Lang (1981) developed a math model of a twintube automotive damper and concluded the observed hysteretic behavior was due to the compressibility of the fluid, cylinder tube elasticity and cavitation. The models of Lang (1977), Segel and Lang (1981) remain the key work on conventional dampers operating at high frequencies. Also, Lee (1997) obtained a complex model of a monotube vehicle suspension damper. The model included compressibility of fluid dampers, floating gas cup inertia and first-order heat transfer effects in addition to a deflected disc piston model. Also, Mollica (1997) proposed a non-linear model of a monotube damper using bond graph techniques. The model of Mollica incorporates friction elements, fluid compressibility, gas, leakage and hydraulic resistance components in the piston (Mollica, 1997). Those studies were a basis for developing the lumped parameter model described in detail below. Specifically, the goal was to obtain a damper model capable of copying the performance characteristics of twin-tube MR dampers and important phenomena occurring inside the device as well as the operational logic of the damper. Also, fluid compressibility effects and fluid inertia are modeled, and their influence on the damping force output of an MR damper is analysed for a selected configuration.

2. Modelling

The MR twin-tube damper concept is illustrated in Fig. 1. The inner tube houses the piston separating the fluid volume into the rebound (upper) chamber volume and the compression (lower) chamber volume. The damper is driven by the displacement (velocity) input x_p (v_p) applied to the rod. MR valve (1) controls the fluid flow between rebound and reservoir chambers. The flow rate through the MR valve is $Q_{v,1}$. The flow through the piston $Q_{v,2}$ is controlled by check valve (2). The valve allows flow in one direction only, from chamber (2) (compression) into chamber (1) (rebound). The flow between chambers (3) (reservoir) and (2) (compression) is controlled by one-way valve (3). This valve allows flow from chamber (3) (reservoir) into (2) (compression). Both valves are schematically shown in Fig. 1 – they may take the form of a standard deflected disc stack assembly or a preloaded spring and plate. The flow rate through check valve (3) is $Q_{v,3}$. The reservoir contains MR fluid and pressurised gas. The fluid rheology in the annulus is controlled by the magnetic field H due to the current I_c in the coil of the piston core. The fluid is described by the yield stress τ_0, viscosity μ, density ρ, and bulk modulus B_f. The MR annulus height is h, and its cross-section area A_g. L_g is the annular length, and the active section length (magnetic poles) is L_a ($L_a < L_g$). In rebound (see Fig. 1), the rod moves out of the damper. The flow is through valves (1) and (3), and there is no flow through valve (2); the flow through MR valve (1) is uni-directional. In compression, the rod would move into the damper. Flow through check valve (3) would be prevented, and it would occur through valves (1) and (2). In the sections that follow below, the author discusses the key phenomena occurring in the damper and outside of the MR valve.

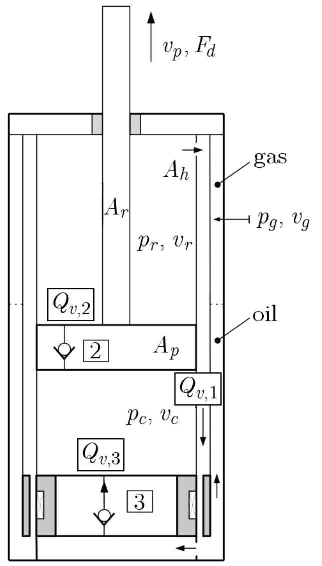

Fig. 1. MR twin-tube damper: internal MR valve

2.1. Damper model

Consider the damper model in Fig. 1. With the inertia of the lumped mass of fluid in the MR valve annulus, the force balance equation is (Gołdasz and Sapiński, 2013)

$$\dot{Q}_{v,1} = \frac{A_g}{\rho L_g}(P_r - P_g - \Delta p_a - \Delta P_H) \tag{2.1}$$

where Δp_a is the field-induced pressure drop along the annular gap, and ΔP_H denotes losses at the holes in the inner cylinder. The term Δp_a is discussed in detail in Section 2.2. Also, fluid continuity expressions for the pressures above and below the piston are

$$\begin{aligned} \dot{P}_r &= \beta(P_r)\frac{(A_p - A_r)v_p - (Q_{v,1} + Q_{v,2})}{V_{r,0} - (A_p - A_r)x_p} \\ \dot{P}_c &= \beta(P_c)\frac{-A_p v_p + (Q_{v,2} + Q_{v,3})}{V_{c,0} + A_p x_p} \end{aligned} \tag{2.2}$$

where $\beta(P)$ refers to the combined bulk modulus due to fluid compressibility and cylinder compliance, whereas $V_{r,0}$ and $V_{c,0}$ are midstroke fluid chamber volumes. Gas pressure in the reservoir P_g can be expressed assuming the adiabatic process, i.e. without heat transfer between the damper and the environment

$$P_g = P_{g,0}\Big(\frac{V_{g,0}}{V_{g,0} - \int(Q_{v,1} - Q_{v,3})\,dt}\Big)^n \tag{2.3}$$

In the above equation, $P_{g,0}$ and $V_{g,0}$ are the initial gas pressure and volume, respectively, and n is the adiabatic gas constant. Also in this analysis, the effects of wall expansion with pressure are combined with the influence of fluid bulk modulus via the relationship

$$\frac{1}{\beta} = \frac{1}{\beta_f} + \frac{1}{\beta_s} \tag{2.4}$$

where the variation of the fluid bulk modulus with pressure can be as

$$\beta_f(P) = \beta_0 \frac{1 + \alpha\Big(\frac{P_a}{P_a+P}\Big)^{\frac{1}{n}}}{1 + \alpha\frac{P_a^{\frac{1}{n}}}{n(P_a+P)^{\frac{1+n}{n}}}} \tag{2.5}$$

Equation (2.5) reveals the bulk modulus variation with pressure of the mixture of the fluid and non-dissolved air (Manring, 2005). β_0 is the pure fluid bulk modulus, P_a refers to the atmospheric (or reference) pressure, and α denotes the relative gas content. The compliance of the steel cylinder β_s is (Mollica, 1997)

$$\frac{1}{\beta_s} = \frac{2}{E_s}\Big(\nu + \frac{D_o^2 + D_p^2}{D_o^2 - D_p^2}\Big) \tag{2.6}$$

where E_s is Young modulus (steel), ν – Poisson's coefficient, D_o – outer diameter of the cylinder. Cavitation effects are simply modeled by imposing a constraint on the pressures P_r and P_c, $P_r \geqslant P_v$ and $P_c \geqslant P_v$. Also, the pressure drop at the holes $\varDelta P_H$ in the inner cylinder is

$$\varDelta P_H = \rho\frac{Q_{v,1}^2}{2(C_H A_H)^2} \tag{2.7}$$

where C_H is the discharge coefficient and A_o cross-sectional area of the holes. Using the one-way valve in the piston, the piston flow rate $Q_{v,2}$ can be

$$Q_{v,2} = \begin{cases} C_2 A_2\sqrt{2\dfrac{|P_r - P_c|}{\rho}} & P_r - P_c < 0 \\ 0 & P_r - P_c \geqslant 0 \end{cases} \tag{2.8}$$

Similarly, the flow rate $Q_{v,3}$ through check valve (3) is

$$Q_{v,3} = \begin{cases} C_3 A_3\sqrt{2\dfrac{|P_c - P_g|}{\rho}} & P_c - P_g < 0 \\ 0 & P_c - P_g \geqslant 0 \end{cases} \tag{2.9}$$

The check valves are assumed to open with no delay. Considering forces on the piston, the damping force F_d including friction F_f becomes

$$F_d = (A_p - A_r)P_r - A_p P_c + F_f\big(\operatorname{sgn}(v_p)\big) \tag{2.10}$$

To summarize, equations from (2.1) to (2.10) form a set of expressions for simulating the output of a twin-tube MR damper.

2.2. MR valve model

This Section shows the application of a biplastic Bingham scheme for deriving the pressure vs. flow rate characteristics of an MR valve model. The MR valve (annulus) contains a parallel flux bypass feature. The flux bypass often takes the form of a slot feature on either surface constituting the annulus. Due to the increased (local) height of the annulus, it is characterized by a region of low flux density (yield stress) (Gołdasz and Sapiński, 2012) where the MR fluid is allowed to flow through the flux bypass section at a lower breakaway pressure drop than in the other portion of the flow channel. As a result, low forces are achieved at near-zero flow rates through the MR piston. Medium and high flow rate performance is not affected. Application of the bi-plastic scheme is based on the assumption that the dual behavior can be described with the artificial material model of parameters related to both material properties of the MR (Bingham) fluid and the piston geometry. By expressing the pressure drop Δp_a across the control valve in terms of the dimensionless pressure number G and the plasticity S, the equation linking the term Δp_a with the flow rate through the MR valve $Q_{v,1}$ is (Gołdasz and Sapiński, 2012)

$$\begin{aligned} &\Delta p_a = \frac{2\tau_2 L_a}{h}G(S) + C\frac{\rho Q_{v,1}^2}{A_g^2} = \frac{2\tau_0 L_a}{h[1-\gamma(1-\delta)]}G(S) + C\frac{\rho Q_{v,1}^2}{A_g^2} \\ &G = -\frac{h\Delta p_a}{2L_a\tau_2} \qquad\qquad S = \frac{12\mu Q_{v,1}}{wh^2\tau_2} \end{aligned} \tag{2.11}$$

In equation (2.11), high velocity losses are accounted for in the model in quadratic form, and the tuning coefficient C captures the effects of the fluid entry and exit, flow development, turbulent losses, etc. The parameters γ and δ refer to the slope of the damper force (pressure) variation against velocity (flow rate) and the interception force in the pre-yield region, and τ_2 is the bi-plastic material yield stress. The pre-yield viscosity (slope) μ_r is related to the material viscosity μ via $\gamma = \mu/\mu_r$, and the yield stress τ_2 is linked to the yield stress τ_0 through the equation $\tau_0 = \tau_2[1-\gamma(1-\delta)]$. At $\gamma \to \infty$ and $\delta \to 1$, the model would reduce to that of classic Bingham's.

The bi-plastic model was studied by various authors (Gołdasz and Sapiński, 2012, 2013; Dimock *et al.*, 2002). For example, Gołdasz and Sapiński (2012) analyzed the performance of a dual coil MR piston with the flux bypass feature and extracted non-dimensional parameters for it. The authors concluded that the non-dimensional viscosity γ was relatively invariant of the magnetic field, whereas the yield stress parameter δ varied with the current level (or flux density). The model allows for separating the flow regime into two distinct flow regimes with the threshold plasticity $S_0 = \gamma(2-3\delta+\delta^3)$. Briefly, the pre-yield (bypass) regime is characterized by the plasticity number $S < S_0$ and the post-yield regime by $S \geqslant S_0$. In the model, the post-yield relationship between the pressure drop and the flow rate through the annulus for ($S \geqslant S_0$ and $G \geqslant 1$) is

$$G = \frac{1}{6}[3(1-\gamma(1-\delta)) + S]\Big[2\cos\Big(\frac{1}{3}\arctan 2(y,x)\Big) + 1\Big] \tag{2.12}$$

where

$$\begin{aligned} &y = 12\sqrt{-81b^2 + 12ba^3} \qquad\qquad x = -108b + 8a^3 \\ &a = \frac{3}{2}(1-\gamma(1-\delta)) + \frac{1}{2}S \qquad\qquad b = \frac{1}{2}(1-\gamma(1-\delta^3)) \end{aligned} \tag{2.13}$$

In the pre-yield flow regime, $S < S_0$, the material behavior is governed by the modified Bingham plastic formula

$$G = \delta\frac{1}{6}\Big(\frac{S}{\delta\gamma} + 3\Big)\Big[2\cos\Big(\frac{1}{3}\arctan 2(y',x')\Big) + 1\Big] \tag{2.14}$$

where

$$
\begin{aligned}
x' &= -27 + 27\frac{S}{\gamma\delta} + 9\Big(\frac{S}{\gamma\delta}\Big)^2 + \Big(\frac{S}{\gamma\delta}\Big)^3 \\
y' &= 6\sqrt{3}\sqrt{27\frac{S}{\gamma\delta} + 9\Big(\frac{S}{\gamma\delta}\Big)^2 + \Big(\frac{S}{\gamma\delta}\Big)^3}
\end{aligned}
\tag{2.15}
$$

To summarize, equation (2.11) accompanied by equations (2.14) and (2.15) allow for calculation of the pressure drop Δp_a across the energized annulus.

3. Simulations

The simulations involved the MR twin-tube damper model subjected to a displacement waveform at the rod as in Fig. 1 and used the data in Table 1. The friction estimate F_f of 70 N has been obtained from a real damper; the gas pressure $P_{g,0}$ is equal to 0.8 MPa, and the adiabatic constant 1.4. The MR fluid bulk modulus β_f is 1500 MPa, the density ρ is 2.68 g/cc, and its air contents α equal to 0.001. The viscosity of the fluid μ is 62 cP at the temperature T_a of 30°C – see Fig. 2. The steel modulus of elasticity E_s is $2.1 \cdot 10^5$ MPa, and the Poisson coefficient equals to 0.29.

Table 1. Twin-tube damper model inputs

Symbol	Description	Value
$L_{r,0}$	Initial rebound chamber length, [mm]	150
$L_{c,0}$	Initial compression chamber length, [mm]	150
$A_{eff} = Ap - A_r$	Upper chamber cross-section area, [mm^2]	683.48
A_p	Cylinder cross-section area, [mm^2]	804.24
$V_{r,0}$	Initial rebound chamber volume, [mm^3]	$1.206 \cdot 10^5$
$V_{c,0}$	Initial compression chamber volume, [mm^3]	$1.025 \cdot 10^5$
$V_{g,0}$	Initial gas chamber volume, [mm^3]	$0.861 \cdot 10^5$
A_2, A_3	Check valve flow areas, [mm^2]	220
C_2, C_3, C_H	Discharge coefficients, [–]	0.7
A_H	Cylinder holes area, [mm^2]	301
t_w	Cylinder wall thickness, [mm]	1.8
L_a	Active length, [mm]	25.8
L	Annulus length, [mm]	37
h	Annulus height, [mm]	0.89
w	Mean circumferential width, [mm]	88.60
C	Flow coefficient, [–]	0.1

The piston parameters, the yield stress ratio and the viscosity ratio variation with current, respectively, copy the dual-coil assembly by Gołdasz and Sapiński (2012). In the study, the two parameters γ and δ are identified from real piston performance data. The identified viscosity ratio γ varied from 0.0175 at the coil current I_c of 1 A through 0.0167 at 3 A to 0.0149 at the maximum coil current level of 5 A. The yield stress ratio varied from 0.179 ($I_c = 1$ A) through 0.363 ($I_c = 3$ A) to 0.492 ($I_c = 5$ A). Here, the MR piston is simply described by the steady-state pressure vs. flow rate characteristics in Fig. 3. The $\Delta p_a - Q_{v,1}$ characteristics in Fig. 3 are based on the geometry and material properties, and then input into the Simulink model. The fluid data are in Fig. 2; B – magnetic flux density, H – field strength. The results given by equations (2.2) through (2.10) are presented in Figs. 4 through 7. Briefly, the model

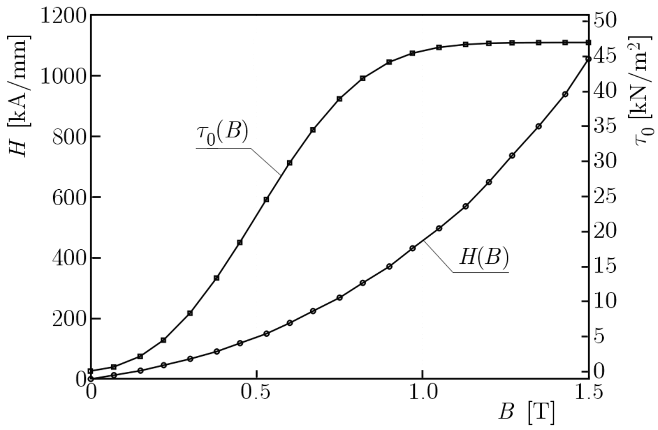

Fig. 2. MR fluid characteristics: B-H, τ_0-B (Gołdasz and Sapiński, 2012)

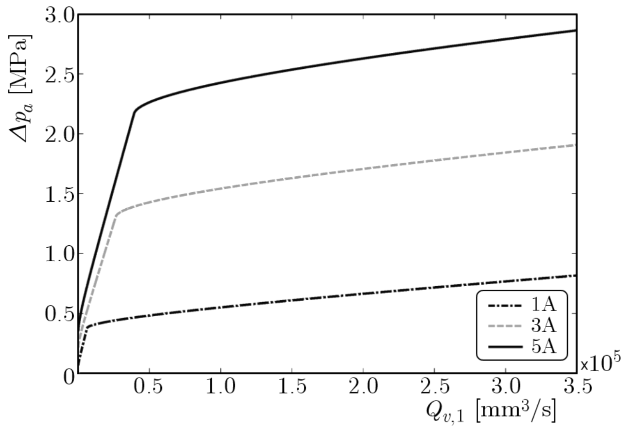

Fig. 3. MR piston steady-state characteristics: Δp_a vs. $Q_{v,1}$

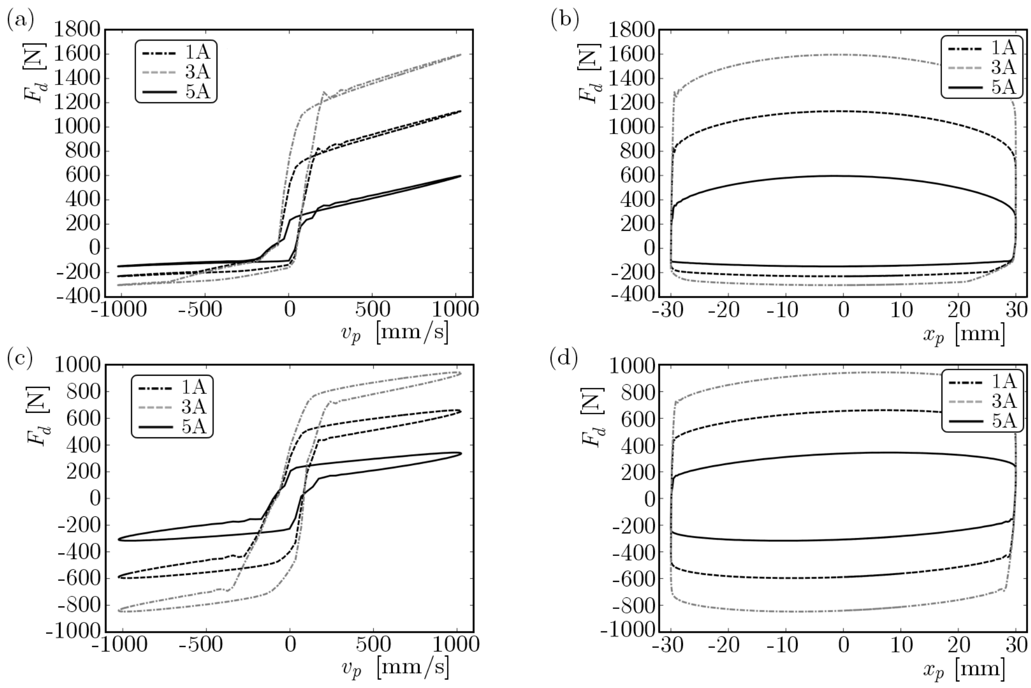

Fig. 4. Influence of rod size on the damping force; $X_p = 30\,\text{mm}$, $V_p = 1024\,\text{mm/s}$

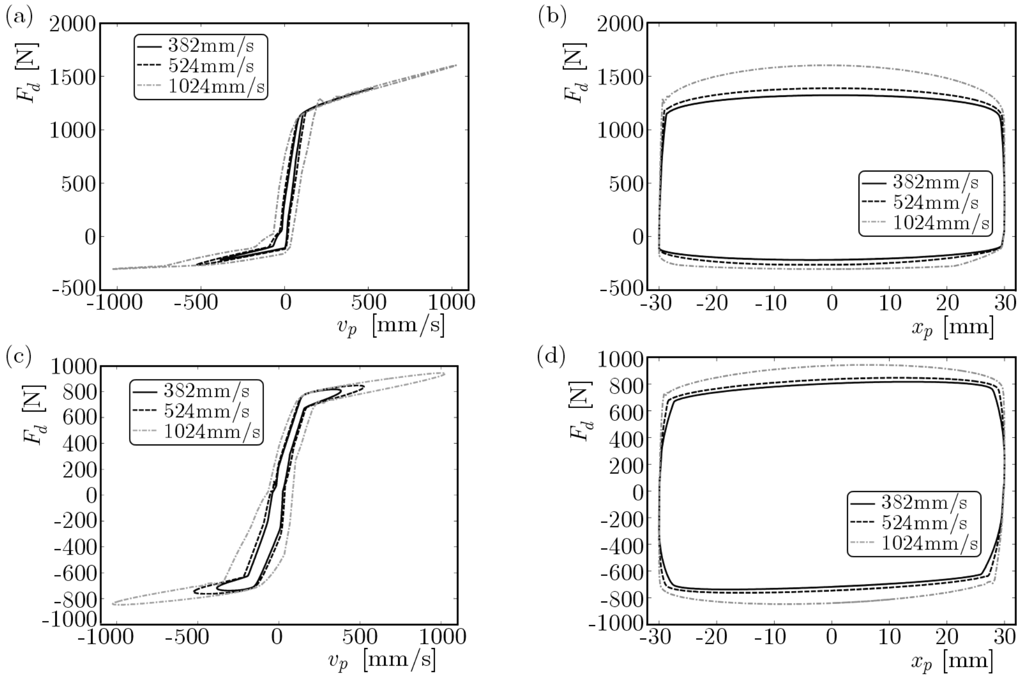

Fig. 5. Graphs of force-displacement and force-velocity; $X_p = 30\,\mathrm{mm}$, $I_c = 5\,\mathrm{A}$

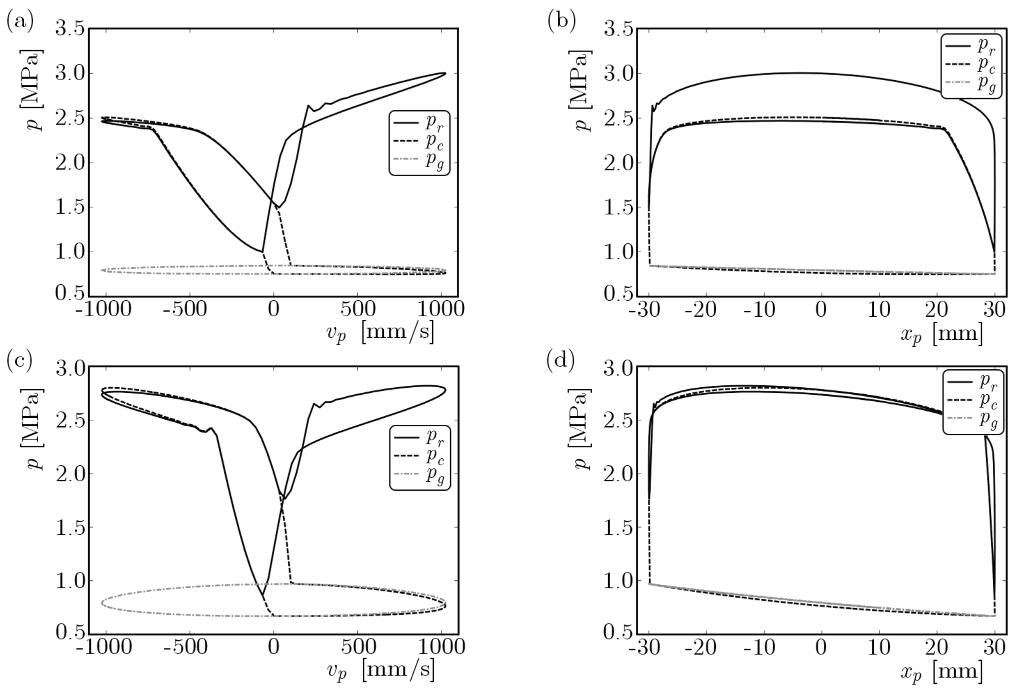

Fig. 6. Graphs of pressure-displacement and pressure-velocity; $X_p = 30\,\mathrm{mm}$, $I_c = 5\,\mathrm{A}$

is subjected to the displacement $x_p(t) = X_p \sin \omega t$ applied to the rod. The results are shown as force-velocity and force-displacement loops. In the simulations, the effects of velocity, coil current and rod size on the damping force output are examined. Specifically, Fig. 4 shows the impact the rod diameter (area) has on the damper force. As seen in Figs. 4a through 4d, smaller rod sizes ($D_p = 12.4\,\mathrm{mm}$) contribute to major asymmetry in the damping force. The rebound-to-compression ratio (asymmetry ratio) for the damping force is above 5:1 at the peak velocity of 1024 mm/s. In the cases shown, the rebound forces decreased when the piston diameter increased

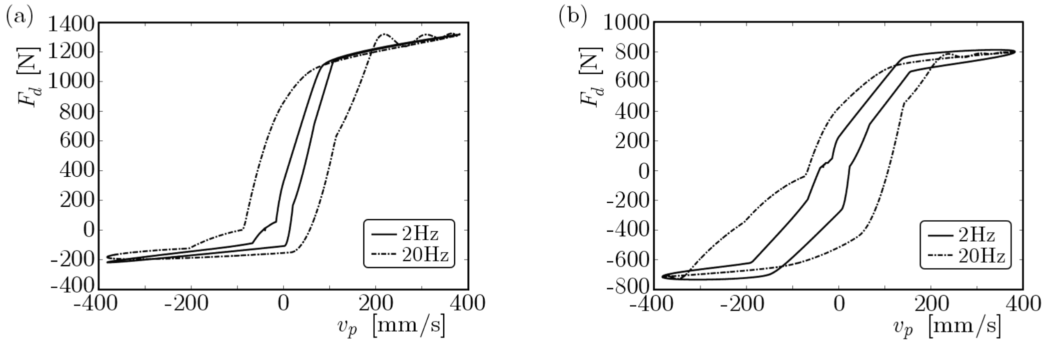

Fig. 7. Influence of the frequency; $V_p = 382\,\mathrm{mm/s}$

up to 22 mm. The asymmetry decreased at the expense of rebound forces. It can be shown that as the piston rod is in compression, check valve (2) in the piston is opened, and check valve (3) in the base valve is closed, so that the annular flow rate is related to the rod area A_r. Smaller rod sizes develop larger force output asymmetry. Increasing the rod size impacts the hysteresis between the force and velocity (see Figs. 4a and 4c and 5) and rotates the damping force ellipses into the first quadrant of the force-displacement plane due to the gas force. The hysteresis is larger when in compression than in rebound. Also, it can be shown that the gas force change magnitude is directly related to the rod area. Next, Fig. 6 reveals the pressures in each chamber of the damper vs. piston displacement and velocity. Note that the rebound chamber pressure dominates regardless of the damper operating conditions, i.e. it is clear that when the damper is in rebound the pressure in the lower chamber drops below gas pressure. Check valve (3) in the base valve opens, and there is flow through check valve (3) from the reservoir and into the compression chamber. In compression, the check valve in the piston opens and there is flow from the compression chamber into the rebound one. The effect of frequency manifested by an increase in the hysteresis in the force-velocity loops and force oscillations are shown in Fig. 7.

4. Conclusions

The author has analysed a novel model of a twin-tube MR damper concept. The study shows numerical results, however, the MR valve model is based on a verified bi-plastic theory and against real data which allows one to analyze the results with confidence (Gołdasz and Sapiński, 2012, 2013). Apart from the MR valve, the damper utilizes two one-way check valves in the piston and the base valve, respectively. The check valves offer extra means of tuning the output force in off-state conditions; this aspect of the concept is beyond the scope of this paper. Additionally, by using the check valves at the piston and the base of the damper, the flow through the piston is always in the same direction. To the author's knowledge no such model has been developed so far. As opposed to present MR structures, this configuration is asymmetric rebound-to-compression; the asymmetry is related to the rod size. To conclude, larger rod sizes minimize the asymmetry at the cost of rebound forces. The damper is more complex than single-tube structures but any performance and cost benefits, namely, lower friction, less stringent cylinder surface finish, may favour its applications. The damper works at a lower gas pressure than other MR damper structures, too. The twin-tube damper model can be a useful tool in various studies. The model relies on the information extracted mainly from engineering drawings and fluid data, which makes it suitable for fast sizing studies early in the design development stage. Transient studies through the B-τ_0 coupling are possible, too.

References

1. de Carbon Ch., 1952, *Shock absorbers*, US Patent No. 2774446
2. Dimock G.A., Yoo J.-H., Wereley N.M., 2002, Quasi-steady Bingham biplastic analysis of electrorheological and magnetorheological dampers, *Journal of Intelligent Material Systems and Structures*, **13**, 9, 549-559
3. Gołdasz J., Sapiński, B., 2012, Nondimensional characterization of flow-mode magnetorheological fluid dampers, *Journal of Intelligent Material Systems and Structures*, **23**, 14, 1545-1562
4. Gołdasz J., Sapiński B., 2013, Verification of magnetorheological shock absorber models with various piston configurations, *Journal of Intelligent Material Systems and Structures*, **24**, 15, 1846-1864
5. Hong S.R., Gang W., Hu W., Wereley N.M., 2006, Liquid spring shock absorber with controllable magnetorheological damping, *Proceedings of the Institution of Mechanical Engineers. Part D: Journal of Automotive Engineering*, **220**, 1019-1029
6. Jensen E., Oliver M.L., Kruckemeyer W.C., 2001, *Twin-tube magnetorheological damper*, US Patent Application No. 20020139624 A1
7. Lang H., 1977, A study of the characteristics of automotive hydraulic dampers at high stroking frequencies, Ph.D. Thesis, University of Michigan, US
8. Lee L., 1997, Numerical modeling for the hydraulic performance prediction of automotive monotube dampers, *Vehicle System Dynamics*, **28**, 25-39
9. Manring N.D., 2005, *Hydraulic Control Systems*, John Wiley and Sons, New York
10. Mollica M., 1997, Nonlinear dynamic model and simulation of a high pressure monotube shock absorber using the bond graph method, M.Sc. Thesis, MIT, US
11. Oakley R., 2006, *Twin-tube magnetorheological damper*, European Patent Application No. 1908985 A1
12. Poynor J.C., 2001, Innovative designs for magnetorheological dampers, M.Sc. Thesis, Virginia Polytechnic Institute and State University, US
13. Segel L., Lang H., 1981, The mechanics of automotive hydraulic dampers at high stroking frequencies, *Vehicle System Dynamics*, **10**, 2, 82-85

Manuscript received September 23, 2014; accepted for print May 8, 2015

JOURNAL OF THEORETICAL
AND APPLIED MECHANICS
53, 4, pp. 895-910, Warsaw 2015
DOI: 10.15632/jtam-pl.53.4.895

DETERMINATION OF MATERIAL PARAMETERS OF ISOTROPIC AND ANISOTROPIC HYPER-ELASTIC MATERIALS USING BOUNDARY MEASURED DATA

Maedeh Hajhashemkhani, Mohammad R. Hematiyan
Shiraz University, Department of Mechanical Engineering, Shiraz, Iran
e-mail: maedeh.hajhashemkhani@gmail.com; mhemat@shirazu.ac.ir

Identification of mechanical properties of isotropic and anisotropic materials that demonstrate non-linear elastic behavior, such as rubbers and soft tissues of human body, is critical for many industrial and medical purposes. In this paper, a method is presented to obtain the mechanical constants of Mooney-Rivlin and Holzapfel hyper-elastic material models which are employed to describe the behavior of isotropic and anisotropic hyper-elastic materials, respectively. By using boundary measured data from a sample with non-standard geometry, and by using an iterative inverse analysis technique, the material constants are obtained. The method uses the results of different experiments simultaneously to obtain the material parameters more accurately. The effectiveness of the proposed method is demonstrated through three examples. In the two first examples, the simulated measured data are used, while in the third example, the experimental data obtained from a polyvinyl alcohol sample are used.

Keywords: hyper-elstic material, inverse analysis, anisotropic, polyvinyl alcohol

1. Introduction

Many materials such as rubbers, elastomers and tissues of human body experience large deformation under small loads. Further, some materials such as wood, fiber-reinforced composites and some body tissues like arterial walls, show anisotropic behavior in addition to large elastic deformation due to the presence of preferred directions in their structure. The large strains in the response of these materials clarify that their mechanical behavior is nonlinear, and getting back to the reference configuration after load removal demonstrates their elastic response. Because of the wide use of these materials in industry and the crucial role of different tissues in human body, presenting a model with known parameters that can predict the mechanical behavior of these materials is essential. When these materials experience small deformations (less than 2 to 5 percent), their mechanical behavior can be modeled using common linear elastic models (Czabanowski, 2010), but under large deformations, their mechanical response must be represented by nonlinear models such as hyper-elastic material models. Therefore, many efforts have been made to present constitutive laws that model the behavior of these materials properly. Pamidi and Advani (1987) proposed nonlinear constitutive relations for human brain tissue. Fung (1993) showed that the elastic properties of rabbits' mesentery could be simply modeled as an exponential function. Holzapfel and Gasser (2000) considered arterial walls as thin-walled cylinders and presented a constitutive equation for describing their behavior. They obtained the numerical values of the constants of their model using experimental data. A constitutive law for arterial layers with distributed collagen fiber orientation was presented in the work of Gasser *et al.* (2006).

Many researchers used hyper-elastic models to predict material behavior especially for human body tissues. Moulton *et al.* (1995) used a combination of finite element model, nonlinear optimization algorithm, and a set of strains obtained by magnetic resonance imaging (MRI) to determine passive myocardial material properties. Miller and Chinzei (1997) conducted pressure experiments on brain tissue to model the destructions that may happen during brain surgery. They obtained force-displacement diagrams from the experiments. Then, they computed the unknown constants for different hyper-elastic models using the least squares method. Krouskop *et al.* (1998) conducted some pressure experiments on different parts of breast and prostate tissue, such as fat, and obtained Young's modules for each part.

Hartman (2001) conducted some tension and torsion tests on different samples made of rubber to identify their properties based on incompressible Rivlin's hyper-elastic model. Ogden *et al.* (2004) used a non-linear least squares optimization method to obtain the constants of hyper-elastic models for incompressible materials by fitting experimental data to their model. In the work of Hu and Desai (2004), a tissue indentation test was conducted on liver to identify its biomechanical properties.

Balaraman *et al.* (2005) conducted different experiments on 19 samples of muscle tissue and used the experimental data in a finite element analysis. They obtained mechanical properties of the muscle by an inverse method using Taguchi's approach. Mehrabian (2008) estimated the constants of an incompressible hyper-elastic material based on three different energy functions. Some samples made of polyvinyl alcohol were used in pressure experiments. The tests were modeled in the finite element analysis and the unknown constants were computed using the least square method.

Ahn *et al.* (2008) conducted biomechanical experiments on macro and micro liver samples to characterize their mechanical behavior using a nonlinear least squares method and an inverse finite element (FE) method based on a parameter estimation algorithm. In the work of Mesa-Múnera *et al.* (2012), several hyper-elastic models were used to predict and model mechanical behavior of a silicone rubber. They conducted a uniaxial compression test on a phantom with mechanical properties close to brain tissue. They could obtain force-displacement diagrams for compression tests on the phantom.

Rauchs *et al.* (2010) used a depth-sensing spherical indentation technique to determine the parameters of different rubber materials by using an inverse method based on a gradient-based numerical optimization method. Czabanowski (2010) conducted some pressure experiments on machinery elastomers to obtain their material properties. Czabanowski obtained force-displacement diagrams first. Then, by using a function in ABAQUS finite element software, he determined the constants of Mooney-Rivlin model for the materials.

Abyaneh *et al.* (2013) used an inverse method to obtain viscoelastic material properties of porcine cornea by performing tension and indentation tests. They used a sample with possible maximum length for the tension test. Using the results of the tension test, material properties for an isotropic viscoelastic material were obtained using a curve fitting procedure. Due to insufficiency of this model, to match the indentation test results, an anisotropic model with the results of the indentation test was also used in an inverse algorithm to obtain anisotropic parameters. Parameters of the isotropic model were the initial guesses for the inverse algorithm. Baker and Shrot (2013) proposed a new method for inverse identification of material parameters. They used auxiliary quantities to describe material behavior.

In all of the works reviewed above, the sample that was used to obtain the measurement data was cut to a cubic or cylindrical shape to provide standard test specimens. Therefore, these methods cannot be applicable to find the material constants of a hyper-elastic material with a non-standard shape nondestructively. The inverse method presented in this paper uses the measured displacement data from a sufficient number of sampling points on the original hyperelastic body to obtain unknown material constants. If the properties of the material are dependent on size and geometry, the properties, which are obtained by this method, are suitable for that special shape. Unlike previous researches, the method presented in this research uses the results of different experiments simultaneously to obtain the material parameters more accurately. This inverse problem is highly nonlinear and encounters various difficulties. Simultaneous use of measured data from several experiments with different load cases reduces the ill-posedness of the inverse problem. It is observed that using the measured data from several experiments results in a better solution than the case where only the measured data from one experiment is used. The Mooney-Rivlin and Holzapfel models are considered for isotropic and anisotropic materials, respectively. The Tikhonov regularization method is used in the inverse analysis. A method to determine the initial guesses for the unknown constants is also presented. The inverse method needs a sensitivity analysis, which is carried out using the finite element method (FEM).

2. Materials modeling

2.1. Hyper-elastic materials

For hyper-elastic materials, the stress-strain relations are determined using the strain energy density function ψ which is defined in terms of a deformation gradient or strain tensor. The derivative of ψ with respect to a component of strain gives its corresponding stress component (Holzapfel, 2000)

$$S_{ij} = \frac{\partial\psi}{\partial\varepsilon_{ij}} \tag{2.1}$$

where $\mathbf{S}$ is the second Piola-Kirchhoff stress tensor and $\boldsymbol{\varepsilon}$ is the Lagrangian strain tensor defined as follows

$$\varepsilon_{ij} = \frac{1}{2}(C_{ij} - \delta_{ij}) \tag{2.2}$$

In Eq. (2.2), $\mathbf{C}$ is the right Cauchy-Green deformation tensor ($\mathbf{C} = \mathbf{F}^{\mathrm{T}}\mathbf{F}$). $\mathbf{F}$ is the deformation gradient, which can be expressed in terms of the displacement vector $\mathbf{u}$ ($\mathbf{F} = \nabla\mathbf{u} + \mathbf{I}$).

Local shape deformation of a material element is described by $\mathbf{F}$. The strain energy function is usually a function of deformation gradient $\mathbf{F}$. Indeed, the function ψ is expressed in terms of the right Cauchy-Green deformation tensor, i.e., $\psi = \psi(\mathbf{C})$. The following relation holds between the second Piola-Kirchhoff and Cauchy stress tensors (Holzapfel, 2000)

$$\mathbf{S} = J\mathbf{F}^{-1}\boldsymbol{\sigma}\mathbf{F}^{-T} \tag{2.3}$$

where $J = \det\mathbf{F}$. Therefore, according to Eqs. (2.1), (2.2) and (2.3) the Cauchy stress tensor is defined as follows

$$\boldsymbol{\sigma} = 2J^{-1}\mathbf{F}\frac{\partial\psi}{\partial\mathbf{C}}\mathbf{F}^{\mathrm{T}} \tag{2.4}$$

For an isotropic material, ψ is dependent on $\mathbf{C}$ based on its invariants. The invariants of $\mathbf{C}$ are

$$I_1 = \operatorname{tr}\mathbf{C} \qquad I_2 = \frac{1}{2}[(\operatorname{tr}\mathbf{C})^2 - \operatorname{tr}\mathbf{C}^2] \qquad I_3 = \det\mathbf{C} \tag{2.5}$$

For an isotropic material ψ is just dependent on I_1, I_2 and I_3 (Holzapfel and Ogden, 2010) and the Cauchy stress equation is expanded as follows

$$\boldsymbol{\sigma} = 2J^{-1}\Big(\mathbf{F}\frac{\partial\psi}{\partial I_1}\frac{\partial I_1}{\partial\mathbf{C}}\mathbf{F}^{\mathrm{T}} + \mathbf{F}\frac{\partial\psi}{\partial I_2}\frac{\partial I_2}{\partial\mathbf{C}}\mathbf{F}^{\mathrm{T}} + \mathbf{F}\frac{\partial\psi}{\partial I_3}\frac{\partial I_3}{\partial\mathbf{C}}\mathbf{F}^{\mathrm{T}}\Big) \tag{2.6}$$

By obtaining the derivatives of the invariants with respect to $\mathbf{C}$ (Holzapfel, 2000) and knowing that $\mathbf{B} = \mathbf{F}\mathbf{F}^{\mathrm{T}}$ Eq. (2.6) yields to

$$\boldsymbol{\sigma} = 2J^{-1}[\psi_1\mathbf{B} + \psi_2(I_1\mathbf{B} - \mathbf{B}^2) + I_3\psi_3\mathbf{I}] \tag{2.7}$$

where $\psi_i = \partial\psi/\partial I_i$. For an incompressible isotropic material $I_3 = \det\mathbf{F} = 1$ and the Cauchy stress tensor is modified as follows (Holzapfel, 2000)

$$\boldsymbol{\sigma} = -p\mathbf{I} + 2\mathbf{F}\frac{\partial\psi}{\partial\mathbf{C}}\mathbf{F}^{\mathrm{T}} \tag{2.8}$$

where p is a scalar identified as hydrostatic pressure. Therefore, the Cauchy stress tensor for an incompressible material with respect to $\mathbf{B}$ is expressed as follows

$$\boldsymbol{\sigma} = -p\mathbf{I} + 2\psi_1\mathbf{B} + 2\psi_2(I_1\mathbf{B} - \mathbf{B}^2) \tag{2.9}$$

2.2. Isotropic hyper-elastic materials

The polynomial hyper-elastic model is a proper model for rubbers and other soft materials with isotropic behavior. In this research, the Mooney-Rivlin hyper-elastic model, which is obtained from the polynomial model, is used to predict the mechanical behavior of isotropic materials. In this model, density of strain energy for an incompressible material is a function of the first and second invariants of the left Cauchy-Green deformation tensor. The strain energy function for the polynomial model is defined as follows (Rivlin and Saunder, 1951)

$$\psi = \sum_{i,j=0}^{n} A_{ij}(I_1 - 3)^i(I_2 - 3)^j \tag{2.10}$$

where A_{ij} are the constants of the material and $A_{00} = 0$. The Mooney-Rivlin strain energy function is obtained by considering $n = 1$ and $A_{11} = 0$ in equation (2.10), i.e.

$$\psi = A_{10}(I_1 - 3) + A_{01}(I_2 - 3) \tag{2.11}$$

By considering relations (2.9) and (2.11), the Cauchy stress for the Mooney-Rivlin hyper-elastic material is obtained as follows

$$\boldsymbol{\sigma} = -p\mathbf{I} + 2A_{10}\mathbf{B} + 2A_{01}(I_1\mathbf{B} - \mathbf{B}^2) \tag{2.12}$$

2.3. Anisotropic hyper-elastic materials

In the structure of human soft tissues, the presence of collagen fibers (Unnikrishnan, 2012) causes the material to have one or more preferred direction. This preferred direction is presented here by $\mathbf{M}$. In this case, the strain energy density is a function of both $\mathbf{C}$ and $\mathbf{M}$. Two more dependent pseudo invariants are defined for these materials (Holzapfel and Gasser, 2000)

$$I_4 = \mathbf{M}(\mathbf{C}\mathbf{M}) \qquad I_5 = \mathbf{M}(\mathbf{C}^2\mathbf{M}) \tag{2.13}$$

where, for example, $\mathbf{CM}$ represents the action of the second order tensor $\mathbf{C}$ on the vector $\mathbf{M}$.

For an incompressible material reinforced with one family of fibers, ψ is dependent on I_1, I_2, I_4 and I_5. In this case, the Cauchy stress has two additional terms which show the effect of anisotropy. Therefore, the Cauchy stress tensor can be expressed as follows (Holzapfel and Ogden, 2010)

$$\boldsymbol{\sigma} = -p\mathbf{I} + 2\psi_1\mathbf{B} + 2\psi_2(I_1\mathbf{B} - \mathbf{B})^2 + 2\psi_4\mathbf{m}\otimes\mathbf{m} + 2\psi_5[\mathbf{m}\otimes\mathbf{Bm} + \mathbf{Bm}\otimes\mathbf{m}] \tag{2.14}$$

where $\otimes$ denotes the dyadic product of two vectors and $\mathbf{m} = \mathbf{FM}$ is the deformed form of the vector $\mathbf{M}$ in current configuration. For some tissues like arterial walls, two families of fibers with different directions can be detected within the tissue. $\mathbf{M}'$ is considered to be the unit vector in the direction of the second family of fibers. In this case, three more invariants are considered, which are expressed as follows (Holzapfel and Ogden, 2010)

$$I_6 = \mathbf{M}'(\mathbf{C}\mathbf{M}') \qquad I_7 = \mathbf{M}'(\mathbf{C}^2\mathbf{M}') \qquad I_8 = [\mathbf{M}(\mathbf{C}\mathbf{M}')](\mathbf{M}\mathbf{M}') \tag{2.15}$$

In this case, the Cauchy stress is expressed as follows (Holzapfel and Ogden, 2010)

$$\begin{aligned}\boldsymbol{\sigma} = &-p\mathbf{I} + 2\psi_1\mathbf{B} + 2\psi_2(I_1\mathbf{B} - \mathbf{B})^2 + 2\psi_4\mathbf{m}\otimes\mathbf{m} + 2\psi_5[\mathbf{m}\otimes\mathbf{Bm} + \mathbf{Bm}\otimes\mathbf{m}] \\ &+ 2\psi_6\mathbf{m}'\otimes\mathbf{m}' + 2\psi_7[\mathbf{m}'\otimes\mathbf{Bm}' + \mathbf{Bm}'\otimes\mathbf{m}'] + 2\psi_8(\mathbf{M}\otimes\mathbf{M}')(\mathbf{m}\otimes\mathbf{m}' + \mathbf{m}'\otimes\mathbf{m})\end{aligned} \tag{2.16}$$

In this research, the Holzapfel's strain energy function for anisotropic materials is used. This function is described as follows (Holzapfel and Ogden, 2010)

$$\psi = R_{10}(I_1 - 3) + \frac{k_1}{k_2}\{\exp[k_2(I_4^* - 1)^2] - 1\} \tag{2.17}$$

R_{10}, k_1, k_2 and κ are material constants and I_4^* is defined as follows

$$I_4^* = \kappa I_1 + (1 - 3\kappa)I_4 \tag{2.18}$$

In this model, it is assumed that the direction of each family of fibers is dispersed around a mean direction. This dispersion is shown by κ ($0 \leqslant \kappa \leqslant 1/3$) (Holzapfel and Ogden, 2010). By using relations (2.16), (2.17) and (2.18), the Cauchy stress tensor can be obtained.

3. Computation of unknown material parameters of hyper-elastic materials

In this paper, an inverse method is used to obtain the constants of hyper-elastic material models. The inverse analysis is used to convert the measured data to some information about the material or system under study. In the inverse analysis, the outputs of the system may be available from an experiment but loading parameters, material properties, geometry of structure, boundary conditions or a combination of these factors have to be determined (Liu and Han, 2003). In the present study, unknowns are constants of hyperelastic materials. These unknowns are found using the measured displacements at some sampling points on the boundary of the body. The measured displacements are collected from a few load cases (for example, 3 cases). Then by using the inverse analysis in an iterative process, the constants are obtained. A proper initial guess is required for the iterative process.

3.1. Inverse analysis

In this section, the inverse formulation for evaluation of constants of isotropic and anisotropic hyper-elastic material models is presented.

For an incompressible material, the Mooney-Rivlin hyper-elastic model constants are A_{10} and A_{01}. Therefore, the vector of unknowns for the problem is defined as follows

$$\mathbf{x} = \begin{bmatrix} x_1 & x_2 \end{bmatrix}^{\mathrm{T}} \tag{3.1}$$

where $x_1 = A_{10}$ and $x_2 = A_{01}$. For the Holzapfel hyper-elastic model, these constants are R_{10}, k_1, k_2 and κ. The vector of unknowns for this case is defined as follows

$$\mathbf{x} = \begin{bmatrix} x_1 & x_2 & x_3 & x_4 \end{bmatrix}^{\mathrm{T}} = \begin{bmatrix} R_{10} & k_1 & k_2 & \kappa \end{bmatrix}^{\mathrm{T}} \tag{3.2}$$

In order to obtain material constants, a few experiments (load cases) are performed on the material. These experiments must be different with each other to provide suitable data for the inverse analysis. The number of these experiments is 2, 3 or more. In this work, 3 load cases are considered for describing the formulation.

In each experiment, the displacement at some boundary points is measured and restored in vectors $\mathbf{Y}^{(1)}$, $\mathbf{Y}^{(2)}$ and $\mathbf{Y}^{(3)}$. If they are N_1, N_2 and N_3 measured data in load cases 1, 2 and 3, respectively, $\mathbf{Y}^{(i)}$ $(i = 1, 2, 3)$ are defined as follows

$$\mathbf{Y}^{(i)} = \begin{bmatrix} Y_1^{(i)} & Y_2^{(i)} & \cdots & Y_{N_i}^{(i)} \end{bmatrix} \qquad i = 1, 2, 3 \tag{3.3}$$

By solving the problem numerically using the estimated constants, the displacement vector at sampling points is obtained and stored in $\mathbf{D}^{(1)}$, $\mathbf{D}^{(2)}$ and $\mathbf{D}^{(3)}$ which are defined as follows

$$\mathbf{D}^{(i)} = \begin{bmatrix} D_1^{(i)} & D_2^{(i)} & \cdots & D_{N_i}^{(i)} \end{bmatrix} \qquad i = 1, 2, 3 \tag{3.4}$$

In order to find the constants of the material, the Tikhonov regularization method is used. In this method, the objective function Π is defined as follows

$$\Pi = (\mathbf{Y} - \mathbf{D})^{\mathrm{T}}(\mathbf{Y} - \mathbf{D}) + \alpha \mathbf{X}^{\mathrm{T}}\mathbf{X} \tag{3.5}$$

where the vectors $\mathbf{Y}$ and $\mathbf{D}$ are defined as follows

$$\mathbf{Y} = \begin{bmatrix} \mathbf{Y}^{(1)} & \mathbf{Y}^{(2)} & \mathbf{Y}^{(3)} \end{bmatrix}^{\mathrm{T}} \qquad \mathbf{D} = \begin{bmatrix} \mathbf{D}^{(1)} & \mathbf{D}^{(2)} & \mathbf{D}^{(3)} \end{bmatrix}^{\mathrm{T}} \tag{3.6}$$

In equation (3.5), α is the regularization parameter. The objective function Π should be minimized to find the unknown vector $\mathbf{X}$. By taking the derivative of Π with respect to $\mathbf{X}$ and equating to zero, the following equation is obtained

$$\frac{\partial \Pi}{\partial \mathbf{X}} = -2\mathbf{S}^{\mathrm{T}}(\mathbf{Y} - \mathbf{D}) + 2\alpha\mathbf{X} = 0 \tag{3.7}$$

In Eq. (3.7), $\mathbf{S}$ is the sensitivity matrix and is defined as follows

$$\mathbf{S}^{(L)} = \begin{bmatrix} S_{11}^{(L)} & S_{12}^{(L)} & \cdots & S_{1q}^{(L)} \\ S_{21}^{(L)} & S_{22}^{(L)} & \cdots & S_{2q}^{(L)} \\ \vdots & \vdots & \ddots & \vdots \\ S_{N_L 1}^{(L)} & S_{N_L 2}^{(L)} & \cdots & S_{N_L q}^{(L)} \end{bmatrix} \tag{3.8}$$

where L is the number of the load case and q is the number of unknowns or the number of components of $\mathbf{X}$.

The components of the sensitivity matrix are defined as follows

$$S_{ij}^{(L)} = \frac{\partial D_i^{(L)}}{\partial X_j} \tag{3.9}$$

In order to compute the constants in an iterative process and calculate the sensitivity matrix, a program is written in python for the finite element software ABAQUS. This program uses the finite difference method to calculate the sensitivity matrix. For this purpose, each material constant is changed by a very small value and displacements at sampling points are obtained. The differences between these displacements are used to compute the sensitivity coefficients. The sensitivity coefficient $S_{ij}^{(L)}$ is computed through the following finite difference equation

$$S_{ij}^{(L)} = \frac{D_i^{(L)}(X_1, \ldots, X_j + \mu X_j, \ldots, X_q) - D_i^{(L)}(X_1, \ldots, X_q)}{\mu X_j} \tag{3.10}$$

where μ is a small value such as 0.001.

For example, if there are four unknown material constants, the sensitivity of the displacement at sampling point 3 with respect to material constant 2 is computed as follows

$$S_{32}^{(2)} = \frac{D_3^{(2)}(X_1, X_2 + \mu X_2, X_3, X_4) - D_3^{(2)}(X_1, X_2, X_3, X_4)}{\mu X_2} \tag{3.11}$$

It is possible to obtain the unknown vector $\mathbf{X}$ through equation (3.7). Let the vector of unknown constants in the current step of the iterative process is represented by $\mathbf{X}_c$ and the corresponding displacement vectors for load cases 1, 2, and 3 are represented by $\mathbf{D}_c^{(1)}$, $\mathbf{D}_c^{(2)}$ and $\mathbf{D}_c^{(3)}$, respectively. The total displacement vector $\mathbf{D}_c$ is defined as follows

$$\mathbf{D}_c = \Big[\mathbf{D}_c^{(1)} \quad \mathbf{D}_c^{(2)} \quad \mathbf{D}_c^{(3)}\Big]^{\mathrm{T}} \tag{3.12}$$

The total displacement vector in the new step, i.e. $\mathbf{D}$, can be expressed as follows

$$\mathbf{D} = \mathbf{D}_c + \mathbf{S}(\mathbf{X} - \mathbf{X}_c) \tag{3.13}$$

where $\mathbf{X}$ is the vector of unknown constants in the new step. By using Eqs. (3.13) and (3.7) the following equation is obtained

$$\mathbf{X} = [\mathbf{S}^{\mathrm{T}}\mathbf{S} + \alpha\mathbf{I}]^{-1}[\mathbf{S}^{\mathrm{T}}(\mathbf{Y} - \mathbf{D}_c) + \mathbf{S}^{\mathrm{T}}\mathbf{S}\mathbf{X}_c] \tag{3.14}$$

Equation (3.14) is used iteratively through the following equation to obtain the constants

$$\mathbf{X}^{k+1} = [(\mathbf{S}^k)^{\mathrm{T}}\mathbf{S}^k + \alpha^k\mathbf{I}]^{-1}[(\mathbf{S}^k)^{\mathrm{T}}(\mathbf{Y} - \mathbf{D}^k) + (\mathbf{S}^k)^{\mathrm{T}}\mathbf{S}^k\mathbf{X}^k] \tag{3.15}$$

k and $k+1$ are the numbers of iterations, and the convergence rule is defined as follows

$$\|\mathbf{X}^{k+1} - \mathbf{X}^k\| \leqslant e \tag{3.16}$$

where e is the specified tolerance. In the cases where a large number of sampling points and/or many load cases are considered, selecting a small value or even zero for α results in stable solutions.

Inequality constraints on material constants (for example $0 \leqslant \kappa \leqslant 1/3$) are not considered in the inverse formulation of this study. In other words, the inverse formulation of this research uses an unconstrained optimization formulation. However, the obtained results must satisfy all the constraints. Otherwise, the problem has to be solved with different initial guesses.

3.2. Initial guesses

In order to start the iterative process and obtain the material constants, proper initial guesses are required. Selecting appropriate initial guesses reduces the number of iterations and increases the convergence rate. To find proper initial guesses for the unknown parameters of the hyper-elastic material, we try to find unknown Young's modulus E and Poisson's ratio ν for an isotropic linear elastic material, which can approximately reconstruct the measured data for the original hyper-elastic material. For this purpose, the measured data Y are used in a simple inverse analysis to find appropriate values for the two parameters of the pseudo linear elastic material. Then, the calculated parameters are used to compute initial guesses for the original material parameters. A similar approach has been used by Hematiyan *et al.* (2012) for providing initial guesses for identification of material constants of linear elastic anisotropic materials.

The pseudo material is assumed incompressible with $\nu = 0.5$. The displacement vector obtained from the experiments on the hyper-elastic material, i.e. $\mathbf{Y}$, is assumed to be the displacement vector for the pseudo material with unknown E. The unknown parameter E can be simply found as follows.

The displacement vector at the sampling points of the pseudo material can be computed as

$$\mathbf{D} = \frac{\overline{\mathbf{D}}}{E} \tag{3.17}$$

where $\overline{\mathbf{D}}$ is the displacement vector at the same sampling points for a linear elastic material with $E = 1\,\mathrm{Pa}$ and $\nu = 0.5$. The vector $\overline{\mathbf{D}}$ can be computed using a direct analysis by the FEM. To find a suitable value of E, we minimize the difference between $\mathbf{D}$ and $\mathbf{Y}$. This can be carried out by minimizing the following expression

$$F = \Big(\mathbf{Y} - \frac{\overline{\mathbf{D}}}{E}\Big)^{\mathrm{T}}\Big(\mathbf{Y} - \frac{\overline{\mathbf{D}}}{E}\Big) \tag{3.18}$$

which gives

$$E = \frac{\overline{\mathbf{D}}^{\mathrm{T}}\overline{\mathbf{D}}}{\overline{\mathbf{D}}^{\mathrm{T}}\mathbf{Y}} \tag{3.19}$$

Now, we have found elastic constants of a pseudo linear elastic isotropic material for the inverse problem. After obtaining the Young modulus from equation (3.19), by selecting different values for ε, a set of stress-strain data is provided using the relation $\sigma = E\varepsilon$. This set of data is used to find initial guesses for the unknown constants of the original hyper-elastic material.

Consider a case of uniaxial loading with the axial stress σ which causes the axial strain ε in direction 1 for the pseudo material. The deformation of the material can be expressed as follows

$$x_1 = \lambda_1 X_1 \qquad x_2 = \lambda_2 X_2 \qquad x_3 = \lambda_3 X_3 \tag{3.20}$$

where (X_1, X_2, X_3) are rectangular Cartesian coordinates that identify material particles in some unstressed reference configuration, (x_1, x_2, x_3) are the corresponding coordinates after deformation with respect to the same axes, and the coefficients $(\lambda_1, \lambda_2, \lambda_3)$ are principal stretches of the deformation. Therefore, the deformation gradient tensor $F_{ij} = \partial x_i/\partial X_j$ is expressed as follows

$$\mathbf{F} = \begin{bmatrix} \lambda_1 & 0 & 0 \\ 0 & \lambda_2 & 0 \\ 0 & 0 & \lambda_3 \end{bmatrix} \tag{3.21}$$

Substituting $B_{ij} = F_{ik}F_{jk}$ in equation (2.12), the following equation is obtained

$$\sigma = 2\Big(\lambda_1^2 - \frac{1}{\lambda_1}\Big)\Big(A_{10} + \frac{1}{\lambda_1}A_{01}\Big) \tag{3.22}$$

On the other hand, for the pseudo material we have

$$\varepsilon = \frac{\partial(x_1 - X_1)}{\partial X_1} = 1 - \lambda_1 \tag{3.23}$$

Substituting $\lambda_1 = 1 + \varepsilon$ into Eq. (3.22) results in

$$\sigma = 2\Big[(1+\varepsilon)^2 - \frac{1}{1+\varepsilon}\Big]\Big(A_{10} + \frac{1}{1+\varepsilon}A_{01}\Big) \tag{3.24}$$

Equation (3.24) can be written in the following form

$$Y = A_{10}X + A_{01} \tag{3.25}$$

where Y and X are

$$Y = \frac{\sigma(1+\varepsilon)}{2\Big[(1+\varepsilon)^2 - \frac{1}{1+\varepsilon}\Big]} \qquad\qquad X = 1+\varepsilon \tag{3.26}$$

By using the previously generated set of stress-strain data, a set of X-Y data is computed using Eq. (3.26). Then a line is fitted through the X-Y data by a simple linear regression. Considering Eq. (3.25) and by using the coefficients of the fitted line, the values of A_{10} and A_{01} are obtained. These values are considered as initial guesses for the inverse analysis.

A method to obtain the initial guesses for constants of anisotropic hyper-elastic materials is also presented here. These constants are R_{10}, k_1, k_2, and κ, see Eqs (2.17) and (2.18). Since $0 \leqslant \kappa \leqslant 1/3$, we simply select the value of 0.25 as an initial guess for κ. To simplify the process of obtaining the initial guesses we also set $k_1 = k_2$. Therefore, only the initial guesses for R_{10} and k_1 should be determined. Substituting Eqs. (2.17) and (2.18) into Eq. (2.16), the Cauchy stress is expressed as follows

$$\boldsymbol{\sigma} = 2R_{10}\mathbf{B} + k_1\Big(\frac{I_1}{4} + \frac{I_4}{4} - 1\Big)\exp\Big[k_1\Big(\frac{I_1}{4} + \frac{I_4}{4} - 1\Big)^2\Big](\mathbf{B} + \mathbf{m}\otimes\mathbf{m}) \tag{3.27}$$

As discussed for the isotropic case, by using Eq. (3.19) Young modulus is obtained for the pseudo incompressible linear elastic material. Using the calculated Young's modulus and Hooke's law, the components of the stress tensor $\boldsymbol{\sigma}$ and the strain tensor $\boldsymbol{\varepsilon}$ at two different points are computed. The strain tensor is used in Eq. (2.2) to obtain the right Cauchy-Green deformation tensor $\mathbf{C}$ from which the deformation gradient tensor $\mathbf{F}$ and the tensor $\mathbf{B}$ can be obtained. Having $\mathbf{F}$ and $\mathbf{M}$, the vector $\mathbf{m} = \mathbf{FM}$ is also known and the unknowns in Eq. (3.27), i.e. R_{10} and k_1, can be found. These computed values are considered as initial guesses for the corresponding parameters.

4. Numerical examples

In this Section, three examples are presented to show the efficiency of the presented method. In the two first examples, numerically simulated measured data are used; however, in the third example, the experimental data obtained from a polyvinyl alcohol sample are used for the identification of material parameters.

4.1. Example 1. Isotropic hyper-elastic material

In this example, a rectangular plate with a non-circular hole made of an isotropic hyper-elastic material is considered. As shown in Fig. 1, the body is subjected to three load cases. The loading location and directions vary in each case to obtain more useful measurement data. The measurement data were numerically simulated. For this purpose, three direct problems corresponding to the three load cases were solved by the exact material constants and displacement at sampling points where obtained. Then, some errors with a normal distribution were added to the displacement data to account for practical inaccuracies.

The exact material constants of the Mooney-Rivlin hyper-elastic model for the material are assumed 80 Pa and 20 Pa for A_{10} and A_{01}, respectively. The initial guesses for the material constants obtained from the method presented in Section 3.2, are $A_{10} = 90.34$ Pa and $A_{01} = 3.497$ Pa. These initial guesses are used in the developed program, and by using equation (3.15) the unknowns are updated in each step until they satisfy convergence rule.

At first, the problem was solved without any measurement error. Table 1 shows the number of iterations and obtained values for the constants when the results of the load cases where used separately (1, 2 or 3) or together (1+2 or 1+2+3) for the inverse analysis. The tolerance

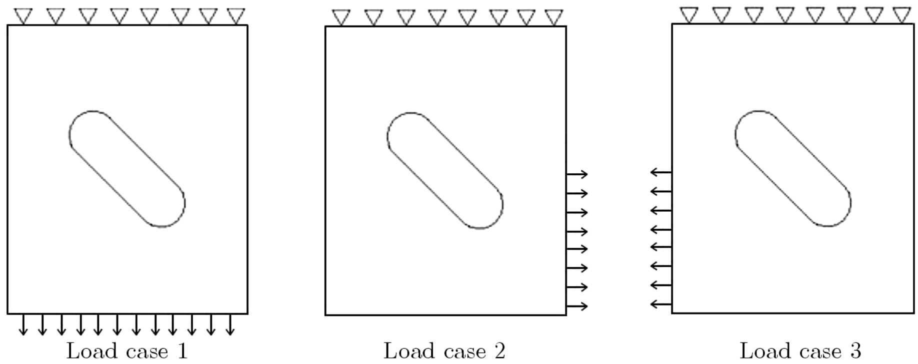

Fig. 1. Load cases applied to the material

for the convergence rule was assumed 0.01. Then the problem was solved by applying 1 and 5 percent error in the measurement data. These errors are applied in the exact solution of the problem using the normal distribution function. The results of these cases are shown in Table 1 as well. The convergence process for the case with 5% measurement error is shown in Fig. 2. From the results of Table 1, it is clear that when there is no error in the measurements, the solution for all load cases converge easily to the material constants and the number of iterations is almost the same whether the load cases are solved together or separately. Further, when the error percentage in measurements increases, the number of iterations and errors in the obtained results increase too. In addition, the number of iterations is less for the cases that the problem is solved by using 2 or 3 load cases. Moreover, it is seen that the obtained results are more accurate when more than one load case is considered in the inverse analysis.

Table 1. Results for material constants with different values of measurement errors, Example 1

Load case		1	2	3	1+2	1+2+3
without measurement error	No. of iterations	6	6	6	5	5
	Constants [Pa] (Error [%])	$A_{10}=80$ (0) $A_{01}=20$ (0)	$A_{10}=80$ (0) $A_{01}=20$ (0)	$A_{10}=80$ (0) $A_{01}=20$ (0)	$A_{10}=80$ (0) $A_{01}=20$ (0)	$A_{10}=80$ (0) $A_{01}=20$ (0)
1% measurement error	No. of iterations	8	12	8	6	7
	Constants [Pa] (Error [%])	$A_{10}=77.17$ (3.5) $A_{01}=23.18$ (15.9)	$A_{10}=80.36$ (0.4) $A_{01}=19.52$ (2.4)	$A_{10}=77.66$ (2.9) $A_{01}=22.15$ (10.7)	$A_{10}=81.15$ (1.4) $A_{01}=18.74$ (6.3)	$A_{10}=80.81$ (1) $A_{01}=19.04$ (4.8)
5% measurement error	No. of iterations	10	11	17	4	5
	Constants [Pa] (Error [%])	$A_{10}=70.058$ (12.4) $A_{01}=31.09$ (55.4)	$A_{10}=72.97$ (8.7) $A_{01}=25.93$ (29.6)	$A_{10}=75.66$ (5.4) $A_{01}=25.18$ (25.9)	$A_{10}=86.43$ (8) $A_{01}=12.60$ (36.9)	$A_{10}=80.53$ (0.6) $A_{01}=19.39$ (3)

4.2. Example 2. Anisotropic hyper-elastic material

In this example, the same geometry of the previous example but with an anisotropic hyper--elastic material is considered. The exact material constants of the Holzapfel hyper-elastic model for this material are assumed 7.64 Pa, 996.6, 524.6 and 0.226 for R_{10}, k_1, k_2 and κ, respectively. The direction of the fibers in a hyper-elastic material that determines the $\mathbf{M}$ and $\mathbf{M}'$ vectors can be obtained from two-dimensional images of soft biological tissues (Schriefl *et al.*, 2012). In this

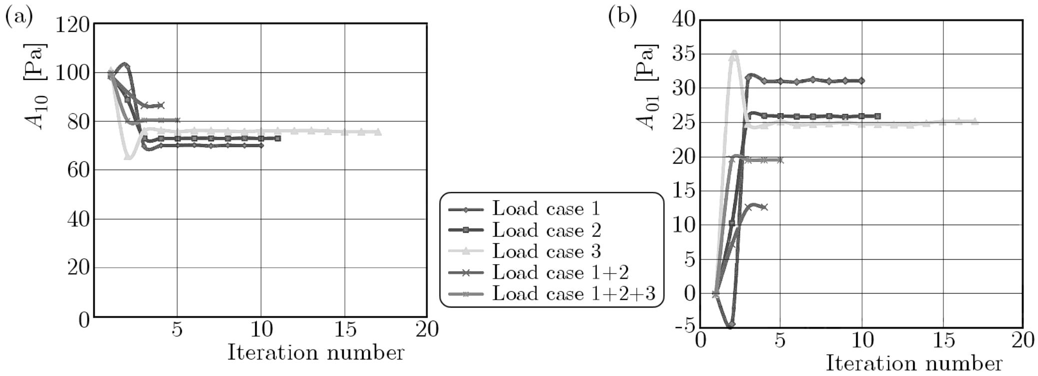

Fig. 2. Convergence of (a) A_{10} and (b) A_{01} for different load cases with 5% error in measurements

example, these vectors are assumed to be known ($\mathbf{M} = 0.766\mathbf{e}_1 - 0.643\mathbf{e}_2$, $\mathbf{M}' = 0.5\mathbf{e}_1 - 0.866\mathbf{e}_2$). The initial guesses for the material constant, which are obtained from the method presented in Section 3.2, are $R_{10} = 10.65$ Pa, $k_1 = k_2 = 144.2$ and $\kappa = 0.25$. At first, the problem was solved without any measurement error. Table 2 shows the number of iterations and obtained constants when the results of different load cases were used separately or together. The tolerance for the convergence rule was assumed 0.01. Then, the problem was solved by considering 1 and 5 percent error in the measurement data. The results of these cases are shown in Table 2. The convergence process of constants for the case with 1% error in measurements is shown in Fig. 3. From the results given in Table 2, it is seen that the inverse solution diverges for load cases 2 and 3 even without any measurement error. Further, it is seen that when an error exists in measurements, the solution cannot be obtained by only one load case. It is also observed that the number of iterations for the solution with 3 load cases is smaller than the solution with 2 load cases.

Table 2. Results for material constants with different values of measurement errors, Example 2

Load case		1	2	3	1+2	1+2+3
without measurement error	No. of iterat.	7	Diverged	Diverged	7	8
	Constants (Error [%])	$R_{10} = 7.640$ Pa (0) $k_1 = 996.6$ (0) $k_2 = 524.6$ (0) $\kappa = 0.226$ (0)			$R_{10} = 7.640$ Pa (0) $k_1 = 996.6$ (0) $k_2 = 524.6$ (0) $\kappa = 0.226$ (0)	$R_{10} = 7.640$ Pa (0) $k_1 = 996.6$ (0) $k_2 = 524.6$ (0) $\kappa = 0.226$ (0)
1% measurement error	No. of iterat.	Diverged	Diverged	Diverged	18	7
	Constants (Error [%])				$R_{10} = 7.645$ Pa (0.06) $k_1 = 1015$ (1.8) $k_2 = 528.8$ (0.8) $\kappa = 0.227$ (0.4)	$R_{10} = 7.645$ Pa (0.06) $k_1 = 1020$ (2.3) $k_2 = 527.3$ (0.5) $\kappa = 0.227$ (0.4)
5% measurement error	No. of iterat.	Diverged	Diverged	Diverged	37	15
	Constants (Error [%])				$R_{10} = 7.607$ Pa (0.4) $k_1 = 1079$ (8.2) $k_2 = 509.8$ (2.8) $\kappa = 0.228$ (0.8)	$R_{10} = 7.650$ Pa (0.1) $k_1 = 926.0$ (7) $k_2 = 572.8$ (9.1) $\kappa = 0.225$ (0.4)

4.3. Example 3. A rectangular plate with a hole made of polyvinyl alcohol

In order to verify the proposed method for obtaining material constants of hyper-elastic materials, a sample was made of polyvinyl alcohol which exhibits hyperelastic mechanical behavior. Polyvinyl alcohol is usually used to simulate soft tissues of human body (Hebden *et al.*,

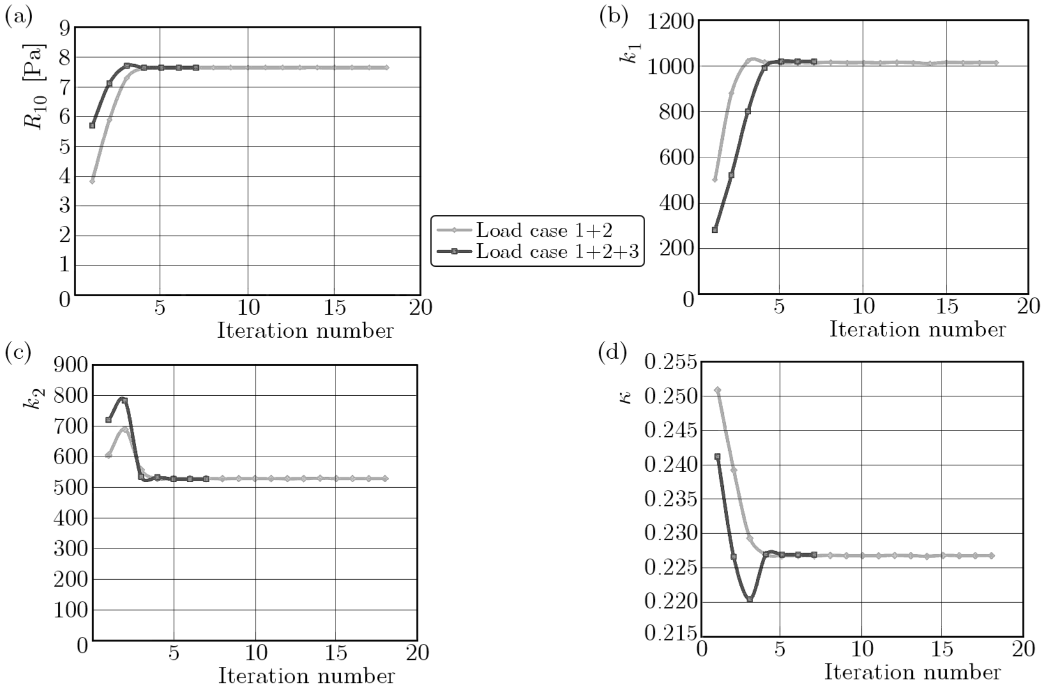

Fig. 3. Convergence of (a) R_{10}, (b) k_1, (c) k_2 and (d) κ for different load cases with 1% error in measurements

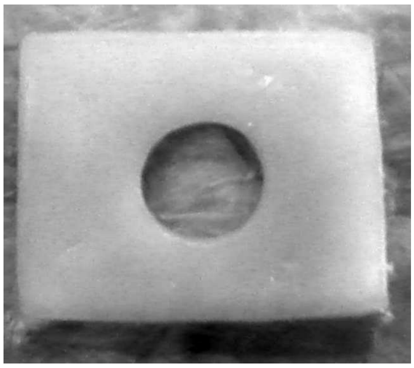

Fig. 4. The polyvinyl alcohol sample used in the experiments

2006). The sample used in the experiments (Fig. 4) is a rectangular plate with dimensions of 80.04 mm×10.02 containing a 33.28 mm diameter hole.

Two load cases are considered for the polyvinyl alcohol sample. In the first case, the sample is placed horizontally on the desk and by using a force meter, a load is applied to one end while the other end is fixed. This load case is shown in Fig. 5. In this case, a load of 1.2 N is applied to the sample.

In the second case, the sample is hanged by its weight and by using a hook, a load is applied to the sample. This case is shown in Fig. 6. A load of 1.5 N is applied in this case. It should be mentioned that, in this case, there exists a body force in the same direction of loading too. Therefore, the deflection of the member in the second case is much more than the deflection in the first load case.

For measuring the displacement at the sampling points, these points were marked before the test. By using the measured displacements, the material constants are obtained for a simple cylindrical sample and for the rectangular sample with a hole. The finite element model (con-

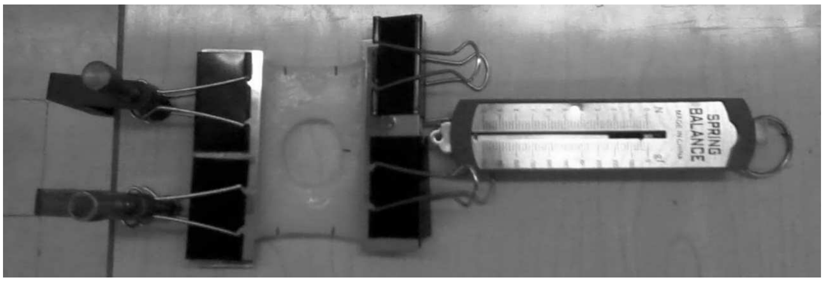

Fig. 5. First load case for the rectangular sample

Fig. 6. Second load case for the rectangular sample

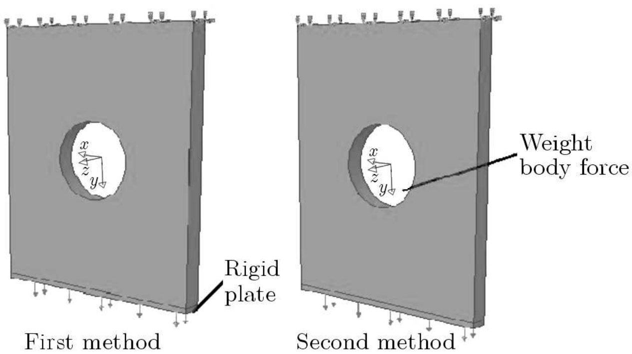

Fig. 7. Load application in FEA for the two cases

structed in ABAQUS) and displacement for the two load cases are shown in Figs. 7 and 8. As it is shown in Fig. 7, the load is not directly applied to the material. A rigid plate is used in the FEA model for load application in order to simulate the experiment more accurately.

The material constants obtained from loading the cylindrical sample are presented in Table 3. The material constants obtained for the rectangular sample are presented in Table 4, where the results of the first and second cases are used separately and together. From Table 4 it is seen that when each test is used separately to obtain the material constants, the number of iterations is larger and the constants deviate more from those obtained for the cylindrical sample in Table 3. Further, when two tests are used together to obtain the constants, the deviation from constants of Table 3 and number of iterations are smaller.

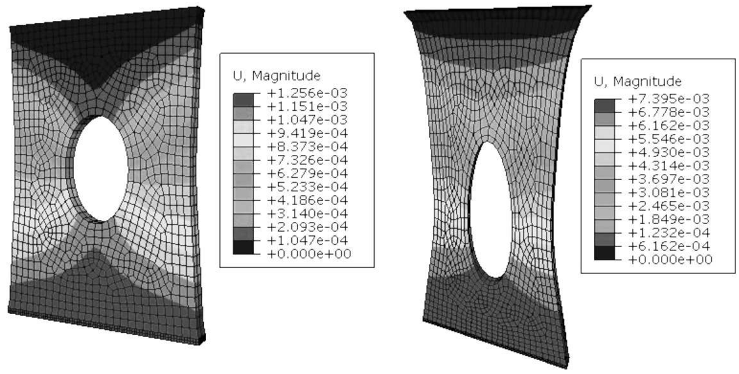

First method Second method

Fig. 8. Displacement contours in the sample for two load cases

Table 3. Material constants obtained for the cylindrical sample

C_{10} [Pa]	C_{01} [Pa]	Number of iterations
4.964	0.541	19

Table 4. Material constants obtained for the rectangular sample with a hole

Test	C_{10} [Pa]	C_{01} [Pa]	Number of iterations
1	6.231	0.756	28
2	5.843	0.641	43
1+2	5.006	0.524	13

5. Conclusions

A method to obtain the constants of isotropic and anisotropic incompressible hyper-elastic materials is presented. In the proposed method, by using the measured displacements at some sampling points on the boundary of a member with a non-standard shape, the unknown material constants of the material are computed. The measured data are obtained from more than one test with different load cases. It is shown that the method is more efficient when the results of two or three load cases are simultaneously used to solve the problem.

From the results of the numerical examples, it is concluded that when the measurement error is zero for isotropic materials, the solution process corresponding to all load cases easily converge to the exact solution and the number of iterations is almost the same whether the load cases are solved together or separately. However, for anisotropic hyper-elastic materials, even in the cases without any measurement error, the solution corresponding to some load cases may diverge. Since the number of constants to be determined in the anisotropic case is more than the isotropic case, more load cases are needed to find the unknown constants of hyper-elastic anisotropic materials.

For both isotropic and anisotropic hyper-elastic materials, when the measurement error increases, the number of iterations and the error in the obtained results increase too. Further, it can be seen that usually the number of iterations is smaller for the cases that the problem is solved by using the measured data from 2 or 3 load cases and the results obtained are more accurate.

In this research, the preferred direction vectors are considered to be known. However, if one considers these parameters as unknowns, the number of the unknowns of the inverse problem increases. This will complicate the problem more and more, and the need for conducting more experiments increases as well.

References

1. Abyaneh M.H., Wildman R.D., Ashcroft I.A., Ruiz P.D., 2013, A hybrid approach to determining cornea mechanical properties in-vivo using a combination of nano-indentation and inverse finite element analysis, *Journal of the Mechanical Behavior of Biomedical Materials*, **27**, 239-248
2. Ahn B., Kim Y., Kim J., 2008, Biomechanical characterization with inverse FE model parameter estimation: Macro and Micro applications, International Conference on Control, *Automation and Systems*, 1769-1772
3. Baker M., Shrot A., 2013, Inverse parameter identification with finite element simulation using knowledge-based descriptors, *Computational Materials Science*, **69**, 128-136
4. Balaraman K., Mukherjee S., Chawla A., Malhotra R., 2005, Inverse finite element characterization of soft tissue using impact experiments and Taguchi method, *SAE Internationals*, 2005-01-4044
5. Czabanowski R., 2010, Experimental identification of hyperelastic material parameters for calculations by the finite element method, *Journal of KONES*, **17**, 1, 87-92
6. Fung Y.C., 1993, *Biomechanics: Mechanical Properties of Living Tissues*, Springer, New York
7. Gasser T.C., Ogden R.W., Holzapfel G.A., 2006, Hyperelastic modeling of arterial layers with distributed collagen fiber orientations, *Journal of Royal Society Interface*, **3**, 6, 15-35
8. Hartman S., 2001, Numerical studies on the identification of the material parameters of Rivlin's hyper-elasticity using tension-torsion tests, *Acta Mechanica*, **148**, 129-155
9. Hebden J.C., Price B.D., Gibson A.P., Royle G., 2006, A soft deformable tissue equivalent phantom for diffuse optical tomography, *Physics in Medicine and Biology*, **51**, 21, 5581-5590
10. Hematiyan M.R., Khosravifard A., Siah Y.C., Tan C.L., 2012, Identification of material parameters of two-dimensional anisotropic bodies using an inverse multi loading boundary element technique, *Computer Modeling in Engineering and Science*, **87**, 1, 55-76
11. Holzapfel G.A., Gasser T.C., 2000, A new constitutive framework for arterial wall mechanics and a comparative study of material models, *Journal of Elasticity*, **61**, 1-48
12. Holzapfel G.A., 2000, *Nonlinear Solid Mechanics*, Technical University Graz, Austria
13. Holzapfel G.A., Ogden R.W., 2010, Constitutive modeling of arteries, *Journal of Royal Society*, **466**, 2118, 1551-1597
14. Hu T., Desai J.P., 2004, *Characterization of Soft-Tissue Material Properties: Large Deformation Analysis*, Drexel University, Philadelphia
15. Krouskop T.A., Wheeler T.M., Kallel F., Garra B.S. Hall T., 1998, Elastic moduli of breast and prostate tissues under compression, *Ultrasonic Imaging*, **20**, 260-274
16. Liu G.R., Han X., 2003, *Computational Inverse Techniques in Nondestructive Evaluation*, CRC Press, Boca Raton, London, New York, Washington, D.C.
17. Miller K., Chinzei K., 1997, Constitutive modeling of brain tissue: experiment and theory, *Journal of Biomechanics*, **30**, 1115-1121
18. Mehrabian H., 2008, Soft tissue hyper-elastic parameter reconstruction for breast cancer assessment, Mastered Engineering Science Thesis, University of Toronto
19. Mesa-Múnera E., Ramírez-Salazar J.F., Boulanger P., Branch J.W., 2012, Inverse-FEM characterization of a brain tissue phantom to simulate compression and indentation, *Ingeniería y Cienc*, **8**, 11-36
20. Moulton M.J., Creswell L.L., Actis R.L., Myers K.W., Vannier M.W., Szabo B.A., Pasque M.K., 1995, An inverse approach to determining myocardial material properties, *Journal of Biomechanics*, **28**, 8, 935-948

21. Ogden R.W., Saccomandi G., Sgura I., 2004, Fitting hyper-elastic models to experimental data, *Computational Mechanics*, **34**, 6, 484-502

22. Pamidi M.R., Advani S.H., 1978, Nonlinear constitutive relations for human brain tissue, *Journal of Biomechanical Engineering*, **100**, 1, 44-48

23. Rauchs G., Bardon J., Georges D., 2010, Identification of the material parameters of a viscous hyper-elastic constitutive law from spherical indentation tests of rubber and validation by tensile tests, *Mechanic of Materials*, **42**, 961-973

24. Rivlin R.S., Saunder D.W., 1951, Large elastic deformations of isotropic materials VII. Experiments on the deformation of rubber, *Journal of Royal Society*, **243**, 865, 251-288

25. Schriefl A.J., Reinisch A.J., Sankaran S., Pierce D.M., Holzapfel G.A., 2012, Quantitative assessment of collagen fibre orientations from two-dimensional images of soft biological tissues, *Journal of Royal Society*, **9**, 76, 3081-3093

26. Unnikrishnan V.U., Unnikrishnan G.U., Reddy J.N., 2012, Biomechanics of breast tumor: effect of collagen and tissue density, *International Journal of Mechanics and Materials in Design*, **8**, 3, 257-267

Manuscript received August 25, 2014; accepted for print May 8, 2015

**JOURNAL OF THEORETICAL
AND APPLIED MECHANICS**
53, 4, pp. 911-923, Warsaw 2015
DOI: 10.15632/jtam-pl.53.4.911

PAYLOAD MAXIMIZATION FOR MOBILE FLEXIBLE MANIPULATORS IN ENVIRONMENT WITH AN OBSTACLE

Hamidreza Heidari
College of Mechanical Engineering, Malayer University, Malayer, Iran
e-mail: hr.heidari@malayeru.ac.ir

Mohammad Haghpanahi, Moharam Habibnejad Korayem
College of Mechanical Engineering, Iran University of Science and Technology, Tehran, Iran

A mobile flexible manipulator is developed in order to achieve high performance requirements such as high-speed operation, increased high payload to mass ratio, less weight, and safer operation due to reduced inertia. Hence, this paper presents a method for finding the Maximum Allowable Dynamic Load (MADL) of geometrically nonlinear flexible link mobile manipulators. The full dynamic model of a wheeled mobile base and the mounted flexible manipulator is considered with respect to dynamics of non-holonomic constraint in environment including an obstacle. In dynamical analysis, an efficient model is employed to describe the treatment of a flexible structure in which both the geometric elastic nonlinearity and the foreshortening effects are considered. Then, a path planning algorithm is developed to find the maximum payload that the optimal strategy is based on the indirect solution to the open-loop optimal control problem. In order to verify the effectiveness of the presented algorithm, several simulation studies are carried out for finding the optimal path between two points in the presence of obstacles. The results clearly show the effect of flexibility and the proposed approach on mobile flexible manipulators.

Keywords: flexible link, nonholonomic mobile manipulator, optimal control, obstacle, path planning

1. Introduction

Mobile manipulators that are required to have a long reach, fast motion and reduced weight typically also possess significant structural flexibility. For example, mobile flexible manipulators have important application in space stations, manufacturing automation, nuclear contaminated environments, and many other areas. A common task for mobile robots is handling heavy loads from one place to another, particularly for wheeled mobile flexible manipulators when operating in high speeds with long arms. For such systems, to make an effective use of robotic systems, it is important to consider the path planning of the system for finding full-load motion in point--to-point maneuvers since it increases the productivity and economic usage of robotic systems. However, kinematic and dynamic analysis of such a nonholonomic wheeled mobile robot (WMR) is challenging due to complex wheel/manipulator interactions, flexibility and kinematic constraints. An efficient model should be employed to describe the treatment of a flexible structure in which both the geometric elastic nonlinearity and the foreshortening effects are considered.

In this investigation, the optimal strategy is based on the indirect solution to the open-loop optimal control problem. In the open loop optimal control, in spite of the closed-loop ones, many difficulties like process nonlinearities and all types of constraints can be explicitly considered because of the off-line computation of optimal trajectories. On the other hand, the indirect solution method appears to be a well suited approach for this kind of problems, which is based on Pontryagin's minimum principle. Combining this approach with an iterative algorithm, the optimal paths and maximum load for WMM in the presence of obstacles can be achieved.

Many researchers have studied the problems of mobile manipulators for the last few years. The dynamic model for links in most of these researches is often based on rigid or small deflection theory, but for applications like light-weight links, high-precision elements or high speed maneuver, it is necessary to capture the deflection caused by nonlinear terms. Seraji (1998) reported a simple on-line approach for motion control of mobile manipulators using the augmented Jacobian matrix. Yamamoto and Yun (1994) focused their research on the modeling and compensation of the dynamic interaction between the manipulator and the mobile platform of a mobile manipulator, and developed a coordination algorithm based on the concept of a preferred operating region. Korayem *et al.* (2012) and Xi and Fenton (1991) designed an algorithm for motion planning of flexible manipulators in quasi-static operations. A concise motion expression for flexible manipulators was developed to reflect the contributions of joint motions and link deflections to the motion of the end effector by three respective Jacobians. It was found that the algorithm was efficient and accurate for motion planning of flexible link manipulators. Damaren and Sharf (1995) presented and classified different types of inertial and geometric nonlinearities in the dynamical equation for flexible multibody systems. They observed that for sufficiently fast maneuvers of the flexible-link manipulators, the ruthlessly linearized approximation completely inadequate.

Several papers tried to give an answer to the path planning problem and calculate the MADL for rigid and flexible manipulators. For instance, Wang *et al.* (2001) developed an algorithm that maximized the robot payload while taking into account realistic constraints such as joint torque limits and velocity bounds. The governing optimal control problem was converted into a direct, SQP parameter optimization in which the joint trajectories were defined by B-spline polynomials along with a time-scale factor. Park (2003) presented a method for generating the path of a redundant flexible manipulator which significantly reduced residual vibration in the presence of obstacles. The proposed method was based on an optimized path that was constructed from a combined Fourier series and polynomial with coefficients of each harmonic term selected to minimize the residual vibration.

One of the most popular methods for obstacle avoidance is the artificial potential field method (Castro *et al.* 2002). In contrast to many methods, the robot motion planning through artificial potential fields (APF) is able to take into account simultaneously the problems of obstacle avoidance and trajectory planning. The first use of the APF concept for obstacle avoidance was presented by Khatib (1986). He proposed the force involving an artificial repulsion from the surface which should be non-negative, continuous and differentiable. More recently, a new version such as the repulsive artificial potential field has been proposed (Agirrebeitia *et al.*, 2005). In most of the previous works, flexibility and nonholonomic constraints of the wheeled mobile manipulator in the path planning problem have not been considered. Hence, this paper proposes a method for planning the trajectory of the nonholonomic mobile flexible manipulator for determining the maximum allowable load and considering the effect of flexibility to achieve the specified point to point maneuver in the presence of an obstacle.

2. Kinematic and dynamic model of the mobile flexible manipulator

In this Section, for the sake of modeling and analysis, a mobile flexible manipulator comprising a manipulator flexible arm mounted on a nonholonomic mobile base is considered, as shown in Fig. 1. The motion of the system has to be decomposed into the motion of the flexible manipulator and the motion of the base. The unidirectional platform shown in Fig. 2 is a typical example of a nonholonomic WMR which has two rear driving wheels and two castor wheels.

The two driving wheels are powered by DC motors and have the same wheel radius r. The point P_b is the origin of WMR axis, which is located at the intersection of the longitudinal x-axis and the lateral y-axis. L_0 and b are length and width or WMR body, respectively. The origin of the inertial frame $\{X, Y\}$ is shown as O and as such allows the position of the WMR to be completely specified through the following vector of generalized coordinates with respect to $\{X, Y\}$, $\mathbf{q}_b = [X_b, Y_b, \varphi, \theta_r, \theta_l]$, where X_b and Y_b are the coordinates of the center of mass. The orientation of the WMR frame from the inertial frame is denoted by φ. θ_r and θ_l are the angular displacements of the right and left driving wheel, respectively. Due to the nonholonomic nature of the system, the constraint equation obeys the ideal no-slip condition. The rolling and the knife edge constraint equations for this system can be found in Yamamoto and Yun (1994). In the next Section, these constraints will be explained.

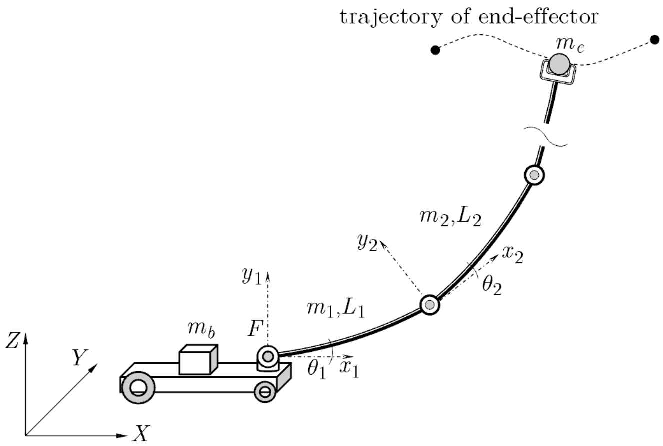

Fig. 1. Schematic view of a mobile flexible manipulator

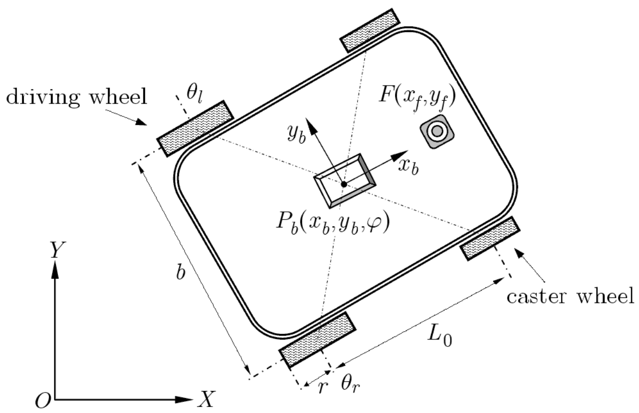

Fig. 2. Nonholonomic wheeled mobile robot platform

The global position vector of the end-effector $\mathbf{r}$ can be defined by appropriately considering the position vector of the corresponding local coordinate in the global reference system as

$$\mathbf{r}_i = \mathbf{r}_b + \mathbf{r}_{m/b} = \mathbf{r}_b + {}_{i-1}^{0}\mathbf{r} + \mathbf{R}\begin{Bmatrix} x+u \\ v \\ w \end{Bmatrix} \tag{2.1}$$

where $\mathbf{r}_b$ is the position of the mobile platform, $\mathbf{R}$ is the transformation matrix and u, v, w denote the longitudinal and transverse displacements.

The analysis of the flexible link can be modeled by slender elastic beams. In this investigation, a more efficient computationally model is employed, in which both the geometric elastic nonlinearity and the foreshortening effects are considered. The model takes into account the distinction between the longitudinal displacement due to axial deformation, denoted as s, and the longitudinal displacement that can occur due to the foreshortening effect, denoted by u_{fs}. The longitudinal displacement caused by transverse deflection of the neutral axis of the beam can be expressed as (Korayem *et al.*, 2012)

$$u_{fs} = -\frac{1}{2}\int_0^x \Big[\Big(\frac{\partial v}{\partial x}\Big)^2 + \Big(\frac{\partial w}{\partial x}\Big)^2\Big]\, dx \tag{2.2}$$

The assumed field of displacements for $\mathbf{u}$ can be written as

$$\mathbf{u} = \begin{bmatrix} u \\ v \\ w \end{bmatrix} = \begin{bmatrix} s + u_{fs} \\ v \\ w \end{bmatrix} \tag{2.3}$$

The general expression of the strain energy is written in terms of s,v and w, as below (Korayem *et al.*, 2012)

$$U = \frac{EA}{2}\int_0^l \Big(\frac{\partial s}{\partial x}\Big)^2\, dx + \frac{EI}{2}\int_0^l \Big(\frac{\partial^2 v}{\partial x^2}\Big)^2\, dx + \frac{EI}{2}\int_0^l \Big(\frac{\partial^2 w}{\partial x^2}\Big)^2\, dx \tag{2.4}$$

where E, A, I, and l denote Young's modulus, cross-sectional area, moment of inertia of the cross section, and length, respectively. This formulation brings nonlinear inertia terms and a constant stiffness matrix in the equations of motion.

The Lagrangian method is utilized to formulate the dynamic equations governing the motion of mobile flexible manipulator systems. In order to derive dynamic equations, the kinetic energy and the potential energy are computed for the entire system. The kinetic energy for the overall system is obtained by computing the kinetic energy for each element ij and then by summing over all the elements. The potential energy of the manipulator is obtained by computing the strain energy for each element ij due to elasticity and gravity of any link. After calculation of these energies, by applying the Lagrangian multipliers procedure and performing some algebraic manipulations, the compact form of the governing equations of a two-link flexible mobile manipulator can be obtained from

$$\begin{bmatrix} M_{bb} & M_{bm} & M_{bf} \\ M_{mb} & M_{mm} & M_{mf} \\ M_{fb} & M_{fm} & M_{ff} \end{bmatrix}\begin{bmatrix} \ddot{q}_b \\ \ddot{q}_m \\ \ddot{q}_f \end{bmatrix} + \begin{bmatrix} C_b(q_b, q_m, q_f, \dot{q}_b, \dot{q}_m, \dot{q}_f) \\ C_m(q_b, q_m, q_f, \dot{q}_b, \dot{q}_m, \dot{q}_f) \\ C_f(q_b, q_m, q_f, \dot{q}_b, \dot{q}_m, \dot{q}_f) \end{bmatrix} + \begin{bmatrix} G_b(q_b, q_m, q_f) \\ G_m(q_b, q_m, q_f) \\ G_f(q_b, q_m, q_f) \end{bmatrix} = \begin{bmatrix} F_b - A^{\mathrm{T}}(q)\lambda \\ F_m \\ 0 \end{bmatrix} \tag{2.5}$$

where $\mathbf{M}$ is the nonlinear mass matrix, $\mathbf{C}$ is the vector of Coriolis and centrifugal forces, $\mathbf{G}$ describes the gravity effects, and $\mathbf{A}$ denotes the nonholonomic constraints. The generalized coordinates $\mathbf{q}$ and the generalized force $\mathbf{F}$ are the following vectors

$$\begin{aligned} \mathbf{q} &= [q_b, q_m, q_f] = [X_f, Y_f, \varphi, \theta_r, \theta_l, \theta_1, \theta_2, q_{f1}, \dots, q_{fn}] \\ \mathbf{F} &= [F_b, F_m, 0] = [0, 0, 0, \tau_{wr}, \tau_{wl}, \tau_1, \tau_2, 0, \dots, 0] \end{aligned} \tag{2.6}$$

The WMRs are called nonholonomic mobile robots because of their no-slip kinematic constraints. The vehicle is prevented from sliding sideways relative to its instantaneous heading, and each drive wheel is assumed to roll without slipping. These three independent nonholonomic constraints are represented as

$$\begin{aligned} &\dot{Y}_f \cos\varphi - \dot{X}_f \sin\varphi - d\dot{\varphi} = 0 \\ &\dot{Y}_f \sin\varphi + \dot{X}_f \cos\varphi + b\dot{\varphi} = r\dot{\theta}_r \\ &\dot{Y}_f \sin\varphi + \dot{X}_f \cos\varphi - b\dot{\varphi} = r\dot{\theta}_l \end{aligned} \tag{2.7}$$

The compact form of the nonholonomic constraints can be written as

$$\mathbf{A}(\mathbf{q})\dot{\mathbf{q}} = \mathbf{0} \tag{2.8}$$

and

$$\mathbf{A} = \begin{bmatrix} -\sin\varphi & \cos\varphi & -d & 0 & 0 & 0 & 0 & 0 & \dots & 0 \\ -\cos\varphi & -\sin\varphi & -b & r & 0 & 0 & 0 & 0 & \dots & 0 \\ -\cos\varphi & -\sin\varphi & b & 0 & r & 0 & 0 & 0 & \dots & 0 \end{bmatrix} \tag{2.9}$$

where r is the radius of the driving wheel, b is the distance of two wheels and d is the distance between the front and rear wheels.

By defining the matrix $\mathbf{B}(\mathbf{q})$, which is the null space of the matrix $\mathbf{A}(\mathbf{q})$, the Lagrange multipliers can be eliminated

$$\mathbf{A}(\mathbf{q})\mathbf{B}(\mathbf{q}) = 0 \tag{2.10}$$

One choice of $\mathbf{B}(\mathbf{q})$ is as follows

$$\mathbf{B} = \begin{bmatrix} (r/2b)(b\cos\varphi - d\sin\varphi) & (r/2b)(b\cos\varphi + d\sin\varphi) & 0 & 0 & 0 & \dots & 0 \\ (r/2b)(b\sin\varphi + d\cos\varphi) & (r/2b)(b\sin\varphi - d\cos\varphi\Big)n & 0 & 0 & 0 & \dots & 0 \\ (r/2b) & -(r/2b) & 0 & 0 & 0 & \dots & 0 \\ 1 & 0 & 0 & 0 & 0 & \dots & 0 \\ 0 & 1 & 0 & 0 & 0 & \dots & 0 \\ 0 & 0 & 1 & 0 & 0 & \dots & 0 \\ 0 & 0 & 0 & 1 & 0 & \dots & 0 \\ 0 & 0 & 0 & 0 & 1 & \dots & 0 \\ \vdots & \vdots & \vdots & \vdots & \vdots & \vdots & 0 \\ 0 & 0 & 0 & 0 & 0 & 0 & 1 \end{bmatrix} \tag{2.11}$$

as well as $\dot{\mathbf{q}}$ can be expressed as follows

$$\dot{\mathbf{q}} = \mathbf{B}(\mathbf{q})\mathbf{v} \tag{2.12}$$

where

$$\mathbf{v} = [\dot{\theta}_r, \dot{\theta}_l, \dot{\theta}_1, \dot{\theta}_2, \dot{q}_{f1}, \dots, \dot{q}_{fn}]^{\mathrm{T}} \tag{2.13}$$

By differentiating equation (2.12)

$$\ddot{\mathbf{q}} = \mathbf{B}(\mathbf{q})\dot{\mathbf{v}} + \dot{\mathbf{B}}(\mathbf{q})\mathbf{v} \tag{2.14}$$

after performing some algebraic manipulations, the dynamic equation of the mobile flexible manipulator is

$$\mathbf{B}^{\mathrm{T}}(\mathbf{q})\mathbf{M}[\mathbf{B}(\mathbf{q})\dot{\mathbf{v}} + \dot{\mathbf{B}}(\mathbf{q})\mathbf{v}] + \mathbf{B}^{\mathrm{T}}(\mathbf{q})(\mathbf{C} + \mathbf{G}) = \mathbf{B}^{\mathrm{T}}(\mathbf{q})\mathbf{F} \tag{2.15}$$

Finally, the dynamic equations in the state space are as follow

$$\dot{\mathbf{x}} = \begin{bmatrix} \mathbf{B}\mathbf{v} \\ (\mathbf{B}^{\mathrm{T}}\mathbf{M}\mathbf{B})^{-1}(-\mathbf{B}^{\mathrm{T}}\mathbf{M}\dot{\mathbf{B}}\mathbf{v} - \mathbf{B}^{\mathrm{T}}\mathbf{C}) \end{bmatrix} + \begin{bmatrix} \mathbf{0} \\ (\mathbf{B}^{\mathrm{T}}\mathbf{M}\mathbf{B})^{-1} \end{bmatrix} \mathbf{F} \tag{2.16}$$

By using these equations, the optimal trajectory planning problem can be formulated.

3. Optimization strategy

Path planning in the case of a mobile flexible manipulator is complex due to flexibility of the manipulator arm. In this Section, an indirect solution to the optimal control problem is applied for the off-line global trajectory planning of the mobile flexible manipulator. The purpose of the optimal control problem is to determine the control $u(t)$ that minimizes the performance index $J(u)$. In this investigation, the specific objective functional J is to obtain the optimal paths with minimum effort and vibration. The general expression which minimizes the cost functional means that (Wang *et al.*, 2001)

$$\min J = \int\limits_{t_0}^{t_f} L(\mathbf{X}(t), \mathbf{U}(t), t)\ dt = \frac{1}{2}\|\mathbf{X}_1\|^2_{\mathbf{W}_P} + \frac{1}{2}\|\mathbf{X}_2\|^2_{\mathbf{W}_V} + \frac{1}{2}\|\mathbf{U}\|^2_R \tag{3.1}$$

Here, the integrand $L(\cdot)$ is a smooth differentiable function in the arguments, $\mathbf{X}(t)$ and $\mathbf{U}(t)$ denote the state space form of the generalized coordinate and the joint torque, respectively. $\|\mathbf{X}\|^2_{\mathbf{K}} = \mathbf{X}^{\mathrm{T}}\mathbf{K}\mathbf{X}$ is the generalized squared norm, $\mathbf{W}_P$, $\mathbf{W}_V$ are symmetric, positive semi--definite $(k \times k)$ weighting matrix, and $\mathbf{R}$ is the symmetric, positive definite $(k \times k)$ matrix. The designer can decide on the relative importance among the angular position, angular velocity, vibration amplitude and control effort by the numerical choice of penalty matrices $\mathbf{W}_P$, $\mathbf{W}_V$ and $\mathbf{R}$. In order to minimize the objective function subjected to the nonlinear dynamic equations, the well-known Pontryagin minimum principle is used. By introducing the cost vector $\boldsymbol{\psi}$, the Hamiltonian function of the system can be defined as

$$H(\mathbf{X}, \mathbf{U}, \boldsymbol{\psi}, t) = L(\mathbf{X}, \mathbf{U}) + \boldsymbol{\psi}^{\mathrm{T}}\dot{\mathbf{X}} \tag{3.2}$$

The PMP then implies that the necessary condition for a local minimum is that H be minimized with respect to $u(t)$ at all times. If it is assumed that the set of admissible inputs is bounded $U_i^- \leqslant u_i^* \leqslant U_i^+$, this condition is equivalent to

$$\dot{\mathbf{X}} = \frac{\partial H}{\partial \boldsymbol{\psi}} \qquad \dot{\boldsymbol{\psi}} = \frac{-\partial H}{\partial \mathbf{X}} \qquad \mathbf{0} = \frac{\partial H}{\partial \mathbf{U}} \tag{3.3}$$

The considered boundary conditions are

$$\mathbf{X}(t_i) = \mathbf{X}_i \qquad \mathbf{X}(t_f) = \mathbf{X}_f \tag{3.4}$$

where $\mathbf{X}(t_i)$ and $\mathbf{X}(t_f)$ represent positions and velocities of the links at the beginning and at the end of the maneuver. The optimal trajectory is then obtained by solving the $2n$ differential equations

$$\begin{aligned} &\dot{x}^*(t) = \frac{\partial H}{\partial p}(x^*(t), u^*(t), p^*(t), t) \\ &\dot{p}^*(t) = -\frac{\partial H}{\partial x}(x^*(t), u^*(t), p^*(t), t) \\ &H(x^*(t), u^*(t), p^*(t), t) \leqslant H(x^*(t), u(t), p^*(t), t) \end{aligned} \tag{3.5}$$

The control values are limited with the upper and lower bounds. One of the most commonly used motors for actuating the joints of small and medium size mobile robots are permanent magnet DC motors. Typical speed-torque characteristics of DC motors in which the relationship between speed and torque is linear are defined as below (Wang *et al.*, 2001)

$$\mathbf{U}^{(+)}_{allow} = \mathbf{K}_1 - \mathbf{K}_2\dot{\mathbf{q}} \qquad \mathbf{U}^{(-)}_{allow} = -\mathbf{K}_1 - \mathbf{K}_2\dot{\mathbf{q}} \tag{3.6}$$

where

$$\mathbf{K}_1 = \begin{bmatrix} \tau_{s1} & \tau_{s2} & \dots & \tau_{sm} \end{bmatrix}^{\mathrm{T}} \qquad \mathbf{K}_2 = \mathrm{diag}\begin{bmatrix} \frac{\tau_{s1}}{\omega_1} & \frac{\tau_{s2}}{\omega_2} & \dots & \frac{\tau_{sm}}{\omega_m} \end{bmatrix}^{\mathrm{T}}$$

the stall torque (torque generated by the motor when fully "ON" but unable to move) and no--load speed (output speed of the motor when running without load) are denoted by τ_s and ω_m, respectively.

3.1. Maximum payload algorithm

The set of dynamic equations, the governing optimal control problem and the boundary conditions lead to the standard form of a two-point boundary value problem (TPBVP). The collocation method is one of the basic ways of solving TPBVP. The method iterates on the initial values of the co-state until the final boundary conditions are satisfied by the following desired accuracy

$$h(\mathbf{X}(t_f), t_f) = \frac{1}{2}\|\mathbf{X}_1(t_f) - \mathbf{X}_{1f}\|^2_{\mathbf{W}_p} + \frac{1}{2}\|\mathbf{X}_2(t_f) - \mathbf{X}_{2f}\|^2_{\mathbf{W}_V} \leqslant \varepsilon \tag{3.7}$$

In this Section, an algorithm is proposed to find the maximum payload shown in Fig. 3. The proposed method considers torque bounds and is based on increasing the payload until one point

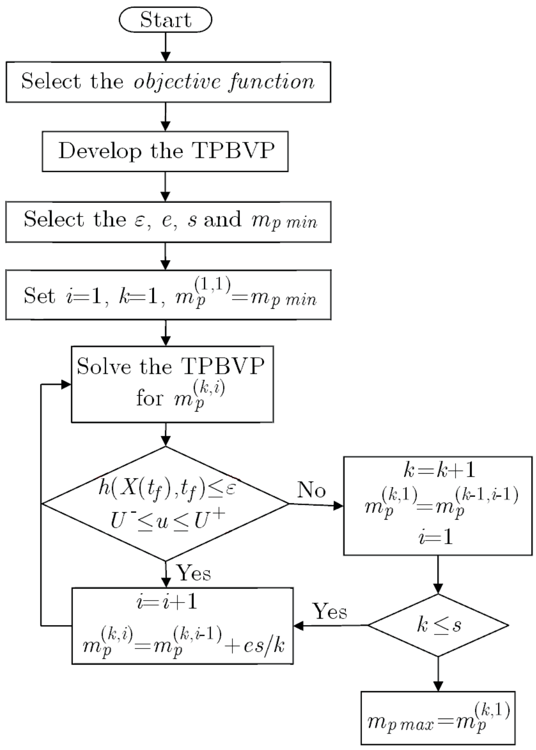

Fig. 3. The algorithm for calculation of the maximum payload

of one of the actuators torque reach the upper or lower torque bounds. As shown in Fig. 3, the proposed algorithm includes two stages; the first stage index i increases the tip mass mp until the actuators torque reach the upper or lower torque constraints. The desired accuracy ε in TPBVP solution must be satisfied for the payload in each step. A further increase in the payload exceeds the torque limits. Consequently, the desired accuracy ε in TPBVP solution could not be satisfied and the boundary conditions at yhe final time may be obtained incorrectly. At this status, while one point of one of the actuators torque reach the upper or lower torque bounds; the second stage index k decreases the payload until the maximum payload for the supposed penalty matrices is obtained with the accuracy ε. The accuracy of the maximum payload mp_{max} calculation depends on the value e. The iteration number is denoted by s symbol in this algorithm.

3.2. Path planning in the presence of an obstacle

In order for mobile flexible manipulators to successfully carry out tasks, especially in carrying heavy loads on different trajectories, the Artificial Potential Fields (APFs) is used throughout the robot workspace with each point in the workspace having an associated potential. The idea used in APF-based obstacle avoidance is to position a mobile manipulator in the workspace such that the overall potential encountered by the mobile manipulator is minimized while still accomplishing the desired task. A repulsive potential formulation based on the distance between parts of the WMM and obstacles is used in the cost function for obstacle avoidance. The most commonly used repulsive potential takes the form (Khatib, 1986)

$$\mathbf{U}_{rep} = \begin{cases} \dfrac{1}{2}\eta\Big(\dfrac{1}{\rho(q,q_{obs})} - \dfrac{1}{\rho_0}\Big) & \text{if} \quad \rho(q,q_{obs}) \leqslant \rho_0 \\ 0 & \text{if} \quad \rho(q,q_{obs}) > \rho_0 \end{cases} \tag{3.8}$$

where η is a positive weighting matrix, $\rho(q,q_{obs})$ denotes the minimal distance from the robot q to the obstacle, q_{obs} denotes the point on the obstacle such that the distance between this point and the robot is minimal between the obstacle and the robot, and ρ_0 is a positive constant denoting the distance of influence of the obstacle.

The obstacle avoidance problem is formulated in terms of collision avoidance of the base, links and joints with the obstacles. In order to add the penalty function to the performance index in order to guarantee free-collision motion of the mobile body, the distance between the center of the mobile base and the center of the obstacle will be

$$\rho_b = \|\mathbf{P}_{obs} - \mathbf{P}_b\| = \sqrt{(\mathbf{X}_{obs} - \mathbf{X}_b)^2 + (\mathbf{Y}_{obs} - \mathbf{Y}_b)^2} \tag{3.9}$$

By assuming the links as lines, the minimal distance between ij link and the center of the obstacle can be calculated as

$$\rho_{ij} = \frac{1}{\sqrt{(\mathbf{X}_j - \mathbf{X}_i)^2 + (\mathbf{Y}_j - \mathbf{Y}_i)^2}} \left| \det \begin{bmatrix} \mathbf{X}_j - \mathbf{X}_i & \mathbf{X}_{obs} - \mathbf{X}_i \\ \mathbf{X}_j - \mathbf{X}_i & \mathbf{Y}_{obs} - \mathbf{Y}_i \end{bmatrix} \right| \tag{3.10}$$

The position of parts in the workspace is denoted by $\mathbf{X}_i$ and $\mathbf{Y}_i$. Therefore, the objective function to guarantee the free-collision motion can be defined as

$$J(u) = \int\limits_{t_0}^{t_f} L(\mathbf{X},\mathbf{U},t)\;dt = \frac{1}{2}\|\mathbf{X}_1\|^2_{\mathbf{W}_1} + \frac{1}{2}\|\mathbf{X}_2\|^2_{\mathbf{W}_2} + \frac{1}{2}\|\mathbf{U}\|^2_{\mathbf{R}} + \frac{1}{2}\Big\|\frac{1}{\boldsymbol{\rho}} - \frac{1}{\boldsymbol{\rho}_0}\Big\|^2_\eta \tag{3.11}$$

The new objective function is used to obtain the trajectory optimization problem to avoid collision of the WMM parts with the obstacles. Figure 4 shows the wheeled mobile robot in the presence of an obstacle.

4. Simulation results

A simulation study has been carried out to investigate further the validity and effectiveness of the mobile flexible manipulators in finding the optimal path between two points with different objective functions. A two-link planar manipulator is considered. It is mounted on a differentially driven mobile base at point F on the main axis of the base (Fig. 4). The parameters of the mobile flexible manipulator are given in Table 1.

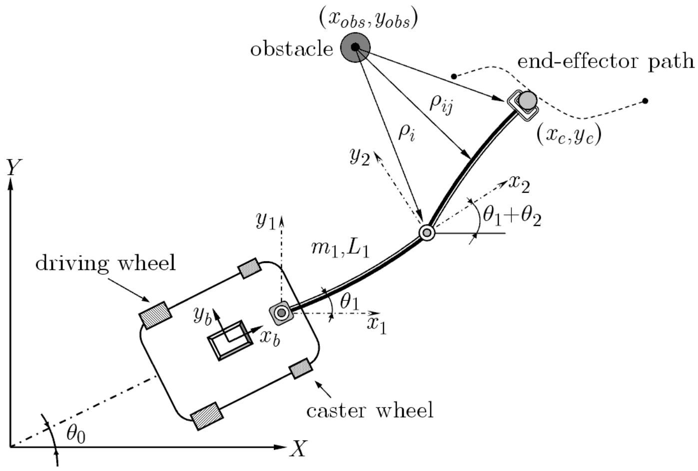

Fig. 4. WMM in the presence of an obstacle

Table 1. Simulation of parameters

Parameter	Value (base)	Value (manipulator)
Length [m]	$L_0 = 0.4$	$L_1 = L_2 = 1$
Mass [kg]	$m_b = 94$	$m_1 = m_2 = 3$, $mp = 0.5$
Cross section area [m^2]	–	$A_1 = A_2 = 4 \cdot 10^{-8}$
Moment of inertia [m^4]	$I_b = 6.609$	$I_1 = 0.416$, $I_2 = 0.0625$
Young's modulus of the material [N/m^2]	–	$E_1 = E_2 = 2 \cdot 10^{10}$

4.1. First case study: optimal path for minimum effort

The motion planning problem is to find the optimal trajectory with minimum effort. The main motivation behind the minimum effort is to find a path to reduce the amount of torques and hence to lower energy consumption. According to the algorithm presented in Fig. 3, the general solution method is based on increasing the payload from its minimum value mp_{min} up to the maximum payload can be found. Therefore, in this case, the initial payload, initial values of the co-state vector, accuracy values, and penalty matrices are considered as follows

$$\begin{array}{llll} mp_{min} = 0.5\,\mathrm{kg} & \psi(0) = 0 & e = 0.1 & \varepsilon = 0.0001 \\ \mathbf{W}_p = \mathbf{W}_V = \mathbf{0} & \mathbf{R} = \mathrm{diag}\,(1) & & \end{array} \tag{4.1}$$

This cost function is typical for systems that need to conserve energy during a particular operation. The actuator constants are given as follows

$$\begin{aligned} \mathbf{K}_1 &= \begin{bmatrix} 20 & 20 & 50 & 50 \end{bmatrix}^{\mathrm{T}}\ \mathrm{N \cdot m} \\ \mathbf{K}_2 &= \mathrm{diag}\begin{bmatrix} 1.5 & 1.5 & 2.5 & 2.5 \end{bmatrix} \frac{\mathrm{N \cdot m \cdot s}}{\mathrm{rad}} \end{aligned} \tag{4.2}$$

The system is initially at rest, thus the mobile base is initially at the point ($x_F = 0.75\,\mathrm{m}$, $y_F = -0.5\,\mathrm{m}$, $\varphi = 0°$) and moves to its final position ($x_F = 1.6\,\mathrm{m}$, $y_F = -0.2\,\mathrm{m}$, $\varphi = 15°$). The initial conditions of the manipulator are $\theta_1(0) = 1.5\,\mathrm{rad}$, $\theta_2(0) = 2\,\mathrm{rad}$, $\dot{\theta}_1(0) = 0$, $\dot{\theta}_2(0) = 0$ (point A in Fig. 5a) and the final conditions are $\theta_1(t_f) = -0.86\,\mathrm{rad}$, $\theta_2(t_f) = 1.09\,\mathrm{rad}$, $\dot{\theta}_1(t_f) = 0$, $\dot{\theta}_2(t_f) = 0$ (point B in Fig. 5a) during the overall time $t_f = 1.9\,\mathrm{s}$ (see Fig. 5a) and also the remaining boundary conditions are equal to zero.

A comparative study is carried out between the rigid model and flexible models (linear and nonlinear models) as shown in Fig. 5b. The optimal angular positions of the link and wheels, corresponding to the minimum effort are shown in Figs. 6a and 6b.

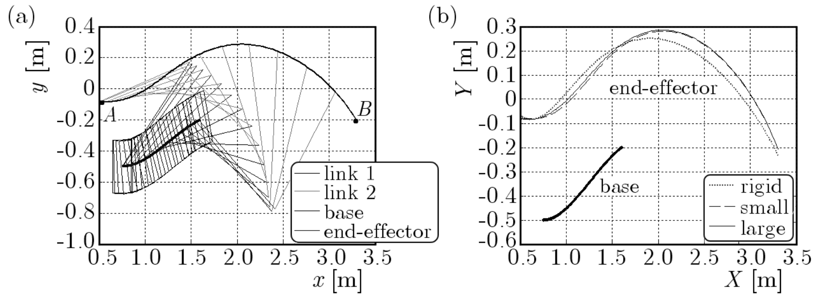

Fig. 5. The optimal paths between point A and B via minimum effort (a) and for different models (b)

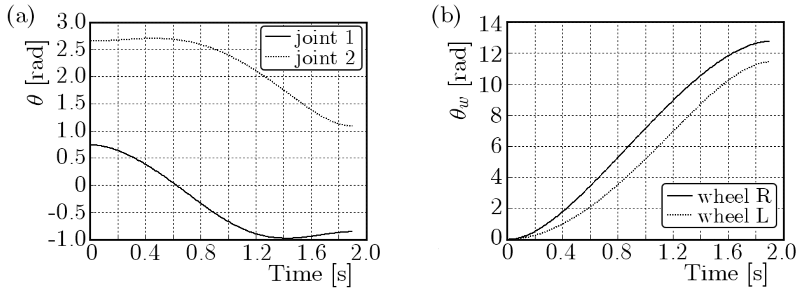

Fig. 6. The optimal angular positions of the first and second joints (a) and the right and left wheels (b)

The simulation results presented in Fig. 7 illustrate the optimal controls to carry the maximum payload, which also show the upper and lower bounds of the actuator torque capacity. By increasing the payload from mp_{min} to mp_{max}, the required torque grows until one point of one of the actuators torque reach the upper or lower torque bounds. It can be seen that, the second motor reaches its maximum capacity. In this case study, the maximum payload is obtained to be $mp_{max} = 2.45\,\mathrm{kg}$, while by considering the rigid link and Nikoobin's method (Korayem *et al.*, 2012), the maximum payload is found to be $mp_{max} = 8.25\,\mathrm{kg}$. This difference is due to flexibility of the link which increases the oscillation of torque curves.

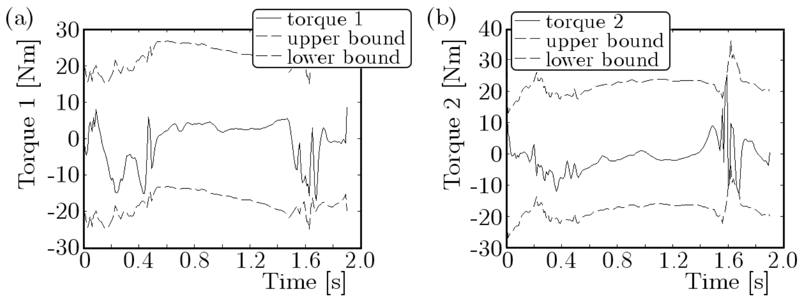

Fig. 7. Minimum effort of the first and second motors within upper and lower acceptable boundaries

4.2. Second case study: minimum vibration trajectory

In the motion planning of flexible robots, obtaining the minimum vibration trajectory is one of the most frequently encountered problems. The optimization objective is to minimize the vibration excitation during motion. By increasing the weighting factors corresponding to the derivative of flexural displacements ($\dot{q}_{f1}, \ldots, \dot{q}_{fn}$), the vibrational motions will be suppressed. The bounds of the motor capacity are not considered. Hence, the proper penalty matrices are selected to be $\mathbf{R} = \mathrm{diag}\,(0.01)$ and $\mathbf{W}_p = \mathbf{0}$, $\mathbf{W}_V = \mathrm{diag}\,(0, 0, 1, \ldots, 1)$. The load must be carried from the initial point with coordinate ($x_e = 0.5\,\mathrm{m}$, $y_e = -0.08\,\mathrm{m}$) to the final point with coordinate ($x_e = 3.31$ m, $y_e = -0.25$ m). The optimal trajectory between these two points during the overall time $t_f = 1.9$ s is desired for the rest-to-rest maneuver. The other conditions remain the same with the previous case study. The characteristics of the parts are shown in Table 1.

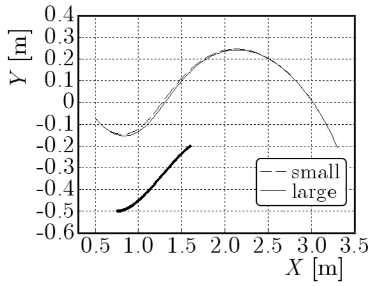

Fig. 8. The optimal paths via minimum vibration

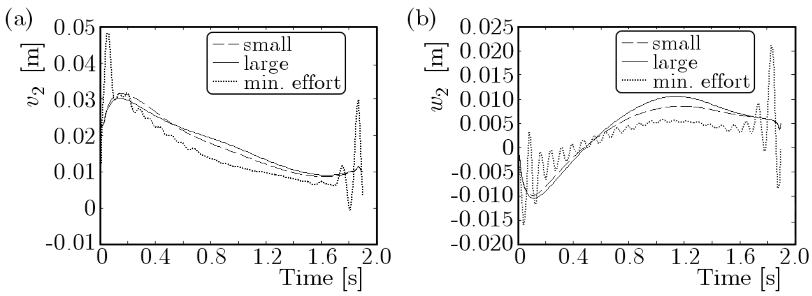

Fig. 9. The optimal flexural deflections of the first link (a) and the optimal flexural displacements of the second link (b)

The simulation results (small and large models) are illustrated in Fig. 8. The obtained optimal flexural deflections, corresponding to the minimum vibration are shown in Figs. 9a and 9b. The simulation results show that a significant reduction in manipulator vibration can be achieved by employing the proposed optimization procedure. As expected, it can be seen, by decreasing the amplitude vibration, that the linear and nonlinear models come closer together. Also, it is shown that application of the proper input torque may decrease the end effector vibration significantly.

4.3. Third case study: trajectory optimization in the presence of an obstacle

Recently, there has been a great deal of interest in path planning for autonomous mobile manipulators in the presence of an obstacle because of their ability to replace objects in a wide workspace. Hence, the problem is how to find a feasible trajectory for all components in order to carry the maximum payload in environment with an obstacle. The characteristics of the non-holonomic mobile manipulator, penalty matrices, accuracy value, and the actuator constants are the same as in the first case study. Moreover, the augmented functional obstacle avoidance is considered in the cost function. The task is considered to move the end effector from the initial point $p_0 = (0.5, -0.08)$ to the final configuration $p_f = (3.31, -0.25)$ for the rest-to-rest maneuver during the overall time $t_f = 1.9$ s. Also, there is an obstacle with $r_{obs} = 0.05$ m at a point with coordinates $p_{obs} = (x_{obs} = 1.1\,\mathrm{m},\ y_{obs} = -0.55\,\mathrm{m})$. The simulation parameters are shown in Table 1.

In this condition, the maximum payload is found to be 2.05 kg. To avoid the obstacle, the manipulator moves far from it and causes a decrease in the allowable payload. The schematic of the obstacle and the obtained optimal paths of the end-effector and the mobile base are shown in Fig. 10a. A comparative study is performed between the rigid model and flexible models (linear and nonlinear models) as shown in Fig. 10b.

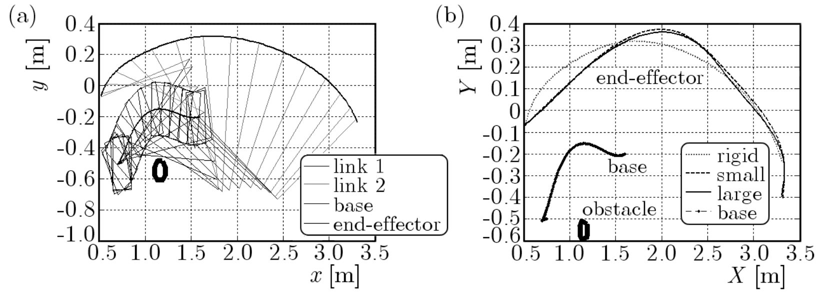

Fig. 10. The schematic view of obtained optimal paths in the presence of an obstacle (a) and the obtained optimal paths of the end-effector and mobile base for different models (b)

5. Conclusions

The main objective of this investigation is to determine the trajectory optimization for calculating the MADL of flexible-link mobile manipulators in the point-to-point maneuver in the presence of an obstacle, based on the indirect solution to the optimal control problem. The effect of dynamic interaction between the flexible manipulator and the mobile platform is considered to characterize the motion of a nonholonomic mobile manipulator with the compliant link capable of large deflection, in which both the geometric elastic nonlinearity and the foreshortening effects are considered. This model leads to a constant stiffness matrix and makes the formulation particularly efficient in computational terms and numerically more stable than alternative geometrically nonlinear formulations based on lower-order terms. Pontryagin's minimum principle is used to obtain the optimality conditions, which leads to a standard form of a two-point boundary value problem. An augmented objective function based on an artificial potential field is considered to avoid the obstacle during point-to-point maneuvers. Several simulation studies on a nonholonomic wheeled mobile manipulator are carried out for finding the MADL and optimal paths with different objective functions like minimum effort and minimum vibration. The numerical results indicate the effect of employing trajectory optimization in the performance improvement of the mobile flexible manipulator. It is shown that the presence of the obstacle causes the manipulator moves far from it; therefore, it reduces the maximum load-carrying capacity. Moreover, in this method, the designer can compromise between different objectives by considering proper penalty matrices, and may choose the proper trajectory between various paths. The obtained results illustrate the power and efficiency of the model in overcomming the highly nonlinear nature of the large deflection and optimization problem, which with other methods may be very difficult or impossible to achieve.

References

1. Agirrebeitia J., Aviles R., Ajuria G., 2005, A new APF strategy for path planning in environments with obstacles, *Mechanism and Machine Theory*, **40**, 1, 645-658

2. Castro D., Nunes U., Ruano A., 2002, Obstacle avoidance in local navigation, *Proceedings of the 10th Mediterranean Conference on Control and Automation*, Lisbon, Portugal

3. Damaren C., Sharf L., 1995, Simulation of flexible-link manipulators with inertia and geometric nonlinearities, *ASME Journal of Dynamic Systems, Measurement, and Control*, **117**, 1, 74-87

4. Khatib O., 1986, Real-time obstacle avoidance for manipulators and mobile robots, *The International Journal of Robotics Research*, **5**, 1, 90-98

5. Korayem M.H., Haghpanahi M., Heidari H.R., 2012, Analysis of flexible mobile manipulators undergoing large deformation with stability consideration, *Latin American Applied Research*, **42**, 2

6. Park K.J., 2003, Path design of redundant flexible robot manipulators to reduce residual vibration in the presence of obstacles, *Robotica*, **21**, 1, 335-340
7. Seraji H., 1998, A unified approach to motion control of mobile manipulators, *The International Journal of Robotics Research*, **17**, 12, 107-118
8. Wang C.Y.E., Timoszyk W.K., Bobrow J.E., 2001, Payload maximization for open chained manipulator: finding weightlifting motions for a Puma 762 robot, *IEEE Transactions on Robotics and Automation*, **17**, 1, 218-224
9. Xi F., Fenton R.G., 1991, A quasi-static motion planner for flexible manipulators using the algebra of rotations, *IEEE International Conference on Robotics and Automation*, **3**, 1, 2363-2368
10. Yamamoto Y., Yun X., 1994, Coordinating locomotion and manipulation of a mobile manipulator, *IEEE Transactions on Robotics and Automation*, **39**, 6, 1326-1332

Manuscript received March 12, 2015; accepted for print May 8, 2015

JOURNAL OF THEORETICAL
AND APPLIED MECHANICS
53, 4, pp. 925-934, Warsaw 2015
DOI: 10.15632/jtam-pl.53.4.925

EFFECTS OF LIQUID LOADINGS ON LAMB WAVES IN CONTEXT OF SIZE DEPENDENT COUPLE STRESS THEORY

Vikas Sharma
Department of Mathematics, Lovely Professional University, Phagwara, Punjab, India
e-mail: vikas.sharma@lpu.co.in; vikassharma10a@yahoo.co.in

Satish Kumar
School of Mathematics and Computer Applications, Thapar University, Patiala, Punjab, India
e-mail: satishk.sharma@thapar.edu

For understanding the effects of an internal microstructure, generalised microcontinuum theories with additional microstructural parameters are developed. One such a parameter, called the characteristic length of the material comparable with the internal cell size of the material is involved in the couple stress theory. The problem of propagation of Lamb waves in a plate with an internal microstructure and loaded with an inviscid liquid on both sides is studied using the couple stress theory. The dispersion equation of Lamb waves with the liquid loadings is derived. The impact of the liquid loadings is studied on the propagation of Lamb waves. The effect of the characteristic length is also studied on the phase velocity of Lamb waves in the plate for various modes in the presence of liquid loadings.

Keywords: couple stress, characteristic length, Lamb waves, elastic waves, liquid loadings

1. Introduction

Classical theory of elasticity is inadequate to capture the size effects, as the atomic structure of the material is ignored in this theory, and it is based on the assumption of homogeneity of the material. It can describe elastic deformations and properties of materials at macroscale. However, experimental evidences show that mechanical behaviour of the material at microscale is different from its behaviour at macroscale. To explain this, there was a need to develop a new theory or to modify existing ones, which can fill this gap of theoretical and experimental results. Microcontinuum theories such as micropolar theory (Eringen, 1968), strain gradient (Mindlin, 1964) and couple stress theory (Toupin, 1962; Mindlin and Tiersten, 1962; Koiter, 1964; Hadjesfandiari and Dargush, 2011) were developed to investigate the microstructural effects in the material.

Voigt (1887) was the first to create the idea of couple stresses in the materials by assuming that an infinitesimal surface element transmits both Cauchy stresses and couple stresses. Cosserat and Cosserat (1909) gave the mathematical model to analyse materials with couple stresses by considering that the deformation of the medium is described by a displacement vector and an independent rotation vector. This theory was not recognised at that time. Later on, this concept was used by many researchers like Toupin (1962), Mindlin and Tiersten (1962), Koiter (1964), Eringen (1968), Nowacki (1974) to explore microstructural effects in the material. Many problems of wave propagation in an elastic medium with a microstructure under different conditions have been studied by applying the couple stress theory. Sengupta and Ghosh (1974) studied the effects of couple stresses on wave propagation in an elastic layer and they observed that couple stresses affect the velocity of propagation of waves in the elastic layer. Das *et al.*

(1991) studied thermo-viscoelastic Rayleigh waves under the influence of couple stress and gravity. They derived more general equations of phase velocity for these waves and showed that it reduces to classical elastic Rayleigh waves in the absence of couple stresses, viscosity and gravity. Ottosen *et al.* (2000) studied Rayleigh waves by applying the indeterminate couple stress theory. Georgiadis and Velgaki (2003) shown the dispersive nature of Rayleigh waves propagating along the surface of a half-space at high frequencies using the couple stress theory and also tried to estimate the values of microstructural parameters in couple stress theory. Akgoz and Civalek (2013) did the modeling and analysis of micro-sized plates resting on an elastic medium using the modified couple stress theory. Chen and Li (2014) proposed a new modified couple stress theory for anisotropic elasticity containing three length scale parameters and developed composite laminated Kirchhoff plate models under this theory.

Hadjesfandiari and Dargush (2011) formulated a couple stress theory for an isotropic material involving three parameters λ, μ and η. The constants λ, μ have the same meaning as Lamé constants in Cauchy elasticity and η is a length scale parameter which accounts for couple stress effects for isotropic solids. Evaluation of η requires characteristic material length l which is absent in Cauchy elasticity. One of the major problems in these size dependent elastic theories (Cosseret, 1909), micropolar (Eringen, 1968) and couple stress (Toupin, 1962; Mindlin and Tiersten, 1962; Koiter, 1964; Hadjesfandiari and Dargush, 2011) is determination of these length scale parameters. It was observed (Lakes, 1991) that the characteristic length would be undetectable in any macroscopic mechanical experiment, but have relevance in studies involving composite and cellular solids. In fibrous composites, the characteristic length may be of the order of spacing between the fibres. In cellular solids, it may be comparable to the average cell size of the material.

Lakes *et al.* (1986), while studying propagation of an ultrasonic wave in wet bone, pointed out that bone may be regarded as a composite with particulate, porous and fibrous structural elements at different levels of scale. Vavva *et al.* (2009) also described bone as a strongly heterogeneous natural composite with a complex structure and carried out the study by taking the characteristic length comparable to the size of the bone microstructure that is of the order of 10 to 500 μm.

Lamb waves travel in thin stress free elastic plates and were originally studied by Horace Lamb (1917). These waves are extremely useful for detection of cracks, corrosion and other defects in materials using non destructive testing techniques and have immense applications in aerospace, industrial and engineering fields. Viktorov (1967) gave the further details by providing dispersive nature of Lamb waves and explained that they are formed by interference of multiple reflections and mode conversion of longitudinal and shear waves at the free surfaces of the plate. Osborne and Hart (1945) examined Lamb waves activated in steel plates in underwater explosions and made a comparison between theoretical and experimental results. Schoch (1952) investigated the effect of an inviscid liquid loading on the propagation of Lamb waves and derived the dispersion relation for leaky Lamb waves for an isotropic plate. Wu and Zhu (1992) studied the propagation of Lamb waves in a plate bordered with inviscid liquid layers on both sides. The dispersion equations of this case were derived and showed that phase velocity varies with thickness of the liquid layers. Sharma and Pathania (2003) studied generalized thermoelastic Lamb waves in a homogeneous isotropic, thermally conducted plate bordered with layers of an inviscid liquid or inviscid half space. Sharma and Kumar (2009) studied Lamb waves in micropolar thermoelastic solid plates immersed in a liquid with varying temperature. They studied the effect of the characteristic length and coupling factor on the phase velocity of the Lamb wave. Vavva *et al.* (2009) discussed velocity dispersion of guided waves propagating in a free gradient elastic plate by showing its application to cortical bone. They studied microstructural effects on the propagation of guided waves by applying gradient elasticity and concluded that this theory can provide additional information for better understanding of the waves. Wu *et al.* (2009) investigated vibration characteristics in a microscale fluid loaded rectangular isotropic plate attached to a uniformly distributed mass. They studied plate vibrations under the simultaneous effect of fluid loadings and attached mass loadings.

In an earlier work, the authors (2014) successfully employed the couple stress model (Hadjesfandiari and Dargush, 2011) to capture size effects on velocity dispersion in an elastic plate. It was observed that the microstructural parameter affected the dispersion of the Lamb wave. The dynamical characteristics of a structure get affected when it is surrounded by a fluid. This study becomes more important when the material under consideration exhibits internal microstructure. Lamb waves are guided waves propagating in a traction free plate surface, however if the surface of the plate is in contact with the fluid, a part of energy will leak into the liquid, and this phenomenon may find possible applications not only in non destructive evaluation of materials, but also in biomedical field. Keeping this in mind, the fluid-solid model adopted by Sharma and Kumar (2009) is applied to extend the study of Lamb waves (Sharma and Kumar, 2014) in a thin elastic plate with a microstructure. The study is carried out for a thin elastic plate having mechanical properties similar to bone, bordered on both sides with an inviscid liquid by applying the couple stress theory (Hadjesfandiari and Dargush, 2011) to capture the effects of both liquid loading and microstructure in terms of the internal characteristic length of the material.

2. Formulation and solution of the problem

Consider an infinite homogeneous isotropic, elastic plate of thickness $2d$. The plate is bordered both on the top and bottom with infinitely large homogeneous inviscid liquid layers of thickness H. Consider the origin of the coordinate system (x, y, z) in the middle of the plate. The XY-plane is chosen to coincide with the middle surface of the plate and z-axis is normal to the plate, along the thickness of the plate pointing vertically downwards. We consider the XZ-plane as the plane of incidence and assume that the solutions are explicitly independent of y.

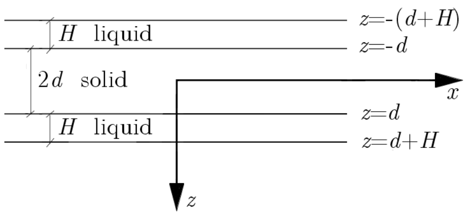

Fig. 1. Geometry of the considered structure

The basic governing equation of motion and constitutive relations of couple stress elasticity for an isotropic material in the absence of body forces (Hadjesfandiari and Dargush, 2011) are given by

$$\begin{aligned}
&(\lambda+\mu+\eta\nabla^2)u_{k,ki}+(\mu-\eta\nabla^2)\nabla^2u_i=\rho\ddot{u}_i\\
&\sigma_{ji}=\lambda u_{k,k}\delta_{ij}+\mu(u_{i,j}+u_{j,i})-\eta\nabla^2(u_{i,j}-u_{j,i})\\
&\mu_{ji}=4\eta(\omega_{i,j}-\omega_{j,i}) \qquad \omega_i=\frac{1}{2}\epsilon_{ijk}u_{k,j}
\end{aligned} \tag{2.1}$$

where λ and μ are Lamé constants, $\eta=\mu l^2$ is the couple-stress coefficient, l is the characteristic length, ρ is the density of the plate, u_i are the displacement components, commas are used for partial differentiation and dot notation $(\cdot)$ is used for partial differentiation with time. Here, σ_{ji} is the non-symmetric force-stress tensor, μ_{ji} is skew symmetric couple-stress tensor, ω_i is the rotation vector, δ_{ij} is Kronecker's delta and ϵ_{ijk} is the permutation tensor.

In the solid, we take

$$u = \frac{\partial\phi}{\partial x} - \frac{\partial\psi}{\partial z} \qquad w = \frac{\partial\phi}{\partial z} + \frac{\partial\psi}{\partial x} \tag{2.2}$$

where u and w are the x and z components of the particle displacement in the plate. ϕ and $\vec{\psi} = (0, \psi, 0)$ are the potential functions of the longitudinal and shear waves in the solid. In the liquid boundary layers, we have

$$\begin{aligned} u_1' &= \frac{\partial\phi_1}{\partial x} - \frac{\partial\psi_1}{\partial z} \qquad & w_1' &= \frac{\partial\phi_1}{\partial z} + \frac{\partial\psi_1}{\partial x} \\ u_2' &= \frac{\partial\phi_2}{\partial x} - \frac{\partial\psi_2}{\partial z} \qquad & w_2' &= \frac{\partial\phi_2}{\partial z} + \frac{\partial\psi_2}{\partial x} \end{aligned} \tag{2.3}$$

where ϕ_j and ψ_j, $j = 1, 2$ are the scalar potential and vector potential for the bottom liquid layer ($j = 1$) and for the top liquid layer ($j = 2$), u_j' and w_j' are respectively x and z components of the particle displacement in the layers of the liquid. Because the inviscid liquid does not support the shear motion, so the shear modulus of the liquid vanishes and hence $\psi_j = 0$, $j = 1, 2$. The potential functions ϕ, ψ and ϕ_j satisfy the basic governing equations

$$\nabla^2\phi = \frac{1}{C_1^2}\frac{\partial^2\phi}{\partial t^2} \qquad \nabla^2\psi - l^2\nabla^4\psi = \frac{1}{C_2^2}\frac{\partial^2\psi}{\partial t^2} \qquad \nabla^2\phi_j = \frac{1}{C_L^2}\frac{\partial^2\phi_j}{\partial t^2} \tag{2.4}$$

and for the liquid the stresses are $\sigma_{ji}' = \lambda_L u_{k,k}'\delta_{ij}$ and the couple stresses in the case of the liquid are all zero. $C_1^2 = (\lambda + 2\mu)/\rho$, $C_2^2 = \mu/\rho$ are the dilatational and shear wave speeds, respectively, in the classical theory of elasticity $C_L^2 = \lambda_L/\rho_L$. Here C_L is the velocity of sound in the liquid and λ_L is the bulk modulus. Prime denotes the same quantities for the liquid layer.

Using equations (2.2) and (2.3) in equations $(2.1)_{2,3}$, we get stresses and couple stresses in terms of the potential functions as

$$\begin{aligned} \sigma_{zx} &= \mu\Big(\frac{\partial^2\psi}{\partial x^2} - \frac{\partial^2\psi}{\partial z^2} + 2\frac{\partial^2\phi}{\partial x\partial z}\Big) + \mu l^2\Big(\frac{\partial^4\psi}{\partial x^4} + \frac{\partial^4\psi}{\partial z^4} + 2\frac{\partial^4\psi}{\partial x^2\partial z^2}\Big) \\ \sigma_{zz} &= \mu\Big[\frac{C_1^2}{C_2^2}\Big(\frac{\partial^2\phi}{\partial x^2} + \frac{\partial^2\phi}{\partial z^2}\Big) - 2\frac{\partial^2\phi}{\partial x^2} + 2\frac{\partial^2\psi}{\partial x\partial z}\Big] \\ \mu_{zy} &= -2\mu l^2\Big(\frac{\partial^3\psi}{\partial z^3} + \frac{\partial^3\psi}{\partial z\partial x^2}\Big) \end{aligned} \tag{2.5}$$

and the value of stresses in the liquid in terms of the potential function becomes

$$\sigma_{zz}' = \lambda_L\Big(\frac{\partial^2\phi_j}{\partial x^2} + \frac{\partial^2\phi_j}{\partial z^2}\Big) \tag{2.6}$$

We assume solutions of the form

$$\{\phi, \psi, \phi_j\} = \{f(z), g(z), \overline{\phi}_j(z)\}\mathrm{e}^{\mathrm{i}\xi(x-ct)} \tag{2.7}$$

where $c = \omega/\xi$ is the phase velocity, ω is the frequency and ξ is the wave number. Using solutions (2.7) in Eqs. (2.4) and solving the resulting differential equations, we get the expressions for ϕ, ψ and ϕ_j as

$$\begin{aligned} \phi &= (A_1\cos\alpha z + A_2\sin\alpha z)\mathrm{e}^{\mathrm{i}\xi(x-ct)} \\ \psi &= (A_3\cos\beta z + A_4\sin\beta z + A_5\cos\gamma z + A_6\sin\gamma z)\mathrm{e}^{\mathrm{i}\xi(x-ct)} \\ \phi_1 &= A_7\sin\delta[z - (d+H)]\mathrm{e}^{\mathrm{i}\xi(x-ct)} \qquad & d < z < d+H \\ \phi_2 &= A_8\sin\delta(z + d + H)\mathrm{e}^{\mathrm{i}\xi(x-ct)} \qquad & -(d+H) < z < -d \end{aligned} \tag{2.8}$$

where

$$\alpha^2 = \xi^2\Big(\frac{c^2}{C_1^2} - 1\Big) \qquad \beta^2 + \gamma^2 = -\Big(2\xi^2 + \frac{1}{l^2}\Big)$$
$$\beta^2\gamma^2 = \frac{\xi^2}{l^2}\Big(1 + \xi^2 l^2 - \frac{c^2}{C_2^2}\Big) \qquad \delta^2 = \xi^2\Big(\frac{c^2}{C_L^2} - 1\Big)$$

Here ϕ_1 and ϕ_2 are solutions of standing waves and are chosen in such a way that the acoustical pressure is zero at $z = \pm(d + H)$.

The boundary conditions at the solid-liquid interfaces $z = \pm d$ to be satisfied are:

(i) The magnitude of the normal component of the stress tensor of the plate should be equal to the pressure of the liquid, that is $\sigma_{zz} = \sigma'_{zz}$

(ii) Since the liquid does not support the shear motion so, the tangential component of the stress tensor should be equal to zero, which implies $\sigma_{zx} = 0$

(iii) Couple stress tensor, μ_{zy} should vanish, that is $\mu_{zy} = 0$

(iv) Normal component of the displacement of the solid should be equal to that of the liquid, that is $w = w'_j$ where $j = 1, 2$

Imposing these above mentioned boundary conditions and using Eqs. (2.8), we get the following four equations

$$\begin{aligned}
&\mu\Big[\Big(-\frac{C_1^2}{C_2^2}(\xi^2+\alpha^2)+2\xi^2\Big)C_{11}A_1 + \Big(-\frac{C_1^2}{C_2^2}(\xi^2+\alpha^2)+2\xi^2\Big)S_1A_2 - (2\mathrm{i}\xi\beta)S_2A_3 \\
&\qquad + (2\mathrm{i}\xi\beta)C_{22}A_4 - (2\mathrm{i}\xi\gamma)S_3A_5 + (2\mathrm{i}\xi\gamma)C_3A_6\Big] - \lambda_L(\xi^2+\delta^2)A_7S_4 = 0 \\
&\mu[(-2\mathrm{i}\xi\alpha)S_1A_1 + (2\mathrm{i}\xi\alpha)C_{11}A_2 + (-\xi^2+\beta^2+l^2\xi^4+l^2\beta^4+2l^2\xi^2\beta^2)C_{22}A_3 \\
&\qquad + (-\xi^2+\beta^2+l^2\xi^4+l^2\beta^4+2l^2\xi^2\beta^2)S_2A_4 + (-\xi^2+\gamma^2+l^2\xi^4+l^2\gamma^4+2l^2\xi^2\gamma^2)C_3A_5 \\
&\qquad + (-\xi^2+\gamma^2+l^2\xi^4+l^2\gamma^4+2l^2\xi^2\gamma^2)S_3A_6] = 0 \\
&-2\eta[(\beta^3+\xi^2\beta)S_2A_3 - (\beta^3+\xi^2\beta)C_{22}A_4 + (\gamma^3+\xi^2\gamma)S_3A_5 - (\gamma^3+\xi^2\gamma)C_3A_6] = 0 \\
&-A_1\alpha S_1 + A_2\alpha C_{11} + A_3\mathrm{i}\xi C_{22} + A_4\mathrm{i}\xi S_2 + A_5\mathrm{i}\xi C_3 + A_6\mathrm{i}\xi S_3 - A_7\delta C_4 = 0
\end{aligned} \tag{2.9}$$

Here $S_1 = \sin(\alpha d)$, $S_2 = \sin(\beta d)$, $S_3 = \sin(\gamma d)$, $C_{11} = \cos(\alpha d)$, $C_{22} = \cos(\beta d)$, $C_3 = \cos(\gamma d)$, $S_4 = \sin(\delta H)$ and $C_4 = \cos(\delta H)$.

Equations (2.9) will have a non-trivial solution if the determinant of coefficients of the unknowns A_1, A_2, A_3, A_4, A_5, A_6 and A_7 vanishes. After applying this condition to the above system of equations and with a series of tedious mathematical calculations, we obtain the following secular equations for the Lamb waves in a plate loaded with an inviscid liquid layer on both sides

$$\begin{aligned}
&\pm\,\alpha\lambda_L K_\beta K_\gamma K_\delta\Big[-\beta(1+l^2K_\gamma)\frac{t_4}{t_3^{\pm 1}} + \gamma(1+l^2K_\beta)\frac{t_4}{t_2^{\pm 1}}\Big] \\
&\qquad + \beta K_\beta[(\gamma^2-\xi^2)+l^2K_\gamma^2]\mu\delta P\Big(\frac{t_1}{t_3}\Big)^{\pm 1} - \gamma K_\gamma[(\beta^2-\xi^2)+l^2K_\beta^2]\mu\delta P\Big(\frac{t_1}{t_2}\Big)^{\pm 1} \\
&\qquad = 4\alpha\beta\gamma\delta\mu\xi^2(K_\beta - K_\gamma)
\end{aligned} \tag{2.10}$$

where $K_\beta = \beta^2 + \xi^2$, $K_\gamma = \gamma^2 + \xi^2$, $K_\delta = \delta^2 + \xi^2$, $P = -(C_1^2/C_2^2)(\xi^2 + \alpha^2) + 2\xi^2$, $t_1 = S_1/C_{11}$, $t_2 = S_2/C_{22}$, $t_3 = S_3/C_3$ and $t_4 = S_4/C_4$.

Here "+" sign corresponds to skew symmetric and "−" sign refers to symmetric modes of the Lamb waves.

In the absence of the liquid layer, ($\lambda_L \to 0$), Eq. (2.10) reduces to

$$\beta K_\beta[(\gamma^2-\xi^2)+l^2K_\gamma^2]\Big(\frac{t_1}{t_3}\Big)^{\pm 1} - \gamma K_\gamma[(\beta^2-\xi^2)+l^2K_\beta^2]\Big(\frac{t_1}{t_2}\Big)^{\pm 1} = \frac{4\alpha\beta\gamma\xi^2(K_\beta - K_\gamma)}{P} \tag{2.11}$$

This equation is the same as the obtained and studied by the authors (Sharma and Kumar, 2014) for Lamb waves in an isotropic elastic plate within the couple stress theory.

3. Numerical results and discussion

To investigate the effects of characteristic length and inner microstructure on the propagation of Lamb waves, the material of the plate is assumed to have properties similar to cortical bone, so following Vavva *et al.* (2009), the material properties are Young's modulus $E = \mu(3\lambda + 2\mu)/(\lambda + \mu) = 14\,\mathrm{GPa}$, Poisson ratio $\nu = \lambda/[2(\lambda + \mu)] = 0.37$ and density $\rho = 1500\,\mathrm{kg/m^3}$, the values of bulk longitudinal and shear velocities are $C_1 = 4063\,\mathrm{m/s}$, $C_2 = 1846\,\mathrm{m/s}$, respectively. The fluid medium used is an inviscid liquid with $C_L = 1.5\cdot 10^3\,\mathrm{m/s}$ and density $\rho_L = 1000\,\mathrm{kg/m^3}$. The size of bone internal microstructure (internal cell size) ranges from 10 to 500 μm. Here, to study the impact of characteristic length, different cases of characteristic lengths l, comparable with the internal cell size h such as $l = 0.0003\,\mathrm{m}$, $l = 0.0001\,\mathrm{m}$, $l = 0.00003\,\mathrm{m}$ are considered.

Figures 2 and 3 show the phase velocity profile of Lamb waves in an elastic plate under the effect of an inviscid liquid layer on both sides for a fixed characteristic length ($l = 0.0001\,\mathrm{m}$) and fixed thickness of the liquid layer ($H = 0.02\,\mathrm{m}$). Figure 2 shows the phase velocity profiles of fundamental modes of symmetric (S0) and skew symmetric (A0) Lamb waves. The phase velocity profiles of skew symmetric Lamb waves for different modes (M = 1, M = 2 and M = 3) are shown in Fig. 3. It is observed that in the wave number range 0-2, the secular equation has only one root – these are the fundamental modes (S0 and A0) of Lamb waves. As the wave number increases, new roots start appearing for both symmetric and skew symmetric modes. The behaviour of these profiles is quite in agreement with the earlier findings. It is observed that the magnitude of phase velocity of these profiles is quite high for the lower wave number, which decreases at a steady rate and becomes asymptotic for higher wave numbers.

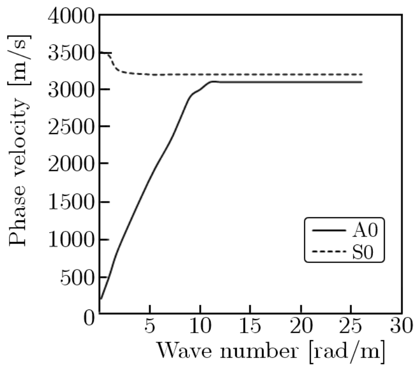

Fig. 2. Phase velocity profile of fundamental modes of Lamb waves (symmetrical (S0) and skew symmetrical (A0)) with the wave number in an elastic plate bordered with a liquid layer

Lamb waves propagating in a plate bounded by a liquid on both sides leak some of its energy into the liquid and this situation has practical importance in the field of NDT. To study the impact of loadings on Lamb waves, Figs. 4a and 4b are drawn showing phase velocity profiles of skew symmetrical Lamb waves for two different values of thickness of the liquid layer (H1 = 0.01 m and H2 = 0.02 m), and the profiles are compared with the case of no liquid

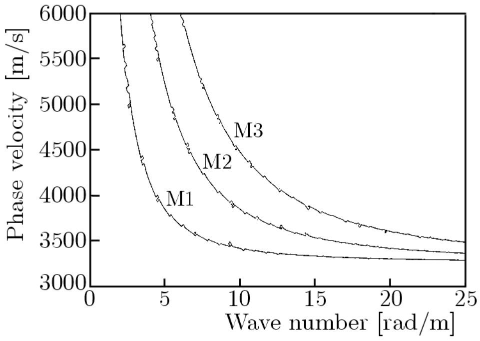

Fig. 3. Phase velocity profiles of skew symmetrical modes (M1, M2 and M3 for M = 1, 2, 3, respectively) of Lamb waves with the wave number in an elastic plate bordered with a liquid layer

loadings H0. Figure 4a is for M = 1 skew symmetrical mode and Fig. 4b is for M = 2 mode. In both cases, the characteristic length ($l = 0.0001$ m) is kept fixed. It can be seen that with an increase in the thickness of the liquid loadings, the phase velocity of the skew symmetrical Lamb waves decreases for the same wave number. As the variation in the phase velocity is very small with the increasing value of thickness of the liquid layer and it is not possible to show these variations graphically for a wide range of wave numbers, so the figures are drawn with very small variations in the wave numbers to depict the effects more precisely.

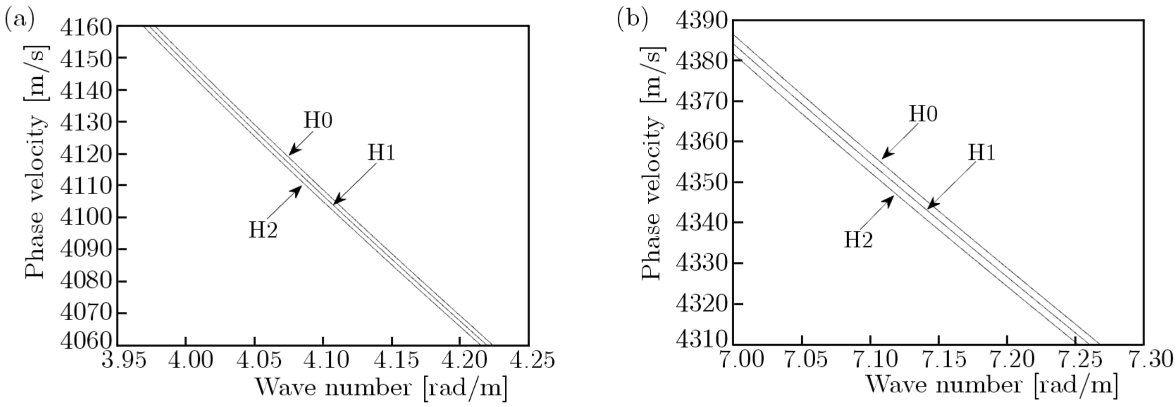

Fig. 4. Phase velocity profile of Lamb waves for skew symmetrical mode ((a) M = 1, (b) M = 2) with the wave number in an elastic plate bordered with a liquid layer of different thicknesses (H0 = 0.00 m, H1 = 0.01 m and H2 = 0.02 m)

The effect of the characteristic length parameter l, on the phase velocity profiles of skew symmetric Lamb waves are shown in Figs. 5a and 5b. The characteristic length parameter l is a microstructural parameter involved in the couple stress theory and is assumed to be of the order of internal cell size of the considered material. The material of the considered plate has properties similar to cortical bone and the internal cell size of cortical bone varies from 10 to 500 μm (Vavva *et al.*, 2009). So, here three different values of characteristic lengths are considered, for profile L1, the characteristic length is 0.00003 m, for L2 profile, the characteristic length is 0.0001 m and for L3, it is 0.0003 m. In all the three cases, the considered characteristic length of the material lies in the range of internal cell size of the material. As the problem deals with the study of microstructural effects and to observe these effects again, graphs are drawn again with a very small variation in the wave number and phase velocity of Lamb waves. Figure 5a shows the phase velocity profiles of skew symmetric Lamb waves for M = 1 mode, with three different values of the characteristic length and fixed thickness of the liquid layer (H = 0.02 m). Figure 5b shows the phase velocity profiles of skew symmetric Lamb waves for M = 2 mode, again with

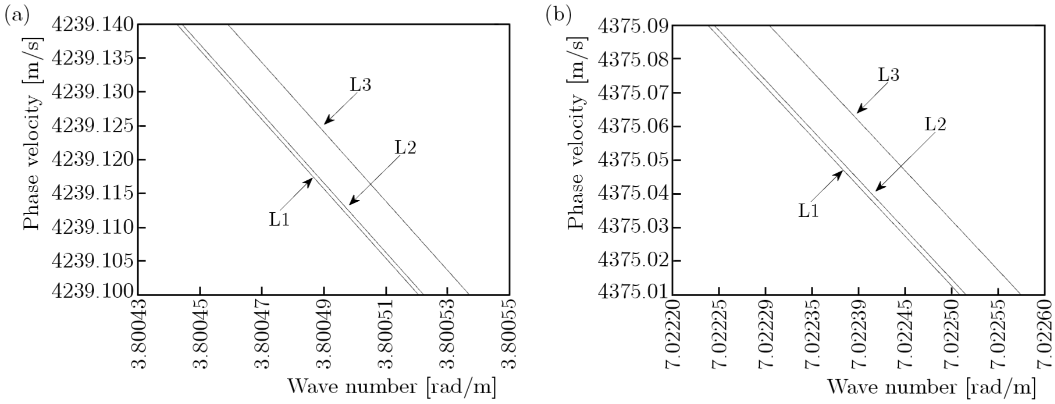

Fig. 5. Phase velocity profile of Lamb waves for skew symmetrical mode ((a) M = 1, (b) M = 2) with the wave number in an elastic plate bordered with a liquid layer of fixed thickness and different characteristic lengths L1 = 0.00003 m, L2 = 0.0001 m and L3 = 0.0003 m

the same considered values of the characteristic length and fixed thickness of the liquid layer (H = 0.02 m). From both figures, it is observed that with an increase in the characteristic length parameter l, the phase velocity of skew symmetric Lamb waves is also increasing for the same wave number.

4. Conclusion

As the physical model of the problem consists of a thin plate loaded with an inviscid liquid on both sides, it is of practical use in ultrasonic immersion testing of plates. The impact of liquid loadings is studied on the propagation of phase velocity of Lamb waves. Three different cases for thickness of the liquid loaded on both sides of the plate are considered. It is observed that with an increase in the thickness of the loadings, the phase velocity tends to decrease. The material of the plate considered is assumed to have properties similar to cortical bone (Vavva *et al.*, 2009), so it also enhances the applicability of this model in characterisation of the properties of bones loaded with different type of fluids.

To find the impact of the microstructural parameter, the problem is solved by applying the couple stress theory (Hadjesfandiari and Dargush, 2011). This theory involves only one microstructural parameter, called the characteristic length (l) and is assumed to be of the order of internal cell size of the material (Georgiadis and Velgaki, 2003; Vavva *et al.*, 2009). Here, three different values of the characteristic length are considered. They are comparable with the internal cell size of the material and their effect is studied on the phase velocity of the Lamb waves. It is observed that with an increase in the value of this parameter, the phase velocity of the Lamb wave also increases.

References

1. Akgoz B., Civalek O., 2013, Modeling and analysis of micro-sized plates resting on elastic medium using the modified couple stress theory, *Meccanica*, **48**, 863-873

2. Chen W., Li X., 2014, A new modified couple stress theory for anisotropic elasticity and microscale laminated Kirchhoff plate model, *Archive of Applied Mechanics*, **84**, 323-341

3. Cosserat E., Cosserat F., 1909, *Théorie des corps déformables (Theory of Deformable Bodies)*, A. Hermann et Fils, Paris

4. Das T.K., Sengupta P.R., Debnath L., 1991, Thermo-visco-elastic Rayleigh waves under the influence of couple stress and gravity, *International Journal of Mathematics and Mathematical Sciences*, **14**, 3, 553-560
5. Eringen A.C., 1968, Theory of micropolar elasticity, [In:] *Fracture*, Liebowitz H. (Ed.), vol. 2, Academic Press, New York, 662-729
6. Georgiadis H.G., Velgaki E.G., 2003, High-frequency Rayleigh waves in materials with microstructure and couple-stress effects, *International Journal of Solids and Structures*, **40**, 2501-2520
7. Hadjesfandiari A.R., Dargush G.F., 2011, Couple stress theory for solids, *International Journal of Solids and Structures*, **48**, 2496-2510
8. Koiter W.T., 1964, Couple stresses in the theory of elasticity, I and II, *Proceedings of the Koninklijke Nederlandse Akademie Van Wetenschappen B*, **67**, 17-44
9. Lakes R.S., 1991, Experimental micro mechanics methods for conventional and negative Poisson's ratio cellular solids as Cosserat continua, *Journal of Engineering Materials and Technology*, **113**, 148-155
10. Lakes R.S., Yoon H.S., Katz J.L., 1986, Ultrasonic wave propagation and attenuation in wet bone, *Journal Biomedical Engineering*, **8**, 143-148
11. Lamb H., 1917, On waves in an elastic plate, *Proceedings of the Royal Society of London*, 114-128
12. Mindlin R.D., 1964, Micro-structure in linear elasticity, *Archive for Rational Mechanics and Analysis*, 16, 51–78
13. Mindlin R.D., Tiersten H.F., 1962, Effects of couple-stresses in linear elasticity, *Archive for Rational Mechanics and Analysis*, **11**, 415-488
14. Nowacki W., 1974, *Micropolar Elasticity, International Center for Mechanical Sciences*, Courses and Lectures No. 151, Udine, Springer-Verlag, Wien-New York
15. Osborne M.F.M., Hart S.D., 1945, Transmission, reflection and guiding of an exponential pulse by a steel plate in water, I: theory, *Journal of the Acoustical Society of America*, **17**, 1-18
16. Ottosen N.S., Ristinmaa M., Ljung C., 2000, Rayleigh waves by the indeterminate couple-stress theory, *European Journal of Mechanics – A/Solids*, **19**, 929-947
17. Schoch V.A., 1952, Der schalldurchgang durch platten (Sound transmission in plates), *Acoustica*, **2**, 1-17
18. Sengupta P.R., Ghosh B., 1974, Effects of couple stresses on the propagation of waves in an elastic layer, *Pure and Applied Geophysic*, **112**, 331-338
19. Sharma J.N., Kumar S., 2009, Lamb waves in micropolar thermoelastic solid plates immersed in liquid with varying temperature, *Meccanica*, **44**, 305-319
20. Sharma V., Kumar S., 2014, Velocity dispersion in an elastic plate with microstructure: effects of characteristic length in a couple stress model, *Meccanica*, **49**, 1083-1090
21. Sharma J.N., Pathania V., 2003, Generalized thermoelastic Lamb waves in a plate bordered with layers of inviscid liquid, *Journal of Sound and Vibration*, **268**, 897-916
22. Toupin R.A., 1962, Elastic materials with couple-stresses, *Archive for Rational Mechanics and Analysis*, **11**, 385-414
23. Vavva M.G., Protopappas V.C., Gergidis L.N., Charalambopoulos A., Fotiadis D.I., Polyzos D., 2009, Velocity dispersion of guided waves propagating in a free gradient elastic plates: application to cortical bone, *Journal of the Acoustical Society of America*, **125**, 5, 3414-3427
24. Viktorov I.A., 1967, *Rayleigh and Lamb Waves*, Plenum Press, New York

25. Voigt W., 1887, Theoretische Studien fiber die Elastizitatsverhiltnisse der Kristalle (Theoretical studies on the elasticity relationships of crystals), *Abh Gesch Wissenschaften*, **34**

26. Wu J., Zhu Z., 1992, The propagation of Lamb waves in a plate bordered with layers of a liquid, *Journal of the Acoustical Society of America*, **91**, 861-867

27. Wu Z., Ma X., Brett P.N., Xu J., 2009, Vibration analysis of submerged rectangular microplates with distributed mass loading, *Proceedings of the Royal Society A*, **465**, 2104, 1323-1336

Manuscript received October 2, 2014; accepted for print May 10, 2015

JOURNAL OF THEORETICAL
AND APPLIED MECHANICS
53, 4, pp. 935-945, Warsaw 2015
DOI: 10.15632/jtam-pl.53.4.935

VIBRATION OF A DISCRETE-CONTINUOUS STRUCTURE UNDER MOVING LOAD WITH ONE OR TWO CONTACT POINTS

Anna Kumaniecka
Cracow University of Technology, Institute of Mathematics, Kraków, Poland
e-mail: pukumani@cyf-kr.edu.pl

Michał Prącik
Cracow University of Technology, Institute of Applied Mechanics, Kraków, Poland
e-mail: mp@sparc2.mech.pk.edu.pl

What is of particular importance in view of the development and operation of fast railway transport is the overhead system vibration excited by pantograph motion. The problems discussed in the paper are related to continuous system vibration under moving loads. Modelling the catenary-pantograph system is connected with motion of two subsystems, namely: continuous (contact wire) and discrete (pantograph). In the paper, the results of research on dynamical phenomena caused by the interaction between the pantograph and catenary are presented. The stiffness of the catenary wire is taken into account. The dynamical phenomena occurring in the system are described by a set of partial and ordinary differential equations. The solution to these equations has been obtained using approximate numerical methods.

Keywords: dynamics of pantograph, stiffness of catenary system

1. Introduction

The theoretical problem discussed in the paper is a technical problem connected with the dynamics of systems under moving loads (Bajer and Dyniewicz, 2012; Bogacz and Szolc, 1993; Fryba, 1999; Szolc, 2003). As a vibrating discrete-continuous structure, the pantograph-catenary system has been chosen for analysis.

In any high voltage electric traction system, the current needed for operating a train is collected from an overhead contact system by some form of sliding electrical contact. Such a system usually consists of a horizontal wire with which the pantograph makes continuous contact, and a catenary cable slung between the supports from which the contact wire is suspended at intervals by vertical dropper wires.

The complex behaviour of the catenary-pantograph system has been the focus of attention of many researchers for several years (Poetsch *et al.*, 1997; Wu and Brennan, 1998). Over the last sixty years, many studies of the catenary-pantograph dynamic behaviour have been undertaken (Kumaniecka and Grzyb, 2000; Kumaniecka and Nizioł, 2000; Zhang *et al.*, 2002).

In the past years, many researchers attempted to improve current collection quality in order to reduce wear and maintenance costs of both the overhead line and pantograph. Numerous studies on rail vehicles proved that the processes describing their dynamic state have a complex and non-periodic character (Poetsch *et al.*, 1997; Kumaniecka, 2007). To improve the pantograph-catenary interface, it is essential to understand better the complex behaviour of this couple. The pantograph-catenary interaction at high speed is the critical factor for reliability and safety of high speed railways. The large amplitudes of transversal vibration of the messenger and contact wires can result in pantograph strip wear, loss of contact or disturbance of mutual interaction.

With an increase in the train speed, the catenary-pantograph system with its dynamic behaviour proved to be a very important component for new train systems required to run at higher speed. This speed can be limited by the power supply through the overhead catenary system. The key point that describes the efficiency of the current collection is the contact force. The zero value of this force induces the brake in the current collection, but too large value can result in wear of the contact wire and pantograph strips.

The aim of the paper is to obtain a better understanding of the pantograph-catenary system dynamics. The emphasis of studies is placed on the description of contact loss and proper description of contact wire stiffness. A relatively simple analytical model presented in the paper is appropriate to gain physical insight into the pantograph-catenary system.

In the paper, an analytical method for calculating the response of a catenary to a uniformly moving pantograph is presented. To the authors' knowledge, the loss of contact of such a system has not been investigated so far.

The paper is organized in five Sections. Following Introduction 1, the models of the catenary--pantograph system including the contact wire, messenger wire, droppers, supporting towers and the pantograph itself are described in Section 2. In Section 3 an analytical method for calculating the response of a catenary to a uniformly moving pantograph is presented. The simulation results are given in Section 4. Final concluding remarks are formulated in Section 5.

2. Modelling of the catenary-pantograph system

The presented models belong to the class of continuous systems excited by a uniformly moving load. In the literature, many physical and a lot of different analytical models of the catenary--pantograph system have been proposed. Both the contact and carrying wire are one-dimensional systems. The contact and carrying cables have been modelled by infinite or non-infinite homogenous strings or Bernoulli-Euler beams. The pantograph has been modelled by an oscillator with two or four degrees of freedom. Such systems were studied in the past by a number of researchers employing different methods. A review paper describing the pantograph-catenary systems was presented by Poetsch *et al.* (1997) and by Kumaniecka (2007). The dynamic interaction between a discrete oscillator with four degrees of freedom and a continuous beam was also studied by Kumaniecka and Prącik (2011).

The simplified model of the catenary with one contact point introduced in the paper, shown in Fig. 1, is composed of two parallel infinitely long homogenous beams (the contact and carrying cables) connected by lumped elements (suspension rods), which are positioned equidistantly along the beams. The upper beam (carrying cable) is fixed at periodically spaced elastic supports. The lower beam (contact wire) is suspended from the upper beam by visco-elastic elements. These elements are used as a model of suspension rods. They are periodically placed at points along the beams. It is assumed that the distance between the supports of carrying cable is equal l and between the droppers $2l_w$. In the adopted model, the bending stiffness of the contact wire is taken into account (Wu and Brennan, 1999; Kumaniecka and Prącik, 2011).

The system in question is subjected to a concentrated force (model of pantograph), which is applied to the lower beam. This load moves along the lower beam at a constant velocity v.

Between the contact wire and pantograph there also appears the friction force. In the presented study, the friction force is neglected.

The physical model of the catenary with two contact points is presented in Fig. 2.

The mathematical model for a physical model of the catenary system adopted in this paper and shown in Fig. 2, was discussed in detail and presented in the monograph by Kumaniecka (2007).

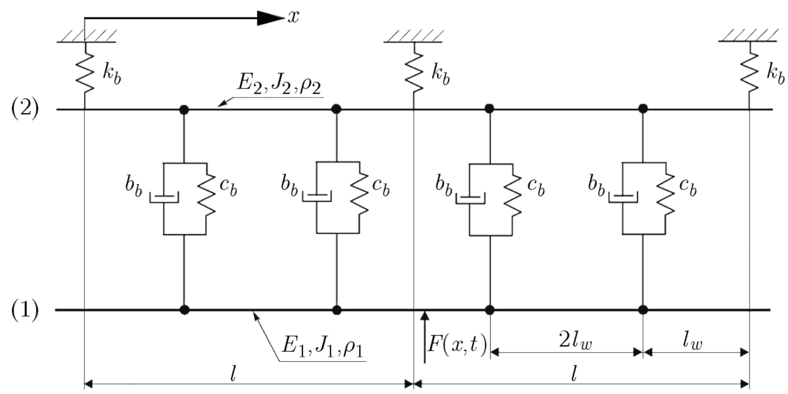

Fig. 1. Physical model of catenary with one contact point

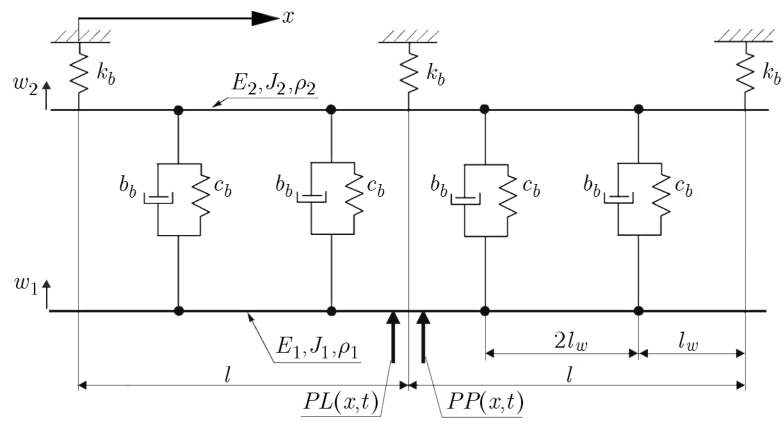

Fig. 2. Physical model of catenary with two contact points

Motion of the catenary in the vertical plane is governed by equations

$$\begin{aligned} &E_1J_1\frac{\partial^4 w_1}{\partial x^4} - N_1\frac{\partial^2 w_1}{\partial x^2} + \rho_1\frac{\partial^2 w_1}{\partial t^2} - p + p_F - p_{m1} = 0 \\ &E_2J_2\frac{\partial^4 w_2}{\partial x^4} - N_2\frac{\partial^2 w_2}{\partial x^2} + \rho_2\frac{\partial^2 w_2}{\partial t^2} + p - p_{m2} = 0 \end{aligned} \tag{2.1}$$

where the following notation is used: E_1, E_2 – Young's modulus of lower and upper beam, respectively, J_i – cross-sectional moment of inertia ($i = 1,2$), N_i – tensile force in the beams, ρ_i – mass density, $w_i(x,t)$ – transversal displacements, x – spatial coordinate measured along the non-deformed axis of beams, t – time. The functions $w_1(x,t)$ and $w_2(x,t)$ describe the lower and upper beam transversal displacements, respectively.

The loads $p(x,t)$ acting on the beams and caused by internal forces in the springs and damping elements are treated as continuous. They can be expressed in the form

$$p(x,t) = \sum_{(n)}\{c_b[w_2(x,t) - w_1(x,t)] + b_b[\dot{w}_2(x,t) - \dot{w}_1(x,t)]\}\delta(x - x_n) \tag{2.2}$$

where: c_b is the coefficient of spring elasticity, b_b – damping coefficient, x_n – coordinates of droppers spacing (concentrated masses), $x_n = 2l_w(2s-1)$, $s \in N$, $2l_w$ – distance between the droppers, δ – Dirac's function.

The interaction force between the pantograph and contact wire p_F can be described by the term

$$p_F(x,t) = F(t)\delta(x - vt) \tag{2.3}$$

The reaction force p_{mi} $(i = 1, 2)$ that comes from concentrated masses m spaced on the lower and upper beams acting at points x_n can be treated as distributed and written in the form:
— for the lower beam

$$p_{m1}(x,t) = \sum_{(n)} m\ddot{w}_1(x,t)\delta(x - x_n) \tag{2.4}$$

— for the upper beam

$$p_{m2}(x,t) = \sum_{(n)} m\ddot{w}_2(x,t)\delta(x - x_n) \tag{2.5}$$

The boundary and initial conditions adopted for numerical simulation have been based on the assumed vibration model of a linear system (data from identification research).

In the present paper, the pantograph has been modelled as an oscillator with four degrees of freedom. The model refers to a real system designed by engineers from Schunk Wien GmbH. The basic pantograph is the standard WBL-85/3kV. The collector strips are represented by masses m1L and m1P, the equivalent masses of the frames are denoted by m_2 and m_3. The masses are connected by springs c_{11} and c_{22} to provide a nominally constant uplift force. The aerodynamic force is taken into account (Bacciolone *et al.*, 2005). The physical model of the pantograph investigated in our studies is shown in Fig. 3.

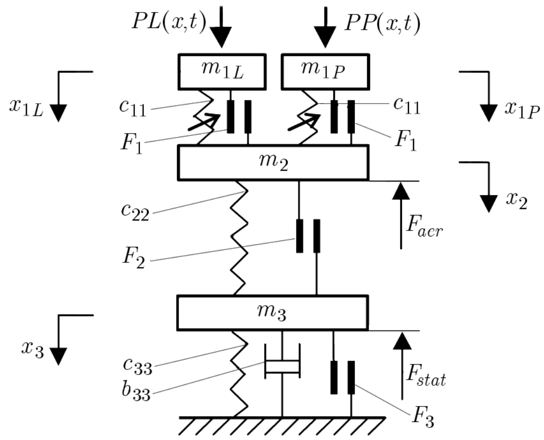

Fig. 3. Model of pantograph

The mathematical model for a physical model of the pantograph adopted in this paper and shown in Fig. 3 was discussed in detail and presented in the monograph by Kumaniecka (2007). In many real pantograph systems, the springs are guided in telescopic sliders, which gives reasons to apply dry friction elements in the physical model. The structure of the simulation model has been based on the formal notation of motion in form of ordinary differential equations.

Motion of the pantograph in the vertical plane is governed by equations

$$\begin{aligned} m_{1L}\ddot{x}_{1L} &= m_{1L}g - |F_1|\,\mathrm{sgn}\,(\dot{x}_{1L} - \dot{x}_2) - c_{11}(x_{1L} - x_2) + PL(x,t) \\ m_{1P}\ddot{x}_{1P} &= m_{1P}g - |F_1|\,\mathrm{sgn}\,(\dot{x}_{1P} - \dot{x}_2) - c_{11}(x_{1P} - x_2) + PP(x,t) \\ m_2\ddot{x}_2 &= m_2g - |F_2|\,\mathrm{sgn}\,(\dot{x}_2 - \dot{x}_3) + |F_1|[\,\mathrm{sgn}\,(\dot{x}_{1P} - \dot{x}_2) + \,\mathrm{sgn}\,(\dot{x}_{1L} - \dot{x}_2)] \\ &\quad - c_{22}(x_2 - x_3) + c_{11}(x_{1P} - x_2) + c_{11}(x_{1L} - x_2) - F_{aer} \\ m_3\ddot{x}_3 &= m_3g - c_{33}x_3 - b_{33}\dot{x}_3 - |F_3|\,\mathrm{sgn}\,(\dot{x}_3) - F_{stat} + c_{22}(x_2 - x_3) + |F_2|\,\mathrm{sgn}\,(\dot{x}_2 - \dot{x}_3) \end{aligned} \tag{2.6}$$

where: x_1, x_2, x_3, $\dot{x}_1, \dot{x}_2, \dot{x}_3$, m_1, m_2, m_3 are displacements, velocities and masses of the elements, respectively, F_1, F_2, F_3 – friction forces, F_{aer}, F_{stat} – aerodynamic and static forces,

$PL(x,t), PP(x,t)$ – excitation forces, interaction forces between the pantograph and contact wire.

The displacement of the pan-head is the main factor for dynamic performance of the pantograph, and it is related to the contact forces directly.

3. Analytical model of the system vibration

The catenary motion can be described by means of partial differential equations (2.1), which govern small vertical vibrations of each beam in the vicinity of their equilibrium state, induced by the transversal force moving along the lower beam. Some details are presented in the monograph by Kumaniecka (2007) and in the paper by Kumaniecka and Prącik (2011). The mathematical model for a physical model of the pantograph was discussed by Prącik and Furmanik (2000).

The interaction between the pantograph and contact wire is limited to a set of two parallel forces

$$PL(x,t)\delta(x-vt) \qquad PP(x,t)\delta(x-vt+x_{LP}) \tag{3.1}$$

In the above equation, x denotes the spatial horizontal co-ordinate, t time, x_{LP} is the distance between the shoes.

In the case of one contact point, the function describing the contact force can be expressed as

$$F(x,t) = PL(x,t) + PP(x,t) \tag{3.2}$$

According to the results obtained by the authors (2011) and others (Wu and Brennan, 1999), the forces $PL(x,t)$, $PP(x,t)$ can be connected with harmonic changes of catenary stiffness and given in the form

$$\begin{aligned}
PL(x,t) &= k_0 \begin{cases} \Big[1-\alpha\cos\Big(\dfrac{2\pi v}{L}t\Big)\Big](x_{1L0}-x_{1L}) & \text{for} \quad x_{1L0} > x_{1L} \\ 0 & \text{for} \quad x_{1L0} \leqslant x_{1L} \end{cases} \\
PP(x,t) &= k_0 \begin{cases} \Big[1-\alpha\cos\Big(\dfrac{2\pi}{L}(vt+x_{LP})\Big)\Big](x_{1P0}-x_{1P}) & \text{for} \quad x_{1P0} > x_{1P} \\ 0 & \text{for} \quad x_{1P0} \leqslant x_{1P} \end{cases}
\end{aligned} \tag{3.3}$$

In equations (3.3), the following notation is used: x_{1L}, x_{1P} denote vertical displacements of the pantograph contact shoes, x_{1L0}, x_{1P0} – vertical displacements of two points on the wire that are in contact with masses m_{1L} and m_{1P}, respectively, k_0, α – are stiffness coefficients (Wu and Brennan, 1999), given by formulae

$$k_0 = \frac{k_{max}+k_{min}}{2} \qquad \alpha = \frac{k_{max}-k_{min}}{k_{max}+k_{min}} \tag{3.4}$$

where L is the length of one span and k_{max}, k_{min} are the largest and the smallest stiffness values in the span, respectively.

When the model with two contact points is investigated, the contact forces are written as

$$\begin{aligned}
PL(x,t) &= k_0 \begin{cases} \Big[1-\alpha\cos\Big(\frac{2\pi v}{l}t\Big)\Big][x_{1L0}-w_1(x,t)] & \text{for} \quad x_{1L0} > w_1(x,t) \\ 0 & \text{for} \quad x_{1L0} \leqslant w_1(x,t) \end{cases} \\
PP(x,t) &= k_0 \begin{cases} \Big[1-\alpha\cos\Big(\frac{2\pi}{l}(vt+x_{LP})\Big)\Big][x_{1P0}-w_1(x+x_{LP},t)] & \\ & \text{for} \quad x_{1P0} > w_1(x+x_{LP},t) \\ 0 & \text{for} \quad x_{1P0} \leqslant w_1(x+x_{LP},t) \end{cases}
\end{aligned} \tag{3.5}$$

where $w_1(x,t)$ is the transversal displacement of the lower beam, x_{1L}, x_{1P} are coordinates of strips motion (see Fig. 3), $x_{1L} \equiv w_1(x,t)\delta(x-vt)$ and $x_{1P} \equiv w_1(x+x_{LP},t)\delta(x-vt+x_{LP})$.

The equations of catenary motion model (2.1) are presented in the monograph by Kumaniecka (2007). After substituting relations (3.3) or (3.5), in the case of one or two contact points, respectively, to the equations of motion, they include some parameters associated with stiffness of the contact wire k_0, α.

In the case of one contact point, the solutions to set of equations (2.1) have been taken in the form of waves

$$\begin{aligned} w_1(x,t) &= \sum_{p_1}\sum_{r_1} A_{r_1}\frac{\sin\frac{x-vt}{p_1 l_w}}{\frac{x-vt}{p_1 l_w}}\sin(\omega_{r_1}t-\varphi_{r_1}) \\ w_2(x,t) &= \sum_{p_2}\sum_{r_2} A_{r_2}\frac{\sin\frac{x-vt}{p_2 l_w}}{\frac{x-vt}{p_2 l_w}}\sin(\omega_{r_2}t-\varphi_{r_2}) \end{aligned} \tag{3.6}$$

where p_i are associated with the moving modes and r_i with the standing modes for $i = 1, 2$, and the coefficients A_{r_1}, A_{r_2} could be determined numerically using a collocation method.

To solve equations of motion (2.1) and (2.6) for two contact points, it is necessary to employ another expression for functions which describe transversal displacements of the lower beam

$$w_1(x,t) = \sum_{p_1}\sum_{r_1} A_{r1}\frac{\sin\frac{x-vt}{p_1 l_w}}{\frac{x-vt}{p_1 l_w}}\sin(\omega_{r_1}t-\varphi_{r_1}) + \sum_{p_1}\sum_{r_1} B_{r1}\frac{\sin\frac{x+x_{LP}-vt}{p_1 l_w}}{\frac{x+x_{LP}-vt}{p_1 l_w}}\sin(\omega_{r_1}t-\varphi_{r_1}) \tag{3.7}$$

4. Numerical analysis

On the basis of the given mathematical model, a simulation program applying the package VisSim Analyze ver. 3.0 has been built. Numerical simulations have been carried out for different data sets.

The numerical calculations have been done for the following parameters of the system

$m_{1L} = m_{1P} = 7.93\,\mathrm{kg}$	$m_2 = 8.73\,\mathrm{kg}$	$m_3 = 10.15\,\mathrm{kg}$	
$F_1 = 2.0\,\mathrm{N}$	$F_2 = F_3 = 2.5\,\mathrm{N}$	$F_{aer} = 30.0\,\mathrm{N}$	$F_{stat} = 600\,\mathrm{N}$
$F_{aer} = 30\,\mathrm{N}$	$c_3 = 60\,\mathrm{Ns/m}$	$x_{LP} = 1.0\,\mathrm{m}$	

The parameters of the system correspond to the parameters of the real overhead power lines for high speed trains (data set for pantograph WBL 85-3 kV/PKP).

The block schemes of simulation of mass displacements and contact forces of the pantograph model at $F_{stat} = 600\,\mathrm{N}$ and 500 N, $F_{aer} = 30\,\mathrm{N}$ are presented in Figs. 4 and 5.

To investigate the phenomena of contact loss in the overhead system, numerical simulations for the contact force less than the limit force were carried out by Kumaniecka and Prącik (2011).

In Fig. 6, the loss of contact between the pantograph and catenary is illustrated.

The results of simulations of the variability of contact forces of the pantograph (with two contact points), when the vertical displacement amplitude between the contact points spaced by 1 m, is equal 0.03 m, are presented in Fig. 7. The simulations have been done for velocity $v = 55.55\,\mathrm{m/s}$ using the blockscheme of simulation similar to that presented in Fig. 4 but utilizing a different expression for $w_1(x,t)$ (respectively to equation (3.7)).

Based on the results of simulations, we can conclude that the pantograph with two contact strips guarantees better interaction (strips are detached convertible).

The analysis of the simulation results (see Fig. 7) shows that the response of the system in question is not harmonic, it consists of standing and moving modes. To conclude, it can be

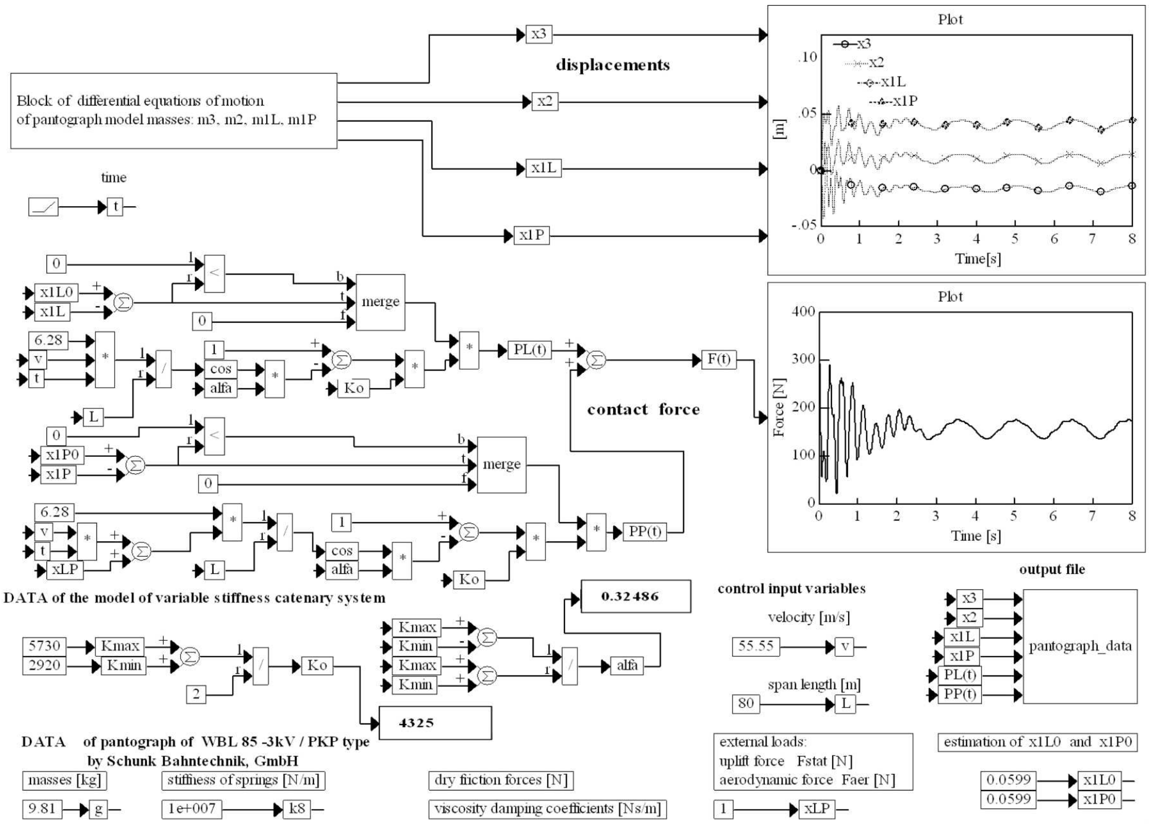

Fig. 4. Block scheme of simulation of mass displacements and contact forces of the pantograph model at $F_{stat} = 600\,\mathrm{N}$, $F_{aer} = 30\,\mathrm{N}$; in the case of one contact point, when $x_{1L} \cong x_{1P}$

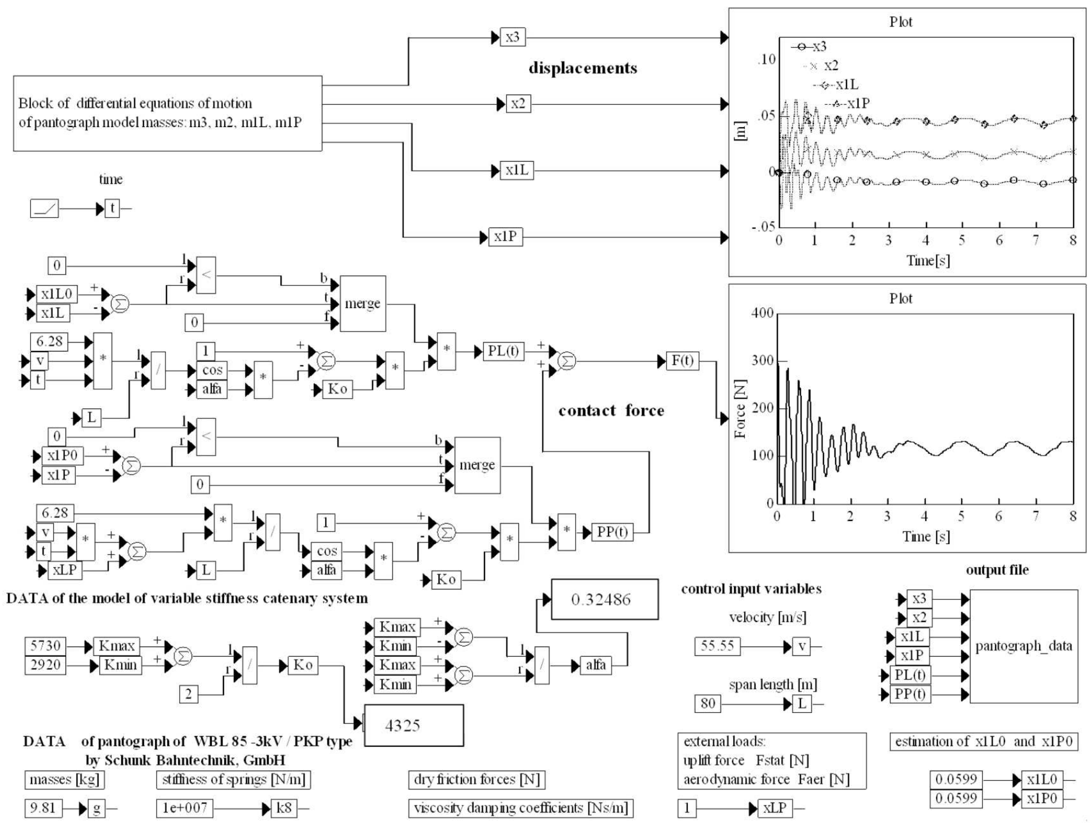

Fig. 5. Block scheme of simulation of contact forces and contact loss at $F_{stat} = 500\,\mathrm{N}$, $F_{aer} = 30\,\mathrm{N}$; in the case of one contact point, when $x_{1L} \cong x_{1P}$

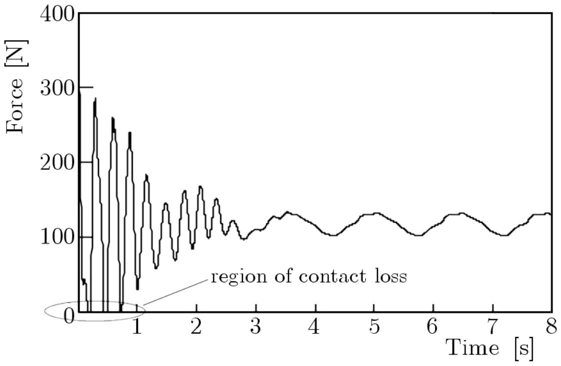

Fig. 6. Contact force for uplift force $F_{stat} = 500\,\mathrm{N}$; loss of contact in the case of one contact point

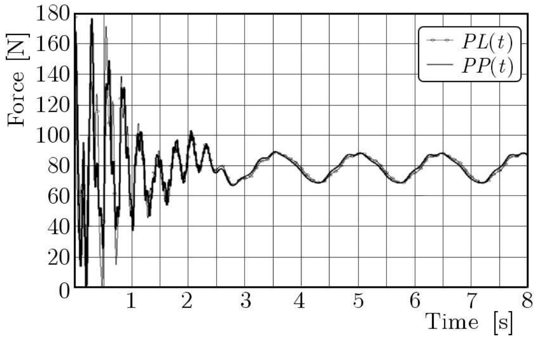

Fig. 7. Variability of contact forces of the pantograph with two contact points

stated that the motion of the contact wire has a wavy character. The calculations have confirmed that the travelling force is a source of waves propagating leftwards and rightwards at different frequencies (Snamina, 2003; Bogacz and Frischmuth, 2013).

The domination of lower frequency modes is visible (see Fig. 8). The same effect is visible in the case of a pantograph with one contact point. For a two contact points pantograph, the modal damping is more effective.

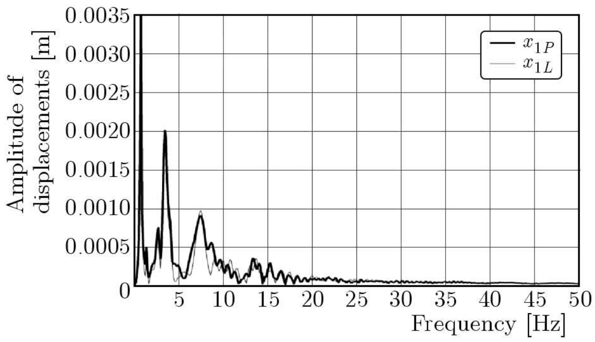

Fig. 8. Spectrum FFT of vibration displacements

In Figs. 9 and 10, some results of the lower beam vibration in the case of one or two contact points are shown. As can be seen in Fig. 10, the critical amplitude value of vibration displacement, critical as referred to displacement values $x_{1L0} = x_{1P0} = 0.03\,\mathrm{m}$ adopted as an example (for the data set taken for numerical simulations at the velocity $v = 55.55\,\mathrm{m/s}$), has been exceeded.

The examples of the results presented above have been obtained with the catenary stiffness parameters and the velocity of pantograph motion $v = 55.55\,\mathrm{m/s}$. At higher velocities taken for

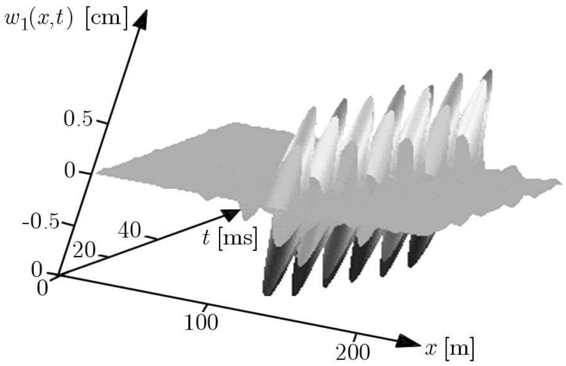

Fig. 9. Results of simulations of the beam displacement function $w_1(x,t)$ for $p_1 = 1$, $r_1 = 1, 2$; in the case of one contact point

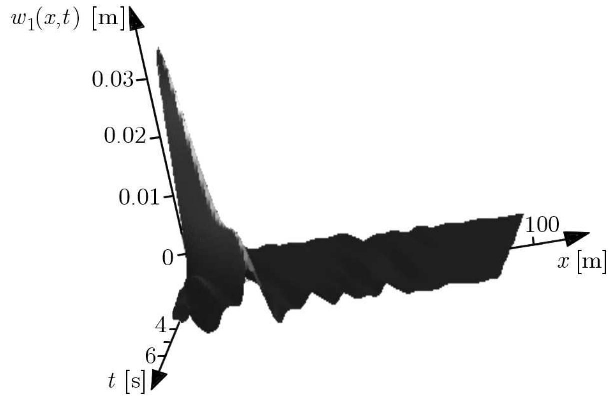

Fig. 10. Simulations of lower beam vibration of the catenary model in the case of two contact points

simulations and the analysis of subsequent excited mode vibration frequencies of the catenary in 3D graphs of displacements. there can be seen a more marked interaction in the case of two contact points pantograph. Also two maxima and minima of waves moving parallel, positioned at an angle to the time axis, are visible.

5. Final conclusions

The state-of-the-art of the theoretical and experimental investigations indicates the need for continuation of the research to improve the modelling of the catenary-pantograph system. In the present paper, a simplified model of the pantograph and catenary has been proposed. The equations of motion are based on a beam model with one or two concentrated varying forces moving along the contact wire at a constant velocity. The structure of the simulation model is based on a formal notation of motion in form of partial and ordinary differential equations. For the simulation, software package VisSim has been applied. The paper has discussed the application of the stiffness formula to the analysis of pantograph-catenary interaction.

On the basis of the results of simulations of the lower beam displacements (Figs. 9 and 10) the following conclusions can be drawn:

- The wave sequence is associated with the pantograph motion (the compound of three modes of moving waves and three standing ones). The frontal maximum and reverse minimum of the displacement are visible. The ratio of the absolute value of the maximum to that of the minimum is equal to 9.

- Damping of the displacement amplitude excited in the lower beam is time and space variable. For example, a reduction of the beam displacement maximum by about 20 dB occurs after approximately 0.6 s, in the case of analysis on the span of length of about 100 m.

The results of analysis of the simulation performed on the adopted model of mutual interaction between the pantograph and catenary have shown the domination of lower frequencies components in the spectrum of the lower beam vibration displacements, similarly to the case of one contact point system (Fig. 8). This fact has been also indicated by others scientists (Poetsch *et al.*, 1997; Szolc, 2003). On the basis of the simulation results of the lower beam displacements, it can be concluded that there is a wave sequence associated with the pantograph motion. Damping of the lower beam vibrations, caused by the moving pantograph, is variable in time and space. The described phenomena should be taken into account in real applications in high speed railways.

References

1. Bajer C.I., Dyniewicz B., 2012, *Numerical Analysis of Vibrations of Structures under Moving Inertial Load*, Springer
2. Bocciolone M., Collina A., Resta F., Rocchi D., Tosi A., 2005, Pantograph aerodynamics effects on the pantograph-catenary interaction, *Proceedings of XIX IAVSD Symposium*, Millano, paper No. 55
3. Bogacz R., Frischmuth K., 2013, Wave propagation in catenaries subjected to moving loads, *ICEDyn/2013/Sesimbro*, K07, 8p
4. Bogacz R., Szolc T., 1993, Analysis of dynamic interaction between the continuous string and moving oscillator, *Engineering Transactions*, **41**, 3/4, 361-380
5. Fryba L., 1999, *Vibration of Solid and Structure Under Moving Loads*, Telford, London
6. Kumaniecka A., 2007, Methods of analysis of discrete-continuous systems vibrations and their applications to the railway transport problems, *Monograph, Mechanics*, **352**, Cracow
7. Kumaniecka A., Grzyb A., 2000, On dynamics of catenary-pantograph system modelled as discrete-continuous system, *Machine Dynamics Problems*, **24**, 1, 105-119
8. Kumaniecka A., Nizioł J., 2000, Dynamical phenomena in catenary-pantograph system, *Scientific Issue of ATR Bydgoszcz, Mechanics*, **228**, 47, 15-26
9. Kumaniecka A., Prącik M., 2003, Modelling and identification of catenary-pantograph system, *Journal of Theoretical and Applied Mechanics*, **41**, 4, 887-901
10. Kumaniecka A., Prącik M., 2011, Modelling of the catenary-pantograph system, *Machine Dynamics Research*, **35**, 4, 74-91
11. Kumaniecka A., Snamina J., 2005, Transient response of the pantograph-catenary system to impulsive loads, *Machine Dynamics Problems*, **29**, 2, 91-105
12. Poetsch G., Evan J., Meisinger R., Kortum W., Baldauf W., Veitl A., Wallaschek J., 1997, Pantograph/catenary dynamics and control, *Vehicle System Dynamics*, **28**, 159-195
13. Prącik M., Furmanik J., 2000, Problems of modelling and simulation of catenary and pantograph cooperation, *Proceedings of VII-th Workshop PTSK*, Warsaw, **7**, 242-250
14. Snamina J., 2003, Mechanical wave phenomena in overhead transmission lines, *Monograph, Mechanics*, **287**, Cracow
15. Szolc T., 2003, Dynamic analysis of complex discrete-continuous mechanical systems, Polish Academy of Sciences – IFTR Reports, 2/2003, D.Sc. dissertation

16. Wu T.X., Brennan M.J., 1998, Basic analytical study of pantograph-catenary system dynamics, *Vehicle System Dynamics*, **30**, 443-456
17. Wu T.X., Brennan M.J., 1999, Dynamic stiffness of a railway overhead wire system and its effect on pantograph-catenary system dynamics, *Journal of Sound and Vibration*, **219**, 483-502
18. Zhang W., Mei G., Wu X., Shen Z., 2002, Hybrid simulation of dynamics for the pantograph--catenary system, *Vehicle System Dynamics*, **38**, 6, 393-414

Manuscript received November 29, 2013; accepted for print May 11, 2015

JOURNAL OF THEORETICAL
AND APPLIED MECHANICS
53, 4, pp. 947-957, Warsaw 2015
DOI: 10.15632/jtam-pl.53.4.947

FLEXURAL VIBRATION OF COUPLED DOUBLE-WALLED CARBON NANOTUBES CONVEYING FLUID UNDER THERMO-MAGNETIC FIELDS BASED ON STRAIN GRADIENT THEORY

Ali Ghorbanpour Arani, Pedram Dashti, Saeed Amir, Mohsen Yousefi

Faculty of Mechanical Engineering, Institute of Nanoscience and Nanotechnology, University of Kashan, Kashan, Iran

e-mail: aghorban@kashanu.ac.ir; pedi_dashti@yahoo.com; samir@kashanu.ac.ir; mohsen_r.yoosefi@yahoo.com

The flexural vibration stability of a coupled double-walled viscoelastic carbon nanotube conveying a fluid based on the Timoshenko beam (TB) model is investigated. The coupled system is surrounded by an elastic medium which is simulated as Pasternak foundation. Van der Waals (vdW) forces between the inner and outer CNTs are taken into account based on the Lenard-Jones model. Using small scale theories, Hamilton's principle and applying two dimensional (2D) magnetic field higher order governing equations are derived. The differential quadrature method (DQM) is applied to solve partial differential equations and investigate natural frequency of the system. The effects of viscoelastic constant, magnetic field with variable magnitudes and surface stresses on natural frequency of the structure are demonstrated in this study.

Keywords: flexural vibration, conveying fluid, coupled-system, thermo-magnetic fields, viscoelasticity

1. Introduction

Since Iijima (1991) discovered Carbon nanotubes (CNTs) many articles have been published in different fields of physics and engineering, which were focused on the CNTs and their applications. For example Ke and Wang (2011) demonstrated the influence of the length scale parameter of modified couple stress theory (MCST) on natural frequency of the double-walled Carbon nanotube (DWCNT). Pradhan and Mandal (2013) investigated the effects of environmental temperature changes on buckling, bending and vibrational stability of the CNT embedded by pinned boundary conditions. Kong *et al.* (2009) illustrated the effects of strain gradient theory (SGT) on the static, dynamic and free vibration response of a microstructure including CNTs. Kiani (2014) presented a single-walled Carbon nanotube (SWCNT) structure introduced to a 3D magnetic field. He investigated the effects of the magnetic field on longitudinal, transverse and lateral frequencies of the structure. According to his results, longitudinal magnetic field was more effective than the transverse one. Lei *et al.* (2013) investigated vibration characteristics of nonlocal viscoelastic nanobeams using the Kelvin-Voigt viscoelastic model based on TB theory. They discussed the effects of the Kelvin-Voigt coefficient, nonlocal constant, external damping ratio, and beam length-to-diameter ratio on natural frequencies of the carbon nanotubes. Ansari *et al.* (2014) illustrated nonlinear free vibration of a TB with different boundary conditions. They used the Gurtin-Murdoch continuum elasticity model to obtain equilibrium equations which were affected by surface stress layers. According to their results, the effects of rigidity of the surface layers and surface residual stress on natural frequency were not neglegible. Lei *et al.* (2012) illustrated the effects of surface elasticity modulus, residual surface stress, nonlocal parameter and aspect ratio on the transverse natural frequency. Xu *et al.* (2010) presented the equilibrium equations of a pipe conveying fluid with the pined-pined boundary condition in order to investigate the effects of the fluid flow velocity on the natural frequency. The results were obtained using Galerkin's method and a complex mode approach. Ghorbanpour Arani *et al.* (2014) presented a mathematical model of a coupled viscoelastic CNT conveying fluid flow based on Euler-Bernoulli beam theory affected by Visco-Pasternak foundation, nonlocal small scale theory, surface stresses and a longitudinal magnetic field. They depicted the effects of surface stresses, viscoelastic constant, nonlocal small scale coefficient and the magnetic field on natural frequency of the system. Khosrozadeh and Hajabasi (2012) investigated the natural frequency of a DWCNT including nonlinear vdW interaction and simply supported, fixed or free boundary conditions. The results revealed that the influence of nonlinear components of vdW forces on natural longitudinal frequency was neglected.

Shen and Zhang (2011) presented post-buckling, nonlinear bending and nonlinear vibration analysis of a nanoscale structure based on nonlocal small scale theory. The system including a thermo-elastic CNT rested on an elastic foundation. The effects of the nonlocal parameter and temperature changes on natural frequency, static bending and buckling load were demonstrated in their work. Ghorbanpour Arani and Amir (2013) investigated free vibration analysis of a coupled-Boron nitride nanotube (BNNT) structure affected by electro-thermal fields. The displacement field and strain-stress relation were based on Euler-Bernoulli beam theory and strain gradient theory, respectively. The effects of fluid velocity, aspect ratio and temperature changes on natural frequencies were demonstrated in their results.

In this study, a double-bonded DWCNT conveying viscous fluid flow is presented. The viscoelastic structure is affected by a surface stress layer, 2D magnetic field, vdW interaction and Pasternak foundation loads. The CNTs are based on Timoshenko beam theory, and the governing equations will be obtained using Hamilton's principle. DQM is used to solve the partial differential equations and investigate natural frequency of the system. Finally, the effects of viscoelastic constant, small scale coefficients, surface stresses and the magnetic field on the natural frequency of the structure are presented in this paper.

2. Governing equations

2.1. TB theory

Figure 1 demonstrates a coupled-structure made of carbon nanotubes based on TB theory in which L is length of the tubes and R and h are outer radius and thickness of the CNTs, respectively. The effects of zigzag graphene sheet rolling procedure are considered in this study. In the zigzag rolling procedure, the radius of CNT is obtained by $R = 0.142p\sqrt{3}/2\pi$ nm in which P denotes the numbers of carbon atoms (Shen and Zhang, 2011). Since the displacement field is based on Timoshenko beam theory, Eq. (2.1) demonstrates strain-displacement relation of TB theory

$$\varepsilon_{xxij} = \frac{\partial U_{ij}(x,t)}{\partial x} + z\frac{\partial \Psi_{ij}(x,t)}{\partial x} \qquad \gamma_{xzij} = 2\varepsilon_{xzij} = \frac{\partial W_{ij}(x,t)}{\partial x} + \Psi_{ij}(x,t) \tag{2.1}$$

where the subscript $i = 1, 2$ indicate the number of upper and lower nanotubes, respectively, $j = 1, 2$ indicate the inner and outer tubes, respectively, and $\Psi_{ij}(x,t)$ is rotation of cross-section of the nanotubes.

2.2. Surface stress effect

Influence of the surface effect on stability of nano or microstructures cannot be ignored because in these structures the surface-to-bulk ratio will increase. An appropriate theoretical notion is offered by Gurtin-Murdoch. It is based on the continuum mechanical model including

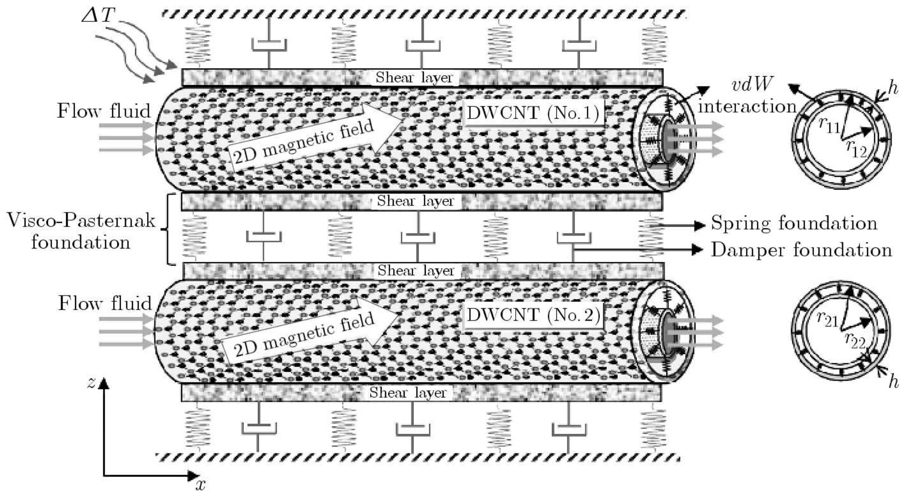

Fig. 1. Schematic of a coupled CNT's deformed element based on the TB model conveying fluid under two dimensional magnetic field

surface stress effects which is well known as the Gurtin-Murdoch model (Ansari *et al.*, 2014; Lu *et al.*, 2006). Mechanical stresses regarding the TB theory are

$$T^s_{xxij} = (\lambda^s + 2\mu^s)\varepsilon_{xxij} + \tau^s \qquad T^s_{xzij} = \tau^s \frac{\partial W_{ij}}{\partial x} \tag{2.2}$$

where τ^s and δ_{nm} are the residual surface stress and Kronecker tensor, respectively, and λ^s and μ^s are surface Lame constants. In this study, we consider that the surface stresses on the layers satisfy the equilibrium relation so T^s_{zzij} cannot be neglected (Lei *et al.*, 2012; Lu *et al.*, 2006), thus the components of stress tensor for the bulk of nanotube can be shown in Eq. $(2.3)_1$ (Ansari *et al.*, 2014; Lu *et al.*, 2006)

$$\begin{aligned} T_{xxij} &= E^*\varepsilon_{xx} + \frac{\nu}{1-\nu}\sigma_{zz} = E^*\Big(\frac{\partial U_{ij}}{\partial x} + z\frac{\partial \Psi_{ij}}{\partial x}\Big) + \frac{2z\nu}{h(1-\nu)}\Big(\tau^S\frac{\partial^2 W_{ij}}{\partial x^2} - \rho^S\frac{\partial^2 W_{ij}}{\partial t^2}\Big) \\ T_{xzij} &= G\kappa_S\gamma_{xzij} = G^* k_s\Big(\frac{\partial W_{ij}}{\partial x} + \Psi_{ij}\Big) \end{aligned} \tag{2.3}$$

where ρ^s is density of the surface layers. $E^* = E(1 + g\partial/\partial t)$ and $G^* = G(1 + g\partial/\partial t)$ are viscoelastic parameters of the CNTs based on the Kelvin-Voigt model (Lei *et al.*, 2013). E and G are elasticity and shear modulus of the CNTs, respectively, which are functions of temperature according to Table 1.

2.3. Hamilton's principle

To develop a comprehensive model for coupled DWCNT, we use extended Hamilton's principle which can be expressed as follows (Ghorbanpour Arani and Amir, 2013)

$$\int_{t_0}^{t_1} \delta\Pi\, dt = \int_{t_0}^{t_1} \delta(U^{strain} - K^{Total} - \Omega^{Total})\, dt = 0 \tag{2.4}$$

where Π indicates total mechanical energy of the structure which includes kinetic energy K^{Total}, external work done by external forces Ω^{Total} and potential energy U^{strain}.

2.3.1. Total kinetic energy

The total kinetic energy of the coupled system contains kinetic energies of nanotubes, surface layer and flow fluid as follows (Ansari *et al.*, 2014; Ghorbanpour Arani *et al.*, 2014)

$$
\begin{aligned}
K^{Total} &= K_{nanotubes} + K^{surface}_{nanotubes} + K_{fluid} \\
&= \frac{1}{2}\rho_f \int\limits_0^l \Big\{ \int\limits_{A_f} \Big[\Big(\frac{\partial U_{i1}}{\partial t} + z\frac{\partial \Psi_{i1}}{\partial t} + U_f\cos\theta\Big)^2 + \Big(\frac{\partial W_{i1}}{\partial t} - U_f\sin\theta\Big)^2\Big]\, dA \Big\}\, dx \\
&+ \frac{\rho^S}{2}\int\limits_0^l \Big\{ \oint\limits_{S_{ij}} \Big[\Big(\frac{\partial U_{ij}}{\partial t} + z\frac{\partial \Psi_{ij}}{\partial t}\Big)^2 + \Big(\frac{\partial W_{ij}}{\partial t}\Big)^2\Big]\, dS \Big\}\, dx \\
&+ \frac{1}{2}\int\limits_0^l \Big\{ \int\limits_{A_{ij}} \rho_{CNT}\Big[\Big(\frac{\partial U_{ij}}{\partial t} + z\frac{\partial \Psi_{ij}}{\partial t}\Big)^2 + \Big(\frac{\partial W_{ij}}{\partial t}\Big)^2\Big]\, dA_{ij} \Big\}\, dx
\end{aligned}
\tag{2.5}
$$

where U_f is the fluid flow velocity and ρ_f, ρ^S, ρ_{CNT} are density of the fluid, surface layer and CNT, respectively.

2.3.2. External work

The external work that includes the elastic medium, thermal and magnetic fields, vdW interactions, and conveying fluid forces are presented as follows (Ghorbanpour Arani *et al.*, 2014)

$$
\begin{aligned}
\varOmega^{Total} &= \underbrace{\frac{1}{2}\int\limits_0^l [(\vec{M}^L_y\Psi_{ij}) + (\vec{F}^L_x U_{ij}) + (\vec{F}^L_z W_{ij})]\, dx}_{\text{Lorentz work}} + \underbrace{\frac{1}{2}\int\limits_0^l (q^{vdW}_{ij} W_{ij} + q^{Pasternak}_{i2} W_{i2})\, dx}_{\text{External work done by vdW \& Pasternak}} \\
&+ \underbrace{\frac{1}{2}\int\limits_0^l -E^* A_{ij}\alpha\Delta T\Big(\frac{\partial W_{ij}}{\partial x}\Big)^2\, dx}_{\text{External work done by thermal changes}} + \underbrace{\frac{1}{2}\int\limits_0^l \Big[-\rho_f U_f^2 A_f \frac{\partial^2 W_{i1}}{\partial x^2}(\cos\theta W_{i1} + \sin\theta U_{i1})\Big]\, dx}_{\text{External work done by centripetal fluid force}} \\
&\underbrace{- \frac{1}{2}\int\limits_0^l \Big[\mu_e A_f \frac{\partial^3 U_{i1}}{\partial x^2 \partial t} + \mu_e A_f U_f\Big(-\sin\theta\frac{\partial^2\theta}{\partial x^2} - \Big(\frac{\partial\theta}{\partial x}\Big)^2\cos\theta\Big)\Big] U_{i1}\, dx}_{\text{External work done by viscous fluid}} \\
&\underbrace{- \frac{1}{2}\int\limits_0^l \Big[\mu_e A_f \frac{\partial^3 W_{i1}}{\partial x^2 \partial t} + \mu_e A_f U_f\Big(-\cos\theta\frac{\partial^2\theta}{\partial x^2} - \Big(\frac{\partial\theta}{\partial x}\Big)^2\sin\theta\Big)\Big] W_{i1}\, dx}_{\text{External work done by viscous fluid}}
\end{aligned}
\tag{2.6}
$$

in which the Lorentz external work is the resultant of two-dimensional (2D) magnetic fields applied along the longitudinal and transverse directions. $\vec{H} = H_x\vec{i} + H_z\vec{k}$ is considered in order to show the effects of this type of magnetic field on stability of our structure. In order to show how the electric and magnetic fields are generated and changed by each other, Maxwell's equations are presented (Ghorbanpour Arani *et al.*, 2014; Kiani, 2014). The load inserted by Pasternak foundation which surrounds the external CNTs and the vdW interaction forces are distributed transverse loads, whose their external works are presented in Eq. (2.7), see Ghorbanpour Arani and Amir (2013), Khosrozadeh and Hajabasi (2012), Shen and Zhang (2011). The structure is introduced to a uniform thermal field. Hence, temperature changes apply an axial compressive load to the system. The external work done by the thermal load is shown in the above equation. Finally, the external work done by the viscous fluid flow is presented in Eq. (2.6), see Ghorbanpour Arani *et al.* (2014), Ghorbanpour Arani and Amir (2013), in which μ_e is the effective viscosity which is modified by the Knudsen number (Ghorbanpour Arani *et al.*, 2014). The Knudsen number is a dimensionless ratio which is used to modify the fluid flow velocity as follows

$$VCF = \frac{V_{ave,slip}}{V_{ave,no-slip}} = (1 + b\mathrm{Kn})\Big(1 + 4\frac{2-\sigma_\nu}{\sigma_\nu}\frac{\mathrm{Kn}}{1+\mathrm{Kn}}\Big) \tag{2.7}$$

where VCF is the correction factor which will be used to modify the fluid flow velocity as $V_{avg,slip} = VCF \cdot V_{avg,no-slip}$ and the governing equations as $U_f = V_{avg,slip}$.

2.3.3. *Strain energy based on Strain gradient theory*

The strain energy of mechanical structures is related to the stress and strain tensors of each structure. Strain gradient and modified couple stress theories are presented in this article in order to obtain strain energy of coupled DWCNT.

In the constitutive equations of the strain gradient theory (Ghorbanpour Arani and Amir, 2013; Kong *et al.*, 2009), for isotropic linear elastic materials there are only three independent higher-order material length scale parameters in addition to the two classical material parameters. Strain stress potential energy of the bulk and surface layer of the system is obtained by strain gradient theory, and will be investigated as below in the general form

$$U = \frac{1}{2}\Bigg(\int\limits_{\varGamma}(T_{kp}\varepsilon_{pq} + p_k\gamma_k + \tau^{(1)}_{ptq}\eta^{(1)}_{ptq} + m_{kp}\chi_{kp})\,dV + \oint\limits_{S}(T^S_{xx}\varepsilon_{xx} + T^S_{xz}\gamma_{xz})\,dS\Bigg) \tag{2.8}$$

in which

$$\begin{aligned} &\varepsilon_{pq} = \frac{1}{2}(\overline{D}_{p,q} + \overline{D}_{q,p}) \qquad \gamma_k = \varepsilon_{mm,k} \qquad \chi_{kp} = \frac{1}{2}(\phi_{k,p} + \phi_{p,k}) \\ &\eta^{(1)}_{ptq} = \frac{1}{2}(\varepsilon_{tq,p} + \varepsilon_{qp,t} + \varepsilon_{pt,q}) - \frac{1}{15}[\delta_{pt}(\varepsilon_{mm,q} + 2\varepsilon_{mq,m})] \\ &\qquad - \frac{1}{15}[\delta_{tq}(\varepsilon_{mm,p} + 2\varepsilon_{mp,m}) + \delta_{qp}(\varepsilon_{mm,t} + 2\varepsilon_{mt,m})] \end{aligned} \tag{2.9}$$

where $\boldsymbol{\varepsilon}$, $\boldsymbol{\gamma}$, $\boldsymbol{\eta}$ and $\boldsymbol{\chi}$ are strain, dilatation gradient, deviatoric stretch gradient and symmetric rotation gradient tensors, respectively. Stresses and higher order stress tensors are mentioned by

$$T_{pg} = \begin{cases} E^*\varepsilon_{pq} & \text{if} \quad p \equiv q \\ 2\kappa_S G^*\varepsilon_{pq} & \text{if} \quad p \neq q \end{cases} \tag{2.10}$$

and

$$p_k = 2G^* l_0^2 \gamma_k \qquad \tau^{(1)}_{ptq} = 2G^* l_1^2 \eta^{(1)}_{ptq} \qquad m_{kp} = 2G^* l_2^2 \chi_{kp} \tag{2.11}$$

where $\mathbf{T}$, $\mathbf{p}$, $\boldsymbol{\tau}$ and $\mathbf{m}$ are stress, higher order stress and deviatoric stress tensors, respectively. According to Eqs. (2.11), l_0, l_1 and l_2 are parameters of small scale theory. Therefore, with respect to Eqs. (2.5), (2.6) and using Hamilton's principle based on strain gradient theory, equations of motion are obtained. Using dimensionless parameters (Ghorbanpour Arani and Amir, 2013; Kong *et al.*, 2009), we have

$$
\begin{array}{llll}
(w_{ij},u_{ij})=\dfrac{(W_{ij},U_{ij})}{R_o} & \zeta=\dfrac{x}{l} & \overline{L}=\dfrac{L}{l} & (\overline{L}_0,\overline{L}_1,\overline{L}_2)=\dfrac{(L_0,L_1,L_2)}{L} \\
g^*=\dfrac{g}{l}\sqrt{\dfrac{E}{\rho_{CNT}}} & \tau=\dfrac{t}{l}\sqrt{\dfrac{E}{\rho_{CNT}}} & \overline{I}_{ij}=\dfrac{I_{ij}}{Al^2} & u_f=\sqrt{\dfrac{\rho_f}{E}}U_f \\
H_x^*=\sqrt{\dfrac{\eta_m H_x^2}{E}} & H_z^*=\sqrt{\dfrac{\eta_m H_z^2}{E}} & \overline{\mu}=\dfrac{\mu}{R_0\sqrt{E\rho_f}} & \beta_{ij}=\dfrac{\kappa_s GA_{ij}}{EA_{ij}} \\
\overline{h}_1=\dfrac{\pi(R_i^3+R_o^3)E_sT_s}{EAl^2} & \overline{h}_2=\dfrac{2\pi(R_i+R_o)E_sT_s}{EA} & \overline{h}_3=\dfrac{2\nu\pi I\tau^sR_o}{(1-\nu)EAhl^3} & \\
\overline{h}_4=\dfrac{2\nu\pi IE\rho^s}{(1-\nu)EAh\rho_{CNT}l^2} & \overline{h}_5=\dfrac{2\pi\rho^s(R_{in}+R_{out})}{\rho_{CNT}A_{11}} & \overline{h}_6=\dfrac{\pi(R_{in}^3+R_{out}^3)\rho^s}{\rho_{CNT}A_{in}l^2} & \\
(\overline{c}_{ij},\overline{c}'_{ij})=\dfrac{(c,c')l^2}{EA_{ij}} & \overline{G}_p=\dfrac{G_p}{EA} & \overline{K}_w=\dfrac{K_wl^2}{EA} & \lambda=\dfrac{l}{R_o} \\
\overline{\mathit{\Pi}}_0=\dfrac{2\pi(R_i+R_o)\tau^s}{EA} & f=\dfrac{A_f}{A} & \overline{\rho}=\dfrac{\rho_f}{\rho_{CNT}} & \overline{\Delta T}=\alpha\Delta T
\end{array}
$$

Therefore, the dimensionless equilibrium equations can be written as:
— for $\delta u_{ij}=0$

$$
\begin{aligned}
&-\frac{1}{\lambda}\frac{\partial^2 u_{ij}}{\partial\zeta^2}-\frac{g^*}{\lambda}\frac{\partial^3 u_{ij}}{\partial\zeta^2\partial\tau}+\frac{2\overline{L}_0\beta_{ij}}{\kappa_s\lambda}\frac{\partial^4 u_{ij}}{\partial\zeta^4}+\frac{2\overline{L}_0g^*\beta_{ij}}{\kappa_s\lambda}\frac{\partial^5 u_{ij}}{\partial\zeta^4\partial\tau}+\frac{20\overline{L}_1\beta_{ij}}{25\kappa_s\lambda}\frac{\partial^4 u_{ij}}{\partial\zeta^4}\\
&\quad+\frac{20\overline{L}_1g^*\beta_{ij}}{25\kappa_s\lambda}\frac{\partial^5 u_{ij}}{\partial\zeta^4\partial\tau}+\frac{H_x^*H_z^*}{\lambda}\frac{\partial^2 w_{ij}}{\partial\zeta^2}-\frac{H_z^{*2}}{\lambda}\frac{\partial^2 u_{ij}}{\partial\zeta^2}-\frac{\overline{h}_2}{\lambda}\frac{\partial^2 u_{ij}}{\partial\zeta^2}+\frac{1}{\lambda}\frac{\partial^2 u_{ij}}{\partial\tau^2}\\
&\quad+\frac{\mathit{\Gamma}_{ij}f_{ij}\overline{\rho}}{\lambda}\frac{\partial^2 u_{ij}}{\partial\tau^2}-\frac{\overline{\mu}\sqrt{\overline{\rho}}}{\lambda}\frac{\partial^3 u_{ij}}{\partial\tau\partial\zeta^2}=0
\end{aligned}
\tag{2.12}
$$

— for $\delta w_{ij}=0$

$$
\begin{aligned}
&-\beta_{ij}\frac{\partial\mathit{\Psi}_{ij}}{\partial\zeta}-\beta_{ij}g^*\frac{\partial^2\mathit{\Psi}_{ij}}{\partial\zeta\partial\tau}-\frac{\beta_{ij}g^*}{\lambda}\frac{\partial^3 w_{ij}}{\partial\zeta^2\partial\tau}-\frac{\beta_{ij}}{\lambda}\frac{\partial^2 w_{ij}}{\partial\zeta^2}+\frac{8\beta_{ij}\overline{L}_1^2}{15\lambda\kappa_s}\frac{\partial^4 w_{ij}}{\partial\zeta^4}+\frac{16\beta_{ij}\overline{L}_1^2}{15\kappa_s}\frac{\partial^3\mathit{\Psi}_{ij}}{\partial\zeta^3}\\
&\quad+\frac{8\beta_{ij}g^*\overline{L}_1^2}{15\lambda\kappa_s}\frac{\partial^5 w_{ij}}{\partial\zeta^4\partial\tau}+\frac{16\beta_{ij}g^*\overline{L}_1^2}{15\kappa_s}\frac{\partial^4\mathit{\Psi}_{ij}}{\partial\zeta^3\partial\tau}+\frac{\beta_{ij}\overline{L}_2^2}{4\lambda\kappa_s}\frac{\partial^4 w_{ij}}{\partial\zeta^4}-\frac{\beta_{ij}\overline{L}_2^2}{4\kappa_s}\frac{\partial^3\mathit{\Psi}_{ij}}{\partial\zeta^3}\\
&\quad-\frac{\beta_{ij}g^*\overline{L}_2^2}{4\kappa_s}\frac{\partial^4\mathit{\Psi}_{ij}}{\partial\zeta^3\partial\tau}+\frac{\beta_{ij}g^*\overline{L}_2^2}{4\lambda\kappa_s}\frac{\partial^5\mathit{\Psi}_{ij}}{\partial\zeta^4\partial\tau}-\frac{2\overline{\mathit{\Pi}}_0}{\lambda}\frac{\partial^2 w_{ij}}{\partial\zeta^2}+\frac{1}{\lambda}\frac{\partial^2 w_{ij}}{\partial\tau^2}+\frac{\mathit{\Gamma}_{ij}\overline{\rho}f_{ij}}{\lambda}\frac{\partial^2 w_{ij}}{\partial\tau^2}\\
&\quad-\frac{H_x^{*2}}{\lambda}\frac{\partial^2 w_{ij}}{\partial\zeta^2}+\frac{H_x^*H_z^*}{\lambda}\frac{\partial^2 u_{ij}}{\partial\zeta^2}-\mathit{\Gamma}_{ij}\sqrt{\overline{\rho}}f_{ij}\frac{\partial\mathit{\Psi}_{ij}}{\partial\tau}+\frac{\mathit{\Gamma}_{ij}u_f^2f_{ij}}{\lambda}\frac{\partial^2 w_{ij}}{\partial\zeta^2}+\frac{\overline{\Delta T}}{\lambda}\frac{\partial^2 w_{ij}}{\partial\zeta^2}\\
&\quad+\frac{\overline{\Delta T}g^*}{\lambda}\frac{\partial^3 w_{ij}}{\partial\zeta^2\partial\tau}\frac{\overline{\mu}u_f}{\lambda}\frac{\partial^3 w_{ij}}{\partial\zeta^3}-\frac{\sqrt{\overline{\rho}\mu}}{\lambda}\frac{\partial^2 w_{ij}}{\partial\zeta^2}-(1-\mathit{\Gamma}_{ij}){q'_{i2}}^{Pasternak}-{q'_{ij}}^{vdW}=0
\end{aligned}
\tag{2.13}
$$

— for $\delta\mathit{\Psi}_{ij}=0$

$$
\begin{aligned}
&-\overline{I}_{ij}\frac{\partial^2\mathit{\Psi}_{ij}}{\partial\zeta^2}+\overline{I}_{ij}g^*\frac{\partial^3\mathit{\Psi}_{ij}}{\partial\zeta^2\partial\tau}+\beta_{ij}\mathit{\Psi}_{ij}+\frac{\beta_{ij}}{\lambda}\frac{\partial w_{ij}}{\partial\zeta}+\beta_{ij}g^*\frac{\partial\mathit{\Psi}_{ij}}{\partial\zeta}+\frac{\beta_{ij}g^*}{\lambda}\frac{\partial^2 w_{ij}}{\partial\zeta\partial\tau}+\frac{\mathit{\Gamma}_{ij}f_{ij}\overline{\rho}u_f}{\lambda}\frac{\partial w_{ij}}{\partial\tau}\\
&\quad-\overline{h}_1\frac{\partial^2\mathit{\Psi}_{ij}}{\partial\zeta^2}+\frac{\overline{\mathit{\Pi}}_0}{\lambda}\frac{\partial w_{ij}}{\partial\zeta}+\overline{I}_{ij}\frac{\partial^2\mathit{\Psi}_{ij}}{\partial\tau^2}+\mathit{\Gamma}_{ij}f_{ij}\overline{\rho}\frac{\partial^2\mathit{\Psi}_{ij}}{\partial\tau^2}-\overline{I}_{ij}H_z^{*2}\frac{\partial^2\mathit{\Psi}_{ij}}{\partial\zeta^2}+\overline{h}_3\frac{\partial^3 w_{ij}}{\partial\zeta^3}+\frac{\overline{h}_4}{\lambda}\frac{\partial^3 w_{ij}}{\partial\zeta\partial\tau^2}\\
&\quad-\frac{2\beta_{ij}\overline{L}_o^2}{\kappa_s}\frac{\partial^2\mathit{\Psi}_{ij}}{\partial\zeta^2}-\frac{2\beta_{ij}g^*\overline{L}_0^2}{\kappa_s}\frac{\partial^3\mathit{\Psi}_{ij}}{\partial\zeta^2\partial\tau}+\frac{2\overline{I}_{ij}\beta_{ij}\overline{L}_0^2}{\kappa_s}\frac{\partial^4\mathit{\Psi}_{ij}}{\partial\zeta^4}+\frac{2\beta_{ij}\overline{I}_{ij}g^*\overline{L}_0^2}{\kappa_s}\frac{\partial^5\mathit{\Psi}_{ij}}{\partial\zeta^4\partial\tau}
\end{aligned}
$$

$$
\begin{aligned}
&+\frac{20\overline{I}_{ij}\beta_{ij}\overline{L}_1^2}{25\kappa_s}\frac{\partial^4\Psi_{ij}}{\partial\zeta^4}+\frac{20\beta_{ij}\overline{I}_{ij}g^*\overline{L}_1^2}{25\kappa_s}\frac{\partial^5\Psi_{ij}}{\partial\zeta^4\partial\tau}+\frac{16\beta_{ij}\overline{L}_1^2}{25\kappa_s\lambda}\frac{\partial^3 w_{ij}}{\partial\zeta^3}-\frac{32\beta_{ij}\overline{L}_1^2}{25\kappa_s}\frac{\partial^2\Psi_{ij}}{\partial\zeta^2}\\
&\quad+\frac{16\beta_{ij}g^*\overline{L}_1^2}{25\kappa_s\lambda}\frac{\partial^4 w_{ij}}{\partial\zeta^3\partial\tau}-\frac{32\beta_{ij}g^*\overline{L}_1^2}{25\kappa_s}\frac{\partial^3\Psi_{ij}}{\partial\zeta^2\partial\tau}+\frac{\beta_{ij}\overline{L}_2^2}{4\kappa_s\lambda}\frac{\partial^3 w_{ij}}{\partial\zeta^3}-\frac{\beta_{ij}\overline{L}_2^2}{4\kappa_s}\frac{\partial^2\Psi_{ij}}{\partial\zeta^2}\\
&\quad+\frac{\beta_{ij}g^*\overline{L}_2^2}{4\kappa_s\lambda}\frac{\partial^4 w_{ij}}{\partial\zeta^3\partial\tau}-\frac{\beta_{ij}g^*\overline{L}_2^2}{4\kappa_s}\frac{\partial^3\Psi_{ij}}{\partial\zeta^2\partial\tau}=0
\end{aligned}
\tag{2.14}
$$

where Γ_{ij} for $j=1$ (inner nanotube) equals 1 and for $j=2$ (outer nanotube) equals 0. By estimating l_0 and l_1, the presented theory converts into the modified couple stress theory.

3. Numerical method

DQM is a numerical method like Galerkin's method, Finite Element, Finite Difference method etc. This method is based on the Gaussian integral method and Lagrange polynomial, and some of its important merits are appropriate accuracy and easy access. Partial differential equations will be converted into algebraic equations in this method in two steps. First of all, Chebyshev points distribute grids along the CNTs, then Lagrange polynomial constructs DQ's weighting coefficient matrix (Ghorbanpour Arani *et al.*, 2014). The components of displacement field will be divided into time dependent and time independent functions

$$
u(\zeta,\tau)=u(\zeta)e^{i\omega\tau}\qquad w(\zeta,\tau)=w(\zeta)e^{i\omega\tau}\qquad \Psi(\zeta,\tau)=\Psi(\zeta)e^{i\omega\tau}
\tag{3.1}
$$

where $\omega=\lambda L\sqrt{\rho_{CNT}/E}$ is the dimensionless natural frequency, λ is the natural frequency and ρ_{CNT} is density of the tubes. According to Eqs. (3.1) and (3.2), the equilibrium and boundary equations will change to algebraic equations

$$
\frac{\partial^n(u_{ij},w_{ij},\Psi_{ij})}{\partial\zeta^n}\bigg|_{\zeta=\zeta_r}=\sum_{k=1}^{N}C_{rk}^n\{u_k(\zeta_k),w_k(\zeta_k),\Psi_k(\zeta_k)\}
\tag{3.2}
$$

By using Eqs. (3.1), (3.2) and some mathematical manipulations, the partial differential equations turn into state space algebraic equations (Ghorbanpour Arani *et al.*, 2014) which are shown by

$$
\left(\begin{bmatrix}\mathbf{0} & \mathbf{I}\\ \mathbf{M}_e^{-1}\mathbf{K}_e & i\mathbf{M}_e^{-1}\mathbf{D}_e\end{bmatrix}-\omega\mathbf{I}\right)\begin{Bmatrix}d_d\\ d^*\end{Bmatrix}=\mathbf{0}
\tag{3.3}
$$

where $\mathbf{K}_e$, $\mathbf{D}_e$, $\mathbf{M}_e$ and $\mathbf{I}$ are the stiffness, damping, mass and unit matrices, respectively. Subscript b is the element related to the boundary points and subscript d indicates the remaining elements. The imaginary part of the eigenvalue $\mathrm{Im}(\omega)t$ is structural damping and the real part $\mathrm{Re}(\omega)$ represents the natural frequency of the structure.

4. Discussion

Some numerical examples and also validation of our results in comparison with other accepted articles are expressed in this Section. Mechanical and geometrical properties of the CNTs are presented in Table 1 (Shen and Zhang, 2011; Zhang and Shen, 2006).

Our purpose is to investigate the natural frequency of the coupled DWCNT. Obviously, it is a nanoscale structure, so small scale theories must be applied in equilibrium equations to obtain appropriate results.

Table 1. Variety of elasticity and shear modulus of CNTs in different temperatures according to the rolling procedure

Rolling procedure	Type of CNT	Inner radius [nm]	Thickness [nm]	Temperature [K]	Young's modulus [TPa]	Shear modulus [TPa]
Zigzag	(17,0)	0.6654	0.088	300	3.9	1.36
				500	3.89	1.36
	(21,0)	0.822	0.087	300	3.81	1.37
				500	3.79	1.37

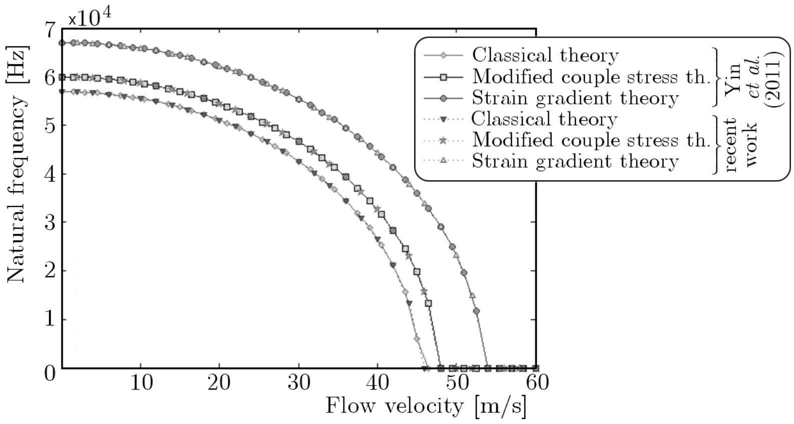

Fig. 2. Comparison of the dimensionless natural frequency with those presented by Yin *et al.* (2011) for MCST, SGT and classical theories

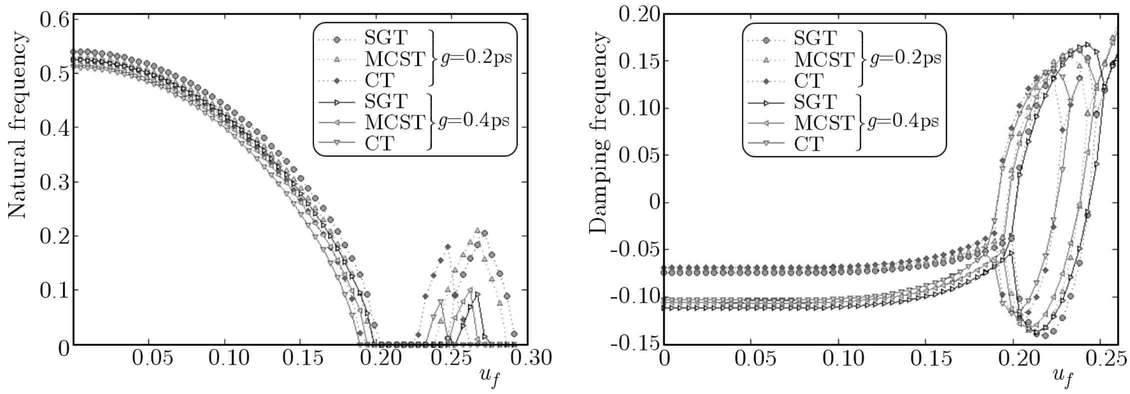

Fig. 3. The effect of structural damping of the CNTs on natural and damping frequencies, $H_x = 0.1\,\mathrm{GA/m}$ (zigzag inner 17.0 and outer 21.0, clamped-clamped, $L_0 = L_1 = L_2 = 0.1\,\mathrm{m}$, $E_sT_s = 0$, $\tau_s = 0$, $H_z = 0$, $\Delta T = 0$)

Figure 2 illustrates the comparison of our results with those by Yin *et al.* (2011), which is based on modified couple stress theory (MCST), strain gradient theory (SGT) and classical theory (CT), respectively. Figures 3a and 3b present the effects of the Kelvin-Voigt coefficient on the zigzag CNT. Before reaching the critical flow velocity, the natural frequency decreases with an increase in the flow velocity while the damping frequency remains negative and its magnitude decreases. Also the viscoelastic constant increases the magnitude of damping frequency. The effects of magnetic fields on stability of the elastic beam are shown in Figs. 4a and 4b. Figure 4a illustrates that stability of the coupled DWCNT increases as the magnitude of longitudinal magnetic field increases. Figure 4b indicates the effect of the transverse magnetic field on foundation frequency of the structure. By comparing Fig. 4a with Fig. 4b, we conclude that the longitudinal magnetic field has a more stabilizing effect on the structure than the transverse magnetic field.

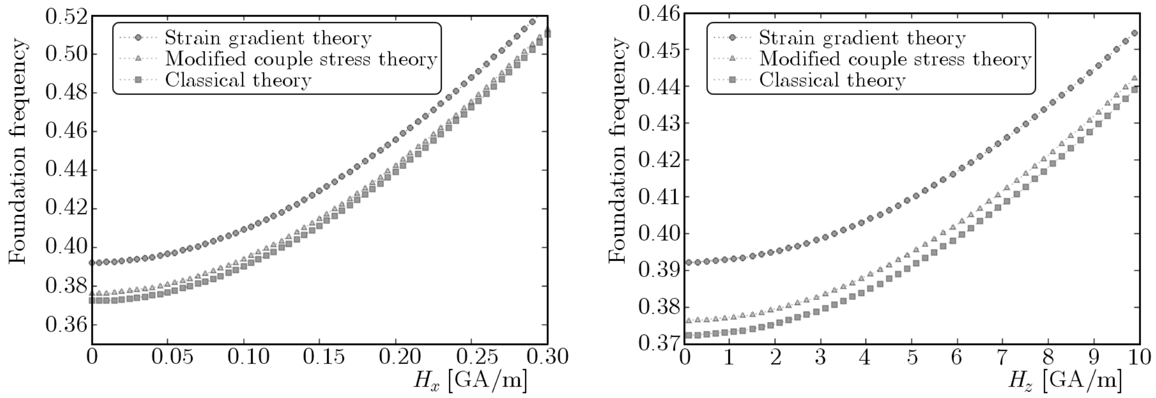

Fig. 4. The influence of 2D-magnetic field on the natural frequency, $\Delta T = 200$ and $g^* = 0$ (zigzag CNT inner 17.0 and outer 21.0, clamped-clamped, $H_z = 0\,\mathrm{GA/m}$, $u_f = 0.01$)

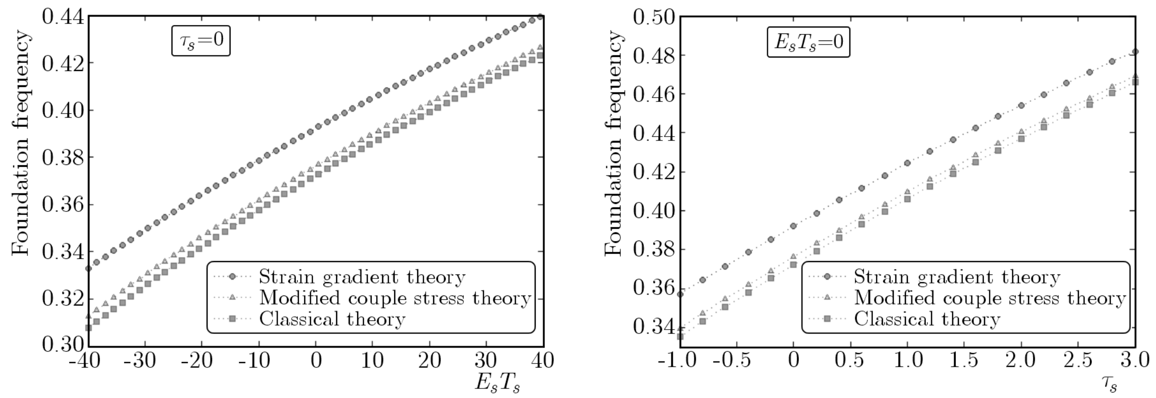

Fig. 5. The effect of surface layer rigidity and layer residual stress constant on the natural frequency $\Delta T = 200$ and $g^* = 0$ (zigzag CNT inner 17.0 and outer 21.0, clamped-clamped, $u_f = 0.01$, $H_x = 0$, $H_z = 0$)

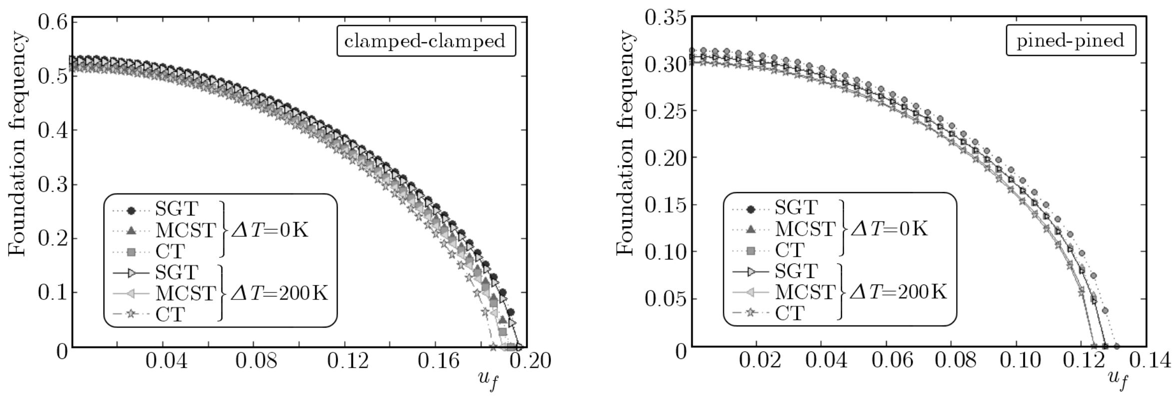

Fig. 6. The effects of different boundary conditions on natural frequency with various temperatures $g^* = 0$ (zigzag inner 17.0 and outer 21.0, $L_0 = L_1 = L_2 = 0.1\,\mathrm{m}$, $E_sT_s = 0$, $\tau_s = 0$, $H_x = H_z = 0$)

The surface stresses divide into two parameters, surface layer rigidity (E_ST_S) and residual surface tension (τ^s). The effects of these parameters are shown in Fig. 5a and Fig. 5b, respectively.

It is obvious that the increasing of the rigidity modulus of the structures reinforces their stability.

Figure 5 demonstrates that the natural frequency of the coupled DWCNT increases with an increase in the surface layer rigidity parameter (E_ST_S). It is also shown in Fig. 5 that the increasing of the residual surface tension (τ^s) increases the natural frequency. Figure 6 illustrates the effects of different boundary conditions and temperatures on the critical flow velocity and natural frequencies. As it can be observed in Fig. 6, strain gradient theory increases the vibration stability region, and the modified couple stress has a more stable region than in the classical theory. It is also shown that the clamped condition is the most stable condition, and the temperature changes have the least effect on the stability of the structure.

5. Conclusion

A viscoelastic couple DWCNTs structure based on the TB theory which is affected by the surface stress layer, magnetic field and temperature changes is presented in this paper. In order to obtain an appropriate compliance with the laboratory model, strain gradient and modified couple stress theories are considered in this study. There is a 3% discrepancy between the stability of CT and other theories. The results reveal that the effect of the viscoelastic coefficient on the vibration response of the system is not negligible. The magnetic field increases the stability region by increasing the rigidity of the system. The effect of the surface stress layer on natural frequency of the structure shows that the surface stress layer is an inherent characteristic for nanostructures. These results are an appropriate guide for designers and engineers to design useful mechanical structures.

Acknowledgement

The author would like to thank the reviewers for their valuable comments and suggestions to improve the clarity of this study. The authors are grateful to University of Kashan for supporting this work by Grant No. 363443/51. They would also like to thank the Iranian Nanotechnology Development Committee for their financial support.

References

1. Ansari R., Mohammadi V., Shojaei M. F., Gholami R., Rouhi H., 2014, Nonlinear vibration analysis of Timoshenko nanobeams based on surface stress elasticity theory, *European Journal of Mechanics A/Solids*, **45**, 143-152
2. Ghorbanpour Arani A., Amir S., 2013, Electro-thermal vibration of visco-elastically coupled BNNT systems conveying fl uid embedded on elastic foundation via strain gradient theory, *Physica B: Physics of Condensed Matter*, **419**, 1-6
3. Ghorbanpour Arani A., Amir S., Dashti P., Yousefi M., 2014, Flow-induced vibration of double bonded visco-CNTs under magnetic fields considering surface effect, *Computational Material Science*, **86**, 144-154
4. Iijima S., 1991, Helical microtubules of graphitic carbon, *Nature*, **354**, 56-58
5. Ke L.L., Wang Y.S., 2011, Flow-induced vibration and instability of embedded double-walled carbon nanotubes based on a modified couple stress theory, *Physica E: Low-Dimensional Systems and Nanostructures*, **43**, 1031-1039
6. Khosrozadeh A., Hajabasi M.A., 2012, Free vibration of embedded double-walled carbon nanotubes considering nonlinear interlayer van der Waals forces, *Applied Mathematical Modelling*, **36**, 997-1007
7. Kiani K., 2014, Vibration and instability of a single-walled carbon nanotube in a three-dimensional magnetic field, *Journal of Physical and Chemistry of Solids*, **75**, 15-22

8. Kong S., Zhou S., Nie Z., Wang K., 2009, Static and dynamic analysis of micro beams based on strain gradient elasticity theory, *International Journal of Engineering Science*, **47**, 487-498

9. Lei X., Natsuki T., Shi J., Ni Q., 2012, Surface effects on the vibrational frequency of double-walled carbon nanotubes using the nonlocal Timoshenko beam model, *Composites Part B: Engineering*, **43**, 64-69

10. Lei Y., Adhikari S., Friswell M. I., 2013, Vibration of nonlocal Kelvin-Voigt viscoelastic damped Timoshenko beams, *International Journal of Engineering Science*, **66/67**, 1-13

11. Lu P., He L.H., Lee H.P., Lu C., 2006, Thin plate theory including surface effects, *International Journal of Solids and Structures*, **43**, 4631-4647

12. Pradhan S.C., Mandal U., 2013, Finite element analysis of CNTs based on nonlocal elasticity and Timoshenko beam theory including thermal effect, *Physica E: Low-Dimensional Systems and Nanostructures*, **53**, 223-232

13. Shen H.S., Zhang C.L., 2011, Nonlocal beam model for nonlinear analysis of carbon nanotubes on elastomeric substrates, *Computational Materials Science*, **50**, 1022-1029

14. Xu M.R., Xu S.P., Guo H.Y., 2010, Determination of natural frequencies of fluid-conveying pipes using homotopy perturbation method, *Computers and Mathematics with Applications*, **60**, 520-527

15. Yin L., Qian Q., Wang L., 2011, Strain gradient beam model for dynamics of microscale pipes conveying fluid, *Applied Mathematical Modelling*, **35**, 2864-2873

16. Zhang C.L., Shen H.S., 2006, Temperature-dependent elastic properties of single-walled carbon nanotubes: Prediction from molecular dynamics simulation, *Applied Physics Letters*, **89**, 081904

Manuscript received November 9, 2014; accepted for print May 18, 2015

JOURNAL OF THEORETICAL
AND APPLIED MECHANICS
53, 4, pp. 959-968, Warsaw 2015
DOI: 10.15632/jtam-pl.53.4.959

NUMERICAL SOLUTION OF NON-HOMOGENOUS FRACTIONAL OSCILLATOR EQUATION IN INTEGRAL FORM

Mariusz Ciesielski
Czestochowa University of Technology, Institute of Computer and Information Sciences, Częstochowa, Poland
e-mail: mariusz.ciesielski@icis.pcz.pl

Tomasz Błaszczyk
Czestochowa University of Technology, Institute of Mathematics, Częstochowa, Poland
e-mail: tomasz.blaszczyk@im.pcz.pl

In this paper, a non-homogenous fractional oscillator equation in finite time interval is considered. The fractional equation with derivatives of order $\alpha \in (0, 1]$ is transformed into its corresponding integral form. Next, a numerical solution of the integral form of the considered equation is presented. In the final part of this paper, some examples of numerical solutions of the considered equation are shown.

Keywords: fractional oscillator equation, fractional integral equation, numerical solution

1. Introduction

Fractional differential equations have numerous applications in physics, engineering and biology. There is a number of monographs (Atanackovic *et al.*, 2014; Baleanu *et al.*, 2012; Hilfer, 2000; Kilbas *et al.*, 2006; Klimek, 2009; Leszczynski, 2011; Magin, 2006; Malinowska and Torres, 2012; Podlubny, 1999) and a huge number of papers (Agrawal, 2002; Ciesielski and Leszczynski, 2006; Katsikadelis, 2012; Klimek, 2001; Riewe, 1996; Sumelka, 2014; Sumelka and Blaszczyk, 2014; Zhang *et al.*, 2014) that cover various problems in fractional calculus. The list is large and is growing rapidly. An important issue is that the derivative of fractional order at any point of the domain has a local property only when the order is an integer number. For non-integer cases, the fractional derivative is a nonlocal operator and depends on the past values of the function (left derivative) or future ones (right derivative).

There are two different ways to formulate differential equations containing derivatives of fractional order. The first way is simply to replace integer order derivatives in differential equations by fractional ones. The second one relies on modifying the variational principle by replacing the integer order derivative by a fractional one. This leads to fractional differential equations which are known in the literature as the fractional Euler-Lagrange equations. It involves different types of Lagrangians, e.g., depending on Riemann-Liouville or Caputo fractional derivatives, fractional integrals, and mixed integer-fractional order operators (Agrawal *et al.*, 2011; Almeida and Malinowska, 2012; Baleanu *et al.*, 2014; Klimek *et al.*, 2014; Odzijewicz *et al.*, 2012). This second approach, in recent years, seems to become increasingly important.

The main feature of the fractional Euler-Lagrange equations is that these equations involve simultaneously the left and right derivatives of fractional order. This is also a fundamental problem in finding solutions to equations of a variational type (Baleanu *et al.*, 2012; Klimek, 2009). Consequently, numerous studies have been devoted to numerical schemes for the fractional Euler-Lagrange equations (Blaszczyk *et al.*, 2011; Blaszczyk and Ciesielski, 2014, 2015a,b; Bourdin *et al.*, 2013; Pooseh *et al.*, 2013; Xu and Agrawal, 2014).

In this paper, we present a numerical solution of the non-homogenous fractional oscillator equation in a finite time interval.

2. Preliminaries

We consider a variational differential equation containing fractional derivatives of order $\alpha \in (0,1]$ in the finite time interval $t \in [0,b]$

$$ {}^C D^{\alpha}_{b-} D^{\alpha}_{0+} x(t) - \omega^{2\alpha} x(t) = f(t) \tag{2.1} $$

where $\omega > 0$, $x(t)$ is an unknown function and $f(t)$ is a given function. Equation (2.1) is supplemented by the following boundary conditions

$$ x(0) = 0 \qquad\qquad x(b) = L \tag{2.2} $$

In this type of equation (derived from the Lagrangian with fractional derivative and the properties of the considered variational problem (Klimek, 2009) we assume $x(0) = 0$ on the left boundary.

We recall some definitions and properties of the fractional operators (Kilbas *et al.*, 2006; Oldham and Spanier, 1974; Podlubny, 1999). The left and right Riemann-Liouville fractional derivatives of order $\alpha \in (0,1)$ are defined by

$$ \begin{aligned} D^{\alpha}_{0+} x(t) &:= D I^{1-\alpha}_{0+} x(t) \\ D^{\alpha}_{b-} x(t) &:= -D I^{1-\alpha}_{b-} x(t) \end{aligned} \tag{2.3} $$

and the left and right Caputo derivatives are defined as follows

$$ \begin{aligned} {}^C D^{\alpha}_{0+} x(t) &:= I^{1-\alpha}_{0+} D x(t) \\ {}^C D^{\alpha}_{b-} x(t) &:= -I^{1-\alpha}_{b-} D x(t) \end{aligned} \tag{2.4} $$

where D is an operator of the first order derivative and the operators I^{α}_{0+} and I^{α}_{b-} are respectively the left and right fractional integrals of order $\alpha > 0$ defined by

$$ \begin{aligned} I^{\alpha}_{0+} x(t) &:= \frac{1}{\Gamma(\alpha)} \int\limits_0^t \frac{x(\tau)}{(t-\tau)^{1-\alpha}}\, d\tau \qquad (t > 0) \\ I^{\alpha}_{b-} x(t) &:= \frac{1}{\Gamma(\alpha)} \int\limits_t^b \frac{x(\tau)}{(\tau-t)^{1-\alpha}}\, d\tau \qquad (t < b) \end{aligned} \tag{2.5} $$

If $\alpha = 1$ then $D^1_{0+} x = {}^C D^1_{0+} x = x'$ and $D^1_{b-} x = {}^C D^1_{b-} x = -x'$. The relations between the Caputo and Riemann-Liouville derivatives are of the form

$$ \begin{aligned} {}^C D^{\alpha}_{0+} x(t) &= D^{\alpha}_{0+} x(t) - \frac{t^{-\alpha}}{\Gamma(1-\alpha)} x(0) \\ {}^C D^{\alpha}_{b-} x(t) &= D^{\alpha}_{b-} x(t) - \frac{(b-t)^{-\alpha}}{\Gamma(1-\alpha)} x(b) \end{aligned} \tag{2.6} $$

The composition rules of the fractional operators (for $\alpha \in (0,1]$) looks as follows

$$ \begin{aligned} I^{\alpha}_{0+} \, {}^C D^{\alpha}_{0+} x(t) &= x(t) - x(0) \\ I^{\alpha}_{b-} \, {}^C D^{\alpha}_{b-} x(t) &= x(t) - x(b) \end{aligned} \tag{2.7} $$

and the fractional integral of a constant C

$$I^{\alpha}_{0+}C = C\frac{t^{\alpha}}{\Gamma(1+\alpha)} \tag{2.8}$$

In particular, when $\alpha = 1$, then ${}^{C}D^{1}_{b-}D^{1}_{0+} = -D^2$ and Eq. (2.1) becomes

$$-D^2 f(t) - \omega^2 x(t) = f(t) \tag{2.9}$$

and its analytical solution with respect to boundary conditions (2.2) has the form

$$x(t) = \frac{\sin(\omega t)}{\sin(\omega b)}[L + F(b)] - F(t) \tag{2.10}$$

where

$$F(t) = \frac{1}{\omega}\int\limits_{0}^{t} f(\tau)\sin(\omega(t-\tau))\,d\tau \tag{2.11}$$

This solution we will apply to verifiction of numerical results obtained by our method for the case $\alpha = 1$.

3. Equivalent integral form

The first step of our method is to transform a differential equation into an integral equation. We integrate Eq. (2.1) twice: the first time by using right fractional integral operator $(2.5)_2$ and the second time by using left fractional integral operator $(2.5)_1$. Finally, we obtain

$$I^{\alpha}_{0+}I^{\alpha}_{b-}\,{}^{C}D^{\alpha}_{b-}D^{\alpha}_{0+}x(t) - \omega^{2\alpha}I^{\alpha}_{0+}I^{\alpha}_{b-}x(t) = I^{\alpha}_{0+}I^{\alpha}_{b-}f(t) \tag{3.1}$$

Next, we use the composition rule of operators $(2.7)_2$ and get

$$I^{\alpha}_{0+}\Big(D^{\alpha}_{0+}x(t) - D^{\alpha}_{0+}x(t)\Big|_{t=b}\Big) - \omega^{2\alpha}I^{\alpha}_{0+}I^{\alpha}_{b-}x(t) = I^{\alpha}_{0+}I^{\alpha}_{b-}f(t) \tag{3.2}$$

In the above equation there occurs the value $D^{\alpha}_{0+}x(t)\big|_{t=b}$, and it is unknown at this stage. Here, we treat it as a constant. By using property $(2.7)_1$ and the assumption $x(0) = 0$ in the boundary condition, and the fractional integral of constant (2.8) we obtain the following form of the considered equation

$$x(t) - D^{\alpha}_{0+}x(t)\Big|_{t=b}\frac{t^{\alpha}}{\Gamma(\alpha+1)} - \omega^{2\alpha}I^{\alpha}_{0+}I^{\alpha}_{b-}x(t) = I^{\alpha}_{0+}I^{\alpha}_{b-}f(t) \tag{3.3}$$

The unknown value $D^{\alpha}_{0+}x(t)\big|_{t=b}$ in the above equation can be determined on the basis of the boundary condition. Substituting the value $t = b$ into Eq. (3.3)

$$x(b) - D^{\alpha}_{0+}x(t)\Big|_{t=b}\frac{b^{\alpha}}{\Gamma(\alpha+1)} - \omega^{2\alpha}I^{\alpha}_{0+}I^{\alpha}_{b-}x(t)\Big|_{t=b} = I^{\alpha}_{0+}I^{\alpha}_{b-}f(t)\Big|_{t=b} \tag{3.4}$$

we obtain

$$D^{\alpha}_{0+}x(t)\Big|_{t=b} = \frac{\Gamma(\alpha+1)}{b^{\alpha}}\Big[x(b) - \omega^{2\alpha}I^{\alpha}_{0+}I^{\alpha}_{b-}x(t)\Big|_{t=b} - I^{\alpha}_{0+}I^{\alpha}_{b-}f(t)\Big|_{t=b}\Big] \tag{3.5}$$

Next, we put the right-hand side of formula (3.5) into Eq. (3.3) and get the integral form of Eq. (2.1)

$$x(t) - \omega^{2\alpha}\Big[I^{\alpha}_{0+}I^{\alpha}_{b-}x(t) - \Big(\frac{t}{b}\Big)^{\alpha}I^{\alpha}_{0+}I^{\alpha}_{b-}x(t)\Big|_{t=b}\Big] = \Big(\frac{t}{b}\Big)^{\alpha}\Big[L - I^{\alpha}_{0+}I^{\alpha}_{b-}f(t)\Big|_{t=b}\Big] + I^{\alpha}_{0+}I^{\alpha}_{b-}f(t) \tag{3.6}$$

4. Numerical solution

In this Section, we present a numerical scheme for Eq. (3.6). We introduce a homogeneous grid of $n+1$ nodes (with the constant time step $\Delta t = b/n$): $0 = t_0 < t_1 < \ldots < t_i < t_{i+1} < \ldots < t_n = b$, and $t_i = i\Delta t$, $i = 0, 1, \ldots, n$. For every grid node t_i, we write the following equation

$$\begin{aligned} & x(t_i) - \omega^{2\alpha}\Big[I^\alpha_{0+}I^\alpha_{b-}x(t)\Big|_{t=t_i} - \Big(\frac{t_i}{t_n}\Big)^\alpha I^\alpha_{0+}I^\alpha_{b-}x(t)\Big|_{t=t_n}\Big] \\ & \quad = \Big(\frac{t_i}{t_n}\Big)^\alpha\Big[L - I^\alpha_{0+}I^\alpha_{b-}f(t)\Big|_{t=t_n}\Big] + I^\alpha_{0+}I^\alpha_{b-}f(t)\Big|_{t=t_i} \end{aligned} \tag{4.1}$$

In order to simplify notation, we denote the values of functions $x(t)$ and $f(t)$ at the node t_i by $x_i = x(t_i)$ and $f_i = f(t_i)$, respectively. The numerical problem is to approximate the values of $I^\alpha_{0+}I^\alpha_{b-}x(t)\big|_{t=t_i}$ and $I^\alpha_{0+}I^\alpha_{b-}f(t)\big|_{t=t_i}$, for $i = 0, 1, \ldots, n$, properly. In our previous works (Blaszczyk and Ciesielski, 2015a,b) we have determined the discrete form of the composition of operators. On the basis of these results, we present the final discrete forms

$$\begin{aligned} I^\alpha_{0+}I^\alpha_{b-}x(t)\Big|_{t=t_i} &\approx \sum_{j=0}^{i} u^{(\alpha)}_{i,j}\sum_{k=j}^{n} v^{(\alpha)}_{j,k}x_k \\ I^\alpha_{0+}I^\alpha_{b-}f(t)\Big|_{t=t_i} &\approx \sum_{j=0}^{i} u^{(\alpha)}_{i,j}\sum_{k=j}^{n} v^{(\alpha)}_{j,k}f_k \end{aligned} \tag{4.2}$$

where the coefficients $u^{(\alpha)}_{i,j}$ and $v^{(\alpha)}_{j,k}$ are as follows

$$\begin{aligned} u^{(\alpha)}_{i,j} &= \frac{(\Delta t)^\alpha}{\Gamma(\alpha+2)}\begin{cases} 0 & \text{for } i = 0 \text{ and } j = 0 \\ (i-1)^{\alpha+1} - i^{\alpha+1} + i^\alpha(\alpha+1) & \text{for } i > 0 \text{ and } j = 0 \\ (i-j+1)^{\alpha+1} - 2(i-j)^{\alpha+1} + (i-j-1)^{\alpha+1} & \text{for } i > 0 \text{ and } 0 < j < i \\ 1 & \text{for } i > 0 \text{ and } j = i \end{cases} \\ v^{(\alpha)}_{j,k} &= \frac{(\Delta t)^\alpha}{\Gamma(\alpha+2)}\begin{cases} 0 & \text{for } j = n \text{ and } k = n \\ (n-j-1)^{\alpha+1} - (n-j)^{\alpha+1} + (n-j)^\alpha(\alpha+1) & \text{for } j < n \text{ and } k = n \\ (k-j+1)^{\alpha+1} - 2(k-j)^{\alpha+1} + (k-j-1)^{\alpha+1} & \text{for } j < n \text{ and } j < k < n \\ 1 & \text{for } j < n \text{ and } k = j \end{cases} \end{aligned} \tag{4.3}$$

One can observe that in order to compute the values of operators (4.2) at every node t_i, we need to use the values of functions at all nodes of the domain.

Now we present the numerical scheme of integral equation (3.6). If we substitute (4.2) into (4.1), then the solution can be written as a system of $n+1$ linear equations

$$\begin{aligned} & x_i - \omega^{2\alpha}\Big[\sum_{j=0}^{i} u^{(\alpha)}_{i,j}\sum_{k=j}^{n} v^{(\alpha)}_{j,k}x_k - \Big(\frac{i}{n}\Big)^\alpha\sum_{j=0}^{n} u^{(\alpha)}_{n,j}\sum_{k=j}^{n} v^{(\alpha)}_{j,k}x_k\Big] \\ & \quad = \Big(\frac{i}{n}\Big)^\alpha\Big[L - \sum_{j=0}^{n} u^{(\alpha)}_{n,j}\sum_{k=j}^{n} v^{(\alpha)}_{j,k}f_k\Big] + \sum_{j=0}^{i} u^{(\alpha)}_{i,j}\sum_{k=j}^{n} v^{(\alpha)}_{j,k}f_k \qquad i = 0, \ldots, n \end{aligned} \tag{4.4}$$

The above system can also be written in the matrix form

$$\mathbf{A}\cdot\mathbf{x}=\mathbf{b} \tag{4.5}$$

with the coefficients of matrices $\mathbf{A}$ and $\mathbf{b}$

$$\begin{aligned} A_{i,j} &= \begin{cases} 1 & \text{if } \; i=j \\ 0 & \text{if } \; i\neq j \end{cases} - \omega^{2\alpha}\Bigg[\sum_{k=0}^{\min(i,j)} u_{i,k}^{(\alpha)} v_{k,j}^{(\alpha)} - \Big(\frac{i}{n}\Big)^{\alpha}\sum_{k=0}^{j} u_{n,k}^{(\alpha)} v_{k,j}^{(\alpha)}\Bigg] \\ & \qquad i=0,\dots,n \qquad\qquad j=0,\dots,n \\ b_i &= \Big(\frac{i}{n}\Big)^{\alpha}\Bigg[L-\sum_{j=0}^{n} u_{n,j}^{(\alpha)}\sum_{k=j}^{n} v_{j,k}^{(\alpha)} f_k\Bigg] + \sum_{j=0}^{i} u_{i,j}^{(\alpha)}\sum_{k=j}^{n} v_{j,k}^{(\alpha)} f_k \qquad\qquad i=0,\dots,n \end{aligned} \tag{4.6}$$

respectively, and $\mathbf{x}=[x_0,x_1,\dots,x_n]^{\mathrm{T}}$.

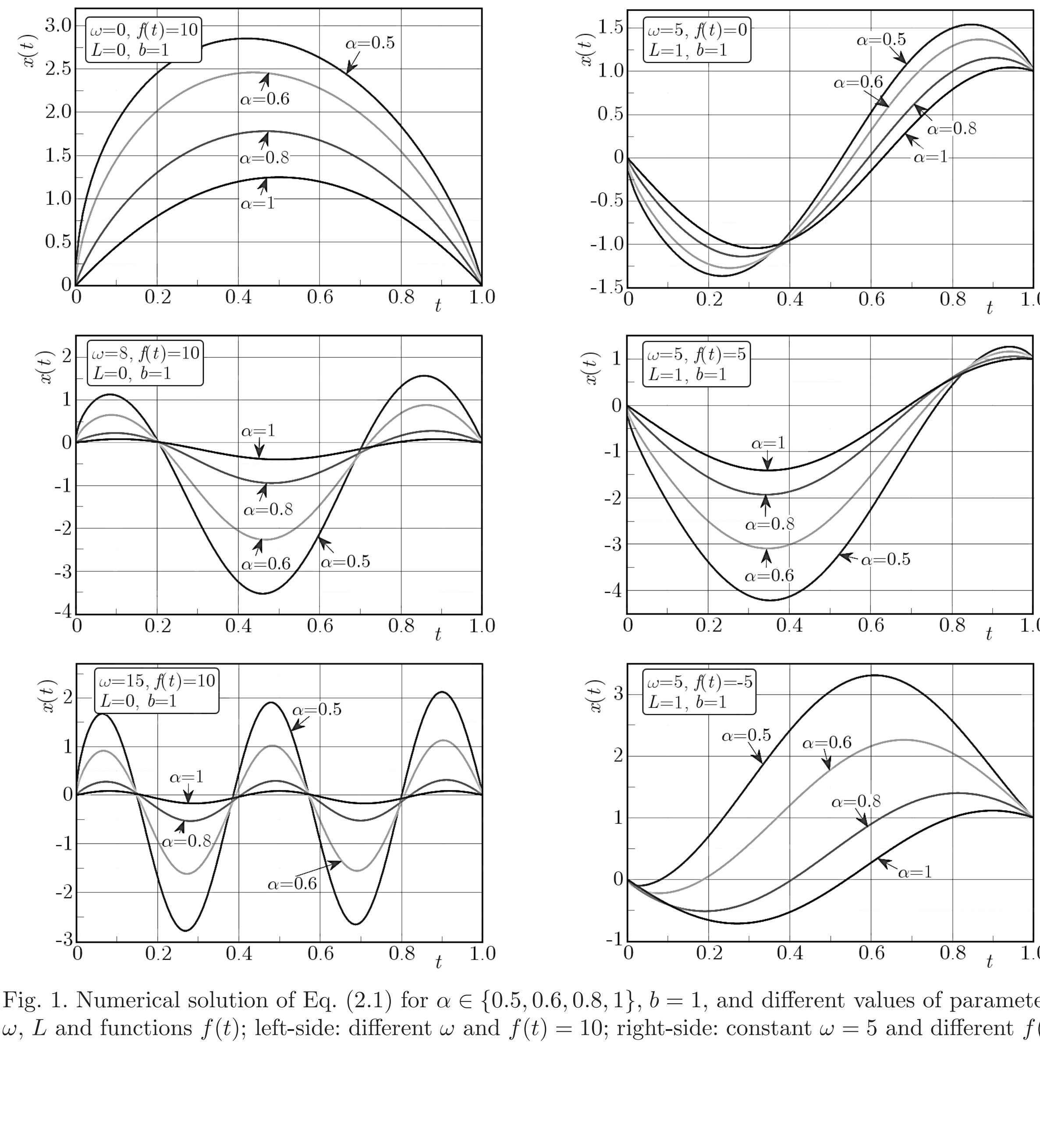

Fig. 1. Numerical solution of Eq. (2.1) for $\alpha\in\{0.5,0.6,0.8,1\}$, $b=1$, and different values of parameters ω, L and functions $f(t)$; left-side: different ω and $f(t)=10$; right-side: constant $\omega=5$ and different $f(t)$

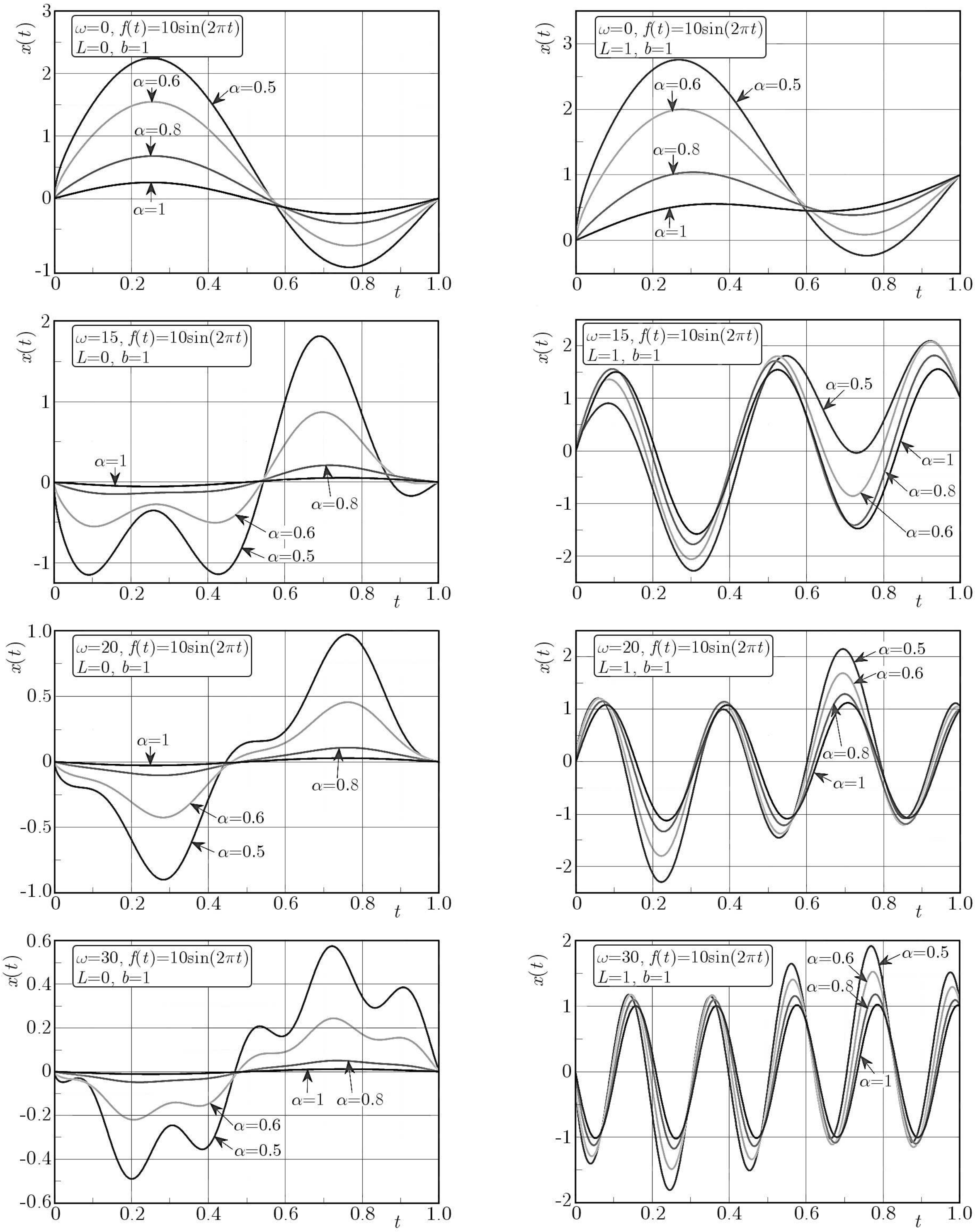

Fig. 2. Numerical solution of Eq. (2.1) for $\alpha \in \{0.5, 0.6, 0.8, 1\}$, $f(t) = 10\sin(2\pi t)$, $b = 1$, different values of parameter ω, and $L = 0$ (left-side), $L = 1$ (right-side)

5. Example of computations

We present the results of computations obtained by our numerical scheme to the forced fractional oscillator equation. The system of linear equations (4.5) has been solved by the Gaussian elimination algorithm (the LUP decomposition (Press *et al.*, 2007)). We present several examples of calculations for different values of the parameters α, ω and different functions f. In the examples we assume: $b = 1$ and $L \in \{0, 1\}$ in the right boundary condition. In Figs. 1 and 2 we present results of the numerical solution of Eq. (2.1). The values of the parameters used in the solution of equation (2.1) are given in plot legends. The time domain $t \in [0, 1]$ has been divided into $n = 1000$ subintervals in all examples.

5.1. Numerical error analysis

The discretization of differential or integral equations always entails certain errors. The knowledge of an analytical solution $x_{anal}(t)$ allows us to evaluate the errors of our numerical solution $x_{num}(t)$. We define the average error as

$$Err_{avg} = \frac{1}{m+1} \sum_{i=0}^{m} |x_{num}(t_i) - x_{anal}(t_i)| \qquad \text{for} \quad i = 0, \dots, m \tag{5.1}$$

where m is the number of measurement points.

Let us consider Eq. (2.1) with the parameters $\omega = 0$, $L = 0$ and the function $f(t) = (b-t)^{2-\alpha}$. In this case

$$I^{\alpha}_{0+} I^{\alpha}_{b-} f(t) = I^{\alpha}_{0+} I^{\alpha}_{b-} (b-t)^{2-\alpha} = t^{\alpha} b^2 \Gamma(3-\alpha) \sum_{j=0}^{2} \frac{(-1)^j}{\Gamma(3-j)\Gamma(\alpha+1+j)} \left(\frac{t}{b}\right)^j \tag{5.2}$$

and the analytical solution (by using Eq. (3.6) and further simplifications) has form

$$x_{anal}(t) = t^{\alpha} b^2 \Gamma(3-\alpha) \sum_{j=0}^{2} \frac{(-1)^j [(t/b)^j - 1]}{\Gamma(3-j)\Gamma(j+\alpha+1)} \tag{5.3}$$

In Tables 1 and 2, we present the values of the analytical (exact) solution $x_{anal}(t)$ for $\alpha \in \{0.5, 0.75\}$ at the selected values of nodes t_i, $i = 0, \dots, 10$ and the corresponding numerical values $x_{num}(t)$ calculated for different numbers of grid nodes ($n \in \{100, 200, 400, 800\}$). The errors generated by numerical schema are also included in Tables 1 and 2. One can note that the error decreases with a decrease in the time step of the grid.

Table 1. Values of analytical and numerical solutions of Eq. (2.1) for $\alpha = 0.5$, $\omega = 0$, $f(t) = (b-t)^{2-\alpha}$, $b = 1$, $L = 0$

t_i	$x_{anal}(t_i)$	$x_{num}(t_i)$ $n = 100$	$x_{num}(t_i)$ $n = 200$	$x_{num}(t_i)$ $n = 400$	$x_{num}(t_i)$ $n = 800$
0	0.000000000000	0.000000000000	0.000000000000	0.000000000000	0.000000000000
0.1	0.159378794072	0.159379032826	0.159378842522	0.159378803745	0.159378795979
0.2	0.186040855728	0.186041292916	0.186040941860	0.186040872522	0.186040858974
0.3	0.184034779322	0.184035363697	0.184034893461	0.184034801419	0.184034783568
0.4	0.166968260457	0.166968963299	0.166968397209	0.166968286848	0.166968265515
0.5	0.141421356237	0.141422156701	0.141421511713	0.141421386199	0.141421361972
0.6	0.111541920371	0.111542800274	0.111542091205	0.111541953283	0.111541926669
0.7	0.080319362547	0.080320302735	0.080319545231	0.080319397768	0.080319369292
0.8	0.050087922696	0.050088897461	0.050088112561	0.050087959382	0.050087929735
0.9	0.022768399153	0.022769357797	0.022768587015	0.022768435655	0.022768406192
1	0.000000000000	0.000000000000	0.000000000000	0.000000000000	0.000000000000
Err_{avg}	–	$5.92466 \cdot 10^{-7}$	$1.15654 \cdot 10^{-7}$	$2.2385 \cdot 10^{-8}$	$4.30118 \cdot 10^{-9}$

Table 2. Values of analytical and numerical solutions of Eq. (2.1) for $\alpha = 0.75$, $\omega = 0$, $f(t) = (b-t)^{2-\alpha}$, $b = 1$, $L = 0$

t_i	$x_{anal}(t_i)$	$x_{num}(t_i)$ $n = 100$	$x_{num}(t_i)$ $n = 200$	$x_{num}(t_i)$ $n = 400$	$x_{num}(t_i)$ $n = 800$
0	0.000000000000	0.000000000000	0.000000000000	0.000000000000	0.000000000000
0.1	0.067645942013	0.067646050586	0.067645965523	0.067645947053	0.067645943086
0.2	0.094996909603	0.094997100277	0.094996949929	0.094996918109	0.094996911394
0.3	0.105395550994	0.105395806812	0.105395604628	0.105395562237	0.105395553351
0.4	0.104362700328	0.104363008356	0.104362764589	0.104362713751	0.104362703135
0.5	0.095196902130	0.095197250210	0.095196974490	0.095196917206	0.095196905277
0.6	0.080331627323	0.080332002341	0.080331705051	0.080331643482	0.080331630691
0.7	0.061751765560	0.061752151496	0.061751845314	0.061751782104	0.061751769002
0.8	0.041170523241	0.041170897406	0.041170600282	0.041170539178	0.041170526550
0.9	0.020119449943	0.020119771392	0.020119515708	0.020119463484	0.020119452744
1	0.000000000000	0.000000000000	0.000000000000	0.000000000000	0.000000000000
Err_{avg}	–	$2.42522 \cdot 10^{-7}$	$5.03981 \cdot 10^{-8}$	$1.04972 \cdot 10^{-8}$	$2.19045 \cdot 10^{-9}$

6. Conclusions

In this work, the method of solving of the non-homogenous fractional oscillator equation with derivatives of order $\alpha \in (0, 1]$ has been presented. First, the equation has been transformed into integral form. Next, the numerical scheme for the integral form of the equation has been proposed. Analysing the solutions of the equation for different values of parameters α, ω, various boundary conditions and different functions $f(t)$ one can understand the influence of these parameters on the solution. One can note that if the value of α decreases then the amplitude of oscillations increases, and if the value of ω increases then the oscillation frequency increases as well. The analytical solution of this type of fractional differential equation (except for the case $\alpha = 1$) is not yet known. Our proposed numerical method of solutions for $\alpha \to 1$ is consistent with the analytical solution for $\alpha = 1$. This type of considered equation can be used in mathematical modelling of the oscillatory behavior of systems where the use of the classical oscillator equation is insufficient.

References

1. Agrawal O.P., 2002, Formulation of Euler-Lagrange equations for fractional variational problems, *Journal of Mathematical Analysis and Applications*, **272**, 368-379
2. Agrawal O.P., Muslih S.I., Baleanu D., 2011, Generalized variational calculus in terms of multi-parameters fractional derivatives, *Communications in Nonlinear Science and Numerical Simulation*, **16**, 4756-4767
3. Almeida R., Malinowska A.B., 2012, Generalized transversality conditions in fractional calculus of variations, *Communications in Nonlinear Science and Numerical Simulation*, **18**, 3, 443-452
4. Atanackovic T.M., Pilipovic S., Stankovic B., Zorica D., 2014, *Fractional Calculus with Applications in Mechanics: Vibrations and Diffusion Processes*, ISTE-Wiley, London
5. Baleanu D., Trujillo J.J., 2008, On exact solutions of a class of fractional Euler-Lagrange equations, *Nonlinear Dynamics*, **52**, 331-335
6. Baleanu D., Asad J.H., Petras I., 2014, Fractional Bateman-Feshbach Tikochinsky oscillator, *Communications in Theoretical Physics*, **61**, 221-225
7. Baleanu D., Diethelm K., Scalas E., Trujillo J.J., 2012, *Fractional Calculus Models and Numerical Methods*, World Scientific, Singapore

8. Blaszczyk T., Ciesielski M., 2014, Numerical solution of fractional Sturm-Liouville equation in integral form, *Fractional Calculus and Applied Analysis*, **17**, 307-320
9. Blaszczyk T., Ciesielski M., 2015a, Fractional oscillator equation: analytical solution and algorithm for its approximate computation, *Journal of Vibration and Control* (in print), http://dx.doi.org/10.1177/1077546314566836
10. Blaszczyk T., Ciesielski M., 2015b, Fractional oscillator equation – transformation into integral equation and numerical solution, *Applied Mathematics and Computation*, **257**, 428-435
11. Blaszczyk T., Ciesielski M., Klimek M., Leszczynski J., 2011, Numerical solution of fractional oscillator equation, *Applied Mathematics and Computation*, **218**, 2480-2488
12. Bourdin L., Cresson J., Greff I., Inizan P., 2013, Variational integrator for fractional Euler-Lagrange equations, *Applied Numerical Mathematics*, **71**, 14-23
13. Ciesielski M., Leszczynski J., 2006, Numerical solutions to boundary value problem for anomalous diffusion equation with Riesz-Feller fractional operator, *Journal of Theoretical and Applied Mechanics*, **44**, 2, 393-403
14. Hilfer R., 2000, *Applications of Fractional Calculus in Physics*, World Scientific, Singapore
15. Katsikadelis J.T., 2012, Nonlinear dynamic analysis of viscoelastic membranes described with fractional differential models, *Journal of Theoretical and Applied Mechanics*, **50**, 3, 743-753
16. Kilbas A.A., Srivastava H.M., Trujillo J.J., 2006, *Theory and Applications of Fractional Differential Equations*, Elsevier, Amsterdam
17. Klimek M., 2001, Fractional sequential mechanics – models with symmetric fractional derivative, *Czechoslovak Journal of Physics*, **51**, 1348-1354
18. Klimek M., 2009, *On Solutions of Linear Fractional Differential Equations of a Variational Type*, Publishing Office of Czestochowa University of Technology, Czestochowa
19. Klimek M., Odzijewicz T., Malinowska A.B., 2014, Variational methods for the fractional Sturm-Liouville problem, *Journal of Mathematical Analysis and Applications.*, **416**, 402-426
20. Leszczynski J.S., 2011, *An Introduction to Fractional Mechanics*, Publishing Office of Czestochowa University of Technology, Czestochowa
21. Magin R.L., 2006, *Fractional Calculus in Bioengineering*, Begell House Inc, Redding
22. Malinowska A.B., Torres D.F.M., 2012, *Introduction to the Fractional Calculus of Variations*, Imperial College Press, London
23. Odzijewicz T., Malinowska A.B., Torres D.F.M., 2012, Fractional variational calculus with classical and combined Caputo derivatives, *Nonlinear Analysis, Theory, Methods and Applications*, **75**, 1507-1515
24. Oldham K.B., Spanier J., 1974, *The Fractional Calculus: Theory and Applications of Differentiation and Integration to Arbitrary Order*, Academic Press, San Diego
25. Podlubny I., 1999, *Fractional Differential Equations*, Academic Press, San Diego
26. Pooseh S., Almeida R., Torres D.F.M., 2013, Discrete direct methods in the fractional calculus of variations, *Computational and Applied Mathematics*, **66**, 668-676
27. Press W.H., Teukolsky S.A., Vetterling W.T., Flannery B.P., 2007, *Numerical Recipes: The Art of Scientific Computing* (3rd ed.), Cambridge University Press, New York
28. Riewe F., 1996, Nonconservative Lagrangian and Hamiltonian mechanics, *Physical Review E*, **53**, 1890-1899
29. Sumelka W., 2014, A note on non-associated Drucker-Prager plastic flow in terms of fractional calculus, *Journal of Theoretical and Applied Mechanics*, **52**, 2, 571-574
30. Sumelka W., Blaszczyk T., 2014, Fractional continua for linear elasticity, *Archives of Mechanics*, **66**, 3, 147-172

31. Xu Y., Agrawal O.P., 2014, Models and numerical solutions of generalized oscillator equations, *Journal of Vibration and Acoustics*, **136**, 051005, 7pp

32. Zhang Y., Chen L., Reeves D.M., Sun H.G., 2014, A fractional-order tempered-stable continuity model to capture surface water runoff, *Journal of Vibration and Control*, http://dx.doi.org//10.1177/1077546314557554

Manuscript received January 29, 2015; accepted for print May 20, 2015

JOURNAL OF THEORETICAL
AND APPLIED MECHANICS
53, 4, pp. 969-980, Warsaw 2015
DOI: 10.15632/jtam-pl.53.4.969

HOMOTOPY PERTURBATION METHOD COMBINED WITH TREFFTZ METHOD IN NUMERICAL IDENTIFICATION OF LIQUID TEMPERATURE IN FLOW BOILING

Sylwia Hożejowska
Kielce University of Technology, Faculty of Management and Computer Modelling, Kielce, Poland
e-mail: ztpsf@tu.kielce.pl

The paper is focused on numerical identification of 2D temperature fields in flow boiling of the liquid through a horizontal minichannel with a rectangular cross-section. The heat transfer process in the minichannel is described by a two-dimensional energy equation with the corresponding boundary conditions. Liquid temperature is determined using the homotopy perturbation method (HPM) with Trefftz functions for Laplace'a equation. The numerical solution to the energy equation found with the HPM is compared with the solution obtained for the simplified form of the energy equation. Considering that only the thermal sublayer is taken into account, both solutions give similar results.

Keywords: homotopy perturbation method, Trefftz method, flow boiling, inverse problem

Nomenclature

a	–	thermal diffusivity [m^2/ s]
a, b, c, d	–	approximation coefficients
c_p	–	specific heat [J/(kg K)]
D	–	hydraulic diametrer [m]
f	–	friction coefficient
G	–	mass flux [kg/(m^{2}s)]
h	–	homotopy
H	–	minichannel length [m]
N, M	–	number of Trefftz functions
p	–	pressure [Pa]
Pr	–	Prandtl number
q	–	heat flux [W/m^2]
q_V	–	volumetric heat flux [W/m^3]
Re	–	Reynolds number
S	–	section area [m^2]
T	–	temperature [K]
u	–	Trefftz function
w	–	velocity [m/s]
x	–	distance along minichannel length [m]
y	–	distance along glass, foil and liquid [m]
α	–	heat transfer coefficient [W/(m^{2}K)]
δ	–	thickness, depth [m]
φ	–	void fraction
λ	–	thermal conductivity [W/(mK)]
μ	–	dynamic viscosity [Pa s]
ρ	–	density [kg/m^3]

Subscripts

ave – average, G – glass, F – foil, f – liquid, h – hydraulic, *in* – inlet, k – measurement point, n – number of function, M – minichannel, *out* – outlet, *sat* – saturation, T – thermal layer, 0 – initial approximation

Superscripts

n – refers to number of function, $\tilde{}$ – refers to particular solution

1. Introduction

The Trefftz method, first described by Trefftz (1926), is used for solving any partial differential equations that are linear. The method involves approximating the unknown solution using a linear combination of functions that exactly satisfy the given differential equation, i.e., Trefftz functions. The linear combination coefficients are determined through minimizing the error functional that describes the mean-square error between the approximate solution and the adopted boundary conditions. In Ciałkowski and Frąckowiak (2002), Herrera (2000), Maciąg (2011), Zieliński (1995) the authors reported the use of Trefftz functions for solving direct and inverse problems in mechanics.

The homotopy perturbation method (HPM) proposed by He (1999) is a useful tool for obtaining exact and approximate solutions to linear and nonlinear partial differential equations. The unknown solution to the differential equation is expressed as the summation of an infinite series that is supposed to be convergent to the exact solution. The HPM procedure generally requires few calculation steps to achieve the accuracy of the solutions. Additional information on HPM can be found in He (2000, 2006), Momani and Odibat (2007), Rajabi *et al.* (2007), Jafari and Seifi (2009), Słota (2011). Application of HPM to the solution of direct and inverse stationary and non stationary heat conduction problems was presented in Hetmaniok *et al.* (2012), Al-Khatib *et al.* (2014) and Grysa *et al.* (2012).

The paper presents a two-dimensional mathematical model describing heat transfer in flow boiling in an asymmetrically heated rectangular minichannel. In each of the three domains of the test section: the glass pane, the heating foil and the liquid, the heat transfer process has been described by different differential equations with appropriate boundary conditions. The solution of these equations leads to the solution of a threefold conjugated heat transfer problem consisting of a direct problem (in the glass pane) and two inverse problems (in the heating foil and boiling liquid). The Trefftz functions for Laplace's equation are used to determine two-dimensional temperature distributions in the glass pane, in the heating foil and in the liquid. The aim of this study is to apply the HPM coupled with the Trefftz method to find the two-dimensional temperature distribution of the boiling liquid flowing in an asymmetrically heated horizontal minichannel. Known liquid and foil temperature distributions help determination of the heat transfer coefficient from the Robin condition.

2. Experiment

Discussed in detail by Piasecka (2013, 2014) the experimental approach to this issue is described below in brief. In the experiment in which the difference between temperatures of the heating foil and the liquid is small, heat transfer enhancement occurs through the phase change that accompanies the boiling process. A microstructured heating surface (the heating foil is enhanced on the side of the fluid) additionally intensifies the process which described Piasecka (2013, 2014).

The basic module of the experimental stand is the test section with a minichannel and cooling liquid FC-72 flowing through it, seeFig. 1. One of the walls of the minichannel, made of the heating foil supplied with the controlled direct current, is isolated with a glass pane from the outside environment. A thin layer of liquid crystals deposited on the exterior of the foil helps measurement of two-dimensional temperature distribution. Boiling liquid flow structures are observed through the glass pane closing the minichannel on the other side of the flow. The measurements included the local temperature of the heating foil, liquid inlet and outlet temperatures and pressure, current and voltage drop of the electric power supplied to the foil, local void fraction and mass flux. Numerical calculations for FC-72 were performed based on the experiment and on the results described in detail in Piasecka (2014).

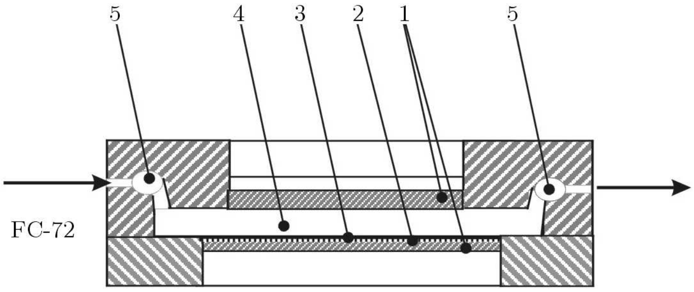

Fig. 1. Measuring module: 1 – glass panes, 2 – heating foil, 3 – thermosensitive liquid crystals, 4 – minichannel, 5 – thermocouples and pressure gauges (pictorial view, not to scale)

3. Mathematical model

For simplicity, only two dimensions are taken into account: dimension x along the flow direction and dimension y, perpendicular to the flow direction, relating to the thickness of the protecting glass (δ_G) and the foil (δ_F), and to the depth of the channel (δ_M), Fig. 2. We focused on the central part of the measurement module (along its length) so that the physical phenomena on the side edges did not affect the thermodynamic parameters within the investigated segment, Fig. 2. The fluid flow in the minichannel was assumed to be steady, stationary and laminar (Re < 2000) with a constant mass flux, (Hożejowska *et al.*, 2014; Hożejowska and Piasecka, 2014). The velocity vector had only one component $w(y)$ parallel to the heating foil (with other components equal to zero) given by the formula

$$w(y) = \frac{\Delta p}{2\mu H}(\delta_M y - y^2) \tag{3.1}$$

Thus the energy equation exclusively for the liquid phase can be written as follows

$$LT_f = AT_f \tag{3.2}$$

where $L = \partial^2/\partial x^2 + \partial^2/\partial y^2$ is the Laplace operator and A is the differential operator defined as

$$A = \frac{w(y)}{a}\frac{\partial}{\partial x} \qquad\qquad a = \frac{\lambda_f}{c_{p,f}\rho_f}$$

The boundary conditions for equation (3.2) are as follows (Bohdal, 2000; Hożejowska *et al.*, 2014):

— liquid temperatures at the inlet and outlet of the minichannel are known

$$\left.\begin{aligned} T_f(0,y) &= T_{in} \\ T_f(H,y) &= T_{out} \end{aligned}\right\} \qquad \text{for} \quad 0 \leqslant y \leqslant \delta_M \tag{3.3}$$

— liquid temperature in the domain of contact with the heating foil meets the condition

$$T_f(x,\delta_G+\delta_F)=\begin{cases} T_F(x,0) & \text{if} \quad T_F(x,0)<T_{sat}(x) \\ T_{sat}(x) & \text{if} \quad T_F(x,0)\geqslant T_{sat}(x) \end{cases} \tag{3.4}$$

where T_{sat} is the saturation temperature dependent on the pressure $p(x)$ which changes linearly along the minichannel,
— the two-phase mixture per unit volume in the minichannel contains vapour phase and liquid phase in proportion φ and $(1-\varphi)$, respectively. The same proportions of vapour and liquid phases are assumed to refer to any cross-sectional area of the minichannel and then to the heat transfer surface. For bubbly and bubbly-slug flows, following Bohdal (2000), Hożejowska *et al.* (2014), the whole heat flux generated in the foil is assumed to be transferred to the liquid phase in proportion carried over from the void fraction

$$\lambda_f\frac{\partial T_f}{\partial y}=\lambda_F(1-\varphi(x))\frac{\partial T_F}{\partial y} \qquad \text{for} \quad y=0 \quad \text{and} \quad 0\leqslant x\leqslant H \tag{3.5}$$

Figure 2 shows a diagram of the unit with the minichannel and the boundary conditions.

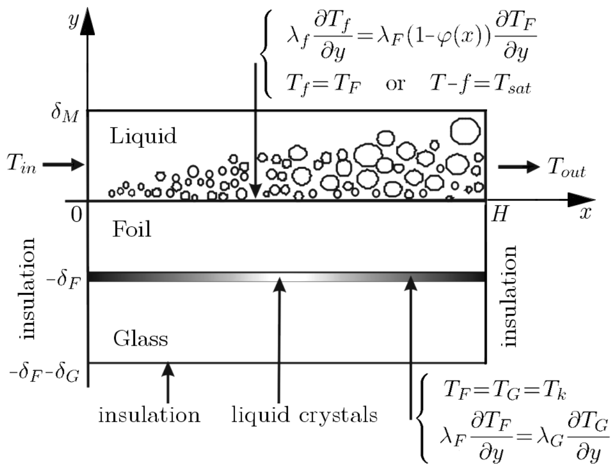

Fig. 2. Scheme of the measuring module with boundary conditions (pictorial view, not to scale)

The temperatures of the heating foil and the glass are assumed to satisfy the following equations (Hożejowska *et al.*, 2009; Piasecka *et al.*, 2004):
— in the glass

$$LT_G=0 \tag{3.6}$$

— in the foil

$$LT_F=-\frac{q_V}{\lambda_F} \tag{3.7}$$

The conditions at the glass-foil contact can be written as

$$\begin{aligned} & T_F(x_k,-\delta_F)=T_G(x_k,-\delta_F)=T_k \\ & \lambda_F\frac{\partial T_F}{\partial y}=\lambda_G\frac{\partial T_G}{\partial y} \qquad y=-\delta_F \qquad 0\leqslant x\leqslant H \end{aligned} \tag{3.8}$$

where T_k denotes the temperature measured at the glass-foil interface at discrete points $(x_k,-\delta_F)$ using liquid crystals thermography. The remaining boundaries are assumed to be isolated, Fig. 2.

When the heating foil temperature distribution and the temperature gradient are known, the heat transfer coefficient $\alpha(x)$ at the foil-liquid interface can be determined from the Robin condition

$$-\lambda_F \frac{\partial T_F}{\partial y}(x,0) = \alpha(x)[T_F(x,0) - T_{f,ave}(x)] \tag{3.9}$$

The reference temperature $T_{f,ave}$ is determined as a mean liquid temperature in the thermal layer

$$T_{f,ave}(x) = \frac{1}{\delta_T} \int\limits_0^{\delta_T} T_f(x,y)\, dy \tag{3.10}$$

where δ_T is the thickness of the thermal boundary layer determined by Bohdal (2000)

$$\delta_T = \mathrm{Pr}^{-\frac{1}{3}} \delta_h \tag{3.11}$$

and

$$\delta_h = \frac{2\mu_f}{f w_{ave} \rho_f} \qquad f = \frac{64}{\mathrm{Re}} \qquad \mathrm{Re} = \frac{w_{ave}\rho_f D}{\mu_f} \tag{3.12}$$

and w_{ave} is the mean velocity of the liquid, calculated from

$$w_{ave} = \frac{1}{0.5\delta_M} \int\limits_0^{0.5\delta_M} w(y)\, dy \tag{3.13}$$

4. Numerical methods

4.1. Trefftz method

The Trefftz method has been used to calculate approximate two-dimensional temperature distributions of the glass pane and the heating foil. The unknown distributions of T_G and T_F have been approximated with a linear combination of the Trefftz functions $u_i(x,y)$ adequate for Laplace's equation (3.6) (Piasecka *et al.*, 2004), in this case harmonic polynomials, that is

$$T_G(x,y) = \sum_{i=1}^{N_G} a_i u_i(x,y) \qquad T_F(x,y) = \widetilde{u}(x,y) + \sum_{j=1}^{N_F} b_j u_j(x,y) \tag{4.1}$$

where $\widetilde{u}(x,y)$ is the particular solution to equation (3.7). The unknown coefficients a_i and b_j of linear combinations (4.1) are calculated using the least square method which led to minimizing the functionals suitable for each function T_G and T_F. These functionals describe the mean squared error between the approximates and prescribed boundary conditions. This procedure was thoroughly discussed in Piasecka *et al.* (2004) and Hożejowska *et al.* (2009).

Numerical computations have been made sequentially. We obtained the solution first in the glass, and then in the heating foil. The approximate functions T_G and T_F, obtained with the Trefftz method, satisfied exactly equations (3.6) and (3.7), respectively, and approximately the adopted boundary conditions. Solving these equations has led to solving two heat transfer problems: the direct problem in the glass and then the inverse problem in the heating foil. Fluid temperature has been computed in the next stage by solving the inverse problem with the HPM and Trefftz method combined.

4.2. Homotopy perturbation method (HPM)

The use of the HPM in combination with the Trefftz method for identifying the source function was presented in Grysa and Maciąg (2013) and Al-Khatib *et al.* (2014). In this study, the above combination is used to find the two-dimensional liquid temperature distribution in the minichannel. According to the homotopy method, a homotopy $h(x, y, p)$ can be constructed as the solution to

$$(1-p)[L(h)-L(u_0)]+p[L(h)-A(h)]=0 \tag{4.2}$$

where the parameter $0 \leqslant p \leqslant 1$ and u_0 is the initial approximation of equation (2) that satisfies boundary conditions (3.3)-(3.5). Substituting $p = 1$ into (4.2), we have

$$L(h)-A(h)=0 \tag{4.3}$$

that is equation (3.2).

Expanding the function h in the power series in p, we obtain

$$h(x,y,p)=h_0(x,y)+h_1(x,y)p+h_2(x,y)p^2+h_3(x,y)p^3+\dots \tag{4.4}$$

and the solution to (3.2) is expressed as

$$T_f(x,y)=\lim_{p\to 1} h(x,y,p)=h_0(x,y)+h_1(x,y)+h_2(x,y)+h_3(x,y)+\dots \tag{4.5}$$

Finally, we take an approximate solution of (3.2) in form of truncated series (4.5)

$$T_f(x,y)=\sum_{i=0}^{N_f} h_i(x,y) \tag{4.6}$$

The convergence of HPM for partial differential equations was proved in Biazar and Ghazvini (2009) and Turkyilmazoglu (2011). The outcome of computations indicates that satisfactory results can be obtained with three or four terms in series (4.6). The assumptions relating to the initial approximation u_0 can be weaker. In further calculation, the initial approximation may be an arbitrary function. Substituting (4.4) into (4.2) and comparing coefficients at subsequent powers of p to zero, we obtain a system of equations from which we calculate $h_0, h_1, h_2, \dots$ sequentially

$$\begin{aligned}
&L(h_0)-L(u_0)=0\\
&L(h_1)+L(u_0)-A(h_0)=0\\
&L(h_2)-A(h_1)=0\\
&\vdots\\
&L(h_{N_f})-A(h_{N_f-1})=0
\end{aligned} \tag{4.7}$$

The Trefftz method is used to determine functions $h_n(x, y)$, $n = 0, 1, \dots, N_f$, which are solutions to successive equations in system (4.7). In this case, the solutions $h_n(x, y)$ contain two terms: a linear combination of the Trefftz functions $u_i(x, y)$ and a particular solution of the n-th equation from system (4.7), see Ciałkowski and Frąckowiak (2000), i.e.

$$
\begin{aligned}
h_0(x,y) &= \sum_{i=1}^{N_0} c_i^{(0)} u_i(x,y) + u_0 \\
h_1(x,y) &= \sum_{i=1}^{N_1} c_i^{(1)} u_i(x,y) + L^{-1}[A(h_0)] - u_0 \\
h_2(x,y) &= \sum_{i=1}^{N_2} c_i^{(2)} u_i(x,y) + L^{-1}[A(h_2)] \\
&\vdots \\
h_n(x,y) &= \sum_{i=1}^{N_n} c_i^{(n)} u_i(x,y) + L^{-1}[A(h_{n-1})]
\end{aligned}
\tag{4.8}
$$

where the functions u_0, $L^{-1}[A(h_0)] - u_0$, $L^{-1}[A(h_n)]$ are particular solutions to the appropriate equations from system (4.7) and L^{-1} is the inverse of operator L. Since the differential operators L and A are linear, one can rewrite recursive formula (4.8) in a more concise form

$$
\begin{aligned}
h_0(x,y) &= \sum_{i=1}^{N_0} c_i^{(0)} u_i(x,y) + u_0 \\
h_n(x,y) &= \sum_{s=0}^{n}\sum_{i=1}^{N_s} c_i^{(s)} L^{-(n-s)}[A^{n-s}(u_i(x,y))] + L^{-n}[A^n(u_0)] - L^{-n+1}[A^{n-1}(u_0)] \\
&\qquad n = 1,2,\dots,N_f
\end{aligned}
\tag{4.9}
$$

where $L^{-n} = L^{-1}(L^{-(n-1)})$ and $A^n = A(A^{n-1})$. The description of the use of inverse operators in the Trefftz method can be found in Ciałkowski and Frąckowiak (2000), Grysa *et al.* (2012).

Known boundary conditions (3.3)-(3.5) help determination of the coefficients of linear combination (4.8) by minimizing the corresponding error functional appropriate for each function $h_n(x,y)$, $n = 0,1,\dots,N_f$. Sequential determination of the functions $h_n(x,y)$ requires each time taking into account the computed functions $h_n(x,y)$ in boundary conditions (3.3)-(3.5) after appropriate modification (Grysa and Maciąg, 2013). The approximate liquid temperature computed from (4.6) satisfies approximately both equation (3.2) and boundary conditions (3.3)-(3.5).

5. Results

Numerical calculations for cooling liquid FC-72 have been performed based on the experimental results described in detail in Piasecka (2013, 2014) concerning a forced flow of FC-72 through an asymmetrically heated minichannel, Fig. 3. The flow structures and the void fraction have also been observed. In further calculations, the local void fraction determined at lengths 0.09 m, 0.133 m, 0.27 m, and 0.34 m is approximated with a quadratic function, Fig. 3.

Approximate temperature distributions of the glass, heating foil and liquid have been determined sequentially. In the first instance, the approximate temperatures of the glass T_G and the heating foil T_F were calculated knowing both the temperature distribution at the foil-glass interface and the heat flux at the foil inside the surface-liquid interface. Fifteen Trefftz functions $u_i(x,y)$ for Laplace's equation were adopted for calculations, i.e. $N_G = N_F = 15$. To determine T_G and T_F, we adopted the particular solution to equation (4.1) in the form $\widetilde{u}(x,y) = -0.5 q_V \lambda_F^{-1} y^2$. The distribution of the fluid temperature could be obtained only after determining the glass and the foil temperature. The liquid temperature T_f in the minichannel was determined based on (4.6) with the initial approximation $u_0 = 0$ (other forms of the initial

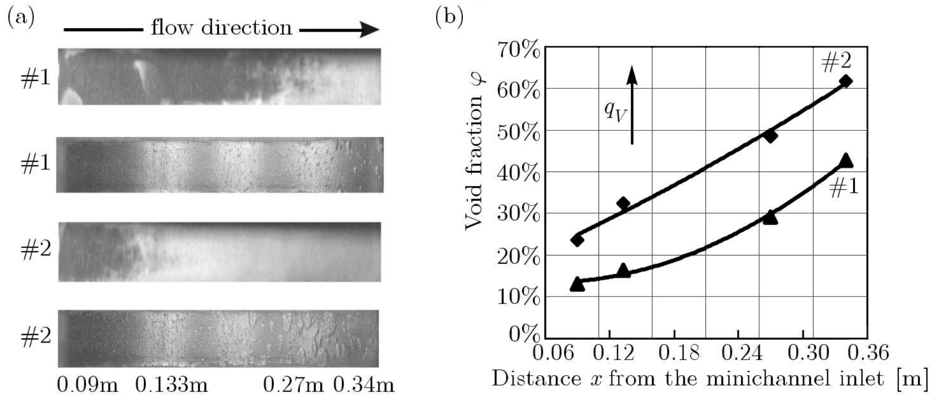

Fig. 3. (a) Hue distribution on the exterior of the minichannel obtained with liquid crystal thermography and the corresponding flow structures observed for the given temperature distribution, (b) void fraction. Experimental parameters of the runs (Piasecka, 2014); foil parameters: $\delta_F = 1.02 \cdot 10^{-4}\,\mathrm{m}$, $H = 0.35\,\mathrm{m}$, $\lambda_F = 8.3\,\mathrm{W/(mK)}$; glass parameters: $\delta_G = 0.006\,\mathrm{m}$, $\lambda_G = 0.71\,\mathrm{W/(mK)}$; for #1: $G = 282\,\mathrm{kg/(m^2s)}$, $\mathrm{Re} = 944$, $p_{in} = 129\,\mathrm{kPa}$, $T_{in} = 293\,\mathrm{K}$, $T_{out} = 319\,\mathrm{K}$, $q_V = 1.92 \cdot 10^5\,\mathrm{kW/m^3}$; for #2: $G = 277\,\mathrm{kg/(m^2s)}$, $\mathrm{Re} = 009$, $p_{in} = 139\,\mathrm{kPa}$, $T_{in} = 293\,\mathrm{K}$, $T_{out} = 334\,\mathrm{K}$, $q_V = 2.99 \cdot 10^5\,\mathrm{kW/m^3}$

approximation u_0, for example, a harmonic function, did not affect the final result). The following quantities were used in calculations: local void fraction, pressure drop, liquid temperature at the inlet and outlet of the minichannel, liquid saturation temperature and the foil temperature gradient in the foil-liquid contact area along the channel. Three steps of recursion were made approximating $h_n(x,y)$ with five Trefftz functions $u_i(x,y)$ in each step, i.e. $N_f = 2$ and $N_n = 5$. Figure 4 presents two-dimensional temperature distribution of the glass, the foil and the flowing liquid. Application of Trefftz method allowed to obtain two-dimensional temperature distributions in the three neighbouring domains.

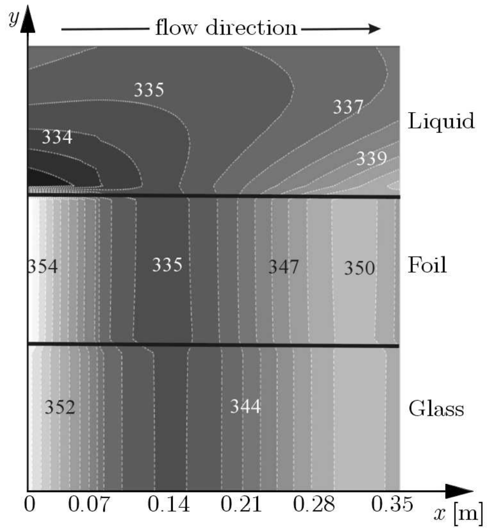

Fig. 4. Temperature of the glass pane and the heating foil determined by the Trefftz method. Temperature of the liquid obtained HPM /Trefftz method. Additional data: as in Fig. 3 for #2

To verify the solution obtained by the HPM combined with the Trefftz method, equation (3.2) has been solved using a different approach with an additional simplification. The liquid temperature change along the whole minichannel length has been replaced with the formula from (Bohdal, 2000)

$$\frac{\partial T_f}{\partial x} = \frac{Dq}{SGc_{p,f}} \tag{5.1}$$

Substituting (5.1) into (3.2), we obtain the Poisson equation. The solution to this equation is given in the form of the sum of the linear combination of the Trefftz functions $u_i(x,y)$ and the particular solution

$$T_F(x,y) = \sum_{j=1}^{M_f} d_j u_j(x,y) + \frac{Dq\rho_f}{SG\lambda_f} L^{-1}[w(y)] \tag{5.2}$$

The coefficients d_j are calculated in the same way as in the Trefftz method. Five Trefftz functions $u_i(x,y)$ are taken, analogously to the combination of the HPM with the Trefftz method.

Figure 5 compares the cooling liquid temperature distribution derived from the solution obtained from formulas (4.6) and (5.2). Both approaches produce very similar results in the thermal layer, Fig. 5. This is the result of the fact that the determination of the liquid temperature in the minichannel leads to the solution of the inverse problem.

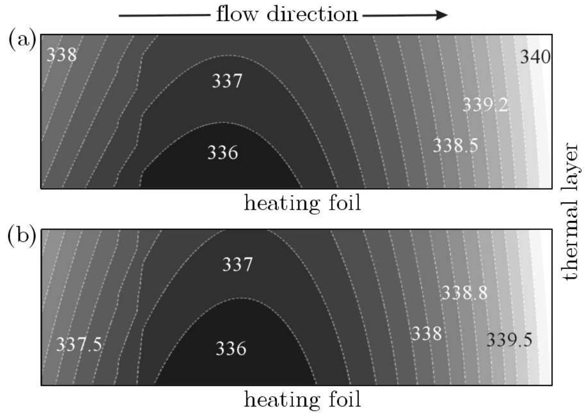

Fig. 5. Temperature of the liquid: (a) obtained by formula (4.6), (b) obtained by formula (5.2), (c) temperature scale; additional data: as in Fig. 3 for #2

For correct interpretation of the temperature distribution shown in Fig. 5, one has to take into account the physics of flow boiling. In the considered case, the heat received from the foil is transferred by the bubbles of gas to the center (axis) of the minichannel which can be seen in Fig. 4. For that reason, once the boiling incipience has taken place, the bubbles lower the temperature of the fluid in the immediate neighbourhood of the foil and the temperature of the foil alone, see Fig. 5. The measured temperature of the heating foil at the foil-glass contact, see Fig. 3, confirms that such a phenomenon is observed (i.e. temperature rise and then a rapid drop after the boiling incipience), see Fig. 4 and Fig. 5 as well as the figures presented in Piasecka (2013, 2014).

In Hożejowska and Piasecka (2014) and Hożejowska *et al.* (2014) in order to determine the temperature of the liquid for equation (3.2), the Trefftz functions were derived assuming the velocity $w(y)$ to be a roof or parabolic function. When the velocity profile has a more complex form, liquid temperature can be calculated from the HPM combined with the Trefftz method.

The known temperature field of the liquid is employed to determine the heat transfer coefficient at the contact point of the foil and liquid, calculated from Robin condition (3.9). Figure 6 presents the heat transfer coefficient calculated from Eq. (3.9) when the liquid temperature is calculated using the HPM plus Trefftz method and when the liquid temperature is obtained by (5.2). Concentrating only on the thermal sublayer, we obtain similar plots of heat transfer coefficients, Fig. 6, with differences that do not exceed $5\,\mathrm{kW/(m^2K)}$ on average. A fast increase in the heat transfer coefficient values results from the phase change which accompanies heat transfer. It is observed that when the heat flux supplied to the heating wall grows, the heat transfer coefficient grows too. A further increase in the heat flux results in an increase in the void fraction and a decrease in the heat transfer coefficient, Fig. 6. In the enhanced boiling region, heat transfer coefficient values decrease with the distance from the minichannel inlet and with the increasing vapour fraction in the flowing mixture.

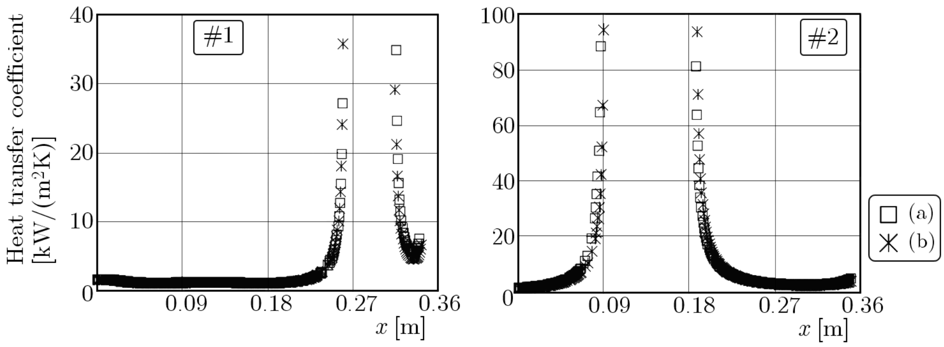

Fig. 6. Heat transfer coefficients as a function of the minichannel length obtained using: (a) HPM plus Trefftz method, (b) Trefftz method and inverse operations; additional data: as in Fig. 3

6. Conclusions

The presented combination of the HPM and the Trefftz method helps determination of the approximate two-dimensional temperature distribution of the boiling liquid. The Trefftz method is used to solve the direct heat transfer problem for the glass pane and the inverse problem in the heating foil, determining their temperatures and gradients. Known temperature distributions in the foil-liquid contact area are used to compute the heat transfer coefficient from the Robin boundary condition. The results are summarized and compared with those obtained from the simplified model. The resulting two-dimensional liquid temperature distributions are similar, in particular when the considerations are limited to the thermal layer. An analogous relationship is observed for the heat transfer coefficient calculated for both models. The advantage of the HPM/Trefftz method combination is its simplicity and a small number of steps of recursion to produce a satisfactory result. The number of Trefftz functions used in calculations is also small. In addition, this combination of methods can be used to solve problems described by non-linear equations. Thus, further work will be directed towards determination of the temperature of the liquid phase, vapour phase and the mixture of these two phases in two-phase flows for more complex models than those presented here.

Acknowledgments

The research has been financially supported by the National Scientific Center from funds granted by virtue of decision No. DEC-2013/09/B/ST8/02825.

References

1. Al-Khatib M.J., Maciąg A., Pawińska A., 2014, The Trefftz functions in different methods of solving the direct and inverse problems for beam with variable stiffness, *8th International Conference on Inverse Problems in Engineering*, 12-15 May, Cracow

2. Biazar J., Ghazvini H., 2009, Convergence of the homotopy perturbation method for partial differential equations, *Nonlinear Analysis: Real World Applications*, **10**, 2633-2640

3. Bohdal T., 2000, Modeling the process of bubble boiling on flows, *Archives of Thermodynamics*, **21**, 34-75

4. Ciałkowski M.J., Frąckowiak A., 2000, *Heat Functions and Their Application to Solving Heat Conduction in Mechanical Problems* (in Polish), Politechnika Poznańska
5. Grysa K., Maciąg A., 2013, Homotopy perturbation method and Trefftz functions in the source function identification, *APCOM&ISCM*, 11-14 December, Singapore
6. Grysa K., Maciąg A., Pawińska A., 2012, Solving nonlinear direct and inverse problems of stationary heat transfer by using Trefftz functions, *International Journal of Heat and Mass Transfer*, **55**, 7336-7340
7. He J.-H., 1999, Homotopy perturbation technique, *Computer Methods in Applied Mechanics and Engineering*, **178**, 3/4, 257-262
8. He J.-H., 2000, A coupling method of homotopy technique and perturbation technique for nonlinear problems, *International Journal of Non-Linear Mechanics*, **35**, 37-43
9. He J.-H., 2006, Some asymptotic methods for strongly nonlinear equations, *International Journal of Modern Physics B*, **20**, 10, 1141-1199
10. Herrera I., 2000, Trefftz method: a general theory, *Numerical Methods for Partial Differential Equations*, **16**, 561-580
11. Hetmaniok E., Nowak I., Słota D., Wituła R., 2012, Application of the homotopy perturbation method for the solution of inverse heat conduction problem, *International Communications in Heat and Mass Transfer*, **39**, 30-35
12. Hożejowska S., Kaniowski R., Poniewski M.E., 2014, Application of adjustment calculus to the Trefftz method for calculating temperature field of the boiling liquid flowing in a minichannel, *International Journal of Numerical Methods for Heat and Fluid Flow*, **24**, 811-824
13. Hożejowska S., Piasecka M., 2014, Equalizing calculus in Trefftz method for solving two--dimensional temperature field of FC-72 flowing along the minichannel, *Heat and Mass Transfer*, **50**, 8, 1053-1063
14. Hożejowska S., Piasecka M., Poniewski M.E., 2009, Boiling heat transfer in vertical minichannels. Liquid crystal experiments and numerical investigations, *International Journal Thermal Sciences*, **48**, 1049-1059
15. Jafari H., Seifi S., 2009, Solving a system of nonlinear fractional partial differential equations using homotopy analysis method, *Communications in Nonlinear Science and Numerical Simulation*, **14**, 5, 1962-1969
16. Maciąg A., 2011, The usage of wave polynomials in solving direct and inverse problems for two-dimensional wave equation, *International Journal for Numerical Methods in Biomedical Engineering*, **27**, 1107-1125
17. Momani S., Odibat Z., 2007, Comparison between the homotopy perturbation method and the variational iteration method for linear fractional partial differential equations, *Computers and Mathematics with Applications*, **54**, 7/8, 910-919
18. Piasecka M., 2013, Heat transfer mechanism, pressure drop and flow patterns during FC-72 flow boiling in horizontal and vertical minichannels with enhanced walls, *International Journal of Heat and Mass Transfer*, **66**, 472-488
19. Piasecka M., 2014, *Flow Boiling on Enhanced Surfaces of Minichannels* (in Polish), Politechnika Świętokrzyska
20. Piasecka M., Poniewski M.E., Hożejowska S., 2004, Experimental evaluation of flow boiling incipience of subcooled fluid in a narrow channel, *International Journal Heat and Fluid Flow*, **25**, 159-172
21. Rajabi A., Ganji D.D., Taherian H., 2007, Application of homotopy perturbation method in nonlinear heat conduction and convection equations, *Physics Letters A*, **360**, 570-573
22. Słota D., 2011, Homotopy perturbation method for solving the two-phase inverse Stefan problem, *Numerical Heat Transfer, Part A*, **59**, 755-768

23. Trefftz E., 1926, Ein Gegenstück zum Ritzschen Verfahren, 2 Int. Kongress für Technische Mechanik, 131-137

24. Turkyilmazoglu M., 2011, Convergence of the homotopy perturbation method, *International Journal of Nonlinear Sciences and Numerical Simulation*, **12**, 9-14

25. Zieliński A.P., 1995, On trial functions applied in the generalized Trefftz method, *Advances in Engineering Software*, **24**, 147-155

Manuscript received November 28, 2014; accepted for print May 21, 2015

JOURNAL OF THEORETICAL
AND APPLIED MECHANICS
54, 1, pp. 981-990, Warsaw 2016
DOI: 10.15632/jtam-pl.54.1.981

THE METHOD OF ESTIMATING LIFETIMES OF AIRCRAFT DEVICES OPERATING UNDER AGEING-ATTRIBUTABLE WEARING CONDITIONS

Mariusz Ważny
Military University of Technology, Warsaw, Poland
e-mail: mariusz.wazny@wat.edu.pl

The paper presents a probabilistic method of assessing lifetimes of selected structural components or assemblies of devices/systems affected by destructive processes that occur during aircraft operation. Reliability status of the device is evaluated by means of diagnostic or operational parameters. It is assumed that these devices (systems, assemblies) operate reliably if effects of wear and tear processes described by diagnostic parameters do not exceed boundary conditions/regimes. From the mathematical aspect, the method has been based on difference equations from which, when rearranged, a partial differential equation of the Fokker-Planck type is derived. A density function of the component wearing is a particular solution to this equation. With the density function of the component wearing applied, after suitable rearrangements, one can determine a density function of time for the exceeding the boundary condition. Now, with the density function of time of reaching the boundary condition found, and after rearrangement of this function, one receives dependences that can be applied to determine lifetime of the device given consideration. An example at the end of the paper illustrates how this method can be applied to analyse an airborne sighting system.

Keywords: reliability, lifetime, destructive processes, permissible condition

1. Introduction

Any manifestations of aeronautical engineering, i.e. aeronautical devices, systems, etc., make design engineers, manufacturers and users meet requirements connected with maintaining high values of safety and reliability parameters. Examining the safety and reliability of an aircraft throughout the operational process involves predictions about health/maintenance status of particular devices and systems of an aircraft and the aircraft itself as a platform combining all the above-mentioned elements. Analyzing an aircraft as an object intended to provide, e.g. transportation of passengers and cargo, we can assume that the operating conditions are of special importance compared with other popular means of transport (Pamuła, 2011). A series of factors make values of parameters that describe health/maintenance status of an aircraft change over time. Destructive processes resulting from overloads, friction, vibration, ageing processes, etc. prove to have the crucial effect on that change.

An aircraft is a platform upon which systems like the following ones are integrated:

- automatic control systems,
- communication systems,
- avionic systems,
- air armament systems,
- sighting systems,
- systems to abandon the aircraft in emergency, etc.

The health/maintenance status of aircraft devices is mainly evaluated with a set of diagnostic parameters. The effect of destructive processes is visible in changes of values of diagnostic parameters, which cause increments in deviations from nominal values of these parameters. Deviations from nominal values of diagnostic parameters are used to estimate reliability of a given device. This question is addressed in (Niu *et al.*, 2011; Tomaszek and Wróblewski, 2001; Tomaszek *et al.*, 2004, 2011, 2013; Tomaszek and Szczepanik, 2005; Ye *et al.*, 2011; Zhanshan and Krings, 2008). Among the above mentioned works, (Niu *et al.*, 2011) is an interesting publication where health/maintenance status of a piece of equipment is analysed with the Mahalanobis distance indicator and the Weibull distribution applied.

This paper is an attempt to analyse and describe degradation of health/maintenance status of selected devices as a result of destructive processes affecting them.

Classification of correlations between effects of destructive processes and changes in values of diagnostic parameters is presented by Ważny (2011a). The density function of changes in deviations of the diagnostic parameter has been determined in this article, with the following assumptions applied:

- the device health is determined by one dominant diagnostic parameter (its current value is denoted by x),
- the change in value of the diagnostic parameter due to the destructive effect of ageing processes occurs as the calendar time passes by,
- the deviation of the diagnostic parameter from the nominal value is

  $$z = |x_p - x_n|$$

  where x_p is measured value of the diagnostic parameter, x_n – nominal value of the diagnostic parameter,
- the value of the diagnostic parameter deviation determines the level of reliability of a given structural component. If it remains within the interval $z \in [0, Z_d]$, the component will be recognised as serviceable (fit for use). Otherwise, it will be recognised unserviceable (unfit for use),
- the increase in the diagnostic parameter deviation against the calendar time satisfies the relationship

  $$\frac{dz}{dt} = c$$

  where c is a random variable that depends on ageing processes, t – the calendar-based time.

2. Determining the density function of changes in values of deviations of the diagnostic parameter

It is assumed that the intensity of growth of the component wear and tear takes the same form as the failure rate for the Weibull distribution

$$\lambda(t) = \frac{\alpha}{\theta} t^{\alpha-1} \tag{2.1}$$

where α and θ are constants in the Weibull distribution with the following denotations: α – the shape factor, θ – the scale factor.

The stochastically approached dynamics of changes in values of diagnostic parameters, including the parameter deviation, is described by difference equation. Let $U_{z,t}$ denote the probability that at the time instance t the diagnostic parameter deviation takes value z.

A difference equation takes the following form for the assumed conditions

$$U_{z,t+\Delta t} = \Big(1 - \frac{\alpha}{\theta}t^{\alpha-1}\Delta t\Big)U_{z,t} + \frac{\alpha}{\theta}t^{\alpha-1}\Delta t U_{z-\Delta z,t} \tag{2.2}$$

where Δz is the increment in the diagnostic parameter deviation in the time interval Δt.

Equation (2.2) written down in functional notation takes the following form

$$u(z,t+\Delta t) = \Big(1 - \frac{\alpha}{\theta}t^{\alpha-1}\Delta t\Big)u(z,t) + \frac{\alpha}{\theta}t^{\alpha-1}\Delta t u(z-\Delta z,t) \tag{2.3}$$

where $u(z,t)$ is the density function of the diagnostic parameter deviation, $[1-(\alpha/\theta)t^{\alpha-1}\Delta t]$ – probability that in the time interval Δt there will be no increment in the diagnostic parameter deviation, $(\alpha/\theta)t^{\alpha-1}\Delta t$ – probability that in the time interval Δt there will be the Δz increment in the parameter deviation, and the following condition is satisfied

$$\frac{\alpha}{\theta}t^{\alpha-1}\Delta t \leqslant 1$$

Rearrangement of equation (2.3) into a partial differential equation results in the following approximation

$$\begin{aligned} u(z,t+\Delta t) &= u(z,t) + \frac{\partial u(z,t)}{\partial t}\Delta t \\ u(z-\Delta z,t) &= u(z,t) - \frac{\partial u(z,t)}{\partial z}\Delta z + \frac{1}{2}\frac{\partial^2 u(z,t)}{\partial z^2}(\Delta z)^2 \end{aligned} \tag{2.4}$$

Having substituted relationships (2.4) into equation (2.3) and with some rearrangements done, the following is arrived at

$$\frac{\partial u(z,t)}{\partial z} = -\frac{\alpha}{\theta}t^{\alpha-1}\Delta z\frac{\partial u(z,t)}{\partial z} + \frac{1}{2}\frac{\alpha}{\theta}t^{\alpha-1}(\Delta z)^2\frac{\partial^2 u(z,t)}{\partial z^2} \tag{2.5}$$

Consideration is given to the increment in the diagnostic parameter deviation per time unit (when $\Delta t = 1$), hence

$$\frac{\Delta z}{\Delta t} = c \quad \Rightarrow \quad \Delta z = c\Delta t \quad \underset{\Delta t=1}{\Longrightarrow} \quad \overline{c}$$

where $\overline{c}$ denotes increment in the diagnostic parameter deviation per one time unit.

The final form of equation (2.5) is as follows

$$\frac{\partial u(z,t)}{\partial z} = -\underbrace{\frac{\alpha\overline{c}}{\theta}t^{\alpha-1}}_{\gamma(t)}\frac{\partial u(z,t)}{\partial z} + \frac{1}{2}\underbrace{\frac{\alpha\overline{c}^2}{\theta}t^{\alpha-1}}_{\beta(t)}\frac{\partial^2 u(z,t)}{\partial z^2} \tag{2.6}$$

The solution to equation (2.6) takes the form

$$u(z,t) = \frac{1}{\sqrt{2\pi A(t)}}\exp\Big(-\frac{(z-B(t))^2}{2A(t)}\Big) \tag{2.7}$$

where $B(t)$ is an average value of the diagnostic parameter deviation for the operating time t

$$B(t) = \int\limits_0^t \gamma(t)\,dt \tag{2.8}$$

$A(t)$ – a variance of the diagnostic parameter deviation for the operating time t

$$A(t) = \int\limits_0^t \beta(t)\,dt \tag{2.9}$$

With integrals (2.8) and (2.9) calculated, the following expressions are arrived at

$$B(t) = \int\limits_0^t \frac{\alpha\overline{c}}{\theta}t^{\alpha-1}\,dt = \frac{\overline{c}}{\theta}t^{\alpha} \qquad\qquad A(t) = \int\limits_0^t \frac{\alpha\overline{c}^2}{\theta}t^{\alpha-1} = \frac{\overline{c}^2}{\theta}t^{\alpha} \tag{2.10}$$

Hence, relationship (2.7) takes the following form

$$u(z,t) = \frac{1}{\sqrt{2\pi\frac{\overline{c}^2}{\theta}t^{\alpha}}}\exp\left(-\frac{\left(z-\frac{\overline{c}}{\theta}t^{\alpha}\right)^2}{2\frac{\overline{c}^2}{\theta}t^{\alpha}}\right) \tag{2.11}$$

Relationship (2.11) presents the density function of the diagnostic parameter deviation from the nominal value.

With the following substitutions

$$\frac{\overline{c}}{\theta} = b \qquad\qquad \frac{\overline{c}^2}{\theta} = a$$

relationship (2.11) takes the following form

$$u(z,t) = \frac{1}{\sqrt{2\pi a t^{\alpha}}}\exp\Big(-\frac{(z-bt^{\alpha})^2}{2at^{\alpha}}\Big) \tag{2.12}$$

With the density function found, one can write down a relationship for reliability with respect to time of the diagnostic parameter deviation increasing up to the boundary value. The formula takes the form

$$R(t) = \int\limits_{-\infty}^{z_d} u(z,t)\,dz \tag{2.13}$$

where z_d is a permissible value of the diagnostic parameter deviation.

3. Determining distribution of time of exceeding the permissible condition by the diagnostic parameter deviation

The probability of exceeding the boundary value by the diagnostic parameter with the density function of changes in the diagnostic parameter deviation can be written down in the following form

$$Q(t,z_d) = \int\limits_{z_d}^{\infty} \frac{1}{\sqrt{2\pi a t^{\alpha}}}\exp\Big(-\frac{(z-bt^{\alpha})^2}{2at^{\alpha}}\Big)\,dz \tag{3.1}$$

The density function of the distribution of time of exceeding the permissible value of the diagnostic parameter z_d equals

$$f(t) = \frac{\partial}{\partial t}Q(t,z_d) \tag{3.2}$$

With (3.1) taken into account, this equation takes the form

$$f(t) = \frac{\partial}{\partial t} \int\limits_{z_d}^{\infty} \frac{1}{\sqrt{2\pi a t^\alpha}} \exp\Big(-\frac{(z - bt^\alpha)^2}{2at^\alpha}\Big)\ dz \tag{3.3}$$

Now, the time derivative of the integrand for relationship (3.3) can be found

$$f(t) = \int\limits_{z_d}^{\infty} \Big[\frac{2(z - bt^\alpha)b\alpha t^\alpha + (z - bt^\alpha)^2\alpha}{2at^{\alpha+1}} - \frac{\alpha}{2t}\Big] u(z,t)\ dz \tag{3.4}$$

In order to calculate integral (3.4), we need to determine an antiderivative. We assume the following form of the antiderivative of the integrand in relationship (3.4)

$$w(z,t) = u(z,t)\theta(z,t) \tag{3.5}$$

The derivative of the indefinite integral with respect to the variable z is equal to the integrand of relationship (3.4). Hence

$$\frac{\partial u(z,t)}{\partial z}\theta(z,t) + u(z,t)\frac{\partial \theta(z,t)}{\partial z} = \Big[\frac{2(z - bt^\alpha)b\alpha t^\alpha + (z - bt^\alpha)^2\alpha}{2at^{\alpha+1}} - \frac{\alpha}{2t}\Big] u(z,t) \tag{3.6}$$

Now, the derivative $\partial u(z,t)/\partial z$ is calculated

$$\frac{\partial u(z,t)}{\partial z} = \frac{1}{\sqrt{2\pi a t^\alpha}} \exp\Big(-\frac{(z - bt^\alpha)^2}{2at^\alpha}\Big)\Big[-\frac{2(z - bt^\alpha)}{2at^\alpha}\Big] = u(z,t)\Big[-\frac{(z - bt^\alpha)}{at^\alpha}\Big] \tag{3.7}$$

After substitution of (3.7) into (3.6), the following relationship can be written down

$$u(z,t)\Big[\underbrace{-\frac{(z - bt^\alpha)}{at^\alpha}\theta(z,t)}_{I-L} + \underbrace{\frac{\partial \theta(z,t)}{\partial z}}_{II-L}\Big] = u(z,t)\Big[\underbrace{\frac{2(z - bt^\alpha)b\alpha t^\alpha + (z - bt^\alpha)^2\alpha}{2at^{\alpha+1}}}_{I-P} \underbrace{-\frac{\alpha}{2t}}_{II-P}\Big] \tag{3.8}$$

Using relationship (3.8), the function $\theta(z,t)$ is determined in such a way that the left side of relationship (3.8) equals its right side. Therefore

$$\begin{aligned} I - L = I - P \ &\Rightarrow\ \theta(z,t) = -\frac{2b\alpha t^\alpha + \alpha(z - bt^\alpha)}{2t} \\ II - L = II - P \ &\Rightarrow\ \frac{\partial \theta(z,t)}{\partial z} = -\frac{\alpha}{2t} \end{aligned} \tag{3.9}$$

After reduction

$$\theta(z,t) = -\frac{\alpha(z + bt^\alpha)}{2t} \tag{3.10}$$

The conclusion is that the primitive of the integrand takes the following form

$$w(z,t) = u(z,t)\Big[-\frac{\alpha(z + bt^\alpha)}{2t}\Big] \tag{3.11}$$

where

$$u(z,t) = \frac{1}{\sqrt{2\pi a t^\alpha}} \exp\Big(-\frac{(z - bt^\alpha)^2}{2at^\alpha}\Big)$$

We calculate integral (3.3)

$$f(t)_{z_d} = u(z_d,t)\frac{\alpha(z_d+bt^\alpha)}{2t} \tag{3.12}$$

where

$$u(z_d,t) = \frac{1}{\sqrt{2\pi a t^\alpha}}\exp\Big(-\frac{(z_d-bt^\alpha)^2}{2at^\alpha}\Big)$$

Thus, relationship (3.12) determines the density function of time of exceeding the boundary (permissible) condition by the diagnostic parameter z_d deviation

$$f(t)_{z_d} = \frac{\alpha(z_d+bt^\alpha)}{2t}\frac{1}{\sqrt{2\pi a t^\alpha}}\exp\Big(-\frac{(z_d-bt^\alpha)^2}{2at^\alpha}\Big) \tag{3.13}$$

4. A method to assess the lifetime of a device with respect to the diagnostic parameter being analyzed

The formula for the reliability of a device with respect to the diagnostic parameter deviation from the nominal value can be expressed as

$$R(\tau) = 1 - \int\limits_0^\tau f(t,z_d)\,dt \tag{4.1}$$

where

$$f(t,z_d) = \frac{\alpha(z_d+bt^\alpha)}{2t}\frac{1}{\sqrt{2\pi a t^\alpha}}\exp\Big(-\frac{(z_d-bt^\alpha)^2}{2at^\alpha}\Big) \tag{4.2}$$

Thus, the unreliability of a device can be expressed by the following formula

$$Q(\tau) = \int\limits_0^\tau \frac{\alpha(z_d+bt^\alpha)}{2t}\frac{1}{\sqrt{2\pi a t^\alpha}}\exp\Big(-\frac{(z_d-bt^\alpha)^2}{2at^\alpha}\Big)\,dt \tag{4.3}$$

One can simplify integral (4.3) by making the following substitution $u = t^\alpha$

$$Q(u) = \int\limits_0^{\sqrt[\alpha]{u}} \frac{z_d+bu}{2u}\frac{1}{\sqrt{2\pi a u}}\exp\Big(-\frac{(z_d-bu)^2}{2au}\Big)\,du \tag{4.4}$$

Integral (4.4) should be converted into a simpler form and the problem comes down to solving the indefinite integral

$$\int f(u,z_d)\,du \tag{4.5}$$

where $f(u,z_d)$ is the integrand of equation (4.5).

For the integrand of integral (4.5), the following change $(z_d-bu)^2 = (bu-z_d)^2$ and substitution are performed $\omega = (bu-z_d)^2/(2au)$

$$\frac{1}{2\sqrt{\pi}}\int\frac{1}{\sqrt{\omega}}\mathrm{e}^{-\omega}\,d\omega \tag{4.6}$$

The following substitution into integral (4.6), $\sqrt{\omega} = w$ results in what follows

$$\frac{1}{2\sqrt{\pi}} \int \frac{1}{\sqrt{\omega}} \mathrm{e}^{-\omega}\, d\omega = \frac{1}{\sqrt{\pi}} \int \mathrm{e}^{-w^2}\, dw \tag{4.7}$$

With one more substitution into the integral (4.7)

$$w^2 = \frac{y^2}{2} \qquad\qquad 2w\, dw = y\, dy \tag{4.8}$$

formula (4.7) can be written down as

$$\frac{1}{\sqrt{\pi}} \int \mathrm{e}^{-w^2}\, dw = \frac{1}{\sqrt{2\pi}} \int \exp\Big(-\frac{y^2}{2}\Big)\, dy \tag{4.9}$$

Considering the above substitution y takes the form expressed by

$$y = \frac{\sqrt{2}(bt^\alpha - z_d)}{\sqrt{2at^\alpha}} \tag{4.10}$$

Hence, remembering about the appropriate notation for the limits of integration, the unreliability of a device with respect to the growth of the diagnostic parameter deviation will be expressed by the following equation

$$Q(\tau) = \frac{1}{\sqrt{2\pi}} \int\limits_{-\infty}^{\frac{\sqrt{2}(bt^\alpha - z_d)}{\sqrt{2at^\alpha}}} \exp\Big(-\frac{y^2}{2}\Big)\, dy \tag{4.11}$$

Assuming some specific level of risk of failure, i.e. the level of probabilities of exceeding the permissible value of the parameter deviation, the following equation can be written down

$$Q(\tau) = Q^* \tag{4.12}$$

Hence

$$Q^* = \frac{1}{\sqrt{2\pi}} \int\limits_{-\infty}^{\gamma} \exp\Big(\frac{-y^2}{2}\Big)\, dy \tag{4.13}$$

For the assumed value of Q^*, the value of the upper limit of integral (4.13) is to be found in the Standard Normal Distribution Table.

In this way, we obtain the value of γ. Thus, the equation to determine lifetime of an element takes the following form

$$\gamma = \frac{\sqrt{2}(bt^\alpha - z_d)}{\sqrt{2at^\alpha}} \tag{4.14}$$

Having solved equation (4.14), one can find the lifetime of a device with respect to the assumed diagnostic parameter.

Therefore, having the value of the parameter $\overline{\gamma}$ and using relation (4.14), one can determine the lifetime of the device with respect to the diagnostic parameter given consideration. The following substitution has been made to do this

$$s = t^\alpha \tag{4.15}$$

Using formula (4.15), one can determine the lifetime of the device on the basis of the following relationship

$$t^* = \frac{1}{a} \ln \frac{2bz_d + \overline{\gamma}^2 a + \overline{\gamma}\sqrt{4bz_d a + \overline{\gamma}^2 a^2}}{2b^2} \tag{4.16}$$

5. Example of calculation

To start verification of the method intended to determine the lifetime of a device with the Weibull distribution parameters applied, the coefficients of this distribution should be determined first. Both the parameter θ reflecting the scale factor and the parameter α representing the ratio of the shape have been pre-assumed to equal unity (determination thereof will provide the basis for further work).

Data recorded in the course of operating one of the sighting system units, i.e. the sighting head, has been assumed a good example, on the basis of which the above-presented model has been verified. The construction of this head enables visualisation of the sighting data in the form of the sighting marker that supports the sighting process while making use of air weapons. Under maintenance procedures/works performed every 100 hours' flight time recorded are values of diagnostic parameters of the sighting head in form of two co-ordinates ε and β that define the co-ordinates of the check position of the sighting marker. Nominal values of these co-ordinates (with permissible error range included) are determined by the aircraft manufacturer responsible for adjusting the sighting head with the sighting system at the stage the aircraft is introduced in service. If in the course of maintenance, the measured values of co-ordinates of the sighting marker position are within the limits of permissible error, no maintenance efforts are taken to correct the sighting marker position. On the other hand, if the value of at least one of the two diagnostic parameters exceeds the permissible error value, the sighting system is subjected to maintenance to remove the error. This is done by means of introducing into the system the co-ordinates that remove the deviation of the sighting marker position from the nominal one.

With data recorded in the course of the operational process $(\varepsilon_1, t_1); (\varepsilon_2, t_2); \ldots ; (\varepsilon_n, t_n)$ and related to changes in values of one of the parameters that define health/maintenance status of the sighting system, the rate of changes (of the increase) in deviation of the diagnostic parameter can be written down as

$$ct_1 = \varepsilon_1 \qquad c = \frac{\varepsilon_1}{t_1} \tag{5.1}$$

For the data presented in Fig. 1, recorded in the course of maintenance works every 100 hours' flight time of the aircraft, the following parameters have been found that enable determination of lifetime described with relationship (4.14)

$$b = 0.00123 \qquad a = 1.524 \cdot 10^{-6} \qquad c = 0.00123 \tag{5.2}$$

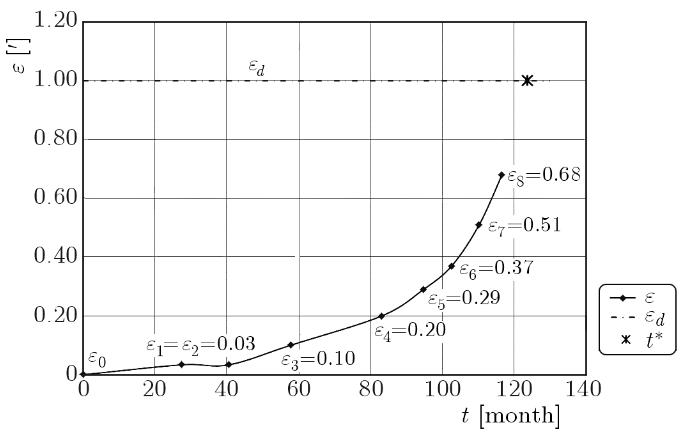

Fig. 1. Changes in the value of the diagnostic parameter that describes the position of the sighting marker and the value of the lifetime found

It is important for aeronautical systems that the level of reliability of the device in question nears unity. That is why the reliability has been assumed close to unity to determine the lifetime of the device. Assuming the level of reliability $R^*(t) = 0.98$, the value of the parameter $\gamma^* = 2.32$ could be found from the Standard Normal Distribution Tables. The parameter ε_d could be found in the system technical documentation (Maintenance Manual), where information is given on the value of permissible deviation of the diagnostic parameter that describes co-ordinates of the sighting marker position. Using operational data (Fig. 1) and the above-determined parameters, the lifetime has been calculated from Eq. (4.14). In the analyzed case, it is

$$t^* = 124 \text{ months} \tag{5.3}$$

6. Summary

The process of operating technical devices installed on an aircraft involves influences of changeable weather and mechanical conditions resulting from, among other things, in-flight overloads. These factors lead to the accumulation of destructive factors affecting the system(s) and causing the nominal performance characteristics of selected system components decline. The material presented in this article is a continuation of analyses to develop methods of finding density function of changes in deviations of parameters, and the time of exceeding the permissible condition by the diagnostic parameter under analysis, the parameter being affected by particular destructive factors (Ważny, 2011a,b). The presented method enables determination of residual lifetime of a device and can be used to modify the process of operating the device in question. In this way, the number of checks of health/maintenance status can be limited, which consequently can reduce the time the device remains beyond the operational-use system.

The relationship for the failure rate described by parameters typical of the Weibull distribution, as applied to determine the rate of wear and tear of the component/device, is an important part of this study. Further work should be focused on verification of the method in question as referred to larger population of objects under analysis. Parameters that describe the rate of the ever increasing intensity of the component/device wear and tear should be found. Both objectives determine future lines of activity for the Author.

The above-presented considerations have been based on analyses of the process of operating aeronautical devices/systems. However, they can be successfully applied for other technical objects, the health/maintenance status of which is usually determined by means of diagnostic parameters. Implementation of this method is possible if we, firstly, have values of diagnostic parameters located along the axis of time of the device service/operation and, secondly, know the value of the boundary/limiting error that – when exceeded by the diagnostic parameter – makes operation of the device less effective (i.e. the device is at the medium level of serviceability).

References

1. Abezgauz G., 1973, *Calculus Probabilistic. Handbook* (in Polish), Wydawnictwo MON, Warszawa

2. Gniedenko B.W., Bielajew J.K., Sołowiew A.D., 1968, *Mathematical Methods in Reliability Theory* (in Polish), WNT, Warszawa

3. Gradsztejn I.S., Ryżyk I.M., 1964, *Tables of Integrals, Sums, Rows and Products* (in Polish), PWN, Warszawa

4. Niu G., Singh S., Holland S., Pecht M., 2011, Health monitoring of electronic products based on Mahalanobis distance and Weibull decision metrics, *Microelectronics Relibility*, **51**, 279-284

5. Pamuła W., 2011, *The Reliability and the Safety* (in Polish), Wydawnictwo Politechniki Śląskiej, Gliwice

6. Tomaszek H., Jasztal M., Zieja M., 2011, A simplified method to assess fatigue life of selected structural components of an aircraft for a variable load spectrum, *Eksploatacja i Niezawodność – Maintenance and Reliability*, **4**, 29-34
7. Tomaszek H., Jasztal M., Zieja M., 2013, Application of the Paris formula with $m = 2$ and the variable load spectrum to a simplified method for evaluation of reliability and fatigue life demonstrated by aircraft components, *Eksploatacja i Niezawodność – Maintenance and Reliability*, **4**, 297-304
8. Tomaszek H., Szczepanik R., 2005, Method of evaluation distribution of time of exceed a limiting state (in Polish), *Zagadnienia Eksploatacji Maszyn*, **40**, 4, 35-44
9. Tomaszek H., Wróblewski M., 2001, *Bases of Assessment of the Effectiveness of the Use of Weapon Systems Air* (in Polish), Dom Wydawniczy Bellona, Warszawa
10. Tomaszek H., Żurek J., Stępień S., 2008, The airship maintenance with its renovation and the risk of its loss, *Scientific Problems of Machines Operation and Maintenance*, **43**, 4, 39-49
11. Tomaszek H., Żurek J., Loroch L., 2004, The outline of a method of estimation reliability and durability of aircraft's structure elements on the basis of destruction process description (in Polish), *Zagadnienia Eksploatacji Maszyn*, **39**, 3, 73-85
12. Ważny M., 2011a, An outline of the method for determining the density function of changes in diagnostic parameter deviations with the use of the Weibull distribution, *Scientific Problems of Machines Operation and Maintenance*, **46**, 2, 105-144
13. Ważny M., 2011b, An outline of a method for determining the density function of the time of exceeding the limit state with the use of the Weibull distribution, *Scientific Problems of Machines Operation and Maintenance*, **46**, 3, 77-91
14. Ważny M., 2013, *Effectiveness Analysis of the Air Sighting System in the Aspect of the Effect of Destructive Processes* (in Polish), WAT
15. Ye Z., Tang L., Xie M., 2011, A burn-in scheme based on precentiles of the residual life, *Journal of Quality Technology*, **43**, 4, 334-345
16. Zhanshan M., Krings, A.W., 2008, Survival analysis approach to reliability, survivability and prognostics and health management (PHM), *Aerospace Conference, IEEE*, 1-20

Manuscript received July 21, 2014; accepted for print May 24, 2015

JOURNAL OF THEORETICAL
AND APPLIED MECHANICS
53, 4, pp. 991-1004, Warsaw 2015
DOI: 10.15632/jtam-pl.53.4.991

ANALYTICAL SOLUTION OF EXCITED TORSIONAL VIBRATIONS OF PRISMATIC THIN-WALLED BEAMS

Elżbieta Augustyn, Marek S. Kozień
Cracow University of Technology, Institute of Applied Mechanics, Kraków, Poland
e-mail: kozien@mech.pk.edu.pl

In the paper, the analytical solution of excited torsional vibrations of prismatic thin-walled beams for different types of boundary conditions and different types of external excitation of torsional moment are formulated. The presented solution can be applied, among others, to preliminary analysis of the optimal position of the actuators and the value of the applied voltage to the elements for minimization of the vibrations of the beams.

Keywords: thin-walled beams, torsional vibrations, excited vibrations

1. Introduction

Knowledge of the analytical solution of externally excited vibrations for a considered model of realistic structures is very useful for preliminary analysis in the design process or choosing parameters and algorithms for vibration control of the systems. The model of an excited prismatic beam response for torsional or coupled bending-torsional vibrations can be applied for analysis of vibration of some machine elements, e.g. turbine-blades (Gryboś, 1996; Łączkowski, 1974; Pust and Pesek, 2014; Rao, 1991). Sometimes, the beam cross-section takes form of an open thin-walled structure. In this paper, thin-walled beams of closed cross-sections as general models of blades are analyzed (Librescu and Na, 1998; Song and Librescu, 1993; Song *et al.*, 2002).

Recently, application of piezoelectric elements for vibration reduction of thin structures are commonly discussed in the literature (Elliott and Nelson, 1997; Hansen and Snyder, 1997; Moheimani and Fleming, 2006; Preumont, 2006). See also the papers by Ferdek and Kozień (2013), Kozień and Kołtowski (2011). These types of vibration cancellation were considered by the authors in preliminary analysis of the possibility of reduction of torsional vibrations of prismatic beams with solid cross-sections (Augustyn and Kozień, 2014).

There are well known analytical solutions for problems of the dynamics of thin walled beams with open cross-section, starting with Gere (1954), Gere with Lin (1958), Aggrawal with Cranch (1967), and Carr (1969) and later e.g. by Bishop *et al.* (1989), Dokumaci (1987), Kaliski and Solarz (1992), Tao (1964), Timoshenko *et al.* (1974) and Yaman (1997). Different cases of vibrations in such a type of structures are discussed in many of articles. A review of these different approaches, theories and models for static and dynamic cases is given by Sapountzakis (2013). The effect of variable cross-section on natural frequencies is discussed in (Eisenberger, 1997). Non-linear models are discussed by Crespo Da Silva (1988a,b), Rozmarynowski with Szymczak (1984) and Di Egidio *et al.* (2003a,b). The steady-state forced vibrations are discussed by Crespo Da Silva (1988b) and Di Egidio *et al.* (2003b). The problem of optimal design of a thin-walled beam for a given natural frequency is analyzed by Szymczak (1984). Torsional vibrations of composite thin-walled beams are analyzed by Song and Librescu (1993). The models with the effect of rotary inertia are analysed by Arpaci *et al.* (2003) and with adaptive capabilities by Song *et al.* (2002). A detailed solution for the general case of excited vibrations, especially in the transient case, are not easily found in the literature. This formulation was given by one of the authors of this paper for bending vibrations of a beam for different types of external excitations (Kozień, 2013).

The main aim of this paper is to formulate the analytical solution for describing the excited torsional-type vibrations of a thin-walled beam for different combinations of boundary conditions (simply supported, free, fixed) and different types of external torsional moment type excitations (harmonic concentrated, harmonic distributed, pulse concentrated, pulse distributed). The presented solution, among others, can be applied to preliminary analysis of the optimal position of the actuators and to calculations of voltage applied to the elements for minimization of vibrations of beams when the application of piezoelectric elements are considered. In this model, the influence of external piezoelectric elements can be modeled by the external concentrated moment of a suitable value, as it was done by Elliott and Nelson (1997), Hansen and Snyder (1997) for pairs of elements in simulations of bending vibrations of beams, as was proposed by Augustyn and Kozień (2014) for double pairs of elements for torsional vibrations of beams.

2. Formulation of the problem

2.1. Equation of motion

Let us consider a prismatic beam with a thin-walled cross section of an open type (Murray, 1986; Piechnik, 2007; Vlasov, 1959) in which it is also assumed that the material is isotropic. The geometry of the cross-section is shown in Fig. 1, where G is the gravity center (centroid), S – shear center. The origin of the co-ordinate system $Sxyz$ lies in the shear center, and the axes Sy and Sz are parallel to the principal axes of the cross-section $(G\eta, G\zeta)$.

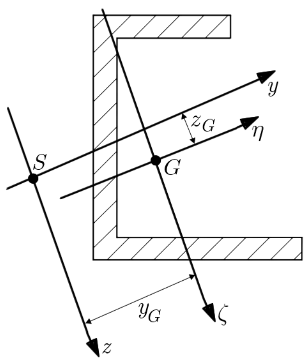

Fig. 1. Geometry of the cross-section

The equations of coupled vibrations of the beam take the following form

$$
\begin{aligned}
&EJ_\zeta \frac{\partial^4 v(x,t)}{\partial x^4} + \rho A\Big[\frac{\partial^2 v(x,t)}{\partial t^2} - z_G \frac{\partial^2 \varphi(x,t)}{\partial t^2}\Big] = q_y(x,t) \\
&EJ_\eta \frac{\partial^4 w(x,t)}{\partial x^4} + \rho A\Big[\frac{\partial^2 w(x,t)}{\partial t^2} + y_G \frac{\partial^2 \varphi(x,t)}{\partial t^2}\Big] = q_z(x,t) \\
&EJ_\omega \frac{\partial^4 \varphi(x,t)}{\partial x^4} - GJ_s \frac{\partial^2 \varphi(x,t)}{\partial x^2} + \rho J_0 \frac{\partial^2 \varphi(x,t)}{\partial t^2} \\
&\qquad + \rho A\Big[-z_G \frac{\partial^2 v(x,t)}{\partial t^2} + y_G \frac{\partial^2 w(x,t)}{\partial t^2}\Big] = m_s(x,t)
\end{aligned}
\tag{2.1}
$$

where $v(x,t)$ is the displacement of the beam in the y direction, $w(x,t)$ is the displacement of the beam in the z direction, $\varphi(x,t)$ is the rotation of the axis of beam around the x direction, J_η is the principal moment of inertia of the cross-section with respect to the η axis, J_ζ is the principal moment of inertia of the cross-section with respect to the ζ axis, J_0 is the polar moment of inertia with respect to the shear center, J_s is the equivalent moment of inertia of the cross-section due to torsion, E is Young's modulus, G is the shear modulus, ρ is the material density, y_G, z_G are the positions of the gravity center G (co-ordinates), $q_y(x,t)$ is the distributed force acting in the y direction (external excitation), $q_z(x,t)$ is the distributed force acting in the z direction (external excitation), $m_s(x,t)$ is the distributed twisting moment (external excitation).

When the considered cross-section is such that the position of the shear center and gravity center is the same (e.g. for the cross-section with two axes of symetry), the following relationship is valid $y_G = z_G = 0$. It means, that the equation of motion for twisting existing in system (2.1) is separated from the equations of bending vibrations, and takes simplified and independent form from bending vibrations form

$$\frac{EJ_\omega}{GJ_s}\frac{\partial^4\varphi(x,t)}{\partial x^4} - \frac{\partial^2\varphi(x,t)}{\partial x^2} + \frac{\rho J_0}{GJ_s}\frac{\partial^2\varphi(x,t)}{\partial t^2} = \frac{1}{GJ_s}m_s(x,t) \tag{2.2}$$

Hence, for the considered cross-section, it is possible to analyze torsional vibrations separately with the bending ones.

If the cross-section is a monolithic type, equation of motion (2.3) takes the following form

$$-GJ_s\frac{\partial^2\varphi(x,t)}{\partial x^2} + \rho J_0\frac{\partial^2\varphi(x,t)}{\partial t^2} = m_s(x,t) \tag{2.3}$$

In general, vibrations of the analyzed structure can be described in form of a three-dimensional model of a solid structure. But for some structures, for which one characteristic dimension (the so-called length) is high enough in comparison to the characteristic dimensions of the cross-section, then so-called one-dimensional models of structures are built for simplicity of the analysis. The results of their application must give good enough results of analysis in comparison with three-dimensional models. The same case takes place during detailed consideration of the cross-section shape. If one characteristic dimension of the cross-section (the so-called thickness) is small enough in comparison with the second one (the so-called width), the whole structure is called a thin-walled one. A detailed rule states that for a thin-walled cross-section, the thickness is more than eight times smaller than the highest way measured along the middle-line of the cross-section between its two end-points. Moreover, the length of this way should be more than eight times smaller than the length of the beam (Piechnik, 2007). For such a beam the assumptions of the Bernoulli-Euler beam theory or the de Saint-Venant rule of loadings, for example, are invalid. Their motion must be analyzed as a three-dimensional body or by the application of an especially formulated theory for thin-walled beams. Due to the form of the middle line of the cross-section, three types of thin-walled beams are defined: with an open cross-section, with a closed cross-section and with a mixed one (Piechnik, 2007). Depending on the type of cross-section, the suitable theory of thin-walled beams should be applied. For a thin-walled beam with an open cross-section, as considered in this article, the Vlasov theory can be applied (Piechnik, 2007; Vlasov, 1959).

2.2. Boundary conditions

The equation of motion of the thin-walled beam is the fourth order due to the spatial variable x. Therefore, a set of the four boundary conditions must be formulated for each beam element. Their formulation is connected with the Vlasov theory of thin-walled beams and must take into account the warping effect.

The following types of boundary conditions can be formulated in a natural way (Gere, 1954; Piechnik, 2007):

- Simply supported:
  — no rotation of the cross-section around the axis of the beam
  $$\varphi = 0 \tag{2.4}$$
  — zero normal stress (free of warping of the cross-section)
  $$\frac{\partial^2\varphi}{\partial x^2} = 0 \tag{2.5}$$
- Fixed:
  — no rotation of the cross-section around the axis of the beam
  $$\varphi = 0 \tag{2.6}$$
  — plain cross-section (blocked warping of the cross-section)
  $$\frac{\partial\varphi}{\partial x} = 0 \tag{2.7}$$
- Free:
  — zeroes for the total torsional moment (free for rotation)
  $$GJ_s\frac{\partial\varphi}{\partial x} - EJ_\omega\frac{\partial\varphi^3}{\partial x^3} = 0 \tag{2.8}$$
  — zero normal stress (free for warping of the cross-section)
  $$\frac{\partial^2\varphi}{\partial x^2} = 0 \tag{2.9}$$

3. Eigen-problem, natural vibrations

Now, the eigen-problem analysis of the thin-walled prismatic beam with length l is considered. The equation of motion has the form

$$\frac{EJ_\omega}{GJ_s}\frac{\partial^4\varphi(x,t)}{\partial x^4} - \frac{\partial^2\varphi(x,t)}{\partial x^2} + \frac{\rho J_0}{GJ_s}\frac{\partial^2\varphi(x,t)}{\partial t^2} = 0 \tag{3.1}$$

The solution to the problem is proposed in form $(3.2)_1$ – the Fourier method of solution. After suitable manipulations, it leads to a solution to the problem of separated variables $(3.2)_2$. It can be written as two independent ordinary differential equations $(3.2)_{3,4}$. The first of the fourth order for the independent spatial variable x, and the second of the second order for the independent variable t (time). The form of unknown functions in the spatial domain can be written in form $(3.2)_5$). For the above given homogeneous boundary conditions, these series of functions satisfy orthogonality conditions (3.4) – see Appendix A for detailed analysis. Finally, the solution can be written in form (3.7), where the series of constants a_n and b_n are determined based on initial conditions (3.6)

$$\begin{gathered}
\varphi(x,t) = \sum_{n=1}^{+\infty} X_n(x)T_n(t) \\
\frac{EJ_\omega}{GJ_s}\frac{\frac{d^4X_n(x)}{dx^4}}{X_n(x)} - \frac{\frac{d^2X_n(x)}{dx^2}}{X_n(x)} = -\frac{\rho J_0}{GJ_s}\frac{\frac{d^2T_n(t)}{dt^2}}{T_n(t)} = \lambda_n^4 \\
\frac{EJ_\omega}{GJ_s}\frac{d^4X_n(x)}{dx^4} - \frac{d^2X_n(x)}{dx^2} - \lambda_n^4X_n(x) = 0 \qquad \frac{d^2T_n(t)}{dt^2} + \underbrace{\lambda_n^4\frac{GJ_s}{\rho J_0}}_{\omega_n^2}T_n(t) = 0 \\
X_n(x) = A_n\sin(\alpha_nx) + B_n\cos(\alpha_nx) + C_n\sinh(\beta_nx) + D_n\cosh(\beta_nx)
\end{gathered} \tag{3.2}$$

where

$$\alpha_n = \sqrt{\frac{-GJ_s + \sqrt{(GJ_s)^2 + 4EJ_\omega GJ_s\lambda_n^4}}{2EJ_\omega}}$$
$$\beta_n = \sqrt{\frac{GJ_s + \sqrt{(GJ_s)^2 + 4EJ_\omega GJ_s\lambda_n^4}}{2EJ_\omega}} \qquad \omega_n = \lambda_n^2\sqrt{\frac{GJ_s}{\rho J_0}} \tag{3.3}$$

and

$$\int_0^l X_n(x)X_m(x)\,dx = \begin{cases} \gamma_n^2 & n = m \\ 0 & n \neq m \end{cases} \tag{3.4}$$

Finding the solution to the system of differential equation $(3.2)_2$ or $(3.2)_{3,4}$ for a given boundary conditions is the well-known eigen-mode problem which gives a set of eigen-values (powered natural frequencies of a system ω_n^2 – solution of equation $(3.2)_4$ and a set of eigen-functions (eigen-modes, waveforms of eigen-functions $X_n(x)$ – solution of equation $(3.2)_3$). The equations, which make possible the finding of natural frequencies ω_n $(3.3)_{1,2,3}$ or exact formula for ω_n for a different combination of typical types of boundary conditions (fixed, simply supported, free) are given in Table 1. Moreover, the analytical form of eigen-functions for the same combination of boundary conditions (simply supported, free, fixed) are also given in Table 1. The other name of the problem is the modal problem and the detailed solution of this problem was done by Gere (1954).

If the solution to the equation of motion fulfills initial conditions (3.6), where $\varphi_0(x)$ is the initial angle of torsion of the beam for $t = 0$, and $\Omega_0(x)$ is the initial angular velocity of the beam for $t = 0$, the problem of natural vibrations is completely defined. These initial conditions should be applied for the detailed solution of the second equation of system $(3.2)_{3,4}$

$$\varphi(x,0) = \varphi_0(x) \qquad \frac{\partial}{\partial t}\varphi(x,0) = \Omega_0(x) \tag{3.5}$$

Solution (3.6) represents the so-called natural vibrations, which are the response of the system to initial conditions written in the time and spatial domains $\varphi(x,t)$

$$\varphi(x,t) = \sum_{n=1}^{+\infty} X_n(x)[a_n\sin(\omega_n t) + b_n\sin(\omega_n t)]$$
$$a_n = \frac{1}{\omega_n\gamma_n^2}\int_0^l \Omega_0(x)X_n(x)\,dx \qquad b_n = \frac{1}{\gamma_n^2}\int_0^l \varphi_0(x)X_n(x)\,dx \tag{3.6}$$

4. Excited vibrations

When analyzing the excited vibrations of a realistic beam (with internal damping), the general solution of the homogeneous differential equation is a function relatively fast tending to zero with respect to time due to the internal and external damping.

The complete solution to the problem of excited vibrations, understood as the particular solution to the non-homogeneous equation (2.2), for the excitation function of harmonic type, has the form of a sum of two components: connected with a set of natural frequencies ω_n and connected with the external loading frequency ν. Note, that the set of constants A_n, B_n, C_n and D_n existing in particular solution $(2.2)_5$, must be found taking into account the complete solution.

Table 1. Formulas for eigenfrequencies and eigenmodes (Gere, 1954)

Boundary conditions	Equation/formula for natural frequency ω_n or parameters α_n and β_n	Eigenfunction $X_n(x)$
Simply supported- -simply supported	$\omega_n = \frac{n\pi}{l^2}\sqrt{\frac{n^2\pi^2 EJ_\omega + l^2 GJ_s}{\rho J_0}}$	$\sin\Big(\frac{n\pi}{l}x\Big)$
Fixed-fixed	$\alpha_n\beta_n = \omega_n\sqrt{\frac{\rho J_0}{EJ_\omega}}$	$\frac{\beta_n[\cosh(\beta_n l)-\cos(\alpha_n l)]}{\alpha_n\sinh(\beta_n l)-\beta_n\sin(\alpha_n l)}\sin(\alpha_n x) - \cos(\alpha_n x)$ $-\frac{\alpha_n[\cosh(\beta_n l)-\cos(\alpha_n l)]}{\alpha_n\sinh(\beta_n l)-\beta_n\sin(\alpha_n l)}\sinh(\beta_n x) + \cosh(\beta_n x)$
Simply supported- -fixed	$\frac{\tanh(\beta_n l)}{\beta_n} = \frac{\tan(\alpha_n l)}{\alpha_n}$	$\sin(\alpha_n x) - \frac{\sin(\alpha_n l)}{\sinh(\beta_n l)}\sinh(\beta_n x)$
Fixed-free	$\frac{\alpha_n^4+\beta_n^4}{\alpha_n^2\beta_n^4}\cos(\alpha_n l)\cosh(\beta_n l)$ $-\frac{\alpha_n^2-\beta_n^2}{\alpha_n\beta_n}\sin(\alpha_n l)\sinh(\beta_n l) + 2 = 0$	$\frac{\beta_n}{\alpha_n}\frac{\alpha_n^2\sinh(\beta_n l)-\alpha_n\beta_n\sin(\alpha_n l)}{\alpha_n^2\cosh(\beta_n l)+\beta_n^2\cos(\alpha_n l)}\sin(\alpha_n x) - \cos(\alpha_n x)$ $-\frac{\alpha_n^2\sinh(\beta_n l)-\alpha_n\beta_n\sin(\alpha_n l)}{\alpha_n^2\cosh(\beta_n l)+\beta_n^2\cos(\alpha_n l)}\sinh(\beta_n x) + \cosh(\beta_n x)$
Simply supported- -free	$\beta_n^2\tanh(\beta_n l) = \alpha_n^2\tan(\alpha_n l)$	$\sin(\alpha_n x) + \frac{\beta_n}{\alpha_n}\frac{cos(\alpha_n l)}{\cosh(\beta_n l)}\sinh(\beta_n x)$
Free-free	$(\beta_n^4 - \alpha_n^4)\sin(\alpha_n l)\sinh(\beta_n l)$ $+2\alpha_n^2\beta_n^2[cos(\alpha_n l)\cosh(\beta_n l) - 1] = 0$	$-\frac{\alpha_n}{\beta_n}\frac{\beta_n^3[\cosh(\beta_n l)-\cos(\alpha_n l)]}{\beta_n^3\sinh(\beta_n l)-\alpha_n^3\sin(\alpha_n l)}\sin(\alpha_n x) + \frac{\beta_n}{\alpha_n}\cos(\alpha_n x)$ $-\frac{\beta_n^3[\cosh(\beta_n l)-\cos(\alpha_n l)]}{\beta_n^3\sinh(\beta_n l)-\alpha_n^3\sin(\alpha_n l)}\sinh(\beta_n x) + \cosh(\beta_n x)$

Due to the same result of action of the internal and external damping (as for free vibrations), the components connected with the set of natural frequencies ω_n are functions relatively fast tending to zero with respect to time. Therefore, the solution of exited vibrations is usually connected with the only external loading frequency ν (Łączkowski, 1974). Such a case of vibrations is called the steady-state case. The complete solution of the problem which includes free vibrations and excited vibrations in general formulation is known as transient vibrations.

As discussed in the Introduction, let us consider the general form of the solution of excited vibrations. In such a case, the solution can be proposed in form (4.1) in terms of the functions $X_n(x)$ and a series of unknown functions of time $H_n(t)$

$$\varphi(x,t)=\sum_{n=1}^{+\infty}X_n(x)H_n(t) \tag{4.1}$$

Putting proposed solution (4.1) into equation (2.2) and taking into account the first of equation of system $(3.2)_{3,4}$ one can obtain

$$\sum_{n=1}^{+\infty}\Big[\Big(\underbrace{\frac{EJ_\omega}{GJ_s}\frac{d^4X_n(x)}{dx^4}-\frac{d^2X_n(x)}{dx^2}}_{\lambda_n^4X_n(x)}\Big)H_n(t)+\frac{\rho J_0}{GJ_s}\frac{d^2H_n(t)}{dt^2}X_n(x)\Big]=\frac{1}{GJ_s}m_s(x,t) \tag{4.2}$$

and then after suitable manipulations

$$\sum_{n=1}^{+\infty}\Big[\frac{d^2H_n(t)}{dt^2}+\underbrace{\frac{GJ_s}{\rho J_0}\lambda_n^4}_{\omega_n^2}H_n(t)\Big]X_n(x)=\frac{GJ_s}{\rho J_0}\frac{1}{GJ_s}m_s(x,t)=\frac{1}{\rho J_0}m_s(x,t) \tag{4.3}$$

The external load function existing in equation (2.2) can be represented in a series form (4.4), in terms of functions $X_n(x)$ and a series of the known functions of time $Q_n(t)$

$$\begin{aligned}&\frac{1}{\rho J_0}m_s(x,t)=\frac{1}{\rho J_0}\sum_{n=1}^{+\infty}X_n(x)Q_n(t)\\ &Q_n(t)=\frac{1}{\gamma_n^2}\int\limits_0^l m_s(x,t)X_n(x)\;dx \qquad\qquad Q_n^*(t)=\frac{1}{\rho J_0}Q_n(t)\end{aligned} \tag{4.4}$$

Substituting formulas (4.1) and (4.4) into equation (2.2), the differential equation for the determination of the unknown functions $H_n(t)$ takes the form

$$\frac{d^2H_n(t)}{dt^2}+\omega_n^2H_n(t)=Q_n^*(t) \tag{4.5}$$

The solution to this equation has the form

$$H_n(t)=\frac{1}{\omega_n}\int\limits_0^t Q_n^*(\tau)\sin[\omega_n(t-\tau)]\;d\tau \tag{4.6}$$

known as the Duhamel integral.

The given formulas make possible the formulation of the analytical solution of excited vibrations of a beam with defined boundary conditions.

Let us formulate the general form of the Duhamel integral for the following types of external excitations and different boundary conditions given by the eigen-functions $X_n(x)$:

— Harmonically distributed moment with a constant amplitude m_0

$$\begin{aligned}&m_s(x,t)=m_0\sin(\nu t) \qquad\qquad [m_0]=N\\ &H_n(t)=m_0\frac{1}{\rho J_0}\frac{1}{\gamma_n^2}\frac{1}{\omega_n^2-\nu^2}\Big[\sin(\nu t)-\frac{\nu}{\omega_n}\sin(\omega_nt)\Big]\int\limits_0^l X_n(x)\;dx\\ &\varphi(x,t)=M_0\frac{1}{\rho J_0}\sum_{n=1}^{\infty}\frac{1}{\gamma_n^2}\frac{1}{\omega_n^2-\nu^2}\Big[\sin(\nu t)-\frac{\nu}{\omega_n}\sin(\omega_nt)\Big]\int\limits_0^l X_n(x)X_n(x)\;dx\end{aligned} \tag{4.7}$$

— Pulsed distributed moment with a constant amplitude Q_m acting at the time $t = t_0$

$$
\begin{aligned}
&m_s(x,t) = Q_m\delta(t-t_0) \qquad\qquad [Q_m] = Ns\\
&H_n(t) = \begin{cases} 0 & t < t_0 \\ Q_M\dfrac{1}{\rho J_0}\dfrac{1}{\gamma_n^2}\dfrac{1}{\omega_n}\sin[\omega_n(t-t_0)]\int\limits_0^l X_n(x)\,dx & t \geqslant t_0 \end{cases}\\
&\varphi(x,t) = \begin{cases} 0 & t < t_0 \\ Q_M\dfrac{1}{\rho J_0}\sum\limits_{n=1}^{\infty}\dfrac{1}{\gamma_n^2}\dfrac{1}{\omega_n}\sin[\omega_n(t-t_0)]\int\limits_0^l X_n(x)X_n(x)\,dx & t \geqslant t_0 \end{cases}
\end{aligned}
\tag{4.8}
$$

— Harmonic concentrated moment with a constant amplitude M_0 applied to the point $x = x_0$

$$
\begin{aligned}
&m_s(x,t) = M_0\delta(x-c)\sin(\nu t) \qquad\qquad [M_0] = Nm\\
&H_n(t) = M_0\frac{1}{\rho J_0}\frac{1}{\gamma_n^2}\frac{1}{\omega_n^2-\nu^2}\Big[\sin(\nu t) - \frac{\nu}{\omega_n}\sin(\omega_n t)\Big]X_n(x_0)\\
&\varphi(x,t) = M_0\frac{1}{\rho J_0}\sum_{n=1}^{\infty}\frac{1}{\gamma_n^2}\frac{1}{\omega_n^2-\nu^2}\Big[\sin(\nu t) - \frac{\nu}{\omega_n}\sin(\omega_n t)\Big]X_n(x_0)X_n(x)
\end{aligned}
\tag{4.9}
$$

— Pulsed concentrated moment with a constant amplitude Q_m acting at the time $t = t_0$ at the point $x = x_0$

$$
\begin{aligned}
&m_s(x,t) = Q_M\delta(x-x_0)\delta(t-t_0) \qquad\qquad [Q_M] = Nms\\
&H_n(t) = \begin{cases} 0 & t < t_0 \\ Q_M\dfrac{1}{\rho J_0}\dfrac{1}{\gamma_n^2}\dfrac{1}{\omega_n}\sin[\omega_n(t-t_0)]X_n(x_0) & t \geqslant t_0 \end{cases}\\
&\varphi(x,t) = \begin{cases} 0 & t < t_0 \\ Q_M\dfrac{1}{\rho J_0}\sum\limits_{n=1}^{\infty}\dfrac{1}{\gamma_n^2}\dfrac{1}{\omega_n}\sin[\omega_n(t-t_0)]X_n(x_0)X_n(x) & t \geqslant t_0 \end{cases}
\end{aligned}
\tag{4.10}
$$

5. Example – excited torsional vibrations of a simply supported thin-walled beam

5.1. Formulation of the problem

As an example, let us consider excited vibrations of a thin-walled beam simply supported on both ends. The beam is made of steel ($E = 2.1 \cdot 10^{11}$ Pa, $G = 8.1 \cdot 10^{10}$ Pa, $\rho = 7800\,\mathrm{kg/m^3}$) and has length $l = 6$ m. The shape of cross-section with its detailed dimensions is shown in Fig. 2.

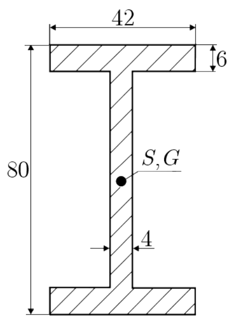

Fig. 2. Cross-section of the analyzed beam (dimensions given in mm)

The boundary conditions take form

$$\begin{aligned} &\varphi(0,t)=0 && \frac{\partial^2}{\partial x^2}\varphi(0,t)=0 \\ &\varphi(l,t)=0 && \frac{\partial^2}{\partial x^2}\varphi(l,t)=0 \end{aligned} \tag{5.1}$$

5.2. Natural vibrations – a comparison of the results for different models

The following models of beam are applied for comparison of the lowest natural frequencies for torsional vibrations:

- three-dimensional solid model solved by application of the finite element method,
- thin-walled Vlasov analytical model,
- model with a monolithic cross-section.

The finite element solution has been obtained by application of the *Ansys* finite element package. The model is built of 76800 three dimensional 8-nodes solid elements of the type *solid45*. The generated mesh is shown in Fig. 3. Due to the degrees of freedom of the applied elements, the boundary conditions on the two ends of the beam are modeled as free sliding along the axis of the beam and as blocked displacements for all nodes in the plane of its ends. Therefore, deplanation of the ends is possible.

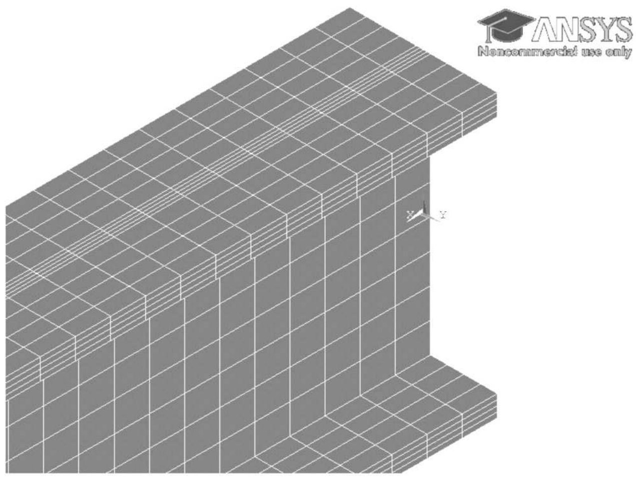

Fig. 3. Part of the FEM mesh of the beam

The second group of values of the natural frequencies is obtained based on the thin-walled model described in the text, especially based on the formula given in the first row in Table 1. The values of J_s, J_ω and J_0 are calculated based on the formulas given by Gere (1954).

The third group of results is obtained for the beam modeled with the assumption of a monolithic type cross-section (shaft) with free-free ($\varphi(0,t) = \varphi(l,t) = 0$) or fixed-fixed ($\partial\varphi(0,t)/\partial x = \partial\varphi(l,t)/\partial x = 0$) boundary conditions. The values of natural frequencies are the same for these cases of boundary conditions (Woroszył, 1984).

In Table 2, a comparison of the lowest natural frequencies for the analyzed beam for the three considered models and the relative percentage error is given to one model obtained from three dimensional solid models, as the reference model. It should be noted that for the considered beam, the values of natural frequencies are correctly estimated theoretically with a monolithic cross-section only for the first few torsional modes. For higher modes, only the theory for thin-walled beam gives good enough results.

Table 2. Comparison of the lowest natural frequencies for the analyzed beam [Hz]

Mode	3-D Solid	Thin-walled		Monolytic	
No.	value [Hz]	value [Hz]	error [%]	value [Hz]	error [%]
1	25.15	25.54	1.6	25.40	1.0
2	50.97	51.89	1.8	50.81	-0.3
3	78.11	79.84	2.2	76.21	-2.4
4	107.16	110.05	2.7	101.62	-5.2
5	138.64	143.16	3.3	127.02	-8.4
6	172.98	179.66	3.9	152.42	-11.9
7	210.56	219.94	4.5	177.83	-15.5
8	251.65	264.36	5.1	203.23	-19.2
9	296.50	313.14	5.6	228.64	-22.9
10	345.26	366.49	6.1	254.04	-26.4

A comparison of the natural frequencies for the two beam models – the thin-walled one and the monolithic one are shown in Fig. 4 in form of the relative percentage error in comparison to the values obtained for the thin-walled model as the reference model. On the horizontal axis, there are identification numbers of the first hundred torsional modes ($n = 1, 2, \ldots, 100$). It can be shown that for the considered beam, the error of the estimated values of natural frequencies found by application of the theory with monolithic cross-section grow rapidly with an increase in the number of torsional modes.

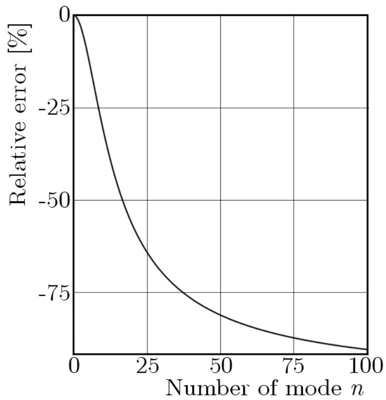

Fig. 4. Relative error of the natural frequencies for torsional modes for the beam models

5.3. Excited vibrations

The vibrations are excited by a concentrated moment with an amplitude $M_0 = 5\,\mathrm{Nm}$ acting at the point distanced $0.4l$ ($2.4\,\mathrm{m}$) from the end of beam.

The initial conditions are zeroes (i.e $\varphi_0(x) = 0$ and $\varOmega_0 = 0$ in formulas (3.6))

$$m_s(x,t) = M_0\delta(x - 0.4l)\sin(\nu t) \tag{5.2}$$

The angular frequency of the excitation is $\nu = 200\,\mathrm{rad/s}$. Material damping is neglected. The analytical solution has the form

$$\varphi(x,t) = \frac{2}{l}\frac{1}{\rho J_0}M_0\sum_{n=1}^{\infty}\frac{1}{\omega_n^2 - \nu^2}\Big[\sin(\nu t) - \frac{\nu}{\omega_n}\sin(\omega_n t)\Big]\sin(\lambda_n 0.4l)\sin(\lambda_n x) \tag{5.3}$$

In the analysis, the first five modes are considered.

The displacement of the middle of the beam just after the beginning of vibrations and for the steady-state are shown in Fig. 5. The control point is the place of action of the concentrated excitation moment. It is distanced by $0.4l$ (2.4 m) from the end of the beam.

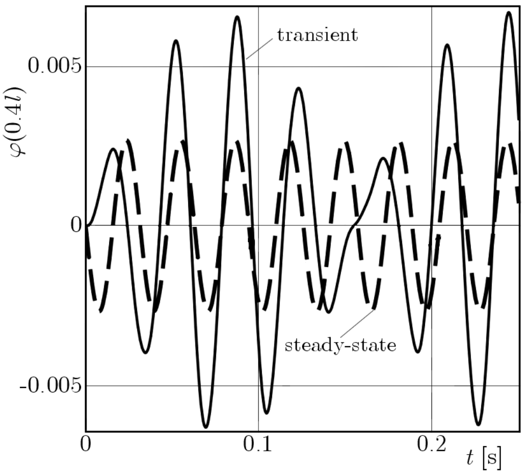

Fig. 5. Displacement at the control point – complete analytical solution, transient and steady-state

The plots show the necessity of taking into account the full solution instead of the steady-state case if the results are important just after the start of action of external loadings. Due to internal material damping (not taken into account in the considered model), the transient component existing in solution is a function that relatively fastly tends to zero. Therefore, enough time after the start of action of the harmonic excitation, the solution takes the steady-state form.

6. Conclusions

- The solution of the problem for a monolithic cross-section is not an asymptotic case of the solution of the thin-walled case if the value of J_ω tends to zero.
- The given formulas can be applied to the analysis of reduction of torsional vibrations by coupled sets of piezoelectric elements. The action of piezoelectric elements can be approximately modeled by a concentrated moment put in the suitable cross-section, see Elliott and Nelson (1997), Hansen and Snyder (1997) for beams.
- The given formulas make it possible to find an analytical solution for the transient case of the response (just after the excitation is applied) and for the steady-state case.
- The solution can be generalized by assuming the Voigt-Kelvin model of the viscous type of damping for description of the internal material damping.

Appendix A. Orthogonality of the eigen-functions

Formula $(3.2)_2$ can be written in the following form

$$\begin{aligned} GJ_s\lambda_n^4X_n(x) &= EJ_\omega\frac{d^4X_n(x)}{dx^4} - GJ_s\frac{d^2X_n(x)}{dx^2} \\ GJ_s\lambda_m^4X_m(x) &= EJ_\omega\frac{d^4X_m(x)}{dx^4} - GJ_s\frac{d^2X_m(x)}{dx^2} \end{aligned} \tag{A.1}$$

Let us multiply the first equation of system (A.1) by the eigen-function $X_m(x)$ and the second equation suitably by $X_n(x)$, and then subtract the equations by sides and integrate.

Finally, formula (A.1) is

$$\begin{aligned} GJ_s(\lambda_n^4-\lambda_m^4)\int\limits_0^l X_n(x)X_m(x)\;dx &= EJ_\omega\int\limits_0^l \frac{d^4X_n(x)}{dx^4}X_m(x)\;dx - EJ_\omega\int\limits_0^l \frac{d^4X_m(x)}{dx^4}X_n(x)\;dx \\ &- GJ_s\int\limits_0^l \frac{d^2X_n(x)}{dx^2}X_m(x)\;dx + GJ_s\int\limits_0^l \frac{d^2X_m(x)}{dx^2}X_n(x)\;dx \end{aligned} \tag{A.2}$$

By integrating the right side of equation (4.2) by parts, one obtains the following formulas for each component

$$\begin{aligned} &EJ_\omega\int\limits_0^l \frac{d^4X_n(x)}{dx^4}X_m(x)\;dx \\ &\quad = EJ_\omega\Big[\frac{d^3X_n(x)}{dx^3}X_m(x)\Big|_0^l - \frac{d^2X_n(x)}{dx^2}\frac{dX_m(x)}{dx}\Big|_0^l + \int\limits_0^l \frac{d^2X_n(x)}{dx^2}\frac{d^2X_m(x)}{dx^2}\;dx\Big] \\ &EJ_\omega\int\limits_0^l \frac{d^4X_m(x)}{dx^4}X_n(x)\;dx \\ &\quad = EJ_\omega\Big[\frac{d^3X_m(x)}{dx^3}X_n(x)\Big|_0^l - \frac{d^2X_m(x)}{dx^2}\frac{dX_n(x)}{dx}\Big|_0^l + \int\limits_0^l \frac{d^2X_m(x)}{dx^2}\frac{d^2X_n(x)}{dx^2}\;dx\Big] \\ &GJ_s\int\limits_0^l \frac{d^2X_n(x)}{dx^2}X_m(x)\;dx = GJ_s\frac{dX_n(x)}{dx}X_m(x)\Big|_0^l - \int\limits_0^l \frac{dX_n(x)}{dx}\frac{dX_m(x)}{dx}\;dx \\ &GJ_s\int\limits_0^l \frac{d^2X_m(x)}{dx^2}X_n(x)\;dx = GJ_s\frac{dX_m(x)}{dx}X_n(x)\Big|_0^l - \int\limits_0^l \frac{dX_m(x)}{dx}\frac{dX_n(x)}{dx}\;dx \end{aligned} \tag{A.3}$$

Finally, the relationship (A.2) can be written in the form

$$\begin{aligned} GJ_s(\lambda_n^4-\lambda_m^4)\int\limits_0^l X_n(x)X_m(x)\;dx &= \Big(EJ_\omega\frac{d^3X_n(l)}{dx^3} - GJ_s\frac{d^2X_n(l)}{dx^2})X_m(l) \\ &- \Big(EJ_\omega\frac{d^3X_n(0)}{dx^3} - GJ_s\frac{d^2X_n(0)}{dx^2}\Big)X_m(0) - \Big(EJ_\omega\frac{d^3X_m(l)}{dx^3} - GJ_s\frac{d^2X_m(l)}{dx^2}\Big)X_n(l) \\ &+ \Big(EJ_\omega\frac{d^3X_m(0)}{dx^3} - GJ_s\frac{d^2X_m(0)}{dx^2}\Big)X_n(0) - EJ_\omega\frac{d^2X_n(l)}{dx^2}\frac{dX_m(l)}{dx} \\ &+ EJ_\omega\frac{d^2X_n(0)}{dx^2}\frac{dX_m(0)}{dx}EJ_\omega\frac{d^2X_m(l)}{dx^2}\frac{dX_n(l)}{dx} - EJ_\omega\frac{d^2X_m(0)}{dx^2}\frac{dX_n(0)}{dx} \end{aligned} \tag{A.4}$$

For any physically possible combination of the discussed boundary conditions, all components existing on the right-hand side are equal to zero. It means that for $n \neq m$

$$\int\limits_0^l X_n(x)X_m(x)\;dx = 0 \tag{A.5}$$

For $n = m$

$$\int\limits_0^l X_n(x)X_n(x)\;dx = \gamma_n^2 \tag{A.6}$$

The value of γ_n^2 depends on the form of the eigen-functions (see Table 1).

These relationships are known as the orthogonality conditions of the eigen-function $X_n(x)$.

References

1. Aggarwal H.R., Cranch E.T., 1967, A theory of torsional and coupled bending torsional waves in thin-walled open section beams, *Journal of Applied Mechanics – Transactions of the ASME*, **34**, 6, 337-343
2. Arpaci A., Bozdag S.E., Sunbuloglu E., 2003, Triply coupled vibrations of thin-walled open cross-section beams including rotary inertia effects, *Journal of Sound and Vibration*, **260**, 889-900
3. Augustyn E., Kozień M.S., 2014, Study of possibility of application of piezoelectric actuators for active reduction of torsional vibrations of beams, *Acta Physica Polonica A*, **125**, 4-A, 164-168
4. Bishop R.E.D., Cannon M., Miao S., 1989, On coupled bending and torsional vibration of uniform beams, *Journal of Sound and Vibration*, **131**, 1, 457-464
5. Carr J.B., 1969, Torsional vibration of uniform thin-walled beams of open section, *Aeronautical Journal*, **73**, 704, 672-674
6. Crespo Da Silva M.R.M., 1988a, Non-linear flexural-flexural-torsional-extensional dynamics of beams – I. Formulation, *International Journal of Solids and Structures*, **24**, 12, 1225-1234
7. Crespo Da Silva M.R.M., 1988b, Non-linear flexural-flexural-torsional-extensional dynamics of beams – II. Response analysis, *International Journal of Solids and Structures*, **24**, 12, 1235-1242
8. Di Egidio A., Luongo A., Vestroni F., 2003a, A non-linear model for the dynamics of open cross-section thin-walled beams – Part I: formulation, *International Journal of Non-Linear Mechanics*, **38**, 7, 1067-1081
9. Di Egidio A., Luongo A., Vestroni F., 2003b, A non-linear model for the dynamics of open cross-section thin-walled beams – Part II: forced motion, *International Journal of Non-Linear Mechanics*, **38**, 7, 1083-1094
10. Dokumaci E., 1987, An exact solution for coupled bending and torsion vibrations of uniform beams having single cross-sectional symmetry, *Journal of Sound and Vibration*, **119**, 3, 443-449
11. Eisenberger M., 1997, Torsional vibrations of open and variable cross-section bars, *Thin-Walled Structures*, **27**, 3/4, 269-278
12. Elliott S.P., Nelson P.A., 1997, *Active Control of Vibrations*, Academic Press, London
13. Ferdek U., Kozień M.S., 2013, FEM simulation of application of FGM piezoelectric actuators for active reduction of beam vibrations, *Acta Physica Polonica A*, **123**, 6, 1044-1047
14. Gere J.M., 1954, Torsional vibrations of beams of thin-walled open section, *Journal of Applied Mechanics – Transactions of the ASME*, **21**, 4, 381-387
15. Gere J.M., Lin Y.K., 1958, Coupled vibrations of thin-walled beams of open cross section, *Journal of Applied Mechanics – Transactions of the ASME*, **25**, 3, 373-378
16. Gryboś R., 1996, *Vibrations of Machines* (in Polish), Politechnika Śląska, Gliwice
17. Hansen C.H., Snyder S.D., 1997, *Active Control of Noise and Vibration*, E&FN Spon, London
18. Kaliski S., Solarz L. (Eds.), 1992, *Vibrations and Waves. Part B: Waves*, Elsevier
19. Kozień M.S., 2013, Analytical solutions of excited vibrations of a beam with application of distribution, *Acta Physica Polonica A*, **123**, 6, 1029-1033
20. Kozień M.S., Kołtowski B., 2011, Comparison of active and passive damping of plate vibration by piezoelectric actuators – FEM simulation, *Acta Physica Polonica A*, **119**, 6-A, 1005-1008
21. Librescu L., Na S., 1998, Dynamic response control of thin-walled beams to blast pulses using structural tailoring and piezoelectric actuation, *Journal of Applied Mechanics*, **65**, 2, 497-504

22. Łączkowski R., 1974, *Vibrations of Elements of Heat Turbines* (in Polish), WNT, Warszawa
23. Moheimani S.O.R., Fleming A.J., 2006, *Piezoelectric Transducers for Vibration Control and Damping*, Springer, London
24. Murray N.W., 1986, *Introduction to the theory of thin-walled structures*, Oxford University Press, Oxford
25. Piechnik S., 2007, *Technical Mechanics of Solid Body*, Politechnika Krakowska, Kraków
26. Pust L., Pesek L., 2014, Blade couple connected by damping element with dry friction, *Journal of Theoretical and Applied Mechanics*, **52**, 3, 815-826
27. Preumont A., 2006, *Mechatronics. Dynamics of Electromechanical and Piezoelectric Systems*, Springer, Berlin
28. Rao J.S., 1991, *Turbomachine Blade Vibration*, Wiley, Chichester
29. Rozmarynowski B., Szymczak C., 1984, Non-linear free torsional vibrations of thin-walled beams with bisymmetric cross-section, *Journal of Sound and Vibration*, **97**, 1, 145-152
30. Sapountzaskis E.J., 2013, Bars under torsional loading: A generalized beam theory approach, *ISRN Civil Engineering*, Article ID 916581, http://dx.doi.org/10.1155/2013/916581
31. Song O., Librescu L., 1993, Free vibrations of anisotropic composite thin-walled beams of closed cross-section contour, *Journal of Sound and Vibration*, **167**, 1, 129-147
32. Song O., Sang-Yong O.H., Librescu L., 2002, Dynamic behavior of elastically tailored rotating blades modeled as pretwisted thin-walled beams and incorporating adaptive capabilities, *International Journal of Rotating Machinery*
33. Szymczak C., 1984, Optimal design of thin-walled I beams for a given natural frequency of torsional vibrations, *Journal of Sound and Vibration*, **97**, 1, 137-144
34. Tao W.K., 1964, Dynamics of thin-walled beams of open section, Ph.D. Thesis, California Institute of Technology, Pasadena
35. Timoshenko S.P., Young D.H., Weaver W. Jr., 1974, *Vibration Problems in Engineering*, Wiley, New York
36. Vlasov V.Z., 1959, *Thin-Walled Elastic Beams* (in Russian), Goz. Izd. Fiz. Mat. Literat., Moskwa
37. Woroszył S., 1984, *Examples and Exercises from Theoty of Vibrations* (in Polish), PWN, Warszawa
38. Yaman Y., 1997, Vibration of open-section channels: a coupled flexural and torsional wave analysis, *Journal of Sound and Vibration*, **204**, 1, 131-158

Manuscript received January 23, 2015; accepted for print May 29, 2015

JOURNAL OF THEORETICAL
AND APPLIED MECHANICS
53, 4, pp. 1005-1018, Warsaw 2015
DOI: 10.15632/jtam-pl.53.4.1005

FREE VIBRATION ANALYSIS OF THICK DISKS WITH VARIABLE THICKNESS CONTAINING ORTHOTROPIC-NONHOMOGENEOUS MATERIAL USING FINITE ELEMENT METHOD

Hassan Zafarmand, Mehran Kadkhodayan
Ferdowsi University of Mashhad, Department of Mechanical Engineering, Mashhad, Iran
e-mail: kadkhoda@um.ac.ir

Free vibration analysis of thick functionally graded nanocomposite annular and solid disks with variable thickness reinforced by single-walled carbon nanotubes (SWCNTs) is presented. Four types of distribution of uniaxial aligned SWCNTs are considered: uniform and three kinds of functionally graded (FG) distribution through radial direction of the disk. The effective material properties of the nanocomposite disk are estimated by a micro mechanical model. The axisymmetric conditions are assumed and employing the graded finite element method (GFEM), the equations are solved. The solution is considered for four different thickness profiles, namely constant, linear, concave and convex. The achieved results show that the type of distribution and volume fraction of CNTs and thickness profile have a great effect on normalized natural frequencies.

Keywords: free vibration, carbon nanotube, functionally graded material, thick disk, variable thickness, graded finite element method

1. Introduction

In the recent years, nano-structured materials such as nanocomposites, have generated considerable interest in the material research community and became an attractive new subject in material science due to their potentially impressive mechanical properties. Carbon nanotubes (CNTs) have illustrated remarkable mechanical, thermal and electrical properties. For example, they could potentially have a Young's modulus as high as 1 TPa and a tensile strength approaching 100 GPa (Odegard *et al.*, 2002). These enormous advantages make them highly desirable candidates for the reinforcement of polymer composites, provided that good interfacial bonding between CNTs and polymer and proper dispersion of the individual CNTs in the polymeric matrix can be assured (Fiedler *et al.*, 2006).

The majority of researches performed on carbon nanotube reinforced composites (CNTRCs) are focused on their material properties (Esawi and Farag, 2007; Thostenson *et al.*, 2001; Dai, 2006; Kang *et al.*, 2006; Lau *et al.*, 2006). Han and Elliott (2007), by the use of molecular dynamic simulation (MD), obtained the elastic modulus of composite structures reinforced by CNTs and studied the effect of volume fraction of SWCNTs on mechanical properties of nanocomposites. Hu *et al.* (2005), by analyzing the elastic deformation of a representative volume element (RVE) under various loading conditions, evaluated the macroscopic elastic properties of CNTRCs. Zhu *et al.* (2007) studied the effect of CNTs on the mechanical properties of polymeric composites. Their results showed that adding CNTs could greatly improve Young's modulus. Due to dependency of the interaction at the polymer and nanotube interface on the local molecular structure and bonding, Odegard *et al.* (2003) a constitutive model for CNTRCs by utilizing an equivalent-continuum modeling method proposed.

Functionally graded materials (FGMs) are special composite materials, microscopically inhomogeneous, in which mechanical properties vary smoothly and continuously from one surface to the other. This idea was used for the first time by Japanese researchers (Koizumi, 1993) and led to the concept of FGMs. A wide range of researches have been carried out on FGMs in various fields of mechanics. Motivated by the concept of FGMs, Shen (2009) presented a kind of CNTRCs in which the volume fraction of CNTs is graded with certain rules through desired directions and demonstrated that using FG-CNTRCs improve the mechanical properties of the structures. Zhu *et al.* (2012) studied bending and free vibration analyses of composite plates reinforced by SWCNTs using the finite element method based on the first order shear deformation plate theory. The effective material properties of the FG-CNTRC are graded in the thickness direction and are estimated according to the rule of mixture. Zafarmand and Kadkhodayan (2015) investigated nonlinear behaviour of FG-CNTRC rotating thick disks with variable thickness where the nonlinear axisymmetric theory of elasticity is employed. The three dimensional free vibration analysis of FC-CNTRC panels was investigated by Yas *et al.* (2013). The boundary conditions were assumed to be simply supported and the equations were solved by a generalized differential quadrature (GDQ) method. Ke *et al.* (2010) performed nonlinear free vibration analysis of FG-CNTRC beams based on Timoshenko beam theory and Von-Karman geometric nonlinearity. The Ritz method was applied to derive the governing eigenvalue equation which was then solved by a direct iterative method to obtain the nonlinear vibration frequencies of FG-CNTRC beams with different end supports. Sobhani Aragh and Yas (2010) investigated the static and free vibration characteristics of continuously graded fiber-reinforced (CGFR) cylindrical shells based on three dimensional elasticity. The boundary conditions were assumed to be simply supported and the equations were solved by a GDQ method. Moreover, several researches were carried out about free vibration analysis of FG disks with variable thickness (Alipour *et al.*, 2010; Gupta *et al.*, 2007; Efraim and Eisenberger, 2007; Tajeddini and Ohadi, 2011).

The purpose of this paper is to investigate free vibration analysis of thick FG-CNTRC annular and solid disks with variable thickness. Material properties are assumed to vary continuously through radial direction. The effective material properties of FG-CNTRC disks are estimated using a micro-mechanical model and the normalized natural frequencies of FG-CNTRC annular and solid disks for various types of distributions and volume fractions of CNTs, boundary conditions and thickness to radius ratios as well as different kinds of thickness profiles are computed and compared. The difficulty in obtaining analytical solutions for the response of graded material systems is due to the dispersive nature of heterogeneous material systems. Therefore, analytical or semi-analytical solutions are available only through a number of problems with simple boundary conditions. Thus, in order to find the solution for a thick FG-CNTRC disk of variable thickness with various boundary conditions, powerful numerical methods such as the graded finite element method (GFEM) are needed. The graded finite element incorporates the gradient of material properties at the element scale in the framework of a generalized isoparametric formulation. Some studies can be found in the literature on the modeling of non-homogenous structures by using GFEM (Kim and Paulino, 2002; Zafarmand and Hassani, 2014; Ashrafi *et al.*, 2013).

2. Problem formulation

In this Section, different types of CNTs distributions through radial direction of the disk is introduced. The axisymmetric governing equations of motion are obtained and the graded finite element method is used for modeling the non-homogeneity of the material.

2.1. Material properties in FG-CNTRC disks

A thick FG-CNTRC disk of inner radius a, outer radius b and variable thickness $h(r)$ is considered. The geometry and coordinate system of the disk is shown in Fig. 1.

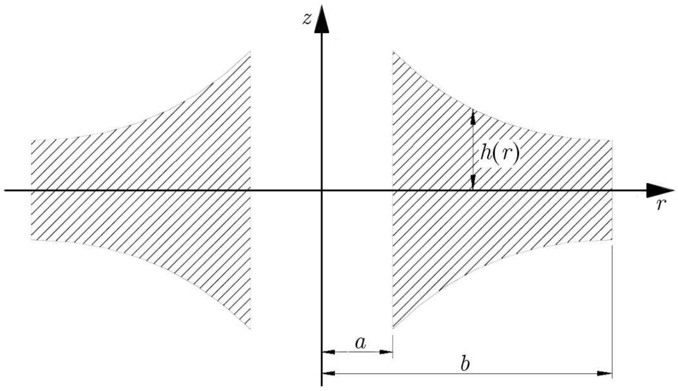

Fig. 1. Axisymmetric thick FG-CNTRC disk

This FG-CNTRC disk consists of SWCNTs (along the radial direction) and an isotropic matrix. UD-CNTRC represents the uniform distribution and FG_V, FG_O and FG_X-CNTRC, the functionally graded distribution of CNTs in the radial direction of the nanocomposite disk. Several studies have been published each with different focuses on mechanical properties of CNTRCs. However, due to the simplicity and convenience, in the present study, the rule of mixture is employed, and thus the effective material properties of CNTRC disk can be obtained as (Shen, 2009)

$$\begin{aligned} & E_1 = \eta_1 V_{CNT} E_1^{CNT} + V_m E^m && \frac{\eta_2}{E_i} = \frac{V_{CNT}}{E_i^{CNT}} + \frac{V_m}{E^m} && (i = 2,3) \\ & \frac{\eta_3}{G_{ij}} = \frac{V_{CNT}}{G_{ij}^{CNT}} + \frac{V_m}{G^m} && \nu_{ij} = V_{CNT}\nu_{ij}^{CNT} + V_m \nu^m && (i \neq j) \\ & \rho = V_{CNT}\rho^{CNT} + V_m \rho^m \end{aligned} \tag{2.1}$$

where E_i^{CNT}, G_{ij}^{CNT}, ν_{ij}^{CNT} and ρ^{CNT} are elasticity modulus, shear modulus, Poisson's ratio and density, respectively, of the CNTs, and E^m, G^m, ν^m and ρ^m are the corresponding properties of the matrix. η_j $(j = 1,2,3)$ is the CNTs' efficiency parameter which can be computed by matching the elastic modulus of CNTRCs observed from the MD simulation results with those obtained from the rule of mixture. V_{CNT} and V_m are volume fractions of the CNTs and matrix, respectively, which are related by $V_{CNT} + V_m = 1$. The type of distribution and volume fraction of the CNTs has serious effects on the disk behavior. As has been mentioned previously, four types of distribution are utilized in this study; that is either uniformly distributed (UD) or functionally graded (FG) in the radial direction of the disk. These types with the distribution for a section in the r-z plane of the disk with a constant thickness profile are depicted in Fig. 2 (the dash lines are CNTs in a huge scale). Distributions of CNTs through the radial direction of these four types of CNTRC disks are assumed to be as (Shen, 2009)

$$\begin{aligned} & V_{CNT} = V_{CNT}^* && \text{type UD} \\ & V_{CNT} = 2\frac{r-a}{b-a}V_{CNT}^* && \text{type FG\_V} \\ & V_{CNT} = 2\frac{b-r}{b-a}V_{CNT}^* && \text{type FG\_O} \\ & V_{CNT} = 4\Big|\frac{r-a}{b-a}\Big|V_{CNT}^* && \text{type FG\_X} \end{aligned} \tag{2.2}$$

in which

$$r_m = \frac{a+b}{2} \qquad V_{CNT}^* = \frac{w_{CNT}}{w_{CNT} + \frac{\rho_{CNT}}{\rho_m}(1 - w_{CNT})} \tag{2.3}$$

where w_{CNT} is the mass fraction of CNTs which does not depend on the variable r and is unique for all types of distribution. ρ_{CNT} and ρ_m are the densities of CNTs and matrix, respectively.

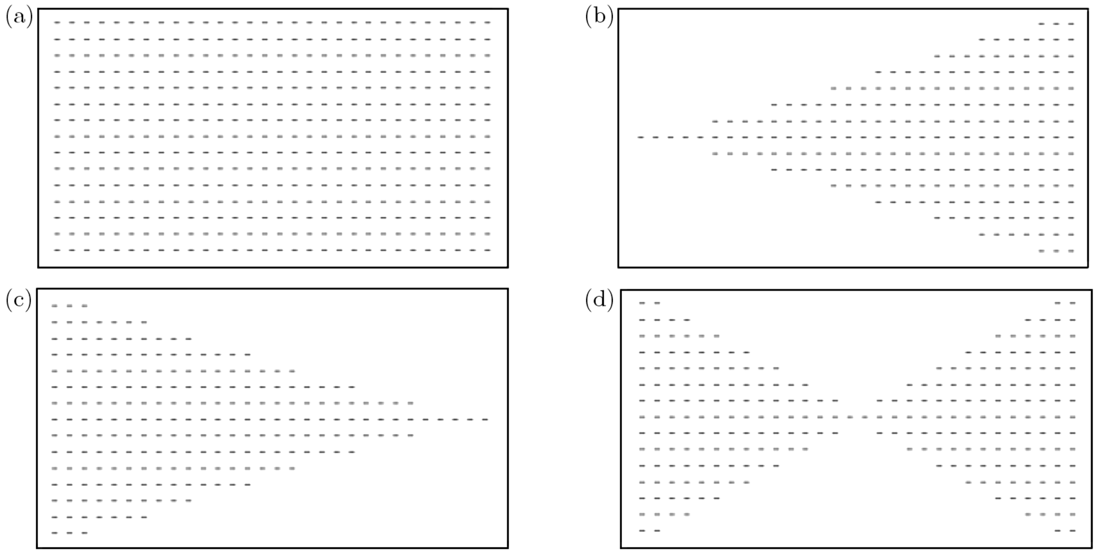

Fig. 2. Different types of distribution: (a) UD, (b) FG_V, (c) FG_O, (d) FG_X

2.2. Governing equations

The governing equations may be obtained based on Hamilton's principle

$$\int_{t_1}^{t_2} \delta I\, dt = \int_{t_1}^{t_2} \delta(\Pi - T)\, dt = 0 \tag{2.4}$$

where Π and T are potential and kinetic energy, respectively. These functions and their variations are

$$\begin{aligned} \Pi &= \frac{1}{2}\iiint_{\Omega} \boldsymbol{\varepsilon}^{\mathrm{T}} \cdot \boldsymbol{\sigma}\, d\Omega \qquad & \delta\Pi &= \frac{1}{2}\iiint_{\Omega} \delta\boldsymbol{\varepsilon}^{\mathrm{T}} \cdot \boldsymbol{\sigma}\, d\Omega \\ T &= \frac{1}{2}\iiint_{\Omega} \rho\dot{\mathbf{U}}^{\mathrm{T}} \cdot \dot{\mathbf{U}}\, d\Omega \qquad & \delta T &= \frac{1}{2}\iiint_{\Omega} \rho\dot{\mathbf{U}}^{\mathrm{T}} \cdot \delta\dot{\mathbf{U}}\, d\Omega \end{aligned} \tag{2.5}$$

where Ω is the volume of the domain under consideration and ρ is the mass density that depends on the r coordinate.

Substituting Eqs. (2.5) into Hamilton's principle (Eq. (2.4)), applying the side conditions $\delta\mathbf{U}|_{t_1,t_2} = \mathbf{0}$ and using part integration, one obtains

$$\iiint_{\Omega} \delta\boldsymbol{\varepsilon}^{\mathrm{T}} \cdot \boldsymbol{\sigma}\, d\Omega + \iiint_{\Omega} \rho\ddot{\mathbf{U}}^{\mathrm{T}} \cdot \delta\dot{\mathbf{U}}\, d\Omega = 0 \tag{2.6}$$

The stress-strain relations from Hook's law in matrix form are as

$$\boldsymbol{\sigma} = \mathbf{D}\boldsymbol{\varepsilon} \tag{2.7}$$

where the stress and strain components and the coefficients of elasticity $\mathbf{D}$ are as in the following relations

$$\boldsymbol{\sigma} = \begin{Bmatrix} \sigma_r & \sigma_\theta & \sigma_z & \sigma_{rz} \end{Bmatrix}^{\mathrm{T}} \qquad \boldsymbol{\varepsilon} = \begin{Bmatrix} \varepsilon_r & \varepsilon_\theta & \varepsilon_z & \gamma_{rz} \end{Bmatrix}^{\mathrm{T}}$$
$$\mathbf{D} = \begin{bmatrix} D_{11} & D_{12} & D_{13} & 0 \\ D_{12} & D_{22} & D_{23} & 0 \\ D_{13} & D_{23} & D_{33} & 0 \\ 0 & 0 & 0 & D_{55} \end{bmatrix} \tag{2.8}$$

in which

$$\begin{aligned} D_{11} &= \frac{1-\nu_{23}\nu_{32}}{E_2E_3\varDelta} & D_{22} &= \frac{1-\nu_{13}\nu_{31}}{E_1E_3\varDelta} & D_{33} &= \frac{1-\nu_{12}\nu_{21}}{E_1E_2\varDelta} \\ D_{12} &= \frac{\nu_{21}+\nu_{31}\nu_{23}}{E_2E_3\varDelta} & D_{13} &= \frac{\nu_{31}+\nu_{21}\nu_{32}}{E_2E_3\varDelta} & D_{23} &= \frac{\nu_{32}+\nu_{12}\nu_{31}}{E_1E_3\varDelta} \\ D_{55} &= G_{13} & \varDelta &= \frac{1-\nu_{12}\nu_{21}-\nu_{23}\nu_{32}-\nu_{13}\nu_{31}-2\nu_{21}\nu_{32}\nu_{13}}{E_1E_2E_3} \end{aligned} \tag{2.9}$$

where E_i, G_{ij} and ν_{ij} are found from (2.1). It is obvious that the matrix $\mathbf{D}$ is dependent on the spatial variable r.

The strain-displacement equations based on the theory of linear theory of elasticity in cylindrical coordinates with the axisymmetric assumption are

$$\varepsilon_r = \frac{\partial u}{\partial r} \qquad \varepsilon_\theta = \frac{u}{r} \qquad \varepsilon_z = \frac{\partial w}{\partial z} \qquad \gamma_{rz} = \frac{\partial u}{\partial z} + \frac{\partial w}{\partial r} \tag{2.10}$$

where u and w are the radial and axial components of the displacement, respectively. Equation (2.10) can be formulated in the matrix form as

$$\boldsymbol{\varepsilon} = \mathbf{LU} \tag{2.11}$$

in which $\mathbf{U}$ is the displacements vector and $\mathbf{L}$ is a matrix containing partial differentiating equations as

$$\mathbf{U} = \begin{Bmatrix} u & v \end{Bmatrix}^{\mathrm{T}} \qquad \mathbf{L} = \begin{bmatrix} \partial_r & 1/r & 0 & \partial_z \\ 0 & 0 & \partial_z & \partial_r \end{bmatrix}^{\mathrm{T}} \tag{2.12}$$

Moreover, the boundary conditions used in this study are defined as follows:

Solid disk:

- Clamped $r = b \;\rightarrow\; u = w = 0$
- Simply supported $r = b \;\rightarrow\; \sigma_r = w = 0$
- Free $r = b \;\rightarrow\; \sigma_r = \sigma_{rz} = 0$

Annular disk:

- Clamped $r = a, b \;\rightarrow\; u = w = 0$
- Simply supported $r = a, b \;\rightarrow\; \sigma_r = w = 0$
- Free $r = a, b \;\rightarrow\; \sigma_r = \sigma_{rz} = 0$

2.3. Graded finite element modeling

In order to solve the governing equations, the isoparametric finite element method with graded element properties is employed. For this purpose, the variational formulation is considered. In conventional finite element formulations, a predetermined set of material properties are used for each element such that the property field is constant within an individual element. For modeling a continuously nonhomogeneous material, the material property function must be discretized according to the size of elements mesh. This approximation can provide significant discontinuities. Based on these facts, the graded finite element is strongly preferable for the modeling of the present problem. Using the graded elements for the modeling of gradation of the material leads to more accurate results than dividing the solution domain into homogenous elements.

The finite element approximation of the domain is in the r-z plane, which is the plane of revolution. The section of the cylinder in the r-z plane is considered and divided into a number of simplex linear quadrilateral elements. For convenience, we use the local coordinate with its variables (ξ,η) between -1 to 1, as shown in Fig. 3.

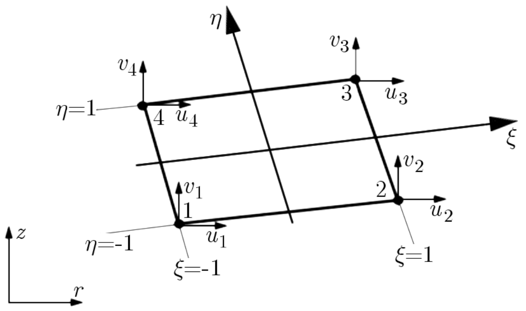

Fig. 3. Local coordinate

For element (e), the displacements are approximated as (Zienkiewicz, 2005)

$$\mathbf{U}^{(e)} = \mathbf{\Phi}\mathbf{\Lambda}^{(e)} \tag{2.13}$$

where $\mathbf{\Phi}$ is the matrix of linear shape functions in the local coordinate and $\mathbf{\Lambda}^{(e)}$ is the nodal displacement vector of the element, which is

$$\begin{aligned}\mathbf{\Phi} &= \begin{bmatrix} \varPhi_1 & 0 & \varPhi_2 & 0 & \varPhi_3 & 0 & \varPhi_4 & 0 \\ 0 & \varPhi_1 & 0 & \varPhi_2 & 0 & \varPhi_3 & 0 & \varPhi_4 \end{bmatrix} \\ \mathbf{\Lambda}^{(e)} &= \Big\{ U_1 \quad V_1 \quad U_2 \quad V_2 \quad U_3 \quad V_3 \quad U_4 \quad V_4 \Big\}^{\mathrm{T}}\end{aligned} \tag{2.14}$$

in which

$$\varPhi_i = \frac{1}{4}(1+\xi_i\xi)(1+\eta_i\eta) \tag{2.15}$$

To treat the material inhomogeneity by using the GFEM, it may be written

$$\varPsi^{(e)} = \sum_{i=1}^{4} \varPsi_i \varPhi_i \tag{2.16}$$

where $\varPsi^{(e)}$ is the material property of the element.

Substituting Eq. (2.13) in Eq. (2.11) gives the strain matrix of element (e) as

$$\boldsymbol{\varepsilon}^{(e)} = \mathbf{B}\mathbf{\Lambda}^{(e)} \tag{2.17}$$

where

$$\mathbf{B} = \mathbf{L}\mathbf{\Phi}^{(e)} \tag{2.18}$$

By imposing Eqs. (2.7), (2.13), (2.17) into Eq. (2.6), it can be achieved as

$$\delta\mathbf{\Lambda}^{(e)\mathrm{T}}\Big(\iiint_{\varOmega} \mathbf{B}^{\mathrm{T}}\mathbf{D}\mathbf{B}\, d\varOmega\Big)\mathbf{\Lambda}^{(e)} + \delta\mathbf{\Lambda}^{(e)\mathrm{T}}\Big(\iiint_{\varOmega} \rho\mathbf{\Phi}^{\mathrm{T}}\mathbf{\Phi}\, d\varOmega\Big)\ddot{\mathbf{\Lambda}}^{(e)} = 0 \tag{2.19}$$

Since $\delta\mathbf{\Lambda}^{(e)^{\mathrm{T}}}$ is the variation of the nodal displacements and is arbitrary, it can be omitted from (2.19), thus this equation can be written as

$$\mathbf{M}^{(e)}\ddot{\mathbf{\Lambda}}^{(e)} + \mathbf{K}^{(e)}\mathbf{\Lambda}^{(e)} = \mathbf{0} \tag{2.20}$$

where the mass and stiffness matrices are defined as

$$\mathbf{M}^{(e)} = \iiint\limits_{\Omega} \rho\mathbf{\Phi}^{\mathrm{T}}\mathbf{\Phi}\, d\Omega \qquad \mathbf{K}^{(e)} = \iiint\limits_{\Omega} \mathbf{B}^{\mathrm{T}}\mathbf{D}\mathbf{B}\, d\Omega \tag{2.21}$$

For finding the components of mass and stiffness matrices, the integral must be taken over the elements volume. As $\mathbf{D}$ and ρ are not constant in the case of FG types distributions, these matrices are evaluated by numerical integration for each element using the Gauss-Legendre technique (Zienkiewicz, 2005). Now by assembling the element matrices, the global equations of motion for the FG-CNTRC disks can be obtained as

$$\mathbf{M}\ddot{\mathbf{\Lambda}} + \mathbf{K}\mathbf{\Lambda} = \mathbf{0} \tag{2.22}$$

Once the finite element equations are estimated, substituting $\mathbf{\Lambda} = \mathbf{\Lambda}_0\mathrm{e}^{\mathrm{i}\omega t}$ (ω is the natural frequency) into Eq. (2.22) leads to an eigenvalue problem that can be solved using standard eigenvalue extraction procedures.

In this regard, for calculating the elemental characteristic matrices (2.21) with the use of Gauss-Legendre technique, obtaining the global ones and solve the eigenvalue problem after imposing the boundary conditions, a FE code is prepared by the authors.

3. Numerical results and discussion

3.1. Validation

To validate the current work, the data of a non-homogeneous solid circular plate with variable thickness can be used (Gupta *et al.*, 2007). The outer radius of the disk is $r_o$and the variable thickness is defined as

$$h(r) = h_0(1 + \alpha r + \beta r^2) \tag{3.1}$$

where h_0, α and β are the thickness at the middle and taper parameters, respectively. The elasticity modulus and density vary in the r direction as below

$$E(r) = E_0\mathrm{e}^{\mu r} \qquad \rho(r) = \rho_0\mathrm{e}^{\eta r} \tag{3.2}$$

in which μ and η are non-homogeneity parameters.

The comparison of the first three frequency parameter ($\Omega = \omega\sqrt{\rho_0 r_0^2(1-\nu^2)/E_0}$) for a circular plate of $\eta = -0.5$, $\mu = 0.1$, $\alpha = -0.5$ and $\beta = 0.5$ with the published data is shown in Table 1 and a good agreement between these results is observed.

3.2. Numerical results

In this Section, the free vibrational response of FG-CNTRC disks with variable thickness is presented. The disk is made of Polymethyl-methacrylate (PMMA) as the matrix, where SWCNTs act as fibers aligned in the radial direction. The properties of basic materials are (Han and Elliott, 2007; Shen, 2009)

$$\begin{array}{lll} E^m = 2.5\,\mathrm{GPa} & \nu^m = 0.34 & \rho^m = 1150\,\mathrm{kg/m^3} \\ E_1^{CNT} = 5.6466\,\mathrm{TPa} & E_2^{CNT} = 7.08\,\mathrm{TPa} & \nu^{CNT} = 0.175 \\ \rho^{CNT} = 1150\,\mathrm{kg/m^3} & & \end{array} \tag{3.3}$$

Table 1. Frequency parameter compared with the result by Gupta (2007)

Boundary condition		$h_0 = 0.1$			$h_0 = 0.2$		
		GFEM	Gupta (2007)	Difference [%]	GFEM	Gupta (2007)	Difference [%]
Clamped	Ω_1	0.4121	0.4083	0.9	0.7765	0.7673	1.2
	Ω_2	1.4657	1.4471	1.2	2.5050	2.4604	1.8
	Ω_3	3.0403	2.9897	1.6	4.7195	4.6123	2.3
Simply supported	Ω_1	0.1857	0.1852	0.3	0.3650	0.3641	0.2
	Ω_2	1.0800	1.0715	0.8	1.9362	1.9258	0.5
	Ω_3	2.5635	2.5349	1.1	4.1489	4.1205	0.7
Free	Ω_1	0.3358	0.3348	0.3	0.6503	0.6480	0.3
	Ω_2	1.3553	1.3436	0.9	2.3823	2.3572	1
	Ω_3	2.9541	2.9159	1.3	4.7125	4.6299	1.8

The key issue for successful application of the extended rule of mixture to CNTRCs is to determine the CNT efficiency parameter η_j $(j = 1, 2, 3)$. However, there are no experiments conducted to determine the value of η_j for CNTRCs (Shen, 2009). Han and Elliott (2007), with the use of MD simulation and energy minimization, obtained the elastic moduli of polymer/CNT composites. In the conventional rule of mixture, the whole system is assumed to be continuum and the interfaces between the matrix and fibers remain fully intact, thus the general macroscopic rule of mixtures cannot be applied straightforwardly to composites with strong interfacial interactions. Besides, micromechanics equations cannot capture the scale difference between the nano and micro levels. For this purpose, CNT efficiency parameters η_j $(j = 1, 2, 3)$ are obtained by comparing Young's moduli E_1^{CNT} and E_2^{CNT} of CNTRCs achieved from the extended rule of mixture to those from MD simulation given by Han and Elliot (2007). It should be noticed that there are no MD results available for shear modulus G_{12} in Han and Elliott (2007). The results are shown in Table 2 and will be used in the present study, in which it is assumed $\eta_3 = 0.7\eta_2$ (Yas *et al.*, 2013).

Table 2. Comparison of Young's moduli for polymer/CNTRC at $T_0 = 300$ (Yas *et al.*, 2013)

	MD (Han*et al.*, 2007)		Extended rule of mixture			
V_{CNT}^*	E_1 [GPa]	E_2 [GPa]	E_1 [GPa]	η_1 [–]	E_2 [GPa]	η_2 [–]
0.12	94.6	2.9	94.78	0.137	2.9	1.022
0.17	138.9	4.9	138.68	0.142	4.9	1.626
0.28	224.2	5.5	224.5	0.141	5.5	1.585

Furthermore, the thickness profile of FG-CNTRC disk is in the form of

$$h(r) = h_0\Big(1 - q\Big(\frac{r}{b}\Big)^m\Big) \tag{3.4}$$

where h_0, q and m are geometric parameters that $0 \leqslant q < 1$ and $m > 0$. By changing the values of q and m, four different thickness profiles, namely constant, linear, concave and convex are introduced in Table 3 and, in the case of $a = 0$, $b = 0.5m$, are shown in Fig. 4.

Table 3. Different kinds of thickness profiles

Constant	Linear	Concave	Convex
$q = 0$	$q = 0.7$ $m = 1$	$q = 0.7$ $m = 0.5$	$q = 0.7$ $m = 2$

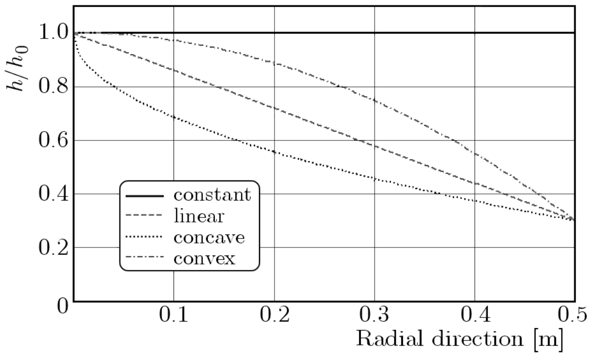

Fig. 4. Different kinds of thickness profiles

It should be also stated that the plane of revolution of the disk (r-$z$plane) is devided into 1200 linear quadrilateral elements with mesh density of 60×20 regularly placed along the r and z direction. In the case of linear thickness profile, a schematic of finite element mesh is illustrated in Fig. 5.

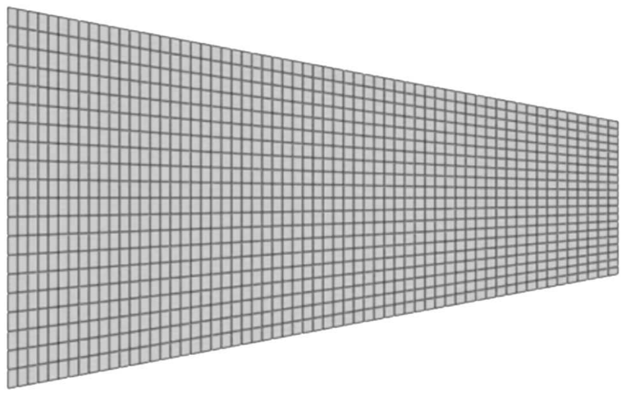

Fig. 5. Finite element mesh

Now, by introducing the normalized natural frequency as

$$\Omega = \omega b \sqrt{\frac{\rho_m}{G_m}} \tag{3.5}$$

the first five normalized natural frequencies for FG-CNTRC annular and solid disks for different types of distribution and volume fractions of CNTs, boundary conditions and thickness to radius ratios (h_0/b) as well as different thickness profiles are presented.

The effect of volume fraction of CNTs (V_{CNT}^*) on the first five normalized natural frequencies (Ω) of the solid UD and FG-CNTRC disk for different types of CNTs distribution is shown in Table 4. In this case, the boundary conditions are assumed to be clamped, the thickness profile to be constant and $h_0/b = 0.5$. As it can be seen; the normalized natural frequencies increase when V_{CNT}^* raises due to growth of the structure stiffness. Moreover, changing the type of CNTs distribution, affects the magnitude of natural frequencies. The FG_V type of distribution has the highest natural frequencies and the FG_O has the lowest ones.

The comparison of first five normalized natural frequencies for UD and FG-CNTRC solid disks for different boundary conditions with the linear thickness profile, $V_{CNT}^* = 0.12$ and $h_0/b = 0.5$ is presented in Table 5. According to the results, boundary conditions have noticeable effects on natural frequencies. Thus, by changing the boundary conditions, the free vibration response of the disk can be controlled.

Table 4. Comparison of the first five normalized natural frequencies (Ω) for clamped UD and FG-CNTRC solid disks for different V^*_{CNT} with constant thickness and $h_0/b = 0.5$

	$V^*_{CNT} = 0.12$				$V^*_{CNT} = 0.17$				$V^*_{CNT} = 0.28$			
	UD	FG_V	FG_O	FG_X	UD	FG_V	FG_O	FG_X	UD	FG_V	FG_O	FG_X
Ω_1	1.977	2.059	1.885	1.953	2.537	2.686	2.385	2.507	2.688	2.981	2.435	2.672
Ω_2	4.669	4.699	4.631	4.576	6.009	6.075	5.943	5.882	6.339	6.536	6.219	6.231
Ω_3	7.381	7.394	7.349	7.32	9.503	9.547	9.455	9.432	10.01	10.18	9.953	9.981
Ω_4	10.13	10.14	10.11	10.06	13.06	13.09	13.02	12.98	13.74	13.91	13.73	13.71
Ω_5	12.94	12.94	12.67	12.42	16.54	16.54	16.03	15.64	17.02	16.70	16.49	16.25

Table 5. Comparison of the first five normalized natural frequencies (Ω) for UD and FG-CNTRC solid disks for different boundary conditions with the linear thickness profile, $V^*_{CNT} = 0.12$ and $h_0/b = 0.5$

	Clamped				Simply supported				Free			
	UD	FG_V	FG_O	FG_X	UD	FG_V	FG_O	FG_X	UD	FG_V	FG_O	FG_X
Ω_1	1.44	1.53	1.323	1.426	1.317	1.427	1.125	1.335	2.942	3.009	2.775	2.723
Ω_2	4.262	4.291	4.21	4.109	4.055	4.109	3.938	3.908	5.399	5.508	5.074	5.37
Ω_3	6.936	6.957	6.884	6.818	6.669	6.709	6.581	6.579	7.945	8.085	7.658	7.905
Ω_4	9.638	9.653	9.582	9.522	9.323	9.348	9.259	9.208	10.65	10.75	10.38	10.64
Ω_5	12.4	12.41	12.35	12.33	12.03	12.04	11.98	11.96	13.41	13.49	10.79	13.39

Table 6 demonstrates the effect of thickness-to-radius ratio on the normalized natural frequencies of UD and FG-CNTRC solid disks for different types of CNTs distribution with the concave thickness profile and $V^*_{CNT} = 0.17$, and the boundary conditions assumed to be simply supported. It is obvious that enlarging the thickness-to-radius ratio leads to growth of natural frequencies, and this growth is larger in the lower natural frequencies.

Table 6. Comparison of the first five normalized natural frequencies (Ω) for simply supported UD and FG-CNTRC solid disks for different thickness-to-radius ratios (h_0/b) with the concave thickness profile and $V^*_{CNT} = 0.17$

	$h_0/b = 0.1$				$h_0/b = 0.2$				$h_0/b = 0.3$			
	UD	FG_V	FG_O	FG_X	UD	FG_V	FG_O	FG_X	UD	FG_V	FG_O	FG_X
Ω_1	0.473	0.562	0.337	0.475	0.881	1.032	0.638	0.889	1.205	1.382	0.905	1.215
Ω_2	2.125	2.203	1.971	1.732	3.493	3.596	3.278	3.01	4.271	4.372	4.057	3.867
Ω_3	4.175	4.154	4.065	3.866	6.284	6.313	6.124	6.053	7.349	7.407	7.184	7.182
Ω_4	6.604	6.467	6.555	6.304	9.35	9.312	9.257	9.022	10.64	10.65	10.55	10.36
Ω_5	9.355	9.113	9.366	9.059	12.65	12.56	12.63	12.41	14.11	14.07	14.08	13.95

The influence of different thickness profiles on the normalized natural frequencies of free UD and FG-CNTRC solid disks with $V^*_{CNT} = 0.28$ and $h_0/b = 0.5$ for different types of CNTs distribution is illustrated in Table 7. The achieved results show that the natural frequencies are highly dependent on the thickness profile. Moreover, the highest natural frequencies occur in the convex thickness profile and the smallest ones occur in the concave thickness profile.

Now, the free vibration response of FG-CNTRC annular disks of variable thickness is discussed. As before, the effect of volume fraction of CNTs, boundary condition, thickness to radius ratio and thickness profile on the first five normalized natural frequencies of annular UD and FG-CNTRC disks are studied, in this case of $a/b = 0.2$. These results are illustrated in Tables 8-11. As it can be concluded from these tables, the normalized natural frequncies increase when

Table 7. Comparison of the first five normalized natural frequencies (Ω) for free UD and FG-CNTRC solid disks for different thickness profiles with $h_0/b = 0.5$ and $V^*_{CNT} = 0.28$

	Linear				Concave				Convex			
	UD	FG_V	FG_O	FG_X	UD	FG_V	FG_O	FG_X	UD	FG_V	FG_O	FG_X
Ω_1	4.027	4.162	3.762	3.585	3.375	3.886	3.401	3.291	4.349	4.459	4.158	3.884
Ω_2	7.38	7.566	6.942	7.257	7.014	7.211	6.479	6.896	7.793	7.95	7.482	7.65
Ω_3	10.87	11.06	10.46	10.71	10.45	10.65	9.991	10.28	11.32	11.49	10.99	11.16
Ω_4	14.49	14.67	14.17	14.42	14.04	14.23	13.71	13.97	14.95	15.13	14.64	14.89
Ω_5	18.21	18.39	15.02	18.18	17.75	17.93	14.76	17.72	18.14	17.31	15.12	17.82

Table 8. Comparison of the first five normalized natural frequencies (Ω) for clamped UD and FG-CNTRC annular disks for different V^*_{CNT} with constant thickness and $h_0/b = 0.5$

	$V^*_{CNT} = 0.12$				$V^*_{CNT} = 0.17$				$V^*_{CNT} = 0.28$			
	UD	FG_V	FG_O	FG_X	UD	FG_V	FG_O	FG_X	UD	FG_V	FG_O	FG_X
Ω_1	3.203	3.237	3.167	3.301	4.122	4.194	4.076	4.314	4.348	4.541	4.321	4.757
Ω_2	6.598	6.609	6.589	6.513	8.493	8.535	8.485	8.419	8.951	9.108	8.977	9.015
Ω_3	10.03	10.04	10.02	10.03	12.93	12.96	12.92	12.98	13.61	13.77	13.66	13.83
Ω_4	13.09	13.13	12.86	12.55	16.66	16.67	16.34	15.82	17.21	17.06	16.81	16.47
Ω_5	13.55	13.56	13.54	13.1	17.47	17.51	17.29	16.61	18.31	18.49	18.09	17.29

Table 9. Comparison of first five normalized natural frequency (Ω) for UD and FG-CNTRC annular disks for different boundary conditions with linear thickness profile, $V^*_{CNT} = 0.12$ and $h_0/b = 0.5$

	Clamped				Simply supported				Free			
	UD	FG_V	FG_O	FG_X	UD	FG_V	FG_O	FG_X	UD	FG_V	FG_O	FG_X
Ω_1	2.829	2.838	2.801	2.928	2.228	2.264	2.124	2.337	3.205	3.234	3.066	2.945
Ω_2	6.155	6.154	6.144	5.984	5.181	5.191	5.125	5.045	6.097	6.129	5.797	6.093
Ω_3	9.478	9.477	9.456	9.422	8.178	8.14	8.152	8.129	9.232	9.215	8.944	9.196
Ω_4	12.88	12.87	12.86	12.83	11.28	11.16	11.27	11.23	12.53	12.46	11.43	12.59
Ω_5	16.37	16.36	16.35	15.49	14.47	14.26	13.39	14.49	15.93	15.09	12.28	15.16

Table 10. Comparison of first five normalized natural frequency (Ω) for simply supported UD and FG-CNTRC annular disks for different thickness to radius ratio (h_0/b) with concave thickness profile and $V^*_{CNT} = 0.17$

	$h_0 = 0.1$				$h_0 = 0.2$				$h_0 = 0.3$			
	UD	FG_V	FG_O	FG_X	UD	FG_V	FG_O	FG_X	UD	FG_V	FG_O	FG_X
Ω_1	1.429	1.193	1.418	1.432	2.212	2.023	2.156	2.329	2.593	2.515	2.488	2.781
Ω_2	3.271	2.927	3.271	3.208	5.011	4.826	4.932	4.776	5.904	5.849	5.812	5.62
Ω_3	5.712	5.279	5.767	5.592	8.421	8.209	8.418	8.285	9.626	9.561	9.609	9.559
Ω_4	8.692	8.223	8.809	8.632	12.25	12.05	12.31	12.15	13.62	13.53	13.67	13.54
Ω_5	12.14	11.69	12.31	12.12	16.37	16.19	16.48	16.34	17.81	17.64	17.76	17.83

Table 11. Comparison of first five normalized natural frequency (Ω) for free UD and FG-CNTRC annular disks for different thickness profile with $h_0/b = 0.5$ and $V^*_{CNT} = 0.28$

	Linear				Concave				Convex			
	UD	FG_V	FG_O	FG_X	UD	FG_V	FG_O	FG_X	UD	FG_V	FG_O	FG_X
Ω_1	4.392	4.448	4.187	3.881	4.077	4.149	3.798	3.56	4.752	4.775	4.628	4.229
Ω_2	8.336	8.399	7.978	8.281	7.928	7.986	7.472	7.887	8.814	8.858	8.585	8.731
Ω_3	12.58	12.59	12.27	12.48	12.11	12.09	11.75	12.01	13.11	13.13	12.86	13.01
Ω_4	17.03	16.98	15.97	17.09	16.54	16.44	15.69	16.61	17.56	16.91	16.07	17.63
Ω_5	21.58	19.22	16.79	21.35	21.13	20.97	16.31	21.22	18.63	17.57	17.31	18.79

the volume fraction of CNTs or thickness-to-radius ratio raises. Moreover, the boundary condition and the type of CNTs distribution as well as the thickness profile have a great influence on the normalized natural frequencies. Besides, in comparison to solid disks, annular disks of the same conditions have larger normalized natural frequencies and, unlike the solid disks, the highest normalized natural frequencies of annular disks occur in the case of FG_X type of CNTs distribution.

Thus, the normalized natural frequencies can be controlled and altered by changing the distribution and volume fraction of CNTs, boundary condition, thickness-to-radius ratio and the thickness profile.

4. Conclusions

In this study, free vibration analysis of thick FG-CNTRC annular and solid disks with variable thickness is presented. The axisymmetric conditions are assumed, volume fraction of CNTs is considered to be graded continuously along the radial direction and material properties are estimated through the extended rule of mixture. By employing the graded finite element method and Hamilton's principle, the free vibrational response of FG-CNTRC disks is investigated. Detailed parametric studies are performed to illustrate the effects of several parameters including the type of distribution and volume fraction of CNTs, boundary condition, thickness-to-radius ratio and the thickness profile on the normalized natural frequencies of FG-CNTRC disks. From this analysis, some typical conclusions can be made:

- The normalized natural frequencies increase when the CNTs volume fraction or thickness--to-radius ratio rises.
- In solid FG-CNTRC disks, the FG_V type of CNTS distribution has higher normalized natural frequencies than the other types, and in the case of annular FG-CNTRC disks, the higher normalized frequencies occur in FG_X type of CNTs distribution.
- By using the variable thickness profile, the normalized natural frequencies can be controlled. Convexing the thickness profile generates larger normalized natural frequencies and concaving the thickness profile, generates smaller ones.

References

1. Alipour M.M., Shariyat M., Shaban M., 2010, A semi-analytical solution for free vibration of variable thickness two-directional-functionally graded plates on elastic foundations, *International Journal of Mechanics and Material in Design*, **6**, 293-304
2. Ashrafi H., Asemi K., Shariyat M., Salehi M., 2013, Two-dimensional modelling of heterogeneous structures using graded finite element and boundary element methods, *Meccanica*, **48**, 663-680

3. Dai H., 2006, Carbon nanotubes: opportunities and challenges, *Surface Science*, **500**, 218-241
4. Efraim E., Eisenberger M., 2007, Exact vibration analysis of variable thickness thick annular isotropic and FGM plates, *Journal of Sound and Vibration*, **299**, 720-738
5. Esawi A.M.K., Farag M.M., 2007, Carbon nanotube reinforced composites: potential and current challenges, *Materials and Design*, **28**, 2394-2401
6. Fiedler B., Gojny F.H., Wichmann M.H.G., Nolte M.C.M., Schulte K., 2006, Fundamental aspects of nano-reinforced composites, *Composites Science and Technology*, **66**, 3115-3125
7. Gupta U.S., Lal R., Sharma S., 2007, Vibration of non-homogeneous circular Mindlin plates with variable thickness, *Journal of Sound and Vibration*, **302**, 1-17
8. Han Y., Elliott J., 2007, Molecular dynamics simulations of the elastic properties of polymer/carbon nanotube composites, *Computational Materials Science*, **39**, 315-323
9. Hu N., Fukunaga H., Lu C., Kameyama M., Yan B., 2005, Prediction of elastic properties of carbon nanotube reinforced composites, *Proceeding of the Royal Society A*, **461**, 1685-1710
10. Kang I., Heung Y., Kim J., Lee J., Gollapudi R., et al., 2006, Introduction to carbon nanotube and nanofiber smart materials, *Composites Part B*, **37**, 382-394
11. Ke L.L., Yang J., Kitipornchai S., 2010, Nonlinear free vibration of functionally graded carbon nanotube-reinforced composite beams, *Composite Structures*, **92**, 676-683
12. Kim J.H., Paulino G.H., 2002, Isoparametric graded finite elements for nonhomogeneous isotropic and orthotropic materials, *Journal of Applied Mechanics*, **69**, 502-514
13. Koizumi M., 1993, The concept of FGM, *Ceramic Transactions, Functionally Gradient Materials*, **34**, 3-10
14. Lau K.T., Gu C., Hui D., 2006, A critical review on nanotube and nanotube/nanoclay related polymer composite materials, *Composites Part B*, **37**, 425-436
15. Odegard G.M., Gates T.S., Nicholson L.M., Wised K.E., 2002, Equivalent-continuum modeling of nano-structured materials, *Composites Science and Technology*, **62**, 1869-1880
16. Odegard G.M., Gates T.S., Wise K.E., Park C., Siochi E.J., 2003, Constitutive modeling of nanotube-reinforced polymer composites, *Composites Science and Technology*, **63**, 1671-1687
17. Shen H.S., 2009, Nonlinear bending of functionally graded carbon nanotube reinforced composite plates in thermal environments, *Composite Structures*, **91**, 9-19
18. Sobhani Aragh B., Yas M.H., 2010, Static and free vibration analyses of continuously graded fiber-reinforced cylindrical shells using generalized power-law distribution, *Acta Mechanica*, **215**, 155-173
19. Tajeddini V., Ohadi A., 2011, Three-dimensional vibration analysis of functionally graded thick, annular plates with variable thickness via polynomial-Ritz method, *Journal of Vibration and Control*, **18**, 1698-1707
20. Thostenson E.T., Ren Z.F., Chou T.W., 2001, Advances in the science and technology of carbon nanotubes and their composites: a review, *Composites Science and Technology*, **61**, 1899-1912
21. Yas M.H., Pourasghar A., Kamarian S., Heshmati M., 2013, Three-dimensional free vibration analysis of functionally graded nanocomposite cylindrical panels reinforced by carbon nanotube, *Materials and Design*, **49**, 583-590
22. Zafarmand H., Hassani B., 2014, Analysis of two-dimensional functionally graded rotating disks with variable thickness, *Acta Mechanica*, **225**, 453-464
23. Zafarmand H., Kadkhodayan M., 2015, Nonlinear analysis of functionally graded nanocomposite rotating thick disks with variable thickness reinforced with carbon nanotubes, *Aerospace Science and Technology*, **41**, 47-54

24. Zhu R., Pan E., Roy A.K., 2007, Molecular dynamics study of the stress-strain behavior of carbon-nanotube reinforced Epon 862 composites, *Material Science and Engineering: A*, **447**, 51-57

25. Zhu P., Lei Z.X., Liew K.M., 2012, Static and free vibration analyses of carbon nanotube reinforced composite plates using finite element method with first order shear deformation plate theory, *Composite Structures*, **94**, 1450-1460

26. Zienkiewicz O.C., Taylor R.L., 2005, *The Finite Element Method for Solid and Structural Mechanics*, Elsevier Butterworth-Heinemann, Oxford

Manuscript received November 1, 2013; accepted for print June 1, 2015

JOURNAL OF THEORETICAL
AND APPLIED MECHANICS
53, 4, pp. 1019-1028, Warsaw 2015
DOI: 10.15632/jtam-pl.53.4.1019

CRACKED BI-MATERIAL STRUCTURE SUBJECTED TO MONOTANICALLY INCREASING THERMAL LOADING. DETERMINATION OF THE INTERFACIAL SHEAR AND PEELING STRESSES

Gergana Nikolova, Jordanka Ivanova
Institute of Mechanics, Bulgarian Academy of Sciences, Sofia, Bulgaria
e-mail: gery@imbm.bas.bg; ivanova@imbm.bas.bg

A modified analytical shear lag model is used for the evaluation of the interfacial shear and peeling stresses in a cracked bi-material structure composed of two elastic plates bonded together by an interface zero thickness material and subjected to monotonically increasing thermal loading. The "peeling" stress can be determined by the aid of the interfacial shear stress and is proportional to deflections of the thinner plate of the structure. The interface is assumed to exhibit brittle failure when the shear stress reaches the critical value. The analytical solution and the length of the debonding and intact zones as well as the interfacial shear and peeling stresses for given material properties and thermal loading are discussed and illustrated in figures.

Keywords: cracked bi-material plates, monotonic thermal loading, interfacial shear and peeling stresses

1. Introduction

Interfacial stresses are the main driving factors for the initiation of delamination. To minimize such failure in multi-layered structures, it is important to develop a better understanding of the stress distribution in the interface. The shear lag approach is one of the most used analytical tools in mechanics of composite materials. The papers of Dowling and Burgan (1990), Nairn (1988a,b) as well as the basic paper of Cox (1952) trace the interest in shear lag of aircraft and ship design from the early days to the more recent attention devoted to it by structural engineers. The shear lag model has been adopted and successfully used by different authors. In the papers of Nikolova *et al.* (2006), Nikolova (2008), Nikolova and Ivanova (2013), the shear lag approach is applied to a bi-material layered structure with the pre-cracked first layer. Different loadings are considered: static, thermal and combined thermo-mechanical ones.

The shear lag approach is also intensively used in the interface fracture mechanics considering the cracking, decohesion and delamination of the thin film on a substrate. A very important basic case in the fracture mechanics of thin films is the problem of a crack in the film oriented perpendicular to the film/substrate interface with the crack tip touching the interface and of a crack of the same geometry, but with length less than the film thickness, so that the crack tip is within the film. This problem was investigated by Beuth (1992) and Beuth and Klingbeil (1996). The plastic yielding of the substrate and film is accompanied by vertical cracking in the films and the interface fracture as well as delamination from the ends of the vertical crack in the film and the crack extension in the substrate along the interface (Hutchinson and Suo, 1991).

Interfacial shear and peeling stresses of layered composite materials under thermal loading were analysed in numerous papers. In most of them, the analysis is based on linear fracture mechanics assumptions when both element cracking and interface debonding are treated as mixed mode crack propagation with critical conditions expressed in terms of stress intensity factors, cf. Zhang (2000), Bleeck *et al.* (1998), Sorensen *et al.* (1998).

The approximate analytical model for the assessment of interfacial stresses in a bi-material soldered assembly with a low-yield-stress of the bonding material was presented by Suhir (2006).

The aim of this paper is to investigate the interfacial shear and peeling stresses at the interface of a cracked bi-material structure subjected to monotonically increasing thermal loading. An approximate predictive model (Nikolova *et al.*, 2006; Nikolova, 2008; Nikolova and Ivanova, 2013) is developed for the evaluation of interfacial thermal stresses in a bi-material structure. This material is considered linearly elastic at the stress level below the critical point and ideally plastic at higher stresses.

The delamination process is analysed for a cracked bi-material structure with stress free boundary. The plates are assumed as linear elastic and isotropic with different stiffness and thermal expansion moduli. The analytic solutions for the shear and peeling stresses are obtained. The main objective of the paper is to discuss the effect of the interface parameters and interfacial stresses on the delamination process.

2. Assumptions and problem formulation

2.1. Assumption

The following major assumptions are made in our analysis:

- The approximate analytical model can be used to present the influence of the temperature on behavior of the peeling stress and length of the interface debonding zone in the pre--cracked two plates structure with an interface zero thickness adhesive layer and subjected to thermal loading.
- At least one of the structure components (the "plate A"/"plate B") is thick and stiff enough, so that this structural component and the construction as a whole do not experience bending deformations.
- The bonding material behaves linearly in the elastic stage. When the induced shearing stress exceeds the critical value, the interface debonding occurs.
- The interfacial stresses can be evaluated based on the concept of the interfacial compliance without considering the effect of "peeling". The "peeling" stress can be then determined from the evaluated interfacial shear stress. Due to this assumption, the "peeling" stress is proportional to the deflections of the thinner plate of the assembly, i.e., to its displacements with respect to the thicker plate.

2.2. Two-plate structure model and basic equations

Let us consider two elastic plates A and B (the plate A has a normal [transverse] crack to the interface). The plates have different material properties and thermal expansion coefficients α_A, α_B and they are bonded along the interface I and loaded by a monotonically increasing thermal loading ΔT (see Fig. 1).

The modified shear lag model is applied and the plate bending is neglected, according to the second assumption (see Section 2.1). The interface is supposed to be with negligible thickness and works only on shear (Nikolova *et al.*, 2006; Nikolova, 2008; Nikolova and Ivanova, 2013).

In view of symmetry, only the solution for the half plate is derived taking the origin of Cartesian coordinate at the centre of interface I. The plates length is denoted by $2L$ and thickness of plates A and B by $2h_A$, $2h_B$, and the Young moduli by E_A and E_B, respectively. The thickness of structures is denoted by $2h = 2h_A + 2h_B$ and is equal to the sum of the thickness of the plate A and B. The uniform temperature of the plates is denoted by ΔT.

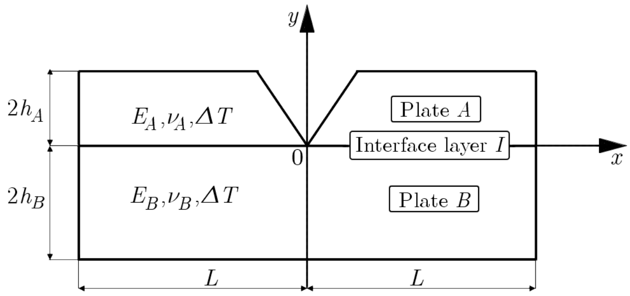

Fig. 1. Model of a Cracked two-plate structure

According to the shear lag hypothesis, the following ordinary differential equations of $1D$ plate equilibrium can be stated

$$\frac{d\sigma_A}{dx} = \frac{\tau^I}{2h_A} \qquad \frac{d\sigma_B}{dx} = -\frac{\tau^I}{2h_B} \tag{2.1}$$

where $\tau^I = \tau^I(x)$ is the interface shear stress.

The following constitutive equations for the plates and interface hold

$$\sigma_A = E_A(\varepsilon_A - \alpha_A \Delta T) \qquad \sigma_B = E_B(\varepsilon_B - \alpha_B \Delta T) \qquad \tau^I = G^I w_I \tag{2.2}$$

where

$$w_I = \frac{u_A - u_B}{h_A + h_B} = \frac{u_I}{h_A + h_B} \qquad \varepsilon_A = \frac{du_A}{dx} \qquad \varepsilon_B = \frac{du_B}{dx} \tag{2.3}$$

and $u_A = u_A(x)$, $u_B = u_B(x)$ and $u_I = u_I(x) = u_A(x) - u_B(x)$ are the displacement fields in the plate A, plate B and the interface. G^I is the representative shear modulus of the interface (adhesive).

Introduce now non-dimensional variables defined as follows

$$\begin{array}{lllll} \overline{x} = \dfrac{x}{h} & \overline{u}_i = \dfrac{u_i}{h} & \overline{\sigma}_i = \dfrac{\sigma_i}{E_B} & \overline{\tau}^I = \dfrac{\tau^I}{E_B} & \overline{G}^I = \dfrac{G^I}{E_B} \\ \overline{h}_A = \dfrac{h_A}{h_A} + h_B & \xi = \dfrac{h_A}{h_B} & \eta = \dfrac{E_A}{E_B} & i = A, B, I & h = h_A + h_B \end{array} \tag{2.4}$$

Then equilibrium equations (2.1) and constitutive equation (2.2) become

$$\frac{d\overline{\sigma}_A}{d\overline{x}} = \frac{\overline{\tau}^I(1+\xi)}{2\xi} \qquad \frac{d\overline{\sigma}_B}{d\overline{x}} = -\frac{\overline{\tau}^I(1+\xi)}{2} \tag{2.5}$$

where

$$\overline{\sigma}_A = \eta(\overline{\varepsilon}_A - \alpha_A \Delta T) \qquad \overline{\sigma}_B = (\overline{\varepsilon}_B - \alpha_B \Delta T)$$

In subsequent derivation, the formulas will be expressed in terms of non-dimensional variables, but the dashes over the parameters will be deleted, but remembered.

2.3. Debonding zone solution

Let us denote $u_I(x)$ as $u_I(x) = u_A(x) - u_B(x)$. Putting the constitutive equations (2.2) in (2.1), we obtain

$$\frac{d^2 u_I}{dx^2} = \lambda^2 u_I - \frac{d}{dx}[(\alpha_A - \alpha_B)\Delta T] \qquad \lambda^2 = \frac{G^I(1+\xi)(1+\xi\eta)}{2\xi\eta} \tag{2.6}$$

Assuming uniform temperature fields in the plates and constant thermal expansion coefficients, equation (2.6) becomes

$$\frac{d^2u_I}{dx^2} = \lambda^2 u_I \tag{2.7}$$

Then equilibrium equations (2.5) can be expressed as follows

$$\frac{d^2u_A}{dx^2} = \frac{\lambda^2}{1+\xi\eta}u_I \qquad\qquad \frac{d^2u_B}{dx^2} = -\frac{\lambda^2}{1+\xi\eta}\xi\eta u_I \tag{2.8}$$

Obviously, the substitution $u_I(x) = u_A(x) - u_B(x)$ has to be satisfied.

The general solution of equation (2.7) has the form

$$u_I = A_1\cosh(\lambda x) + A_2\sinh(\lambda x) \tag{2.9}$$

where are the integration constants which have to be determined.

Considering the two plate structure with a transverse crack in the first plate A, the following boundary and contact conditions are proposed

$$\begin{array}{ll} u_B(0) = 0 \quad \Rightarrow & u_I(0) = u_A(0) \\ \sigma_A(0) = 0 & \sigma_A(L) = \sigma_B(L) = 0 \end{array} \tag{2.10}$$

The strain-stress behavior and respective displacements can be obtained from equations (2.7) and (2.8), satisfying the above-mentioned contact and boundary conditions (2.10). The stress--strain and displacements field is presented in detail by Nikolova *et al.* (2006), Nikolova (2008), Nikolova and Ivanova (2013).

Now the equation for the interfacial shear stress has the following form

$$\tau^I(x) = G^I u_I(x) = \frac{G^I(1+\xi\eta)(\alpha_A-\alpha_B)\Delta T}{\lambda}\frac{\cosh[\lambda(L-x)]}{\sinh(\lambda L)} \tag{2.11}$$

2.4. Length of the debonding zone

The debond length l_d, which gives the magnitude of brittle cracking along the interface layer can be calculated from (2.11) assuming that at $\tau^I(x) = \tau^{cr}$, $u_I(l_d) = u^{cr} = \tau^{cr}/G^I$. Then

$$\tau^I(x) = G^I u_I(x) = \frac{G^I(1+\xi\eta)(\alpha_A-\alpha_B)\Delta T}{\lambda}\frac{\cosh[\lambda(L-x)]}{\sinh(\lambda L)} = \tau^{cr} \tag{2.12}$$

Using the substitution $\exp[\lambda(L-l_d)] = y$, we receive from (2.12) the following equation for

$$y^2 - 2Ay + 1 = 0 \qquad\qquad A = \frac{\lambda\tau^{cr}\sinh(\lambda L)}{G^I(1+\xi\eta)(\alpha_A-\alpha_B)\Delta T} \tag{2.13}$$

Then two roots of (2.13) are available

$$y_{1,2} = A \pm \sqrt{A^2-1} \tag{2.14}$$

Now using the substitution $\exp(\lambda l_d) = y$, we obtain

$$l_{d_{1,2}} = L - \frac{1}{\lambda}\ln(A \pm \sqrt{A^2-1}) \tag{2.15}$$

Obviously, $A^2 - 1 > 0$.

Then we have to choose the length of the debonding zone from the condition that this length has a maximum value, i.e.

$$l_d = L - \frac{1}{\lambda}\ln(A + \sqrt{A^2-1}) \tag{2.16}$$

3. Determination of the peeling stress

3.1. Basic equation of the dimensional peeling stress

The basic equation for the dimensional peeling stress $p(x)$, can be obtained using the following equation of equilibrium for the thinner plate A of the structure treated as an elongated thin plate (Suhir, 2006; Nikolova and Ivanova, 2013)

$$\int\limits_{-x_*}^{x}\int\limits_{-x_*}^{x} p(\varsigma)\,d\varsigma\,d\varsigma + D_1 w''(x) = \frac{h_A}{2}T(x) = \frac{h_A}{2}\Big[\int\limits_{-x_*}^{x} \tau^I(\varsigma)\,d\varsigma - E_B\tau^{cr}(L-l_d)\Big] \tag{3.1}$$

where

$$D_A = \frac{E_A h_A^3}{12(1-\nu_A^2)} \qquad \tau^I(x) = \frac{E_B G^I(1+\xi\eta)(\alpha_A-\alpha_B)\Delta T}{\lambda}\frac{\cosh[\lambda(L-x)]}{\sinh(\lambda L)} \tag{3.2}$$

$w(x)$ is the deflection function of the plate A (with respect to the thicker plate that does not experience bending deformations), D_A is the flexural rigidity of this plate and $\tau^I(x)$ is the dimensional interfacial shear stress, see equations (2.4) and (2.11)

$$T(x) = \int\limits_{-x_*}^{x} \tau(\varsigma)\,d\varsigma - E_B\tau^{cr}(L-l_d) \tag{3.3}$$

are the thermally induced forces acting in the cross-sections of the two-plate structure, τ^{cr} is the dimensional critical stress of the interface and $(L-l_d)$ is length of the intact zone, where L is half the structure length. The length l_d can be defined as $l_d = x_* = L - (1/\lambda)\ln[A+\sqrt{A^2-1}]$. The origin 0 of the coordinate x is in the mid-cross-section of the structure.

The peeling stress $p(x)$ can be evaluated as

$$p(x) = Kw(x) = E_I w(x) \tag{3.4}$$

where K is the spring constant of the elastic foundation, $w(x)$ is the deflection function and E^I is Young's modulus of the bonding material.

We obtain the following integral equation for the peeling stress function $p(x)$

$$\int\limits_{-x_*}^{x}\int\limits_{-x_*}^{x} p(\varsigma)\,d\varsigma\,d\varsigma + \frac{D_A}{K}p''(x) = \frac{h_A}{2}T(x) \tag{3.5}$$

After differentiating this equation twice with respect to the coordinate x and considering relationship (3.3), we obtain the following basic equation for the peeling stress function

$$p^{IV}(x) + 4\beta^4 p(x) = 2\beta^4 h_A E_B \tau'(x) \tag{3.6}$$

where $\beta = \sqrt[4]{K/4D_A}$ is the parameter of the peeling stress.

In the case, when plastic strains occur in the bonding material, the following conditions must be fulfilled at the boundary, $x = x_* = l_d$, between the intact and the debonding zones

$$\tau^I(x_*) = E_B\tau^{cr} \qquad T(x_*) = -E_B\tau^{cr}(L-l_d) \tag{3.7}$$

From (3.5) we find, by differentiation (for more details see Nikolova and Ivanova (2013))

$$\begin{aligned}&\int\limits_{-x_*}^{x} p(\varsigma)\,d\varsigma + \frac{D_A}{K}p'''(x) = \frac{h_A}{2}E_B\tau^I(x)\\ &\int\limits_{-x_*}^{x_*}\int\limits_{-x_*}^{x} p(\varsigma)\,d\varsigma\,d\varsigma = 0 \qquad \int\limits_{-x_*}^{x_*} p(\varsigma)\,d\varsigma = 0\end{aligned} \tag{3.8}$$

With consideration of conditions $(3.8)_2$, relationships (3.5) and $(3.8)_1$ result in the following boundary conditions for the peeling stress function $p(x)$

$$
\begin{aligned}
p''(x_*) &= -\frac{h_A K l_e \tau^{cr}}{4D_A} = -2\beta^4 h_A (L - l_d) E_B \tau^{cr} \\
p'''(x_*) &= \frac{h_A K \tau^{cr}}{2D_A} = 2\beta^4 h_A E_B \tau^{cr}
\end{aligned}
\tag{3.9}
$$

The peeling stress in the debonding zone should be zero as it follows from equation (3.6). The dimensional shear stress is equal to the dimensional critical stress between the intact and the debonding zones.

3.2. Solution to the peeling stress equation

Equation (3.6) has form of an equation of a beam lying on a continuous elastic foundation. We seek a solution to this equation in form

$$
p(x) = C_0 V_0(\beta x) + C_1 V_1(\beta x) + C_2 V_2(\beta x) + C_3 V_3(\beta x) + B \frac{\sinh[\lambda(L - x_*)]}{\sinh(\lambda x)}
\tag{3.10}
$$

These functions $p(x)$ are odd functions, i.e. $p(-x) = -p(x)$. They have their maximum value (zero derivative) at the origin, and are symmetric with respect to the mid-cross-section of the assembly.

The final form of the solution to equation (3.6) is the following

$$
p(x) = C_0 V_0(\beta x) + C_2 V_2(\beta x) + B \frac{\sinh[\lambda(L - x_*)]}{\sinh(\lambda x)}
\tag{3.11}
$$

where the functions $V_i(\beta x)$, $i = 0, 2$ are expressed as follows

$$
V_0(\beta x) = \cosh(\beta x)\cos(\beta x) \qquad V_2(\beta x) = \sinh(\beta x)\sin(\beta x)
\tag{3.12}
$$

The first two terms in (3.11) provide the general solution to the homogeneous equation, which corresponds to non-homogeneous equation (3.6), and the third term is the particular solution to this equation. Introducing this term into equation (3.6), we obtain

$$
(3.13) B = \frac{2G^I E_B h_A \beta^4 (\alpha_A - \alpha_B) \varDelta T (1 + \xi\eta)}{4\beta^4 + \lambda^4}
\tag{3.13}
$$

Using boundary conditions (3.9), we obtain the following algebraic equations for the constants C_0 and C_2 of integration

$$
\begin{aligned}
&-2\beta^3[\sin(\beta x_*)\cosh(\beta x_*) + \sinh(\beta x_*)\cos(\beta x_*)]C_0 \\
&\qquad - 2\beta^3[\sin(\beta x_*)\cosh(\beta x_*) + \sinh(\beta x_*)\cos(\beta x_*)]C_2 = 2\beta^4 h_A E_B \tau^{cr} \\
&-\beta[\sin(\beta x_*)\cosh(\beta x_*) - \sinh(\beta x_*)\cos(\beta x_*)]C_0 \\
&\qquad + \beta[\sin(\beta x_*)\cosh(\beta x_*) + \sinh(\beta x_*)\cos(\beta x_*)]C_2 = -2\beta^4 h_A (L - l_d) E_B \tau^{cr}
\end{aligned}
\tag{3.14}
$$

Algebraic equations (3.14) have the following solutions

$$
\begin{aligned}
C_0 &= \frac{\beta h_A E_B [\sin(\beta x_*)\cosh(\beta x_*)(1 - 2\beta^2 L + 2\beta^2 l_d) + \sinh(\beta x_*)\cos(\beta x_*)(1 + 2\beta^2 L - 2\beta^2 l_d)]\tau^{cr}}{\cos(2\beta x_*) - \cosh(2\beta x_*)} \\
C_2 &= \frac{\beta h_A E_B [\sin(\beta x_*)\cos(\beta x_*)(1 + 2\beta^2 L - 2\beta^2 l_d) - \sinh(\beta x_*)\cos(\beta x_*)(1 - 2\beta^2 L + 2\beta^2 l_d)]\tau^{cr}}{\cos(2\beta x_*) - \cosh(2\beta x_*)}
\end{aligned}
\tag{3.15}
$$

Note that for long enough elastic zones, solution (3.11) can be simplified as follows

$$\begin{aligned} p(x) =& \frac{\beta h_A E_B[\sin(\beta x_*)\cosh(\beta x_*)(1-2\beta^2 L+2\beta^2 l_d)]\tau^{cr}}{\cos(2\beta x_*)-\cosh(2\beta x_*)}\cosh(\beta x)\cos(\beta x) \\ &+ \frac{\beta h_A E_B[\sinh(\beta x_*)\cos(\beta x_*)(1+2\beta^2 L-2\beta^2 l_d)]\tau^{cr}}{\cos(2\beta x_*)-\cosh(2\beta x_*)}\cosh(\beta x)\cos(\beta x) \\ &+ \frac{\beta h_A E_B[\sin(\beta x_*)\cos(\beta x_*)(1+2\beta^2 L-2\beta^2 l_d)]\tau^{cr}}{\cos(2\beta x_*)-\cosh(2\beta x_*)}\sinh(\beta x)\sin(\beta x) \\ &- \frac{\beta h_A E_B[\sinh(\beta x_*)\cos(\beta x_*)(1-2\beta^2 L+2\beta^2 l_d)]\tau^{cr}}{\cos(2\beta x_*)-\cosh(2\beta x_*)}\sinh(\beta x)\sin(\beta x) \\ &+ \frac{2G^I E_B h_A \beta^4(\alpha_A-\alpha_B)\varDelta T(1+\xi\eta)}{4\beta^4+\lambda^4}\frac{\sinh[\lambda(L-x_*)]}{\sinh(\lambda x)} \end{aligned} \tag{3.16}$$

4. Numerical example

Let us consider two elastic plates A (made from ZrO_2) and B (made from Ti_6Al_4V) bonded by the interface with finite lengths $2L = 120\,\mathrm{mm}$ and variable thickness of the first plate h_A $2h_A = [1.6\,\mathrm{mm}, 2\,\mathrm{mm}]$, $2h_B = 2\,\mathrm{mm}$, $h = h_A + h_B = [1.8\,\mathrm{mm}, 2\,\mathrm{mm}]$, $\xi = h_A/h_B = [0.8, 1]$ under monotonic temperature loading $\varDelta T$. The following material characteristics are taken:

- ZrO_2 – Young's modulus $E_A = 132.2\,\mathrm{GPa}$, coefficient of thermal expansion $\alpha_A = 13.3\cdot 10^{-6}\,\mathrm{K}^{-1}$,
- Ti_6Al_4V – Young's modulus $E_B = 122.7\,\mathrm{GPa}$, coefficient of thermal expansion $\alpha_B = 10.291\cdot 10^{-6}\,\mathrm{K}^{-1}$,
- interface layer – Young's modulus $E^I = 2.1\,\mathrm{GPa}$, shear modulus $G^I = 800\,\mathrm{MPa}$ and the critical shear stress $\tau^I = \tau^{cr} = 18\,\mathrm{MPa}$.

In Table 1, the variable parameters of the problem considered are presented.

Table 1. Variable parameter

Name	Variable
Thickness of the first plate A	h_A
Geometric parameter of the structure	$\xi = h_A/h_B$
Non-dimensional parameter	$\lambda = \sqrt{G^I(1+\xi)(1+\xi\eta)/2\xi\eta}$
Flexural rigidity of the plate A	$D_A = E_A h_A^3/[12(1-\nu_A^2)]$
Parameter of the peeling stress	$\beta = \sqrt[4]{K/4D_A}$
Temperature monotonic loading	$\varDelta T$

The behavior of the dimensional interfacial shear and the peeling stresses on x/h, the dimensional peeling stress $p(x)$ for three different temperature of the monotonic loading $\varDelta T$ and as well as the behavior of the respective peeling stresses $p(x)$ for three different values of the parameter $\xi = h_A/h_B$ are illustrated at the given bellow figures (Figs. 2, 3, and 4).

The analytically calculated shear and peeling stresses are plotted in Fig. 2 for a temperature $\varDelta T = 350\,\mathrm{K}$. As shown in this figure, the interfacial shear stress is equal to the critical shear stress at the point between the intact and debonding zones. Thereafter, the shear stress decreases sharply from its maximum value at the interface end (the dependence of the interfacial shear stress for different temperatures is presented in detail in Nikolova *et al.* (2006), Nikolova (2008)).

Contrary to the shear stress, the interfacial peeling stress attains a maximum value at the end of the interface. From the beginning of the intact zone, the peeling stress has a negative value and then increases to its maximum value (less than the critical shear stress value).

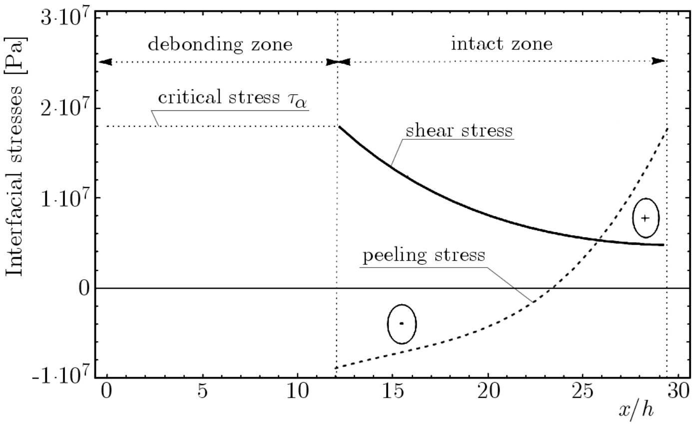

Fig. 2. Calculated interfacial stresses

Figure 3 shows the behavior of the peeling stresses $p(x)$ for $\xi = h_A/h_B = 1$ and three different values of temperature loading ΔT. The peeling stress again attains a maximum value at the end of the interface layer and is negative in the middle of the intact zone.

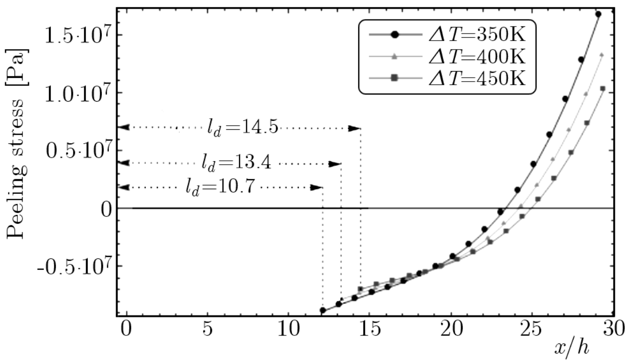

Fig. 3. Dependence of $p(x)$ on x/h for different temperature loadings ΔT

The maximum peeling stress decreases with a rise of the temperature loading ΔT.

For a given value $h_B = 0.001\,\mathrm{m}$, three different thicknesses h_A and $\Delta T = 350\,\mathrm{K}$, the interfacial peeling stresses are plotted as a function of the axial distance in Fig. 4.

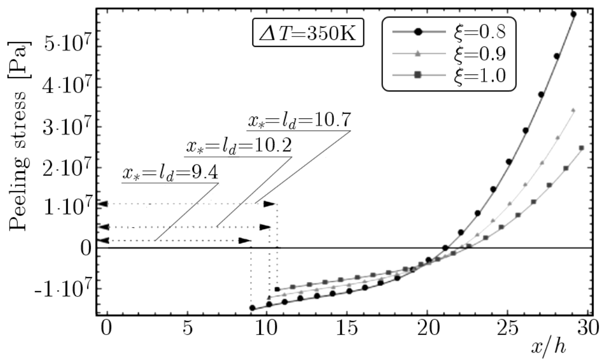

Fig. 4. Dependence of the peeling stresses $p(x)$ on x/h for three different values of the parameter ξ

The thickness of material A is varied in a range $h_A = 0.0008\,\mathrm{m}$-$0.001\,\mathrm{m}$. The peeling stress $p(x)$ decreases with a increase in the parameter ξ and attains its maximum value at the interface end, strongly depending on the thickness of plate (material) A. The maximum peeling stress increases with a decrease in the plate A thickness h_A, while the area for the peeling stress region decreases with the increasing of the thickness h_A.

The dependence of the interfacial peeling stress is sensitive to material properties and geometry of the bi-material structure.

When the thickness of the first plate is very small, the peeling stress increases extremely rapidly and exceeds the critical shear stress value, then in the structure the full debonding of the interface can be observed.

5. Conclusions

The shear lag method, classical plate theory formulation and elastic foundation theory have been used to investigate the interfacial shear and peeling stresses in a pre-cracked bi-material structure subjected to monotonic thermal loading.

The following results can be summarized:

(1) The lengths of the debonding and intact zones are calculated by means of the shear lag analysis associated with constitutive equations.

(2) The peeling stress is sensitive to material properties, geometry of the pre-cracked bi-material structure and the applied thermal loading. Therefore, the thermally induced interfacial peeling stresses in different ceramic-metal composites are preferable to be with low maximum values.

(3) Interfacial shear and peeling stresses due to thermal and elastic mismatch in layered structures are one of the major reasons of mechanical and thermal failure and delamination in multilayered structures.

(4) The obtained from the present analysis results can be used for the assessment of thermally induced stresses in different pre-cracked ceramic-metal composites during production of new ideally designed ceramic-metal composites with optimal properties of combining high temperature resistance and hardness (ceramic), and the ability to undergo plastic deformation (metal).

Acknowledgement

The study has been financially supported by the National Fund "Scientific Research" of Bulgaria, Project DFNI E02/10 121214.

References

1. Beuth J.L., 1992, Cracking of thin films in thin bonded films in residual tension, *International Journal of Solids and Structures*, **29**, 13, 1567-1675
2. Beuth J.L., Klingbeil N.W., 1996, Cracking of thin films bonded to elastic-plastic substrates, *Journal of the Mechanics and Physics of Solids*, **44**, 9, 1411-1428
3. Bleeck O., Munz D., Schaller W., Yang Y.Y., 1998, Effect of a graded interlayer on the stress intensity factor of cracks in a joint under thermal loading, *Engineering Fracture Mechanics*, **60**, 615-623
4. Cox L.H., 1952, The elasticity and strength of paper and other fibrous materials, *British Journal of Applied Physics*, **3**, 72-79
5. Dowling P.J., Burgan B.A., 1990, Shear lag in steel and composite structures, [In:] *Composite Steel Structures. Advances, Design and Construction*, edited by R. Narayanan, Spon Press, London, 1-23
6. Hutchinson J.W., Suo Z., 1991, Mixed mode cracking in layered materials, *Advances in Applied Mechanics*, **29**, 63-191

7. Nairn J.A., 1988a, Fracture mechanics of unidirectional composites using the shear-lag model I: theory, *Journal of Composite Materials*, **22**, 6, 561-588

8. Nairn J.A., 1988b, Fracture mechanics of unidirectional composites using the shear-lag model II: experiment, *Journal of Composite Materials*, **22**, 6, 589-600

9. Nikolova G., 2008, Thermo-mechanical behaviour of thin multilayered structures, Ph.D. Thesis, Institute of Mechanics – BAS, Sofia, Bulgaria

10. Nikolova G., Ivanova J., 2013, Interfacial shear and peeling stresses in a two-plate structure subjected to monotonically increasing thermal loading, *Journal of Theoretical and Applied Mechanics*, **51**, 4, 937-947

11. Nikolova G., Ivanova J., Mroz Z., 2006, Modelling of thermally induced progressive delamination in a two-plate structure, *Journal of Theoretical and Applied Mechanics*, Bulgaria, **36**, 4, 71-92

12. Sorensen B.F., Jorgensen S.O., Horsewell A., 1998, Thermally induced delamination of multilayer, *Acta Matterial*, **46**, 2603-2615

13. Suhir E., 2006, Interfacial thermal stresses in a bi-material assembly with a low-yield-stress bonding layer, *Journal of Physics D: Modeling and Simulation in Materials Science and Engineering*, **14**, 1421-1432

14. Zhang S., 2000, Thermal stress intensities at an interface crack between two elastic layers, *International Journal of Fracture*, **106**, 277-29

Manuscript received June 3, 2014; accepted for print June 25, 2015

JOURNAL OF THEORETICAL AND APPLIED MECHANICS
53, 4, pp. 1029-1039, Warsaw 2015
DOI: 10.15632/jtam-pl.53.4.1029

APPLICATION OF ANTHROPODYNAMIC DUMMIES FOR EVALUATING THE IMPACT OF VEHICLE SEAT VIBRATIONS UPON HUMAN BODY

Tomasz Lech Stańczyk, Andrzej Zuska
Kielce University of Technology, Department of Automotive Vehicles and Transportation, Kielce, Poland
e-mail: a.zuska@tu.kielce.pl

The paper presents the anthropodynamic dummy constructed at the Department of Automotive Vehicles and Transportation of the Kielce University of Technology, Kielce, Poland. The dummy is shown at the concept and design stages, and as a final construction. The first part of the study presents structural and dynamic requirements, and also the structure and construction selected for the dummy. The vertical dynamics of the body of a seated human is accounted for by conducting detailed analysis of the variation range of mass parameters and of the dummy elastic and damping parameters. The second part of the study presents the results of experimental simulations performed for the dummy.

Keywords: anthropodynamic dummy, vibratory comfort

1. Introduction

Initially, the measurements of transfer of vibrations by vehicle seats required participation of human subjects exposed to vibrations. The research results obtained in this way were far from satisfactory due to a significant variety of people's individual body features. Moreover, such measurements require input functions that must be safe for humans. Therefore, for ethical and safety reasons, it is advisable to conduct evaluation of vehicle seats without people being subject to vibrations. On the other hand, using stiff mass or a sand bag instead of a living person fails to ensure results that are satisfactorily consistent with real conditions (Griffin, 1990; Łomako *et al.*, 1998; Mansfield and Griffin, 1996). Much better results can be obtained when the human subject is replaced with a dummy imitating dynamic reactions of a seated person. An example of such dummies is the Memosik. Information about impedance, measured under buttocks of a seated person as well as about the head-seat acceleration transmittance are useful in building the dummies. Memosik I was intended for tests at the 1-50 Hz frequency range. An adequately formed base and low centre of gravity ensure dummy stability during tests (Knoblauch *et al.*, 1995). Memosik 1 dummy was the basis for Memosik II model which is intended for tests at the 0.5-30 Hz frequency range, which is typical for analyzing vibrational comfort in passenger vehicles (Knoblauch, 1992). Memosik III model was based on Memosik II, in which the degrees of freedom were reduced from five to three (Cullmann and Wölfel, 1998). Two subsequent dummy models: Memosik IV (Wölfel, 2006) and Memosik V (Mozaffarin *et al.*, 2008) are active dummies, made on the basis of a passive dummy. Memosik IV enables conduction of tests in vertical direction, whereas Memosik V additionally enables tests in longitudinal and lateral directions.

Using dummies is justified by the requirement of comparability and objectivity of the results. In the course of comparative studies of several constructional solutions of seats, after some time, people change their position to a more comfortable one, stiffen their bodies due to weariness, etc. It distorts the research results. Dummies, on the other hand, manifest no such behaviour.

2. Construction of anthropodynamic dummy

The construction of an anthropodynamic dummy presented in Fig. 1 is based upon the model with four degrees of freedom, which imitates propagation of vertical vibrations to selected body parts of a sitting person (Fig. 2).

Fig. 1. Anthropodynamic dummy on a passenger seat

By means of four masses, the anthropodynamic model imitates four selected parts of the human body:

- mass m_1 imitates mass of the head,
- mass m_2 imitates mass of the pectoral girdle, chest and its internal organs and arms,
- mass m_3 imitates mass of the internal organs, abdominal cavity, diaphragm and abdominal walls,
- mass m_4 imitates mass of the spine, pelvis, thighs, forearms and hands.

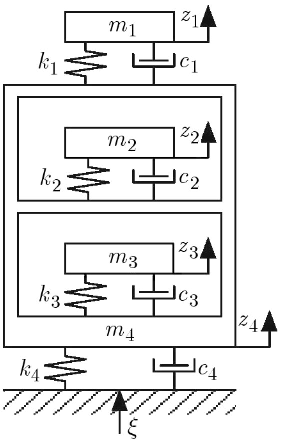

Fig. 2. Anthropodynamic model of a sitting human

The base of the dummy (imitating buttocks) and the support (imitating human back) connected with the basis with a hinged grip is made of epoxy resin. The weight of those elements accounts for 6 percent of the total dummy weight and it has not been taken into consideration in the studies.

The dummy frame consists of guides, fixed and moving discs, clamps and line bearings. The frame is fixed to the base, in which six evenly spaced sockets have been made. Mounted in the sockets are rubber springy-damping elements (Fig. 3), and the entire construction rests upon the dummy base.

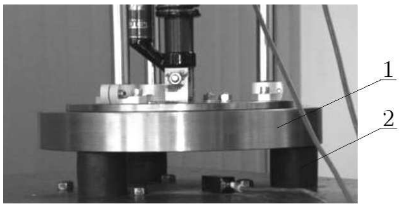

Fig. 3. The base of the dummy frame with rubber spring-damping elements mounted in six sockets: 1 – frame basis, 2 – rubber element

The guides are made of metal rollers. The accurate position of guides is ensured by fixed metal discs connected with the guides by aluminium clamps. Three moving discs slide on the guides, imitating respectively mass of the first (head), second (chest) and the third (abdomen) part of the human body (Fig. 4). Mounting the suitable set of weights to vibrating elements enables one to imitate individual anthropometric features of different body types.

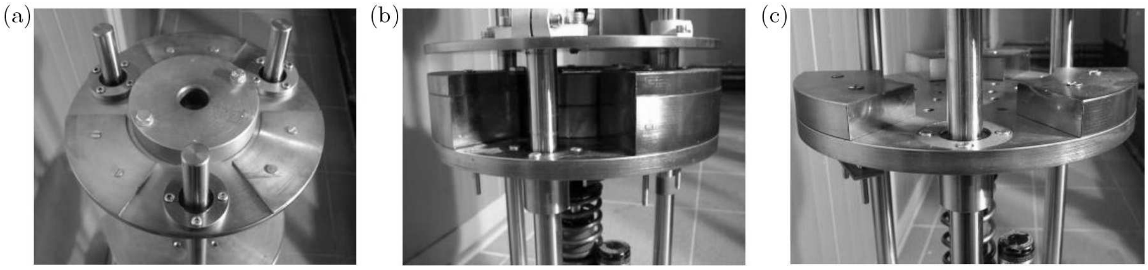

Fig. 4. Moving discs imitating the respective body parts with a sample sets of weights: a – disc 1, b – disc 2, c – disc 3

The moving discs have holes where longitudinal bearings are mounted. The bearings ensure minimal resistance to motion for the discs moving on the guides.

Each moving disc is connected to the dummy frame by means of a spring-damper system consisting of a damper and a spring (Fig. 5).

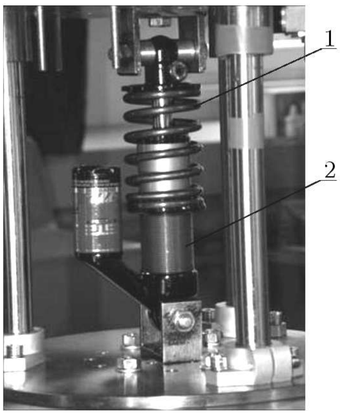

Fig. 5. Spring-damper system: 1 – spring, 2 – damper

Properly selected sets of weights, dampers, springs and rubber elements enable the dummy to imitate the vertical dynamics of various types of the human body.

2.1. Selection of spring-damping elements of the anthropodynamic dummy and identification of their parameters

One of the fundamental requirements to be met by the anthropodynamic dummy is the accurate imitation of the vertical dynamics of a seated human body. For that purpose, a number of tests has been carried out on a stand constructed on the basis of MTS components (Zuska, 2007). The objective of the tests was to determine the transmittance of acceleration for three configurations (output-input): head-seat, chest-seat and abdomen-seat in the selected group of people, Fig. 6 (Zuska, 2007).

Upon the transmittance courses for medians and quantiles 0.1 and 0.9 of the modules designated in laboratory tests, the stiffness (k_1, k_2, k_3, k_4), damping (c_1, c_2, c_3, c_4) and mass parameters of the model presented in Fig. 2 are identified.

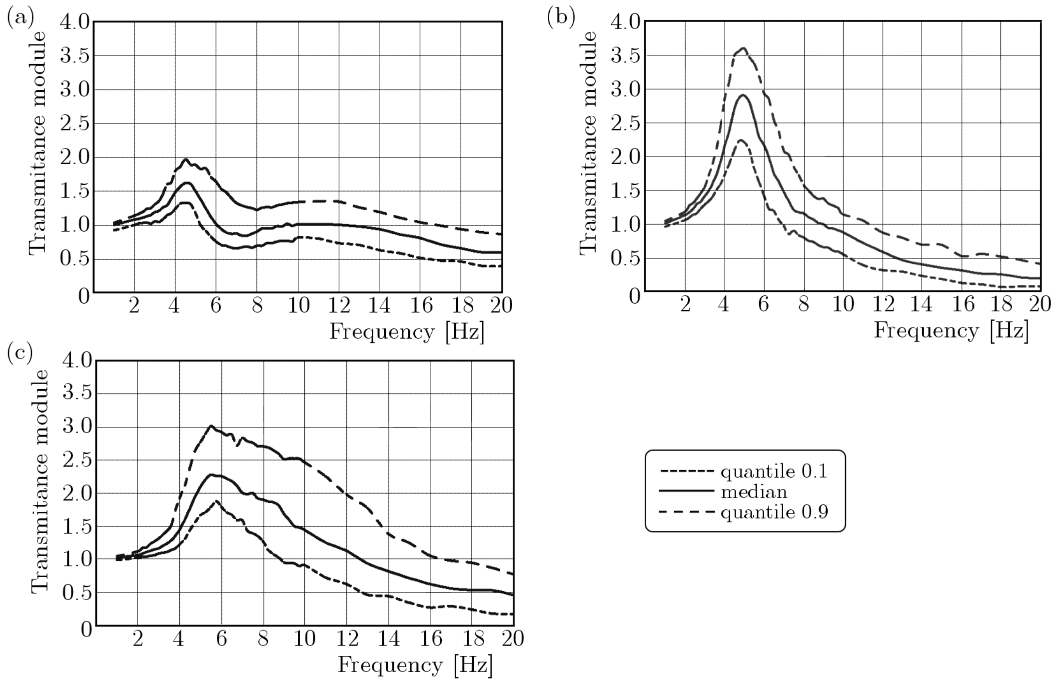

Fig. 6. Courses of transmittance modules: (a) head – seat, (b) chest – seat, (c) abdomen – seat

Before the selection of the supple elements, a number of constructional requirements to be met was adopted. The requirements have been established upon the assumed dimensions of the dummy and the identified parameters of stiffness and damping elements of the mathematic model (Table 1). For the obtained stiffness and damping coefficients, a 15% toleration has been permitted.

Table 1. Parameters of the anthropodynamic model

Parameter		Quantile 0.1	Median	Quantile 0.9
Mass [kg]	m_1	4.83	5.77	7.43
	m_2	13.75	16.43	21.17
	m_3	6.75	8.06	10.38
	m_4	33.05	39.40	50.90
Stiffness coefficient [N/m]	k_1	3898	5098	7169
	k_2	14856	18124	24181
	k_3	11350	14761	20644
	k_4	508863	398800	279187
Damping coefficient [N·s/m]	c_1	200	212	302
	c_2	254	257	349
	c_3	197	209	245
	c_4	13385	1113	17

The tests aimed at determining:

- stiffness coefficient of the springs,
- damping coefficient of the dampers,
- stiffness and damping coefficients of the rubber elements,

and have been carried out on the testing stand adopted for such tests (construction based on a hydraulic actuator manufactured by MTS). They which enabled imitation of the working parameters of dampers, springs and rubber elements (Table 2) as well as recording of the following signals:

- displacement of the plate with the fixed rubber element or spring and displacement of the holder with the fixed cylinder of the damper,
- compressive force affecting the rubber element or spring and damping force of the shock absorber.

Table 2. Working parameters of spring-damping systems

Parameter	System			
	No. 1	No. 2	No. 3	No. 4
Frequency [Hz]	1-20	1-20	1-20	1-20
Amplitude [mm]	0.00-2.73	0.00-4.49	0.00-2.15	0.05-0.62
Pre-load load [kg]	5.77	16.43	8.06	69.66

2.1.1. Selection of coil springs and identification of their stiffness coefficient

Taking into consideration the constructional assumptions and stiffness coefficients (k_1, k_2, k_3) identified for the mathematical model, a pre-selection of springs has been made.

For every pre-selected spring, a test has been carried out to identify their actual stiffness coefficient (Table 3).

Table 3. Parameters of the 50-centile dummy springs

Designation	Stiffness coefficient [N/m]			Deviation from the assumed value [%]
	Assumed value	Catalogue value	Test-determined value	
k_{1m50}	5098	5300	5495	7.8
k_{2m50}	18124	17781	20249	11.7
k_{3m50}	14761	15556	17230	16.7

The obtained values of stiffness coefficients k_{1m50} and k_{2m50} differ from the assumed values by less than 15 percent and fall within the assumed range of toleration, whereas the value of the k_{3m50} stiffness coefficient differs from the assumed one by 16.7 percent and does not meet the 15-percent toleration range. However, a decision has been made to keep the spring and not to reject it until the entire dummy has been examined.

2.1.2. Selection of dampers and identification of their damping coefficient

Taking into consideration the constructional requirements:

- damper maximum length 250 mm,
- minimum stroke of the piston rod 10 mm,

as well as damping coefficients (c_1, c_2, c_3) identified for the mathematical model, a pre-selection of dampers has been made.

The actual characteristics of the selected dampers differed from the required ones. Therefore, constructional changes have been made, which included:

- using oil of various density and viscosity,
- replacing the valves installed in the piston by suitable discs with openings (ducts, bypasses).

After each constructional change in the dampers, a test has been performed to determine the work diagram, which served as a basis for identifying the damping coefficient of the tested dampers (Fig. 7).

The obtained values of the damping coefficient (Table 4) differ from the assumed values by less than 15 percent.

Table 4. Parameters of dampers of the 50-centile dummy

Damping coefficient [N·s/m]			Deviation from the assumed value [%]
Designation	Assumed value	Determined value	
c_{1m50}	212	222.65	5.0
c_{2m50}	257	264.36	2.9
c_{3m50}	209	191.54	8.4

2.1.3. Selection of rubber elements and identification of their damping (c_4) and stiffness (k_4) coefficients

The rubber element in the mathematical model is presented as a Kelvin-Voigt spring-damping element.

Taking into consideration the constructional requirements:

- rubber elements have cylindrical shape of a 50 mm diameter,
- height of the rubber elements falls within the 20-100 mm range,
- quantity of the rubber elements to ensure the dummy stability is either three, four or six items,

as well as the damping (c_4) and stiffness (k_4) coefficients identified for the mathematical models, a pre-selection of the rubber elements has been made (Table 5) followed by identification of actual values of those coefficients.

Table 5. Initial parameters of the selected rubber elements

Hardness [°Sh]	Diameter [mm]	Height [mm]	Shape
40, 50, 60, 70, 80, 90	50	20, 40, 60	cylinder

For every pre-selected rubber element, a test has been carried out to determine its static characteristics (Fig. 8) upon which the stiffness and damping coefficients for the tested elements have been identified.

An assumption has been made that the characteristics of the rubber element $f(\lambda, \dot{\lambda})$ may be presented in an additive form

$$f(\lambda, \dot{\lambda}) = f_s(\lambda) + f_t(\dot{\lambda})$$

where $f_s(\lambda)$ is the stiffness component of the characteristics, $f_t(\dot{\lambda})$ – the damping component of the characteristics.

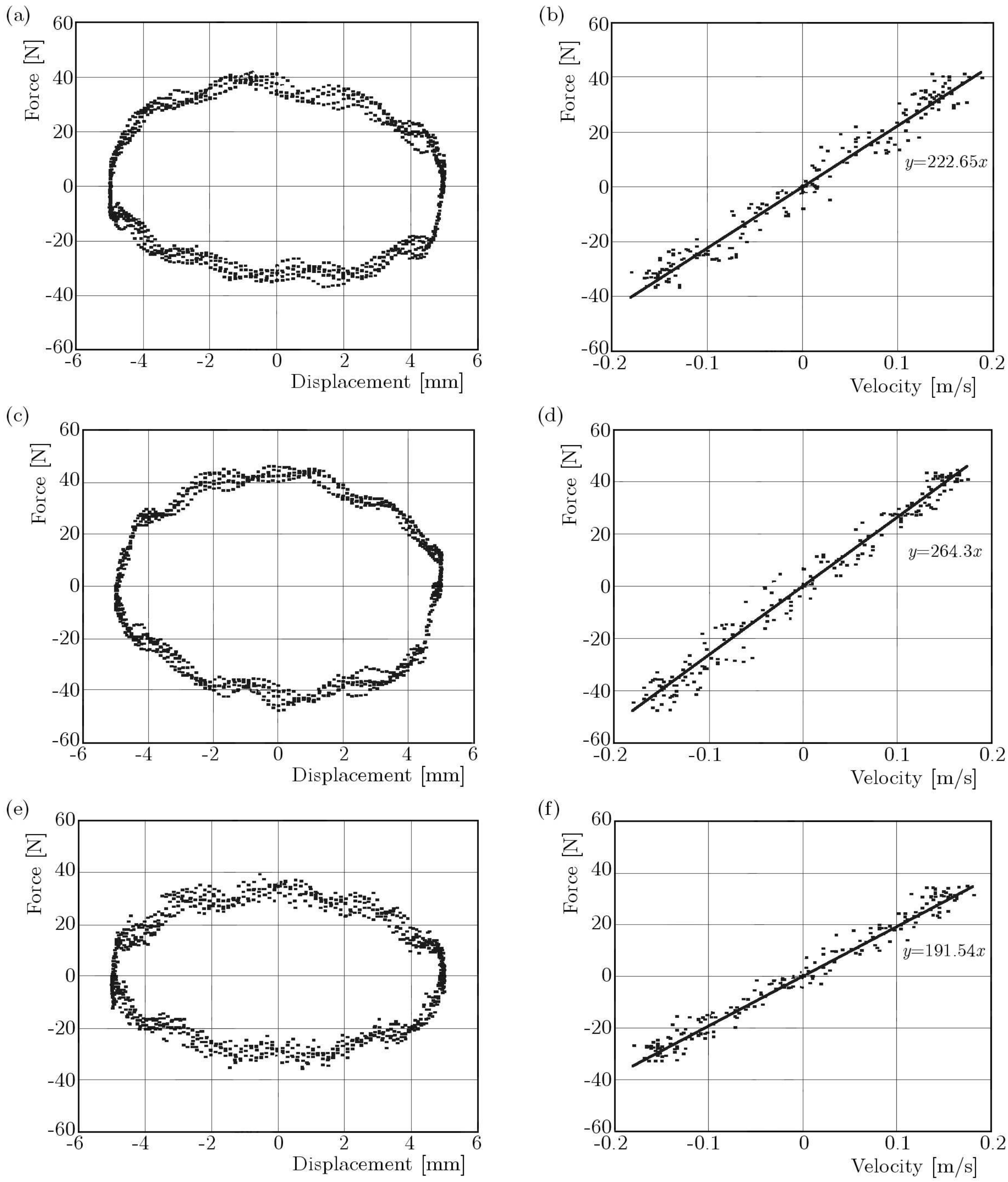

Fig. 7. Work diagrams and the actual characteristics of dampers utilised in the 50-centile anthropodynamic dummy: (a) work diagram of disc 1 support, (b) damping characteristics of disc 1 support, (c) work diagram of disc 2 support, (d) damping characteristics of disc 2 support, (e) work diagram of disc 3 support, (f) damping characteristics of disc 3 support

Given a relatively small nonlinearity of the frame axis within the range of actual work parameters (pre-load load – 23 kg, deflection amplitude – 0.62 mm) it has been assumed that it has a linear shape (Fig. 8b, Fig. 9). The slope of the linear regression line of the frame axis is the required stiffness coefficient of the rubber element (Fig. 11).

Since the velocity of the damper piston rod is known for every point in the diagram (Fig. 10a), it is possible to determine the damping characteristics $f_t(\dot{\lambda})$ (Fig. 10b).

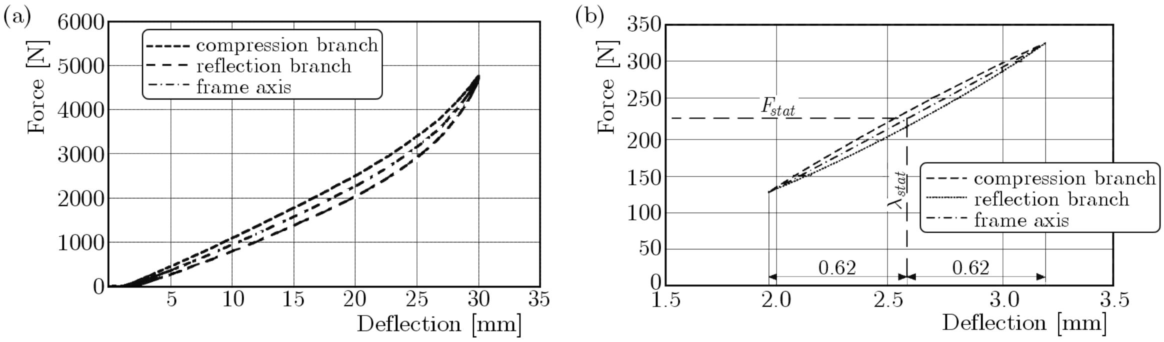

Fig. 8. Characteristics of selected rubber elements: (a) for wide range of loads, (b) made for actual work parameters (actual load range)

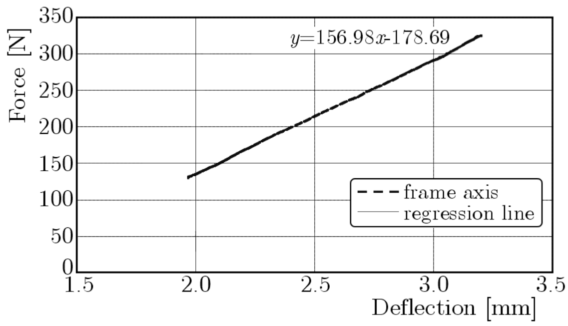

Fig. 9. Stiffness characteristics of the rubber element

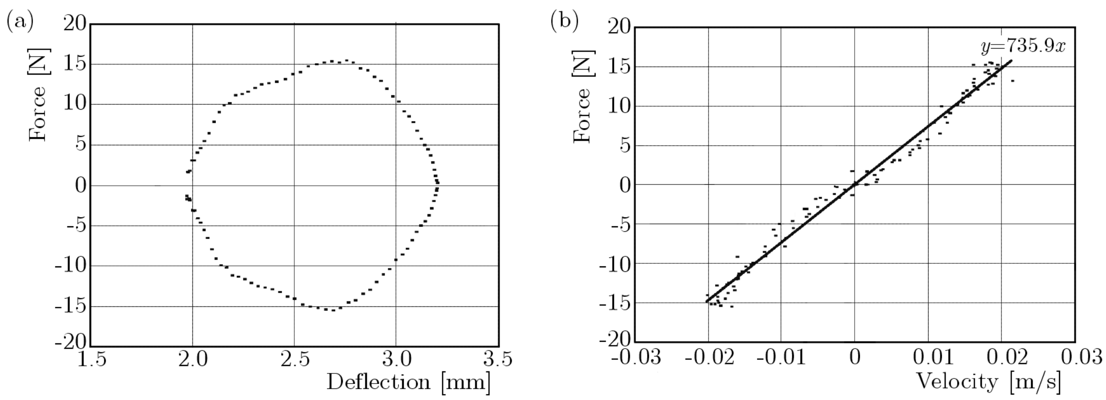

Fig. 10. Characteristics of the rubber element without stiffness component and the damping characteristics based upon it: (a) work diagram of the rubber element, (b) damping characteristics

The slope of the linear regression line of the damping characteristics is the required damping coefficient of a single rubber element (Table 6).

The obtained value of the stiffness coefficient differs from the assumed value by 18 percent and meets the 20 percent tolerance range, whereas the value of the damping coefficient differs from the assumed value by 98% and fails to meet the 20 percent tolerance range. It has been decided to keep the rubber elements and not to reject it until the entire dummy has been examined.

Table 6. Parameters of the selected rubber elements

Coefficient	Designation	Assumed value	Determined value	Deviation from the assumed value [%]
Damping [N·s/m]	c_{4m50}	1113	2207.94	98
Stiffness [N/m]	k_{4m50}	398800	470940	18

3. Anthropodynamic dummy – the results of verification tests

The value measured in the tests has been the acceleration of three moving discs of the dummy (disc 1, disc 2 and disc 3) and the acceleration of the surface of the plate on which the dummy is placed.

The recorded acceleration signals have been used for determining the transmittance of three input-output systems: plate – disc 1, plate – disc 2, plate – disc 3.

The list of the test results conducted for the dummy and the median transmittance courses, determined for 80 tested people, are presented in the Fig. 11.

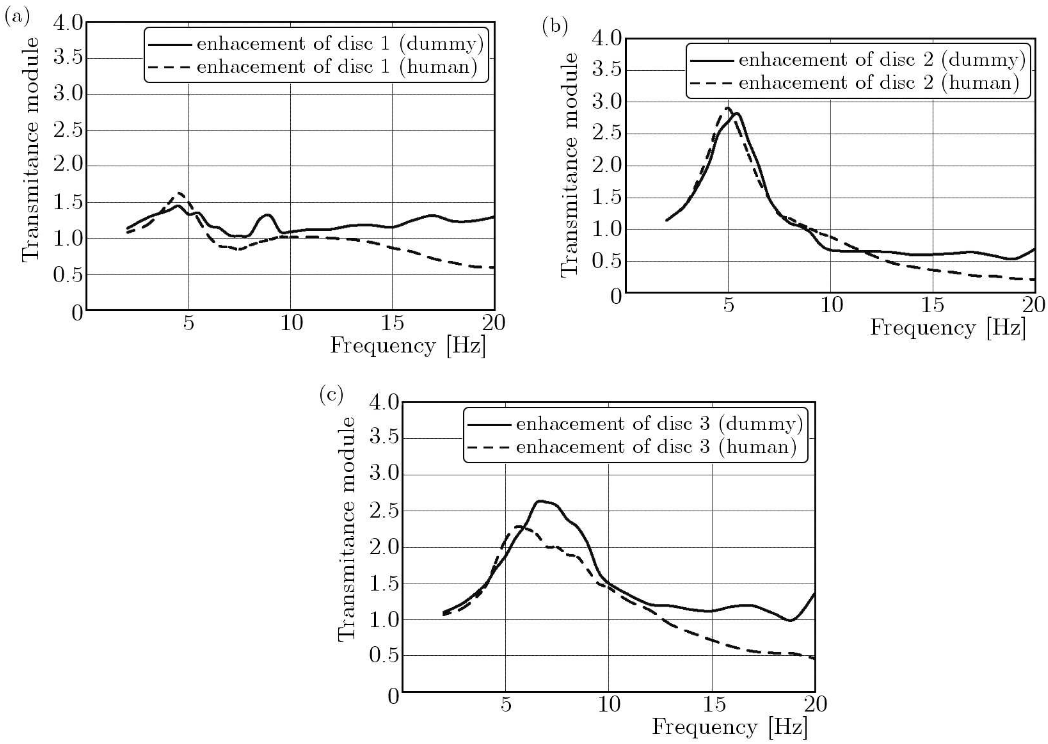

Fig. 11. Results of the experiment – testing of the dummy and the median of tests of 80 people: (a) transmittance of disc 1 and body part 1, (b) transmittance of disc 2 and body part 2, (c) transmittance of disc 3 and body part 3

The highest compatibility is displayed by the transmittance courses of disc 2 and body part 2. As presented in the diagram of transmittance courses, the highest enhancement is observed for frequencies of 5 Hz and 5.5 Hz, respectively. The difference between the maximum enhancement values for these characteristics is 3.3 percent. The courses of the curves for other frequency ranges presented in the diagrams are also very similar.

As indicated by the transmittance courses of body part 1 and disc 1, the highest enhancement for both courses occurs for the same frequency of 4.5 Hz. The difference of enhancement values for this frequency is 10.6 percent. The characteristics have similar courses in the frequency range between 3 and ca. 12 Hz. Above the latter frequency, there are increasing discrepancies between the characteristics.

The transmittance courses for body part 3 and disc 3 are the least compatible. The highest enhancement for both these courses exists in different resonant frequencies, with a 1.5 Hz offset with respect to one another. The difference between the maximum enhancement values is 15 percent. In this instance, the characteristics display the highest compatibility in two frequency ranges: 1-6 Hz and 9-12.5 Hz.

4. Conclusion

Testing vibrational comfort in vehicles may involve either the entire body of a sitting person or its selected parts. For ethical reasons, as well as for ensuring safety and repeatability of obtained results, people are increasingly often replaced with anthropodynamic dummies. The structure of such dummies, used for testing vibrational comfort, should reflect the structure of a sitting human being while taking into consideration the analysed body parts for which test are to be carried out.

The results of the conducted experimental tests indicate that at least three areas of the human body should be distinguished in a dummy, as each one is characterised by a different resonance frequency and various levels of acceleration enhancement. The structure of the dummy presented in this paper comprises these parts. The proposed amount of degrees of freedom is a compromise between obtaining the most accurate representation of the human body structure and the constructional limitations which occurred as the dummy was being built.

The symmetric construction of the dummy prevents the occurrence of forces producing unwanted longitudinal or lateral rocking which, in consequence, increases the dummy stability. Properly formed buttocks and the back ensure the adequate imitation of the distribution of individual pressures produced by a vehicle driver or passenger. The construction of the dummy enables one to imitate mass structures of people of various weight (slim, normal weight, obese).

A significant qualitative and quantitative similarity between the characteristics obtained in laboratory tests of the dummy transmittance and the respective characteristics of human subjects proves that dummies (with a construction based upon the results of the experiment) may be successfully applied to evaluate the impact of vibrations on vehicle passengers.

The assumed solution enables a fairly easy reconfiguration of the dummy to imitate the 10th and the 90th percentile of the weights of tested people.

References

1. Cullmann A., Wölfel H.P., 1998, *Komfortbewertung und Sitzprüfung mittels des Schwingungsdummys MEMOSIK*, Fachtagung, Haus der Technik, Essen

2. Griffin M.J., 1990, *Handbook of Human Vibration*, Academic Pres, London

3. Knoblauch J., 1992, *Entwicklung und Bau eines physikalischen Schwingungsmodells des sitzenden Menschen*, Dissertation, Shaker Verlag

4. Knoblauch J., Wölfel H.P., Buck P., 1995, Ein Schwingungsdummy des sitzenden Menschen, *ATZ – Automobiltechnische Zeitschrift*, **97**, 10

5. Łomako D.M., Stańczyk T. L., Wyrębkiewicz A., 1998, Zagadnienie komfortu jazdy w samochodach z pasywnym zawieszeniem fotela kierowcy, *VI Międzynarodowa Konferencji "Pojazdy Samochodowe. Problemy Rozwoju, Jakości, Eksploatacji AUTOPROGRES"*, **1**

6. Mansfield N.J., Griffin M.J., 1996, Vehicle seat dynamics measured with an anthropodynamic dummy and human subjects, *Proceedings of Inter-Noise 96*, Liverpool UK

7. Mozaffari A., Pankoke S., Wölfel H.P., 2008, MEMOSIK V – An active dummy for determining three-directional transfer functions of vehicle seats and vibration exposure ratings for the seated occupant, *International Journal of Industrial Ergonomics*, **38**
8. Nélisse H., Boileau P.É., Rakheja S., Patra S., Boutin J., 2006, Évaluation de mannequins anthropodynamiques destines aux essais de vibrations des sièges en laboratoires; Études et Recherches, Raport R479
9. Wölfel H.P., 2006, Numerical models and hardware dummies for simulating whole body vibration of human – an overview, *Proceedings of the First American Conference on Human Vibration*, West Virginia, U.S.A., DHHS (NIOSH) Publication No. 2006-140 June
10. Zuska A., 2005, Identyfikacja rozprzestrzeniania się pionowych drgań w organizmie siedzącego człowieka, *Teka Komisji Motoryzacji PAN, Oddz. Kraków*, **29/30**
11. Zuska A., 2007, Analiza porównawcza rozprzestrzeniania się pionowych drgań w organizmach osób o różnej budowie ciała, **Logistyka**, **3**
12. Zuska A., Stańczyk T.L., 2005, Stanowisko do symulacyjnych badań podukładu fotel-kierowca, *Prace Naukowe TRANSPORT, Wydawnictwo Politechniki Radomskiej*, **21**, 1, 149-158

Manuscript received November 29, 2013; accepted for print June 26, 2015

JOURNAL OF THEORETICAL
AND APPLIED MECHANICS
53, 4, pp. 1041-1052, Warsaw 2015
DOI: 10.15632/jtam-pl.53.4.1041

A NONLOCAL TIMOSHENKO BEAM THEORY FOR VIBRATION ANALYSIS OF THICK NANOBEAMS USING DIFFERENTIAL TRANSFORM METHOD

Farzad Ebrahimi, Parisa Nasirzadeh
Department of Mechanical Engineering, Faculty of Engineering, Imam Khomeini International University, Qazvin, Iran
e-mail: febrahimy@eng.ikiu.ac.ir

This article presents the solution for free vibration of nanobeams based on Eringen nonlocal elasticity theory and Timoshenko beam theory. The small scale effect is considered in the first theory, and the transverse shear deformation effects as well as rotary inertia are taken into account in the latter one. Through variational formulation and the Hamilton principle, the governing differential equations of free vibration of the nonlocal Timoshenko beam and the boundary conditions are derived. The obtained equations are solved by the differential transformation method (DTM) for various frequency modes of the beams with different end conditions. In addition, the effects of slenderness and on vibration behavior are presented. It is revealed that the slenderness affects the vibration characteristics slightly whilst the small scale plays a significant role in the vibration behavior of the nanobeam.

Keywords: free vibration, nanobeam, Eringen nonlocal elasticity theory

1. Introduction

Nanostructures have significant mechanical, electrical and thermal performances that are superior to conventional structural materials. They have attracted much attention in modern science and technology. For example, in micro/nano electromechanical systems (MEMS/NEMS); nanostructures have been used in many areas including communications, machinery, information technology, biotechnology technologies, etc. So far, three main methods have been provided to study the mechanical behavior of nanostructures. These are the atomistic (Baughman *et al.*, 2002), semi-continuum (Li and Chou, 2003) and continuum models (Wang and Cai, 2006). However, both atomistic and semi-continuum models are computationally expensive and are not suitable for analyzing large scale systems.

Due to the inherent size effects, at nanoscale, the mechanical characteristics of nanostructures are often significantly different from their behavior at macroscopic scale. Such effects are essential for nanoscale materials or structures and the influence on nano-instruments is great (Maranganti and Sharma, 2007). Generally, theoretical studies on size effects at nanoscale are by means of surface effects (Zhu *et al.*, 2009), strain gradients in elasticity (Mindlin, 1964) and plasticity (Aifantis, 1984) as well as nonlocal stress field theory (Eringen, 1983, 1972a), etc. Unfortunately, the classical continuum theories are deemed to fail for these nanostructures, because length dimensions at nano scale are often sufficiently small such that call the applicability of classical continuum theories into the question. Consequently, the classical continuum models need to be extended to consider the nanoscale effects. This can be achieved through the nonlocal elasticity theory proposed by Eringen (1972a) which considers the size-dependent effect. According to this theory, the stress state at a reference point is considered as a function of strain states of all points in the body. This nonlocal theory is proved to be in accordance with the atomic model of lattice dynamics and with experimental observations on phonon dispersion (Eringen, 1983). In nonlocal theory, nonlocal nanoscale in the constitutive equation could be considered simply as a material-dependent parameter. The ratio of internal characteristic scale (such as the lattice parameter, C-C bond length, granular distance, etc.) to external characteristic scale (such as crack length, wave length, etc.) is defined within a nonlocal nanoscale parameter. If the internal characteristic scale is much smaller than the external characteristic scale, the nonlocal nanoscale parameter approaches zero and the classical continuum theory is recovered.

For analyzing these nanoscale beams, Euler-Bernoulli and Timoshenko beam theories appear to be inadequate, since they are scale free. For this problem, continuum mechanics is needed, and one of the efficient theories for nonlocal continuum mechanics is Eringen's (Eringen, 1983; 1972a,b) theory which allows small scale effect by indicating that stress at one point is a function of strain at all points of the body.

In the recent years, nanobeams and carbon nanotubes (CNTs) have held a wide variety of potential applications (Zhang *et al.*, 2004; Wang, 2005; Wang and Varadan, 2006) such as sensors, actuators, transistors, probes, and resonators in nanoelectromechnical systems (NEMSs). Thus, establishing an accurate model of nanobeams is a key issue for successful NEMS design. As a result, nanotechnological research on free vibration properties of nanobeams is important because such components can be used as design components in nano-sensors and nano-actuators. Furthermore, many researchers worked on bending, buckling and vibration of beam-like elements (Peddieson *et al.*, 2003; Liew *et al.*, 2008; Xu, 2006; Amara *et al.*, 2010) and in some papers the Euler-Bernoulli theory has been applied for vibration of nanobeams (Lu *et al.*, 2006; Zhang *et al.*, 2005; Xu, 2006). But they used the Euler-Bernoulli theory which does not account transverse shear force and rotary inertia which are significant in stubby beams and high vibration frequencies. So in this paper, we used Timoshenko beam theory and the governing equations and boundary conditions for free vibration of a nonlocal Timoshenko beam have been derived via Hamilton's principle. To the author's best knowledge, there is no work reported on the application of DTM on vibration analysis of nonlocal Timoshenko beams with various boundary conditions. Furthermore, the solution procedure in this study is the differential transformation method (DTM) which is a semi analytical-numerical technique depending on Taylor series expansion. This method was first introduced by Zhou (1986) in his study about electrical circuits, and this method has the advantage of its simplicity in use as well as high accuracy. The results in this paper are provided by a MATLAB code with respect to DTM rules, for the first time.

2. Nonlocal Timoshenko beam equations and boundary conditions

Consider a beam with length L and cross sectional area of A. Based on Timoshenko beam theory, strain-displacement and strain energy relations are as follows (Wang *et al.*, 2000)

$$\varepsilon_{xx} = z\frac{d\phi}{dx} \qquad \gamma_{xz} = \phi + \frac{dw}{dx} \tag{2.1}$$

in which x is the longitudinal coordinate measured from the left end of the beam and z is the coordinate measured from the mid-plane of the beam, w represents the transverse displacement and ϕ is rotation of the beam due to bending, ε_{xx} is the normal strain, γ_{xz} is the transverse shear strain, σ_{xx} is normal stress and σ_{xz} – transverse shear stress. The strain energy relation is as follows (Leissa and Qatu, 2011)

$$U = \frac{1}{2}\int\limits_0^L\int\limits_A (\sigma_{xx}\varepsilon_{xx} + \sigma_{xz}\gamma_{xz})\, dA\, dx \tag{2.2}$$

After substituting equations (2.1) into equation (2.2) and putting the bending moment and shear force into relation (2.2), the strain energy becomes

$$
\begin{aligned}
U &= \frac{1}{2}\int_0^L \int_A \Big(\sigma_{xx} z \frac{d\phi}{dx} + \sigma_{xz}\Big(\phi + \frac{dw}{dx}\Big)\Big]\, dA\, dx = \int_0^L \frac{1}{2}\Big[M\frac{d\phi}{dx} + Q\Big(\phi + \frac{dw}{dx}\Big)\Big]\, dx \\
M &= \int_A \sigma_{xx} z\, dA \qquad Q = \int_A \sigma_{xz}\, dA
\end{aligned}
\tag{2.3}
$$

where M is the bending moment and Q is the shear force. The kinetic energy T, by assuming free harmonic motion and rotary inertia effect, is

$$
T = \frac{1}{2}\int_0^L (\rho A \omega^2 w^2 + \rho I \omega^2 \phi^2)\, dx \tag{2.4}
$$

in which ω is the circular frequency of vibration and ρ and I are the mass density and the second moment of area of the beam, respectively. Applying Hamilton's principle (Chow, 2013), requires

$$
\delta(T-U) = 0 = \int_0^L \Big[-M\frac{d\delta\phi}{dx} - Q\Big(\delta\phi + \frac{d\delta w}{dx}\Big) + \rho A\omega^2 w\delta w + \rho I \omega^2 \phi\delta\phi\Big]\, dx \tag{2.5}
$$

After performing integration by parts, we reach

$$
0 = \int_0^L \Big[\Big(\frac{dM}{dx} - Q + \rho I\omega^2\phi\Big)\delta\phi + \frac{dQ}{dx} + \rho A\omega^2 w\Big)\delta w\Big]\, dx - [M\delta\phi]_0^L - [Q\delta w]_0^L \tag{2.6}
$$

This results in the following equations

$$
\frac{dM}{dx} = Q - \rho I\omega^2\phi \qquad \frac{dQ}{dx} = -\rho A\omega^2 w \tag{2.7}
$$

And the boundary conditions are in two forms of below relations

$$
\begin{aligned}
&\text{Either} \qquad w = 0 \qquad \text{or} \qquad Q = 0 \\
&\text{Either} \qquad \phi = 0 \qquad \text{or} \qquad M = 0
\end{aligned}
\tag{2.8}
$$

As can be seen, the equations appear to be the same as in local Timoshenko beam theory, but the shear force and bending moment expressions in nonlocal beam theory must be different. The constitutive equation of classical elasticity is an algebraic relationship between stress and strain tensors while Eringen nonlocal elasticity includes spatial integrals which indicate the average effect of strain of all points of the body to the stress tensor at the given point (Eringen, 1972b; 1983). Since the spatial integrals in constitutive equations are mathematically difficult to solve, they can be converted into equal differential constitutive equations under certain conditions. The nonlocal constitutive stress-strain relation for an elastic material in the one dimensional case beam can be simplified as (Eringen, 1983)

$$
\sigma_{xx} - (e_0 a)^2 \frac{d^2\sigma_{xx}}{dx^2} = E\varepsilon_{xx} \tag{2.9}
$$

in which E is the Young modulus, $e_0 a$ is the scale coefficient that incorporates the small scale effect, a represents the internal characteristic length and e_0 is a constant appropriate to each material which is measured experimentally. The local and nonlocal constitutive shear strain-

-stress relations are the same, since form of the Eringen nonlocal constitutive model cannot be applied in the z direction

$$\sigma_{xz} = G\gamma_{xz} \tag{2.10}$$

in which G is the shear modulus. After multiplying the term $(z\,dA)$ and integrating over the area A, equation (2.9) becomes

$$M - (e_0a)^2\frac{d^2M}{dx^2} = EI\frac{d\phi}{dx} \tag{2.11}$$

By integrating equation (2.10) over the area, we obtain

$$Q = K_sGA\Big(\phi + \frac{dw}{dx}\Big) \tag{2.12}$$

in which K_s is the shear correction factor in the Timoshenko beam theory in order to compensate for the error in assuming equal shear stress or strain in the whole beam thickness. Now by substituting equations (2.7) into equation (2.11), the moment can be reached as below

$$M = EI\frac{d\phi}{dx} - (e_0a)^2\Big(\rho A\omega^2 w + \rho I\omega^2\frac{d\phi}{dx}\Big) \tag{2.13}$$

And by utilizing equations (2.12) and (2.13) in Timoshenko beam equations (2.7), the governing equation for the vibration of nonlocal Timoshenko beam may be obtained as below

$$\begin{aligned}&EI\frac{d^2\phi}{dx^2} - K_sGA\Big(\phi + \frac{dw}{dx}\Big) + \rho I\omega^2\phi - (e_0a)^2\Big(\rho A\omega^2\frac{dw}{dx} + \rho I\omega^2\frac{d^2\phi}{dx^2}\Big) = 0\\ &K_sGA\Big(\frac{d\phi}{dx} + \frac{d^2w}{dx^2}\Big) + \rho Aw\omega^2 = 0\end{aligned} \tag{2.14}$$

On the basis of equation (2.8) and due to various endings of the beam, e.g. for a simply supported end, we have

$$w = 0 \qquad M = EI\frac{d\phi}{dx} - (e_0a)^2\Big(\rho A\omega^2 w + \rho I\omega^2\frac{d\phi}{dx}\Big) = 0 \tag{2.15}$$

and for a clamped end

$$w = 0 \qquad \phi = 0 \tag{2.16}$$

and for a free end

$$\begin{aligned}&M = EI\frac{d\phi}{dx} - (e_0a)^2\Big(\rho A\omega^2 w + \rho I\omega^2\frac{d\phi}{dx}\Big) = 0\\ &Q = K_sGA\Big(\phi + \frac{dw}{dx}\Big) = 0\end{aligned} \tag{2.17}$$

3. Non-dimensional parameters

The non-dimensional parameters contributes to simplification of the equations and to the making of comparisons in the studies possible. The non-dimensional parameters are introduced as the following terms

$$\begin{aligned}&\overline{x} = \frac{x}{L} \qquad &&\overline{w} = \frac{w}{L} \qquad &&\lambda^2 = \omega^2\frac{\rho AL^4}{EI}\\ &\varOmega = \frac{EI}{K_sGAL^2} \qquad &&\alpha = \frac{e_0a}{L} \qquad &&\varepsilon = \frac{L\sqrt{A}}{\sqrt{I}}\end{aligned}$$

where λ^2 is frequency parameter, $\varOmega$ – shear deformation parameter, α – scaling effect arameter, ε – slenderness ratio.

By applying the non-dimensional parameters to governing equations (2.14), the following relations are obtained

$$
\begin{aligned}
&\varOmega\Big(1-\frac{\alpha^2\lambda^2}{\varepsilon^2}\Big)\frac{d^2\phi}{d\overline{x}^2}+\Big(\frac{\varOmega\lambda^2}{\varepsilon^2}-1\Big)\phi-(\alpha^2\lambda^2\varOmega+1)\frac{d\overline{w}}{d\overline{x}}=0\\
&\frac{d\phi}{d\overline{x}}+\frac{d^2\overline{w}}{d\overline{x}^2}+\lambda^2\varOmega\overline{w}=0
\end{aligned}
\tag{3.1}
$$

Also boundary conditions equations (2.15)- (2.17) appear for the simply supported end as

$$
\overline{w}=0 \qquad M=\Big(\varOmega-\frac{\varOmega\alpha^2\lambda^2}{\varepsilon^2}\Big)\frac{d\phi}{d\overline{x}}-\varOmega\alpha^2\lambda^2\overline{w}=0 \tag{3.2}
$$

And for the clamped end as

$$
\overline{w}=0 \qquad \phi=0 \tag{3.3}
$$

And for the free end as

$$
M=\Big(\varOmega-\frac{\varOmega\alpha^2\lambda^2}{\varepsilon^2}\Big)\frac{d\phi}{d\overline{x}}-\varOmega\alpha^2\lambda^2\overline{w}=0 \qquad Q=K_sGA\Big(\phi+\frac{d\overline{w}}{d\overline{x}}=0 \tag{3.4}
$$

4. Differential transformation method

The differential transformation method is one of the useful techniques to solve differential equations with small calculation errors and capable of solving nonlinear equations with boundary condition value problems. Abdel-Halim Hassan (2002) applied the DTM to eigenvalues and normalized eigenfunctions. Also Wang (2013) and Chen and Ju (2004) used the method in their studies. The DTM is a transformation technique based on the Taylor series expansion and is a useful tool to obtain analytical solutions to differential equations. The DTM is proved to be a good computational tool for various engineering problems. Using the differential transformation technique, ordinary and partial differential equations can be transformed into algebraic equations from which a closed-form series solution can be obtained easily. In this method, certain transformation rules are applied to both the governing differential equations of motion and the boundary conditions of the system in order to transform them into a set of algebraic equations as presented in Table 1 and 2.

Table 1. Basics of the differential transform method (Chen and Ju, 2004)

Original function	Transformed function
$f(x)=g(x\pm h(x)$	$F(K)=G(K)\pm H(K)$
$f(x)=\lambda g(x)$	$F(K)=\lambda G(K)$
$f(x)=g(x)h(x)$	$F(K)=\sum\limits_{l=0}^{K}G(K-l)H(l)$
$f(x)=\dfrac{d^ng(x)}{dx^n}$	$F(K)=\dfrac{(k+n)!}{k!}G(K+n)$
$f(x)=x^n$	$F(K)=\delta(k-n)=\begin{cases}0 & \text{if} \quad k\neq n\\ 1 & \text{if} \quad k=n\end{cases}$

Table 2. Transformed boundary conditions (BC) based on DTM (Chen and Ju, 2004)

$X=0$		$X=1$	
Original BC	Transformed BC	Original BC	Transformed BC
$f(0)=0$	$F[0]=0$	$f(1)=0$	$\sum\limits_{k=0}^{\infty} F[k]=0$
$\dfrac{df}{dx}(0)=0$	$F[1]=0$	$\dfrac{df}{dx}(1)=0$	$\sum\limits_{k=0}^{\infty} kF[k]=0$
$\dfrac{d^2f}{dx^2}(0)=0$	$F[2]=0$	$\dfrac{d^2f}{dx^2}(1)=0$	$\sum\limits_{k=0}^{\infty} k(k-1)F[k]=0$
$\dfrac{d^3f}{dx^3}(0)=0$	$F[3]=0$	$\dfrac{d^3f}{dx^3}(1)=0$	$\sum\limits_{k=0}^{\infty} k(k-1)(k-2)F[k]=0$

The solution of these algebraic equations gives the desired results of the problem. It is different from the high-order Taylor series method because the Taylor series method requires symbolic computation of necessary derivatives of data functions and is expensive for large orders.

The basic definitions and the application procedure of this method can be introduced as follows:

The transformation equation of the function $f(x)$ can be defined as (Chen and Ju, 2004)

$$F[k]=\frac{1}{k!}\frac{d^kf(x)}{dx^k}\Big|_{x=x_0} \tag{4.1}$$

where $f(x)$ the original function and $F[k]$ is the transformed function.

The inverse transformation is defined as

$$f(x)=\sum_{k=0}^{\infty}(x-x_0)^kF[k] \tag{4.2}$$

Combining equations (4.1) and (4.2), one obtains

$$f(x)=\sum_{k=0}^{\infty}\frac{(x-x_0)^k}{k!}\frac{d^kf(x)}{dx^k}\Big|_{x=x_0} \tag{4.3}$$

Considering equation (4.3), it is noticed that the concept of the differential transform is derived from Taylor series expansion. In actual application, the function $f(x)$ is expressed by a finite series, and equation (4.3) can be written as follows

$$f(x)=\sum_{k=0}^{n}\frac{(x-x_0)^k}{k!}\frac{d^kf(x)}{dx^k}\Big|_{x=x_0} \tag{4.4}$$

which implies that the term in relation (4.5) is negligible

$$f(x)=\sum_{k=n+1}^{\infty}\frac{(x-x_0)^k}{k!}\frac{d^kf(x)}{dx^k}\Big|_{x=x_0} \tag{4.5}$$

In this study, the natural frequencies determine the value of n.

5. Solution with DTM

According to the DTM rules given in Table 1, equations (3.1) will be transformed into the following equations

$$\begin{aligned}&\Omega\Big(1-\frac{\alpha^2\lambda^2}{\varepsilon^2}\Big)(k+1)(k+2)\Phi(k+2)+\Big(\frac{\Omega\lambda^2}{\varepsilon^2}-1\Big)\Phi(k)-(\alpha^2\lambda^2\Omega+1)(k+1)\overline{W}(k+1)=0\\&(K+1)\Phi(k+1)+(k+1)(k+2)\overline{W}(k+2)+\lambda^2\Omega\overline{W}(k)=0\end{aligned} \tag{5.1}$$

The rules of the DTM for defining boundary conditions are given in Table 2. $\overline{W}(k)$ and $\Phi(k)$ are transforms of $w(x)$ and $\phi(x)$, respectively. By substituting values for $k = 0, 1, 2, \ldots$, $\alpha = 0$, $\varepsilon = 34.641$ and $\Omega = 0.2436$ into equations (5.1), we can evaluate the amounts of $\overline{W}(2), \overline{W}(3), \ldots$ and $\Phi(2), \Phi(3), \ldots$ in terms of ω^2 and some constants like $c_1, \ldots$. The values can be achieved with a computer program, and after substituting $\overline{W}(i)$ and $\Phi(i)$ into boundary conditions the following equation is obtained

$$N_r1^{(n)}(\omega)c_1 + N_r2^{(n)}(\omega)c_2 = 0 \qquad r = 1, 2, \ldots, n \tag{5.2}$$

in which N_s are polynomials in terms of ω corresponding to the n-th term. When solving equation (5.2) in matrix form, the following eigenvalue equation may be obtained

$$\begin{vmatrix} N_{11}^n(\omega) & N_{12}^n(\omega) \\ N_{21}^n(\omega) & N_{22}^n(\omega) \end{vmatrix} = 0 \tag{5.3}$$

The solution to equation (5.3) gives ω_r^n which is the r-th estimated eigenvalue for the n-th repeat. The number of repeats can be obtained by equation (5.4) as

$$|\omega_r^n - \omega_r^{n-1}| < \delta \tag{5.4}$$

In the present study, $\delta = 0.0001$ and this shows the accuracy of calculations. With respect to the differential transformation method and the algorithm above, a MATLAB code has been developed in order to determine vibration characteristics of the nonlocal Timoshenko nanobeam.

6. Results and discussion

In the present study, the impact of the small scale coefficient as well as the effect of slenderness on the first, second and third frequencies of the nonlocal Timoshenko nanobeam are presented. Also, three types of boundary conditions are compared. In order to validate the computed results, a comparison between the present paper and the results obtained by Wang *et al.* (2007) is performed. The mechanical properties of the nonlocal Timoshenko nanobeam are given in Table 3.

Table 3. Mechanical properties of the nonlocal Timoshenko nanobeam (Wang *et al.*, 2007)

Property	Unit	
E	T·Pa	5.5
P	g·cm^{-3}	2.3
ν	–	0.19

Also, the Timoshenko shear correction factor k_s is taken 0.563. For calculating the exact difference between the results of the present paper and the available results in literature, relation (6.1) has been applied

$$\%\text{difference} = 100 \cdot \frac{|\text{reference} - \text{present}|}{\text{present}} \tag{6.1}$$

As shown by the comparisons given in Tables 4 and 5, a close correlation between these results validates the proposed method of solution.

Table 4. First three nondimensional frequencies $\sqrt{\lambda}$ of the nonlocal Timoshenko beam for both clamped ends and $L/d = 10$

α	Mode 1			Mode 2			Mode 3		
	present	Wang *et al.* (2007)	diff. [%]	present	Wang *et al.* (2007)	diff. [%]	present	Wang *et al.* (2007)	diff. [%]
0	4.53	4.45	1.766	7.19	6.95	3.33	9.6	9.2	4.1
0.1	4.4233	4.3471	1.72	6.67	6.4952	2.62	8.4	8.2	2.38
0.3	3.83	3.7895	1.057	5	4.9428	1.14	5.95	5.846	1.74
0.5	3.2657	3.242	0.725	4	3.994	0.15	4.75	4.6769	1.53
0.7	2.85	2.8383	0.41	3.45	3.4192	0.89	4.05	3.9961	1.33

Table 5. First nondimensional natural frequency $\sqrt{\lambda}$ of the nonlocal Timoshenko beam for two kinds of boundary conditions and $L/d = 10$

α	Clamped-simple			Simple-free		
	present	Wang *et al.* (2007)	diff. [%]	present	Wang *et al.* (2007)	diff. [%]
0	3.82	3.7845	0.929	3.08	3.0929	0.418
0.1	3.73	3.6939	0.967	3.059	3.0243	1.13
0.3	3.23	3.2115	0.5727	2.91	2.6538	8.8
0.7	2.415	2.4059	0.37	2.4	2.0106	16

In addition, the convergence of the differential transformation method is perused. In Fig. 1, the convergence of the third frequency of the nonlocal Timoshenko beam with both clamped ends is presented. It illustrates that the third frequency converges at the 46th repeat, while the first and the second frequencies converged before, in this example at the 29th and 37th repeats.

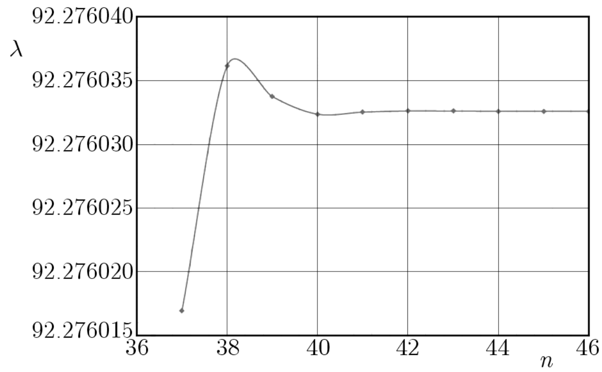

Fig. 1. Convergence of the third frequency, $L/d = 10$, $\alpha = 0$

The variables in governing equations (3.1) are α, ε and Ω. α relates to the small scale effect, ε is in terms of the slenderness (L/d) and Ω relates to the mechanical properties and slenderness. So, it is possible to investigate the effects of slenderness and small scale on various frequencies and mode shapes of the nonlocal Timoshenko beam. Furthermore, determination of the magnitude of e_0 is significant due to its prominent effect on the small scale coefficient. Some researchers worked on estimating the magnitude of e_0a. For instance, Zhang *et al.* (2005) estimated the magnitude of the parameter for carbon nanotubes to be approximately 0.82. In this study, we adopt $0 \leqslant \alpha < 0.8$ in our investigations as reported by Lu *et al.* (2006). As Figs. 2a,b,c show when the coefficient α equals zero, the frequency of the nonlocal Timoshenko beam equals its local counterpart. As the coefficient increases, the frequency ratio decreases, which means that the nonlocal beam frequency becomes smaller than the local counterparts. This reduction is especially noticeable in higher modes and cannot be neglected. In sum, the small scale effect makes the beam more flexible since in nonlocal theory elastic springs link the atoms together (Liew *et al.*, 2008).

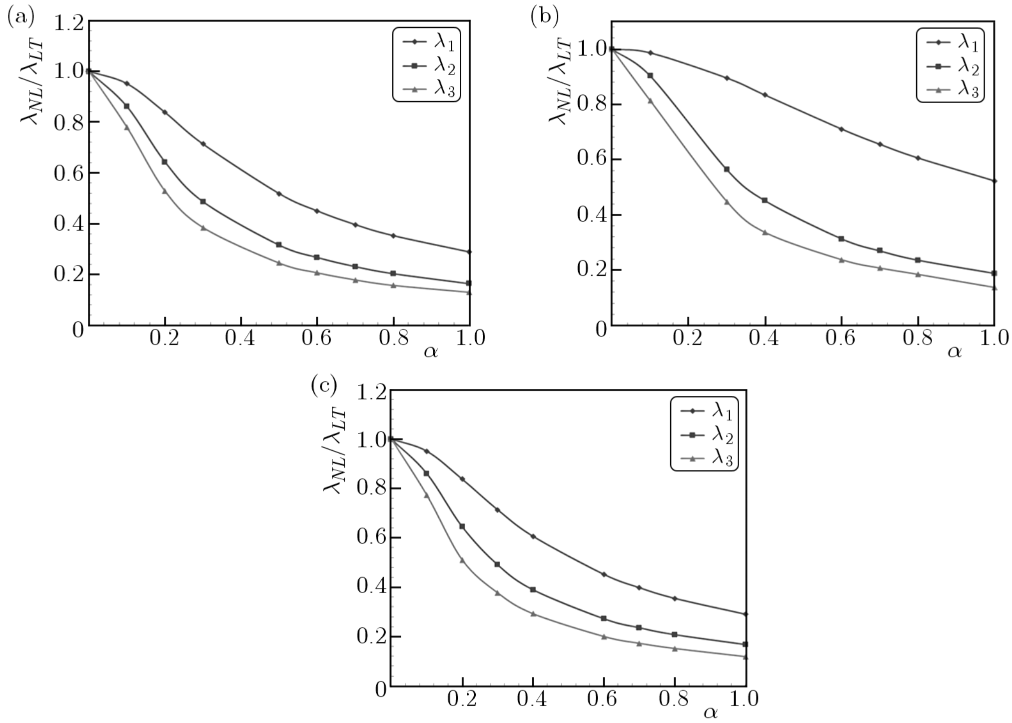

Fig. 2. Effect of small scale on different frequency modes, $L/d = 10$: (a) clamped ends, (b) simply supported beam, (c) clamped-simply beam

Figure 3 indicates that the small scale have significant effect on short beams and, as the beam gets longer, its impact becomes gradually negligible. So, the small scale will diminish for a very long and thin (slender) beam. Also, Fig. 4 illustrates that the nonlocal Timoshenko beam frequency approaches the local Timoshenko beam frequency as the slenderness increases.

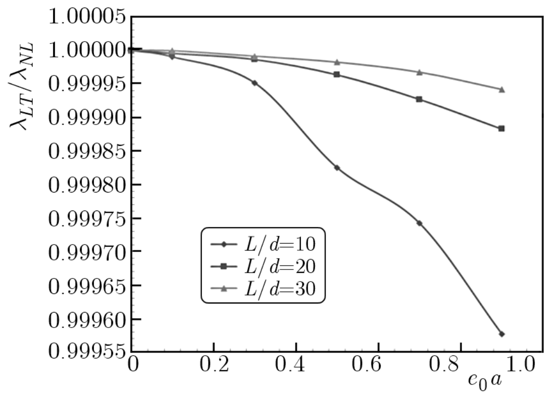

Fig. 3. Small scale effect on the frequency ratio with different values of L/d (both ends clamped)

Table 6. First three frequencies $\sqrt{\lambda}$ of the nonlocal Timoshenko beam with two kinds of boundary conditions

e_0a	Mode	$L/d = 10$	$L/d = 20$	$L/d = 30$
Simply supported-simply supported beam				
0	1	3.08057	3.12577	3.13451
0.1		3.08056	3.12577	3.13451
0.3		3.08056	3.12577	3.1345
0.5		3.08052	3.12576	3.1345
0.7		3.08047	3.12574	3.13449
0.9		3.08040	3.12572	3.13448
0	2	5.94588	6.18907	6.24037
0.1		5.94584	6.18906	6.24036
0.3		5.94558	6.18898	6.24033
0.5		5.94466	6.18882	6.24025
0.7		5.94425	6.18858	6.24015
0.9		5.94318	6.18826	6.24000
0	3	8.53236	9.15198	9.29787
0.1		8.53225	9.15194	9.29785
0.3		8.53139	9.15165	9.29771
0.5		8.52995	9.15107	9.29743
0.7		8.52936	9.15020	9.29702
0.9		8.52366	9.14904	9.29647
Clamped-simply supported beam				
0	1	3.829744	3.901179	3.915187
0.1		3.829726	3.901175	3.915186
0.3		3.829653	3.901155	3.915176
0.5		3.829491	3.901111	3.915155
0.7		3.829248	3.901045	3.915136
0.9		3.828925	3.900957	3.915086
1		3.828732	3.900904	3.915063
0	2	6.644277	6.948166	7.01359
0.1		6.644219	6.948148	7.013581
0.3		6.642754	6.948008	7.013516
0.5		6.642824	6.947726	7.013386
0.7		6.641431	6.947305	7.013191
0.9		6.639576	6.946740	7.01293
1		6.638475	9.946408	7.012778
0	3	9.177342	9.888691	10.05988
0.1		9.177189	9.888635	10.05986
0.3		9.175962	9.888215	10.05966
0.5		9.173494	9.887381	10.05925
0.7		9.169836	9.886127	10.05866
0.9		9.164950	9.883445	10.05853
1		9.162052	9.883461	10.05806

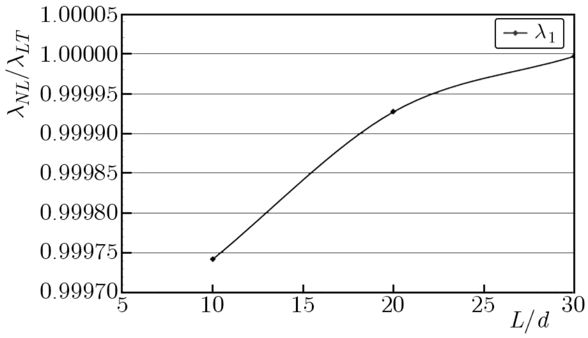

Fig. 4. Effect of slenderness on the nonlocal beam frequency ($\alpha = 0.7$, both ends clamped)

7. Conclusion

A semi-analytical method called the differential transformation method is generalized to analyze vibration characteristics of a nanobeam. The formulation is based on the assumptions of Timoshenko beam theory and the nonlocal differential constitutive relations of Eringen. The transverse shear force and rotary inertia that become significant at short beams and higher frequencies are taken into account in the equations. Also, the effect of the small scale coefficient as well as the slenderness and boundary conditions in various frequency ratios are investigated. It is demonstrated that the DTM has high precision and computational efficiency in the vibration analysis of nanobeams.

References

1. Abdel-Halim Hassan I.H., 2002, On solving some eigenvalue problems by using a differential transformation, *Applied Mathematics and Computation*, **127**, 1, 1-22
2. Aifantis E.C., 1984, On the microstructural origin of certain inelastic models, *Journal of Engineering Materials and Technology*, **106**, 4, 326-330
3. Amara K., Tounsi A., Mechab I., Adda-Bedia E.A., 2010, Nonlocal elasticity effect on column buckling of multiwalled carbon nanotubes under temperature field, *Applied Mathematical Modeling*, **34**, 12, 3933-3942
4. Baughman R.H., Zakhidov A.A., de Heer W.A., 2002, Carbon nanotubes – the route toward applications, *Science*, **297**, 5582, 787-792
5. Chen C.O.K., Ju S.P., 2004, Application of differential transformation to transient advective-dispersive transport equation, *Applied Mathematics and Computation*, **155**, 1, 25-38
6. Chow T.L., 2013, *Classical Mechanics*, CRC Press, Boca Raton, Florida, USA
7. Eringen A.C., 1972a, Linear theory of nonlocal elasticity and dispersion of plane waves, *International Journal of Engineering Science*, **10**, 5, 425-435
8. Eringen A.C., 1972b, Nonlocal polar elastic continua, *International Journal of Engineering Science*, **10**, 1, 1-16
9. Eringen A.C., 1983, On differential equations of nonlocal elasticity and solutions of screw dislocation and surface waves, *Journal of Applied Physics*, **54**, 9, 4703-4710
10. Eringen A.C., Edelen D.G.B., 1972, On nonlocal elasticity, *International Journal of Engineering Science*, **10**, 3, 233-248
11. Lee Y.Y., Wang C.M., Kitipornchai S., 2003, Vibration of Timoshenko beams with internal hinge, *Journal of Engineering Mechanics*, **129**, 3, 293-301
12. Leissa A.W., Qatu M.S., 2011, *Vibration of Continuous Systems*, McGraw Hill Professional

13. Li C., Chou T.W., 2003, A structural mechanics approach for the analysis of carbon nanotubes, *International Journal of Solids and Structures*, **40**, 10, 2487-2499

14. Liew K.M., Hu Y., He X.Q., 2008, Flexural wave propagation in single-walled carbon nanotubes, *Journal of Computational and Theoretical Nanoscience*, **5**, 4, 581-586

15. Lu P., Lee H.P., Lu C., Zhang P.Q., 2006, Dynamic properties of flexural beams using a nonlocal elasticity model, *Journal of Applied Physics*, **99**, 7, 073510

16. Maranganti R., Sharma P., 2007, Length scales at which classical elasticity breaks down for various materials, *Physical Review Letters*, **98**, 19, 195504

17. Mindlin R.D., 1964, Micro-structure in linear elasticity, *Archive for Rational Mechanics and Analysis*, **16**, 51-78

18. Peddieson J., Buchanan G.R., McNitt R.P., 2003, Application of nonlocal continuum models to nanotechnology, *International Journal of Engineering Science*, **41**, 3, 305-312

19. Wang C.M., Reddy J.N., Lee K.H., Eds., 2000, *Shear Deformable Beams and Plates: Relationships with Classical Solutions*, Elsevier

20. Wang C.M., Zhang Y.Y., He X.Q., 2007, Vibration of nonlocal Timoshenko beams, *Nanotechnology*, **18**, 10, 105401

21. Wang Q., 2005, Wave propagation in carbon nanotubes via nonlocal continuum mechanics, *Journal of Applied Physics*, **98**, 12, 124301

22. Wang Q., Varadan V.K., 2006, Vibration of carbon nanotubes studied using nonlocal continuum mechanics, *Smart Materials and Structures*, **15**, 2, 659

23. Wang X., Cai H., 2006, Effects of initial stress on non-coaxial resonance of multi-wall carbon nanotubes, *Acta Materialia*, **54**, 8, 2067-2074

24. Wang Z.G., 2013, Axial vibration analysis of stepped bar by differential transformation method, *Applied Mechanics and Materials*, **419**, 273-279

25. Xu M., 2006, Free transverse vibrations of nano-to-micron scale beams, *Proceedings of the Royal Society A: Mathematical, Physical and Engineering Science*, **462**, 2074, 2977-2995

26. Zhang Y.Q., Liu G.R., Wang J.S., 2004, Small-scale effects on buckling of multiwalled carbon nanotubes under axial compression, *Physical Review B*, **70**, 20, 205430

27. Zhang Y.Q., Liu G.R., Xie X.Y., 2005, Free transverse vibrations of double-walled carbon nanotubes using a theory of nonlocal elasticity, *Physical Review B*, **71**, 19, 195404

28. Zhou J.K., 1986, *Differential Transformation and its Applications for Electrical Circuits*, Huazhong University Press, Wuhan, China

29. Zhu H., Wang J., Karihaloo B., 2009, Effects of surface and initial stresses on the bending stiffness of trilayer plates and nanofilms, *Journal of Mechanics of Materials and Structures*, **4**, 3, 589-604

Manuscript received April 3, 2014; accepted for print July 1, 2015

JOURNAL OF THEORETICAL
AND APPLIED MECHANICS
53, 4, pp. 1053-1065, Warsaw 2015
DOI: 10.15632/jtam-pl.53.4.1053

TIME-DEPENDENT THERMO-ELASTIC CREEP ANALYSIS OF THICK-WALLED SPHERICAL PRESSURE VESSELS MADE OF FUNCTIONALLY GRADED MATERIALS

Mosayeb Davoudi Kashkoli, Mohammad Zamani Nejad
Mechanical Engineering Department, Yasouj University, Yasouj, Iran
e-mail: m.zamani.n@gmail.com; m_zamani@yu.ac.ir

Assuming that the thermo-elastic creep response of the material is governed by Norton's law and material properties, except Poisson's ratio, are considered as a function of the radius of the spherical vessel, an analytical solution is presented for calculation of stresses and displacements of axisymmetric thick-walled spherical pressure vessels made of functionally graded materials. This analytical solution could be used to study the time and temperature dependence of stresses in spherical vessels made of functionally graded materials. Creep stresses and displacements are plotted against dimensionless radius and time for different values of the powers of the material properties.

Keywords: spherical pressure vessels, creep, time-dependent, thermo-elastic, functionally graded material

1. Introduction

Composites are commonly employed in various structural and engineering applications. Recently, a new class of composite materials known as functionally graded materials (FGMs) has drawn considerable attention. From viewpoints of solid mechanics, FGMs are non-homogeneous elastic mediums (Ghannad and Nejad, 2013). FGMs are those in which two or more different material ingredients change continuously and gradually along a certain direction (Noda *et al.*, 2012). The mechanical and thermal responses of materials with spatial gradients in composition are of considerable interests in numerous industrial applications such as tribology, biomechanics, nanotechnology and high temperature technologies. These materials are usually mixtures of metal and ceramic which exhibit excellent thermal resistance with low levels of thermal stresses (Alashti *et al.*, 2013).

Extensive studies have been carried out, both theoretically and numerically, on thermo-elastic creep stress distribution in functionally gradient materials. Time-dependent creep analysis of FGM spheres and cylinders has been an active area of research over the past decade.

Assuming the infinitesimal strain theory, Finnie and Heller (1959) studied creep problems in engineering materials and a steady-state creep solution for a spherical vessel under internal pressure. Johnson and Khan (1963) obtained a theoretical analysis of the distribution of stress and strain in metallic thick-walled spherical pressure vessels subject to internal and external pressures at elevated temperatures. Penny (1967) investigated creep of spherical shells containing discontinuities.

In this study, the solution procedure has been applied to pressurized spherical shells containing discontinuities with a view to discovering, in broad terms, how stresses change with time and how strains accumulate during the creep process. Bhatnagar and Arya (1975) obtained creep analysis of a pressurized thick-walled spherical vessel made of a homogeneous and isotropic material by making use of the finite strain theory, and with considering large strains. Miyazaki *et al.* (1977) presented a parametric analysis of the creep buckling of a shallow spherical shell subjected to uniform external pressure using the finite element incremental method. Xirouchakis and Jones (1979) investigated creep buckling behavior of a geometrically imperfect complete spherical shell subjected to a uniform external pressure using Sanders' equilibrium and kinematic equations appropriately modified to include the influence of initial stress-free imperfections in the radius.

In this study, the Norton-Bailey constitutive equations are used to describe the secondary creep behavior, and elastic effects are retained. Arya *et al.* (1980) studied effect of material anisotropy on creep of pressurized thick-walled spherical vessel considering the large strain theory. Kao (1981) obtained creep deformations and creep buckling times for axisymmetric shallow spherical shells with and without initial imperfections. For nonlinear creeps, both strain-hardening and time-hardening rules are employed in this study. Creep of a sphere subjected to inner and outer pressures, and also thermal stress, was discussed by Sakaki *et al.* (1990) by using internal stress arising from a spherically symmetric, finite plastic strain. Assuming that the elastic behavior of the material is undergoing both creep and dimensional changes, Miller (1995) presented a solution for stresses and displacements in a thick spherical shell subjected to internal and external pressure loads. Based on basic equations of steady-state creep of spherically symmetric problems, You *et al.* (2008) proposed a simple and efficient iterative method to determine creep deformations and stresses in thick-walled spherical vessels with varying creep properties subjected to internal pressure. Using a long-term material creep constitutive model defined by the Θ projection concept, Loghman and Shokouhi (2009) evaluated the damage histories of a thick-walled sphere subjected to an internal pressure and a thermal gradient. They studied the creep stress and damage histories of thick-walled spheres using the material constant creep and creep rupture properties defined by the theta projection concept. Aleayoub and Loghman (2010) studied time-dependent creep stress redistribution analysis of thick-walled FGM spheres subjected to internal pressure and a uniform temperature field.

In this study, using equations of equilibrium, compatibility and stress-strain relations, a differential equation, containing creep strains, for radial stress is obtained. Ignoring creep strains in this differential equation, a closed-form solution for initial thermo-elastic stresses at zero time is presented. Pankaj (2011) investigated creep stresses for a thick isotropic spherical shell by finitesimal deformation under steady-state temperature and internal pressure by using Seth's transition theory. Marcadon (2011) presented mechanical modelling of the creep behavior of Hollow-Sphere Structures. Based on basic equations of steady-state creep of spherically symmetric problems, Nejad *et al.* (2011) presented a new exact closed form solution for creep stresses in isotropic and homogeneous thick spherical pressure vessels. Loghman *et al.* (2011) investigated time-dependent creep stress redistribution analysis of thick-walled spheres made of a functionally graded material (FGM) subjected to internal pressure. In another study, Loghman *et al.* (2012) investigated magneto-thermo-elastic creep behavior of thick-walled spheres made of functionally graded materials (FGM) placed in uniform magnetic and distributed temperature fields and subjected to internal pressure using the method of successive elastic solution. They developed a semi-analytical method in conjunction with Mendelson's method of successive elastic solution to obtain history of stresses and strains. Assuming that the creep response of the material is governed by Norton's law, Nejad *et al.* (2013) presented a new exact solution for steady state creep stresses of hollow thick-walled spherical shells subjected to internal and external pressure, made of functionally graded materials (FGMs). By using the method of successive elastic solution, Fesharaki *et al.* (2014) presented a semi-analytical solution for the time-dependent creep behavior of hollow spheres under thermomechanical loads.

In this study, assuming that the thermo-elastic creep response of the material is governed by Norton's law, an analytical solution is presented for the calculation of stresses and displacements of FGM thick-walled spherical pressure vessels. For the creep material behavior, the solution is asymptotic. For the stress analysis after creeping for a long time, an iterative procedure is necessary.

2. Geometry and loading condition, material properties and creep constitutive model

2.1. Geometry and loading condition

A thick-walled spherical vessel made of a functionally graded material with inner radius a, and outer radius b, subjected to internal pressure P_i and external pressure P_o and a distributed temperature field due to steady-state heat conduction from the inner surface to the outer surface of the vessel is considered.

2.2. Material properties

The material properties are assumed to be radially dependent

$$E(r) = E_i\Big(\frac{r}{a}\Big)^{n_1} \qquad \alpha(r) = \alpha_i\Big(\frac{r}{a}\Big)^{n_2} \qquad \lambda(r) = \lambda_i\Big(\frac{r}{a}\Big)^{n_3} \tag{2.1}$$

Here E_i, α_i and λ_i are the modulus of elasticity, linear expansion and thermal conductivity on the linear surface, $r = a$ and n_1, n_2 and n_3 are inhomogeneity constants determined empirically.

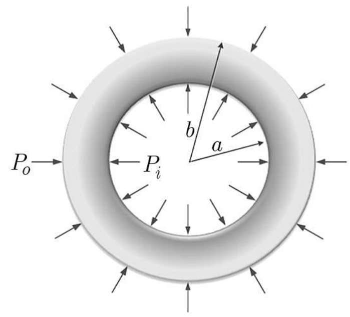

Fig. 1. Geometry and boundary conditions of the sphere

2.3. Creep constitutive model

For materials with creep behavior, Norton's law (1956) is used to describe the relations between the rates of stress $\dot{\sigma}_{ij}$ and strain $\dot{\varepsilon}_{ij}$ in the multi-axial form

$$\dot{\varepsilon}_{ij} = \frac{1+\nu}{E}\dot{\sigma}_{ij} - \frac{\nu}{E}\dot{\sigma}_{kk}\delta_{ij} + \frac{3}{2}D\sigma_{\mathit{eff}}^{(N-1)}S_{ij} \tag{2.2}$$

and

$$\begin{aligned}
S_{ij} &= \sigma_{ij} - \frac{1}{3}\sigma_{kk}\delta_{ij} \\
\sigma_{\mathit{eff}} &= \sqrt{\frac{3}{2}S_{ij}S_{ij}} = \frac{1}{\sqrt{2}}\sqrt{(\sigma_{rr}-\sigma_{\theta\theta})^2 + (\sigma_{rr}-\sigma_{\phi\phi})^2 + (\sigma_{\phi\phi}-\sigma_{\theta\theta})^2} = \sigma_{rr} - \sigma_{\theta\theta}
\end{aligned} \tag{2.3}$$

where D and N are material constants for creep. σ_{eff} is the effective stress, S_{ij} is the deviator stress tensor and σ_{rr} and $\sigma_{\theta\theta} = \sigma_{\phi\phi}$ are respectively the radial and circumferential stresses.

3. Heat conduction formulation

In the steady-state case, the heat conduction equation for the one-dimensional problem in spherical coordinates simplifies to

$$\frac{1}{r^2}\frac{\partial}{\partial r}\Big(r^2\lambda\frac{\partial T}{\partial r}\Big)=0 \tag{3.1}$$

We can determine the temperature distribution in the spherical vessel by solving Eq. (3.1) and applying appropriate boundary conditions. Equation (3.1) may be integrated twice to obtain the general solution

$$T(r)=A_1r^{-n_3-1}+A_2 \tag{3.2}$$

It is assumed that the inner surface is exposed to uniform heat flux, whereas the outer surface is exposed to airstream. To obtain the constants of integration A_1 and A_2, we introduce the following boundary conditions

$$-\lambda T'=\begin{cases} q_a & \text{for} \quad r=a \\ h_\infty(T-T_\infty) & \text{for} \quad r=b \end{cases} \tag{3.3}$$

where $T'=dT/dr$.

Applying these conditions to the general solution, we obtain

$$A_1=\frac{a^{n_3+2}q_a}{(n_3+1)\lambda_i} \qquad A_2=T_\infty+\frac{q_a}{h_\infty}\Big(\frac{a}{b}\Big)^2-\frac{a^{n_3+2}q_a}{\lambda_i(n_3+1)b^{n_3+1}} \tag{3.4}$$

Substituting the constants of integration A_1 and A_2 into the general solution, we obtain the temperature distribution

$$T(r)=T_\infty+\frac{q_a}{h_\infty}\Big(\frac{a}{b}\Big)^2+\frac{a^{n_3+2}q_a}{(n_3+1)\lambda_i}(r^{-n_3-1}-b^{-n_3-1}) \tag{3.5}$$

4. Formulation of the thermo-elastic creep analysis

4.1. Solution for linear elastic behavior of FGM thick spherical pressure vessels

For the stress analysis inan FGM thick spherical pressure vessel, having material creep behavior, solutions of the stresses at a time equal to zero (i.e. the initial stress state) are needed, which correspond to the solution of materials with linear elastic behavior. In this Section, equations to calculate such linear stresses in FGM thick spherical pressure vessel analytically will be given. The elastic stress-strain relations in each material read

$$\begin{aligned}\sigma_{rr}&=\frac{E}{(1+\nu)(1-2\nu)}[(1-\nu)\varepsilon_{rr}+2\nu\varepsilon_{\theta\theta}-(1+\nu)\alpha T]\\ \sigma_{\theta\theta}=\sigma_{\phi\phi}&=\frac{E}{(1+\nu)(1-2\nu)}[\varepsilon_{\theta\theta}+\nu\varepsilon_{rr}-(1+\nu)\alpha T]\end{aligned} \tag{4.1}$$

where σ_{rr} and $\sigma_{\theta\theta}=\sigma_{\phi\phi}$ are radial and circumferential stresses, respectively. Here E, ν and α are Young's modulus, Poisson's ratio and thermal expansion coefficient, respectively, and $T=T(r)$ is the temperature distribution in the sphere. The strain displacement relation is written as

$$\varepsilon_{rr}=\frac{du_r}{dr} \qquad \varepsilon_{\theta\theta}=\frac{u_r}{r} \tag{4.2}$$

where ε_{rr} and $\varepsilon_{\theta\theta} = \varepsilon_{\phi\phi}$ are radial and circumferential strains and u_r is the displacement in the r-direction. The equation of the stress equilibrium inside the FGM spherical pressure vessel is

$$\frac{d\sigma_{rr}}{dr} + \frac{2}{r}(\sigma_{rr} - \sigma_{\theta\theta}) = 0 \tag{4.3}$$

Using Eqs. (4.1)-(4.3), the essential differential equation for the displacement u_r can be obtained as

$$\begin{aligned} &\frac{d^2u_r}{dr^2} + \frac{n_1+2}{r}\frac{du_r}{dr} + \frac{\nu''n_1-2}{r^2}u_r = \nu'(Ar^{n_2-1} + Br^{n_2-n_3-2}) \\ &\nu' = \frac{1+\nu}{1-\nu} \qquad \nu'' = \frac{2\nu}{1-\nu} \end{aligned} \tag{4.4}$$

where

$$\begin{aligned} A &= (n_1+n_2)\Big[\frac{T_\infty\alpha_i}{a^{n_2}} + \frac{q_a\alpha_i}{h_\infty a^{n_2}}\Big(\frac{a}{b}\Big)^2\Big] - \frac{a^{n_3-n_2+2}q_a\alpha_i(n_1+1)b^{-n_3-1}}{\lambda_i(n_3+1)} \\ B &= \frac{(n_1+1)a^{n_3-n_2+2}q_a\alpha_i}{\lambda_i(n_3+1)} - \frac{a^{n_3-n_2+2}q_a\alpha_i}{\lambda_i} \end{aligned} \tag{4.5}$$

It is obvious that the homogeneous solution for Eq. (4.4) can be obtained by assuming

$$u_r = Cr^x \tag{4.6}$$

Substituting Eq. (4.6) into Eq. (4.4) one can obtain the following characteristic equation

$$x^2 + (n_1+1)x + (\nu''n_1 - 2) = 0 \tag{4.7}$$

The roots of Eq. (4.7) are

$$\begin{aligned} x_1 &= \frac{-(n_1+1) + \sqrt{(n_1+1)^2 - 4(\nu''n_1-2)}}{2} \\ x_2 &= \frac{-(n_1+1) - \sqrt{(n_1+1)^2 - 4(\nu''n_1-2)}}{2} \end{aligned} \tag{4.8}$$

For selected common values of $n_1 = \pm 0.4, \pm 0.8$ and $\nu = 0.292$ in this study, the discriminant of Eqs. (4.8) is always greater than zero; therefore, x_1 and x_2 are real and distinct. The homogeneous solution to Eq. (4.4) is then as follows

$$u_h = C_1r^{x_1} + C_2r^{x_2} \tag{4.9}$$

The particular solution to differential equation (4.4) can be obtained as

$$u_p = u_1r^{x_1} + u_2r^{x_2} \tag{4.10}$$

where

$$u_1 = \int \frac{-r^{x_2}P(r)}{W(r^{x_1}, r^{x_2})}\,dr \qquad u_2 = \int \frac{r^{x_1}P(r)}{W(r^{x_1}, r^{x_2})}\,dr \tag{4.11}$$

in which

$$P(r) = \nu'(Ar^{n_2-1} + Br^{n_2-n_3-2}) \tag{4.12}$$

is the expression on the right-hand side of Eq. (4.4), and W is defined as

$$W(r^{x_1}, r^{x_2}) = \begin{vmatrix} r^{x_1} & r^{x_2} \\ x_1r^{x_1-1} & x_2r^{x_2-1} \end{vmatrix} = (x_2 - x_1)r^{x_1+x_2-1} \tag{4.13}$$

Therefore, u_1 and u_2 can be obtained by the following integration

$$\begin{aligned}
u_1 &= \nu'\Big[\int \frac{-r^{x_2}Ar^{n_2-1}}{(x_2-x_1)r^{x_1+x_2-1}}\,dr + \int \frac{-r^{x_2}Br^{n_2-n_3-2}}{(x_2-x_1)r^{x_1+x_2-1}}\,dr\Big] \\
&= -\nu'\Big[\frac{Ar^{n_2-x_1+1}}{(x_2-x_1)(n_2-x_1+1)} + \frac{Br^{n_2-n_3-x_1}}{(x_2-x_1)(n_2-n_3-x_1)}\Big] \\
u_2 &= \nu'\Big[\int \frac{r^{x_1}Ar^{n_2-1}}{(x_2-x_1)r^{x_1+x_2-1}}\,dr + \int \frac{r^{x_1}Br^{n_2-n_3-2}}{(x_2-x_1)r^{x_1+x_2-1}}\,dr\Big] \\
&= \nu'\Big[\frac{Ar^{n_2-x_2+1}}{(x_2-x_1)(n_2-x_2+1)} + \frac{Br^{n_2-n_3-x_2}}{(x_2-x_1)(n_2-n_3-x_2)}\Big]
\end{aligned} \tag{4.14}$$

Substituting Eqs. (4.14) into Eq. (4.10), one can obtain the particular solution as

$$u_p = \nu'\Big[\frac{Ar^{n_2+1}}{(n_2-x_2+1)(n_2-x_1+1)} + \frac{Br^{n_2-n_3}}{(n_2-n_3-x_2)(n_2-n_3-x_1)}\Big] \tag{4.15}$$

The complete solution to Eq. (4.4) can be written as

$$u_r(r) = C_1r^{x_1} + C_2r^{x2} + \nu'\Big[\frac{Ar^{n_2+1}}{(n_2-x_2+1)(n_2-x_1+1)} + \frac{Br^{n_2-n_3}}{(n_2-n_3-x_2)(n_2-n_3-x_1)}\Big] \tag{4.16}$$

The corresponding stresses are

$$\begin{aligned}
\sigma_{rr} &= \frac{E_i\left(\frac{r}{a}\right)^{n_1}}{(1+\nu)(1-2\nu)}\Big\{C_1r^{x_1-1}[2\nu+(1-\nu)x_1] + C_2r^{x_2-1}[2\nu+(1-\nu)x_2] \\
&\quad + \frac{A\nu'[(n_2+1)(1-\nu)+2\nu]r^{n_2}}{(n_2-x_2+1)(n_2-x_1+1)} + \frac{B\nu'[(n_2-n_3)(1-\nu)+2\nu]r^{n_2-n_3-1}}{(n_2-n_3-x_2)(n_2-n_3-x_1)} \\
&\quad - (1+\nu)\Big[\Big(\frac{T_\infty\alpha_i}{a^{n_2}} + \frac{q_a\alpha_i}{h_\infty a^{n_2}}\Big(\frac{a}{b}\Big)^2 - \frac{a^{n_3-n_2+2}q_a\alpha_i b^{-n_3-1}}{\lambda_i(n_3+1)}\Big)r^{n_2} \\
&\quad + \frac{a^{n_3-n_2+2}q_a\alpha_i}{\lambda_i(n_3+1)}r^{n_2-n_3-1}\Big]\Big\} \\
\sigma_{\theta\theta} &= \frac{E_i\left(\frac{r}{a}\right)^{n_1}}{(1+\nu)(1-2\nu)}\Big\{C_1r^{x_1-1}(1+x_1\nu) + C_2r^{x_2-1}(1+\nu x_2) \\
&\quad + \frac{A\nu'[(n_2+1)\nu+1]r^{n_2}}{(n_2-x_2+1)(n_2-x_1+1)} + \frac{B\nu'[(n_2-n_3)\nu+1]r^{n_2-n_3-1}}{(n_2-n_3-x_2)(n_2-n_3-x_1)} \\
&\quad - (1+\nu)\Big[\Big(\frac{T_\infty\alpha_i}{a^{n_2}} + \frac{q_a\alpha_i}{h_\infty a^{n_2}}\Big(\frac{a}{b}\Big)^2 - \frac{a^{n_3-n_2+2}q_a\alpha_i b^{-n_3-1}}{\lambda_i(n_3+1)}\Big)r^{n_2} \\
&\quad + \frac{a^{n_3-n_2+2}q_a\alpha_i}{\lambda_i(n_3+1)}r^{n_2-n_3-1}\Big]\Big\}
\end{aligned} \tag{4.17}$$

To determine the unknown constants C_1 and C_2 in each material, boundary conditions have to be used, which are

$$\sigma_{rr} = \begin{cases} -P_i & \text{for} \quad r=a \\ -P_o & \text{for} \quad r=b \end{cases} \tag{4.18}$$

The unknown constants C_1 and C_2 are given in Appendix.

4.2. Solution for creep behavior of FGM thick spherical pressure vessel

The relations between the rates of strain and displacement are

$$\dot{\varepsilon}_{rr} = \frac{d\dot{u}_r}{dr} \qquad \dot{\varepsilon}_{\theta\theta} = \frac{\dot{u}_r}{r} \tag{4.19}$$

And the equilibrium equation of the stress rate is

$$\frac{d\dot{\sigma}_{rr}}{dr} + \frac{2}{r}(\dot{\sigma}_{rr} - \dot{\sigma}_{\theta\theta}) = 0 \tag{4.20}$$

The relations between the rates of stress and strain are

$$\begin{aligned} \dot{\sigma}_{rr} &= \frac{E}{(1+\nu)(1-2\nu)}[(1-\nu)\dot{\varepsilon}_{rr} + 2\nu\dot{\varepsilon}_{\theta\theta}] - \frac{3}{2}\frac{E}{(1-\nu)(1-2\nu)}D\sigma_{\mathit{eff}}^{(N-1)}S'_{rr} \\ \dot{\sigma}_{\theta\theta} &= \frac{E}{(1+\nu)(1-2\nu)}[\dot{\varepsilon}_{\theta\theta} + \nu\dot{\varepsilon}_{rr}] - \frac{3}{2}\frac{E}{(1-\nu)(1-2\nu)}D\sigma_{\mathit{eff}}^{(N-1)}S'_{\theta\theta} \end{aligned} \tag{4.21}$$

where

$$S'_{rr} = (1-\nu)S_{rr} + 2\nu S_{\theta\theta} \qquad S'_{\theta\theta} = S_{\theta\theta} + \nu S_{rr} \tag{4.22}$$

Using Eqs. (4.19)-(4.22), the essential differential equation for the displacement rate $\dot{u}_r$ in FGM spherical vessel can be obtained as

$$\begin{aligned} &\frac{d^2\dot{u}_r}{dr^2} + \frac{d\dot{u}_r}{dr}\Big(\frac{2}{r} + \frac{d\ln E}{dr}\Big) + \frac{\dot{u}_r}{r}\Big(\frac{2\nu}{1-\nu}\frac{d\ln E}{dr} - \frac{2}{r}\Big) = \frac{d\ln E}{dr}\frac{3}{2(1-\nu)}D\sigma_{\mathit{eff}}^{(N-1)}S'_{rr} \\ &\qquad + \frac{1}{1-\nu}\frac{d}{dr}\Big(\frac{3}{2}D\sigma_{\mathit{eff}}^{(N-1)}S'_{rr}\Big) + \frac{3}{r(1-\nu)}D\sigma_{\mathit{eff}}^{(N-1)}(S'_{rr} - S'_{\theta\theta}) \end{aligned} \tag{4.23}$$

In general, the quantities σ_{eff}, S'_{rr} and $S'_{\theta\theta}$ are very complicated functions of the coordinate r, even in an implicit function form. Therefore, it is almost impossible to find an exact analytical solution to Eq. (4.23). We can alternatively find an asymptotical solution to Eq. (4.23). At first, we assume that σ_{eff}, S'_{rr} and $S'_{\theta\theta}$ are constant, i.e. they are independent of the coordinate r

$$\frac{d^2\dot{u}_r}{dr^2} + \frac{1+n_1}{r}\frac{d\dot{u}_r}{dr} - \frac{\nu n_1 - 1}{r^2}\dot{u}_r = \frac{3}{2}\frac{D}{r}\sigma_{\mathit{eff}}^{(N-1)}[S'_{rr}(1+n_1-v') + S'_{\theta\theta}(n_1\nu' - 1 + \nu')] \tag{4.24}$$

The homogeneous solution to Eq. (4.24) is then

$$u_h = D_1 r^{x_1} + D_2 r^{x_2} \tag{4.25}$$

The particular solution to differential equation (4.24) can be obtained as

$$u_p = u'_1 r^{x_1} + u'_2 r^{x_2} \tag{4.26}$$

where

$$\begin{aligned} u'_1 &= \int \frac{-r^{x_2}Hr^{-1}}{(x_2 - x_1)r^{x_1+x_2-1}}\,dr \qquad u'_2 = \int \frac{r^{x_1}Hr^{-1}}{(x_2 - x_1)r^{x_1+x_2-1}}\,dr \\ H &= \frac{3}{2}\frac{D}{(1-\nu)}\sigma_{\mathit{eff}}^{(N-1)}[S'_{rr}(2+n_1) - 2S'_{\theta\theta}] \end{aligned} \tag{4.27}$$

The complete solution to Eq. (4.24) can be written as

$$\dot{u}_r(r) = D_1 r^{x_1} + D_2 r^{x_2} + \frac{3}{2}\frac{Dr\sigma_{\mathit{eff}}^{(N-1)}[(n_1+2)S'_{rr} - 2S'_{\theta\theta}]}{(1-\nu)[n_1(\nu''-1) - 2]} \tag{4.28}$$

where the unknown constants D_1 and D_2 can be determined from the boundary conditions. The corresponding stress rates are

$$\begin{aligned}\dot{\sigma}_{rr} &= \frac{E_i\left(\frac{r}{a}\right)^{n_1}}{(1-2\nu)(1+\nu)}\Big\{D_1 r^{x_1-1}[2\nu+(1-\nu)x_1] + D_2 r^{x_2-1}[2\nu+(1-\nu)x_2] \\ &\quad + \frac{3}{2}\frac{\nu'}{n_1(\nu''-1)-2} D\sigma_{\mathit{eff}}^{(N-1)}[(n_1+2)S'_{rr} - 2S'_{\theta\theta}] - \frac{3}{2}D\sigma_{\mathit{eff}}^{(N-1)}S'_{rr}\Big\} \\ \dot{\sigma}_{\theta\theta} &= \frac{E_i\left(\frac{r}{a}\right)^{n_1}}{(1-2\nu)(1+\nu)}\Big\{D_1 r^{x_1-1}(1+\nu x_1) + D_2 r^{x_2-1}(1+\nu x_2) \\ &\quad + \frac{3}{2}\frac{1+\nu}{n_1(\nu''-1)-2} D\sigma_{\mathit{eff}}^{(N-1)}[(n_1+2)S'_{rr} - 2S'_{\theta\theta}] - \frac{3}{2}D\sigma_{\mathit{eff}}^{(N-1)}S'_{\theta\theta}\Big\}\end{aligned} \tag{4.29}$$

To determine the unknown constants D_1 and D_2 in each material, boundary conditions have to be used. Since the inside and outside pressures do not change with time, the boundary conditions for stress rates on the inner and outer surfaces may be written as

$$\dot{\sigma}_{rr} = \begin{cases} 0 & \text{for} \quad r=a \\ 0 & \text{for} \quad r=b \end{cases} \tag{4.30}$$

The unknown constants D_1 and D_2 are given in Appendix. When the stress rate is known, the calculation of stresses at any time t_i should be performed iteratively

$$\sigma_{ij}^{(i)}(r,t_i) = \sigma_{ij}^{(i-1)}(r,t_{i-1}) + \dot{\sigma}_{ij}^{(i)}(r,t_i)dt^{(i)} \qquad t_i = \sum_{k=0}^{i} dt^{(k)} \tag{4.31}$$

To obtain a generally useful solution, a higher-order approximation of σ_{eff}, S'_{rr} and $S'_{\theta\theta}$ should be made

$$\begin{aligned}\sigma_{\mathit{eff}}(r) &= \sigma_{\mathit{eff}}(\overline{r}) + \frac{\frac{d}{dr}[\sigma_{\mathit{eff}}(r)]\Big|_{r=\overline{r}}}{1!}(r-\overline{r}) + \frac{\frac{d^2}{dr^2}[\sigma_{\mathit{eff}}(r)]\Big|_{r=\overline{r}}}{2!}(r-\overline{r})^2 + \frac{\frac{d^3}{dr^3}[\sigma_{\mathit{eff}}(r)]\Big|_{r=\overline{r}}}{3!}(r-\overline{r})^3 \\ S'_{rr}(r) &= S'_{rr}(\overline{r}) + \frac{\frac{d}{dr}[S'_{rr}(r)]\Big|_{r=\overline{r}}}{1!}(r-\overline{r}) + \frac{\frac{d^2}{dr^2}[S'_{rr}(r)]\Big|_{r=\overline{r}}}{2!}(r-\overline{r})^2 + \frac{\frac{d^3}{dr^3}[S'_{rr}(r)]\Big|_{r=\overline{r}}}{3!}(r-\overline{r})^3 \\ S'_{\theta\theta}(r) &= S'_{\theta\theta}(\overline{r}) + \frac{\frac{d}{dr}[S'_{\theta\theta}(r)]\Big|_{r=\overline{r}}}{1!}(r-\overline{r}) + \frac{\frac{d^2}{dr^2}[S'_{\theta\theta}(r)]\Big|_{r=\overline{r}}}{2!}(r-\overline{r})^2 + \frac{\frac{d^3}{dr^3}[S'_{\theta\theta}(r)]\Big|_{r=\overline{r}}}{3!}(r-\overline{r})^3\end{aligned} \tag{4.32}$$

where $\overline{r}$ is the center point of the wall thickness in the following analysis.

5. Numerical results and discussion

In the previous Sections, the analytical solution of creep stresses for FGM thick-walled spherical vessels subjected to uniform pressures on the inner and outer surfaces has been obtained. In this Section, some profiles are plotted for the radial displacement, radial stress and circumferential stress as a function of the radial direction and time. An FGM thick-walled spherical vessel with creep behavior under internal and external pressure is considered. Radii of the sphere are $a = 20\,\mathrm{mm}$, $b = 40\,\mathrm{mm}$. Mechanical properties of the sphere such as modulus of elasticity, linear expansion and thermal conductivity are assumed to be varying through the radius. The inhomogeneity constants $n_1 = n_2 = n_3 = n$, and n ranges from -0.8 to $+0.8$. The following data for loading and material properties are used in this investigation: $E_i = 207\,\mathrm{GPa}$,

$\nu = 0.292$, $\alpha_i = 10.8 \cdot 10^{-6}\,\mathrm{K}^{-1}$, $P_i = 80\,\mathrm{MPa}$, $P_o = 0\,\mathrm{MPa}$, $q_a = 500\,\mathrm{W/m^2}$, $\lambda_i = 43\,\mathrm{W/(m^\circ C)}$, $h_\infty = 6.5\,\mathrm{W/(m^2\,{}^\circ C)}$, $T_\infty = 25^\circ\mathrm{C}$, $D = 1.4 \cdot 10^{-8}$, $N = 2.25$.

The distributions of creep stress components σ_{rr} and $\sigma_{\theta\theta}$ after 10h of creeping for values of $n = \pm 0.4$, ± 0.8 are plotted in Fig. 2. It must be noted from Fig. 2a that the radial stress increases as n decreases, and that the radial stress for different values of n is compressive. The absolute maximums of radial stress occur at the outer edge. It means the maximum shear stress, which is $\tau_{max} = (\sigma_{\theta\theta} - \sigma_{rr})/2$ for each value of n will be very high on the outer surface of the vessel.

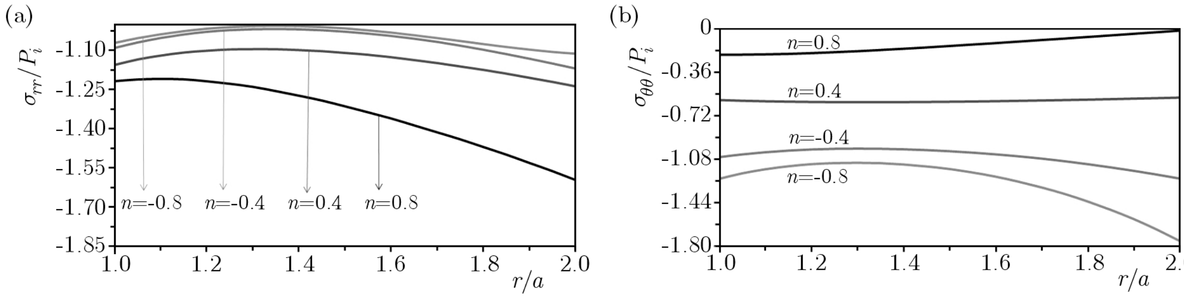

Fig. 2. Normalized radial and circumferential stresses versus dimensionless radius after 10h of creeping

It is also clear from Fig. 2a that the maximum changes in the radial stresses with time take place for the material $n = 0.8$ and the minimum changes occur for $n = \pm 0.4$, -0.8. The circumferential stress shown in Fig. 2b remains compressive throughout and is observed to decrease with the increasing radius for $n = -0.4$, -0.8, and reaches the minimum value somewhere towards the inner radius followed by an increase with a further increase in the radius. It also can be seen from Fig. 2b that the circumferential stress remains compressive throughout the cylinder for $n = +0.8$ with the maximum value at the inner radius and zero at the outer radius under the imposed boundary conditions, and that the minimum changes occur for $n = 0.4$.

Time dependent stress redistributions at the point $r = 30\,\mathrm{mm}$ are shown in Fig. 3. It can be seen in Fig. 3a that the radial stress increases as time increases. It must be noted from Fig. 3b that, for $n = +0.4$, $+0.8$ the circumferential stress decreases as time increases, whereas for $n = -0.4$, -0.8 the circumferential stress increases as time increases.

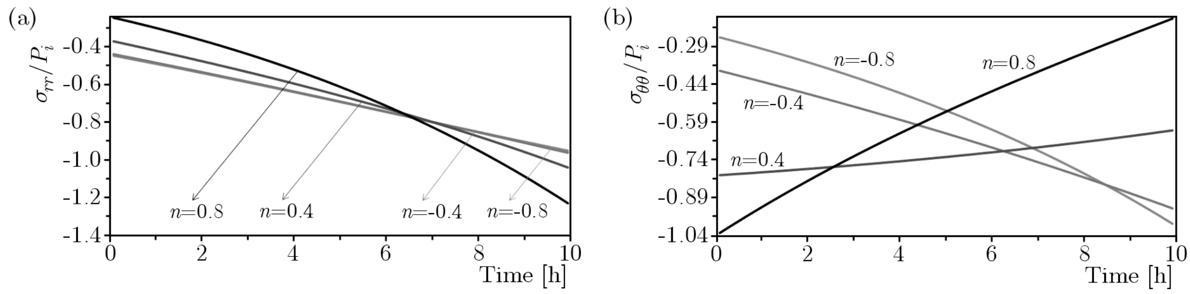

Fig. 3. Time-dependent radial and circumferential stresses at the point $r = 30\,\mathrm{mm}$

The radial displacement along the radius is plotted in Fig. 4a. There is an increase in the value of the radial displacement as n increases and the maximum value of radial displacement occurs at the outer edge. The time-dependent radial displacement at the point $r = 30\,\mathrm{mm}$ is shown in Fig. 4b. Figure 4b shows that the radial displacement redistribution at the point

$r = 30\,\text{mm}$ increases as time increases for $n = -0.4$, -0.8, while for $n = +0.4$, $+0.8$ the radial displacement decreases as time increases. Figure 5 shows the effect of adding external pressure to the radial and circumferential stresses. It can be seen in Fig. 5 that the radial stress decreases as the external pressure increases while the circumferential stress increases as the external pressure increases.

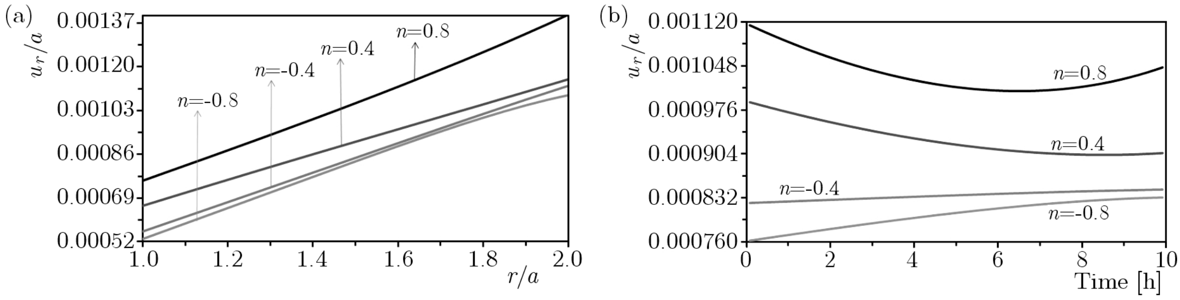

Fig. 4. (a) Normalized radial displacement versus dimensionless radius after 10h of creeping, (b) time-dependent radial displacement at the point $r = 30\,\text{mm}$

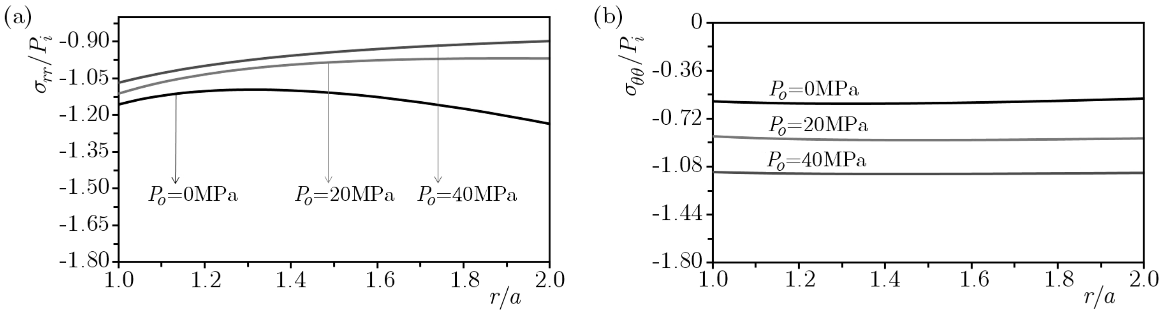

Fig. 5. The effect of adding external pressure to the radial and circumferential stresses

Temperature distribution of four different values of n is shown in Fig. 6. It can be seen in Fig. 6 that the maximum values of temperature occur at the inner radius for $n = -0.8$ and that the minimum values of temperature occur at the outer radius for all values of n under the imposed boundary conditions.

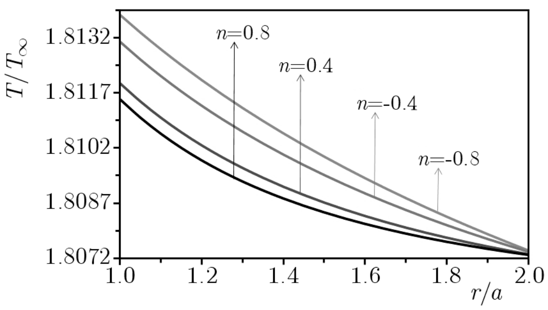

Fig. 6. Temperature distribution of FGM thick-walled spherical vessel for values of $n = \pm 0.4, \pm 0.8$

6. Conclusions

In this paper, assuming that the thermo-creep response of the material is governed by Norton's law, an analytical solution is presented for the calculation of stresses and displacements of FGM thick-walled spherical pressure vessels. For the stress analysis inasphere, having material creep behavior, the solutions of the stresses at a time equal to zero (i.e. the initial stress state) are needed, which corresponds to the solution of materials with linear elastic behavior. It is assumed that the material properties change as graded in the radial direction to a power law function. To show the effect of inhomogeneity on the stress distributions, different values are considered for inhomogeneity constants. The pressure, inner radius and outer radius are considered constant. The heat conduction equation for the one-dimensional problem in spherical coordinates is used to obtain temperature distribution in the sphere. For the creep material behavior, the solution is asymptotic. For the stress analysis after creeping for a long time, the iterative procedure is necessary. It could be seen that the inhomogeneity constants have significant influence on the distributions of the creep stresses and radial displacement. By increasing the grading parameter n, the normalized radial stress increases due to internal pressure and temperature distribution while the normalized circumferential stress decreases (Fig. 2). The absolute maximums of radial and circumferential stresses occur at the outer edge. It must be noted that the radial and circumferential stresses at the point $r = 30$ mm for different values of n are compressive. As can be seen, the absolute maximum of radial stress at the point $r = 30$ mm occurs at a time equal to 10 hours for different values of n, whereas for $n = +0.4$, $+0.8$ the absolute maximum of circumferential stress occurs at a time equal to zero, and for $n = -0.4$, -0.8 the absolute maximum of circumferential stress occurs at a time equal to 10 hours.

Appendix

The unknown constants in Eqs. (4.17) are

$$
\begin{aligned}
C_1 &= \frac{-P_i(1+\nu)(1-2\nu)}{E_i[2\nu+(1-\nu)x_1]a^{x_1-1}} - \frac{C_2[2\nu+(1-\nu)x_2]a^{x_2-1}}{[2\nu+(1-\nu)x_1]a^{x_1-1}} \\
&- \frac{A\nu'[(n_2+1)(1-\nu)+2\nu]a^{n_2}}{(n_2-x_2+1)(n_2-x_1+1)[2\nu+(1-\nu)x_1]a^{x_1-1}} \\
&- \frac{B\nu'[(n_2-n_3)(1-\nu)+2\nu]a^{n_2-n_3-1}}{(n_2-n_3-x_2)(n_2-n_3-x_1)[2\nu+(1-\nu)x_1]a^{x_1-1}} \\
&+ \frac{1+\nu}{[2\nu+(1-\nu)x_1]a^{x_1-1}}\Big\{\Big[\frac{T_\infty\alpha_i}{a^{n_2}} + \frac{q_a\alpha_i}{h_\infty a^{n_2}}\Big(\frac{a}{b}\Big)^2 - \frac{a^{n_3-n_2+2}q_a\alpha_i b^{-n_3-1}}{\lambda_i(n_3+1)}\Big]a^{n_2} \\
&+ \frac{aq_a\alpha_i}{\lambda_i(n_3+1)}\Big\}
\end{aligned}
\tag{A.1}
$$

$$
\begin{aligned}
C_2 &= \frac{\Big(P_ib^{x_1-1} - \frac{P_oa^{n_1+x_1-1}}{b^{n_1}}\Big)(1+\nu)(1-2\nu)}{E_i[2\nu+(1-\nu)x_2](b^{x_2-1}a^{x_1-1}-b^{x_1-1}a^{x_2-1})} \\
&- \frac{A\nu'[(n_2+1)(1-\nu)+2\nu](n_2+\nu'+1)(b^{n_2}a^{x_1-1}-b^{x_1-1}a^{n_2})}{(n_2-x_2+1)(n_2-x_1+1)[2\nu+(1-\nu)x_2](b^{x_2-1}a^{x_1-1}-b^{x_1-1}a^{x_2-1})} \\
&- \frac{B\nu'[(n_2-n_3)(1-\nu)+2\nu](b^{n_2-n_3-1}a^{x_1-1}-b^{x_1-1}a^{n_2-n_3-1})}{(n_2-n_3-x_2)(n_2-n_3-x_1)[2\nu+(1-\nu)x_2](b^{x_2-1}a^{x_1-1}-b^{x_1-1}a^{x_2-1})} \\
&+ \frac{1+\nu}{[2\nu+(1-\nu)x_2](b^{x_2-1}a^{x_1-1}-b^{x_1-1}a^{x_2-1})}\Big\{\Big[\frac{T_\infty\alpha_i}{a^{n_2}} + \frac{q_a\alpha_i}{h_\infty a^{n_2}}\Big(\frac{a}{b}\Big)^2 \\
&- \frac{a^{n_3-n_2+2}q_a\alpha_i b^{-n_3-1}}{\lambda_i(n_3+1)}\Big](b^{n_2}a^{x_1-1}-b^{x_1-1}a^{n_2}) \\
&+ \frac{q_a\alpha_i}{\lambda_i(n_3+1)}(b^{n_2-n_3+1}a^{n_3-n_2+x_1+1}-b^{x_1-1}a)\Big\}
\end{aligned}
\tag{A.2}
$$

The unknown constants in Eqs. (4.29) are

$$D_1 = \frac{\frac{3}{2}\nu' D\sigma_{\mathit{eff}}^{(N-1)}(a^{x_2-1} - b^{x_2-1})[(n_1+2)S'_{rr} - 2S'_{\theta\theta}]}{[2\nu + (1-\nu)x_1][n_1(\nu''-1) - 2](a^{x_1-1}b^{x_2-1} - b^{x_1-1}a^{x_2-1})} + \frac{\frac{3}{2}D\sigma_{\mathit{eff}}^{(N-1)}S'_{rr}(b^{x_2-1} - a^{x_2-1})}{[2\nu + (1-\nu)x_1](a^{x_1-1}b^{x_2-1} - b^{x_1-1}a^{x_2-1})} \tag{A.3}$$

$$D_2 = \frac{\frac{3}{2}\nu' D\sigma_{\mathit{eff}}^{(N-1)}(a^{x_1-1} - b^{x_1-1})[(n_1+2)S'_{rr} - 2S'_{\theta\theta}]}{[2\nu + (1-\nu)x_2][n_1(\nu''-1) - 2](a^{x_2-1}b^{x_1-1} - b^{x_2-1}a^{x_1-1})} + \frac{\frac{3}{2}D\sigma_{\mathit{eff}}^{(N-1)}S'_{rr}(b^{x_1-1} - a^{x_1-1})}{[2\nu + (1-\nu)x_2](a^{x_2-1}b^{x_1-1} - b^{x_2-1}a^{x_1-1})} \tag{A.4}$$

References

1. Alashti R.A., Khorsand M., Tarahhomi M.H., 2013, Three-dimensional asymmetric thermoelastic analysis of a functionally graded rotating cylindrical shell, *Journal of Theoretical and Applied Mechanics*, **51**, 1, 143-158
2. Aleayoub S.M.A., Loghman A., 2010, Creep stress redistribution analysis of thick-walled FGM spheres, *Journal of Solid Mechanics*, **2**, 10, 115-128
3. Arya V.K., Debnath K.K, Bhatnagar N.S., 1980, The spherical vessel with anisotropic creep properties considering large strains, *International Journal of Non-Linear Mechanics*, **15**, 185-193
4. Bhatnagar N.S., Arya V.K., 1975, Creep of thick-walled spherical vessels under internal pressure considering large strains, *Indian Journal of Pure and Applied Mathematics*, **6**, 10, 1080-1089
5. Bhatnagar N.S., Pradnya K., Arya V.K., 1987, Primary creep analysis of an anisotropic thick-walled spherical shell, *Journal of Pressure Vessel Technology*, **109**, 347-351
6. Finnie I., Heller W.R., 1959, *Creep of Engineering Materials*, McGraw-Hill Book Co. Inc., New York
7. Ghannad M., Nejad M.Z., 2013, Elastic solution of pressurized clamped-clamped thick cylindrical shells made of functionally graded materials, *Journal of Theoretical and Applied Mechanics*, **51**, 4, 1067-1079
8. Fesharaki J., Loghman A., Yazdipoor M., Golabi S., 2014, Semi-analytical solution of time-dependent thermomechanical creep behavior of FGM hollow spheres, *Mechanics of Time-Dependent Materials*, **18**, 41-53
9. Johnson A.E., Khan B., 1963, Creep of metallic thick-walled spherical vessels subject to pressure and radial thermal gradient at elevated temperatures, *International Journal of Mechanical Sciences*, **5**, 507-532
10. Kao R., 1981, Nonlinear creep buckling analysis of initially imperfect shallow spherical shells, *Computers and Structures*, **14**, 1/2, 111-122
11. Loghman A., Aleayoub S.M.A., Hasani Sadi M., 2012, Time-dependent magnetothermoelastic creep modeling of FGM spheres using method of successive elastic solution, *Applied Mathematical Modelling*, **36**, 836-845
12. Loghman A., Ghorbanpourarani A., Aleayoub S.M.A., 2011, Time-dependent creep stress redistribution analysis of thick-walled functionally graded spheres, *Mechanics of Time-Dependent Materials*, **15**, 353-365
13. Loghman A., Shokouhi N., 2009, Creep damage evaluation of thick-walled spheres using a long--term creep constitutive model, *Journal of Mechanical Science and Technology*, **23**, 2577-2582

14. Marcadon V., 2011, Mechanical modelling of the creep behaviour of hollow-sphere structures, *Computational Materials Science*, **50**, 3005-3015
15. Miller G.K., 1995, Stresses in a spherical pressure vessel undergoing creep and dimensional changes, *International Journal of Solids and Structures*, **32**, 14, 2077-2093
16. Miyazaki N., Yagawa G., Ando Y., 1977, A parametric analysis of creep buckling of a shallow spherical shell by the finite element method, *Nuclear Engineering and Design*, **41**, 257-263
17. Nejad M.Z., Hoseini Z., Niknejad A., Ghannad M., 2011, A new analytical solution for creep stresses in thick-walled spherical pressure vessels, *Journal of Basic and Applied Scientific Research*, **1**, 11, 2162-2166
18. Nejad M.Z., Hoseini Z., Taghizadeh T., Niknejad A., 2013, Closed-form analytical solution for creep stresses of pressurized functionally graded material thick spherical shells, *Advanced Science Letters*, **19**, 2, 464-467
19. Noda N., Ootao Y., Tanigawa Y., 2012, Transient thermoelastic analysis for a functionally graded circular disk with piecewise power law, *Journal of Theoretical and Applied Mechanics*, **50**, 3, 831-839
20. Pankaj T., 2011, Creep transition stresses of a thick isotropic spherical shell by finitesimal deformation under steady-state of temperature and internal pressure, *Thermal Science*, **15**, 2, 157-165
21. Penny R.K., 1967, The creep of spherical shells containing discontinuities, *International Journal of Mechanical Sciences*, **5**, 373-388
22. Sakaki T., Kuroki T., Sugimoto K., 1990, Creep of a hollow sphere, *Journal of Applied Mechanics, Transactions ASME*, **57**, 276-281
23. Xirouchakis P.C., Jones N., 1979, Axisymmetric and bifurcation creep buckling of externally pressurized spherical shells, *International Journal of Solids and Structures*, **16**, 131-148
24. You L.H., Ou H., Zheng Z.Y., 2008, Steady-state creep analysis of thick-walled spherical pressure vessels with varying creep properties, *Journal of Pressure Vessel Technology*, **130**, 0145011--0145015

Manuscript received March 8, 2014; accepted for print July 15, 2015

JOURNAL OF THEORETICAL
AND APPLIED MECHANICS
53, 4, pp. 1067-1081, Warsaw 2015
DOI: 10.15632/jtam-pl.53.4.1067

LINEAR STABILITY ANALYSIS FOR FERROMAGNETIC FLUIDS IN THE PRESENCE OF MAGNETIC FIELD, COMPRESSIBILITY, INTERNAL HEAT SOURCE AND ROTATION THROUGH A POROUS MEDIUM

Kapil Kumar
Department of Mathematics and Statistics, Gurukula Kangri Vishwavidyalaya, Haridwar, India
e-mail: kkchaudhary000@gmail.com

V. Singh
Department of Applied Sciences, Moradabad Institute of Technology, Moradabad, India

Seema Sharma
Department of Mathematics and Statistics, Gurukula Kangri Vishwavidyalaya, Haridwar, India

The effects of magnetic field and heat source strength on thermal convection of a compressible rotating ferromagnetic fluid through a porous medium are investigated theoretically using linear stability theory. A normal mode analysis method is employed to find solutions for the fluid layer confined between parallel planes with free boundaries. The cases of stationary and oscillatory instabilities are discussed. For the stationary state, compressibility, medium porosity and temperature gradient due to heat source have destabilizing effects, whereas rotation and ratio of magnetic permeability delay the onset of convection. The magnetic field and medium permeability have both stabilizing and destabilizing effects under certain conditions. The variations in the stationary critical thermal Rayleigh number and neutral instability curves in (Ra_1, x)-plane for various values of physical parameters are shown graphically to depict the stability characteristics. The sufficient conditions for the non-existence of overstability are obtained and the principle of exchange of stabilities holds true in the absence of magnetic field and rotation under certain conditions.

Keywords: ferrofluids, rotation, magnetic field, porous medium, heat source, compressibility

1. Introduction

Ferrofluids (also known as magnetic fluids) are electrically non-conducting colloidal suspensions of fine solid ferromagnetic particles or nanoparticles (iron, nickel, cobalt etc.) and their study opens a wide range of attractive and futuristic applications in various engineering and medical science purposes like vacuum technology, instrumentation, lubrication mechanism, acoustics theory, recovery of metals, detection of tumours, drug delivery to a target site, magnetic fluid bearings, non-destructive testing, sensors and actuators, sorting of industrial scrap metals. They also serve as a challenging subject for scientists interested in the basics of fluid mechanics. The ferromagnetic nanoparticles are coated with a surfactant to prevent their agglomeration. Rosensweig (1985, 1987) discussed the fundamental concepts related to the use of ferrofluids and provides a comprehensive and detailed application of ferrohydrodynamics (also known as FHD) in various commercial usages such as novel zero-leakage rotary shaft seals used in computer disk drives (Bailey, 1983); semiconductor manufacturing (Moskowitz, 1975); pressure seals for compressor and blowers (Rosensweig, 1985); tracer of blood flow in non-invasive circulatory measurements (Newbower, 1972) and in loudspeakers to conduct heat away from the speakers coil (Hathaway, 1979). The thermal instability problem of ferrofluids is a current topic of frontier research and also attractive from a theoretical point of view. Thus, the overall field of ferrofluid research has a highly interdisciplinary character bringing physicists, engineers, chemists and mathematicians together. Finlayson (1970) discussed the convective instability problem of a ferromagnetic fluid layer heated from below when under the effect of a uniform vertical magnetic field with or without considering the effect of body force (gravity force). He quantified that the magnetization of a ferromagnetic fluid depends upon the magnetic field strength, temperature gradient and density of fluid, and is known as ferroconvection (which is very similar to Bénard convection as noted by Chandrasekhar, 1981). Lalas and Carmi (1971) studied a thermoconvective instability problem of ferrofluids without considering buoyancy effects, whereas the problem of thermal convection in a ferromagnetic fluid saturating a porous medium under the influence of rotation and/or suspended dust particles was simulated by Sunil *et al.* (2005a,b). Copious literatures (Odenbach, 2002; Neuringer and Rosensweig, 1964; Berkovsky and Bashtovoy, 1996; Sherman and Sutton, 1962) are available to deal with the hydrodynamic and hydromagnetic instability problems of ferrofluids and forcing further investigation in the whole research area.

The thermo-convective transport phenomenon in a rotating porous medium is of significant importance in modern science and engineering problems such as rotating machinery, crystal growth, food processing engineering, centrifugal filtration processes, biomechanics and in thermal power plants (to generate electricity by rotation of turbine blades). Magneto-hydrodynamics (MHD) theory of electrically conducting fluids has several scientific and practical applications in atmospheric physics, astronomy and astrophysics, space sciences, etc. Magnetic field is also used in several clinical areas such as neurology and orthopaedics for probing and curing the internal organs of the body in several diseases like tumours detection, heart and brain diseases, stroke damage, etc. Aggarwal and Makhija (2014) studied the effect of Hall current on thermal instability of ferromagnetic fluid in the presence of horizontal magnetic field through a porous medium. Spiegel and Veronis (1960) simplified the set of equations for compressible fluids by assuming that the vertical height of the fluid is much smaller than the scale height as defined by them, and the fluctuations in density, temperature and pressure did not exceed their total static variations. The thermal instability problem for a compressible fluid in the presence of rotation and magnetic field was studied by Sharma (1997).

Detailed investigations related with the problem of convection through various porous mediums were supplied and very well defined by Nield and Bejan (2006). The fluid flow problems saturating a porous medium plays a key role in petroleum and chemical industry, geophysical fluid dynamics, filtering technology, recovery of crude oil from Earth's interior, etc. Kumar *et al.* (2014a,b, 2015) addressed theoretically the thermal instability problems of couple-stress and ferromagnetic fluids by considering the effects of various parameters such as rotation, suspended particles, compressibility, heat source and variable gravity through Darcy and/or Brinkman porous medium. The physical properties of comets, meteorites and interplanetary dust strongly suggest the importance of porosity in astrophysical situations (McDonnel, 1978). The governing hydrodynamic equations of motion are solved using a regular perturbation technique. The objective of the present study is to discuss the influence of rotation, compressibility and heat source on thermal stability of a ferromagnetic fluid layer heated from below through a porous medium using linear stability analysis. The understanding of rotating ferrofluid instability problems plays a key role in microgravity environmental applications. Some existing results are recovered as a particular case of the present study.

2. Governing equations

Consider an infinite horizontal porous layer saturated with a non-conducting compressible ferromagnetic fluid confined between the parallel planes $z = 0$ and $z = d$ subject to a uniform vertical magnetic field of intensity $\mathbf{H}(0, 0, H)$ and uniform vertical rotation $\mathbf{\Omega}(0, 0, \Omega)$. A Cartesian frame of reference is chosen with the z-axis directed vertically upwards and the x- and y-axes at the lower boundary plane. It is also assumed that the flow in the porous medium is governed by

Darcy's law in the equation of motion with medium porosity ε and permeability k_1 for the case of free and perfect conducting boundaries. The geometrical configuration of the present problem is shown in Fig. 1.

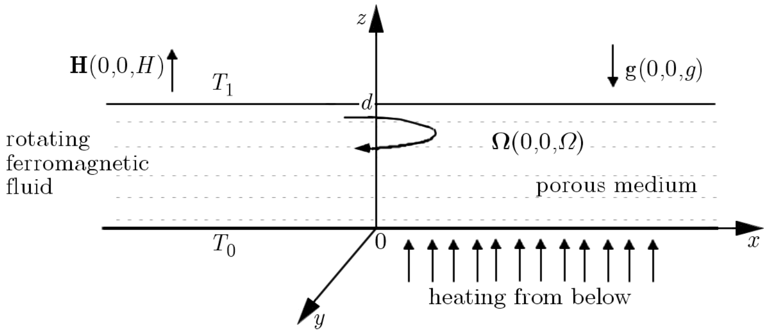

Fig. 1. Geometrical sketch of the physical problem

The basic governing equations of motion, continuity, energy and Maxwell equations for a magnetized ferrofluid saturating a homogenous porous medium with constant viscosity under Boussinesq approximation are given as follows (Finlayson, 1970; Rosensweig, 1985; Sunil *et al.*, 2005a,b)

$$
\begin{aligned}
&\frac{\rho}{\varepsilon}\Big[\frac{\partial \mathbf{q}}{\partial t}+\frac{1}{\varepsilon}(\mathbf{q}\cdot\nabla)\mathbf{q}\Big]=-\nabla p+\rho\mathbf{X}_i+\mu_0(\mathbf{M}\cdot\nabla)\mathbf{H}-\Big(\frac{\mu}{k_1}\Big)\mathbf{q}+\frac{2\rho}{\varepsilon}(\mathbf{q}\times\boldsymbol{\Omega})\\
&\qquad+\frac{\mu_e}{4\pi}[(\nabla\times\mathbf{H})\times\mathbf{H}]\\
&\varepsilon\frac{\partial\rho}{\partial t}+\nabla\cdot(\rho\mathbf{q})=0\\
&[\varepsilon\rho c_v+\rho_s c_s(1-\varepsilon)]\frac{\partial T}{\partial t}+\rho c_v(\mathbf{q}\cdot\nabla)T=k_T\nabla^2T+\varPhi\\
&\varepsilon\Big(\frac{\partial\mathbf{H}}{\partial t}\Big)=[\nabla\times(\mathbf{q}\times\mathbf{H})]+\varepsilon\eta(\nabla^2\mathbf{H}\qquad\qquad \nabla\cdot\mathbf{H}=0
\end{aligned}
\tag{2.1}
$$

where the symbols ρ, t, μ, $\mathbf{q}$, ∇p, μ_e, μ_0, $\mathbf{H}$, $\mathbf{X}_i=-g\boldsymbol{\lambda}_i$, ρ_s, c_s, c_v, T, k_T, $\varPhi$ and η denote, respectively, density of the compressible fluid, time, co-efficient of viscosity, fluid velocity, pressure gradient term, magnetic permeability of the medium, magnetic permeability of vacuum $4\pi\cdot10^{-7}$ H/m (H – Henry), magnetic field intensity, gravitational acceleration term, density of the solid material, heat capacity of the solid material, specific heat at constant volume, temperature, effective thermal conductivity, internal heat source strength and electrical resistivity.

The rotational effect induces two terms in the equation of motion, namely, the Centrifugal force $(-0.5\,\mathrm{grad}\,|\boldsymbol{\Omega}\times\mathbf{r}|^2)$ and the Coriolis force $2(\mathbf{q}\times\boldsymbol{\Omega})$. In Eq. $(2.1)_1$, $p=(p_f-0.5\rho|\boldsymbol{\Omega}\times\mathbf{r}|^2)$ is the reduced pressure, where p_f stands for the fluid pressure and $\boldsymbol{\Omega}$ denotes the angular velocity.

Maxwell's equations for an electrically non-conducting fluid with no displacement currents are

$$
\nabla\cdot\mathbf{B}=0\qquad\qquad \nabla\times\mathbf{H}=\mathbf{0}
\tag{2.2}
$$

The magnetic induction $\mathbf{B}$, magnetization $\mathbf{M}$ and the intensity of magnetic field $\mathbf{H}$ are related by (Penfield and Haus, 1967)

$$
\mathbf{B}=\mu_0(\mathbf{H}+\mathbf{M})
\tag{2.3}
$$

In general, the magnetization $\mathbf{M}$ of a ferrofluid depends upon the magnitude of magnetic field $\mathbf{H}$ and temperature T, but in the present study it is assumed that the magnetization does not depend upon the magnetic field strength and is a function of temperature only. So, the magnetic equation of state takes the form

$$\mathbf{M} = \mathbf{M}_0[1 + \chi(T_0 - T)] \tag{2.4}$$

where T_0 and $\mathbf{M}_0$ are the reference temperature and reference magnetization, respectively, with $\mathbf{M}_0 = \mathbf{M}(T_0)$. $\chi = -(1/\mathbf{M}_0)(\partial\mathbf{M}/\partial T)_{\mathbf{H}_0}$ stands for the pyromagnetic co-efficient and $\mathbf{H}_0$ is the uniform magnetic field of the fluid layer when placed in an external magnetic field $\mathbf{H} = \mathbf{H}_0^{ext} \times \boldsymbol{\lambda}_i$, where $\boldsymbol{\lambda}_i$ is the unit vector in the vertical direction.

According to Spiegel and Veronis (1960), the equations for compressible fluids are equivalent to those for incompressible fluids if the static temperature gradient β is replaced by the term $(\beta - g/c_p)$ and f is defined as any of the state variable (p, ρ, T) and is expressed in the form

$$f(x, y, z, t) = f_m + f_0(z) + f'(x, y, z, t) \tag{2.5}$$

where f_m is the constant space distribution of f, f_0 is the variation in the absence of motion, $f'(x, y, z, t)$ stands for the fluctuations in f resulting from motion of the fluid and c_p stands for the specific heat at constant pressure.

The quantities of the basic state are given by

$$\begin{aligned}
&\mathbf{q} = \mathbf{q}_b = [0, 0, 0] \qquad p = p_b(z) \qquad \rho = \rho_b(z) = \rho_0(1 + \alpha\beta z)\\
&\mathbf{H} = \mathbf{H}_b(0, 0, H_z) \qquad \mathbf{M} = \mathbf{M}_b(z) \qquad \beta = \frac{T_0 - T_1}{d}\\
&T = T_b(z) = T_0 - \Big(\beta - \frac{g}{c_p}\Big)z + \frac{\Phi}{2\kappa}(zd - z^2) \qquad \mathbf{H}_0 + \mathbf{M}_0 = \mathbf{H}_0^{ext}
\end{aligned} \tag{2.6}$$

and

$$\begin{aligned}
&\rho = \rho_m[1 - \alpha_m(T - T_m) + K_m(p - p_m)] \qquad \alpha_m = -\Big(\frac{1}{\rho}\frac{\partial\rho}{\partial T}\Big)_m\\
&K_m = \Big(\frac{1}{\rho}\frac{\partial\rho}{\partial p}\Big)_m \qquad p(z) = p_m - g\int\limits_0^z (\rho_0 + \rho_m)\,dz
\end{aligned} \tag{2.7}$$

where ρ_0 and T_0 stands for the density and temperature of the fluid at the lower boundary, whereas p_m and ρ_m stand for a constant space distribution of pressure p and density ρ, respectively. The subscript b denotes the basic state, α is the coefficient of thermal expansion and β denotes the basic temperature gradient.

Now, to analyze the stability of the basic state using the perturbation technique, infinitesimal perturbations are assumed around the basic state solutions of the following form

$$\begin{aligned}
&\mathbf{q} = \mathbf{q}_b + \mathbf{q}' \qquad p = p_b(z) + p' \qquad T = T_b(z) + \theta \qquad \rho = \rho_b(z) + \rho'\\
&\mathbf{M} = \mathbf{M}_b(\mathbf{z}) + \mathbf{M}'(m_x, m_y, m_z) \qquad \mathbf{H} = \mathbf{H}_b + \mathbf{h}(h_x, h_y, h_z)
\end{aligned} \tag{2.8}$$

where $\mathbf{q}'(u, v, w)$, p', θ, ρ', $\mathbf{M}'$, $\mathbf{h}(h_x, h_y, h_z)$ are the perturbations in velocity $\mathbf{q}$, pressure p, temperature T, density ρ, magnetization $\mathbf{M}$ and magnetic field intensity $\mathbf{H}$, respectively. The changes in density and magnetization $\mathbf{M}'$ caused by perturbation θ in temperature T are defined as

$$\rho' = -\alpha\rho_m\theta \qquad \mathbf{M}' = -\chi\mathbf{M}_0\theta \tag{2.9}$$

Using equation (2.8) in equations (2.1) and assuming the perturbation quantities to be very small, the following linearized perturbation equations are obtained as follows

$$
\begin{aligned}
&\frac{1}{\varepsilon}\Big(\frac{\partial \mathbf{q}'}{\partial t}\Big) = -\frac{1}{\rho_m}(\nabla p') - \mathbf{g}\Big(\frac{\rho'}{\rho_m}\Big)\boldsymbol{\lambda}_i - \frac{\mu_0\chi\mathbf{M}_0(\nabla\mathbf{H})\theta}{\rho_m} + \frac{\mu_0(\mathbf{M}\cdot\nabla)\mathbf{h}}{\rho_m} - \frac{\upsilon}{k_1}\mathbf{q}' \\
&\qquad + \frac{2}{\varepsilon}(\mathbf{q}'\times\boldsymbol{\Omega}) + \frac{\mu_e}{4\pi\rho_m}[(\nabla\times\mathbf{h})\times\mathbf{H}] \\
&\nabla\cdot\mathbf{q}' = 0 \qquad\qquad E\Big(\frac{\partial\theta}{\partial t}\Big) = -\Big(\frac{\partial T_b}{\partial z}\Big)w + \kappa(\nabla^2\theta) \\
&\nabla\cdot\mathbf{h} = 0 \qquad\qquad \varepsilon\Big(\frac{\partial\mathbf{h}}{\partial t}\Big) = (\nabla\mathbf{H})\mathbf{q}' + \varepsilon\eta(\nabla^2\mathbf{h})
\end{aligned}
\tag{2.10}
$$

where $E = \varepsilon + (1-\varepsilon)[\rho_s c_s/(\rho_m c_v)]$, $\boldsymbol{\lambda}_i = [0,0,1]$ and $\mathbf{w}$ stands for the vertical fluid velocity. Eliminating u, v and $\nabla p'$ from the momentum equation and retaining the vertical component of fluid velocity, the following perturbation equations are obtained

$$
\begin{aligned}
&\frac{1}{\varepsilon}\frac{\partial}{\partial t}(\nabla^2\mathbf{w}) = \Big(\mathbf{g}\alpha - \frac{\mu_0\chi\mathbf{M}_0\nabla\mathbf{H}}{\rho_m}\Big]\nabla_1^2\theta + \frac{\mu_0\mathbf{M}_0(1+\chi\Delta T)}{\rho_m}\nabla_1^2\Big(\frac{\partial\mathbf{h}_z}{\partial z}\Big) - \frac{\upsilon}{k_1}(\nabla^2\mathbf{w}) \\
&\qquad - \frac{2\boldsymbol{\Omega}}{\varepsilon}\Big(\frac{\partial\boldsymbol{\zeta}}{\partial z}\Big) + \frac{\mu_e\mathbf{H}}{4\pi\rho_m}\Big[\frac{\partial}{\partial z}(\nabla^2\mathbf{h}_z)\Big] \\
&\frac{1}{\varepsilon}\Big(\frac{\partial\boldsymbol{\zeta}}{\partial t}\Big) = -\frac{\upsilon}{k_1}\boldsymbol{\zeta} + \frac{2\boldsymbol{\Omega}}{\varepsilon}\Big(\frac{\partial\mathbf{w}}{\partial z}\Big) + \frac{\mu_e\mathbf{H}}{4\pi\rho_m}\Big(\frac{\partial\boldsymbol{\xi}}{\partial z}\Big) \qquad \Big(E\frac{\partial}{\partial t} - \kappa\nabla^2\Big)\theta = \beta L h(z) w \\
&\varepsilon\Big(\frac{\partial\mathbf{h}_z}{\partial t}\Big) = \mathbf{H}\Big(\frac{\partial\mathbf{w}}{\partial z}\Big) + \varepsilon\eta(\nabla^2\mathbf{h}_z) \qquad \varepsilon\Big(\frac{\partial\boldsymbol{\xi}}{\partial t}\Big) = \mathbf{H}\Big(\frac{\partial\boldsymbol{\zeta}}{\partial z}\Big) + \varepsilon\eta(\nabla^2\boldsymbol{\xi})
\end{aligned}
\tag{2.11}
$$

where $\boldsymbol{\xi} = \frac{\partial\mathbf{h}_y}{\partial x} - \frac{\partial\mathbf{h}_x}{\partial y}$ (z-components of current density), $\boldsymbol{\zeta} = \frac{\partial\mathbf{v}}{\partial x} - \frac{\partial\mathbf{u}}{\partial y}$ (z-component of vorticity), $\nabla^2 = \frac{\partial^2}{\partial x^2} + \frac{\partial^2}{\partial y^2} + \frac{\partial^2}{\partial z^2}$ (three dimensional Laplacian operator), $\nabla_1^2 = \frac{\partial^2}{\partial x^2} + \frac{\partial^2}{\partial y^2}$ (two dimensional horizontal Laplacian operator), $L = 1 - \frac{1}{G} = 1 - \frac{\beta c_p}{g}$ (modified dimensionless compressibility parameter), $S = \frac{\Phi d}{2\beta\kappa L}$ (dimensionless heat source parameter), $h(z) = 1 - S\Big(1 - \frac{2z}{d}\Big)$ (non-uniform temperature gradient) and $\kappa = \frac{k_T}{\rho_m c_v}$ (thermal diffusivity of the fluid).

3. Normal modes and linear stability analysis

The system of equations (2.11) can be solved by using the method of normal modes in which the perturbation quantities have solutions with dependence upon x, y and t of the following form

$$
[w,\theta,\zeta,h_z,\xi] = [W(z),\Theta(z),Z(z),K(z),X(z)]\exp[\mathrm{i}(k_x x + k_y y) + nt]
\tag{3.1}
$$

where k_x and k_y are the horizontal wave numbers along the x and y directions, respectively, $k^2 = k_x^2 + k_y^2$ is a dimensionless resultant wave number and n is the growth rate of harmonic disturbance. Infinitesimal perturbations of the state may either grow or damp depending upon the growth rate n. Substituting expression (3.1) into linearized differential equations (2.11) along with $z = z^* d$, $a = kd$, $\sigma = nd^2/\upsilon$, $D = \partial/\partial z^*$, the following non-dimensional form is obtained (after ignoring the asterisk)

$$
\begin{aligned}
&\Big(\frac{\sigma}{\varepsilon} + \frac{1}{P_l}\Big)(D^2 - a^2)W(z) = -\Big(g - \frac{\mu_0\chi M_0\nabla H}{\rho_m\alpha}\Big)\frac{\alpha a^2 d^2\Theta}{\upsilon} \\
&\qquad - \Big[\frac{\mu_0 M_0(1+\chi\Delta T)}{\rho_m}\frac{a^2 d}{\upsilon} - \frac{\mu_e H d}{4\pi\rho_m\upsilon}(D^2 - a^2)\Big]DK - \frac{2\Omega d_3}{\varepsilon\upsilon}DZ
\end{aligned}
\tag{3.2}
$$

and

$$
\begin{aligned}
&\Big(\frac{\sigma}{\varepsilon}+\frac{1}{P_l}\Big)Z=\frac{2\Omega d}{\varepsilon\upsilon}DW+\frac{\mu_e Hd}{4\pi\rho_m\upsilon}DX \qquad && [(D^2-a^2)-Ep_1\sigma]\Theta=-\frac{\beta d^2}{\kappa}Lh(z)W\\
&[(D^2-a^2)-p_2\sigma]K=-\frac{Hd}{\varepsilon\eta}DW && [(D^2-a^2)-p_2\sigma]X=-\frac{Hd}{\varepsilon\eta}DZ
\end{aligned}
\tag{3.3}
$$

The dimensionless parameters in equations (3.2) and (3.3) are the thermal Prandtl number $\mathrm{Pr}_1=\upsilon/\kappa$, the magnetic Prandtl number $\mathrm{Pr}_2=\upsilon/\eta$ and the dimensionless medium permeability $P_l=k_1/d^2$.

The boundary conditions appropriate for the case of two free boundaries are defined as

$$
\begin{cases}
W=D^2W=DZ=\Theta=0 \qquad \text{at} \quad z=0 \quad \text{and} \quad z=1\\
h_x,h_y,h_z \quad \text{are continuous at the boundaries}
\end{cases}
\tag{3.4}
$$

The solution to equations (3.2) and (3.3) satisfying boundary conditions (3.4) can be taken in the form

$$
W=W_0\sin(l\pi z) \qquad l=1,2,3,\ldots
\tag{3.5}
$$

where W_0 is a constant. The most suitable mode corresponds to $l=1$ (fundamental mode). Therefore, using solution (3.5) with $l=1$ into equations (3.2) and (3.3), the dispersion relation is obtained as follows (after eliminating Θ, X, Z and K)

$$
\begin{aligned}
(1+x)(1+x+iE\mathrm{Pr}_1\sigma_i)(1+x+i\mathrm{Pr}_2\sigma_i)&=\mathrm{Ra}_1 x\varepsilon PLh(z)\frac{1+x+i\sigma_i\mathrm{Pr}_2}{\varepsilon+i\sigma_i P}\\
&-\frac{PQ_1}{\varepsilon+i\sigma_i P}[x\Gamma+(1+x)](1+x+i\sigma_i E\mathrm{Pr}_1)\\
&-T_{A_1}P^2(1+x+i\sigma_i E\mathrm{Pr}_1)(1+x+i\sigma_i\mathrm{Pr}_2)^2\frac{1}{1+x+i\sigma_i\mathrm{Pr}_2+Q_1P}
\end{aligned}
\tag{3.6}
$$

where Ra_F is the thermal Rayleigh number for ferromagnetic fluids, Q – Chandrasekhar number, Q_M – modified Chandrasekhar number for ferromagnetic fluids, Γ – ratio of magnetic permeability with magnetization to magnetic strength and T_A – Taylor number

$$
\begin{aligned}
&\mathrm{Ra}_F=\Big(g-\frac{\mu_0\chi M_0\nabla H}{\rho_m\alpha}\Big)\frac{\alpha\beta d^4}{\upsilon\kappa} \qquad && Q=\frac{\mu_e H^2d^2}{4\pi\rho_m\upsilon\eta} \qquad && Q_M=\frac{\mu_0M_0(1+\chi\Delta T)}{\rho_m}\frac{Hd^2}{\upsilon\eta}\\
&\Gamma=\frac{Q_{M_1}}{Q_M}=\frac{4\pi\mu_0 M}{\mu_e H} && T_A=\frac{4\Omega^2d^4}{\upsilon^2}
\end{aligned}
$$

and

$$
\begin{aligned}
&\mathrm{Ra}_1=\frac{\mathrm{Ra}_F}{\pi^4} \qquad && x=\frac{a^2}{\pi^2} \qquad && i\sigma_i=\frac{\sigma}{\pi^2} \qquad && P=\pi^2P_l\\
&Q_1=\frac{Q}{\pi^2} && Q_{M_1}=\frac{Q_M}{\pi^2} && T_{A_1}=\frac{T_A}{\pi^4}
\end{aligned}
$$

Equation (3.6) is the required dispersion relationship that accounts for the effects of rotation, medium permeability, medium porosity, compressibility, uniform heat source and magnetic field on thermal instability of the ferromagnetic fluid in a porous medium.

From equation (3.6), the thermal Rayleigh number Ra_1 can be separated into the real and imaginary parts as

$$
\mathrm{Ra}_1=X_1+i\sigma_iX_2
\tag{3.7}
$$

where X_1, X_2 and σ_i are real numbers defined as

$$
\begin{aligned}
X_1 = \frac{1}{x\varepsilon PLh(z)}\Big(& [(1+x)^2\varepsilon - \sigma_i^2 P\mathrm{Pr}_1 E(1+x)] \\
& + \frac{PQ_1[x\Gamma + (1+x)][(1+x)^2 + \sigma_i^2\mathrm{Pr}_1\mathrm{Pr}_2 E]}{(1+x)^2 + \sigma_i^2\mathrm{Pr}_2^2} \\
& + \frac{T_{A_1}P^2}{[(1+x)+Q_1P]^2 + \sigma_i^2\mathrm{Pr}_2^2}\Big\{[(1+x)^2 - \sigma_i^2\mathrm{Pr}_1\mathrm{Pr}_2E][(1+x+Q_1P)\varepsilon + \sigma_i^2 P\mathrm{Pr}_2] \\
& - \sigma_i^2[(1+x)(\mathrm{Pr}_2 + \mathrm{Pr}_1E)][(1+x)P + Q_1P^2 - \mathrm{Pr}_2\varepsilon]\Big\}\Big)
\end{aligned}
\tag{3.8}
$$

$$
\begin{aligned}
X_2 = \frac{1}{x\varepsilon PLh(z)}\Big(& [(1+x)^2P + \mathrm{Pr}_1E\varepsilon(1+x)] + \frac{PQ_1[x\Gamma + (1+x)](1+x)(\mathrm{Pr}_1E - \mathrm{Pr}_2)}{(1+x)^2 + \sigma_i^2\mathrm{Pr}_2^2} \\
& + \frac{T_{A_1}P^2}{[(1+x)+Q_1P]^2 + \sigma_i^2\mathrm{Pr}_2^2}\Big\{[(1+x)^2 - \sigma_i^2\mathrm{Pr}_1\mathrm{Pr}_2E][(1+x+Q_1P)P - \mathrm{Pr}_2\varepsilon] \\
& + [(1+x+Q_1P)\varepsilon + \sigma_i^2 P\mathrm{Pr}_2](1+x)(\mathrm{Pr}_2 + \mathrm{Pr}_1E)\Big\}\Big)
\end{aligned}
$$

Since Ra_1 is a physical quantity, it must be real. Hence, from equation (3.7) it follows that either $\sigma_i = 0$ (stationary state) or $X_2 = 0$, $\sigma_i \neq 0$ (oscillatory state). It should also be noted that when $\mu_0 = 0$ (i.e. $\Gamma = 0$) then from equation $(3.8)_2$ X_2 cannot vanish and therefore, σ_i must be zero. This implies that for an ordinary viscous fluid, the principle of exchange of stabilities is valid even in the presence of a porous medium, and this statement is verified in Section 6.

3.1. The stationary state

For real σ_i, the marginal instability (or neutral instability) occurs when $\sigma_i = 0$. Substituting $\sigma_i = 0$ into equations (3.7) and $(3.8)_1$, the modified thermal Rayleigh number is obtained for the onset of stationary convection in the following form

$$
\mathrm{Ra}_1^{stat} = \frac{1}{x\varepsilon PLh(z)}\Big\{(1+x)^2\varepsilon + PQ_1[x\Gamma + (1+x)] + T_{A_1}P^2\frac{(1+x)^2\varepsilon}{Q_1P + (1+x)}\Big\}
\tag{3.9}
$$

Equation (3.9) leads to the marginal instability curves in stationary conditions.

For higher values of permeability ($P \to \infty$) which correspond to the case of pure fluids, equation (3.9) gives

$$
\mathrm{Ra}_1^{stat} = \frac{1}{Lh(z)}\Big\{\frac{Q_1[x\Gamma + (1+x)]}{\varepsilon x} + \frac{T_{A_1}(1+x)^2}{Q_1x}\Big\}
\tag{3.10}
$$

Minimizing equation (3.9) with respect to x yields an equation of degree four in x as

$$
x^4 + A_1x^3 + A_2x^2 + A_3x + A_4 = 0
\tag{3.11}
$$

where

$$
\begin{aligned}
A_1 &= 2(1 + Q_1P) \\
A_2 &= Q_1^2P^2 + 2Q_1P - \frac{Q_1P}{\varepsilon} + T_{A_1}Q_1P^3 - T_{A_1}P^2 \\
A_3 &= -\Big[2(1+Q_1P) + 2T_{A_1}P^2 + \frac{2Q_1P(1+Q_1P)}{\varepsilon}\Big] \\
A_4 &= -1 + Q_1^2P^2 + 2Q_1P - \frac{Q_1P}{\varepsilon} - T_{A_1}Q_1P^3 - T_{A_1}P^2 - \frac{(Q_1^2P^2 + 2Q_1P)Q_1P}{\varepsilon}
\end{aligned}
$$

In the absence of heat source parameter (i.e. $h(z) = 1$), equation (3.9) gives

$$\mathrm{Ra}_1^{stat} = \frac{1}{x\varepsilon PL}\Big\{(1+x)^2\varepsilon + PQ_1[x\varGamma + (1+x)] + T_{A_1}P^2\frac{(1+x)^2\varepsilon}{Q_1P+(1+x)}\Big\} \tag{3.12}$$

which agrees with the previous published work by Aggarwal and Makhija (2014) in the absence of the Hall effect but in the presence of rotation and compressibility.

The classical results for Newtonian fluids can be obtained as a particular case of the present study.

For an incompressible ($L = 1$), non-rotatory and non-magnetized system, equation (3.12) reduces to

$$\mathrm{Ra}_1^{stat} = \frac{(1+x)^2}{Px} \tag{3.13}$$

This coincides with the classical Rayleigh-Bénard result for a Newtonian fluid in a porous medium.

To analyze the effects of various parameters such as modified compressibility, medium porosity, temperature gradient due to internal heating, rotation, magnetic field and medium permeability, the behaviour of $d\mathrm{Ra}_1^{stat}/dL$, $d\mathrm{Ra}_1^{stat}/d\varepsilon$, $d\mathrm{Ra}_1^{stat}/dh(z)$, $d\mathrm{Ra}_1^{stat}/dT_{A_1}$, $d\mathrm{Ra}_1^{stat}/dQ_1$ and $d\mathrm{Ra}_1^{stat}/dP$ is examined analytically.

Differentiating equation (3.9) with respect to various parameters, i.e. L, ε, $h(z)$, T_{A_1}, Q_1, P, leads to following expressions

$$\begin{aligned}
&\frac{d\mathrm{Ra}_1^{stat}}{dL} = -\frac{R^{\oplus}}{L^2h(z)} \qquad \frac{d\mathrm{Ra}_1^{stat}}{d\varepsilon} = -\frac{1}{Lh(z)}\Big\{\frac{[x\varGamma+(1+x)]Q_1}{\varepsilon^2 x}\Big\}\\
&\frac{d\mathrm{Ra}_1^{stat}}{dh(z)} = \begin{cases} \dfrac{1}{L(1-S)^2}R^{\oplus} & \text{at} \quad z=0 \\ -\dfrac{1}{L(1+S)^2}R^{\oplus} & \text{at} \quad z=d \end{cases}
\end{aligned} \tag{3.14}$$

This shows that the modified compressibility, medium porosity and temperature gradient (except for the lower boundary) have a destabilizing effect

$$\frac{d\mathrm{Ra}_1^{stat}}{dT_{A_1}} = \frac{1}{Lh(z)}\Big\{\frac{P(1+x)^2}{x[Q_1P+(1+x)]}\Big\} \tag{3.15}$$

which is positive, thereby implying the stabilizing effect of the rotational parameter

$$\begin{aligned}
\frac{d\mathrm{Ra}_1^{stat}}{dQ_1} &= \frac{1}{Lh(z)}\Big\{\frac{x\varGamma+(1+x)}{\varepsilon x} - \frac{T_{A_1}P^2(1+x)^2}{x[Q_1P+(1+x)]^2}\Big\}\\
\frac{d\mathrm{Ra}_1^{stat}}{dP} &= \frac{1}{Lh(z)}\Big\{\frac{T_{A_1}(1+x)^2}{x[Q_1P+(1+x)]} - \frac{PQT_{A_1}(1+x)^2}{x[Q_1P+(1+x)]^2} - \frac{(1+x)^2}{P^2x}\Big\}
\end{aligned} \tag{3.16}$$

Equations (3.16) show that the magnetic field and medium permeability have dual effects. In a non-rotating frame, the magnetic field has a stabilizing effect, whereas permeability has a destabilizing effect where

$$R^{\oplus} = \frac{(1+x)^2}{Px} + \frac{[x\varGamma+(1+x)]Q_1}{\varepsilon x} + \frac{T_{A_1}P(1+x)^2}{x[Q_1P+(1+x)]}$$

3.2. The oscillatory state

For an oscillatory state, setting $X_2 = 0$, $\sigma_i \neq 0$ in equation $(3.8)_2$ gives a polynomial in σ_i^2 of degree two in the form

$$a_0\sigma_i^4 + a_1\sigma_i^2 + a_2 = 0 \tag{3.17}$$

Solving equation (3.17) for σ_i^2, one gets

$$\sigma_i^2 = \frac{-a_1 \pm \sqrt{a_1^2 - 4a_0a_2}}{2a_0} \tag{3.18}$$

For simplicity, the values of coefficients a_0, a_1 and a_2 are not mentioned here to save spaces.

With σ_i^2 determined from equation (3.18), the Rayleigh number for an oscillatory instability can be obtained with the help of equations (3.7) and $(3.8)_1$ as

$$\begin{aligned}\mathrm{Ra}_1^{osc} &= \frac{1}{x\varepsilon PLh(z)}\Bigg((1+x)^2\varepsilon - \sigma_i^2 P\mathrm{Pr}_1E(1+x) \\ &+ \frac{PQ_1[x\Gamma + (1+x)][(1+x)^2 + \sigma_i^2\mathrm{Pr}_1\mathrm{Pr}_2E]}{(1+x)^2 + \sigma_i^2\mathrm{Pr}_2^2} \\ &+ \frac{T_{A_1}P^2}{[(1+x)+Q_1P]^2 + \sigma_i^2\mathrm{Pr}_2^2}\Big\{\Big[(1+x)^2 - \sigma_i^2\mathrm{Pr}_1\mathrm{Pr}_2E\Big][(1+x+Q_1P)\varepsilon + \sigma_i^2P\mathrm{Pr}_2] \\ &- \sigma_i^2(1+x)(\mathrm{Pr}_2 + \mathrm{Pr}_1E)[(1+x)P + Q_1P^2 - \mathrm{Pr}_2\varepsilon]\Big\}\Bigg)\end{aligned} \tag{3.19}$$

The values of the critical wave number x_c for the oscillatory case can be obtained from equation (3.19) with the condition $d\mathrm{Ra}_1^{osc}/dx = 0$ and then substituting this critical wave number x_c into equation (3.19) yields the critical Rayleigh number Ra_{1c}^{osc} for the oscillatory instability. Further, substituting these critical wave number and the critical Rayleigh number of oscillatory instability into equation (3.18) gives the critical frequency for the oscillatory case.

4. Results and discussion

In the present Section, we mainly focused on the determination of critical wave numbers and critical thermal Rayleigh numbers for the stationary case. The values of the critical wave number x_c for the onset of stationary instability are determined numerically from equation (3.11) with the condition $d\mathrm{Ra}_1^{stat}/dx = 0$, and then equation (3.9) will give the critical thermal Rayleigh number for the stationary state. The variations in critical thermal Rayleigh numbers Ra_{1c}^{stat} for various values of physical parameters are depicted graphically in Fig. 2. Also, the variations of marginal (neutral) instability curves in the $(\mathrm{Ra}_1 - x)$ plane for different parametric values $(L, h(z), \varepsilon, T_{A_1}, Q_1, P)$ are shown in Fig. 3. We fixed the values of the parameters except for the varying parameter.

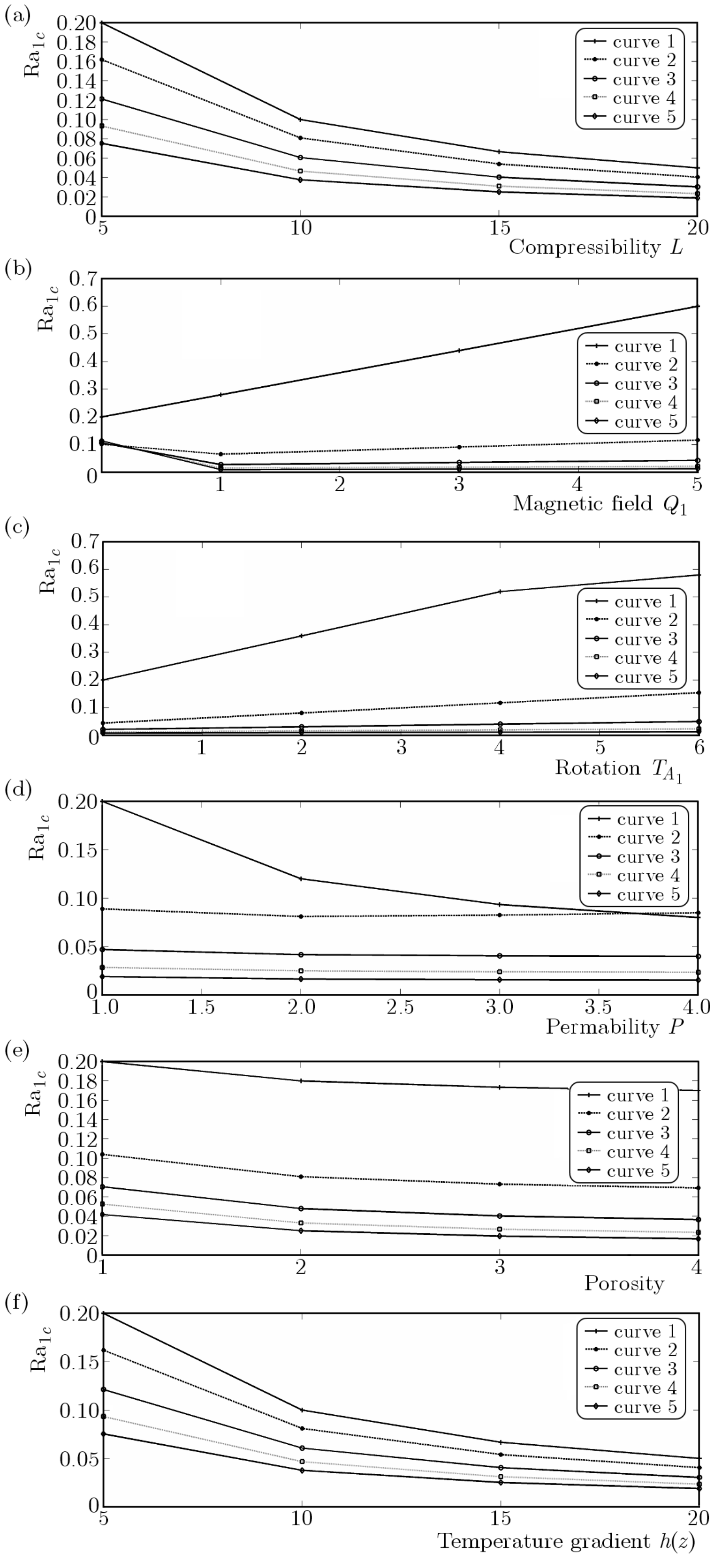

Fig. 2. Variation of Ra_{1c} verrsus L (a), T_{A_1} (b), Q_1 (c), P (d), ε (e), $h(z)$ (f)various valuesof physical parameters; curve 1: $Q_1 = 0$, $Q_{M_1} = 1$, $\varepsilon = 1$, $P = 1$, $h(z) = 5$, $L = 5$, $T_{A_1} = 0$, curve 2: $Q_1 = 1$, $Q_{M_1} = 3$, $\varepsilon = 2$, $P = 2$, $h(z) = 10$, $L = 10$, $T_{A_1} = 2$, curve 3: $Q_1 = 3$, $Q_{M_1} = 5$, $\varepsilon = 3$, $P = 3$, $h(z) = 15$, $L = 15$, $T_{A_1} = 4$, curve 4: $Q_1 = 5$, $Q_{M_1} = 7$, $\varepsilon = 4$, $P = 4$, $h(z) = 20$, $L = 20$, $T_{A_1} = 6$, curve 5: $Q_1 = 7$, $Q_{M_1} = 9$, $\varepsilon = 5$, $P = 5$, $h(z) = 25$, $L = 25$, $T_{A_1} = 8$

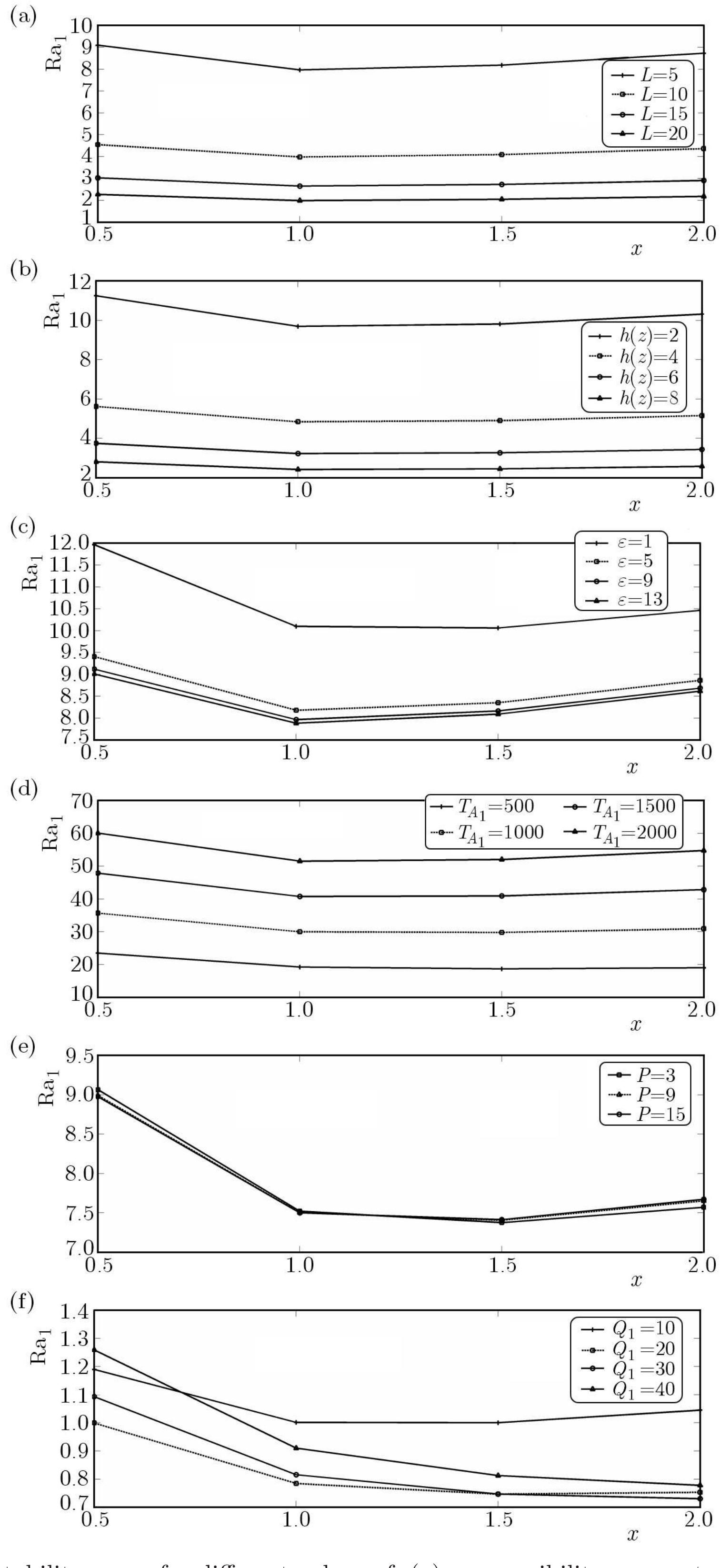

Fig. 3. Neural instability curve for different values of: (a) comprssibility parameter, $h(z) = 5$, $P = 5$, $\varepsilon = 5$, $Q_1 = 10$, $Q_{M_1} = 10$, $T_{A_1} = 500$; (b) temperature gradient, $L = 10$, $P = 2$, $\varepsilon = 3$, $Q_1 = 10$, $Q_{M_1} = 10$, $T_{A_1} = 500$; (c) porosity, $L = 5$, $h(z) = 5$, $P = 2$, $Q_1 = 20$, $Q_{M_1} = 20$, $T_{A_1} = 1000$; (d) rotation parameter, $L = 3$, $h(z) = 3$, $P = 3$, $\varepsilon = 2$, $Q_1 = 50$, $Q_{M_1} = 50$; (e) permeability, $L = 2$, $h(z) = 2$, $P = 5$, $\varepsilon = 3$, $Q_1 = 10$, $Q_{M_1} = 10$, $T_{A_1} = 50$; (f) magnetic field parameter, $L = 5$, $h(z) = 5$, $P = 5$, $\varepsilon = 5$, $Q_{M_1} = 5$, $T_{A_1} = 50$

5. The overstable case

Now, the possibility whether the instability may occur as overstability is examined. Equating the real and imaginary parts of equation (3.6) leads to

$$
\begin{aligned}
&[(1+x)^2-\sigma_i^2 E\mathrm{Pr}_1\mathrm{Pr}_2](1+x)=\mathrm{Ra}_1 x\varepsilon PLh(z)\frac{(1+x)\varepsilon+\sigma_i^2 P\mathrm{Pr}_2}{\varepsilon^2+\sigma_i^2P^2}\\
&\quad -P[(1+x)\varepsilon+\sigma_i^2\mathrm{Pr}_1PE]\frac{(1+x)Q_1+Q_{M_1}x}{\varepsilon^2+\sigma_i^2P^2}\\
&\quad -T_{A_1}P^2\Big\{[(1+x)^2+\sigma_i^2\mathrm{Pr}_2(\mathrm{Pr}_2-\mathrm{Pr}_1E)](1+x)^2\\
&\quad +[(1+x)^2-\sigma_i^2\mathrm{Pr}_2(\mathrm{Pr}_2+2\mathrm{Pr}_1E)]Q_1P(1+x)-\sigma_i^4E\mathrm{Pr}_1\mathrm{Pr}_2^3\Big\}\\
&\sigma_i(\mathrm{Pr}_2+\mathrm{Pr}_1E)(1+x)^2=\mathrm{Ra}_1x\varepsilon PLh(z)\frac{\sigma_i[\mathrm{Pr}_2\varepsilon-P(1+x)]}{\varepsilon^2+\sigma_i^2P^2}\\
&\quad -\frac{\sigma_iP[\mathrm{Pr}_1E\varepsilon-P(1+x)][(1+x)Q_1+Q_{M_1}x]}{\varepsilon^2+\sigma_i^2P^2}-T_{A_1}P^2\sigma_i\Big[(\mathrm{Pr}_2+\mathrm{Pr}_1E)(1+x)^3\\
&\quad +Q_1P(2\mathrm{Pr}_2+\mathrm{Pr}_1E)(1+x)^2+\sigma_i^2\mathrm{Pr}_2^2(\mathrm{Pr}_2+\mathrm{Pr}_1E)(1+x)-\sigma_i^2\mathrm{Pr}_1\mathrm{Pr}_2^2Q_1PE\Big]
\end{aligned}
\tag{5.1}
$$

Eliminating Ra_1 between equations (5.1) and assuming $\sigma_i^2=y$, a four degree polynomial in y is obtained as follows

$$
b_0y^4+b_1y^3+b_2y^2+b_3y+b_4=0 \tag{5.2}
$$

where

$$
\begin{aligned}
b_0&=T_{A_1}P^6\mathrm{Pr}_2^3[P\mathrm{Pr}_2(1+x)-\mathrm{Pr}_1E(\mathrm{Pr}_2\varepsilon+Q_1P^2)]\\
b_4&=T_{A_1}P^3\varepsilon^4(1+x)^5+[P\varepsilon^4+T_{A_1}P^2\varepsilon^4(\mathrm{Pr}_1E\varepsilon+Q_1P^2)](1+x)^4\\
&\quad +[\mathrm{Pr}_1E\varepsilon^5+T_{A_1}Q_1P^3\varepsilon^5(\mathrm{Pr}_1E+\mathrm{Pr}_2)](1+x)^3+[Q_1P\varepsilon^4(\mathrm{Pr}_1E-\mathrm{Pr}_2)](1+x)^2\\
&\quad +[Q_{M_1}P\varepsilon^4x(\mathrm{Pr}_1E-\mathrm{Pr}_2)](1+x)
\end{aligned}
\tag{5.3}
$$

The coefficients b_1, b_2 and b_3 involving the large number of terms are not written here as they do not play any role in determining the overstability. Since σ_i is real for overstability to occur, therefore all the roots of y should be positive. So, from equation (5.2), the product of roots equals b_4/b_0 must be positive. b_0 is negative if

$$
P\mathrm{Pr}_2(1+x)<\mathrm{Pr}_1E(\mathrm{Pr}_2\varepsilon+Q_1P^2) \qquad \text{i.e.} \qquad P\kappa(1+x)<\eta E(\mathrm{Pr}_2\varepsilon+Q_1P^2) \tag{5.4}
$$

and b_4 is positive if

$$
\mathrm{Pr}_1E>\mathrm{Pr}_2 \qquad \text{i.e.} \qquad \eta E>\kappa \tag{5.5}
$$

Thus, for inequalities (5.4) and (5.5), the overstability cannot occur and the principle of exchange of stabilities holds true. Therefore, the aforementioned inequalities are the sufficient conditions for the non-existence of overstability, violation of which does not necessarily imply the occurrence of overstability.

6. Principal of exchange of stabilities and oscillatory modes

Here, the conditions have been derived, if any, under which the principle of exchange of stabilities is satisfied and the possibility of oscillatory modes for the ferromagnetic fluid takes place. For this purpose, equation (3.2) is multiplied by W^* (the complex conjugate of W) and then integrated over the range of z using equations (3.3). With the help of boundary conditions (3.4), it gives

$$\begin{aligned}
&\Big(\frac{\sigma}{\varepsilon}+\frac{1}{P_l}\Big)I_1-\Big(g-\frac{\mu_0\chi M_0\nabla H}{\rho_m\alpha}\Big)\frac{\kappa\alpha a^2}{\beta\upsilon Lh(z)}(I_2+E\mathrm{Pr}_1\sigma^*I_3)\\
&\quad+\frac{\mu_0M_0(1+\chi\varDelta T)}{\rho_m}\frac{a^2\varepsilon}{\mathrm{Pr}_2H}(I_4+\mathrm{Pr}_2\sigma^*I_5)\\
&\quad+\frac{\mu_e\varepsilon}{4\pi\rho_m\mathrm{Pr}_2}(I_6+\mathrm{Pr}_2\sigma^*I_4)+d^2\Big[\Big(\frac{\sigma^*}{\varepsilon}+\frac{1}{P_l}\Big)I_7+\frac{\mu_e\varepsilon}{4\pi\rho_m\mathrm{Pr}_2}(I_8+\mathrm{Pr}_2\sigma^*I_9)\Big]=0
\end{aligned} \tag{6.1}$$

where the integrals I_1-I_9 are positive definite and defined as

$$\begin{aligned}
&I_1=\int_0^1(|DW|^2+a^2|W|^2)\,dz && I_2=\int_0^1(|D\varTheta|^2+a^2|\varTheta|^2)\,dz && I_3=\int_0^1(|\varTheta|^2)\,dz\\
&I_4=\int_0^1(|DK|^2+a^2|K|^2)\,dz && I_5=\int_0^1|K|^2\,dz\\
&I_6=\int_0^1(|D^2K|^2+a^4|K|^2+2a^2|DK|^2)\,dz && I_7=\int_0^1(|Z|^2)\,dz\\
&I_8=\int_0^1(|DX|^2+a^2|X|^2)\,dz && I_9=\int_0^1(|X|^2)\,dz
\end{aligned} \tag{6.2}$$

Putting $\sigma=i\sigma_i$ in equation (6.1) and equating the imaginary part leads to

$$\begin{aligned}
\sigma_i\Big[&\frac{I_1}{\varepsilon}+\Big(g-\frac{\mu_0\chi M_0\nabla H}{\rho_m\alpha}\Big)\frac{\kappa\alpha a^2}{\beta\upsilon Lh(z)}\mathrm{Pr}_1EI_3-\frac{\mu_0M_0(1+\chi\varDelta T)}{\rho_m}\frac{a^2\varepsilon}{\mathrm{Pr}_2H}\mathrm{Pr}_2I_5\\
&-\frac{\mu_e\varepsilon\mathrm{Pr}_2I_4}{4\pi\rho_m\mathrm{Pr}_2}-\frac{d^2I_7}{\varepsilon}+\frac{\mu_e\varepsilon d^2\mathrm{Pr}_2I_9}{4\pi\rho_m\mathrm{Pr}_2}\Big]=0
\end{aligned} \tag{6.3}$$

From equation (6.3), it is concluded that either $\sigma_i=0$ or $\sigma_i\neq 0$, i.e. the modes may be non-oscillatory or oscillatory, respectively.

For a non-magneto-rotatory system (i.e. $I_4=I_5=I_7=0$), equation (6.2) reduces to

$$\sigma_i\Big[\frac{I_1}{\varepsilon}+\Big(g-\frac{\mu_0\chi M_0\nabla H}{\rho_m\alpha}\Big)\frac{\kappa\alpha a^2}{\beta\upsilon Lh(z)}\mathrm{Pr}_1EI_3\Big]=0 \tag{6.4}$$

It is obvious from equation (6.4) that if $g>\mu_0\chi M_0\nabla H/(\rho_m\alpha)$ then the term inside the square bracket will surely be positive, which leads to $\sigma_i=0$. Therefore, the modes are non-oscillatory and the principle of exchange of stabilities is satisfied. The oscillatory modes are introduced due to the presence of magnetic field and rotation. Thus the sufficient condition for the oscillatory modes to appear in the system is that the inequality $g<\mu_0\chi M_0\nabla H/(\rho_m\alpha)$ is satisfied.

Further, for an ordinary viscous fluid $\mu_0=0$ (i.e. $\varGamma=0$), equation (6.3) reduces to

$$\sigma_i\Big[\frac{I_1}{\varepsilon}+\frac{g\kappa\alpha a^2}{\beta\upsilon Lh(z)}\mathrm{Pr}_1EI_3\Big]=0 \tag{6.5}$$

which implies that $\sigma_i=0$ and the principles of exchange of stabilities is found to hold good.

7. Conclusions

In this study, linear stability theory is used to find the critical Rayleigh number for the onset of both stationary and oscillatory thermal instabilities. The effects of various embedded parameters (rotation, magnetic field, compressibility, heat source, permeability and porosity) on thermal instability of a ferrofluid have been analyzed for the stationary state. The main conclusions drawn are presented as:

- For the case of stationary convection, compressibility, medium porosity and temperature gradient due to heat source (except at the lower boundary) accelerate the onset of convection, whereas rotation and ratio of magnetic permeability delay the onset of convection. The magnetic field and medium permeability have dual effects on thermal instability of the system, whereas in the absence of rotation, the stabilizing effect of the magnetic field and the destabilizing effect of the medium permeability is obvious from equations (3.16).
- The conditions $P\kappa(1+x) < \eta E(\mathrm{Pr}_2\varepsilon + Q_1 P^2)$ and $\eta E > \kappa$ are the sufficient conditions for the non-existence of overstability. The principle of exchange of stabilities holds good for an ordinary viscous fluid and also in the absence of magnetic field and rotation for $g > \mu_0\chi M_0\nabla H/(\rho_m\alpha)$. Hence, the oscillatory modes are due to the presence of magnetic field and rotation only.
- Finally, from the present study, it is concluded that the compressibility, porosity, permeability, rotation, magnetic field and heat source parameter have profound effects on the onset of ferroconvection saturating a porous medium. The present work will also be useful for understanding more complex problems under different physical parameters mentioned above, and it is also possible to suppress the convective instability in a ferromagnetic fluid layer by controlling the magnitude of heat source, compressibility and medium porosity.

References

1. Aggarwal A.K., Makhija S., 2014, Hall effect on thermal stability of ferromagnetic fluid in porous medium in presence of horizontal magnetic field, *Thermal Science*, **18**, 2, 503-514
2. Bailey R.L., 1983, Lesser known applications of ferrofluids, *Journal of Magnetism and Magnetic Materials*, **39**, 178-182
3. Berkovsky B.M., Bashtovoy V.G., 1996, *Magnetic Fluids and Applications Handbook*, Begell House, New York
4. Chandrasekhar S.C., 1981, *Hydrodynamic and Hydromagnetic Stability*, Dover, New York
5. FINLAYSON B.A., 1970, Convective instability in ferromagnetic fluids, *Journal of Fluid Mechanics*, **40**, 4, 753-767
6. Hathaway D.B., 1979, Use of ferrofluid in moving coil loudspeakers, *dB Sound Engineering Magazine*, **13**, 42-44
7. Kumar K., Singh V., Sharma S., 2014a, Thermo-magnetic convection in a rotating couple-stress fluid through a Brinkman porous medium, *International Journal of Applied Mathematics and Mechanics*, **10**, 8, 78-93
8. Kumar K., Singh V., Sharma S., 2014b, Magneto-rotational convection for ferromagnetic fluids in the presence of compressibility and heat source through a porous medium, *Special Topics and Reviews in Porous Media*, **5**, 4, 311-323
9. Kumar K., Singh V., Sharma S., 2015, On the onset of convection in a dusty couple-stress fluid with variable gravity through a porous medium in hydromagnetics, *Journal of Applied Fluid Mechanics*, **8**, 1, 55-63

10. Lalas D.P., Carmi S., 1971, Thermoconvective stability of ferrofluids, *Physics of Fluids*, **14**, 2, 436-437
11. McDonnel J.A.M., 1978, *Cosmic Dust*, John Wiley and Sons, Toronto
12. Moskowitz R., 1975, Dynamic sealing with magnetic fluids, *ASLE Transactions*, **18**, 2, 135-143
13. Neuringer J.L., Rosensweig R.E., 1964, Ferrohydrodynamics, *Physics of Fluids*, **7**, 12, 1927-1937
14. Newbower R.S., 1972, A new technique for circulatory measurements employing magnetic fluid tracers, *Proceedings Biomedical Symposium*, San Diego
15. Nield D.A., Bejan A., 2006, *Convection in Porous Media*, Springer, New-York
16. Odenbach S., 2002, *Magnetoviscous Effects in Ferrofluids*, Springer-Verlag, Berlin
17. Penfield P., Haus H.A., 1967, *Electrodynamics of Moving Media*, Institute of Technology Press, Cambridge
18. Rosensweig R.E., 1985, *Ferrohydrodynamics*, Cambridge University Press, Cambridge
19. Rosensweig R.E., 1987, Magnetic fluids, *Review of Fluid Mechanics*, **19**, 437-463
20. Sharma R.C., 1997, Thermal instability of compressible fluid in the presence of rotation and magnetic field, *Journal of Mathematical Analysis and Applications*, **60**, 227-235
21. Sherman A., Sutton G.W., 1962,*Magnetohydrodynamic*, Northwestern University Press, Illinois
22. Spiegal E.A., Veronis G., 1960, On the Boussinesq approximation for a compressible fluid, *Astrophysical Journal*, **131**, 442-447
23. Sunil, Sharma D., Sharma R.C., 2005a, Effect of dust particles on thermal convection in ferromagnetic fluid saturating a porous medium, *Journal of Magnetism and Magnetic Materials*, **288**, 183-195
24. Sunil, Sharma D., Sharma V., 2005b, Effect of dust particles on rotating ferromagnetic fluid heated from below saturating a porous medium, *Journal of Colloid and Interface Science*, **291**, 152-161

Manuscript received January 28, 2014; accepted for print July 7, 2015

INFORMATION FOR AUTHORS

Journal of Theoretical and Applied Mechanics (***JTAM***) is devoted to all aspects of solid mechanics, fluid mechanics, thermodynamics and applied problems of structural mechanics, mechatronics, biomechanics and robotics. Both theoretical and experimental papers as well as survey papers can be proposed.

We accept articles in English only. The text of a *JTAM* paper should not exceed **12 pages of standard format A4** (11-point type size, including abstract, figures, tables and references).

- The material for publication should be sent to the Editorial Office via electronic journal system: http://www.ptmts.org.pl/jtam/index.php/jtam

Papers are accepted for publication after the review process. Blind review model is applied, which means that the reviewers' names are kept confidential to the authors. The final decision on paper acceptance belongs to the Editorial Board.

- After qualifying your paper for publication we will require the following:
  - LaTeX or TeX or Word document file
  - graphical files in grey scale, 300 dpi, in print quality (e.g.: ∗.png, ∗.bmp, ∗.jpg, ∗.eps).

Requirements for paper preparation

Contents of the manuscripts should appear in the following order:

- Title of the paper
- Authors' full name, affiliation and e-mail
- Short abstract (maximum 100 words) and 3-5 key words (1 line)
- Article text (equations should be numbered separately in each section; each reference should be cited in the text by the last name(s) of the author(s) and the publication year)
- References in alphabetical order. See the following:
  1. Achen S.C., 1989, A new boundary integral equation formulation, *Journal of Applied Mechanics*, **56**, 2, 297-303
  2. Boley B.A., Weiner J.H., 1960, *Theory of Thermal Stresses*, Wiley, New York
  3. Canon W., 1955, Vibrations of heated beams, Ph.D. Thesis, Columbia University, New York
  4. Deresiewicz H., 1958, Solution of the equations of thermoelasticity, *Proceedings of Third U.S. National Congress of Applied Mechanics*, 287-305
- Titles of references originally published not in English, should be translated into English and formulated as follows:
  5. Huber M.T., 1904, Specific work of strain as a measure of material effort (in Polish), *Czasopismo Techniczne*, **XXII**, 3, 80-81

All the data should be reported in SI units.

New *JTAM* offer for short communication!

Since July 2013, short research communications have been accepted for publication in *JTAM* with all the requirements concerning standard publications, except for their volume that is limited to 4 pages.
